Challenges in CMB Lensing Data Analysis and Scientific Exploitation of Current and Future CMB Polarization Experiments

Dominic Beck

Université de Paris

STEP'UP ÉCOLE DOCTORALE

Thèse de doctorat de physique (cosmologie) préparée à
l'Université de Paris,
l'Ecole Doctorale STEP'UP (560)
et le
Laboratoire AstroParticule et Cosmologie

Challenges in CMB Lensing Data Analysis and Scientific Exploitation of Current and Future CMB Polarization Experiments

v1007

présentée et soutenue publiquement le
2 octobre 2019

par
Dominic BECK

dirigée par
Dr. Radek STOMPOR

devant un jury composé de

Prof. Anthony CHALLINOR (University of Cambridge) ..... Rapporteur
Dr. Juan-Francisco MACÍAS-PEREZ (LPSC Grenoble) ..... Rapporteur
Dr. Sophie HENROT-VERSILLE (LAL Orsay) ..... Examinateur
Dr. Valeria PETTORINO (CEA Saclay) ..... Examinateur
Prof. Danièle STEER (APC Paris) ..... Examinateur
Dr. Radek STOMPOR (APC Paris) ..... Directeur de thèse
Dr. Josquin ERRARD (APC Paris) ..... Co-encadrant de thèse

Challenges in CMB Lensing Data Analysis and Scientific Exploitation of Current and Future CMB Polarization Experiments

Abstract

Next-generation cosmic microwave background (CMB) measurements will further establish the field of cosmology as a high-precision science and continue opening new frontiers of fundamental physics. Cosmic-variance limited measurements not only of the CMB temperature but also its polarization down to arcminute scales will allow for precise measurements of our cosmological model, which is sensitive to the elusive physics of dark matter, dark energy and neutrinos. Furthermore, a large-scale measurement of B-mode CMB polarization permits a determination of the power of primordial gravitational waves, generated by processes potentially happening in the very early universe at energies close to the scale of the Grand Unified Theory. Entering a new sensitivity regime entails the necessity to improve our physical understanding and analysis methods of astronomical and instrumental systematics.

This thesis presents within this context several analyses of potential astronomical and instrumental systematics, primarily focusing on CMB measurements related to weak gravitational lensing. The latter distorts the path of the primary CMB's photons, such that the statistical properties of the measured signal deviate from the primary signal and, hence, has to be accounted for. This thesis describes the underlying physics, analysis methods and applications to current data sets of the POLARBEAR CMB experiment in the context of CMB lensing science.

In particular, this thesis shows that future high-precision measurements of CMB lensing have to account for the high complexity of this effect, primarily caused by multiple deflections within an evolving, non-linear large-scale structure distribution. Furthermore, the impact of higher-order correlations introduced by galactic foregrounds and CMB lensing when jointly analyzing CMB data sets on both large and small scales is investigated, showing the need for small-scale multi-frequency observations and foreground removal techniques to obtain an unbiased estimate of the tensor-to-scalar ratio.

Keywords:
cosmology, cosmic microwave background, weak gravitational lensing, large-scale structure, data analysis

Défis de l'analyse de données du lentillage gravitationnel et de l'exploitation scientifique des expériences, actuelles et futures, d'observation de la polarisation du fond diffus cosmologique

Résumé

La prochaine génération de mesures du fond diffus cosmologique (CMB) continuera d'établir le domaine de la cosmologie comme une science de haute précision et ne cessera d'ouvrir de nouvelles frontières en physique fondamentale. Les mesures limitées par la variance cosmique de la température du CMB, mais aussi de sa polarisation jusqu'aux minutes d'arc, permettent des mesures précises de notre modèle cosmologique, qui est sensible à la physique insaisissable de la matière noire, de l'énergie noire et des neutrinos. De plus, une mesure aux grandes échelles de la polarisation CMB, dite "mode B", permettra de déterminer la puissance des ondes gravitationnelles primordiales, générées par des phénomènes potentiellement présents dans le tout jeune univers, à des échelles d'énergie qui s'approchent de la théorie de grande unification. L'entrée dans un nouveau régime de sensibilité implique la nécessité d'améliorer notre compréhension de la physique et des méthodes d'analyse des effets systématiques astronomiques et instrumentaux.

Dans ce contexte, cette thèse présente plusieurs analyses des possibles effets systématiques astronomiques et instrumentaux, principalement centrés sur les mesures CMB dans le cadre du lentillage gravitationnelle faible. Cet effet déforme le trajet des photons primaires du CMB, de sorte que les propriétés statistiques du signal mesuré s'écartent du signal primaire, et il faut donc prendre en compte cette distorsion. Cette thèse décrit la physique fondamentale, les méthodes d'analyse et les applications aux ensembles de données actuels de POLARBEAR, une expérience CMB dans le contexte scientifique des lentilles gravitationnelles.

En particulier, cette thèse établit que les futures mesures de haute précision des lentilles gravitationnelles devront prendre en compte la haute complexité de cet effet, principalement causée par des déflexions multiples, induites par une distribution non linéaire des structures à grande échelle en évolution. De plus, l'impact des corrélations d'ordre supérieur, introduites par les avant-plans galactiques et par l'analyse jointe de données aux petites et aux grandes échelles, est étudié. Cette thèse démontre la nécessité d'observations des petites échelles dans plusieurs bandes de fréquences, ainsi que l'utilisation de techniques pour supprimer les avant-plans, afin d'obtenir une estimation sans biais du rapport tenseur-sur-scalaire.

Mots clefs:
cosmologie, fond diffus cosmologique, lentille gravitationnelle faible, structure à grande échelle, analyse des données

Preface

Since its discovery 50 years ago by Arno Penzias and Robert W. Wilson, measurements of the cosmic microwave background (CMB) paved the way towards the high-precision cosmology we experience today. With the help of the CMB, along with new advances in technology and ever increasing data sets, it was possible to pin down the parameters of the standard model of cosmology, ΛCDM, to great precision, showing (almost) no signs of discrepancies. Future CMB experiments will reach sensitivities that will allow to probe for those discrepancies on the sub-percent level, and, maybe more importantly, are envisioned to uncover signatures of some of the most elusive sectors of physics today. In my thesis I will mainly focus on two of those. On one hand there is the prospect of cosmological measurements of neutrino physics, a highly active field in both particle physics and astronomy today, which are complementary to those measurements we can perform in a particle physics laboratory. On the other hand there is the target to understand the physics in the very early state of the Universe and thus at extremely high energies.

These two targets, measuring the primordial as well as the neutrino physics in the CMB, are the context of this thesis. I will provide the broad scientific context of my work in Chapter 1, which I tried to keep brief but also rather self-contained. This will lead to a more focused description of data analysis techniques to extract the CMB lensing signal from CMB datasets in Chapter 2. I made use of some of these techniques and implemented them within a lensing reconstruction software package[1], which capitalizes on modern supercomputer frameworks and was made publicly available.

In Chapter 3 I will discuss data analysis methods to measure another CMB observable besides the CMB lensing signal, which is the primordial B-mode power spectrum. It is clear that a clean measurement of this signal, and a measurement of so-called Inflation theories that comes along with it, will have to take into account signals from our own Galaxy as well as the lensing effect that the large-scale structure (LSS) distribution has on CMB photons, to properly disentangle them from the primordial signal. I will give a higher-level overview of the techniques I implemented and used in this Chapter, upon which following chapters will built.

In Chapter 4 I will tackle this issue from the observational side of cosmology and will introduce the work of the collaborations I am part of and will describe my major contributions to this work within the collaborations. This work lead to collaboration papers that I co-authored that can be found in Refs. [378, 386, 399, 363, 255, 82, 385], papers in preparation in Refs. [380, 381, 82] as well as a conference proceedings, of which I am first author, in Ref. [34].

In the following Chapter 5 I will present my work on the theoretical and phenomenological investigation of the robustness of CMB lensing reconstruction methods to effects induced by nonlinear large-scale structure formation as well as effects that appear when the Born approximation in CMB lensing is dropped. This work was published in Refs. [33, 114]. In Chapter 6 I will focus on the effect of galactic foreground emission, in particular polarized emission, that can bias CMB lensing estimates. I will present results of a paper in preparation [32] on CMB lensing potential power spectrum biases, how this can be mitigated with component separation techniques and how the effect of galactic foregrounds propagate to the measured B-modes, after attempting to remove the lensing effect in this measurement with the help of the CMB measurement itself.

[1] https://github.com/doicbek/lensquest/

Acknowledgments

I'm incredibly grateful for the help of as well as collaboration and discussions with numerous people over the last three years, who helped to influence the work written down in the following pages. First and foremost there are the members of my local group at APC in Paris, including Hamza El Bouhargani, Josquin Errard, Maude Le Jeune, Clément Leloup, Aygul Jamal, Baptiste Jost, Radek Stompor & Clara Vergès, as well as the extended group of Polarbear Europe consisting of Carlo Baccigalupi, Giulio Fabbian, Nicoletta Krachmalnicoff, Julien Peloton, Davide Poletti & Giuseppe Puglisi.

Special thanks and best wishes go to fellow students, colleagues and administration at APC throughout the years: Jean-Christophe Hamilton, Danièle Steer, Ken Ganga, Yannick Giraud-Héraud, Alessandra Tonazzo, Melissa Ridel, François Carré, Georgette Diaby, Monia Mestar, Nelly Nganta, Beatrice Silva, Olga Szydlowska, Joëlle Taïeb, Sabine Tesson, Marc Arène, Philippe Bacon, Ranajoy Banerji, Jean-Baptiste Bayle, Cyrille Doux, Hoang Duc Thuong, Ileyk El Mellah, Jie Hu, Thomas Montandon, Louise Mousset, Calum Murray, Pierros Ntelis, Guillaume Stankowiak, Alessandro Traini, Alexandre Toubiana & Tuan Van Bui.

Many thanks also to my close collaborators of Polarbear and Simons Array who are scattered around the world for the help analyzing the data and hosting me at my visits to Berkeley: Darcy Barron, Shawn Beckman, Federico Bianchini, Julian Borril, Julien Carron, Kolen Cheung, Yuji Chinone, Ari Cukierman, Chang Feng, Neil Goeckner-Wald, John Groh, Charlie Hill, Oliver Jeong, Reijo Keskitalo, Akito Kusaka, Adrian Lee, David Leon, Daisy Mak, Frederick Matsuda, Anh Pham, Ben Westbrook & the whole Polarbear and Simons Array collaboration.

Furthermore I want to thank Vanessa Böhm, Emanuele Castorina, Anthony Challinor, Simone Ferraro, Silvia Galli, Antony Lewis, Luca Pagano, Jan Papež, Emmanuel Schaan, Blake Sherwin, Alexander van Engelen, Flavien Vansyngel & everyone I forgot for help, comments and discussions on (parts of) the manuscript and beyond. A special thanks goes to the selected group of people who endured reading significant parts of this thesis and provided very useful comments: Anthony Challinor, Josquin Errard, Giulio Fabbian, Juan-Francisco Macías-Perez, Davide Poletti & Radek Stompor. If anyone is ever reading this line and thinks he or she should be considered to be included in this exclusive group of readers of this thesis, please contact me (dmncbck@gmail.com) and I will make up for the suffering by paying for a cold drink of his or her choice.

I thank all members of the jury of my PhD defense, Anthony Challinor, Juan-Francisco Macías-Perez, Sophie Henrot-Versillé, Valeria Pettorino & Danièle Steer.

Finally I want to thank all authors of the following publicly available software packages, without which this work would not have been possible in this form: Python, NumPy, SciPy, HEALPix, healpy, Matplotlib, fgbuster, lensingbiases, S^{2}HAT, libsharp, lenS^{2}HAT, flints, LensPix, X^{2}Pure, NaMaster, wignerSymbols, CAMB, CLASS, MontePython, CosmoMC & emcee.

Contents

Listing of figures

1

The Foundation of Modern Cosmology

It was no more than 100 years ago when astronomers discovered that there are other galaxies in the Universe besides the Milky Way, our home [170, 171]. It was at that time when people realized the vastness of our Universe, consisting of an unfathomable number of galaxies, stars and planets. Since then tremendous technical advances like the increasing size of telescopes and the invention of modern technologies such as CCDs made it possible to further study our Universe at its largest scales, in the domain which has become to be called *Cosmology*. Today both experimental and theoretical efforts allowed us to establish a Standard Model of Cosmology called ΛCDM [286]. It is named after the two major components thought to be making up most matter in our Universe, dark energy (Λ) and (cold) dark matter (CDM). Both these components are very unlike the matter we see around us every day, called baryonic or ordinary matter, non-luminous and hardly understood. This means we can not observe them with our conventional methods, with telescopes detecting light with a particular spectrum. As of now, the only way to know both components do exist is through their gravitational interaction with ordinary matter. That dark matter has to make up most matter in galaxies was established by galaxy observations with radio, optical and X-Ray telescopes, in order to match observations with Einstein's theory of Gravity [408, 51, 312]. Evidence from distance Supernovae of type 1a suggests that our Universe is undergoing an accelerated expansion, which can be explained within Einstein's General Relativity with a non-zero cosmological constant, Λ, that can be interpreted as a type of matter that experiences a repellent rather than attractive force under Gravity [272, 310].

Besides that, we know now that this model can describe extremely well the physical processes of our Universe evolving from very early times, when it was merely seconds old and so hot that no atoms or even nucleons could have been formed yet. This hot and dense early stage in our Universe cooled down due to its expansion and through gravitational instabilities, caused by tiny fluctuations in this primordial plasma, lumps of matter have formed that eventually evolved into the large scale structure in our Universe, within which clusters, galaxies, suns, planets and life could have formed. The direct evidence of this early phase in our Universe is the measurement of the light that reaches us today from the time the Universe became transparent. This light constitutes the Cosmic Microwave Background (CMB). Thanks to extensive experimental efforts that produced huge datasets from the CMB, we can determine parameters of the ΛCDM model, a total of six, to sub-percent precision, which establishes this model describing our Universe from tiny early matter fluctuations to the Universe we can see today (up to a significant tension of unknown origin between model-dependent and direct measurements of the expansion rate of the Universe [309]).

This begs the question, where do these fluctuations come from? Extrapolating our expanding Universe back in time we arrive at a singularity, when the physical size of the Universe approaches zero. At times, when the Universe was extremely small, we expect the theory of General Relativity to break down and Quantum Gravity, whatever it is, to take over. In so-called Inflation theories, the fluctuations of a field, the so-called inflaton field that eventually decays into the matter (and energy) as well as the fundamental forces we see today, are believed to be the origin of those fluctuations we see in the CMB today. Currently, there are major experimental endeavors undertaken to provide decisive evidence for Inflation theories, a characteristic feature of which is a rapid exponential expansion in the early Universe. This would make visible, for the first time, physics at ultra-high energies, more than nine orders of magnitude larger than what could so far be reached on earth, at the large hadron collider (LHC) at CERN. And much like the detection of the Higgs particle by the LHC, the detection of the inflaton in the CMB turns out to be extremely challenging due to complex background noise (in the context of CMB referred to as foreground noise). The subject of the following thesis is the challenging path towards a detection of an inflationary early phase in our Universe, taking into account foregrounds and systematics in an ever growing complexity.

While the ultimate goal of this endeavor has not been reached yet, significant progress has been accomplished over the last few years. This thesis describes my contributions to this global effort. In this chapter I will set the scientific context of my work by describing the cosmological and astrophysical concepts lying at the basis of my research. For reference, common notation and natural constants are summarized in Tabs. 1.1 and 1.2. If not stated otherwise, I will use natural units throughout this thesis. Large parts of this chapter's content follow roughly the lecture notes in Refs. [30, 29].

1.1 THE HOMOGENEOUS UNIVERSE

The basis of our cosmological model is General Relativity. Observations of our Universe like the CMB indicate that in our vicinity the Universe tends to become progressively more homogeneous on gradually larger and larger scales. Grounded on the Copernican principle, that us humans are not in a special position within our Universe, we assume our Universe to be statistically homogeneous and isotropic at all times. Later, this homogeneous and isotropic model will be perturbed to describe the tiny fluctuations we observe today at large scales.

1.1.1 THE METRIC

To start, we need to conceptualize the structure of space-time, which will be used in Einstein's field equations. Based on the assumption of spatially homogeneity and isotropy, the most general metric satisfying these symmetries is the Friedman–Lemaître–Robertson–Walker (FLRW) metric given by

$$\begin{aligned} ds^2 &= g_{\mu\nu} dx^\mu dx^\nu = && (1.1)\\ &= -dt^2 + a^2(t) \left[\frac{dr^2}{1-kr^2} + r^2 \left(d\theta^2 + \sin^2\theta d\phi^2 \right) \right] = \\ &= -dt^2 + a^2(t) \left[d\chi^2 + S_k^2(\chi) \left(d\theta^2 + \sin^2\theta d\phi^2 \right) \right], && (1.2) \end{aligned}$$

where

$$\begin{aligned} &S_k(\chi) \equiv \sinh(\chi) \text{ for } k = +1, \\ &S_k(\chi) \equiv \chi \text{ for } k = 0, \\ &S_k(\chi) \equiv \sin(\chi) \text{ for } k = -1. \end{aligned} \quad (1.3)$$

Symbol	Description	Defined in ...
A_s	the normalization of the primordial scalar power spectrum	Eq. 1.189
$a(t)$	scale factor	Eq. 1.2
$a^T_{\ell m}$, $a^E_{\ell m}$ & $a^B_{\ell m}$	CMB spherical harmonic coefficients with well defined parity	Eq. 1.142 and 1.156
$\boldsymbol{\alpha}$	deflection angle two-dimensional vector field	Eq. 1.244
$B_\nu(T)$	Planck black body spectrum	Eq. 1.77
$b^{XYZ}_{\ell_1\ell_2\ell_3}$	reduced harmonic space bispectrum of (polarized) CMB fluctuations X, Y and Z	Eq. 1.164
C^{XY}_ℓ	harmonic space power spectrum of (polarized) CMB fluctuations X and Y	Eq. 1.160
χ	comoving radial coordiante	Eq. 1.2
$\mathbf{D}$	deflection operator	Eq. 2.1
δ_m	fractional total matter density perturbation / total matter density contrast	Eq. 1.231
E	energy	Eq. 1.30
e^-	electron	Tab. 1.3
η	baryon-to-photon ratio	Eq. 1.46
η	conformal time	Eq. 1.6
$f(\mathbf{x}, \mathbf{p}, E, \eta)$	phase space distribution of particles	Eq. 1.116
g_*	total number of relativistic degrees of freedom (in energy)	Eq. 1.37
g^S_*	total number of relativistic degrees of freedom (in entropy)	Eq. 1.38
$g_{\mu\nu}$	space-time metric	Eq. 1.2
Γ	interaction rate	
$\Gamma^\mu_{\alpha\beta}$	Christoffel symbols	Eq. A.3
γ	photon	Tab. 1.3
H	hydrogen	Sec. 1.2.8
$H(t)$	Hubble rate	Eq. 1.4
H_0	Hubble constant	Sec. 1.1.1
h_{ij}	transverse traceless part of the metric tensor perturbation	Eq. 1.100
k	curvature parameter	Eq. 1.3
Λ	cosmological constant	Eq. 1.17
M_ν	total mass of (non-sterile) neutrinos	Sec. 1.2.6
$M_{\rm pl} \equiv \sqrt{\hbar c/G}$	Planck mass	Tab. 1.1
$\mathbf{M}$	magnification matrix	Eq. 1.250
m	rest mass	Tab. 1.3
N_ℓ	harmonic space power spectrum of noise fluctuations	Sec. 3.1
$N_{\rm eff}$	effective number of neutrino species	Eq. 1.63
n	neutron	Tab. 1.3
n_i	number density of particle i	Sec. 1.2
n_s	tilt of the primordial scalar power spectrum	Eq. 1.189
n_t	tensor spectral index	Eq. 1.191
ν	frequency	
ν	neutrino	Tab. 1.3
p	proton	Tab. 1.3
Ω	area element of the unit sphere	Eq. A.5
Ω_Λ	dark energy density today and	Sec. 1.2.10
$\Omega_{\rm cdm}$	energy density of cold dark matter today	Sec. 1.2.7
Ω_b	energy density of baryons today	Sec. 1.2.8
P	pressure	Eq. 1.32
$P_\delta(k, z)$	matter powr spectrum at redshift z	Eq. 1.6.2
$\mathbf{p}$	physical momentum	
Ψ & Φ	scalar metric perturbations	Eq. 1.100
ϕ	lensing potential	Eq. 1.263
$R_{\mu\nu}$	Ricci curvature tensor	Eq. A.1
R	Ricci scalar	Eq. A.2
r	tensor-to-scalar ratio	Eq. 1.193
r, θ, ϕ	spherical coordinates	Eq. A.4
$\mathcal{R}$	comoving curvature perturbation	Eq. 1.186
ρ_i	energy density of particle i	Eq. 1.32
S	entropy	Sec. 1.2
s_i	entropy density of particle i	Eq. 1.32
σ_T	Thomson cross-section	Eq. 1.92
T	temperature (of the thermal bath)	Sec. 1.2
T, Q, U & V	Stokes parameters	Eq. 1.133
$T_{\mu\nu}$	stress-energy tensor	Eq. 1.17
t	proper time	Sec. 1.1.1
τ	optical depth	Eq. 1.206
$\tau_{\rm reio.}$	optical depth to reionization	Eq. 1.6.1
U	free energy	Sec. 1.2
x_μ	coordinate system	Sec. 1.1.1
${}_{\pm s}Y_{\ell m}$	spin-weighted spherical harmonic functions	Sec. 1.3.7
z	cosmological redshift	Eq. 1.12

Table 1.1: Summary of notation conventions used in this thesis.

Symbol	Quantity	Value (SI)	Value (natural units)
c	speed of light	$299\,792\,458\ \mathrm{ms}^{-1}$	1
$\hbar$	reduced Planck constant	$6.582119514 \cdot 10^{22}$ MeV s	1
G	gravitational constant	$6.70861 \cdot 10^{-39} \hbar c (\mathrm{GeV}/c^2)^{-2}$	$1/8\pi$
k_B	Boltzmann constant	$8.6173303 \cdot 10^{-5} \mathrm{eV\ K}^{-1}$	1
G_F	Fermi coupling constant	$1.1663787 \cdot 10^{-5} (\hbar c)^3 \mathrm{GeV}^2$	

Table 1.2: Summary of natural constants used in this thesis. Values are taken from Ref. [365].

This metric represents a space-time with a spatial slicing associated with a changing scale factor, $a(t)$, for each time slice, t. It includes the three cases of a spatially flat Universe ($k = 0$) , as well as spherical ($k = +1$) or hyperbolic ($k = -1$) space. The spatial coordinates χ (the radial coordinate), ϕ (the polar coordinate) and θ (the azimuthal coordinate) are comoving coordinates, defining an inertial frame associated with them, i.e. the comoving coordinates of an object don't change as long as no force is acting. Physical (or proper) distances scale with the scale factor as $d_p(t) = a(t) \cdot d$, given a comoving distance d. It follows that the distance between two objects changes locally as

$$\dot{d_p}(t) = \frac{\dot{a}}{a}(t) d_p(t) \equiv H(t) d_p(t), \tag{1.4}$$

where we defined the Hubble rate, H, which is the relative change of the scale factor with time. This equation, applied to the present time, is called the Hubble's law, with $H_0 \equiv H(t_0)$.

Photon trajectories are null geodesics in space-time, $ds^2 = 0$, and, when only considering radial propagation with $d\phi = d\theta = 0$, satisfy the simple equations

$$\chi(\eta) = \pm\eta + \text{const.}, \tag{1.5}$$

where we introduce the conformal time

$$\eta = \int \frac{dt}{a(t)}. \tag{1.6}$$

Hence, photon geodesics move in 45 degree lines in the η-χ plane like in Minkowski space, the so-called light cone, following directly from the fact that the FLRW-metric is *conformally flat*. These equations allows one to introduce the concepts of particle- and event horizon, as well as cosmological redshift. The maximum distance a photon, emitted from a source at the origin of our spatial coordinate system at time t_i, could have traveled at time t, is given by

$$\chi_p(t) \equiv \eta - \eta_i = \int_{t_i}^{t} \frac{dt'}{a(t')}, \tag{1.7}$$

which is called the comoving *particle horizon*. A common definition is $a(t_i = 0) \equiv 0$, i.e. the beginning of time is a initial singularity. Note that $t_i \neq \eta_i$. The particle horizon expressed as a physical distance on a spatial slice is

$$d_p(t) = a(t)\chi_p(t). \tag{1.8}$$

In an inverse sense, the *event horizon* is defined as the points in space-time, beyond which no light signal sent out at time η could ever reach. Given a final moment of time, $t_{\max}$, which could as well be infinite, one has the event horizon distance

$$\chi_e \equiv \eta_{\max} - \eta = \int_{t}^{t_{\max}} \frac{dt'}{a(t')}. \tag{1.9}$$

1.1.2 REDSHIFT

The measurement of distances of cosmological objects relies on the concept of redshift. The distance of two points in comoving space, e.g. an observer and a distant galaxy, can be defined by the time it takes for a photon emitted at time t_1 at point A, e.g. the distant galaxy, to travel to point B, measured at time t_0, e.g. by the observer. At later times, the same comoving distance is traveled by a photon, emitted at time $t_1 + \Delta t_1$ and measured at time $t_0 + \Delta t_0$, such that

$$\int_{t_1}^{t_0} \frac{dt}{a(t)} = \int_{t_1+\Delta t_1}^{t_0+\Delta t_0} \frac{dt}{a(t)} \longrightarrow \int_{t_1}^{t_1+\Delta t_1} \frac{dt}{a(t)} = \int_{t_0}^{t_0+\Delta t_0} \frac{dt}{a(t)}. \tag{1.10}$$

For small Δt_0 and Δt_1, such that one can approximate $a(t)$ to be constant during these time intervals, one can relate the interval between the emission of two light signals to the interval between the arrivals of the signals as

$$\frac{\Delta t_1}{\Delta t_0} = \frac{a(t_1)}{a(t_0)}. \tag{1.11}$$

One can take those signals as two subsequent crests of a single light wave, such that Δt is the inverse of the frequency of the light wave, both at emission and arrival, such that

$$\frac{\nu_1}{\nu_0} = \frac{a(t_0)}{a(t_1)} \equiv 1 + z. \tag{1.12}$$

In the last step the redshift z was defined as the relative frequency difference of emitted and received light compared to the received one. For an increasing scale factor, $a(t)$, two comoving objects are receding from each other, the redshift is positive and light sent between those objects is shifted to lower frequencies, higher wavelengths.

1.1.3 DISTANCES

Generally it is not straightforward to define and measure distances in curved space-time in a meaningful way. In astronomy there are mainly three different concepts of distance. One way to measure distances between an object at large redshifts and the earth is by using the supposedly known absolute luminosity of those objects. One can define the luminosity distance as

$$d_L \equiv \sqrt{\frac{L}{4\pi S}}, \tag{1.13}$$

where L is the known bolometric[2] luminosity of the source and S is the measured, apparent bolometric flux. It is related to the radial, comoving distance $\Delta\chi$ as [398, 125]

$$d_L = (1 + z) S_k(\Delta\chi). \tag{1.14}$$

More relevant in observational astronomy are the quantities of differential or spectral luminosity, L_ν, and differential or spectral flux, S_ν, per frequency, ν. Then, due to redshifting of the photons between emission and measurement, a so-called k-correction function has to be applied, depending on the spectrum of the emitting object (see e.g. [161])

$$d_L = \sqrt{\frac{(1 + z) L_{\nu(1+z)}}{4\pi S_\nu}}. \tag{1.15}$$

The luminosity distance relates to the angular diameter distance, d_A, defined as the ratio between the physical transverse size of an object and its angle subtended on the sky in radians, as [398]

$$d_A = \frac{d_L}{(1 + z)^2} = \frac{S_k(\Delta\chi)}{1 + z}. \tag{1.16}$$

[2] meaning integrated over all frequencies of the measured light

1.1.4 FRIEDMANN EQUATIONS

Einstein's General Relativity relates the space-time metric to the energy density in the Universe to describe the gravitational force. To characterize the dynamics governing the space-time described by the FLRW-metric, the Einstein's field equations can be explicitly simplified. The field equations with a cosmological constant, Λ, can be written as

$$R_{\mu\nu} - \frac{1}{2}g_{\mu\nu}R + \Lambda g_{\mu\nu} = T_{\mu\nu}, \tag{1.17}$$

where $R_{\mu\nu}$ and R are the Ricci curvature tensor and Ricci scalar, respectively. They include first and second order derivatives of the metric tensor, g (see Eq. A.1).

With the help of velocity 4-vector $u_\mu \equiv dx_\mu/d\tau$ one can write the energy-momentum tensor T of an imperfect fluid as

$$T_{\mu\nu} = \rho u_\mu u_\nu + p\left(g_{\mu\nu} + u_\mu u_\nu\right) + 2q_{(\mu}u_{\nu)} + \Sigma_{\mu\nu}, \tag{1.18}$$

with the matter energy density, ρ, the isotropic pressure, p, the energy-flux vector, q_μ, and the anisotropic stress tensor, $\Sigma_{\mu\nu}$.[3] For a perfect fluid ($q_\mu = \Sigma_{\mu\nu} = 0$), the Einstein field equations as well as the stress-energy-tensor-conservation then simplify to two coupled ordinary differential equations, the so-called *Friedmann Equations* (after A. Friedmann, russian А. Фри́дманм, commonly translated with two "n"s)

$$\left(\frac{\dot{a}}{a}\right)^2 = \frac{1}{3}(\rho + \Lambda) - \frac{k}{a^2} \tag{1.19}$$

$$\frac{\ddot{a}}{a} = -\frac{1}{6}\left(\rho + 3p\right) + \frac{\Lambda}{3}, \tag{1.20}$$

where the total time derivatives with respect to the physical time are denoted with a dot. The stress-energy-conservation explicitly leads to the continuity equation, which is for a flat Universe ($k = 0$) colorlinks by

$$\frac{d\rho}{dt} = -3H(1+w)\rho, \tag{1.21}$$

with $w \equiv p/\rho$. One can follow scaling laws for the energy density

$$\rho \sim a^{-3(1+w)} \tag{1.22}$$

and the scale factor

$$a(t) \sim \begin{cases} t^{2/3(1+w)} & , w \neq -1, \\ e^{Ht} & , w = -1. \end{cases} \tag{1.23}$$

Special cases are Universes dominated by radiation, matter or a cosmological constant, where $w = 1/3$, $w = 0$ or $w = -1$, respectively. It is useful to write the energy density and pressure as a sum of distinct species in the Universe, ρ_i and $p_i = w_i\rho_i$, and define the ratios of the present energy density relative to the critical density, $\rho_c \equiv 3H_0^2$,

$$\Omega_i = \frac{\rho_i(t_0)}{\rho_c}. \tag{1.24}$$

[3] The notation $a_{(\mu}b_{\nu)} \equiv \frac{1}{2}\left(a_\mu b_\nu + a_\nu + b_\mu\right)$ to symmetrize a tensor with respect to the two indices μ and ν was introduced here.

This permits to rewrite equation 1.19 as

$$\left(\frac{H}{H_0}\right)^2 = \sum_i \Omega_i a^{-3(1+w_i)} + \Omega_k a^{-2}, \tag{1.25}$$

with the curvature energy density $\Omega_k \equiv -k/a_0^2 H_0^2$. Defining the scale factor to be unity today, $a(t_0) \equiv 1$, yields

$$\sum_i \Omega_i + \Omega_k = 1, \tag{1.26}$$

motivating the interpretation of Ω_i as the relative energy density content in the Universe per species. The second Friedmann equation 1.20 becomes

$$\frac{1}{a_0 H_0^2}\frac{d^2 a}{dt^2} = -\frac{1}{2}\sum_i \Omega_i (1 + 3w_i), \tag{1.27}$$

relating the acceleration of the expansion to the matter content and respective equations of state. The evolution of the relative energy densities is governed by the Friedmann equations and the physical properties, such as the equation of state or mean kinetic energy, of the specific species. Those will be described in the following section.

1.2 THE MATTER CONTENT IN THE UNIVERSE

A central part of the Hot Big Bang model, i.e. an expanding Universe with a hot and dense early state, is the relative strength of the rate of particle interactions, Γ, and the rate of expansion of the Universe, H. When

$$\Gamma \gg H, \tag{1.28}$$

the interactions between particles is efficient enough to reach thermal equilibrium and may be described by simple laws of thermodynamics. Based on the work of Gamow, Alpher and Herman in the 1940s [126, 13, 12, 14], our Universe experienced such a condition in the early stages, such that elementary particles were in thermal equilibrium in the hot and dense early plasma. As the interaction rate decreased due to cosmic expansion, those particles decoupled from the thermal bath and their number density froze, at a time depending on the specific particle's properties. These particles constitute the content of the Universe we see today. This model is not only the basis for the explanation of Big-Bang nucleosynthesis (BBN), but also predicted a cosmic background radiation of about 5 K twenty years before its observation.

In this section I will review our knowledge of the matter content in the Universe. Naturally, our cosmological model should incorporate our understanding of the Standard Model of particle physics, which is used with exceptional success to describe three of the four fundamental forces in physics, the weak-, the strong- and the electromagnetic interactions. To make the connection with the just derived Friedmann equations, one requires energy densities of the particle species that populate our Universe. As will be described in the following, they depend on the particle's masses and the statistics they follow considering an ensamble of many identical particles. The particle species' statistical ensamble follows either Bose-Einstein statistics, for particles with integer-valued spin, or Fermi-Dirac statistics, for particles with half-integer spin, obeying the Pauli exclusion principle. Regarding Tab. 1.3, bosons such as the Higgs-particle or the force carriers, the photon, gluon, Z- and W-bosons, fall into the former category. Fermions such as all quarks and leptons fall in the latter. The density of states for an ensemble

Quarks	**up** u	**charm** c	**top** t
	$2.2^{+0.5}_{-0.4}$ MeV	$1.275^{+0.025}_{-0.035}$ GeV	$173.0^{+0.4}_{-0.4}$ GeV
	down d	**strange** s	**bottom** b
	$4.7^{+0.5}_{-0.3}$ MeV	95^{+9}_{-3} MeV	$4.18^{+0.04}_{-0.03}$ GeV
Leptons	**electron** e	**muon** μ	**tauon** τ
	0.5110 MeV	105.7 MeV	1777 MeV
	electron neutrino ν_e	**muon neutrino** ν_μ	**tauon neutrino** ν_τ
	< 2 eV	< 0.19 MeV	< 18.2 MeV
Scalar Bosons	**Higgs** H^0		
	$125.18^{+0.16}_{-0.16}$ GeV		
Vector Bosons	**photon** γ	W/Z	**gluon** g
	0	80.4/91.2 GeV	0
Tensor Bosons	**graviton**		
	$< 6 \cdot 10^{-32}$ eV		

Table 1.3: The fundamental particles of the Standard Model, together with the corresponding masses [365]. The masses of photons and gluons are zero.

of identical particles of type i is given by

$$dn_i = \frac{g_i}{(2\pi)^3} \left(\exp\left((E(\mathbf{p}_i) - \mu_i)/T_i\right) \pm 1\right)^{-1} d^3\mathbf{p}_i, \tag{1.29}$$

for fermions ($+$ sign) and bosons ($-$ sign), where g_i is the number of degrees of freedom, μ_i the chemical potential and T_i can be interpreted as the mean temperature of particle i in the Universe. Furthermore, the total energy is given by the energy-momentum relation

$$E\left(\mathbf{p}_i\right)^2 = m_i^2 + \mathbf{p}_i^2. \tag{1.30}$$

In thermodynamics, the chemical potential characterizes the response of a system to a change in particle number. At fixed energy and fixed volume, it is defined as [30]

$$\mu \equiv -T \left(\frac{\partial S}{\partial N}\right)_{U,V}, \tag{1.31}$$

with entropy S, free energy U and number of particles N. In particular, it follows from photon number conversion that $\mu_\gamma = 0$ and that the chemical potential of a particle's X antiparticle is $\mu_{\overline{X}} = -\mu_X$.

Energy density, pressure, number density and entropy density follow as

$$\rho_i = \int dn_i E_i \quad , \quad P_i = \frac{1}{3}\int dn_i \frac{\mathbf{p}_i^2}{E_i} \quad , \quad n_i = \int dn_i \quad \text{and} \quad s_i = \frac{\rho_i + p_i - \mu_i n_i}{T_i}. \tag{1.32}$$

Note that this, given Eq. 1.22, means that in a radiation dominated Universe, $T \sim a^{-1}$ [97].

1.2.1 RADIATION

Radiation or relativistic particles are defined by their mass being much smaller than the temperature

$$m_i \ll T_i \quad \text{and} \quad \mu_i \ll T, \tag{1.33}$$

which allows for a straightforward solution to the integrals in Eq. 1.32. It follows for Bosons (B) that [97]

$$\rho_B = \frac{\pi^2}{30} g_B T_B^4 \quad , \quad p_B = \frac{1}{3}\rho_B \quad , \quad n_B = \frac{\zeta(3)}{\pi^2} g_B T_B^3 \quad \text{and} \quad s_B = \frac{4}{3T_B}\rho_B, \tag{1.34}$$

where $\zeta(3)/\pi^2 \approx 0.1218$. For Fermions the corresponding quantities are slightly different [97]

$$\rho_F = \frac{7}{8}\frac{\pi^2}{30} g_F T_F^4 \quad , \quad p_F = \frac{1}{3}\rho_F \quad , \quad n_F = \frac{3}{4}\frac{\zeta(3)}{\pi^2} g_F T_F^3 \quad \text{and} \quad s_F = \frac{4}{3T_F}\rho_F. \tag{1.35}$$

The total energy density of radiation is then given by

$$\rho_r = \frac{\pi^2}{30}\left(\sum_{i\in\text{bosons}} g_i T^4 + \frac{7}{8}\sum_{i\in\text{fermions}} g_i T^4\right) \equiv g_* \frac{\pi^2}{30} T^4, \tag{1.36}$$

summing over all boson and fermion states with $m_i \ll T$. Hence, g_* counts the total number of relativistic degrees of freedom, where fermionic degrees of freedom enter with a factor $7/8$,

$$g_* = \sum_{i\in\text{bosons}} g_i + \frac{7}{8}\sum_{i\in\text{fermions}} g_i. \tag{1.37}$$

A similar equation can be written for the total entropy density of relativistic particles in the Universe

$$s_r = \frac{2\pi^2}{45} g_*^S T^3. \tag{1.38}$$

The g_* and g_*^S parameters are only equal if all relativistic species are in thermal equilibrium at the same temperature. In our Universe this is the case until $t \sim 1\ s$, when neutrinos decouple from the thermal bath (see below).

1.2.2 NON-RELATIVISTIC MATTER AND FREEZE-OUT

The expansion of the Universe cools down the containing matter, such that particle species can become non-relativistic and their energy density gets suppressed rapidly, as we will see in this section. Drops the interaction rate of the processes keeping them in thermal equilibrium with the primordial plasma below the expansion rate, they furthermore can *freeze out*, i.e. their energy density gets frozen in time. For bosons as well as fermions one finds that in the non-relativistic limit

$$m_i \gg T_i \tag{1.39}$$

for the energy density, pressure, number density and entropy density of particles in thermal equilibrium [97]

$$\rho_i = m_i n_i \tag{1.40}$$

$$p_i = n_i T \tag{1.41}$$

$$n_i = g_i m_i \left(\frac{m_i T}{2\pi}\right)^{\frac{3}{2}} \exp\left(-\frac{m_i - \mu_i}{T}\right) \tag{1.42}$$

$$s_F = \frac{(m_i + T) n_i}{T}. \tag{1.43}$$

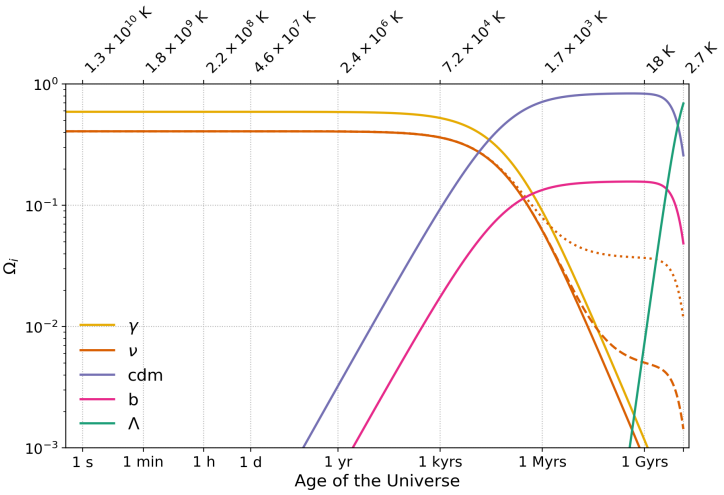

Figure 1.1: The evolution of the energy densities of the different species in our Universe; photons (γ), neutrinos (ν), cold dark matter (cdm), baryons (b) and dark energy (Λ, computed with CAMB using a Planck 2015 cosmology (see Tab. 1.5). The different freeze-out behaviors of neutrinos with $M_\nu = 0$ meV (solid), $M_\nu = 60$ meV (dashed) and $M_\nu = 500$ meV (dotted line) are depicted.

Hence, the abundance of non-relativistic matter in thermal equilibrium is exponentially suppressed by a factor of $\exp(m/T)$ compared to relativistic matter species.

Besides the relative strength of their mean kinetic energy with respect to their mass, one has to factor in another crucial property of a particle species to understand the Universe we see today. In equation 1.28 we established that in order for a particle species to be in thermal equilibrium, the interaction rate of thermalizing processes has to be larger than the expansion rate of the Universe, or, in other words, on average at least one interaction with the primordial plasma has to be occurred during the lifetime of the Universe. When the interaction rate drops below the expansion rate of the Universe

$$\Gamma_\nu(T_d) = H(T_d), \tag{1.44}$$

the particle species freezes out, i.e. it decouples from the thermal bath it was in equilibrium with before. T_d is the so-called decoupling or freeze-out temperature, characteristic for each particle species. The number density of the "frozen-out" species is then called the relic density, which is not further suppressed by a factor $\exp(m/T)$ for the case of non-relativistic particles at freeze-out.

In our model of a hot and dense early Universe relativistic matter is dominating initially. As the Universe expands and cools down, massive particles become non-relativistic, whose energy density would be exponentially suppressed. However, those matter species freeze out, i.e. they decouple from the thermal bath, and are able to form bound states. This enables us to build a theory of the thermal history of the Universe, explaining what we observe today and the effect the various matter species had on the primordial plasma depending on a characteristic energy scale of their associated interactions. In Fig. 1.1 the evolution of the relative energy densities of Eq. 1.24 are shown for the five main particle species we see today and will be introduced in the following sections.

1.2.3 ELECTROWEAK PHASE TRANSITION

At around 100 GeV the force carriers of the weak interaction, the $W^\pm$- and Z-bosons, receive their masses after symmetry breaking through the Higgs mechanism. This is also the maximum energy-scale at which our Standard Model can make predictions.

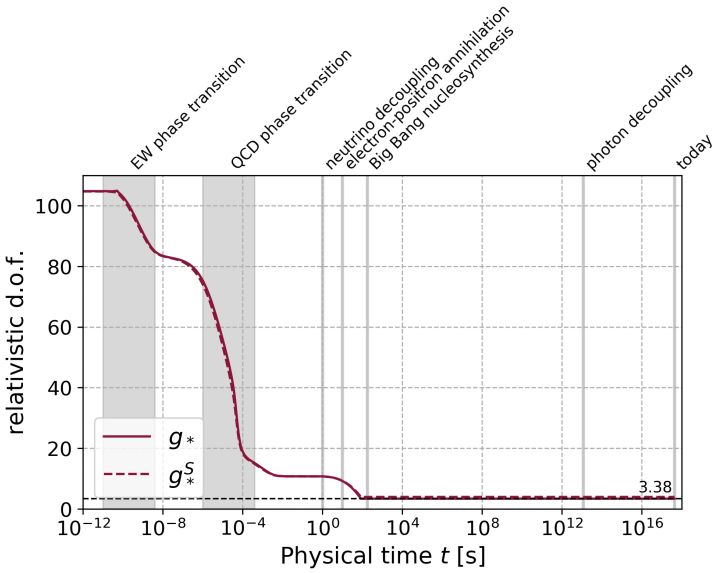

Figure 1.2: The total number of relativistic degrees of freedom, g_* and g_*^S, evolving over the history of the Universe, using the cubic-splined data from lattice QCD computations of Ref. [50]. The rough times of the electroweak (EW) and QCD phase transitions, the time of neutrino decoupling (see Sec. 1.2.6), electron-positron freeze-out, Big Bang nucleosynthesis and photon decoupling (see Sec. 1.2.9) are shown in grey lines.

1.2.4 QCD PHASE TRANSITION

Quarks are asymptotically free at high energies. At the QCD scale of around 150 MeV, the strong interaction between quarks and gluons become important and they can form bound states, so-called mesons, out of a quark and anti-quarks, and so-called hadrons, out of three quarks, such as neutrons and protons.

One can obtain the evolution of the relativistic degrees of freedom, g_*, over time as shown in Fig. 1.2 by using the particles of the Standard Model in Tab. 1.3 and

$$g_* = \sum_{i \in \text{bosons}} g_i \left(\frac{T_i}{T}\right)^4 + \frac{7}{8} \sum_{i \in \text{fermions}} g_i \left(\frac{T_i}{T}\right)^4 , \tag{1.45}$$

where T_i are the specific particle species' freeze-out temperatures. The QCD energy scale, where quarks transform into hadrons, is assumed to be 150 MeV and we require all particles to be in thermal equilibrium initially. At energies above 200 GeV all particles of the Standard Model are relativistic. For bosons, there are in total $g_b = 28$ degrees of freedom, 2 for the two helicity-states of the photon, 3 for each spin-state of the $W^\pm$ and Z-bosons, 2 helicity-states for the 8 types of gluons, as well as 1 for the Higgs particle. Each quark contributes $2 \times 2 \times 3 = 12$ degrees of freedom, coming from its particle and anti-particle, the spin-state and its color charge. The three charged leptons can have 2 different charges and 2 spin-states each. Each flavor of neutrinos also contributes with 2 spin states (assuming them to be Majorana fermions, see below). In total, that makes $g_* = 106.75$ at energies above 200 GeV. Starting at a time of $\sim 10^{-11}$ s, the top quark and anti-quark are the first particles to become non-relativistic and annihilate, followed by the Higgs, $W^\pm$ and Z-bosons. Before all quarks are able to freeze-out or annihilate, at around $T \sim 150$ MeV or $\sim 10^{-5}$ s, the QCD phase transition takes place and quarks form hadrons and mesons. All but the lightest mesons, pions ($m_{\pi^0} = 135.0$ MeV, $m_{\pi^\pm} = 139.6$ MeV [365]), are non-relativistic below the QCD phase transition temperature. The lightest charged leptons, electrons and positrons, are the last to become non-relativistic at $T \sim 0.511$ MeV. The fact that the transition between relativistic to non-relativistic behavior is not instantaneous is not accounted for here. A more precise calculation would rely on high-temperature lattice quantum chromodynamics computations, as can be found in e.g. Ref. [50].

1.2.5 BARYOGENESIS

Today we clearly observe an overabundance of matter over anti-matter, hence not all matter annihilated after freeze-out. Processes of baryogenesis must have been in place in the early Universe which could explain this asymmetry [81]. Baryons, in the cosmological context, mostly refer to protons and neutrons. A characteristic number is the baryon-to-photon ratio

$$\eta = \frac{n_b - n_{\bar{b}}}{n_\gamma}, \tag{1.46}$$

where $n_{\bar{b}}$ is the number density of antibaryons. Today, baryonic matter, meaning protons, neutrons and electrons, cold dark matter, neutrinos and photons constitute the main components that we can, at least indirectly, observe. Furthermore, we deduce from cosmological observations that a fifth component, so-called dark energy has to exist to fit our General Relativity-based models. In the following I will describe those components. The evolution of their energy densities is shown in Fig. 1.1.

1.2.6 Ω_ν: NEUTRINOS

The neutrino was first proposed in 1930 by Wolfgang Pauli as an explanation of the radioactive β-decay's continuous energy spectrum [55]. Precision measurements of the Z-decay at lepton colliders allow for a determination of the number of neutrino flavors that are coupling to observed Standard Model particles. Data from the Large Electron–Positron Collider (LEP) at CERN and the SLAC Linear Collider (SLC) lead to a number of light, non-sterile neutrino species of $N_\nu = 2.9840 \pm 0.0082$, about two standard deviations smaller than three and in agreement with the three observed generations of leptons [370].

PARTICLE NATURE

Neutrinos (ν_l) and antineutrinos ($\bar{\nu}_l$) are important building blocks of the Standard Model of particle physics, coupled via the charged- and neutral-current interactions to the hadronic sector of the Standard Model. They are byproducts of the radioactive β decay, where they couple to the $W^\pm$ bosons and a lepton in the decay of a neutron into a proton, or vice-versa [365]. They are neutral, spin-$\frac{1}{2}$ particles, coming in flavors as counterparts of the electron, muon and tauon ($l = e, \mu, \tau$) and ensure the conservation of the weak isospin within weak interaction decays [365]. In this respect, the three flavors of neutrinos, ν_e, ν_μ and ν_τ, are defined by their products in charged-current weak interactions, which can either a electron, muon or tauon.Experimental evidence favors a left-handed neutrino model in the relativistic regime, meaning they appear only to have a helicity $h = -1/2$ (their spin and momentum vector are anti-parallel) [402]. Alternatively, right-handed relativistic neutrinos could still exist, but do not couple through any interaction to Standard Model particles, so-called "sterile" or "inert" neutrinos. They can be a key element in possible extensions of the Standard model to include neutrino mass creation mechanisms and to explain the disparity in mass scales between neutrinos and other fermions of the Standard Model [8, 365]. Since neutrinos are neutral, there are two options for its representation [273, 365]. Generally it can be represented as a spinor with four degrees of freedom, a so-called Dirac spinor, as it can be done for all fermions. The neutrality of the neutrino would also allow the case of a spinor with two degrees of freedom, a Majorana spinor, in which case the neutrino and antineutrino are identical. In the latter case the lepton number is not a conserved quantity.

NEUTRINO MASS

Measurements of a non-zero neutrino masses are hints for physics beyond the Standard Model of particle physics or even a new fundamental theory of which the Standard Model is only a low-energy effective field theory [365].

The most compelling evidence that neutrinos must be massive are the experimental observations of neutrino oscillations with solar, atmospheric, reactor and accelerator neutrinos. Neutrino oscillations are in-flight transitions between differently flavoured neutrinos. Formally this means that the probability to measure a neutrino with a flavor β, which was produced with a flavour α at an energy E and a distance L, is

$$P(\nu_\alpha \to \nu_\beta, E, L) \neq \delta_{\alpha\beta}. \tag{1.47}$$

Current data favors the mixing between three flavours of neutrinos [365], ν_e, ν_μ and ν_τ, but there is the possibility of more neutrino species, for example heavy sterile neutrinos, to appear in neutrino oscillations. Neutrino oscillations appear when the flavour eigenstates of neutrinos ($|\nu_e\rangle$, $|\nu_\mu\rangle$ and $|\nu_\tau\rangle$) do not coincide with the mass eigenstates of neutrinos, i.e. with the neutrino states which have a defined, observable mass ($|\nu_1\rangle$, $|\nu_2\rangle$ and $|\nu_3\rangle$). The mixture between the two states is described by a unitary 3×3 matrix, the so-called Pontecorvo-Maki-Nakagawa-Sakata (PMNS) mixing-matrix [299], U_{li},

$$|\nu_l\rangle = \sum_{i=1}^{3} U_{li}|\nu_i\rangle \quad , (l = e, \mu, \tau). \tag{1.48}$$

Usually, this matrix is described by three angles (θ_{12}, θ_{23}, θ_{13}) and one (δ) or three phases (δ, α_1 and α_2), depending on whether neutrinos are Dirac or Majorana particles, respectively, given by [365]

$$U = \begin{pmatrix} c_{12}c_{13} & s_{12}c_{13} & s_{13}e^{-i\delta} \\ -s_{12}c_{23} - c_{12}s_{23}s_{13}e^{i\delta} & c_{12}c_{23} - s_{12}s_{23}s_{13}e^{i\delta} & s_{23}c_{13} \\ s_{12}s_{23} - c_{12}c_{23}s_{13}e^{i\delta} & -c_{12}s_{23} - s_{12}c_{23}s_{13}e^{i\delta} & c_{23}c_{13} \end{pmatrix} \begin{pmatrix} 1 & 0 & 0 \\ 0 & e^{i\alpha_1/2} & 0 \\ 0 & 0 & e^{i\alpha_2/2} \end{pmatrix},$$

where $s_{ij} = \sin(\theta_{ij})$ and $c_{ij} = \cos(\theta_{ij})$. One can express the time-dependence of the neutrino mass eigenstates with

$$|\nu_i(t)\rangle = e^{-iE_i t}|\nu_i(t=0)\rangle, \tag{1.49}$$

given the fact that they are eigenstates of the Hamiltonian $\mathcal{H}$, i.e.

$$\mathcal{H}|\nu_i(t)\rangle = E_i|\nu_i(t)\rangle, \tag{1.50}$$

with energy eigenvalues $E_i = \sqrt{m_i^2 + \mathbf{p}_i^2}$. This allows us to write down the neutrino oscillation probability as

$$P(\nu_\alpha \to \nu_\beta, E, L) = \sum_{ij} U^*_{\alpha i} U_{\beta i} U_{\alpha j} U^*_{\beta j} \exp\left(-i\frac{\Delta m^2_{ij} L}{2E}\right), \tag{1.51}$$

where $\Delta m^2_{ij} \equiv m_i^2 - m_j^2$ was defined. In the last equation the approximation for ultrarelativistic neutrinos was used

$$E_i \approx E + \frac{m_i^2}{2E}. \tag{1.52}$$

One cane see immediately that a non-zero neutrino mass introduces neutrino oscillations depending on the energy E and distance L. This principle allows for the measurement of the difference of squared neutrino masses. In the case of three neutrinos, there are two independent neutrino mass

Parameter	Best-fit	2σ range
Δm^2_{21} / $10^{-5}\, eV^2$	7.37	$7.07 - 7.73$
$\lvert\Delta m^2_{31(32)}\rvert$ / $10^{-3}\, eV^2$	2.56 (2.54)	$2.49 - 2.64\,(2.47 - 2.62)$
$\sin^2\theta_{12}$ / 10^{-1}	2.97	$2.65 - 3.34$
$\sin^2\theta_{13}$ / 10^{-2}	2.15 (2.16)	$1.99 - 2.31\,(1.98 - 2.33)$
$\sin^2\theta_{23}$ / 10^{-1}	4.25 (5.89)	$3.95 - 4.70\,(3.99 - 6.21)$
δ / π	1.38 (1.31)	$1.00 - 1.90\,(0.92 - 1.88)$

Table 1.4: The best-fit values and 2σ ranges of neutrino oscillation parameters from [59]. The values correspond to the normal ordering scheme, while the values in brackets indicate the inverted ordering scheme.

squared differences, e.g. $\Delta m^2_{21} \neq 0$ and $\Delta m^2_{31} \neq 0$. The numbering of massive neutrinos, ν_i, is arbitrary. Usually it is convenient to define the ordering of massive neutrinos in such a way that Δm^2_{21} is smaller than Δm^2_{31} and that $\Delta m^2_{21} > 0$ [365]. The mass squared difference Δm^2_{21} is measured by *solar* ν_e oscillations as well as reactor $\overline{\nu}_e$ oscillations. The mass square differences $|\Delta m^2_{31}|$ and $|\Delta m^2_{32}|$ can be associated with the oscillations of *atmospheric* and reactor ν_μ and $\overline{\nu}_\mu$, as well as reactor $\overline{\nu}_e$ at $L \sim 1\ km$ [365]. Since we have only access to the absolute values of the squared mass differences, there remains an ambiguity in the ordering, i.e. either m_3 is the heaviest of the three neutrino mass eigenstates at hand, $m_1 < m_2 < m_3$, or ν_3 is the lightest neutrino mass eigenstate, $m_3 < m_1 < m_2$. This ordering is an open question in neutrino physics, called the neutrino ordering or mass hierarchy, distinguishing between the former, normal ordering (NO), and the latter, inverted ordering (IO). Furthermore, in principle there is a third option, called quasi-degenerate (QD), where $m_1 \approx m_2 \approx m_3$ [365]. However, given the measurement of mass differences through neutrino oscillations, the latter is discouraged. We can set lower bounds to the absolute values of the neutrino mass from neutrino oscillation experiments by zeroing the lightest neutrino mass. Then, given the ordering, we have

$$(m_1, m_2, m_3) \leq \begin{cases} \left(0, \sqrt{\Delta m^2_{21}}, \sqrt{|\Delta m^2_{31}|}\right), & \text{(NO)} \\ \left(\sqrt{|\Delta m^2_{32}| - \Delta m^2_{21}}, \sqrt{|\Delta m^2_{32}|}, 0\right), & \text{(IO)} \\ \left(\sqrt{|\Delta m^2_{31}|}, \sqrt{|\Delta m^2_{31}|}, \sqrt{|\Delta m^2_{31}|}\right), & \text{(QD).} \end{cases} \tag{1.53}$$

Experiments have measured the mixing angles, θ_{ij}, the Dirac phase, δ, as well as the mass splittings Δm^2_{21} (the "solar neutrino" mass splitting) and $|\Delta m^2_{31}|$ (the "atmospheric neutrino" mass splitting). The best-fit values of neutrino oscillation observables, derived from a global fit of neutrino oscillation data, can be found in Tab. 1.4 and is taken from Ref. [59]. They find a preference for normal ordering scheme in their χ^2-fit, $\Delta\chi^2_{\text{IO-NO}} = 3.6$. Lower bounds for the neutrino masses follow as

$$(m_1, m_2, m_3) \leq \begin{cases} (0, 8.6, 50.6)\ \text{meV}, & \text{(NO)} \\ (49.7, 50.6, 0)\ \text{meV}, & \text{(IO).} \end{cases} \tag{1.54}$$

On the other hand, to set upper bounds on neutrino masses, we have to resort to other measurements. In particular, three main observables can probe the absolute neutrino mass spectrum [365]

- the effective neutrino mass in the β-decays, $m_\beta = \sqrt{\sum_i |U_{ei}|^2 m_i^2}$,
- the effective mass in neutrino-less double β-decays, if neutrinos are Majorana fermions, $m_{\beta\beta} = \left|\sum_i |U_{ei}|^2 m_i e^{i\phi_i}\right|$, called the effective Majorana neutrino mass,
- the total neutrino mass $M_\nu \equiv \sum_i m_i$ in cosmology.

The best limits from neutrino-less double β-decays comes from KamLAND-Zen [127]

$$\langle m_{\beta\beta} \rangle < 61 - 165 \text{ meV}. \tag{1.55}$$

Future projects will improve the current sensitivities down to values of the order $\langle m_{\beta\beta} \rangle \sim 10 - 50$ meV [105]. Direct upper-limit constraints on the electron (anti-)neutrino mass come from the Troitsk experiment [20]

$$m_{\bar{\nu}_e} < 2.05 \text{ eV}. \tag{1.56}$$

In the future, experiments like the KATRIN experiment[4] are aiming at reducing that limit to 30 meV [262]. Making use of the lower limits of Eq. 1.54, we find lower bounds of the total neutrino mass, M_ν, to be 59 meV for (NO) and 100 meV for (IO). The tightest constraints on the total mass of neutrinos from cosmology comes from Planck and baryon acoustic oscillations, setting an upper limit of 0.12 eV [286].

As a possible entry point to physics beyond the Standard Model, Neutrino physics is a very active area of research, in which many open questions set the goals for future experimental and phenomenological efforts. Open questions include [365]

- determining if neutrinos are Dirac or Majorana particles, e.g. if they violate lepton number conservation or not,
- determining the neutrino mass spectrum and ordering,
- determining the status of CP-symmetry violation,
- improving on the neutrino oscillation experiments and hence the lower bounds on the neutrino masses,
- and measuring the absolute neutrino mass scale and fixing neutrino mass upper-levels.

Here, cosmology can play an essential part in determining the total mass of neutrinos, with the caveat if e.g., the neutrino masses are generated dynamically at certain relatively late epoch in the evolution of the Universe.

THERMODYNAMICS

Neutrinos are produced in frequent weak interactions in the early Universe at large temperatures, which became possible after electroweak symmetry breaking, when the temperature was below $T \sim 100$ GeV, the mass of the force mediating $W^\pm$- and Z-bosons. After some time, they drop out of equilibrium when their interaction rate, $\Gamma_\nu = \langle n_\nu \sigma_\nu \rangle$, drops below the expansion rate, H. The effective cross section of processes mediated by the weak force is determined by Fermi's constant, G_F, given by $G_F \sim 1.17 \cdot 10^{-5}$ GeV^{-2} [365]. It follows that [210]

$$\frac{\Gamma_\nu}{H} = G_F^2 M_{\text{pl}} T^3, \tag{1.57}$$

which reaches unity when $T \sim 1$ MeV. This is the temperature at which particles that interact with the primordial plasma only through the electroweak force freeze out. Taking into account all possible interactions between the thermal bath and neutrinos, one gets an electron neutrino decoupling temperature of $T_{\nu_e} = 1.34$ MeV and a different muon and tauon neutrino decoupling temperature of

[4] https://www.katrin.kit.edu

$T_{\nu_\mu,\nu_\tau} = 1.5$ MeV [98]. Since they are close to massless, the neutrino temperature scales as $T \sim a^{-1}$. After the temperature drops below $T_e = 0.511$ MeV, electron-positron annihilation

$$e^+ + e^- \to \gamma + \gamma \tag{1.58}$$

becomes effective. The resulting energy and entropy transfers from electrons to photons cause the photon temperature to decrease not as much as the neutrino temperature, since neutrinos are already decoupled from thermal equilibrium. For particles in equilibrium their entropy is conserved. In an adiabatic Universe, i.e. assuming the entropy of the Universe is dominated by the photon bath, the total entropy stays constant. Eq. 1.38 implies that

$$g_*^S T^3 a^3 = \text{const.}\,. \tag{1.59}$$

For the photon thermal bath, we have

$$g_*^S = 2 + \frac{7}{8} 2 \cdot 2 = \frac{11}{2} \tag{1.60}$$

degrees of freedom before electron-positron decoupling at temperatures greater than $m_e = 0.511$ MeV, while after that, only photons remain in thermal equilibrium and

$$g_*^S = 2. \tag{1.61}$$

Then it follows from entropy conservation that the photon temperature gets increased by a factor $\left(\frac{11/2}{2}\right)^{1/3}$, while the neutrino temperature is decoupled from this process. Hence, for temperatures below m_e, one has a neutrino temperature

$$T_\nu = \left(\frac{4}{11}\right)^{1/3} T_\gamma \tag{1.62}$$

as well as the number of relativistic degrees of freedom given by

$$g_* = 2 + \frac{7}{8} \cdot 2 \cdot N_{\text{eff}} \left(\frac{4}{11}\right)^{4/3}, \tag{1.63}$$

where we defined N_{eff} as the effective number of neutrino species in the Universe. If the neutrino decoupling was instantaneous we would have $N_{\text{eff}} = 3$, assuming three flavors of neutrinos. Since neutrinos are still slightly coupled to the photon bath at electron-positron annihilation, non-thermal distortions in the neutrino spectra arise and the photon temperature decreases slightly slower than expected. This leads to a modified effective number of neutrino species. By solving the momentum-dependent kinetic equations for the neutrino spectra one obtains [228]

$$N_{\text{eff}} = 3.046. \tag{1.64}$$

A value of N_{eff} which exceeds this Standard Model predictions could be a hint of new physics beyond the Standard Model (BSM). Additional particles contributing to N_{eff} are referred to as dark radiation and could be explained by

- axions [31], light undetected particles postulated to arise from the spontaneously broken Peccei-Quinn symmetry attempting to explain CP conservation in QCD [365],
- sterile neutrinos [1], neutrino families not interacting with the Standard Model (except gravitation) or
- dark photons [4], the counterpart of photons in the dark sector, coupling to dark matter.

COSMIC NEUTRINO BACKGROUND

Following the previous chapter, there is a sea of decoupled, relic neutrinos at a temperature today of

$$T_\nu = \left(\frac{4}{11}\right)^{1/3} T_\gamma \approx 1.95\ K \tag{1.65}$$

with a corresponding present number density

$$n_\nu = \frac{3}{2}\frac{\xi(3)}{\pi^2} T_\nu^3 \approx 113 \text{ neutrinos and antineutrinos of each flavour per ccm} \tag{1.66}$$

called cosmic neutrino background (CνB). At least two of the three neutrino mass eigenstates we have seen above are non-relativistic today, which can be inferred from current constraints from neutrino oscillations. Given an absolute mass-scale of neutrinos of around 1 eV and current neutrino temperature at $T_\nu = 1.95\ K \approx 0.168$ meV, i.e. assuming all neutrino mass eigenstates to be entirely non-relativistic, one can find

$$\Omega_\nu = \frac{\rho_\nu}{\rho_c} = \frac{M_\nu n_\nu}{\rho_c} = \frac{4\xi(3) T_\nu^3 M_\nu}{\pi H_0^2} = \frac{M_\nu}{93.14\,\text{eV}}\frac{1}{h^2}, \tag{1.67}$$

while, in the case of massless neutrinos, one would have

$$\Omega_\nu = 1.7 \cdot 10^{-5}\frac{1}{h^2}\,, \quad (M_\nu = 0). \tag{1.68}$$

To be precise, the relation between Ω_ν and M_ν has to be computed numerically, for example as in Ref. [228]. Since neutrinos do have a small but non-zero mass, they behave as radiation-like particles in the early Universe, where they fix the expansion rate during the era of radiation domination, and as matter-like particles in the late Universe, where they influence the clustering of large-scale structure.

1.2.7 Ω_{CDM}: (COLD) DARK MATTER

The discovery of dark matter is attributed to the Swiss astronomer Fritz Zwicky, who observed in 1933 the redshift of extragalactic nebulae, concluding that the cluster density must be much higher than expected from luminous matter alone [408]. Dark matter has been, until now, only observed indirectly by its gravitational influence on luminous matter. The discrepancy between predictions from primordial nucleosynthesis and the measured total matter density in the Universe hints at the non-baryonic nature of dark matter. Moreover, astronomical observations show that baryonic Massive Compact Halo Objects (MACHOs) do not substantially contribute to the mass of our Galaxy [28]. Dark matter is conveniently classified into three families; hot, warm and cold-dark matter (HDM, WDM and CDM), depending on their particle mean velocities. For a HDM dominated Universe superclusters would form first and later fragment into galaxies, in contradiction with observations [124]. This also excludes (non-sterile) neutrinos to be the dark matter as examples of hot dark matter [28]. Candidates for CDM are so-called WIMPs (weakly interacting massive particles), which are highly sought after in direct particle detectors like the EDELWEISS[5] [19], DAMIC[6] [7] or XENON[7] [17] experiments, seeking missing momenta in decay processes with bolometric detectors, CCDs or large time projection chambers, respectively. Another candidate for CDM could be axions, which were created non-thermally in the early Universe [28]. Another interesting avenue is the exploration of dark matter through gravitational waves. Although already highly constrained in mass range, primordial black

[5] https://edelweiss.in2p3.fr
[6] https://damic.uchicago.edu
[7] https://www.xenon1t.org

holes could at least make up parts of dark matter in our Universe and could be detected with gravitational wave detectors [63, 26].

Dark matter plays an important role in the history of large-scale structure formation from an initial Gaussian density field. The halos of dark matter are fundamental units of large-scale structure, in which galaxies are able to form. Small structures are the first to decouple from cosmic expansion and are subdued by gravitational instability (they become nonlinear). Larger structures eventually form through mergers of existing halos [124]. Properties such as the Halo mass function and density profile are studied with the help of N-body simulations. An issue in measuring the dark matter distribution in our Universe with galaxy surveys is the problem of relating the galaxy density to the total, dark matter dominated, matter density, since galaxies are positioned only at special positions at the center of dark matter halos. This mismatch is referred to as bias. More details on the bias problem when measuring galaxy correlation functions will follow in Sec. 1.6.2.

1.2.8 Ω_B: BARYONS

Within the first three minutes of our Big-Bang early Universe, the first elements were formed, including hydrogen as well as heavier elements such as deuterium, D, Helium-3, ^{3}He, Helium-4, ^{4}He, and Lithium, ^{7}Li. The underlying model, based on well-established Standard Model physics, the so-called Big Bang Nucleosynthesis, is nowadays well tested and was able to make accurate predictions on the abundances of light elements. Their synthesis starts in the radiation-dominated era at about $T = 1$ MeV, where weak interactions were in thermal equilibrium and the ratio of neutron and proton densities was given by

$$\frac{n_n}{n_p} = \exp\left(-Q/T\right), \tag{1.69}$$

where $Q \equiv m_n - m_p = 1.293$ MeV [365] is the neutron-proton mass difference. Hence, at high temperatures above 1 MeV, this ratio was close to unity, while at smaller temperatures neutrons become less abundant than protons. Hence, neutrons follow the equilibrium abundance

$$X_n(T) = \frac{\exp\left(-Q/T\right)}{1 + \exp\left(-Q/T\right)}, \tag{1.70}$$

where $X_n \equiv n_n/\left(n_p + n_n\right)$, until neutrinos decouple at about $T_\nu \approx 1$ MeV. Then one gets as a rough estimate of the freeze-out abundance [29]

$$X_{nf} \approx X_n(T_\nu) \approx \frac{1}{6}. \tag{1.71}$$

The neutron abundance today, however, is much lower than that. This is because at temperatures below 0.2 MeV the neutron decay into a proton becomes important. Hence the neutron fraction is decreasing further as

$$X_n(t) = \frac{1}{6}\exp\left(t/\tau_n\right), \tag{1.72}$$

with the neutron half-time of $\tau_n = 880.2 \pm 1.0\ s$ [365]. The most relevant chemical reactions for BBN are the neutron decay and the production of deuterium, ^{2}H or D, which unleashes the chain of reactions up to heavier elements such as Boron, Carbon, and Nitride [347, 173]. Some of the most important processes are listed in Eq. 1.73.

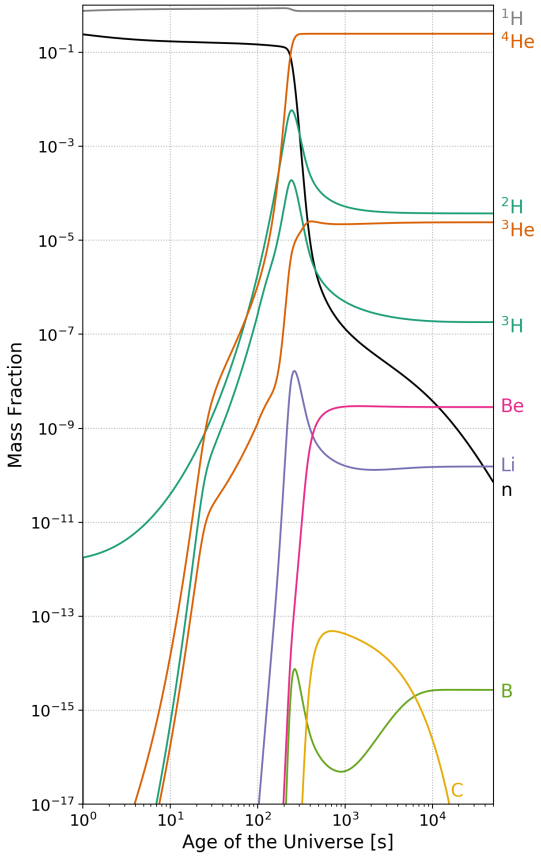

Figure 1.3: The mass fraction evolution during Big Bang nucleosynthesis, including isotopes of the first six elements in the periodic system, hydrogen, H, helium, He, lithium, Li, Beryllium, Be, Boron, B, and Carbon, C, using numerical precision calculations, produced with the PRIMAT code [275].

$$
\begin{aligned}
n &\rightleftharpoons p^+ + e^- + \overline{\nu}_e \\
n + p^+ &\rightleftharpoons {}^2\mathrm{H} + \gamma \\
p^+ + {}^2\mathrm{H} &\rightleftharpoons {}^3\mathrm{He} + \gamma \\
{}^2\mathrm{H} + {}^2\mathrm{H} &\rightleftharpoons {}^3\mathrm{He} + n \\
{}^2\mathrm{H} + {}^2\mathrm{H} &\rightleftharpoons {}^3\mathrm{H} + p^+ \\
{}^3\mathrm{He} + n &\rightleftharpoons {}^3\mathrm{H} + p^+ \\
{}^2\mathrm{H} + {}^3\mathrm{H} &\rightleftharpoons {}^4\mathrm{He} + n \\
{}^2\mathrm{H} + {}^3\mathrm{He} &\rightleftharpoons {}^4\mathrm{He} + p^+ \\
{}^3\mathrm{He} + {}^4\mathrm{He} &\rightleftharpoons {}^7\mathrm{Be} + \gamma \\
{}^3\mathrm{H} + {}^4\mathrm{He} &\rightleftharpoons {}^7\mathrm{Li} + \gamma \\
{}^7\mathrm{Be} + n &\rightleftharpoons {}^7\mathrm{Li} + p^+ \\
{}^7\mathrm{Li} + p^+ &\rightleftharpoons {}^4\mathrm{He} + {}^4\mathrm{He} \\
{}^4\mathrm{He} + {}^2\mathrm{H} &\rightleftharpoons {}^6\mathrm{Li} + \gamma \\
{}^6\mathrm{Li} + p^+ &\rightleftharpoons {}^3\mathrm{He} + {}^4\mathrm{He} \\
{}^7\mathrm{Be} + n &\rightleftharpoons {}^4\mathrm{He} + {}^4\mathrm{He} \\
{}^7\mathrm{Be} + {}^2\mathrm{H} &\rightleftharpoons p^+ + {}^4\mathrm{He} + {}^4\mathrm{He} \qquad (1.73) \\
&\vdots
\end{aligned}
$$

With simple arguments one obtains an estimate of the ^{4}He abundance, a main prediction of BBN. Following for example [97] or [29] one can find for the helium mass fraction

$$Y_p \equiv \frac{4n_{\mathrm{He}}}{n_{\mathrm{H}}} = 0.25. \qquad (1.74)$$

However, to obtain a more precise prediction of this mass fraction, in line with the 1% constraints from observations, as well as the abundance of all light elements produced during BBN, one has to solve a large set of coupled kinetic equations. This is done in numerical codes such as PRIMAT [8] [275], which is used to obtain the mass fractions of hydrogen, helium, lithium, beryllium, boron and carbon in the early Universe.

[8] PRImordial MATter, https://www2.iap.fr/users/pitrou/primat.htm

1.2.9 Ω_γ: PHOTONS

At temperatures above about 1 eV, the Universe consisted of a plasma of free electrons, protons, neutrons and photons. The photon gas was tightly coupled to electrons mainly via so-called double or radiative Compton scattering

$$e^- + \gamma \leftrightarrow e^- + \gamma + \gamma. \tag{1.75}$$

This process is efficient enough to thermalize the photon bath above a redshift of [89]

$$z = 2.0 \times 10^6 \left(1 - \frac{Y_p}{2}\right)^{-2/5} \left(\frac{\Omega_b h^2}{0.02}\right)^{-2/5}. \tag{1.76}$$

The spectrum of the phtotn bath is given by a black body spectrum

$$I_\nu = B_\nu(T) \equiv \frac{2h\nu^3}{e^{h\nu/k_B T} - 1}. \tag{1.77}$$

Below this redshift, which corresponds to a timescale of a few months, the photon bath becomes vulnerable to spectral distortions, caused by processes that drive matter and radiation out of equilibrium depending. These distortions are characterized by the energy exchange between electrons and photons via Compton scattering and bremsstrahlung

$$e^- + \gamma \leftrightarrow e^- + \gamma, \tag{1.78}$$
$$e^- + p \leftrightarrow e^- + p + \gamma. \tag{1.79}$$

The resulting signals are described as Compton y- and chemical potential μ-distortions. At redshifts $z \gtrsim 5 \times 10^4$ [79], Compton scattering is still efficient enough to redistribute photons over frequency, producing a constant chemical potential, μ, at high frequencies, with a residual spectrum [358]

$$\Delta I^\mu_\nu = -\mu \frac{k_B T^2}{h\nu} \frac{\partial B_\nu(T)}{\partial T}, \tag{1.80}$$

which corresponds to the introduction of a small chemical potential, μ, in Eq. 1.77. On the other hand, at lower redshifts $z \lesssim 5 \times 10^4$, Compton scattering is inefficient which only causes an upscattering of photons in the Rayleigh Jeans tail to higher frequencies of the photon bath. In principle the evolution of the Bose-Einstein-distribution is determined by the Boltzmann equation for Compton scattering in a homogeneous medium, the so-called Kompaneets equation [407]. It results in a distortion of the form [407]

$$\Delta I^y_\nu = yT \left(\frac{h\nu}{k_B T} \coth\left(\frac{h\nu}{2k_B T}\right)\right) - 4\frac{\partial B_\nu(T)}{T}. \tag{1.81}$$

Hence we can approximate the photon bath spectrum as

$$I_\nu \approx B_\nu(T) + \Delta I^\mu_\nu + \Delta I^y_\nu. \tag{1.82}$$

The electron gas in turn was tightly coupled to protons via elastic Coulomb scattering. At high temperatures electrons and nuclei could not yet effectively combine to form neutral hydrogen

$$p + e^- \leftrightarrow H + \gamma. \tag{1.83}$$

The epoch in which the temperature fell so low, that this reaction became effective and the abundance of free electrons fell steeply, is called recombination. At that time the mean free path of photons grew and became longer than the horizon. This is the time when photons decoupled from matter and were

able to (mostly) freely travel, unperturbed, as the Universe became essentially transparent. These photons constitute today the Cosmic Microwave Background (CMB).

Since electrons, protons and hydrogen are non-relativistic, one can make use of Eq. 1.43 and in order to eliminate the chemical potentials $\mu_e + \mu_p = \mu_H$ can form the ratio

$$\frac{n_H}{n_e n_p} = \frac{g_H}{g_e g_p} \left(\frac{m_H}{m_p m_e} \frac{2\pi}{T} \right)^{3/2} \exp\left((m_p + m_e - m_H)/T \right). \tag{1.84}$$

The sum in the exponent can be identified as the binding energy of hydrogen, $B_H = 13.6$ eV. By setting $m_p = m_H$ in the prefactor, $g_e = g_p = 2$ and $g_H = 4$, and assume that the Universe is electrically neutral, $n_e = n_p$, we find the so-called Saha equation [97]

$$\frac{1 - X_e}{X_e} = \frac{2\xi(3)}{\pi^2} \eta \left(\frac{2\pi T}{m_e} \right)^{3/2} \exp\left(B_H/T \right). \tag{1.85}$$

This equation gives us the evolution of the free electron fraction $X_e \equiv n_e/n_b$, where n_b is the baryon density, further parametrised by the baryon-to-photon ratio, $\eta \approx 10^{-9}$, as in

$$n_b \equiv \eta n_\gamma = \eta \frac{2\xi(3)}{\pi^2} T^3. \tag{1.86}$$

RECOMBINATION

The Universe becomes substantially neutral at the the temperature $T_{\text{rec.}}$, when electrons and protons recombine into hydrogen. Using the Saha equation in Eq. 1.85 one can find that the free electron fraction falls below $X_e = 0.1$, i.e. 90% of electrons combined with a proton to form hydrogen, at a temperature

$$T_{\text{rec.}} \approx 0.3 \text{ eV} \approx 3600 \text{ K}. \tag{1.87}$$

The recombination temperature is so much lower than the binding energy of hydrogen, $B_H = 13.6$ eV, because of the big abundance of photons making it possible that there are still enough photons in the high-energy tail of the photon distribution to break up the bound between electrons and protons, even though the mean temperature of the photon bath is well below the binding energy. With the measurement of the photon bath temperature today and using our cosmological model, one can find time estimates of the recombination epoch

$$z_{\text{rec.}} \approx 1320, \tag{1.88}$$

$$t_{\text{rec.}} \approx 290\,000 \text{ yrs}. \tag{1.89}$$

Near recombination the Saha equation for electrons is not sufficient to describe the physical processes of non-requilibrium ionization history. Numerical codes like RECFAST take corrections from Helium ionization and multiple excited levels of an atom into account [267, 328].

COSMIC MICROWAVE BACKGROUND

Photons are coupled to the primordial plasma via their interaction with electrons in Compton scattering

$$e^- + \gamma \rightleftharpoons e^- + \gamma. \tag{1.90}$$

The corresponding interaction rate is given by

$$\Gamma = n_e \sigma_T, \tag{1.91}$$

where σ_T is the Thomson cross-section,

$$\sigma_T = \frac{8\pi}{3}\frac{\alpha_e^2}{m_e^2} \approx 2 \cdot 10^{-3}\,\text{MeV}^{-2}. \tag{1.92}$$

This interaction rate decreases as the abundance of free electrons drops. With the Saha equation, Eq. 1.85, and requiring that

$$\Gamma(T_{\text{dec.}}) \sim H(T_{\text{dec.}}), \tag{1.93}$$

one finds that the decoupling temperature, $T_{\text{dec.}}$, for photons is

$$T_{\text{dec.}} \approx 0.27\,\text{eV}, \tag{1.94}$$

not much below the recombination temperature, $T_{\text{rec.}} = 0.3\,\text{eV}$. The free electron fraction, however, decreases significantly, from $X_e(T_{\text{rec.}}) = 0.1$ to $X_e(T_{\text{dec.}}) = 0.01$.

$$z_{\text{dec.}} \approx 1100 \tag{1.95}$$

$$t_{\text{dec.}} \approx 380\,000\,\text{yrs} \tag{1.96}$$

The decoupled photon bath can be measured today in the form of the CMB. COBE FIRAS measurements found found no deviations from a black body spectrum, putting tight constraints on both distortion parameters y and μ, finding 95% confidence upper limits $|\mu| < 9 \cdot 10^{-5}$ and $|y| < 15 \cdot 10^{6}$ [120]. The temperature of the black body spectrum is found to be [119]

$$T_0 = 2.7260 \pm 0.0013\text{K}. \tag{1.97}$$

This corresponds to a number density today of

$$n_\gamma = 2\frac{\xi(3)}{\pi^2}T_\gamma^3 \approx 399\,\text{photons per ccm}. \tag{1.98}$$

1.2.10 Ω_Λ: DARK ENERGY

The fifth component and eponym of our ΛCDM model is dark energy, commonly labeled as Λ referring to its correspondence to the cosmological constant, as already introduced by A. Einstein in his field equations of General Relativity [104]. The cosmological constant, or a constant energy density of the vacuum with repulsive gravitational effect, is just one of three categories of dark energy models considered today [340], all predicting a late-time cosmic expansion to be consistent with the observed accelerated expansion of the Universe [310]. Furthermore, there are models introducing a new dynamical scalar field to describe dark energy (quintessence dark energy) [268]. Lastly, what we consider as dark energy could be merely effects from modifications to General Relativity, so-called modified gravity theories [198].

To parametrize dark energy models, it is common to allow for a general equation of state and linearize it in the scale factor [75]

$$w = \frac{P_\Lambda}{\rho_\Lambda} = w_0 + w_a(1-a). \tag{1.99}$$

Current data from Planck is consistent with ΛCDM predictions of $w_0 = -1$ and $w_a = 0$ [286]. Combined efforts of baryon acoustic oscillation, Supernovae and strong lensing measurements as well as measurements of galaxy and CMB lensing, redshift-space distortions, the thermal Sunyaev-Zeldovich effect and galaxy observations will set tight constraints on dark energy models in the future [340]. The tension between local and early-time measurements of the Hubble parameter, H_0 [309], if not caused by unknown systematic effects [311], could be a hint of physics beyond ΛCDM in the dark sector [300].

1.3 COSMOLOGICAL PERTURBATIONS

In this section I will outline the introduction of small perturbations in our, for now, homogeneous cosmological model. This will allow us to describe the small inhomogeneities we see today in the CMB and large-scale structure formation.

1.3.1 METRIC PERTURBATIONS

A perturbed and flat FLRW-metric 1.2 can be written in general terms as

$$\begin{aligned} g_{00} &= -a^2(\eta)\left[1 + 2\Psi(\eta, \mathbf{x})\right], \\ g_{0i} &= a^2(\eta) w_i(\eta, \mathbf{x}), \\ g_{ij} &= a^2(\eta)\left[\left(1 - 2\Phi(\eta, \mathbf{x})\right)\delta_{ij} + h_{ij}(\eta, \mathbf{x})\right], \end{aligned} \tag{1.100}$$

with scalar (Ψ & Φ), vector (w_i) and tensor (h_{ij}) perturbations. The latter, h_{ij}, is taken to be traceless ($h_{ii} = 0$). Invariance under change of coordinate systems (transformations that keep the spacetime interval constant) allows for a freedom of gauge for these quantities, such that the perturbed metric can be expressed in a more simple form, in the so-called *(conformal) Newtonian gauge* [246]

$$ds^2 = a^2(\eta)\left[-(1 + 2\Psi)d\eta^2 + (1 - 2\Phi)dx^i dx_j\right]. \tag{1.101}$$

In this gauge the metric tensor is diagonal, which leads to simplified geodesic equations. From that one obtains the first order perturbed Einstein field equations [224]

$$-\nabla^2\Phi + 3\frac{\dot{a}}{a}\left(\dot{\Phi} + \frac{\dot{a}}{a}\Psi\right) = \frac{1}{2}a^2\delta T^0_0 \tag{1.102}$$

$$-\nabla^2\left(\dot{\Phi} + \frac{\dot{a}}{a}\Psi\right) = \frac{1}{2}a^2\nabla^j\delta T^0_j \tag{1.103}$$

$$\ddot{\Phi} + \frac{\dot{a}}{a}\left(\dot{\Psi} + 2\dot{\Phi}\right) + \left(2\frac{\ddot{a}}{a} - \frac{\dot{a}^2}{a^2}\right)\Psi - \frac{\nabla^2}{3}(\Phi - \Psi) = \frac{1}{6}a^2\delta T^i_i \tag{1.104}$$

$$-\nabla^2(\Phi - \Psi) = \frac{3}{2}a^2\left(\nabla_i\nabla^j - \frac{1}{3}\delta^j_i\right)\Pi^i_j, \tag{1.105}$$

where Π is the anisotropic stress tensor.

In a radiation-dominated Universe, it follows for the metric perturbations

$$\ddot{\Phi} + 4H\dot{\Phi} = \frac{1}{3a^2}\nabla^2\Phi, \tag{1.106}$$

which can be solved in Fourier space, $\Phi(\eta, \mathbf{x}) = \int \frac{d^3\mathbf{k}}{(2\pi)^3} e^{i\mathbf{k}\cdot\mathbf{x}}\Phi(\eta, \mathbf{k})$, with

$$\Phi(\eta, \mathbf{k}) = -2\Phi(0, \mathbf{k})\frac{\sin y - y\cos y}{y^3} \quad , \; y \equiv \frac{1}{\sqrt{3}}|\mathbf{k}|\eta. \tag{1.107}$$

Outside the sound horizon $y \ll 1$, the solution is close to constant, while inside the horizon (sub-horizon) the solution oscillates and decays as a^{-2} [29]. In a matter-dominated Universe on the other hand, the two solutions to the corresponding differential equation

$$\ddot{\Phi} + 3H\dot{\Phi} = 0, \tag{1.108}$$

are $\Phi =$ const. and $\Phi \sim a^{-5/2}$ [29].

1.3.2 MATTER PERTURBATIONS

The perturbed stress-energy tensor for a fluid reads

$$T_0^0 = \bar{\rho}(\eta) + \delta\rho \tag{1.109}$$
$$T_0^i = \left[\bar{\rho}(\eta) + \bar{P}(\eta)\right] v^i \equiv \partial^i q + q^i \tag{1.110}$$
$$T_j^i = -\left[\bar{P}(\eta) + \delta P\right] \delta_j^i - \Pi_j^i, \tag{1.111}$$

with the bulk velocity v_i. In the so-called comoving gauge we set $q = 0$ [29]. From the conservation of the stress-energy tensor

$$\nabla_\mu T^m u_\nu = 0 \tag{1.112}$$

follows the continuity and Euler equations (see [29] for the derivation)

$$\dot{\delta} = -\left(1 + \frac{\overline{P}}{\overline{\rho}}\right)\left(\frac{1}{a}\partial_i v^i - 3\dot{\Phi}\right) - 3H\left(\frac{\delta P}{\overline{\rho}} - \frac{\overline{P}}{\overline{\rho}}\delta\right) \tag{1.113}$$
$$\dot{v^i} = -\left(H + \frac{\dot{\overline{P}}}{\overline{\rho} + \overline{P}}\right) v^i - \frac{1}{a}\left[\frac{1}{\overline{\rho} + \overline{P}}\left(\partial^i \delta P - \partial_j \Pi^{ij}\right) - \partial^i \Psi\right], \tag{1.114}$$

where we defined $\delta \equiv \delta\rho/\rho$. Furthermore, from the Einstein field equations it follows that

$$\Phi - \Psi = a^2 \Pi, \tag{1.115}$$

i.e. in the absence of anisotropic stress $\Phi = \Psi$. In our cosmological standard model, only free-streaming photons and neutrinos are developing anisotropic stress, in the matter-dominated epoch when their contribution to the total energy is subdominant [29].

1.3.3 BOLTZMANN EQUATION

The phase space distribution of particles

$$f(\mathbf{x}, \mathbf{p}, E, \eta) \equiv \frac{dN}{d\mathbf{x}d\mathbf{p}} \tag{1.116}$$

evolves in (conformal) time following the Boltzmann equation

$$\frac{df}{d\eta} = \left(\frac{\partial f}{\partial \eta}\right)_C, \tag{1.117}$$

where the right-hand-side is the so-called collision term, accounting for particle interactions. It is convenient to split the distribution function in an unperturbed part, $f_0(|\mathbf{p}|)$ (discussed in the previous section), and a (small) perturbation δf,

$$f(\mathbf{x}, \mathbf{p}, E, \eta) = f_0(p)\left(1 + \delta f(\mathbf{x}, p, \mathbf{n}, E, \eta)\right), \tag{1.118}$$

where $p = |\mathbf{p}|$ is the magnitude of the physical momentum and $\mathbf{n}$ its direction. In the conformal Newtonian gauge, together with the previously introduced perturbations of the metric and matter, one can obtain a differential equation for the Fourier-transformed phase space distribution perturbation $\delta f(\mathbf{k})$ [224]

$$\frac{\partial \delta f}{\partial \eta} + i\frac{p}{\sqrt{p^2 + m^2}}(\mathbf{k}\cdot\mathbf{n})\delta f + \frac{d\ln f_0}{d\ln p}\left[\dot{\Phi} - i\frac{\sqrt{p^2 + m^2}}{p}(\mathbf{k}\cdot\mathbf{n})\Psi\right] = \frac{1}{f_0}\left(\frac{\partial f}{\partial \eta}\right)_C. \tag{1.119}$$

The most relevant scattering process for the CMB is Thomson scattering, since it dominates close to recombination. The usual limit used here is that the photon energy $h\nu$ is much lower then the rest mass of the electron $m_e = 0.511$ MeV, such that the recoil of the electron can be neglected. The differential cross-section of Thomson scattering is given by [97]

$$\frac{d\sigma}{d\Omega} = \frac{3}{16\pi}\sigma_T \left[1 + (\hat{\mathbf{p}}_{\rm in} \cdot \hat{\mathbf{p}})^2\right], \tag{1.120}$$

where $\hat{\mathbf{p}}_{\rm in}$ and $\hat{\mathbf{p}}$ are the propagation directions of the incoming and scattered photons, respectively. The Thomson cross section is given by Eq. 1.92. Then the corresponding collision term follows as

$$\left(\frac{\partial f}{\partial \eta}\right)_C = -\Gamma f(\mathbf{x}, \mathbf{p}_{\rm in}, E(1-(\hat{\mathbf{p}}-\hat{\mathbf{p}}_{\rm in})\cdot\mathbf{v}_e), \eta) + \Gamma \int \frac{d\hat{\mathbf{p}}_{\rm in}}{4\pi} f(\mathbf{x}, \mathbf{p}_{\rm in}, E(1-(\hat{\mathbf{p}}-\hat{\mathbf{p}}_{\rm in})\cdot\mathbf{v}_e), \eta),$$

where $\Gamma \equiv a\overline{n}_e\sigma_T$, with the scale factor, a, the background electron density $\overline{n}_e$, and the electron bulk velocity, $\mathbf{v}_e$.

1.3.4 COSMIC MICROWAVE BACKGROUND

The photon brightness temperature perturbations (or otherwise called temperature anisotropies), $\Delta \equiv \frac{\Delta T}{T}$, are then defined by

$$\begin{aligned} f(\mathbf{x}, \mathbf{p}, \eta) &\equiv f_0\left(\frac{\epsilon}{1+\Delta}\right) = \\ &= \left[\exp\left(\frac{\epsilon}{T_0(1+\Delta)}\right) - 1\right]^{-1}, \end{aligned} \tag{1.121}$$

where f_0 is the Bose-Einstein distribution 1.77 and ϵ is the comoving energy, $\epsilon \equiv aE = a\sqrt{p^2+m^2}$. I.e. the CMB still has a Planck spectrum, with a position dependent temperature. To first order in δf, we have

$$\Delta = -\left(\frac{d\ln f_0}{d\ln\epsilon}\right)^{-1}\delta f \tag{1.122}$$

Since the gravitational source terms and the Thomson scattering terms in the Boltzmann equation are proportional to $\frac{d\ln f_0}{d\ln\epsilon}$ [224], Δ is independent of ϵ and consequently the brightness of the perturbed microwave background radiation does not depend on the photon energy, only on its direction, $\mathbf{n}$. In our experiments we are observing this anisotropy in the brightness of photons coming at us in a direction $\mathbf{n}_0$ here at $\mathbf{x}_0$ and now at η_0. To make this connection, we can expand the CMB anisotropy at any point in spacetime η, $\mathbf{x}$ into plane waves

$$\Delta(\mathbf{x}, \mathbf{n}, \eta) \equiv \int d^3\mathbf{k} e^{-i\mathbf{k}\cdot\mathbf{x}} \sum_\ell^\infty (-i)^\ell (2\ell+1)\Delta_\ell(\mathbf{k}, \eta) P_\ell(\mathbf{k}\cdot\mathbf{n}), \tag{1.123}$$

where $\Delta(\mathbf{k}, \mathbf{n}, \eta)$ was further decomposed in Legendre polynomials, P_ℓ. The anisotropy at the origin ($\mathbf{x}_0$) can then be expressed in spherical harmonic functions, $Y_{\ell m}$, (see Sec. 1.3.6)

$$\Delta(\mathbf{x}_0, \mathbf{n}_0, \eta_0) = \sum_{\ell m} a_{\ell m}(\mathbf{x}_0, \eta_0) Y_{\ell m}(\mathbf{n}_0) \tag{1.124}$$

$$a_{\ell m}(\mathbf{x}_0, \eta_0) = 4\pi(-i)^\ell \int d^3\mathbf{k} Y^*_{\ell m}(\mathbf{k}) \Delta_\ell(\mathbf{k}, \eta_0). \tag{1.125}$$

The covariance of the harmonic coefficients is diagonal

$$\left\langle a^{\dagger}_{\ell m} a_{\ell m} \right\rangle = \delta_{\ell \ell'} \delta_{m m'} C_{\ell}, \tag{1.126}$$

which is related to the real space covariance matrix between two directions $\mathbf{n}$ and $\mathbf{n}_0$ by

$$C(\mathbf{n}, \mathbf{n}') = \sum_{\ell}^{\infty} \frac{2\ell + 1}{4\pi} C_{\ell} P_{\ell}(\mathbf{n} \cdot \mathbf{n}'). \tag{1.127}$$

The expansion coefficients of the perturbations $\Delta_{\ell}(\mathbf{k}, \eta)$ are random, complex variables depending on the initial perturbations. One can express them in terms of the initial (comoving curvature) perturbation and a transfer function, $\tilde{\Delta}$, containing the evolution obtained by solving the Boltzmann equation,

$$\Delta_{\ell}(\mathbf{k}, \eta) = \mathcal{R}(\mathbf{k}) \tilde{\Delta}_{\ell}(k, \eta). \tag{1.128}$$

One can then obtain for the harmonic space power spectrum of CMB fluctuations

$$C_{\ell} = (4\pi)^2 \int dk \frac{2\pi^2}{k} P_{\mathcal{R}}(k) \tilde{\Delta}^2_{\ell}(k, \eta). \tag{1.129}$$

To zeroth order the initial perturbations power spectrum Eq. 1.189 is a scale-invariant Harrison-Zel'dovich spectrum. In this case one finds for large angular scales (Sachs-Wolfe effect) [315]

$$\frac{\ell(\ell + 1)}{2\pi} C_{\ell} \approx \frac{32\pi^3}{9} A_s. \tag{1.130}$$

1.3.5 POLARIZED LIGHT

To statistically describe the polarization of the CMB, we start by describing it in terms of two components of an electromagnetic wave in the z-direction with frequency ν

$$E_x(\mathbf{n}) = A_x(t) \cos\left(\nu t - \theta_x(t)\right) \tag{1.131}$$

$$E_y(\mathbf{n}) = A_y(t) \cos\left(\nu t - \theta_y(t)\right). \tag{1.132}$$

The electromagnetic wave is polarized when these two components are correlated. One can locally define Stokes parameters by time-averaging over the amplitude and phases of this electromagnetic wave

$$T = \left\langle A_x^2 \right\rangle + \left\langle A_y^2 \right\rangle \tag{1.133}$$

$$Q = \left\langle A_x^2 \right\rangle - \left\langle A_y^2 \right\rangle \tag{1.134}$$

$$U = \left\langle 2 A_x A_y \cos\left(\theta_x - \theta_y\right) \right\rangle \tag{1.135}$$

$$V = \left\langle 2 A_x A_y \sin\left(\theta_x - \theta_y\right) \right\rangle \tag{1.136}$$

in each direction $\mathbf{n}$ in the sky. Under a rotation by an angle ψ around $\mathbf{n}$, the Q and U parameters transform as

$$\begin{pmatrix} Q' \\ U' \end{pmatrix} = \begin{pmatrix} \cos 2\psi & \sin 2\psi \\ -\sin 2\psi & \cos 2\psi \end{pmatrix} \begin{pmatrix} Q \\ U \end{pmatrix} \tag{1.137}$$

We can form two quantities out of the Q and U Stokes parameters that have a well-defined spin

$$(Q \pm iU)'(\mathbf{n}) = e^{\mp 2i\psi} (Q \pm iU)(\mathbf{n}). \tag{1.138}$$

1.3.6 SCALAR SPHERICAL HARMONIC TRANSFORMS

To continue, we introduce a basis of spherical harmonics, defined by their property of being eigenfunctions of the Laplace operator

$$\nabla^2 Y_{\ell m}(\mathbf{n}) = -\ell(\ell+1) Y_{\ell m}(\mathbf{n}). \tag{1.139}$$

These functions form an orthonormal basis on the sphere

$$\int d\Omega\, Y^*_{\ell m}(\mathbf{n}) Y_{\ell' m'}(\mathbf{n}) = \delta_{\ell\ell'}\delta_{mm'} \tag{1.140}$$

$$\sum_{\ell m} Y^*_{\ell m}(\mathbf{n}) Y_{\ell m}(\mathbf{n}') = \sum_{\ell=0}^{\ell_{\rm max}} \frac{2\ell+1}{4\pi} P_\ell(\mathbf{n}\cdot\mathbf{n}') \xrightarrow{\ell_{\rm max}\to\infty}{}^{10} \delta(\mathbf{n}-\mathbf{n}'). \tag{1.141}$$

One can then expand any scalar field defined on the sphere in a series of harmonic functions

$$T(\mathbf{n}) = \sum_{\ell m} a^T_{\ell m} Y_{\ell m}, \tag{1.142}$$

where the harmonic coefficients $a_{\ell m}$ are given by

$$a^T_{\ell m} = \int d\Omega\, Y^*_{\ell m}(\mathbf{n}) T(\mathbf{n}). \tag{1.143}$$

1.3.7 SPIN SPHERICAL HARMONIC TRANSFORMS

Spherical harmonic transformations of a spin-s field $f(\mathbf{n})$, characterized by its transformation property under coordinate rotation by an angle ψ, $f' = e^{-is\psi} f$, can be defined by introducing spin-weighted spherical harmonic functions, ${}_{\pm s}Y_{\ell m}$, [130, 257, 406]

$${}_{\pm s}a_{\ell m} = \int d\Omega\, f(\mathbf{n})\, {}_{\pm s}Y^\dagger_{\ell m} \tag{1.144}$$

$$f(\mathbf{n}) = \sum_{\ell m} {}_{\pm s}a_{\ell m}\, {}_{\pm s}Y_{\ell m}, \tag{1.145}$$

where

$${}_{s}Y_{\ell m} = \sqrt{\frac{(\ell-s)!}{(\ell+s)!}}\eth^s\, Y_{\ell m} \tag{1.146}$$

$${}_{-s}Y_{\ell m} = (-1)^s \sqrt{\frac{(\ell-s)!}{(\ell+s)!}}\bar{\eth}^s\, Y_{\ell m} \tag{1.147}$$

for $s \geq 0$. The two new operators $\eth$ and $\bar{\eth}$ are covariant derivatives on the sphere with the transformation properties under coordinate rotation by angle ψ

$$(\eth f)' = e^{-i(s+1)\psi}\eth f \tag{1.148}$$

$$(\bar{\eth} f)' = e^{-i(s-1)\psi}\bar{\eth} f \tag{1.149}$$

[10] $\sum_\ell P_\ell(x) w^\ell = \frac{1}{\sqrt{1-2xw+w^2}} \to \sum_\ell (2\ell+1) P_\ell(x) = \frac{0}{\sqrt{2-2x}} \to \delta(x-1)$

where f is a field of spin-weight s. Hence $\eth$ and $\bar{\eth}$ act as spin-raising and -lowering operators. Explicitly they can be written as [406]

$$\eth f(\mathbf{n}) = -\sin^s(\theta)\left[\frac{\partial}{\partial\theta} + i\csc(\theta)\frac{\partial}{\partial\phi}\right]\sin^{-s}(\theta) \tag{1.150}$$

$$\bar{\eth} f(\mathbf{n}) = -\sin^{-s}(\theta)\left[\frac{\partial}{\partial\theta} - i\csc(\theta)\frac{\partial}{\partial\phi}\right]\sin^{s}(\theta). \tag{1.151}$$

It is useful to define the operators

$$\begin{aligned}
{}_E\mathbf{Y}_{s,\ell m} &\equiv \mathbf{D}_s^E\, Y_{\ell m} \\
&= \frac{1}{2}\sqrt{\frac{(\ell-s)!}{(\ell+s)!}}\begin{pmatrix}\eth^s + (-1)^s\bar{\eth}^s \\ -i(\eth^s - (-1)^s\bar{\eth}^s)\end{pmatrix} Y_{\ell m} \\
&= \frac{1}{2}\begin{pmatrix}{}_sY_{\ell m} + (-1)^s{}_{-s}Y_{\ell m} \\ -i({}_sY_{\ell m} - (-1)^s{}_{-s}Y_{\ell m})\end{pmatrix}
\end{aligned} \tag{1.152}$$

$$\begin{aligned}
{}_B\mathbf{Y}_{s,\ell m} &\equiv \mathbf{D}_s^B\, Y_{\ell m} \\
&= -\frac{1}{2}\sqrt{\frac{(\ell-s)!}{(\ell+s)!}}\begin{pmatrix}i(\eth^s - (-1)^s\bar{\eth}^s) \\ \eth^s + (-1)^s\bar{\eth}^s\end{pmatrix} Y_{\ell m} \\
&= -\frac{1}{2}\begin{pmatrix}i({}_sY_{\ell m} - (-1)^s{}_{-s}Y_{\ell m}) \\ {}_sY_{\ell m} + (-1)^s{}_{-s}Y_{\ell m}\end{pmatrix}
\end{aligned} \tag{1.153}$$

such that we can write a decomposition into E- and B-mode spherical harmonics as

$$a^X_{s,\ell m} = \int d\Omega\, {}_X\mathbf{Y}^\dagger_{s,\ell m} f(\mathbf{n}). \tag{1.154}$$

In analogy with the electric and magnetic field, the E-modes remain unchanged under parity transformations, $\mathbf{n} \to -\mathbf{n}$, while the B-modes change sign. With $f^T = (Q, -U)$, one can write

$$\begin{aligned}
a^E_{\ell m} &= \frac{1}{2}\int d\Omega\, ({}_sY_{\ell m} + (-1)^s{}_{-s}Y_{\ell m})Q(\mathbf{n}) + i({}_sY_{\ell m} - (-1)^s{}_{-s}Y_{\ell m})U(\mathbf{n}) = \\
&= \frac{1}{2}\int d\Omega\, {}_sY_{\ell m}(Q(\mathbf{n}) + iU(\mathbf{n})) + (-1)^s{}_{-s}Y_{\ell m}(Q(\mathbf{n}) - iU(\mathbf{n})) = \\
&= \frac{1}{2}\left({}_+a_{\ell m} + (-1)^s{}_{-s}a_{\ell m}\right)
\end{aligned} \tag{1.155}$$

$$\begin{aligned}
a^B_{s,\ell m} &= \frac{1}{2i}\int d\Omega\, ({}_sY_{\ell m} - (-1)^s{}_{-s}Y_{\ell m})Q(\mathbf{n}) + ({}_sY_{\ell m} + (-1)^s{}_{-s}Y_{\ell m})iU(\mathbf{n}) = \\
&= \frac{1}{2i}\int d\Omega\, {}_sY_{\ell m}(Q(\mathbf{n}) + iU(\mathbf{n})) - (-1)^s{}_{-s}Y_{\ell m}(Q(\mathbf{n}) - iU(\mathbf{n})) = \\
&= \frac{1}{2i}\left({}_+a_{\ell m} - (-1)^s{}_{-s}a_{\ell m}\right).
\end{aligned} \tag{1.156}$$

E- and B-modes are only defined in harmonic space. However, one can define the two scalar, real space quantities [406]

$$\tilde{E}(\mathbf{n}) = \sum_{\ell m}\sqrt{\frac{(\ell+s)!}{(\ell-s)!}}a^E_{s,\ell m}Y_{\ell m} \tag{1.157}$$

$$\tilde{B}(\mathbf{n}) = \sum_{\ell m}\sqrt{\frac{(\ell+s)!}{(\ell-s)!}}a^B_{s,\ell m}Y_{\ell m}, \tag{1.158}$$

which are rotationally-invariant.

1.3.8 POWER SPECTRA

Since we assume the CMB to be Gaussian, it is sufficient to define the following rotationally-invariant power spectra from the correlation functions of harmonic coefficients In order to characterize the statistical distribution of CMB perturbations, including polarization,

$$C_\ell^{XY} = \frac{1}{2\ell+1}\sum_m \left\langle a_{\ell m}^{X\,*} a_{\ell m}^{Y} \right\rangle , \tag{1.159}$$

where X and Y can be one of the CMB fields T, E or B. From statistical isotropy of the CMB follows that the covariance matrices of two harmonic coefficients are diagonal in ℓ and m such that we obtain a more general form of Eq. 1.126

$$\left\langle a_{\ell m}^{X\,*} a_{\ell' m'}^{Y} \right\rangle = \delta_{\ell\ell'}\delta_{mm'} C_\ell^{XY} . \tag{1.160}$$

The cross-correlation between T and B as well as E and B vanishes for parity-conserving underlying processes

$$C_\ell^{TB} = C_\ell^{EB} = 0. \tag{1.161}$$

1.3.9 HIGHER-ORDER STATISTICS

In the previous section the CMB fields were assumed to be Gaussian, i.e. the $a_{\ell m}$ taken to be drawn from a Gaussian distribution function with variance given by the C_ℓ^{XY}-spectra

$$P_G\left(\mathbf{a}_{\ell m}\right) \sim \exp\left(-\frac{1}{2}\sum_{\ell m}\sum_{\ell' m'} \mathbf{a}_{\ell m}\mathbf{C}^{-1}_{\ell m \ell' m'}\mathbf{a}_{\ell' m'}\right) . \tag{1.162}$$

Going beyond that assumption, we can introduce the bispectrum, B, measuring the first-order deviation from Gaussianity

$$\left\langle a_{\ell_1 m_1}^{X} a_{\ell_3 m_3}^{Y} a_{\ell_3 m_3}^{Z} \right\rangle \equiv B^{XYZ}_{\ell_1 m_1 \ell_2 m_2 \ell_3 m_3} = \begin{pmatrix} \ell_1 & \ell_2 & \ell_3 \\ m_1 & m_2 & m_3 \end{pmatrix} B^{XYZ}_{\ell_1\ell_2\ell_3}, \tag{1.163}$$

where $B^{XYZ}_{\ell_1\ell_2\ell_3}$ is the angle-averaged bispectrum. The bracketed expression on the right-hand side of Eq. 1.163 is a Wigner 3-j symbol defined analogous to Clebsch-Gordon coefficients as a way to express the summation of angular momenta [394] and appears in this thesis mostly in the context of an integral of three spherical harmonics (see Eq. A.6). The reduced bispectrum, $b^{XYZ}_{\ell_1\ell_2\ell_3}$, is given by

$$\begin{aligned} B^{XYZ}_{\ell_1 m_1 \ell_2 m_2 \ell_3 m_3} &= \int d\Omega\, {}_{s_1}Y_{\ell_1 m_1}(\mathbf{n})\, {}_{s_2}Y_{\ell_2 m_2}(\mathbf{n})\, {}_{s_2}Y_{\ell_2 m_2}(\mathbf{n}) b^{XYZ}_{\ell_1\ell_2\ell_3} = \\ &= \sqrt{\frac{(2\ell_1+1)(2\ell_2+1)(2\ell_3+1)}{4\pi}} \begin{pmatrix} \ell_1 & \ell_2 & \ell_3 \\ -s_1 & -s_2 & -s_3 \end{pmatrix} \begin{pmatrix} \ell_1 & \ell_2 & \ell_3 \\ m_1 & m_2 & m_3 \end{pmatrix} b^{XYZ}_{\ell_1\ell_2\ell_3}, \end{aligned} \tag{1.164}$$

following from statistical isotropy and homogeneity of the bispectrum and using Eq. A.6. For weakly non-Gaussian fields, we can expand their probability distribution function (PDF) in the so-called Edgeworth expansion [304]

$$\begin{aligned} P\left(a_{\ell m}\right) = \Big[1 - B_{\ell_1 m_1 \ell_2 m_2 \ell_3 m_3} &\frac{\partial}{\partial a_{\ell_1 m_1}} \frac{\partial}{\partial a_{\ell_2 m_2}} \frac{\partial}{\partial a_{\ell_3 m_3}} + \\ &+ T_{\ell_1 m_1 \ell_2 m_2 \ell_3 m_3 \ell_4 m_4} \frac{\partial}{\partial a_{\ell_1 m_1}} \frac{\partial}{\partial a_{\ell_2 m_2}} \frac{\partial}{\partial a_{\ell_3 m_3}} \frac{\partial}{\partial a_{\ell_4 m_4}} + \ldots \Big] P_G\left(a_{\ell m}\right), \end{aligned} \tag{1.165}$$

with coefficients given by the bispectrum, B, and trispectrum, T.

1.4 INFLATION

1.4.1 ISSUES WITH THE STANDARD BIG-BANG MODEL

So far I have outlined the standard Big Bang model as a FLRW cosmology and how the early Universe was homogeneous due to the thermal bath in its hot and dense early state. This, however, merely predicts a Universe which is made up of many causally disconnected regions of space. This is not backed up by observations of a homogeneous Universe up to very large scales like the CMB. Going back to the equation defining the particle horizon 1.7

$$\chi_p(t) = \eta - \eta_i = \int_{t_i}^{t} \frac{dt'}{a(t')},$$

one can see that in particular in a radiation-dominated early Universe, where $a(t) \sim \sqrt{t}$, the scale factor would tend to zero, $a \to 0$,and $H \to \infty$ as $t \to 0$. The particle horizon would be of order η, if one sets $\eta_i = 0$ as well. Hence, going back in time, we reach a singularity at $t = 0$ in the Big Bang model. Generally, for a Universe dominated by matter with $w > -\frac{1}{3}$, one finds that

$$\chi_p(t) = \frac{2}{H_0(1+3w)} \left(a^{(1+3w)/2} - a_i^{(1+3w)/2} \right), \tag{1.166}$$

where $a_i = a(t_i) = 0$ is the Big Bang singularity, which means that in an expanding Universe the particle horizon grows with time. One can calculate the ratio of the particle horizon at decoupling of the photons, i.e. the size of the regions in the CMB which could have been in causal contact at decoupling, and the size of the observable Universe today at $t = t_0$ in a radiation dominated Universe[11]. One finds

$$\frac{\int_{t_i}^{t_{\text{dec.}}} \frac{dt'}{a(t')}}{\int_{t_0}^{t_i} \frac{dt'}{a(t')}} \approx 5 \cdot 10^{-4}, \tag{1.167}$$

with $t_{\text{dec.}} = 380\,000$ yrs and $t_0 = 13.7$ Gyrs. That means that an observer today could observe roughly 10 000 independent patches of space on the full sky, according the standard Big Bang model. That apparent disagreement with CMB observations, measuring a homogeneous radiation on large angular scales up to small fluctuations of about 50 ppm, is called the horizon problem. A way to rectify this is to allow the conformal time to extend to negative values. Naturally one achieves that by requiring a phase with $w < -\frac{1}{3}$, such that the singularity moves to infinite conformal time

$$\tau_i = \frac{2}{H_0(1+3w)} a_i^{(1+3w)/2} \xrightarrow{a_i \to 0} -\infty. \tag{1.168}$$

In this picture the Universe would undergo a transition to the standard Big Bang model at $\eta = 0$, while now there could have been enough time in the past for the different regions the CMB is originating from to be in causal contact. However, this also implies that before $\eta = 0$, the Universe is dominated by matter with an equation of state with $w < -\frac{1}{3}$, a so-called strong energy condition (SEC)-violating fluid. Fig. 1.4 shows a schematic of the past light cone of an observer, looking at the CMB today, and how a viable negative conformal time could ameliorate the horizon problem to allow all point observed in the CMB to have intersecting past light cones.

Further problems associated with the standard Big-Bang model are the fine-tuning problem of the initial conditions, that would be necessary to produce a current value of the total energy so close to critical (flatness problem), and the problem of galaxy formation, requiring tiny fluctuations in the otherwise homogeneous early plasma [217].

[11] neglecting the rather recent period of matter and dark energy domination in our Universe

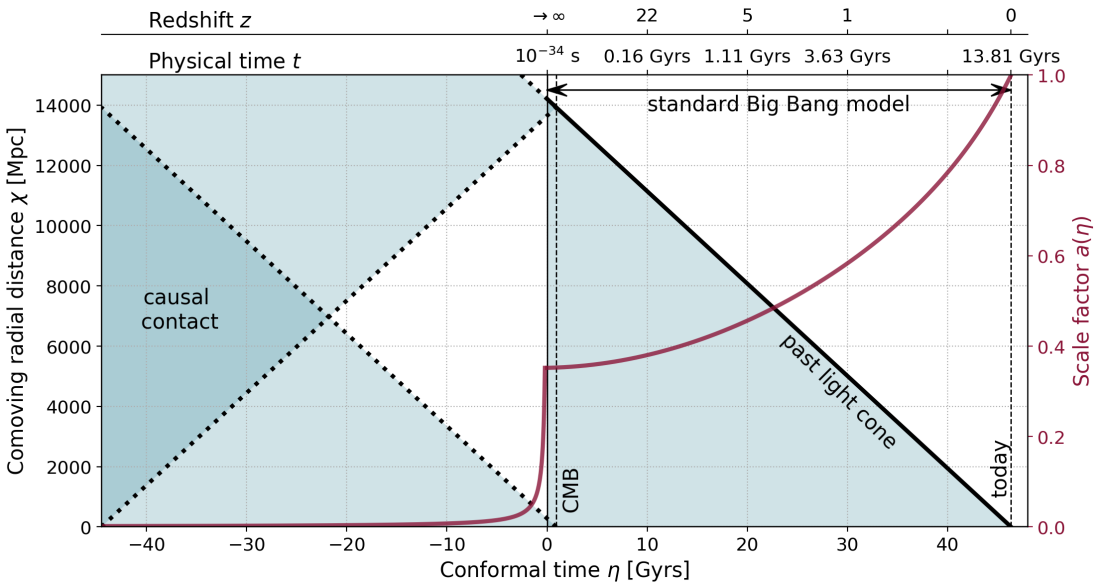

Figure 1.4: Schematic view of a past light cone of a CMB observer today. This observer sees a part of the Universe, in which many points could not have been in causal contact ever before, i.e. don't have intersecting past light cones, in the Standard Big Bang model with a singularity at $\eta = 0$. Moving this singularity to $\eta \to -\infty$ allows for an extension of the past light cones to become intersecting for all points in the observable Universe during photon decoupling.

1.4.2 INFLATION MODELS

The issues with the standard cosmological model lead to the emergence of led to the emergence of models of Inflation [353, 137, 245, 218, 9, 219].

A simple case of an inflationary model is driven by a single scalar field, ϕ, running down a close to flat potential, $V(\phi)$. The action, including the Einstein-Hilbert term of General Relativity, is given by

$$S = \int d^4x\sqrt{-g}\left(\frac{M_{\rm pl}^2}{2}R + \frac{1}{2}g^{\mu\nu}\partial_\mu\phi\partial_\nu\phi - V(\phi)\right). \tag{1.169}$$

In the case of a homogeneous scalar field, ϕ, computing the resulting stress-energy tensor and identifying the density and pressure of the scalar field yields [334]

$$\rho_\phi = \frac{1}{2}\dot{\phi}^2 + V(\phi) \tag{1.170}$$

$$p_\phi = \frac{1}{2}\dot{\phi}^2 - V(\phi). \tag{1.171}$$

If the potential energy dominates over the kinetic energy

$$V(\phi) \ll \dot{\phi}^2 \tag{1.172}$$

one can fullfill the requirement for an inflationary phase

$$w_\phi = \frac{p_\phi}{\rho_\phi} \approx -1 < -\frac{1}{3}. \tag{1.173}$$

This led to the name of these theories, so-called slow-roll inflation. The equation-of-motion for the scalar potential follows as [30]

$$\ddot{\phi}^2 + 3H\dot{\phi} + \frac{\partial V(\phi)}{\partial \phi} = 0, \tag{1.174}$$

where the second term describes the Hubble friction, and

$$H^2 = \frac{1}{3}\left(\frac{1}{2}\dot{\phi}^2 + V(\phi)\right). \tag{1.175}$$

One can define slow roll parameters to make it easier to relate the shape of the potential to observables. The first one is [30]

$$\epsilon \equiv \frac{3}{2}(1 + w_\phi) = -\frac{\dot{H}}{H^2} = -\frac{d\ln H}{dN}, \tag{1.176}$$

where $dN = Hdt$, which sets the slow roll requirement following Eq. 1.173 to be $\epsilon \ll 1$. Since $\ddot{a}/a = H^2(1-\epsilon)$ [30] the slow-roll inflationary phase inhibits an accelerated expansion. To allow the inflationary phase to go on for a sufficient amount of time (to solve the horizon problem) one has to ensure that the Hubble friction in the inflaton field's equation of motion is large enough. That is related to the second slow roll parameter [30]

$$\mathcal{R} \equiv -\frac{\ddot{\phi}}{H\dot{\phi}}\epsilon - \frac{1}{2\epsilon}\frac{d\epsilon}{dN}. \tag{1.177}$$

These two parameters determine the shape of the inflaton potential to second order in ϕ in slow roll approximation [30]

$$\epsilon \approx \frac{M_{\rm pl}^2}{2}\left(\frac{1}{V}\frac{dV}{d\phi}\right)^2 \tag{1.178}$$

$$\eta \equiv -\frac{\ddot{\phi}}{H\dot{\phi}} \approx M_{\rm pl}^2\frac{1}{V}\frac{d^2V}{d\phi^2} - \frac{M_{\rm pl}^2}{2}\left(\frac{1}{V}\frac{dV}{d\phi}\right)^2. \tag{1.179}$$

From that, it is straightforward to compute the number of e-folds before inflation ends

$$N \equiv \ln\frac{a_{\rm end}}{a} \tag{1.180}$$

in terms of the slow roll parameter [30]

$$N = \int_{\phi_{\rm end}}^{\phi}\frac{d\phi}{\sqrt{2\epsilon}}. \tag{1.181}$$

In order to solve the horizon problem and achieve a ratio in Eq. 1.167 larger than unity inflation has to last at least 60 e-folds [30].

At the end of inflation the inflaton begins to oscillate around the minimum of the potential. We achieved a homogenization of the Universe, however, this often entails that the Universe is left at effectively zero temperature [27]. Hence a mechanism must exist to *reheat* the Universe in order to initiate the hot Big Bang evolution of the Universe, including baryogenesis and nucleosynthesis. This could happen by inflaton field(s) decays through its (their) coupling to Standard Model particles [27].

Nowadays exist a wide range of single field slow roll inflationary models. So-called large field inflation models have potentials like

$$V(\phi) = M^4\left(\frac{\phi^\alpha}{M_{\rm pl}}\right)^p, \tag{1.182}$$

while so-called small field inflation or hilltop models have potentials of the form

$$V(\phi) = M^4 \left(1 - \left(\frac{\phi}{\mu}\right)^p\right), \tag{1.183}$$

for some exponent $p > 0$, normalization M and mass scale μ [80]. One example of so-called plateau models is the Starobinsky model [80]

$$V(\phi) = M^4 \left(1 - \exp\left(-\sqrt{\frac{2}{3}}\frac{\phi}{M_{\rm pl}}\right)\right)^2. \tag{1.184}$$

This model is related via a conformal transformation to an $f(R)$ modified gravity theory with action

$$S = \frac{1}{2}\int d^4x \left(R + \frac{R^2}{6M^2}\right), \tag{1.185}$$

which is why it is also called R^2-inflation [353]. Furthermore, the potential matches with the Higgs inflation model, where the inflaton coincides with the Higgs particle, non-minimally coupled to gravity [46]. The latter type of models are favoured by CMB data from Planck [288, 80].

1.4.3 INITIAL CONDITIONS

Necessary for the solution of the network of Einstein field equations and Boltzmann equations for the Big-Bang evolution are initial conditions, which have to be set a priori or predicited by theories such as inflation. These determine the evolution of the metric perturbations that were introduced in Sec. 1.3. It is useful to set the initial conditions with respect to a variable called the comoving curvature perturbation

$$\mathcal{R} \equiv -\Phi + \frac{aH}{\bar{\rho} + \bar{P}}\delta q, \tag{1.186}$$

especially since it can be easily connected to inflation theories and it is conserved on super-Hubble scales ($|\mathbf{k}|\eta \gg 1$) [23]. We can only predict the statistics of the initial conditions, i.e. the statistical distribution of which our Universe is one realization of. This comes from the underlying theory based on quantum mechanical principles, only allowing to make predicitions over a statistical ensamble. This is made manifest by specifying the initial conditions by its statistical distribution, which is Gaussian with a covariance given by

$$\langle \mathcal{R}(\mathbf{x})\mathcal{R}(\mathbf{x}')\rangle \equiv \xi(\mathbf{x}, \mathbf{x}'), \tag{1.187}$$

or its Fourier transform

$$\langle \mathcal{R}^*(\mathbf{k})\mathcal{R}(\mathbf{k}')\rangle \equiv \frac{2\pi^2}{k^3} P_{\mathcal{R}}(k)\delta(\mathbf{k} - \mathbf{k}'), \tag{1.188}$$

assuming statistical homogeneity and isotropy. $P_{\mathcal{R}}(k)$ is the primordial power spectrum of curvature perturbations and can be modeled with a power law as [211]

$$\ln P_{\mathcal{R}}(k) = \ln A_s + (n_s - 1)\ln\left(\frac{k}{k_s}\right) + \frac{n_{s,\rm run}}{2}\left(\ln\left(\frac{k}{k_s}\right)\right)^2 + \ldots, \tag{1.189}$$

where k_s is the pivot scale, n_s the scalar spectral index, $n_{s,\rm run}$ the running scalar parameter and A_s is the primordial comoving curvature power spectrum amplitude. The pivot scale is usually set to

$k_s = 0.05\,\mathrm{Mpc}^{-1}$. Likewise, one can define the power spectrum of the transverse traceless part of the metric tensor, h_{ij},

$$\left\langle h^*_{ij}(\mathbf{k}) h^{ij}(\mathbf{k}') \right\rangle = \delta(\mathbf{k} - \mathbf{k}') \delta_{ij} \frac{2\pi^2}{k^3} P_h(k), \tag{1.190}$$

where $P_h(k)$ is the primordial tensor power spectrum, which can be parametrised as [211]

$$\ln P_h(k) = \ln A_t + n_t \ln\left(\frac{k}{k_t}\right) + \frac{n_{t,\mathrm{run}}}{2}\left(\ln\left(\frac{k}{k_t}\right)\right)^2 + \dots . \tag{1.191}$$

Here we introduce the tensor pivot scale, k_t, the tensor spectral index, n_t, and the tensor power amplitude, A_t, which is usually related to the scalar amplitude by

$$A_t \equiv r A_s. \tag{1.192}$$

The tensor-to-scalar ratio, r, can be rewritten in an alternative form as

$$r = \frac{P_h(k_*)}{P_{\mathcal{R}}(k_*)}, \tag{1.193}$$

if $k_s = k_t = k_*$.

1.4.4 CONNECTION WITH INFLATION

To describe the dynamics of inflation theories we require a theory which is valid beyond the Standard model. We have a good understanding of the history of the Universe starting at the electroweak phase transition at energies of about 100 GeV or an age of the Universe of about 1 ns. But how to describe earlier times, the era of Inflation? For now we just extrapolated our expanding ΛCDM model to $t = 0$, arriving at a singularity where $a = 0$. But we already know, that all our knowledge of physics breaks down at regimes where we cannot neglect one of both, gravitational force or quantum dynamical effects. In our early Universe, which was very dense and hot, we are not able to make viable predictions due to the lack of a unifying theory of quantum gravity.

However, one encounters similar situations in numerous fields of physics. For example, in order to describe the physics of a falling apple, Isaac Newton required neither a detailed quantum dynamical description of the apple nor a general relativistic description of the Earth's gravitational field. This is because the scales (in terms of space dimension, energy and time) involved in the problem do not necessitate to invoke physics to describe much smaller or larger scales. This concept is the central point of so-called effective field theories, describing the physics of a particular scale with an effective version of the theory at respective shorter scales. The physics of the early Universe is clearly pushing to extreme scales. So is it possible to have an effective field theory of the creation of our Universe without knowing the details of the physics of creating a Universe?

One common way to create an effective field theory, especially in particle physics, is starting with a theory by writing down a most general Lagrangian obeying given symmetries and then introducing a mechanism to break this symmetry. This symmetry breaking introduces a new particle associated to the broken symmetry, called a Goldstone boson, π. For details on the construction of the Inflation effective field theory Lagrangian with broken time translation symmetry the reader is referred to Ref. [74]. One can show [74] that the comoving curvature perturbation, $\mathcal{R}$, is related to the Goldstone boson associated to the broken symmetry of time translations as

$$\mathcal{R}(\mathbf{x}, t) = -H(t)\pi(\mathbf{x}, t). \tag{1.194}$$

The Lagrangian formulation makes it now possible to follow the textbook procedure of canonical quantization of the π-field. This allows to elevate the comoving curvature perturbation $\mathcal{R}$ to an operator given by [334]

$$\mathcal{R} = \frac{c_s}{\sqrt{2\epsilon}M_{\rm pl}}\frac{1}{(2c_sk)^{3/2}}(1-ik\eta)e^{ic_sk\eta}a^\dagger_{\mathbf{k}} + \frac{c_s}{\sqrt{2\epsilon}M_{\rm pl}}\frac{1}{(2c_sk)^{3/2}}(1+ic_sk\eta)e^{-ik\eta}a_{-\mathbf{k}}, \quad (1.195)$$

where $a_{\mathbf{k}}$ and $a^\dagger_{\mathbf{k}}$ are annihilation and creation operators, removing or creating excitations acting on the vacuum state $|0\rangle$. Also the sound speed of π-waves is defined as

$$c_s^{-2} \equiv 1 - \frac{2M_2^4}{M_{\rm pl}^2\dot{H}}, \quad (1.196)$$

where M_2 can be interpreted as the mass of π. Using the fact that $\mathcal{R}$ is conserved at super-horizon scales [23], one obtains the power spectrum [74]

$$\langle 0|\mathcal{R}(\mathbf{k}_1)\mathcal{R}(\mathbf{k}_2)|0\rangle = (2\pi)^3\delta(\mathbf{k}_1+\mathbf{k}_2)\frac{2\pi^2}{k_1^3}\underbrace{\frac{1}{c_s}\frac{H_*^2}{8\pi^2\epsilon_* M_{\rm pl}^2}}_{\equiv P_{\mathcal{R}}(k_1)}, \quad (1.197)$$

where the starred quantities are evaluated at horizon-crossing. The power spectrum can also be interpreted as the variance of the fluctuating time delays in different parts of the Universe, ending inflation at slightly different times. Using the parametrized form of Eq. 1.189 of the power spectrum one finds at leading order in slow roll [74, 334]

$$n_s - 1 = 4\frac{\dot{H}_*}{H_*^2} - \frac{\ddot{H}_*}{H_*\dot{H}_*} \approx -4\epsilon_* - 2\eta_* + \frac{\dot{c}_s}{Hc_s} \neq 0. \quad (1.198)$$

Furthermore, one can compute the three-point function of the comoving curvature perturbation, arising from self-interactions of π, which yield [334]

$$\langle \mathcal{R}(\mathbf{k})\mathcal{R}(\mathbf{k})\mathcal{R}(\mathbf{k})\rangle \equiv (2\pi)^3\delta(\mathbf{k})\frac{10}{k^6}\frac{H^2}{4\epsilon c_s M_{\rm pl}^2}f_{\rm NL}, \quad (1.199)$$

where

$$f_{\rm NL} \sim \left(1-\frac{1}{c_s}\right)^2. \quad (1.200)$$

Following the quantization of the tensor modes, h_{ij}, one obtains a power spectrum for tensor fluctuations given by [30, 334]

$$P_h = \frac{2}{\pi}\frac{H_*^2}{M_{\rm pl}^2}. \quad (1.201)$$

For the spectral tilt one finds [30, 334]

$$n_t = -2\epsilon_*. \quad (1.202)$$

For the tensor-to-scalar ratio follows

$$r = 16\epsilon_* = -8n_t. \quad (1.203)$$

This can also be directly related to the energy scale of inflation [390, 193]

$$V_*^{1/4} \approx \left(\frac{r}{0.001}\right)^{1/4} 10^{16}\ \text{GeV}, \quad (1.204)$$

showing the huge energies that Inflation theories are probing, close to the expected energy scale of the Grand Unified Theory (GUT).

1.5 EVOLUTION OF PERTURBATIONS TO ANISOTROPIES

Previously, we have seen how the measured power spectrum of the CMB (temperature) relates to the power spectrum of primordial fluctuations via a transfer functions for scalar perturbations, $\tilde{\Delta}^2_\ell(k,\eta)$, and tensor perturbations, $\tilde{\Delta}^{T\,2}_\ell(k,\eta)$,

$$C_\ell = (4\pi)^2 \int dk \frac{2\pi^2}{k} P_{\mathcal{R}}(k) \tilde{\Delta}^2_\ell(k,\eta) + (4\pi)^2 \int dk k \frac{2\pi^2}{k} P_h(k) \tilde{\Delta}^{T\,2}_\ell(k,\eta). \tag{1.205}$$

In this section I will outline the different physics that go into this transfer function. The general picture is

$$\mathcal{R}(\mathbf{k}) \xrightarrow{\text{Boltzmann eq.}} \delta_\gamma,\ \Phi,\ \mathbf{v}_e \text{ at recombination} \xrightarrow[\text{(secondary anisotropies)}]{\text{free-streaming, projection}} \begin{pmatrix} T \\ Q \\ U \end{pmatrix}(\mathbf{n}) \xrightarrow{\text{correlations}} C_\ell^{XY}.$$

1.5.1 FREE-STREAMING

The anisotropy observed in direction $\mathbf{n}$ is obtained by line-of-sight integration of the Boltzmann equation of the temperature perturbation at point $\mathbf{x}_* \equiv \mathbf{x}_0 + (\eta_0 - \eta_*)\mathbf{n}$. To do so we define the optical depth between today, η_0, and a conformal time η as

$$\tau(\eta) \equiv \int_\eta^{\eta_0} \Gamma(\eta') d\eta' \tag{1.206}$$

and the visibility function

$$g(\eta) \equiv -\dot{\tau}(\eta) e^{-\tau(\eta)}. \tag{1.207}$$

The optical depth drops at recombination to almost zero, when the mean-free-path of photons become very long. The visibility function is sharply peaked around the time of recombination. The Boltzmann equation for scalar perturbations with Thomson collison term then reads [97]

$$\frac{d}{d\eta} e^{-\tau}(\Delta + \Psi) = e^{-\tau}(\dot{\Phi} + \dot{\Psi}) + g\left(\frac{\delta_\gamma}{4} + \Psi - \mathbf{n}\cdot\mathbf{v}_e\right) \equiv S(k,\eta). \tag{1.208}$$

After performing the line-of-sight integral of this equation and extracting the harmonic coefficients after a plane-wave expansion as in Eq. 1.123 one obtains [97]

$$\tilde{\Delta}_\ell(\eta_0,k) = \int_0^{\eta_0} d\eta \left[\underbrace{g\left(\frac{\delta_\gamma}{4} + \Psi\right) j_\ell(k\chi)}_{\text{Sachs-Wolfe}} - \underbrace{g v_e a \dot{j}_\ell(k\chi)}_{\text{Doppler}} + \underbrace{e^{-\tau}(\dot{\Phi} + \dot{\Psi}) j_\ell(k\chi)}_{\text{integrated Sachs-Wolfe}} \right], \tag{1.209}$$

where we can identify three terms responsible for three different effects. The Sachs-Wolfe term contains the intrinsic temperature fluctuation at recombination and a gravitational redshift term arising from photons climbing out of the gravitational potential Ψ at last scattering. The Doppler term comes from the electron movement, shifting the photon energy during Thomson scattering. The integrated Sachs-Wolfe effect encapsulates the gravitational redshifting of photons due to changing gravitational potentials along the line of sight.

1.5.2 CMB POLARIZATION

The differential Thomson cross section, accounting for the photon polarization, is given by [165]

$$\frac{d\sigma}{d\Omega} = \frac{3}{8\pi}\sigma_T |\mathbf{E}' \cdot \mathbf{E}|^2, \tag{1.210}$$

Isotropic radiation would not create any polarized light, since there would be no preferred direction. Only a quadrupolar temperature fluctuation anisotropy, Δ_2, can generate linear polarized light in the direction of line-of-sight. Polarization arises through scattering in optically thin conditions [165], which is why it is primarily probing recombination and reionization.

Another effect specifically influencing the temperature fluctuation quadrupole is the tensor distortion of space, i.e. gravitational waves. Due to their azimuthal symmetry, scalar perturbations in the temperature field can only produce E-mode polarization (see Fig. 1.11) [169]. Gravitational waves break this symmetry, causing non-zero B-mode fluctuations. Quadrupoles are rescattered during recombination, causing a peak in the E- and B-mode power spectrum at around $\ell \approx 80$ [169]. Reionization, a phase where the Universe becomes optically thin again happening between $z \approx 5 - 20$, produces excess polarization power at $\ell < 30$ [169].

One can obtain similar line-of-sight integral equations as Eq. 1.209 for the polarization fluctuations by solving the corresponding Boltzmann equations [196, 181, 333, 406]. In particular, the B-mode power spectrum from tensor perturbations by using [406]

$$\tilde{\Delta}_\ell(k,\eta) = 0 \tag{1.211}$$

$$\tilde{\Delta}^T_\ell(k,\eta) = \int_0^{\eta_0} d\eta \left[g\left(\frac{4\psi}{k\chi} + \frac{2\dot{\psi}}{k}\right) + 2\dot{g}\frac{\psi}{k}\right] j_\ell(k\chi) \tag{1.212}$$

in Eq. 1.205, where ψ is a result of the Boltzmann equation solution [298]. Assuming Eq. 1.193 is valid for all scales, k, one can write

$$C_\ell^{BB} = r \cdot C_\ell^{BB}\big|_{r=1}\,. \tag{1.213}$$

1.5.3 ACOUSTIC OSCILLATIONS

From the Boltzmann equation for the primordial photon-baryon fluid with Thomson collision term we obtain an evolution equation for the photon density contrast (or the temperature fluctuation monopole $\Delta_0 = \delta_\gamma/4$)

$$\ddot{\delta}_\gamma + \frac{HR}{1+R}\dot{\delta}_\gamma + c_s^2 a^2 k^2 \delta_\gamma = -\frac{4}{3}a^2k^2\Psi + 4\ddot{\Phi} + \frac{4\dot{R}}{1+R}\dot{\Phi}, \tag{1.214}$$

where we introduced the sound speed of the photon-baryon fluid

$$c_s \equiv \frac{1}{3(1+R)}, \quad \text{with} \quad R \equiv \frac{3}{4}\frac{\overline{\rho}_b}{\overline{\rho}_\gamma} = 0.6\left(\frac{\Omega_b h^2}{0.02}\right)\left(\frac{a}{10^{-3}}\right). \tag{1.215}$$

There are three length scales associated to the solution to this equation. The *Hubble radius*

$$r_H \equiv (aH)^{-1}, \tag{1.216}$$

outside of which modes of the metric perturbations are frozen, i.e. remain constant, and only start to evolve once they cross the Hubble radius. Photon fluctuations are frozen outside of the sound horizon

$$r_s \equiv c_s(aH)^{-1}, \tag{1.217}$$

and start to oscillate after entering the horizon. Solving Eq. 1.214 for early times when $\overline{\rho}_b \ll \overline{\rho}_\gamma$ gives a photon fluctuation which oscillates, caused by interplay of pressure and gravity,

$$\delta_\gamma(\eta, \mathbf{k}) + 4\Psi(\mathbf{k}) = -\frac{4}{5}\mathcal{R}(\mathbf{k})\cos(kr_s). \tag{1.218}$$

These are called *acoustic oscillations*. At the time of decoupling different modes will be in different phases of this oscillation, hitting extrema at discrete wavenumber magnitudes given by

$$k_n = \frac{n\pi}{r_s(\eta_*)}. \tag{1.219}$$

These peaks of acoustic oscillations manifest themselves as peaks in the CMB power spectra. The characteristic scale in the power spectrum, the acoustic scale, is given by [163]

$$\ell_A = \frac{n\pi d_{A*}}{r_s(\eta_*)}, \tag{1.220}$$

where d_{A*} is the angular diameter distance to recombination. Hence, the first peak is around $\ell \approx 200 \approx 2^\circ$. On small scales CMB fluctuations are damped due to the break-down of the tight-coupling approximation, i.e. radiative viscosity and heat conduction become important. The relevant scale is the diffusion scale

$$r_d \equiv \sqrt{\tau\lambda_C}, \tag{1.221}$$

which is the distance a photon can random walk in time τ, where λ_C is the comoving mean free path defined by

$$\lambda_C \equiv \frac{1}{a\overline{n}_e\sigma_T}. \tag{1.222}$$

Given the diffusion scale at recombination one obtains a power spectrum [164]

$$\frac{\ell(\ell+1)}{2\pi}C_\ell^{TT} \sim \exp(-(\ell/\ell_d)^{1.25}), \tag{1.223}$$

where the damping scale is given by

$$\ell_d = \frac{2\pi d_{A*}}{r_d}, \tag{1.224}$$

where the damping scale at recombination can be approximated with

$$r_d \approx 64.5\left(\frac{\Omega_m h^2}{0.14}\right)^{-0.278}\left(\frac{\Omega_b h^2}{0.024}\right)^{-0.18}\ \text{Mpc}. \tag{1.225}$$

The conditions in the damping regime also provide the necessary conditions for polarization of the CMB: radiative viscosity, π_γ, which is equivalent to photon density contrast quadrupolar anisotropy. One has [168]

$$\pi_\gamma = \frac{v_\gamma}{k_d\tau_*}\frac{k}{k_d}, \tag{1.226}$$

with the photon bulk velocity v_γ. This leads to a rough scaling in the power spectrum of ℓ/ℓ_d. Since v_γ is out of phase with the temperature fluctuations

$$v_\gamma \sim \sin(kr_s), \tag{1.227}$$

the peaks in the temperature and polarization power spectra are out of phase as well. The correlation between temperature and E-modes then has a power spectrum which oscillates at twice the acoustic frequency, since

$$(\Delta + \Psi)v_\gamma \sim \cos(kr_s)\sin(kr_s) \sim \sin(2kr_s). \tag{1.228}$$

1.6 SECONDARY ANISOTROPIES

The are multiple secondary anisotropies imprinted in the CMB we measure today. Those are anisotropies that that were created between recombination and our measurement in the CMB photon field. In this section I will focus on astrophysical secondaries, and roughly distinguish between two categories, scattering and gravitational effects. The basis of this section is the review article in Ref. [6].

1.6.1 SCATTERING EFFECTS

SUNYAEV ZEL'DOVICH EFFECTS

The Sunyaev Zel'dovich (SZ) effect [359] is the distortion of the CMB spectrum, i.e. upscattering of photons in the low-frequency tail (Rayleigh-Jeans tail) of the blackboday spectrum to higher frequencies (Wien tail), caused by inverse Compton interaction between the CMB photons and a free electrons in the hot gas within galaxy clusters or superclusters. It can be divided into two phenomena, the thermal SZ (tSZ) effect, caused by scattering on thermal electrons, and the kinethic SZ (kSZ) effect, which is the scattering of CMB photons off of electrons in a bulk motion. The thermal SZ effect is creating local Compton-y distortions, with a local spectrum given by Eq. 1.81. The non-linear version of the kSZ is called Ostriker-Vishniac effect.

A polarized tSZ signal (pSZ) can arise from Thomson scattering of photon quadrupoles by (free electrons in) distant galaxy clusters [317]. This signal is expected to be detectable for near-future multi-frequency CMB polarization measurements [139].

REIONISATION

At a redshift of about $z_{\rm reio.} \approx 8$ [286] the Universe became ionized again, called *reionization*, where the first generations of galaxies start to radiate ultraviolet and X-ray photons, which starts to heat and ionize their surroundings and eventually the entire intergalactic medium [401]. The optical depth to reionization is the line-of-sight integral along the free electron fraction from reionization, X_e, [286]

$$\tau_{\rm reio.} \equiv n_H \sigma_T \int_0^{z_{\rm max}} dz X_e(z) \frac{(1+z)^2}{H(z)}, \tag{1.229}$$

where n_H is the total number density of hydrogen nuclei today. Its effect on the temperature power spectrum is a suppression by the factor $e^{-2\tau_{\rm reio.}}$ at scales smaller than the horizon at the epoch of reionization ($\ell \gtrsim 20$) [305]. In polarization it additionally creates a bump at $\ell \lesssim 20$, which scales in power as $\tau^2_{\rm reio.}$ [305]. At scales $\ell \gtrsim 20$ those scales it is heavily correlated with the A_s parameter, effectively modulating the power spectrum amplitude by $A_s e^{-2\tau_{\rm reio.}}$, which is why an improvement in large scale E-mode measurement is crucial to improve our constraints on $\tau_{\rm reio.}$ [11].

1.6.2 GRAVITATIONAL EFFECTS

CMB photons detected today have interacted with the matter distribution in the Universe throughout their journey from the last scattering surface towards us. Such interactions result in the generation of the so-called secondary anisotropies, i.e. fluctuations generated after the epoch of matter-radiation decoupling. These can be due to interactions of the photons with gravitational potential wells, e.g. the integrated Sachs-Wolfe [315] or Rees-Sciama [303] effects. In this class of secondary anisotropies is also the weak gravitational lensing effect on CMB primary anisotropies in temperature and polarization, which we will focus on in this section.

LARGE-SCALE STRUCTURE FORMATION

The cosmology at largest scales is determined by the previously discussed Einstein and Boltzmann equations for the metric and matter perturbations. In practice, the resulting coupled differential equations can be solved with codes like CAMB[12] and CLASS[13] rather quickly. A simple picture is that the growth of inhomogeneities is determined by two competing effects: Gravity, which attracts matter into overdense regions, and pressure, which pushes matter out of overdensities. Explicitly, one can rewrite the continuity and Euler equations to find

$$\ddot{\delta} + (1 - 3w)H\dot{\delta} - c_s^2\nabla^2\delta = (1 + w)\nabla^2\Phi. \tag{1.230}$$

On the left hand side one can identify the second term as the friction and the third term as the pressure contribution. The right hand side represents the gravity effect. For small scales, $k > k_J$, the pressure term dominates and one finds that the matter fluctuations oscillate. On large scales, $k < k_J$, the gravity effect prevails and inhomogeneities grow. Here we defined the sound speed $c_s \equiv \delta P/\delta\rho$ and the Jeans' scale $k_J \equiv (1 + w)\frac{a^2\bar{\rho}}{2c_s^2}$.

MATTER POWER SPECTRUM

The evolution of matter in our Universe is usually encoded in a transfer function or linear growth factor $T(k, z)$, depending on the redshift, z, and the mode, k. The fractional total matter density perturbation can then be related to the primordial perturbation $\mathcal{R}(\mathbf{k})$ in the linear regime by

$$\delta_m(\mathbf{k}, z) \equiv \frac{\delta\rho_m}{\bar{\rho}_m}(\mathbf{k}, z) = T(k, z)\mathcal{R}(\mathbf{k}). \tag{1.231}$$

It is then sufficient to solve Eq. 1.230 for $T(k, z)$. For a matter dominated Universe for example one finds for the growing mode [43]

$$T(k, z) \sim a, \tag{1.232}$$

while for a Universe including matter and dark energy one can find the approximation [204]

$$T(k, z) \sim \frac{5}{2}\frac{a\Omega_m}{\Omega_m^{4/7} - \Omega_\Lambda + (1 + \Omega_m/2)(1 + \Omega_\Lambda/70)}. \tag{1.233}$$

We can again define a power spectrum as the variance of the Fourier modes, the so-called matter power spectrum, $P_\delta(k, z)$, and relate it to the primordial power spectrum, $P_\mathcal{R}$,

$$P_\delta(k, z) = \frac{2\pi^2}{k^3}T^2(k, z)P_\mathcal{R}(k). \tag{1.234}$$

In Fig. 1.5 we show the matter power spectrum at redshift $z = 0$. For scales $k < k_{\rm eq} \approx 0.01\,Mpc^{-1}$, corresponding to the horizon size at radiation-matter equality, the spectrum grows as $P_\delta(k) \sim k$. For smaller scales, $k > k_{\rm eq}$, the spectrum scales as $P_\delta(k) \sim k^{-3}$.

[12] https://camb.info/
[13] http://class-code.net/

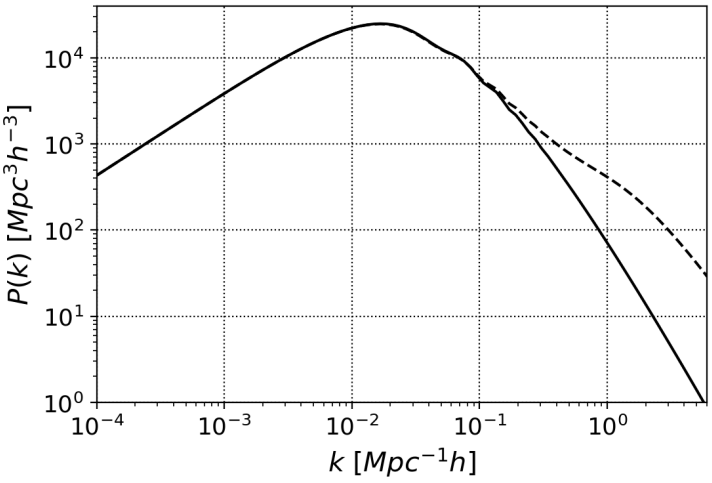

Figure 1.5: The total matter power spectrum at redshift $z = 0$ computed with CAMB. The excess in the dashed line at small scales is caused by the nonlinear evolution of matter, computed with the Mead [236] Halofit version.

THE NON-LINEAR REGIME

Instead of Eq. 1.231 we can more generally write

$$\delta_m(\mathbf{k}, z) = \sum_i \delta_m^{(i)}(\mathbf{k}, z), \tag{1.235}$$

where $\delta_m^{(1)}$ is linear in the initial density field and $\delta_m^{(i)}$ are ith order in the initial density field. One Ansatz made in Einstein-de-Sitter space is taking [43]

$$\delta_m^{(i)}(\mathbf{k}, z) = a^i(z)\delta_m^{(i)}(\mathbf{k}). \tag{1.236}$$

Again, using the Euler equation one finds [131, 43]

$$\delta_m^{(i)}(\mathbf{k}) = \int d^3\mathbf{q}_1 ... \int d^3\mathbf{q}_i \delta \left(\mathbf{k} - \sum_n^i \mathbf{q}_n \right) F_i \left(\mathbf{q}_1, ..., \mathbf{q}_i \right) \delta_m^{(1)} \left(\mathbf{q}_1 \right) ... \delta_m^{(1)} \left(\mathbf{q}_i \right), \tag{1.237}$$

where, for $n = 2$,

$$F_2 \left(\mathbf{k}_1, \mathbf{k}_2 \right) = \frac{5}{7} + \frac{1}{2} \frac{\mathbf{k}_1 \cdot k_2}{k_1 k_2} \left(\frac{k_1}{k_2} + \frac{k_2}{k_1} \right) + \frac{2}{7} \frac{\left(\mathbf{k}_1 \cdot \mathbf{k}_2 \right)^2}{k_1^2 k_2^2}. \tag{1.238}$$

The matter power spectrum can then be written in an expansion, including so-called one-loop corrections,

$$P_\delta(k, z) = \underbrace{T^2(k, z) P_{\rm lin}(k)}_{= P_{\rm lin}(k, z)} + P^{(1)}(k, z), \tag{1.239}$$

where the one-loop correction consists of two terms [43]

$$P^{(1)}(k, z) = 2 \int d^3\mathbf{q} F_2^2(\mathbf{k}-\mathbf{q}, \mathbf{q}) P_{\rm lin}(|\mathbf{k}-\mathbf{q}|, z) P_{\rm lin}(q, z) + 6 \int d^3\mathbf{q} F_3(\mathbf{k}, \mathbf{q}, -\mathbf{q}) P_{\rm lin}(k, z) P_{\rm lin}(q, z).$$

Furthermore, one is able to write down a bispectrum of matter density fields [43]

$$\langle \delta_m(\mathbf{k}_1) \delta_m(\mathbf{k}_2) \delta_m(\mathbf{k}_3) \rangle = \delta(\mathbf{k}_1 + \mathbf{k}_2 + \mathbf{k}_3) \left(2 F_2(\mathbf{k}_1, \mathbf{k}_2) P_\delta(k_1) P_\delta(k_2) + \text{cycl.} \right). \tag{1.240}$$

In practice, fitting formula are used to obtain nonlinear matter power spectra in a given cosmology. Commonly used is the HALOFIT code [348, 362], modeling the power spectrum as a quasi-linear part and a *one-halo* term, caused by self-correlations of dark matter halos,

$$P_\delta(k,z) = P_L(k,z) + P_H(k,z) \tag{1.241}$$

Likewise for the bispectrum, which is modeled by N-body simulations and matched to so-called fitting formulae. These use the effective kernel

$$\hat{F}_2\left(\mathbf{k}_1,\mathbf{k}_2\right) = \frac{5}{7} a\left(n,k_1\right) a\left(n,k_2\right) + \frac{1}{2}\frac{\mathbf{k}_1\cdot k_2}{k_1 k_2}\left(\frac{k_1}{k_2} b\left(n,k_1\right) b\left(n,k_2\right) + \frac{k_2}{k_1}\right) + \tag{1.242}$$

$$+ \frac{2}{7}\frac{\left(\mathbf{k}_1\cdot\mathbf{k}_2\right)^2}{k_1^2 k_2^2} c\left(n,k_1\right) c\left(n,k_2\right), \tag{1.243}$$

where a, b and c are free functions. Those are given for example in Ref. [326] or Ref. [129].

CMB LENSING

Going back to the CMB we will account for the effect that clustering of large-scale structure has gravitationally on CMB photons. The gravitational potentials of the intermediate matter distribution between recombination and observation leave small imprints on the measured temperature and polarization fields, called weak-gravitational lensing. This effect can be modeled with a two-dimensional vector field on the sphere, $\boldsymbol{\alpha}$, which re-maps each line-of-sight direction according to

$$\mathbf{n} \to \mathbf{n}' = \mathbf{n} + \boldsymbol{\alpha}(\mathbf{n}). \tag{1.244}$$

There are several ways to express this remapping, either with potential functions of $\boldsymbol{\alpha}$ or in its linearized form. The remapping function can be decomposed in a longitudal part generated by the lensing potential ϕ and a transversal part generated by the lensing curl-potential Ω

$$\mathbf{n}' = \mathbf{n} + \boldsymbol{\alpha} \equiv \tag{1.245}$$

$$\equiv \mathbf{n} + \nabla\phi + \nabla\times\Omega = \tag{1.246}$$

$$= \begin{pmatrix}\theta\\ \varphi\end{pmatrix} + \begin{pmatrix}\partial_\theta\phi\\ \partial_\varphi\phi\end{pmatrix} + \begin{pmatrix}\partial_\varphi\Omega\\ -\partial_\theta\Omega\end{pmatrix} = \tag{1.247}$$

$$= \mathbf{M}(\mathbf{n})\cdot\mathbf{n}. \tag{1.248}$$

In the second equation we define the cross product $(\nabla\times\Omega)_i \equiv \epsilon_{ij}\partial_j\Omega$, where ϵ_{ij} is the Levi-Civita symbol in two dimensions

$$\epsilon_{ij} = \begin{cases} +1, \text{ for } (i,j) = (1,2) \\ -1, \text{ for } (i,j) = (2,1) \\ 0, \text{ for } i = j \end{cases}. \tag{1.249}$$

At first order in perturbation theory the curl potential can be neglected. Furthermore, in the weak lensing regime we can define the magnification matrix $\mathbf{M}$ as

$$\mathbf{M}(\mathbf{n}) = \begin{pmatrix} \frac{\partial\mathbf{n}'_\theta}{\partial\theta} & \frac{\partial\mathbf{n}'_\theta}{\partial\varphi} \\ \frac{\partial\mathbf{n}'_\varphi}{\partial\theta} & \frac{\partial\mathbf{n}'_\varphi}{\partial\varphi}\end{pmatrix} = \begin{pmatrix} 1+\partial_\theta^2\phi + \partial_\theta\partial_\varphi\Omega & \partial_\theta\partial_\varphi\phi + \partial_\varphi^2\Omega \\ \partial_\theta\partial_\varphi\phi - \partial_\varphi^2\Omega & 1+\partial_\varphi^2\phi - \partial_\theta\partial_\varphi\Omega\end{pmatrix}$$

$$\equiv \begin{pmatrix} 1-\kappa+\gamma_Q & \gamma_U-\omega \\ \gamma_U+\omega & 1-\kappa-\gamma_Q\end{pmatrix}. \tag{1.250}$$

The combination

$$\psi \equiv \mathbf{M} - \mathbf{1} \tag{1.251}$$

is called deformation matrix. All components of this matrix a position dependent on the sky. The herein defined quantities comprise the convergence, κ, the two shear components, γ_Q and γ_U, as well as the rotation component, ω. The convergence causes a magnification of a feature at the last-scattering surface with angular size ϑ to appear at an apparent anular size $(1+\kappa)\vartheta$. The rotation component rotates this feature by ω radians. The shear component γ_Q stretches the feature along the x-axis by $(1+\gamma_Q)$ and compresses it by $(1-\gamma_Q)$ along the y-axis. The γ_U component has a similar effect, but along axes rotated clockwise by $45°$. The latter two are not needed for CMB lensing studies, but they are important quantities in weak lensing of galaxies. Similar to the CMB fields one can decompose the spin-2 fields γ_Q and γ_U shear fields into E- and B-modes as

$$a^{\epsilon}_{\ell m} \pm i a^{\beta}_{\ell m} \equiv \int d\Omega (\gamma_Q \pm i\gamma_U)_{\pm 2} Y_{\ell m}. \tag{1.252}$$

GENERAL RELATIVITY AND CMB LENSING

The first-order perturbed metric in conformal Newtonian gauge in Eq. 1.101 can be written as

$$ds^2 = a^2(\eta)(1-2\Phi)\left[-(1+4\Psi_W)d\eta^2 + dx^i dx_j\right], \tag{1.253}$$

where the Weyl potential $\Psi_W \equiv (\Psi+\Phi)/2$ was introduced. It follows directly that the null geodesics $ds^2 = 0$ only depends on the Weyl potential. With this one can bring the affine parametrization of the null geodesics

$$\frac{dx^\sigma}{d\lambda} + \Gamma^\sigma_{\mu\nu}\frac{dx^\mu}{d\lambda}\frac{dx^\nu}{d\lambda} = 0 \tag{1.254}$$

in the form of three equations determining the light ray perturbation up to first order in Ψ_W [212]

$$\frac{d^2\chi}{d\eta^2} + 2\frac{d\Psi_W}{d\eta} = 0 \tag{1.255}$$

$$\frac{d^2\theta}{d\eta^2} - 2\frac{d\ln S_k(\chi)}{d\chi}\frac{d\theta}{d\eta} + \frac{2}{S_k(\chi)^2}\frac{d\Psi_W}{d\theta} = 0 \tag{1.256}$$

$$\frac{d^2\varphi}{d\eta^2} - 2\frac{d\ln S_k(\chi)}{d\chi}\frac{d\varphi}{d\eta} + \frac{2}{S_k(\chi)^2}\frac{1}{\sin^2\theta}\frac{d\Psi_W}{d\eta} = 0, \tag{1.257}$$

where the light ray focuses at $x_i = 0$. The first equation characterizes the time delay or radial displacement of CMB photons due to lensing

$$d\chi = -d\eta - 2\Psi_W(\eta)d\eta. \tag{1.258}$$

This effect is small in the CMB due to geometric considerations and it being coherent on large scales $\sim 1\,Mpc$ and hence only relevant for cross-power spectra on the order of $0.1\,\%$ [167]. The latter two equations can be summarized to one equation for the differential deflection angle $d\boldsymbol{\beta}$ experiencing a potential angular gradient $\nabla\Psi_W$ during a conformal time $d\eta$

$$d\boldsymbol{\beta}(\mathbf{x},\eta) = -\frac{2}{S_k(\chi)}\nabla\Psi_W(\mathbf{x},\eta)d\eta, \tag{1.259}$$

where χ is the radial distance to the source.

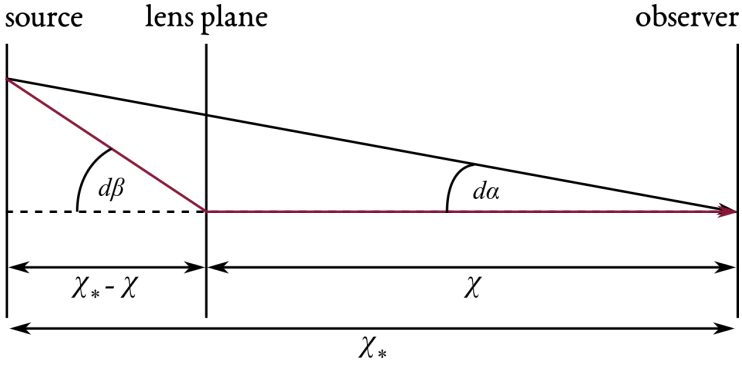

Figure 1.6: The schematic view of the relation in Eq. 1.260, showing the relation between the apparent deflection angle, $d\alpha$, and the deflection angle of the photon at the lensing event, $d\beta$, in the lensing plane at a distance χ from center of the coordinate system, $\mathbf{x} = 0$.

As illustrated in Fig. 1.6, the transverse shift of a light ray emitted at a time $\eta = 0$, arriving at the center of the coordinate system, $\mathbf{x} = 0$, at time η_* from a direction $\mathbf{n}$, resulting from a single deflection at time η, is then given by

$$S_k(\chi_*) d\boldsymbol{\alpha}(0, \eta_*) = S_k(\chi_* - \chi) d\boldsymbol{\beta}(\mathbf{n}(\chi_* - \chi), \eta), \tag{1.260}$$

where $d\boldsymbol{\alpha}$ is the angular shift of the light ray at the origin. We can then compute the deflection angle at the origin, $\mathbf{x} = 0$, and time of observation, η_0, in sky-direction, $\mathbf{n}$, by integrating back in comoving distance, $\chi = \eta_0 - \eta$,

$$\boldsymbol{\alpha}(\mathbf{n}) = -2 \int_0^{\chi_*} d\chi \frac{S_k(\chi_* - \chi)}{S_k(\chi_*) S_k(\chi)} \nabla \Psi_W(\mathbf{s}(\mathbf{n}, \eta), \eta), \tag{1.261}$$

where $\mathbf{s}(\mathbf{n}, \eta)$ is a parametrization of the perturbed photon geodesic reaching the observer at $\mathbf{x} = 0$ from direction $\mathbf{n}$. This is general for all cases where light is emitted at a distance χ_* and lensed by an intermediate gravitational potential Ψ_W. One can define a window function like

$$W(\chi) = \int_0^{\chi} d\chi' \frac{S_k(\chi' - \chi)}{S_k(\chi') S_k(\chi)} f(\chi') \tag{1.262}$$

and obtain a more general expression for the deflection angle

$$\boldsymbol{\alpha}(\mathbf{n}) = -2 \int_0^{\chi_*} d\chi W(\chi) \nabla \Psi_W(\mathbf{s}(\mathbf{n}, \chi), \eta), \tag{1.263}$$

to allow for a custom distribution function of light sources $f(\chi)$, which is normalized to one. For the CMB this is simply the Thompson visibility function, which can be approximated by a delta function at the look-back time of last-scattering

$$f(\chi) = \delta(\chi_* - \chi). \tag{1.264}$$

It is useful to discretize this equation [90]

$$\boldsymbol{\alpha}(\mathbf{n}) = -2 \sum_j W(\chi_j) \int_{\eta_j - \Delta\chi/2}^{\chi_j + \Delta\chi/2} d\chi \nabla \Psi_W(\chi \mathbf{n}_j, \eta), \tag{1.265}$$

where we assume that the photon geodesic to be given as a straight, unperturbed line, $\chi \mathbf{n}_j$, in each discretized interval $[\chi_j - \Delta\chi/2, \chi_j + \Delta\chi/2]$. This is called *Born approximation*. The $\mathbf{n}_j$ for each time interval can be obtained with so-called ray-tracing (see Sec. 5.2). Taking this interval to be the whole age of the Universe, we obtain the usual Born-approximated deflection angle of CMB photons

$$\boldsymbol{\alpha}(\mathbf{n}) = -2 \int_0^{\chi_*} d\chi W(\chi) \nabla \Psi_W(\chi \mathbf{n}, \eta). \tag{1.266}$$

The corresponding lensing potential is then given by

$$\phi(\mathbf{n}) = -2\int_0^{\chi_*} d\chi W(\chi)\Psi_W(\chi\mathbf{n},\eta), \tag{1.267}$$

which is a (weighted) integral of the gravitational potential along the line-of-sight.

CMB LENSING POTENTIAL POWER SPECTRUM

Again, the physical information lies in the statistical properties of the lensing fields. To make this apparent, one can compute spherical harmonic coefficients and their power spectrum of the lensing potential, ϕ,

$$\phi_{LM} = \int d\Omega Y^*_{LM}\phi(\mathbf{n}) \tag{1.268}$$

$$\langle\phi^*_{LM}\phi_{L'M'}\rangle = \delta_{LL'}\delta_{MM'}C_L^{\phi\phi}. \tag{1.269}$$

Assuming a statistically homogeneous gravitational potential with power spectrum

$$\langle\Psi_W(\mathbf{k},\eta)\Psi_W(\mathbf{k}',\eta')\rangle \equiv \frac{2\pi^2}{k}P_\Psi(k,\eta,\eta')\delta(\mathbf{k}-\mathbf{k}'), \tag{1.270}$$

one can write [212]

$$C_L^{\phi\phi} = 16\pi\int\frac{dk}{k}\int_0^{\chi_*}d\chi\int_0^{\chi_*}d\chi' P_\Psi(k,\eta_0-\chi,\eta_0-\chi')j_L(k\chi)j_L(k\chi')W(\chi)W(\chi'). \tag{1.271}$$

LIMBER APPROXIMATION

For a slowly varying integration kernel one can make use of the equation

$$\int dk k^2 j_L(k\chi)j_L(k\chi') = \frac{\pi}{2\chi}\delta(\chi-\chi'), \tag{1.272}$$

such that the lensing power spectrum in Limber approximation [216] can be written as a simple line-of-sight integral

$$C_L^{\phi\phi} \approx \frac{8\pi^2}{L^3}\int_0^{\chi_*} d\chi\,\chi P_\Psi((L+1/2)/\chi,\eta(\chi))W(\chi)W(\chi). \tag{1.273}$$

Effectively the Limber approximation removes the mixing of contributions of the matter power spectrum at different redshifts. Furthermore one can relate the power spectrum P_Ψ to the previously introduced (comoving) matter power spectrum, using the Poisson equation [25] in the case of a flat and matter dominated Universe

$$\Delta\Psi_W = \frac{1}{2}a^2\bar{\rho}\delta = \frac{3}{2}H_0^2\Omega_m\frac{\delta}{a}, \tag{1.274}$$

which leads to

$$P_\Psi(k,\eta) = \frac{9\Omega_m^2(\eta)H_0^4}{8\pi^2a^2k}P_\delta(k,\eta). \tag{1.275}$$

This mean the lensing potential power spectrum is a probe of the statistical properties of large-scale structure formation. Its relation with the matter power spectrum is shown in Fig. 1.7. This figure also shows the lensing power spectrum for our fiducial cosmological model of Tab. 1.5.

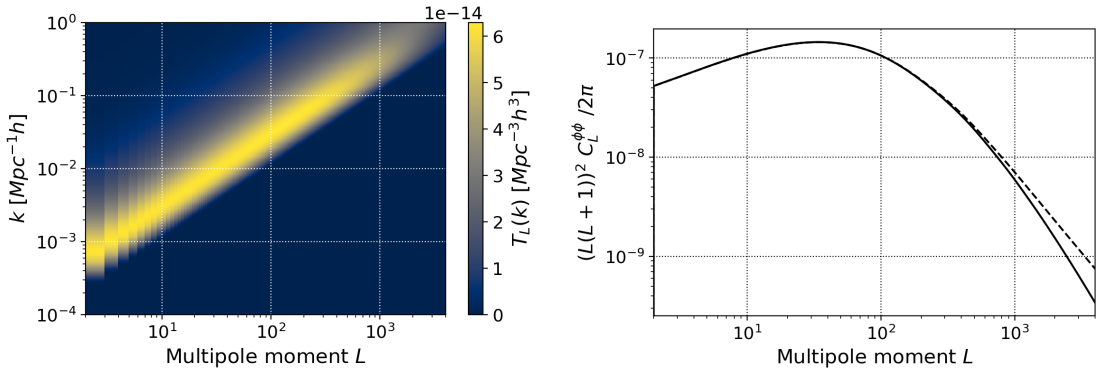

Figure 1.7: The lensing power spectrum computed in the Limber approximation using the linear (nonlinear) matter power spectrum of Fig. 1.5 in the solid (dashed) line on the right hand side. The left hand side shows the contribution of each k-mode of $P(k, z = 0)$ to the L-mode of $C_L^{\phi\phi}$ by plotting $T_L(k)$, which is defined by $(L(L+1))^2\, C_L^{\phi\phi}\, 2\pi \equiv \sum_k T_L(k) P(k, z = 0)$.

EFFECT ON THE CMB

We can now model the effect of weak gravitational lensing on CMB observables. We are working with the three observables with well-defined spin T and ${}_{\pm}X = Q \pm iU$ and are going to denote lensed quantities with a tilde, $\tilde{\bullet}$. Using Eq. 1.263 (and neglecting the curl potential for now) we can write the lensed quantities in terms of the unlensed ones as

$$\tilde{T}(\mathbf{n}) = T(\mathbf{n} + \nabla\phi(\mathbf{n})) \tag{1.276}$$

$${}_{\pm}\tilde{X}(\mathbf{n}) = {}_{\pm}X(\mathbf{n} + \nabla\phi(\mathbf{n})). \tag{1.277}$$

Since the deflection is small we can perform a Taylor expansion around the unperturbed line-of-sight $\mathbf{n}$ up to second order in ϕ

$$\tilde{T}(\mathbf{n}) = T(\mathbf{n}) + \nabla_i T(\mathbf{n})\nabla^i\phi(\mathbf{n}) + \frac{1}{2}\left(\nabla_i\nabla_j T(\mathbf{n})\right)\nabla^i\phi(\mathbf{n})\nabla^j\phi(\mathbf{n}) + \mathcal{O}(\phi^3) \tag{1.278}$$

$${}_{\pm}\tilde{X}(\mathbf{n}) = {}_{\pm}X(\mathbf{n}) + \nabla_i {}_{\pm}X(\mathbf{n})\nabla^i\phi(\mathbf{n}) + \frac{1}{2}\left(\nabla_i\nabla_j {}_{\pm}X(\mathbf{n})\right)\nabla^i\phi(\mathbf{n})\nabla^j\phi(\mathbf{n}) + \mathcal{O}(\phi^3).$$

To obtain expressions for the power spectra one has to perform spherical harmonic transformation. We find for the harmonic coefficients

$$\tilde{a}^T_{\ell m} = a^T_{\ell m} + \sum_{\ell' m'}\sum_{LM}\phi_{LM}a^T_{\ell' m'}\left(F_{\ell m LM\ell' m'} + \frac{1}{2}\phi^*_{L'M'}G_{\ell m LM\ell' m' L' M'}\right) \tag{1.279}$$

$${}_{\pm2}\tilde{a}_{\ell m} = {}_{\pm2}a_{\ell m} + \sum_{\ell' m'}\sum_{LM}\phi_{LM}\,{}_{\pm2}a_{\ell' m'}\left({}_{\pm2}F_{\ell m LM\ell' m'} + \frac{1}{2}\phi^*_{L'M'}\,{}_{\pm2}G_{\ell m LM\ell' m' L' M'}\right).$$

This makes the convolution lensing introduces in the harmonic coefficients of the CMB fields apparent, with convolution kernels given by (expressions for G can be found in Ref. [166])

$${}_{\pm s}F_{\ell m LM\ell' m'} = \int d\Omega\, {}_{\pm s}Y^*_{\ell m}\left(\nabla^i Y_{LM}\right)\left(\nabla_i\, {}_{\pm s}Y_{\ell' m'}\right) = \tag{1.280}$$

$$= (-1)^m\, {}_{\pm s}F_{\ell L\ell'}\begin{pmatrix}\ell & L & \ell'\\ -m & M & m'\end{pmatrix} \tag{1.281}$$

$${}_{\pm s}G_{\ell m LM\ell' m' L' M'} = \int d\Omega\, {}_{\pm s}Y^*_{\ell m}\left(\nabla^i Y_{LM}\right)\left(\nabla^j Y^*_{L'M'}\right)\left(\nabla_i\nabla_j\, {}_{\pm s}Y_{\ell' m'}\right), \tag{1.282}$$

and the definitions of the reduced kernel

$$ {}_{\pm s}F_{\ell L\ell'} \equiv \frac{1}{2}\left(-\ell(\ell+1)+L(L+1)+\ell'(\ell'+1)\right)\times \tag{1.283} $$

$$ \times\sqrt{\frac{(2\ell+1)(2L+1)(2\ell'+1)}{4\pi}}\begin{pmatrix}\ell & L & \ell'\\ \pm s & 0 & \mp s\end{pmatrix}, \tag{1.284} $$

This function has the useful properties

$$ F_{\ell L\ell'} \equiv {}_0F_{\ell L\ell'} \tag{1.285} $$

$$ {}_{\mp s}F_{\ell L\ell'} = (-1)^{\ell+L+\ell'}\,{}_{\pm s}F_{\ell L\ell'}. \tag{1.286} $$

The first order equations in ϕ for the parity eigenstates E and B follow as

$$ \tilde{a}^E_{\ell m} = a^E_{\ell m} + \sum_{\ell' m'}\sum_{LM}\phi_{LM}(-1)^m\,{}_2F_{\ell L\ell'}\begin{pmatrix}\ell & L & \ell'\\ m & -M & -m'\end{pmatrix}\left(\epsilon_{\ell L\ell'}a^E_{\ell' m'} + \beta_{\ell L\ell'}ia^B_{\ell' m'}\right) $$

$$ \tilde{a}^B_{\ell m} = a^B_{\ell m} + \sum_{\ell' m'}\sum_{LM}\phi_{LM}(-1)^m\,{}_2F_{\ell L\ell'}\begin{pmatrix}\ell & L & \ell'\\ m & -M & -m'\end{pmatrix}\left(\epsilon_{\ell L\ell'}a^B_{\ell' m'} - \beta_{\ell L\ell'}ia^E_{\ell' m'}\right), $$

where the tensors ϵ and β are nonzero only when the sum $\ell + L + \ell'$ is odd or even, respectively,

$$ \epsilon_{\ell L\ell'} \equiv \frac{1+(-1)^{\ell+L+\ell'}}{2} \tag{1.287} $$

$$ \beta_{\ell L\ell'} \equiv \frac{1-(-1)^{\ell+L+\ell'}}{2}. \tag{1.288} $$

One can see that gravitational lensing mixes the flavors of polarization parity fields E and B. Especially the B-mode signal, that is not directly sourced by the power-dominating density perturbations, can still get a significant contribution from the leaking E-mode signal through the convolution with the CMB lensing potential.

LENSED CMB POWER SPECTRA

One direct implication of these equations are the lensed CMB power spectra in terms of the unlensed ones and the lensing potential power spectra. By calculating the diagonal terms in $\left\langle a^{X\,*}_{\ell m}a^Y_{\ell' m'}\right\rangle$ one obtains [166]

$$ \tilde{C}^{TT}_\ell = (1-\ell(\ell+1)R)C^{TT}_\ell + \sum_{L\ell'}\frac{F^2_{\ell L\ell'}}{2\ell+1}C^{\phi\phi}_L C^{TT}_{\ell'} \tag{1.289} $$

$$ \tilde{C}^{TE}_\ell = (1-(\ell^2+\ell-2)R)C^{TE}_\ell + \sum_{L\ell'}\frac{F_{\ell L\ell'}\,{}_2F_{\ell L\ell'}}{2\ell+1}C^{\phi\phi}_L C^{TE}_{\ell'} \tag{1.290} $$

$$ \tilde{C}^{EE}_\ell = (1-(\ell^2+\ell-4)R)C^{EE}_\ell + \frac{1}{2}\sum_{L\ell'}\frac{{}_2F^2_{\ell L\ell'}}{2\ell+1}C^{\phi\phi}_L\left(\epsilon_{\ell L\ell'}C^{EE}_{\ell'} + \beta_{\ell L\ell'}C^{BB}_{\ell'}\right) \tag{1.291} $$

$$ \tilde{C}^{TB}_\ell = (1-(\ell^2+\ell-2)R)C^{TB}_\ell + \sum_{L\ell'}\frac{F_{\ell L\ell'}\,{}_2F_{\ell L\ell'}}{2\ell+1}C^{\phi\phi}_L C^{TB}_{\ell'} \tag{1.292} $$

$$ \tilde{C}^{EB}_\ell = (1-(\ell^2+\ell-4)R)C^{EB}_\ell + \frac{1}{2}\sum_{L\ell'}\frac{{}_2F^2_{\ell L\ell'}}{2\ell+1}C^{\phi\phi}_L\left(\epsilon_{\ell L\ell'}C^{EB}_{\ell'} - \beta_{\ell L\ell'}C^{EB}_{\ell'}\right) \tag{1.293} $$

$$ \tilde{C}^{BB}_\ell = (1-(\ell^2+\ell-4)R)C^{BB}_\ell + \frac{1}{2}\sum_{L\ell'}\frac{{}_2F^2_{\ell L\ell'}}{2\ell+1}C^{\phi\phi}_L\left(\beta_{\ell L\ell'}C^{EE}_{\ell'} + \epsilon_{\ell L\ell'}C^{BB}_{\ell'}\right), \tag{1.294} $$

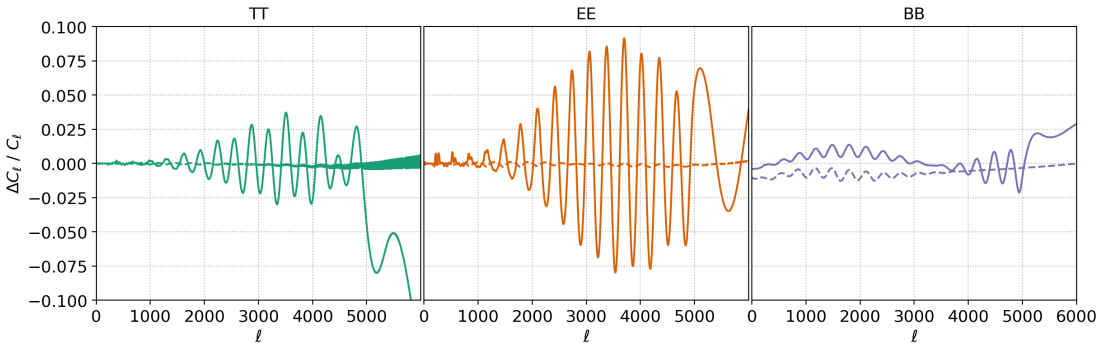

Figure 1.8: The relative difference of lensed power spectra C_ℓ^{TT}, C_ℓ^{EE} and C_ℓ^{BB} using different methods for their computation. In the solid lines show the relative error made by the second order Taylor series expansion derived in this section, while the dashed lines show the relative error made by using the flat-sky approximation (see Appendix B.1)

where

$$R \equiv \frac{1}{2}\sum_L L(L+1)\frac{2L+1}{4\pi}C_L^{\phi\phi}. \tag{1.295}$$

These equations give the correct answer only on the 10% level [212]. For more accurate results one has to take all orders of the series expansion of Eq. 1.278 into account, as implemented in CAMB [72]. Fig. 1.8 shows the accuracy of the equations derived above compared to the exact, non-perturbative computation. The error can reach up to 9% for EE at small scales. For TT and BB the error is smaller on the level of 1% and 2%, respectively. Another issue is the question of truncating the sums in these equation by setting a $\ell_{\rm max}$. Due to the spread of the convolution kernel, setting an $\ell_{\rm max}$ gives accurate results of the lensed power spectra up to $\ell_{\rm max}/2$.

The final CMB power spectra, including the effect of gravitational lensing, are shown in Fig. 1.11. It shows (slightly) the smoothing of the acoustic oscillation peaks and the transfer of power to smaller scales in the temperature and E-mode power spectra. In the B-mode spectrum, gravitational lensing induces small-scale power peaking around $\ell = 1000$, which spoils the density-perturbation-free CMB measurement through the B-mode power spectrum.

CMB LENSING CROSS-CORRELATIONS

One of the great successes of the cosmological concordance model, ΛCDM, is its ability to predict the formation of large-scale structure (LSS) by evolving perturbations in the early matter density distribution up until very late times. Assuming this model, it is possible to infer the matter power spectrum using different cosmological probes of the matter distribution in the Universe, starting at the CMB at an redshift of $z \approx 1100$ and going to galaxy clustering surveys at low redshifts [367, 71]. This allows to produce summary plots such as Fig. 1.9, showing measurements of the matter power spectrum at $z = 0$ from Planck CMB data, galaxy clustering and Lyα data from SDSS [306] as well as DES cosmic shear data.

LSS surveys usually probe the projected matter distribution in the Universe projected along some distance within the line-of-sight, sensitive to different times in the history of gravitational instability and LSS formation. Formally, it can be written as

$$\delta(\mathbf{n}) = \int d\chi W(\chi)\delta(\chi\mathbf{n}, \eta = \eta_0 - \chi), \tag{1.296}$$

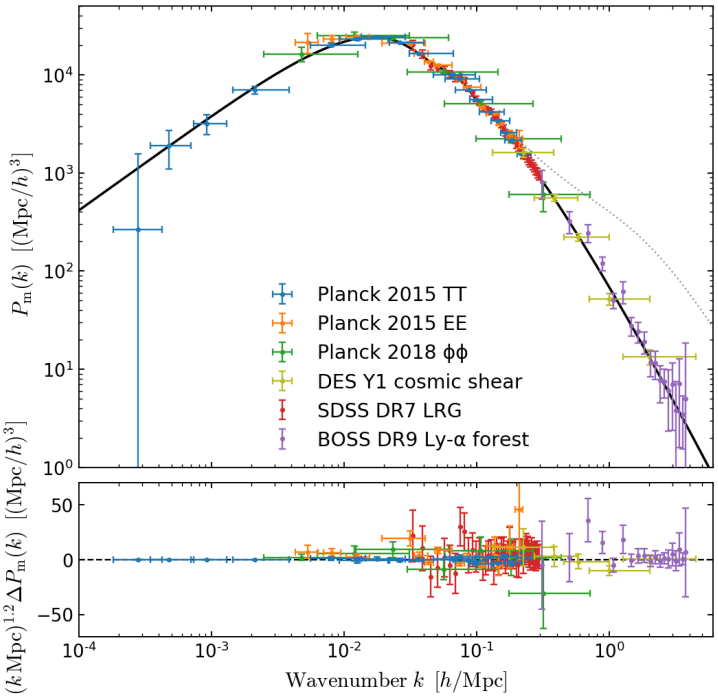

Figure 1.9: Measurements of the linear matter power spectrum at $z = 0$ using Planck data at the largest scales, SDSS galaxy clustering at intermediate scales and Lyα clustering from SDSS as well as cosmic shear data from DES on small scales. The Planck 2018 bets-fit ΛCDM model is used for the theoretical computation (black solid line). Non linear effects are shown in the dotted line. The figure is taken from Ref. [71].

making use of the Born approximation. The kernel or selection function $W(\chi)$ takes into account the sensitivity of different LSS surveys to the matter distribution at different times. Using the Limber approximation, we can write the cross-correlation power spectrum of two LSS surveys A and B as

$$C_L^{AB} = \int \frac{d\chi}{\chi^2} W^A(\chi) W^B(\chi) P_\delta \left(\frac{L+1/2}{\chi}, \eta(\chi) \right). \tag{1.297}$$

Since CMB photons travel from redshift $z \approx 1100$ up until today at $z = 0$, they are sensitive to the entire cosmological history of gravitational instability and formation of LSS. Hence, the signal will be correlated with the many other probes of the matter distribution at different times in the history of our Universe. Form Eqs. 1.262 and 1.275 follow a kernel for the CMB lensing convergence κ as

$$W^{\kappa_{\rm CMB}}(\chi) = \frac{3}{2}\Omega_m \frac{H_0^2}{a} \chi^2 \frac{\chi_* - \chi}{\chi_* \chi} \quad (\chi < \chi_*). \tag{1.298}$$

COSMIC SHEAR Light from any luminous matter is experiencing distortions by the gravitational field of the foreground matter distribution, much like we have seen for the special case of the CMB. In the case of galaxy lensing the lensing observables are inferred from images of galaxies. One way of doing this is by measuring their shear. One can describe the shape of a galaxy by its intrinsic ellipticity ϵ^I. Cosmic shear then modifies this ellipticity of the so-called source galaxy, which is given in terms of the local lens parameters κ and $\gamma = \gamma_U + i\gamma_Q$ as

$$\epsilon = \frac{\epsilon^I + g(z)}{1 + g^*(z)\epsilon^I} \quad , |g| < 1, \tag{1.299}$$

where $g = \frac{\gamma(z)}{1-\kappa(z)}$ [330]. This relation is usually approximated by the simple sum of intrinsic shear and extrinsic or cosmic shear

$$\epsilon = \epsilon^I + \gamma. \tag{1.300}$$

If there is no preferred orientation of the intrinsic ellipticity of galaxies, $\langle \epsilon^I \rangle$, then the measurement of the galaxy ellipticity is an unbiased estimator of the cosmic shear. This is not the case in the presence of intrinsic alignment, which is a major bias in cosmic shear measurements and subject to ongoing efforts to properly account for it (see references in [189]). These include theoretical modeling, e.g. assuming that the observed shape of a galaxy is in part determined by its dark matter halo's shape as in Refs. [70, 52], or N-body and hydro-dynamical simulations. The source of intrinsic alignment is the gravitational interaction between galaxies and surrounding tidal fields. Generally, an observed ellipticity will be subject to multiplicative and additive biases from astrophysical and instrumental systematics [152]

$$\hat{\epsilon} = (1+m)\epsilon + c. \tag{1.301}$$

The former can in principle be calibrated in cross-correlation with CMB lensing [91, 320].

One can use the kernel introduced in Eq. 1.262 to get the convergence of a population of source galaxies with probability distribution $f(\chi)$. It follows that

$$W^{\kappa_{\rm galaxy}}(\chi) = \frac{3}{2}\Omega_m \frac{H_0^2}{a}\chi^2 \int_\chi^\infty \chi' \frac{\chi'-\chi}{\chi'\chi} f(\chi'), \tag{1.302}$$

which is similar to the kernel of CMB lensing, but instead of a single source χ_* there is a distribution of source galaxies $f(\chi)d\chi = f(z)dz$. The resulting power spectrum of the convergence can be directly related to the power spectrum of the shear E-mode (cf. Eq. 1.252) [166]

$$C_L^{\epsilon\epsilon} = \left(1 - \frac{2}{L(L+1)}\right) C_L^{\kappa\kappa}. \tag{1.303}$$

Following Refs. [70, 52] one can formulate a model for intrinsic alignment given

$$W^{\rm IA}(\chi) = -\frac{3}{2}\Omega_m \frac{H_0^2}{a} A^{\rm IA} \frac{2C_1}{(1+z)D(z)} f(\chi), \tag{1.304}$$

where $D(z)$ is the linear growth function and $C_1 = 5\cdot 10^{-14} h^{-2} M_\odot^{-1} Mpc^3$, obtained by matching with observations [52]. $A^{\rm IA}$ is a dimensionless constant. In practice $f(\chi)$ is determined with photometric redshifts by fitting the measured flux in a given band to a template SED, which is another major source of systematics. The information on the redshift distribution of source galaxies allows for a tomographic view of the large-scale structure by redshift binning the cosmic shear measurements.

The variance of the measured shear power spectrum, $\hat{C}_L^{\kappa\kappa}$, can be written in Gaussian approximation as

$$\mathrm{var}\left(\hat{C}_L^{\epsilon\epsilon}\right) = \frac{1}{2L+1}\frac{1}{f_{\rm sky}}\left(C_L^{\epsilon\epsilon} + \frac{\sigma_\epsilon^2}{2\overline{n}}\right)^2, \tag{1.305}$$

where the last term within the brackets is the so-called shot noise, arising from the finite number density of lensing galaxies, $\overline{n}$, which is proportional to the variance of intrinsic ellipticities, $\sigma_\epsilon^2 = \langle |\epsilon^I|^2 \rangle$.

The current generation of surveys targeting cosmic shear include the Dark Energy Survey[14] (DES), the Kilo-Degree Survey[15] (KiDS) and the Hyper-Supreme Cam[16] (HSC) project. Future projects include the Large Synoptic Survey Telescope (LSST) on the ground and two space-based missions, Euclid[17] (ESA) and WFIRST[18] (NASA).

[14] https://www.darkenergysurvey.org/
[15] https://kids.strw.leidenuniv.nl/
[16] https://www.naoj.org/Projects/HSC/HSCProject.html
[17] https://sci.esa.int/euclid/
[18] https://www.nasa.gov/wfirst

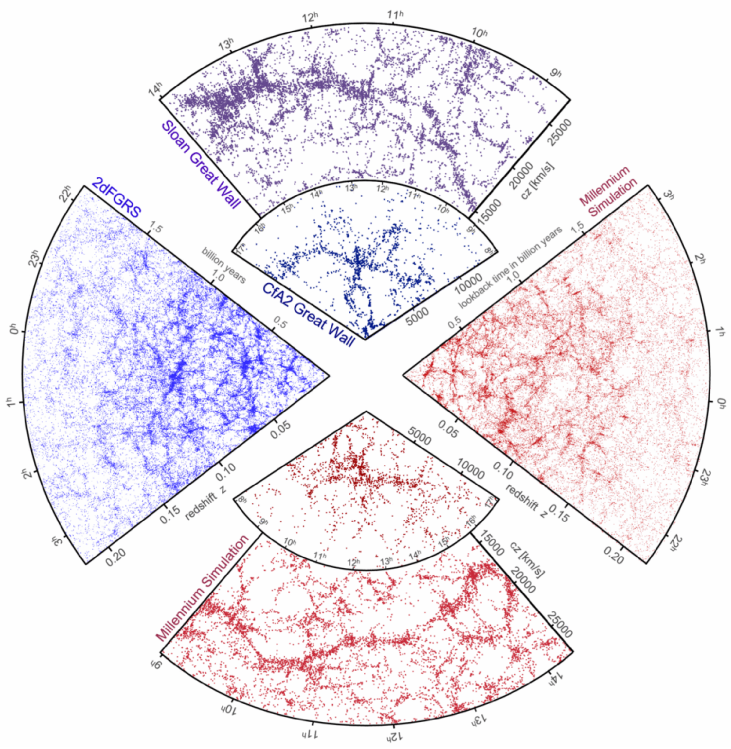

Figure 1.10: The galaxy distribution, obtained from spectroscopic redshift surveys (CfA2 and SDSS) in blue and from massive N-body simulations (the Millenium simulation) in red, where semianalytic techniques were used to simulate the formation of galaxies within dark matter halos. The qualitative similarity between real data and simulation is apparent. The figure is taken from Ref. [350].

Photons from both the CMB and luminous galaxies are affected by some of the same intervening matter distribution, causing a non-zero cross-correlation between CMB lensing and cosmic shear. It has the advantage of increased signal-to-noise and possibly lower systematics compared to the auto-correlation spectra. Cross-correlation between CMB lensing and cosmic shear has been successfully measured in Refs. [144, 191, 220, 339, 146, 147], which also includes cross-correlation between CMB lensing convergence from polarization data of POLARBEAR and cosmic shear from HSC [255]. The highest significance of such a measurement was achieved by the DES and SPT collaborations, by cross-correlating first-year DES cosmic shear data with CMB lensing from SPT and Planck [260].

GALAXY CLUSTERING Another major cosmological probe is the measurement of galaxy locations across the sky in photometric or spectroscopic redshift surveys. Fig. 1.10 shows two examples of such galaxy surveys, CfA2 and SDSS, as well as the galaxy distribution obtained by simulating the galaxy formation within the evolving dark matter distribution of the Millenium simulation, a large-volume, high-resolution N-body simulation of dark matter particles [351].

One important aspect of galaxy surveys is that observables such as the density contrasts of galaxies or clusters are biased tracers of the underlying matter density field, $\delta(\mathbf{x})$, which was realized when observing different correlation functions of galaxies and clusters [180]. Formally the galaxy density contrast can be written at any given time as

$$\delta_g(\mathbf{x}) = \frac{n_g(\mathbf{x})}{\overline{n}_g} - 1 = b_1\delta(\mathbf{x}) + \frac{b_2}{2}\delta^2(\mathbf{x}) + ..., \tag{1.306}$$

where $n_g(\mathbf{x})$ and $\overline{n}_g$ are the local and the mean number density of galaxies. The parameters b_1 and b_2 are so-called local bias parameters, used in a subset of bias models called local-in-matter-density (LIMD) bias [94]. It follows for the galaxy auto-power spectrum, $P_{gg}(k)$, and the galaxy-matter cross-

power spectrum, $P_{gm}(k)$ at leading order that

$$P_{gg}(k) = (2\pi)^2\delta(\mathbf{k}-\mathbf{k}')\left\langle\delta_g(\mathbf{k})\delta_g(\mathbf{k}')\right\rangle = b_1^2 P_\delta(k) \tag{1.307}$$

$$P_{gm}(k) = (2\pi)^2\delta(\mathbf{k}-\mathbf{k}')\left\langle\delta_g(\mathbf{k})\delta(\mathbf{k}')\right\rangle = b_1 P_\delta(k), \tag{1.308}$$

where higher order terms will arise from nonlinear evolution of both matter and the bias. To compute angular (cross-)power spectra, the associated weight function follows directly as

$$W^g(\chi) = b_1(z)\frac{\frac{dN}{dz}}{\int dz' \frac{dN}{dz'}}, \tag{1.309}$$

where dN/dz is the number of galaxies surveyed depending on redshift.

1.7 COSMOLOGICAL PARAMETERS AND POWER SPECTRA

We have now seen the main effects influencing the shape of the measured CMB power spectra, originating in density and tensor perturbations in the early plasma, as well as scattering and gravitational effects between us and recombination. The standard cosmological model, ΛCDM depends on six parameters. Additionally we allow for 3 additional parameters, M_ν, $N_{\rm eff}$ and r. In my thesis I will mainly focus on the nine following parameters,

A_s, the normalization of the primordial scalar power spectrum,
n_s, the tilt of the primordial scalar power spectrum,
Ω_b, the energy density of baryons today,
$\Omega_{\rm cdm}$, the energy density of cold dark matter today,
Ω_Λ, the dark energy density today and
$\tau_{\rm reio.}$, the optical depth to reionization as well as
M_ν, the total mass of (non-sterile) neutrinos,
$N_{\rm eff}$, the effective number of neutrino species and
r, the tensor-to-scalar ratio.

If not mentioned otherwise we use the cosmology from the best-fit ΛCDM model from Planck (`TT`, `TE`, `EE+lowP+lensing+ext`) [279] with the updated estimation of the optical depth to reionization of Ref. [294]. The best fit values and their associated 68 % confidence limits are given in Tab. 1.5. Fig. 1.11 shows the power spectra C_ℓ^{TT}, C_ℓ^{EE} and C_ℓ^{BB}, corresponding to our fiducial cosmological model. It also distinguishes the different contributions from density or tensor perturbations and gravitational lensing.

EFFECTS FROM $N_{\rm EFF}$

A higher number of effective relativistic degrees of freedom, $N_{\rm eff}$, while fixing the energy density of all other species, shifts the time of radiation-to-matter equality to later times. This causes a suppression of the CMB peaks. Fig. 1.12 show the temperature, E-mode and B-mode auto-power spectra for varying values of $N_{\rm eff}$. Keeping the time of radiation-to-matter equality fixed, i.e. by increasing the energy density of other species by the same amount as the radiation density, the main effect of $N_{\rm eff}$ is the increase of the diffusion scale at the time of decoupling. Hence a larger $N_{\rm eff}$ increases the damping at high-ℓ of CMB power spectra. Furthermore, with higher $N_{\rm eff}$ photons are affected by a denser neutrino fluid, reinforcing the effect of gravitational lensing on the CMB, i.e. smoothing of the acoustic peaks [365].

Parameter	Value (1σ-error)
$\Omega_b h^2$	0.02230 ± 0.00014
$\Omega_{cdm} h^2$	0.1188 ± 0.0010
H_0 [km s^{-1} Mpc^{-1}]	67.74 ± 0.46
$\tau_{\text{reio.}}$	0.055 ± 0.009
$\ln\left(10^{10} A_s\right)$	3.064 ± 0.023
n_s	0.9667 ± 0.0040
M_ν [meV]	0
N_{eff}	3.04
r	0.001

Table 1.5: The cosmological parameters used as the fiducial cosmology throughout this thesis. The ΛCDM parameters are taken from the parameters estimation results of [279, 294], given in terms of their best-fit value and 68 % confidence limits.

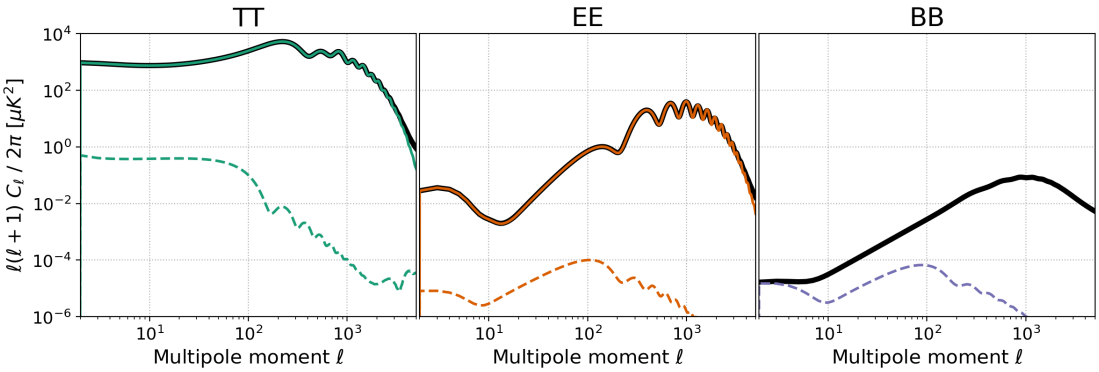

Figure 1.11: The TT, EE and BB power spectra of the fiducial cosmology in Tab. 1.5. The total power spectrum, including the effect of gravitational lensing, is shown in the thick black line. The colored solid and dashed lines show the contributions from scalar and tensor perturbations to the primordial, unlensed power spectrum, respectively.

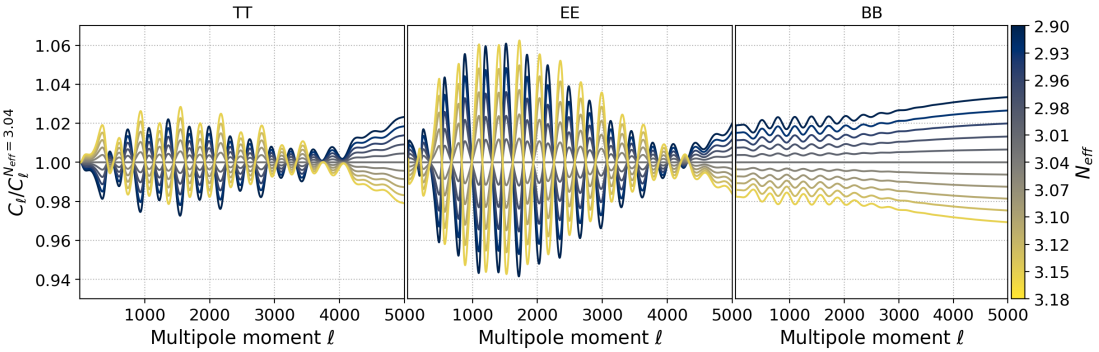

Figure 1.12: The effect of changing effective number of neutrino species, N_{eff}, on the lensed CMB power spectra, computed with CAMB.

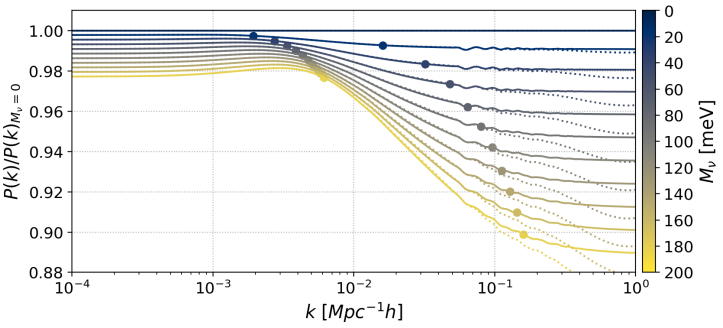

Figure 1.13: The effect the total neutrino mass parameter has on the matter power spectrum. We also show the respective characteristic scales k_{nr} and $k_{fs} > k_{nr}$ in the circles along the curves. The dotted lines show the same, but including nonlinear effects in the matter power spectrum (neutrinos not accounted in the nonlinear computation). CAMB was used in the creation of this figure.

EFFECTS FROM M_ν

As we have seen Neutrinos behave like radiation at early, primordial times, while their mass becomes relevant relatively late when the Universe is sufficiently cold. Prior to becoming non-relativistic they free-stream out of potential wells, causing an erasing of primordial fluctuations of the neutrino density at scales $k > k_{\rm nr}$, where $k_{\rm nr}$ is the scale corresponding to the Hubble horizon at the time neutrinos become non-relativistic. On scales larger than $k_{\rm nr}$ the neutrino density contrast contributes together with cold dark matter and baryons to the total matter contrast δ_m. Hence, we have for the matter power spectrum today [210]

$$P(k) \sim \left\langle \left(\frac{\Omega_{cdm}\delta_{cdm} + \Omega_b\delta_b + \Omega_\nu\delta_\nu}{\Omega_{cdm} + \Omega_b + \Omega_\nu} \right)^2 \right\rangle = \begin{cases} \left\langle \delta^2_{cdm} \right\rangle, & \text{if } k < k_{\rm nr} \\ \left[1 - \Omega_\nu/\Omega_m\right]^2 \left\langle \delta^2_{cdm} \right\rangle, & \text{if } k \gg k_{\rm nr} \end{cases} .$$

Additionally cold dark matter and baryon perturbations grow slower in a Universe with massive neutrinos, since in both cases, massive or massless, the neutrino energy density contributes to the expansion rate. Neutrinos remain relatively smooth above the free-streaming scale $k_{\rm fs}$. This scale is related to the typical distance a neutrino travels during a Hubble time and is given by [210]

$$k_{\rm fs} \equiv \sqrt{\frac{3}{2}} \frac{aH}{v_\nu} \tag{1.310}$$

where v_ν is the mean neutrino velocity. This explains Fig. 1.13, i.e. a suppression of the matter power spectrum at scales $k > k_{\rm fs}$ compared to a matter power spectrum in a Universe with massless neutrinos and also compared to scales $k < k_{\rm nr}$. Hence, measuring the free streaming scale in the matter power spectrum is the most direct way to measure the total neutrino mass. Measuring the matter power spectrum at late times is hence most sensitive to a neutrino mass measurement. This includes the measurement of the CMB lensing potential. Constraining the total mass of neutrinos requires breaking degenaracies, primarily caused by the cold dark matter energy density (see Fig. 1.13), and measuring the amplitude of primordial fluctuations A_s. The latter measurement allows to normalize the matter power spectrum at high redshifts. However, a measurement of A_s in the CMB anisotropies above $\ell = 20$ is degenerate with $\tau_{\rm reio.}$, which is limiting the constraining power for the mass of neutrinos [11]. Fig. 1.14 depicts the effect of massive neutrinos on the CMB lensing power spectrum compared to a Universe with massless neutrinos, showing the suppression of small-scale lensing with increasing total neutrino mass.

Weaker constraints of the total neutrino mass can come from the primordial TT and EE power spectra. For sufficiently high masses neutrinos become non-relativistic before recombination, impacting the location of acoustic peaks and the damping scale.

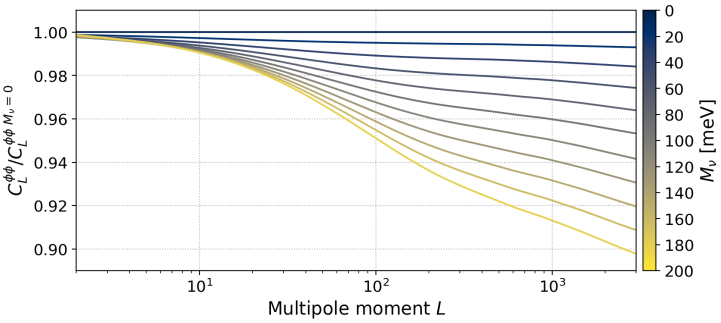

Figure 1.14: The effect the total neutrino mass parameter has on the CMB lensing power spectrum. CAMB was used in the creation of this figure.

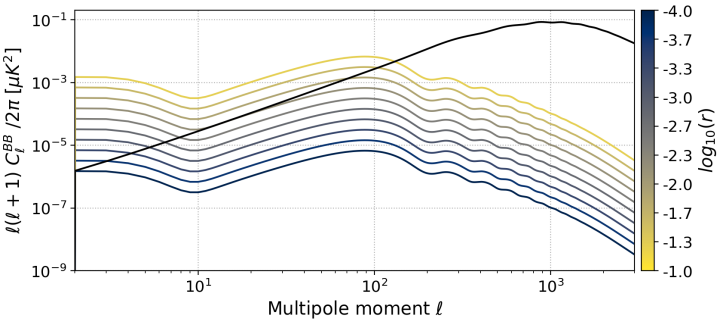

Figure 1.15: The effect of r is mainly linearly scaling the primordial B-mode power spectrum. The B-mode from density perturbations through the conversion of E-modes due to the weak gravitational lensing effect is shown in black.

EFFECTS FROM PRIMORDIAL GRAVITATIONAL WAVES

Fig. 1.11 clearly shows the difficulty of measuring tensor perturbations in temperature and E-mode power spectra, which was until recently the major driver in constraining r [281]. After measuring the large-scale temperature and E-mode spectra to cosmic variance limit, constraints on the tensor-to-scalar ratio, r, will come from the large-scale B-mode power spectrum. Making use of Eq. 1.213 we can show its dependence on r in Fig. 1.15. Besides r, constraints on Inflation physics come from measurements of the spectral index of density perturbations, n_s, and the Hubble parameter, H_0.

1.8 FOREGROUNDS

In this section I will review the most prominent sky components besides the CMB that contribute to the signal in microwave observations.

1.8.1 A NOTE ON UNITS

To relate between the various units of temperature and brightness used in different fields of astronomy, we start by the observable quantity in CMB measurements, the map of the sky, $\mathbf{m}$, made by a single detector, which is given by [276]

$$\mathbf{m} = C \int d\nu b(\nu) dT_\nu, \tag{1.311}$$

where dT_ν is the differential intensity or surface brightness of the sky signal. The parameter C is a calibration factor, relating the brightness measured in W to the temperature of the CMB measured in K_{CMB}. The surface brightness is integrated over a normalized window function, $b(\nu)$, which is called the (detector) bandpass. The surface brightness of the CMB is given by the Planck spectrum Eq. 1.77, now given explicitly in SI units

$$T_\nu = B_\nu(T_{\mathrm{CMB}}) = \frac{2h\nu^3/c^2}{e^{h\nu/kT_{\mathrm{CMB}}} - 1} \quad \left[\frac{\mathrm{W}}{\mathrm{Hz\,m^2\,sr}}\right], \tag{1.312}$$

and its differential then results in

$$dT_\nu = \frac{\partial B_\nu}{\partial T} dT_{\mathrm{CMB}}. \tag{1.313}$$

A convenient unit, which is heavily used in radio astronomy is the Rayleigh-Jeans brightness temperature, which is defined to be the temperature of the Rayleigh-Jeans spectrum that would result in a given surface brightness, T_ν,

$$dT_\nu = 2k_B\nu^2 dT_{\mathrm{RJ}}, \tag{1.314}$$

The Rayleigh-Jeans spectrum is obtained as the limit of the Planck spectrum if $h\nu \ll k_B T$. The brightness temperature is often denoted with a unit $\mathrm{K_{RJ}}$. A third common unit when dealing with the brightness of point sources is the Jansky, Jy, where

$$1\,\mathrm{Jy} = 10^{-26}\,\frac{\mathrm{W}}{\mathrm{Hz\,m^2}}. \tag{1.315}$$

Hence, intensity can be measured in Jy/sr. Two different telescopes do not measure the same intensity and brightness temperature. The flux, defined as

$$S_\nu = T_\nu \cdot \Omega_{\mathrm{beam}} \tag{1.316}$$

is independent of the telescope, where Ω_{beam} is the (effective) beam area.

1.8.2 GALACTIC FOREGROUNDS

One major foreground to CMB measurements originates from the emission of the Milky Way. Thankfully, our Galaxy is transparent to CMB photons, however, especially in the vicinity of the galactic plane, its own emission in the sub-Millimeter spectrum can massively outshine the CMB. Moreover, the emission of some components in the Milky Way are known to be polarized. This section is based in parts on Ref. [285].

SYNCHROTRON

Relativistic electrons in cosmic rays spiral in the galactic magnetic field (GMF) emitting synchrotron radiation which dominates the sky temperature at frequencies < 10 GHz [282]. We can model its brightness temperature with a power-law spectrum

$$T_\nu^{\text{sync.}} = A_{\text{sync.}} \left(\frac{\nu}{\nu_{ref}} \right)^{\beta_{\text{sync.}}} . \tag{1.317}$$

At 1 GHz the spectral index is $\beta_{\text{sync.}} \approx -2.7$ and steepens at higher frequencies to $\beta_{\text{sync.}} \approx -3.0$ [282]. It is polarized, being a strong foreground to CMB polarization up to frequencies of 100 GHz. In the frequency range between 2.3 and 33 GHz the spectral index can go down to $\beta_{\text{sync}} \approx -3.2$ [200] for polarization. Furthermore, the spectral index varies depending on the direction on the sky, between values of -4.4 and -2.5.

ANOMALOUS MICROWAVE EMISSION (AME)

Anomalous Microwave Emission (AME) is measured to be more intense at frequencies $10 - 60$ GHz. It can be, at least in part, explained as dipole radiation from spinning interstellar dust grains [100]. Its polarization properties are relatively unknown. At frequencies ~ 30 GHz, where the AME is peaking, the polarization fraction is on the level of $\sim 1\%$, which corresponds to an equivalent of $r = 0.2$ in primordial B-mode power at this frequency [313]. The ongoing low-frequency experiments S-PASS [64], C-BASS[19] and QUIJOTE[20] [221] will improve constraints on the polarized AME. The spectral energy density is usually modeled with the help of templates using codes such as SpDust [21] [10].

FREE-FREE EMISSION / BREMSSTRAHLUNG

Radiation from collisions of electrons with ions are called free-free emission or bremsstrahlung. Its spectrum is well known and can be modeled as [99]

$$T_\nu^{\text{free-free}} = 10^6 T_e (1 - e^{-\tau}) \tag{1.318}$$

$$\tau = 0.05468 T_e^{-3/2} \left(\frac{\nu}{10^9\, Hz} \right)^{-2} EM g_{\text{ff}} \tag{1.319}$$

$$g_{\text{ff}} = \log \left(\exp \left(5.96 - \frac{\sqrt{3}}{\pi} \log \left(\frac{\nu}{10^9\ \text{Hz}} \left(\frac{T_e}{10^4} \right)^{-3/2} \right) \right) + e \right) , \tag{1.320}$$

with two free parameters, the electron temperature, T_e, and the integrated squared electron density along a line of sight, EM.

THERMAL DUST

The most prominent galactic foreground is the emission from thermal dust, since it is the dominating foreground at frequencies larger than 100 GHz. It is the emission of the solid phase of the inter-stellar medium (ISM), consisting of Carbon, Silicon, Magnesium, Iron and Oxide, mainly forming silicate and amorphous carbon molecules such as graphite (C), enstatite ($(\text{Mg, Fe})\text{SiO}_3$), olivine ($(\text{Mg, Fe})_2\text{SiO}_4$), silicon carbide (SiC), iron (Fe) and magnetude Fe_3O_4 [177, 101]. These molecules form the dust grains with sizes of $0.005 - 0.25\ \mu$m [234]. Dust grains are not spherical, consequently

[19] https://www2.physics.ox.ac.uk/research/c-bass

[20] http://www.iac.es/proyecto/cmb/pages/en/quijote-cmb-experiment.php

[21] http://pages.jh.edu/~yalihai1/spdust/spdust.html

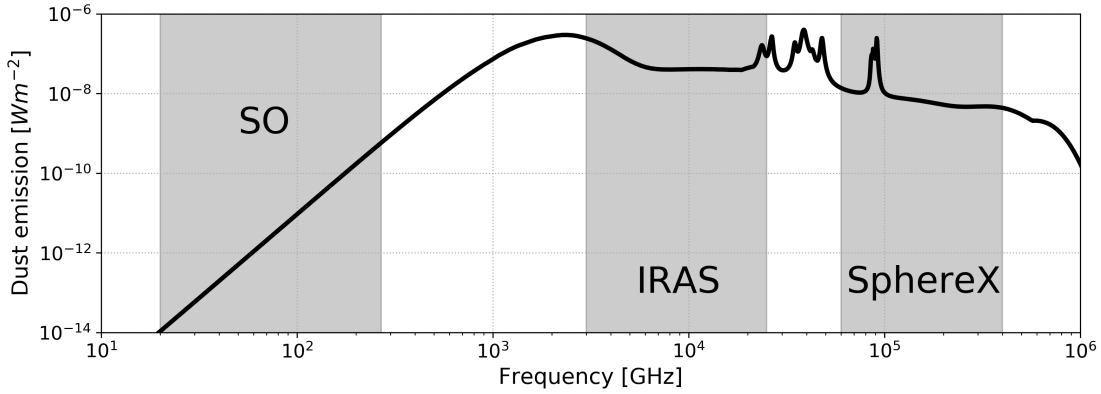

Figure 1.16: Figure showing the dust SED between 10 GHz and 1000 THz computed with the model of [83] using the DustEM code. The frequency coverage of three experiments, Simons Obervatory (SO), IRAS and SphereX are shown in grey bands.

are electric dipoles and at least partially aligned with the galactic magnetic field [93]. The absorption and scattering of light by dust grains is called extinction. Extinction is relevant for light at sub-mm wavelengths, i.e. from ultraviolet to near-infrared-emission [101]. Dust grains are heated by stellar photons, which causes them to radiate in mid-infrared to milimeter-wavelengths. Their emission spectrum is shown in Fig. 1.16, which is computed with the DustEM[22] code using modeling of dust grains [83]. The alignment of the asymmetric dust grains along the galactic magnetic field causes polarization of the thermal dust.

Following Refs.[208, 396, 295] we can model the Stokes parameters of thermal dust emission due to optically thin ISM as line-of-sight integrals given by

$$T = \int d\chi\, n_d B_\nu(T_d) C_{\rm avg} \left(1 - p_0 \left(\cos^2\gamma - \frac{2}{3}\right)\right) \tag{1.321}$$

$$Q = \int d\chi\, n_d B_\nu(T_d) C_{\rm avg} p_0 \cos(2\phi)\cos^2\gamma \tag{1.322}$$

$$U = \int d\chi\, n_d B_\nu(T_d) C_{\rm avg} p_0 \sin(2\phi)\cos^2\gamma, \tag{1.323}$$

where $C_{\rm avg}$ is the average dust absorption cross section and n_d is the dust grain number density. The angle γ is determined by the local orientation of the galactic magnetic field with respect to the plane, (x, y), perpendicular to the line of sight. The (x, y) coordinate system also defines the Q and U Stokes parameters and the associated local polarization angle ϕ. The integration is done along the z-axis, the line-of-sight with line element ds. Furthermore, the parameter p_0 is the intrinsic polarization fraction and in this model given by

$$p_0 = \frac{C_{\rm pol}}{C_{\rm avg}} \frac{3}{2} \left(\langle \cos^2\beta \rangle - \frac{1}{3}\right) = \frac{C_{\rm pol}}{C_{\rm avg}} R, \tag{1.324}$$

where β is the angle between the spin axis of the rotating grain and the galactic magnetic field, R is the so-called Rayleigh reduction factor and $C_{\rm pol}$ is the dust polarization absorption cross section. The

[22] https://www.ias.u-psud.fr/DUSTEM/

absorption cross sections depend on the shape of the dust grains given by

$$C_{\text{avg}} = \frac{2C_\perp + C_\parallel}{3} \tag{1.325}$$

$$C_{\text{pol}} = \begin{cases} \frac{C_\perp - C_\parallel}{2} & \text{(oblate grains)} \\ \frac{C_\parallel - C_\perp}{4} & \text{(prolate grains)} \end{cases}, \tag{1.326}$$

where $C_\perp$ and $C_\parallel$ are the absorption cross sections perpendicular or parallel to the dust grain symmetry axis. For spherical dust grains $C_\perp = C_\parallel$. We have the relations for the frequency-dependent dust optical depth [277]

$$d\tau_\nu = n_d C_{\text{avg}} ds = \sigma_\nu n_H ds, \tag{1.327}$$

where σ_ν is the frequency-dependent dust opacity and n_H is the gas density of hydrogen atoms due to its coexistence with dust grains within the ISM. The column gas density is then just the line-of-sight integrated density

$$N_H(\mathbf{n}) = \int ds n_H(\mathbf{x}). \tag{1.328}$$

Important observables in context of the polarized diffuse foreground emission are the local polarization fraction

$$p \equiv \frac{\sqrt{Q^2 + U^2}}{T} \tag{1.329}$$

and the local polarization angle, defined in the HEALPix (+) or IAU (−) convention, respectively,

$$\phi_\pm = \frac{1}{2} \arctan\left(\frac{\pm U}{Q}\right). \tag{1.330}$$

Note that $p_0 \neq p$ Furthermore, it is useful to define the polarization angle dispersion relation

$$\Delta\phi^2(\mathbf{n}, \delta) \equiv \int d^2\Omega' \delta(|\mathbf{n}'| - \delta) \left(\phi(\mathbf{n}) - \phi(\mathbf{n} + \mathbf{n}')\right), \tag{1.331}$$

which can be related to the structure of the (plane-of-the-sky projected) galactic magnetic field [155].

A simple model of the spectral emissivity of (polarized) thermal dust is a modified black-body spectrum with temperature T_d and spectral parameter β_d

$$T_\nu^{\text{dust}} = A_d \left(\frac{\nu}{\nu_{\text{ref}}}\right)^{\beta_d - 2} \frac{B_\nu(T_d)}{B_{\nu_{\text{ref}}}(T_d)}, \tag{1.332}$$

i.e. $\sigma_\nu \sim (\nu/\nu_{\text{ref}})^{\beta_d - 2}$. In sky regions with low galactic foreground contamination the spectrum of thermal galactic dust emission is strongly degenerate with the signal from dusty extra-galactic sources, the cosmic infrared background (CIB). Improved modelling accounts for multiple dust components, each having a modified black-body spectrum [237], taking into account the distinct optical properties of silicate and carbon molecules.

The Planck satellite mission (see Sec. 4.1) has measured the polarized galactic dust foreground extensively, however, with low signal-to-noise at high galactic latitudes. The mean spectral indices are found to be $\beta_d = 1.51 \pm 0.01$ for total intensity and $\beta_d = 1.53 \pm 0.02$ for polarization with significant variations across the sky, while the mean dust temperature is measured at $T_d \approx 19.6\ K$ [295, 289].

The maximum polarization fraction was found to be $p_{\max} = 19.8 \pm 0.7\%$ [292], setting a lower limit to the intrinsic polarization fraction p_0. Furthermore, there is an anti-correlation between the polarization fraction for a given column density and the total value of the column density, N_H, which is consistent with models where photon interactions cause the dust grain alignment. The additionally observed anti-correlation between polarization fraction and the polarization angle dispersion is likely caused by field rotation along the line of sight [292].

Planck also observed a decorrelation of thermal dust emission between different frequency channels. The $B-mode$ cross-power spectra of thermal dust between frequency channels ν_1 and ν_2 can be modeled as

$$\ell(\ell+1)C_\ell^{BB}[\nu_1,\nu_2] = A_\ell^2 \left(\frac{\nu_1\nu_2}{\nu_{\text{ref}}^2}\right)^{\beta_d-2} \frac{B_{\nu_1}}{B_{\nu_{\text{ref}}}} \frac{B_{\nu_2}}{B_{\nu_{\text{ref}}}} f_d(\delta_d,\nu_1,\nu_2), \tag{1.333}$$

with the decorrelation parameter, δ_d, defined in the function

$$f_d(\delta_d,\nu_1,\nu_2) \equiv \exp\left(-\delta_d \left(\ln(\nu_1/\nu_2)\right)^2\right). \tag{1.334}$$

Alternatively, one can define the correlation ratio

$$\mathcal{R}_\ell^{XY} = \frac{C_\ell^{XY}[\nu_1,\nu_2]}{\sqrt{C_\ell^{XY}[\nu_1,\nu_1]C_\ell^{XY}[\nu_2,\nu_2]}}. \tag{1.335}$$

Refs. [289, 336] find that the Planck data is consistent with no dust B-mode decorrelation between frequency channels. This property is a crucial factor in a future primordial B-mode detection and these current upper-levels seem to allow for a measurement of $r > 0.01$ [289]. Note that frequency decorrelation can arise due to variations of the spectral indices across the sky, if not accounted for in the analysis, as well as along the line of sight.

... AND MORE

Besides these major foregrounds, there is emission from carbon-oxide (CO) in our galaxy in form of emission lines, which are usually avoided by CMB bandpasses, or zodiacal light at low frequencies [95].

1.8.3 EXTRAGALACTIC FOREGROUNDS

COSMIC INFRARED BACKGROUND (CIB)

The cosmic infrared background (CIB) consists of stellar dust of the sum of all galaxy luminosities integrated over the entire evolution of the Universe [182]. Hence it is a powerful probe of a broad redshift range. It is spectrally degenerate with the emission of our own galaxy. Hence spatial information has to be used to distinguish between both, galactic dust and the CIB [209]. It is, however, not only a nuisance for CMB measurements and component separation, but can also be a source of information, e.g. in order to improve cosmological parameter constraints [229] or to remove cosmic variance from CMB lensing [207, 230] (see also Sec. 3.3).

Effects like galaxy intrinsic alignment could cause a net polarization of the summed individual galaxies' dust emission, but the effect is expected to be not detectable for current CMB experiment sensitivities [355, 154, 117].

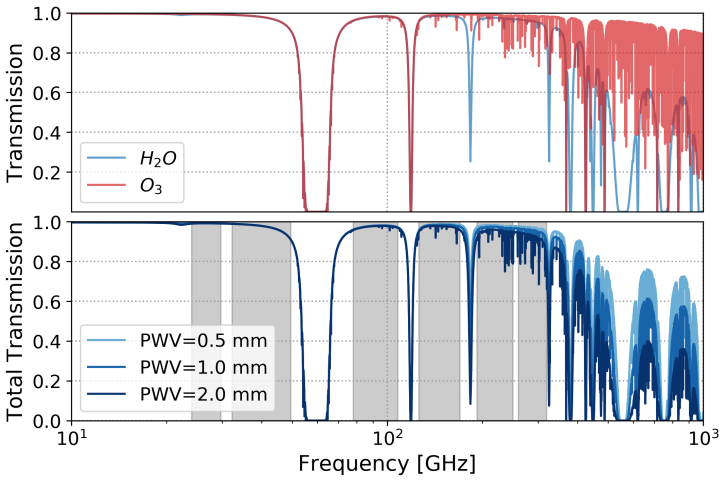

Figure 1.17: The atmosphere transmission coefficient for different components, water vapor, H_2O and ozone, O_3, and different levels of the PWV. The curves are simulation produced with the AM atmospheric modeling code [263], assuming conditions as in the Atacama desert in Chile. The anticipated observation bands of the Simons Observatory (see Sec. 4.5.1) are shown in grey bands.

RADIO AND SUB-MM SOURCES

Some point sources emit in the radio-millimetric domain and are usually masked out in the data analysis, if detected. However, unresolved point sources can still bias CMB observables. They can also emit polarized light, hence being an important foreground for lensing reconstruction from polarized CMB data. Details on the treatment of polarized point sources in the analysis of data are given in Sec. 4.3.3.

1.8.4 ATMOSPHERIC FOREGROUNDS

A major foreground for ground-based CMB observations is emission from the earth's atmosphere, causing correlated noise between close detectors, causing low-frequency noise in CMB power-spectra. That's why CMB observatories are situated at high altitudes, where the atmosphere is especially thin. The relevant parameter is the Precipitable Water Vapor (PWV), indicating the water vapor in a column of the atmosphere. Fig. 1.17 shows the transmission spectra of the atmosphere at the Atacama desert in Chile, produced with the AM atmospheric modeling code[23] [263]. Rotational and vibrational excited states of aerosols such as water or ozone absorb light in the for us interesting microwave spectrum.

[23] https://www.cfa.harvard.edu/~spaine/am/

Ihr sagt "das ist dunkel". Ich stellte euch eine Wolke vor die Sonne. Aber seht wie die Ränder der Wolke glühen und licht werden!

Friedrich Wilhelm Nietzsche

2 Reconstructing CMB Lensing

Measuring the effect of weak gravitational lensing in the CMB allows for a direct measurement of the line-of-sight-projected gravitational potential and hence a way to measure a two-dimensional map of the matter distribution in our sky. A pathway to a measurement like that is by capitalizing of the particular statistical properties which CMB lensing imprints in the maps of CMB temperature and polarisation anisotropies. I will first formally review those statistical properties, before I will describe my work on the implementation of a CMB lensing reconstruction method using quadratic estimators.

2.1 THE STATISTICS OF THE LENSED CMB

One can go beyond the diagonal part of the two-point function we investigated in Sec. 1.6.2 and don't discard the non-diagonal terms of the two-point function of the lensed CMB fields. First, we introduce the deflection operator $\mathbf{D}$ defined by its action on a field defined on the sphere, $X(\mathbf{n})$,

$$\mathbf{D}_{\mathbf{d}} X(\mathbf{n}) = X(\mathbf{n} + \mathbf{d}(\mathbf{n})). \tag{2.1}$$

It is linear

$$\mathbf{D}_{\mathbf{d}}(X + Y)(\mathbf{n}) = \mathbf{D}_{\mathbf{d}} X(\mathbf{n}) + \mathbf{D}_{\mathbf{d}} Y(\mathbf{n}) \tag{2.2}$$

and can be written in its integral-form as

$$\mathbf{D}_{\mathbf{d}} X(\mathbf{n}) = \int d\Omega' \delta(\mathbf{n} + \mathbf{d}(\mathbf{n}) - \mathbf{n}') X(\mathbf{n}'). \tag{2.3}$$

The inverse deflection operator, however, is not $\mathbf{D}_{\mathbf{d}}^{-1} \neq \mathbf{D}_{-\mathbf{d}}$, but

$$\mathbf{D}_{\mathbf{d}}^{-1} \equiv \mathbf{D}_{-\mathbf{d}'}, \tag{2.4}$$

where the new deflection $\mathbf{d}'$ is implicitly given by [66]

$$\mathbf{d}(\mathbf{n}) = \mathbf{d}'(\mathbf{n} + \mathbf{d}(\mathbf{n})). \tag{2.5}$$

This is because deflected positions are computed with respect to the lensing deflection field at the initial position, hence the inverse mapping has to be computed not at the new, deflected position, but at the initial one. This simplifies at first order to the naive relation for the inverse deflection

$$\mathbf{d}(\mathbf{n}) = \mathbf{d}'(\mathbf{n}) + \left(\mathbf{M}'(\mathbf{n}) - \mathbf{1}\right) \cdot \mathbf{d}(\mathbf{n}) + \mathcal{O}(\phi^3). \tag{2.6}$$

We can define a vector including temperature and polarization fields

$$\mathbf{s}(\mathbf{n}) = (T(\mathbf{n}), Q(\mathbf{n}), U(\mathbf{n}))^T, \tag{2.7}$$

which is *not* a vector field on the sphere, and its corresponding vector in harmonic-space

$$\mathbf{s}_{\ell m} = (a^T_{\ell m}, a^E_{\ell m}, a^B_{\ell m})^T. \tag{2.8}$$

One can transform between the two spaces via

$$\mathbf{s}_{\ell m} = \mathbf{Y}^\dagger \cdot \mathbf{s}(\mathbf{n}) \tag{2.9}$$
$$\mathbf{s}(\mathbf{n}) = \mathbf{Y} \cdot \mathbf{s}_{\ell m}, \tag{2.10}$$

defining the operators

$$\mathbf{Y} \cdot \mathbf{s}_{\ell m} \equiv \sum_{\ell m} \begin{pmatrix} Y_{\ell m} & 0 & 0 \\ 0 & \frac{1}{2}({}_2Y_{\ell m} + {}_{-2}Y_{\ell m}) & \frac{i}{2}({}_2Y_{\ell m} - {}_{-2}Y_{\ell m}) \\ 0 & -\frac{i}{2}({}_2Y_{\ell m} - {}_{-2}Y_{\ell m}) & \frac{1}{2}({}_2Y_{\ell m} + {}_{-2}Y_{\ell m}) \end{pmatrix} \cdot \mathbf{s}_{\ell m} \tag{2.11}$$

$$\mathbf{Y}^\dagger \cdot \mathbf{s}(\mathbf{n}) \equiv \int d\Omega \begin{pmatrix} Y^*_{\ell m} & 0 & 0 \\ 0 & \frac{1}{2}({}_2Y^*_{\ell m} + {}_{-2}Y^*_{\ell m}) & \frac{i}{2}({}_2Y^*_{\ell m} - {}_{-2}Y^*_{\ell m}) \\ 0 & -\frac{i}{2}({}_2Y^*_{\ell m} - {}_{-2}Y^*_{\ell m}) & \frac{1}{2}({}_2Y^*_{\ell m} + {}_{-2}Y^*_{\ell m}) \end{pmatrix} \cdot \mathbf{s}(\mathbf{n}). \tag{2.12}$$

The purpose of the $\mathbf{Y}$- and $\mathbf{Y}^\dagger$-operators is to perform (inverse) spherical harmonic transformations on the CMB fields, $\mathbf{s}$. To first order in ϕ one can make use of the Taylor expansion to first order in Eq. 1.279 and get explicit expressions for $\mathbf{D}$ acting in pixel-space on $\mathbf{s}(\mathbf{n})$

$$\mathbf{D}(\mathbf{n}) = \mathbf{1} + \nabla_i \phi(\mathbf{n}) \nabla^i \tag{2.13}$$

and in harmonic space on $\mathbf{s}_{\ell m}$

$$\begin{aligned} \mathbf{D}_{\ell m \ell' m'} &= \delta_{\ell m \ell' m'} + \sum_{LM} \phi_{LM} (-1)^m \begin{pmatrix} \ell & L & \ell' \\ m & -M & -m' \end{pmatrix} \begin{pmatrix} F_{\ell L \ell'} & 0 & 0 \\ 0 & {}_2F_{\ell L \ell'} \epsilon_{\ell L \ell'} & i\,{}_2F_{\ell L \ell'} \beta_{\ell L \ell'} \\ 0 & -i\,{}_2F_{\ell L \ell'} \beta_{\ell L \ell'} & {}_2F_{\ell L \ell'} \epsilon_{\ell L \ell'} \end{pmatrix} \\ &= \delta_{\ell m \ell' m'} + \sum_{LM} \phi_{LM} (-1)^m \begin{pmatrix} \ell & L & \ell' \\ m & -M & -m' \end{pmatrix} \mathbf{F}_{\ell L \ell'}. \end{aligned} \tag{2.14}$$

In the following we will omit the subscripts and parantheses of $\mathbf{s}$ when it is clear which basis it is referred to. Additional to the notation of lensed CMB fields denoted by a tilde, $\tilde{\bullet}$, we are going to use a hat, $\hat{\bullet}$, for measured quantities. The latter will mean in the following that a noise field, $\mathbf{n}$, is added to the lensed and beam-convolved CMB fields

$$\hat{\mathbf{s}} \equiv \mathbf{B}\tilde{\mathbf{s}} + \mathbf{n}, \tag{2.15}$$

which has the covariance

$$\left\langle \mathbf{n}\mathbf{n}^\dagger \right\rangle \equiv \mathbf{N}. \tag{2.16}$$

We also introduced an operator $\mathbf{B}$, which convolves subsequent fields with the instrument's beam function and other imaginable transfer functions arising from the lower level data analysis. In the following we assume orthonormality of this operator, $\mathbf{B}\mathbf{B}^\dagger = \mathbf{1}$.

The unlensed CMB signals are assumed to be Gaussian and we suppose from hereon that the Universe is statistically parity-invariant. For the unlensed CMB power spectra follows then that their covariance is diagonal in harmonic space and given by

$$\mathbf{C} \equiv \left\langle \mathbf{s}\mathbf{s}^\dagger \right\rangle = \delta_{\ell\ell'}\delta_{mm'} \underbrace{\begin{pmatrix} C_\ell^{TT} & C_\ell^{TE} & 0 \\ C_\ell^{TE} & C_\ell^{EE} & 0 \\ 0 & 0 & C_\ell^{BB} \end{pmatrix}}_{\mathbf{C}_\ell} \tag{2.17}$$

. Occasionally it is instructive and useful to assume the noise to be white, i.e. diagonal in pixel- as well as harmonic space and uncorrelated with the CMB signal,

$$\mathbf{N} = \delta_{\ell\ell'}\delta_{mm'} \begin{pmatrix} N_\ell^{TT} & 0 & 0 \\ 0 & N_\ell^{EE} & N_\ell^{EB} \\ 0 & N_\ell^{EB} & N_\ell^{BB} \end{pmatrix} \tag{2.18}$$

.

The covariance matrix of the measured CMB can then be written as (e.g. [157])

$$\hat{\mathbf{C}} = \langle \hat{\mathbf{s}}\hat{\mathbf{s}}^\dagger \rangle = \mathbf{B}\tilde{\mathbf{C}}\mathbf{B}^\dagger + \mathbf{N} = \mathbf{B}\mathbf{D}\mathbf{C}\mathbf{D}^\dagger\mathbf{B}^\dagger + \mathbf{N}. \tag{2.19}$$

2.2 THE LIKELIHOOD PROBLEM

With a fixed large-scale structure realization the measured CMB is Gaussian if the primordial CMB and the noise is Gaussian. This can be used to write down a Gaussian likelihood of the measured CMB, $\hat{\mathbf{s}}$, given a deflection field, ϕ,

$$-2\ln\mathcal{L}(\hat{\mathbf{s}}|\phi) = \ln\det\hat{\mathbf{C}} + \hat{\mathbf{s}}^\dagger\hat{\mathbf{C}}^{-1}\hat{\mathbf{s}}. \tag{2.20}$$

The gradient of the (log-)likelihood, its derivative with respect to $\phi^\dagger$, is given by

$$\frac{\delta(-2\ln\mathcal{L})}{\delta\phi^\dagger_{LM}} = \mathrm{Tr}\left(\hat{\mathbf{C}}^{-1}\mathbf{B}\frac{\delta\mathbf{D}}{\delta\phi^\dagger_{LM}}\mathbf{C}\mathbf{D}^\dagger\mathbf{B}^\dagger\right) + \mathrm{Tr}\left(\hat{\mathbf{C}}^{-1}\mathbf{B}\mathbf{D}^\dagger\mathbf{C}\frac{\delta\mathbf{D}^\dagger}{\delta\phi^\dagger_{LM}}\mathbf{B}^\dagger\right) \tag{2.21}$$

$$- \hat{\mathbf{s}}^\dagger\hat{\mathbf{C}}^{-1}\mathbf{B}\frac{\delta\mathbf{D}}{\delta\phi^\dagger_{LM}}\mathbf{C}\mathbf{D}^\dagger\mathbf{B}^\dagger\hat{\mathbf{C}}^{-1}\hat{\mathbf{s}} - \hat{\mathbf{s}}^\dagger\hat{\mathbf{C}}^{-1}\mathbf{B}\mathbf{D}\mathbf{C}\frac{\delta\mathbf{D}^\dagger}{\delta\phi^\dagger_{LM}}\mathbf{B}^\dagger\hat{\mathbf{C}}^{-1}\hat{\mathbf{s}}, \tag{2.22}$$

using the matrix relations

$$(\ln\det\mathbf{M})' = \mathrm{Tr}(\mathbf{M}^{-1}\mathbf{M}') \tag{2.23}$$

$$(\mathbf{M}^{-1})' = -\mathbf{M}^{-1}\mathbf{M}'\mathbf{M}^{-1}. \tag{2.24}$$

One can identify the total-power-filtered signal vector (which is similar to Wiener-filtering up to an application of the signal covariance) in the likelihood above

$$\bar{\mathbf{s}} \equiv \mathbf{B}^\dagger\hat{\mathbf{C}}^{-1}\hat{\mathbf{s}}. \tag{2.25}$$

The posterior of the deflection, ϕ, given the measured CMB, $\hat{\mathbf{s}}$, can be obtained by introducing a Gaussian prior on the lensing field, which regularizes the problem of having too many degrees of freedom within the lensing field

$$-2\ln p(\phi|\hat{\mathbf{s}}) = -2\ln\mathcal{L}(\hat{\mathbf{s}}|\phi) + \sum_{LM}\frac{|\phi_{LM}|^2}{C_L^{\phi\phi}}. \tag{2.26}$$

The maximum posterior estimate for the mode LM can be constructed by setting $\frac{\delta(-2\ln p(\phi|\bar{\mathbf{s}}))}{\delta\phi_{LM}} = 0$. One obtains

$$\left(C_L^{\phi\phi}\right)^{-1}\hat{\phi}_{LM} = -\frac{1}{2}\frac{\delta(-2\ln\mathcal{L})}{\delta\phi^\dagger_{LM}} \tag{2.27}$$

We now take a closer look at the two latter terms in the likelihood gradient which are quadratic in the CMB fields. Working in harmonic space we find

$$\begin{aligned}\left(\frac{\delta(-2\ln\mathcal{L})}{\delta\phi^\dagger_{LM}}\right)_{\text{quadratic}} &= -\bar{\mathbf{s}}^\dagger_{\ell m}(-1)^{m+M}\begin{pmatrix}\ell & L & \ell'\\ m & M & -m'\end{pmatrix}\mathbf{F}_{\ell L\ell'}\mathbf{C}_{\ell'}\mathbf{D}^\dagger\bar{\mathbf{s}}_{\ell' m'}\\ &\quad -\bar{\mathbf{s}}^\dagger_{\ell m}(-1)^{m+M}\begin{pmatrix}\ell' & L & \ell\\ m' & -M & -m\end{pmatrix}\mathbf{D}\mathbf{C}_{\ell}\mathbf{F}^\dagger_{\ell' L\ell}\bar{\mathbf{s}}_{\ell' m'}\\ &= -(-1)^{m+M}\begin{pmatrix}\ell & \ell' & L\\ -m & m' & -M\end{pmatrix}\bar{\mathbf{s}}^\dagger_{\ell m}\left[\mathbf{F}_{\ell L\ell'}\mathbf{C}_{\ell'}+\mathbf{C}_{\ell}\mathbf{F}^\dagger_{\ell' L\ell}\right]\bar{\mathbf{s}}_{\ell' m'},\end{aligned} \tag{2.28}$$

where in the last equation we averaged over the large scale structure, such that $\langle\mathbf{D}\rangle = 1$, and $\mathbf{F}$ was introduced in Eq. 1.284. Note that this also affects the total-power-filtered quantities, $\bar{\mathbf{s}}$, since they are now filtered with a LSS-averaged total covariance. The obtained estimator, after combining with Eq. 2.27, is a Wiener-filtered version of the estimator we will obtain in the following section.

Although estimators of the type introduced in the next section still prevail in current data analysis efforts due to its simplicity, likelihood implementations are tested and used on data and simulations and allow for a more optimal lensing reconstruction. These include Ref. [66] using a maximum a posteriori technique and Ref. [240] using Bayesian sampling of the likelihood.

2.3 QUADRATIC ESTIMATOR

We have seen in the previous section that quadratic combinations of lensed CMB fields are sensitive to the lensing potential, ϕ, for a fixed realization of the matter distribution in the Universe. One can compute the CMB-averaged two-point correlation function of a general quadratic combination up to first order in ϕ, with the help of Eq. 2.14, as

$$\left\langle\tilde{\mathbf{s}}_{\ell m}\tilde{\mathbf{s}}^\dagger_{\ell' m'}\right\rangle_{\text{CMB}} = \delta_{\ell\ell'}\delta_{mm'}\mathbf{C}_\ell + \sum_{LM}(-1)^m\begin{pmatrix}\ell & \ell' & L\\ -m & m' & M\end{pmatrix}\mathbf{f}_{\ell L\ell'}\phi_{LM}. \tag{2.29}$$

One defines the so-called response functions $\mathbf{f}$ as

$$\mathbf{f}_{\ell L\ell'} \equiv \mathbf{F}_{\ell L\ell'}\mathbf{C}_{\ell'} + \mathbf{C}_\ell\mathbf{F}^\dagger_{\ell' L\ell}. \tag{2.30}$$

This is a 3×3 matrix for a given set of (ℓ, L, ℓ'), where the entries correspond to the 9 quadratic combinations of CMB fields T, E and B, of which 6 are independent due to symmetry. Performing

the matrix multiplication explicitly leads to

$$\begin{aligned}
f^{TT}_{\ell L\ell'} &= \left(F_{\ell' L\ell} C^{TT}_{\ell} + F_{\ell L\ell'} C^{TT}_{\ell'}\right) \epsilon_{\ell L\ell'} \\
f^{TE}_{\ell L\ell'} &= \left({}_2F_{\ell' L\ell} C^{TE}_{\ell} + F_{\ell L\ell'} C^{TE}_{\ell'}\right) \epsilon_{\ell L\ell'} \\
f^{ET}_{\ell L\ell'} &= \left(F_{\ell' L\ell} C^{TE}_{\ell} + {}_2F_{\ell L\ell'} C^{TE}_{\ell'}\right) \epsilon_{\ell L\ell'} \\
f^{TB}_{\ell L\ell'} &= i\left({}_2F_{\ell' L\ell} C^{TE}_{\ell}\right) \beta_{\ell L\ell'} \\
f^{BT}_{\ell L\ell'} &= -i\left({}_2F_{\ell L\ell'} C^{TE}_{\ell'}\right) \beta_{\ell L\ell'} \\
f^{EE}_{\ell L\ell'} &= \left({}_2F_{\ell' L\ell} C^{EE}_{\ell} + {}_2F_{\ell L\ell'} C^{EE}_{\ell'}\right) \epsilon_{\ell L\ell'} \\
f^{EB}_{\ell L\ell'} &= i\left({}_2F_{\ell' L\ell} C^{EE}_{\ell} + {}_2F_{\ell L\ell'} C^{BB}_{\ell'}\right) \beta_{\ell L\ell'} \\
f^{BE}_{\ell L\ell'} &= -i\left({}_2F_{\ell' L\ell} C^{BB}_{\ell} + {}_2F_{\ell L\ell'} C^{EE}_{\ell'}\right) \beta_{\ell L\ell'} \\
f^{BB}_{\ell L\ell'} &= \left({}_2F_{\ell' L\ell} C^{BB}_{\ell} + {}_2F_{\ell L\ell'} C^{BB}_{\ell'}\right) \epsilon_{\ell L\ell'}.
\end{aligned} \tag{2.31}$$

These weights are consistent with Tab. 1 of Ref. [258], except for a flipped sign in the EB (and BE) estimator weights. Simulations confirm that the weights given above are necessary to get consistent results. These weights satisfy the relation

$$\mathbf{f}_{\ell L\ell'} = \mathbf{f}^{\dagger}_{\ell' L\ell}. \tag{2.32}$$

We can follow Refs. [213, 145, 114] and generalize the concept of the response function by defining

$$\mathbf{f}_{\ell L\ell'} \equiv \sum_{mMm'} (-1)^m \begin{pmatrix} \ell & \ell' & L \\ -m & m' & M \end{pmatrix} \frac{\delta}{\delta\phi_{LM}} \left\langle \tilde{\mathbf{s}}_{\ell m} \tilde{\mathbf{s}}^{\dagger}_{\ell' m'} \right\rangle_{\text{CMB}}. \tag{2.33}$$

This is equivalent to the previous result, if we consider $\left\langle \tilde{\mathbf{s}}_{\ell m} \tilde{\mathbf{s}}^{\dagger}_{\ell' m'} \right\rangle$ up to first order in ϕ, but also allows to incorporate higher-order effects in the response functions. The exact flat-sky, non-perturbative mode response functions are given in Appendix B.1. In good approximation they only lead to slight modifications of the response functions 2.30, which amounts to replacing the matrix $\mathbf{C}_\ell$ with [213, 270]

$$\mathbf{C}^g_\ell = \begin{pmatrix} C^{T\nabla T}_\ell & C^{T\nabla E}_\ell & 0 \\ C^{T\nabla E}_\ell & C^{E\nabla E}_\ell & 0 \\ 0 & 0 & C^{B\nabla B}_\ell \end{pmatrix}. \tag{2.34}$$

The gradient power spectra are defined by

$$\left\langle \tilde{s}_{\ell m} \tilde{s}^{g\,\dagger}_{\ell' m'} \right\rangle \equiv \delta_{\ell\ell'} \delta_{mm'} \mathbf{C}^g_\ell, \tag{2.35}$$

where

$$\tilde{\mathbf{s}}^g_{\ell m} \equiv \mathbf{Y}^{\dagger} \nabla \tilde{\mathbf{s}}(\mathbf{n}). \tag{2.36}$$

A way to compute them is presented in the appendix of Ref. [213]. In practice the gradient power spectra can be reasonably well approximated with the corresponding lensing power spectra, $\tilde{\mathbf{C}}_\ell$ [213], which leads to the usual substitution in Eq. 2.30

$$\mathbf{f}_{\ell L\ell'} \equiv \mathbf{F}_{\ell L\ell'} \tilde{\mathbf{C}}_{\ell'} + \tilde{\mathbf{C}}_\ell \mathbf{F}^{\dagger}_{\ell' L\ell}. \tag{2.37}$$

Fig. 2.1 shows a comparison of the two types of spectra. Both coincide well for larger scales in the case of TT, EE and BB, but start to deviate significantly at small scales.

With this one can start with an Ansatz for a quadratic estimator for ϕ_{LM}

$$\hat{\phi}_{LM} = \bar{\mathbf{s}}^{\dagger} \mathbf{G}_{LM} \bar{\mathbf{s}} = \sum_{\ell m} \sum_{\ell' m'} \bar{\mathbf{s}}^{\dagger}_{\ell m} \mathbf{G}_{\ell m L M \ell' m'} \bar{\mathbf{s}}_{\ell' m'}, \tag{2.38}$$

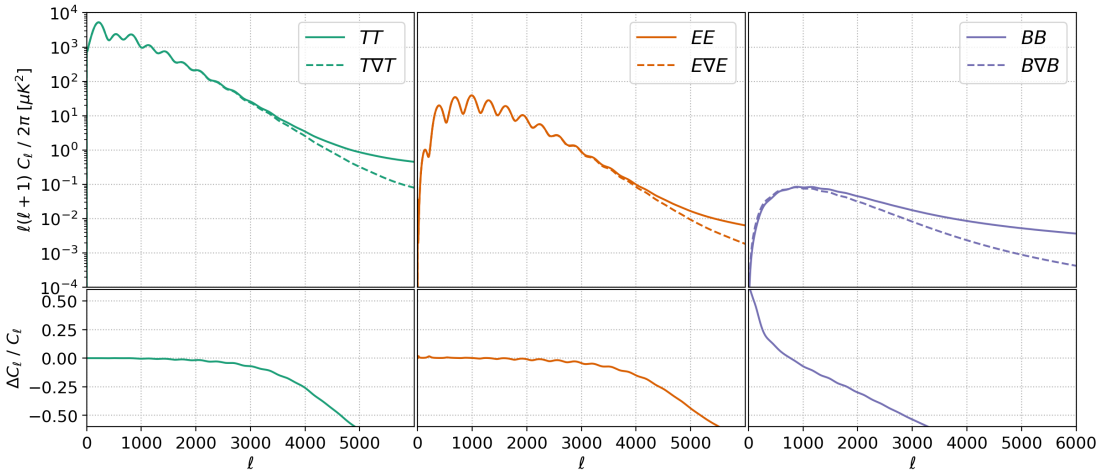

Figure 2.1: Comparison of the lensed power spectra and gradient power spectra introduced in Eq. 2.34 computed with CAMB. The relative comparison is shown in the bottom line, exhibiting large deviations at very small scales. On small scales $\ell > 3000$ the TT and EE spectra start to differ significantly, while the BB spectrum shows a discrepancy already at larger scales.

where the estimator is chosen to be quadratic in the filtered CMB fields as defined in Eq. 2.25, to simplify the final result, and introduced a free matrix, $\mathbf{G}$. This matrix is set by two requirements. The estimator is supposed to be unbiased and has minimum variance per mode LM. The first condition is

$$\left\langle \hat{\phi}_{LM} \right\rangle_{\text{CMB}} = \left\langle \bar{\mathbf{s}}^\dagger \mathbf{G}_{LM} \bar{\mathbf{s}} \right\rangle_{\text{CMB}} \overset{!}{=} \phi_{LM}. \tag{2.39}$$

Using the two-point correlation function of lensed CMB fields up to first order in ϕ of Eq. 2.29 this can be translated in a condition for $\mathbf{G}$

$$\phi_{LM} = \text{Tr}\left(\mathbf{G}_{LM} \mathbf{B}^\dagger \hat{\mathbf{C}}^{-1} \left\langle \hat{\mathbf{s}}\hat{\mathbf{s}}^\dagger \right\rangle_{\text{CMB}} \hat{\mathbf{C}}^{-\dagger} \mathbf{B} \right) \tag{2.40}$$

$$= \text{Tr}\left(\mathbf{G}_{LM} \mathbf{B}^\dagger \hat{\mathbf{C}}^{-1} \mathbf{B} \left\langle \tilde{\mathbf{s}}\tilde{\mathbf{s}}^\dagger \right\rangle_{\text{CMB}} \mathbf{B}^\dagger \hat{\mathbf{C}}^{-\dagger} \mathbf{B} \right) + \text{Tr}\left(\mathbf{G}_{LM} \mathbf{B}^\dagger \hat{\mathbf{C}}^{-1} \mathbf{B} \mathbf{N} \mathbf{B}^\dagger \hat{\mathbf{C}}^{-\dagger} \mathbf{B} \right). \tag{2.41}$$

Following [258] one can parametrize $\mathbf{G}$ as

$$\mathbf{G}_{\ell m L M \ell' m'} = (-1)^{m'} \begin{pmatrix} \ell & \ell' & L \\ -m & m' & -M \end{pmatrix} \mathbf{G}_{\ell L \ell'}. \tag{2.42}$$

Since in this case

$$\sum_m \mathbf{G}_{\ell m L M \ell' m} \sim \delta_{L0} \tag{2.43}$$

one can see directly from Eq. 2.41 that the second term only contributes to the monopole of the estimator if both $\mathbf{N}$ and $\mathbf{B}$ (and therefore $\hat{\mathbf{C}}$) are diagonal in harmonic space. In the contrary, the estimator will be biased for $L > 0$. In the former case the full Eq. 2.41 yields

$$\sum_{\ell\ell'} \mathbf{G}_{\ell L \ell'} \hat{\mathbf{C}}_{\ell'}^{-1} \mathbf{f}_{\ell' L \ell} \hat{\mathbf{C}}_{\ell}^{-1} = 2L + 1. \tag{2.44}$$

To make the connection to Ref. [258], we can define

$$\mathbf{G}_{\ell L \ell'} \equiv \frac{1}{L(L+1)} \hat{\mathbf{C}}_\ell \begin{pmatrix} A_L^{TT} g_{\ell L \ell'}^{TT} & A_L^{TE} g_{\ell L \ell'}^{TE} & A_L^{TB} g_{\ell L \ell'}^{TB} \\ A_L^{ET} g_{\ell L \ell'}^{ET} & A_L^{EE} g_{\ell L \ell'}^{EE} & A_L^{EB} g_{\ell L \ell'}^{EB} \\ A_L^{BT} g_{\ell L \ell'}^{BT} & A_L^{BE} g_{\ell L \ell'}^{BE} & A_L^{BB} g_{\ell L \ell'}^{BB} \end{pmatrix} \hat{\mathbf{C}}_{\ell'} \tag{2.45}$$

and separate the above combined estimator in contributions from the different quadratic combinations of CMB fields. The condition above then reduces to a condition on the normalization of the quadratic estimator in order for it being unbiased

$$A_L^{XY} = L(L+1)(2L+1)\left[\sum_{\ell\ell'} g^{XY}_{\ell L\ell'} f^{XY}_{\ell L\ell'}\right]^{-1}. \tag{2.46}$$

Next we compute the variance per LM-mode of the quadratic estimator as the second condition. Computing the variance of the quadratic estimator, we obtain terms which are proportional to four-point functions of the CMB fields. One finds

$$\left\langle \hat{\phi}_{LM}\hat{\phi}^\dagger_{LM}\right\rangle = \left\langle \hat{\mathbf{s}}^\dagger \hat{\mathbf{C}}^{-\dagger}\mathbf{B}\mathbf{G}_{LM}\mathbf{B}^\dagger\hat{\mathbf{C}}^{-1}\hat{\mathbf{s}}\hat{\mathbf{s}}^\dagger\hat{\mathbf{C}}^{-\dagger}\mathbf{B}\mathbf{G}^\dagger_{LM}\mathbf{B}^\dagger\hat{\mathbf{C}}^{-1}\hat{\mathbf{s}}\right\rangle \tag{2.47}$$

$$=(-1)^{m_1+m_3}\begin{pmatrix}\ell_1 & \ell_2 & L\\ -m_1 & m_2 & -M\end{pmatrix}\begin{pmatrix}\ell_3 & \ell_4 & L\\ -m_3 & m_4 & -M\end{pmatrix}\times \tag{2.48}$$

$$\times\left\langle \hat{\mathbf{s}}^\dagger_{\ell_1 m_1}\mathbf{G}_{\ell_1 L\ell_2}\hat{\mathbf{s}}_{\ell_2 m_2}\hat{\mathbf{s}}^\dagger_{\ell_4 m_4}\mathbf{G}^\dagger_{\ell_3 L'\ell_4}\hat{\mathbf{s}}_{\ell_3 m_3}\right\rangle.$$

Again, using the definition in Eq. 2.45 one finds expressions for the weights $g^{XY}_{\ell L\ell'}$ equivalent to Ref. [258]

$$g^{XY}_{\ell L\ell'} = \frac{C^{XX}_{\ell'}C^{YY}_{\ell} f^{XY\,*}_{\ell L\ell'} - (-1)^{\ell+L+\ell'}C^{XY}_{\ell}C^{XY}_{\ell'} f^{XY\,*}_{\ell' L\ell}}{C^{XX}_{\ell}C^{XX}_{\ell'}C^{XX}_{\ell}C^{YY}_{\ell'} - \left(C^{XY}_{\ell}C^{XY}_{\ell'}\right)^2}. \tag{2.49}$$

There are two sets of special cases, one if $X = Y$, i.e. for TT, EE and BB, where

$$g^{XX}_{\ell L\ell'} = \frac{f^{XX\,*}_{\ell L\ell'}}{2\hat{C}^{XX}_{\ell}\hat{C}^{XX}_{\ell'}}, \tag{2.50}$$

and second if $\hat{C}^{XY}_{\ell'} = 0$, i.e. for TB and EB, where

$$g^{XY}_{\ell L\ell'} = \frac{f^{XY\,*}_{\ell L\ell'}}{\hat{C}^{XX}_{\ell}\hat{C}^{YY}_{\ell'}}. \tag{2.51}$$

To summarize, for an isotropic and full sky, we can reconstruct ϕ_{LM} with minimal variance with the help of the quadratic estimator of Ref. [258]

$$\hat{\phi}^{XY}_{LM} = \frac{A^{XY}_L}{L(L+1)}\sum_{\ell m}\sum_{\ell' m'}(-1)^{m'}\begin{pmatrix}\ell & \ell' & L\\ -m & m' & -M\end{pmatrix} g^{XY}_{\ell L\ell'}\hat{a}^{X\,\dagger}_{\ell m}\hat{a}^{Y}_{\ell' m'}. \tag{2.52}$$

With this method we obtain six independent estimators of the lensing potential from the combination of CMB fields TT, TE, TB, EE, EB and BB.

2.4 EFFICIENT ESTIMATORS

The two-dimensional sum and computation of the Wigner-3j symbols is not as efficient as it would allow for a lensing reconstruction in a reasonable time. An alternative way, similar to the method already proposed in Ref. [258], is grounded in the fact that we can write

$${}_sF_{\ell L\ell'}(-1)^{\ell+L+\ell'}(-1)^{m'}\begin{pmatrix}\ell & \ell' & L\\ -m & m' & -M\end{pmatrix} = \tag{2.53}$$

$$= \frac{1}{2}\left(-\ell(\ell+1)+L(L+1)+\ell'(\ell'+1)\right)\int d\Omega\, {}_sY^*_{\ell m}Y^*_{LM}\,{}_sY_{\ell' m'}$$

using Eq. A.6, which we already used before in the derivation of the lensing response functions, $\mathbf{F}$. This allows us to write the estimator in Eq. 2.52 as

$$\hat{\phi}^{XY}_{LM} = \frac{A^{XY}_L}{L(L+1)} \sum_{\ell m} \sum_{\ell' m'} \left(\sum_i^N \alpha^i_\ell \beta^i_L \gamma^i_{\ell'} \right) \int d\Omega \, {}_sY^*_{\ell m} Y^*_{LM} \, {}_sY_{\ell' m'} \hat{a}^{X\,\dagger}_{\ell m} \hat{a}^Y_{\ell' m'} = \tag{2.54}$$

$$= \frac{A^{XY}_L}{L(L+1)} \sum_i \beta^i_L \int d\Omega Y^*_{LM} \left(\sum_{\ell m} {}_{-s}Y_{\ell m} \alpha^i_\ell \hat{a}^X_{\ell m} \right) \left(\sum_{\ell' m'} {}_sY_{\ell' m'} \gamma^i_{\ell'} \hat{a}^Y_{\ell' m'} \right) \tag{2.55}$$

with a set of simple, one-dimensional functions α^i, β^i and γ^i for each estimator, where N can be up to 12. The two CMB fields X and Y are multiplied by the functions α and γ in harmonic space, then transformed back into pixel-space, where the two resulting maps are multiplied. The product is then transformed back into harmonic space, where it is weighted by β. This has to be done N times, then summed together and properly normalized with A_L. While a brute-force implementation of the estimator in Eq. 2.52 has a computational cost of $\mathcal{O}(\ell^5_{\rm max})$, the pixel-space implementation is using at most 12×3 spherical harmonic transformations with computational cost $\mathcal{O}(\ell^3_{\rm max})$. Note that strictly speaking this can not be done for the TE estimator, since the $g^{TE}_{\ell L \ell'}$ weighting function can not be separated in a product of the functions α_ℓ, β_ℓ and γ_ℓ. However, by setting $\hat{C}^{TE}_{\ell m}/\hat{C}^{TT}_{\ell m} \approx 0$ and $\hat{C}^{TE}_{\ell m}/\hat{C}^{EE}_{\ell m} \approx 0$ one can sidestep this issue with negligible loss in being optimal.

2.5 CHARACTERIZATION OF THE QUADRATIC ESTIMATOR

The average of reconstructed lensing potentials from many realizations of the CMB gives by design an unbiased result in the absence of inhomogeneous noise or sky masking. The major interest, however, lies in the two-point function, or lensing potential power spectrum, $C^{\phi\phi}_L$, which we can simply estimate from reconstructed $\hat{\phi}_{LM}$s as

$$\hat{C}^{ABCD}_L = \frac{1}{2L+1} \sum_M \hat{\phi}^{AB}_{LM} \hat{\phi}^{CD\,\dagger}_{LM}. \tag{2.56}$$

What can be seen in the following is that this estimator is biased. It is convenient to express the CMB- and LSS-averaged estimator as a series of powers in $C^{\phi\phi}_L$

$$\left\langle \hat{C}^{\phi\phi}_L \right\rangle = C^{\phi\phi}_L + N^{(0)}_L + N^{(1)}_L + N^{(2)}_L + ..., \tag{2.57}$$

where the superscript specifies the power of explicit appearances of $C^{\phi\phi}_L$. The quadratic estimator is a complex combination of two CMB fields, which introduces complex mode-mixing when computing its two-point correlation function. Fig. 2.2 shows the contribution of the modes of the E- and B-fields, contributing to one L mode of the EB quadratic estimator auto-power spectrum.

2.5.1 ZEROTH ORDER BIAS

Taking the form of the quadratic estimator in Eq. 2.52 the expectation of the power spectrum estimator can be expressed as

$$\hat{C}^{ABCD}_L = \frac{1}{2L+1} \sum_M \frac{A^{AB}_L A^{CD\,*}_L}{(L(L+1))^2} \sum_{\ell_1 m_1} \sum_{\ell_2 m_2} \sum_{\ell_3 m_3} \sum_{\ell_4 m_4} (-1)^{m_2+m_4} \times \tag{2.58}$$

$$\times \begin{pmatrix} \ell_1 & \ell_2 & L \\ -m_1 & m_2 & -M \end{pmatrix} \begin{pmatrix} \ell_3 & \ell_4 & L \\ -m_3 & m_4 & -M \end{pmatrix} g^{AB}_{\ell_1 L \ell_2} g^{CD\,*}_{\ell_3 L \ell_4} \left\langle \hat{a}^{A\,\dagger}_{\ell_1 m_1} \hat{a}^B_{\ell_2 m_2} \hat{a}^C_{\ell_3 m_3} \hat{a}^{D\,\dagger}_{\ell_4 m_4} \right\rangle.$$

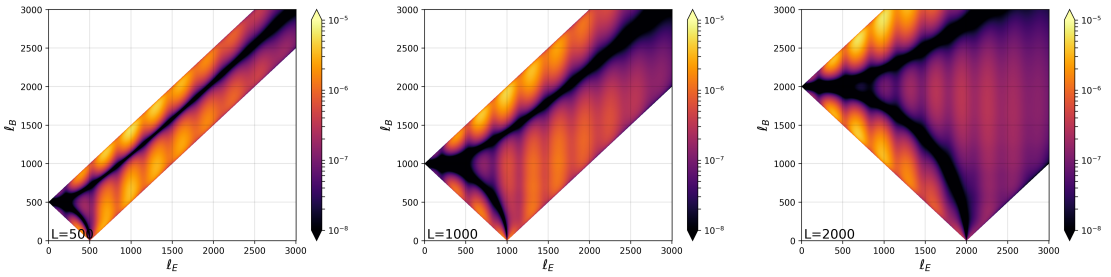

Figure 2.2: This figure shows the mixing of the modes of the CMB E- and B-fields in the EB quadratic estimator modes of $L = 500$ (left), $L = 1000$ (middle) and $L = 2000$ (right). Summing the matrices over ℓ_B and ℓ_E would give the value for $N_L^{(0)}$ at the given L-mode.

The power spectrum estimator is thus sensitive to the four-point function of CMB fields. One can use Wick's theorem to evaluate this four-point function. The disconnected part, assuming the lensed CMB fields to be Gaussian and isotropic fields on the sphere, gives

$$\begin{aligned}\left\langle \hat{a}^{A\,\dagger}_{\ell_1 m_1} \hat{a}^{B}_{\ell_2 m_2} \hat{a}^{C}_{\ell_3 m_3} \hat{a}^{D\,\dagger}_{\ell_4 m_4} \right\rangle_D =& \delta_{\ell_1\ell_2}\delta_{\ell_3\ell_4}\delta_{m_1 m_2}\delta_{m_3 m_4}\hat{C}^{AB}_{\ell_1}\hat{C}^{CD}_{\ell_3} + \\ &+ \delta_{\ell_1\ell_3}\delta_{\ell_2\ell_4}\delta_{m_1 m_3}\delta_{m_2 m_4}\hat{C}^{AC}_{\ell_1}\hat{C}^{BD}_{\ell_2} + \\ &+ \delta_{\ell_1\ell_4}\delta_{\ell_2\ell_3}\delta_{m_1 -m_4}\delta_{m_2 -m_3}(-1)^{m_3+m_4}\hat{C}^{AD}_{\ell_1}\hat{C}^{BC}_{\ell_2}.\end{aligned}$$

After plugging this into Eq. 2.58, one can observe that the first term only contributes to the monopole $L = 0$ due to the properties of the Wigner-3j symbols (see Appendix A), such that one has for $L > 0$

$$\begin{aligned}N_L^{(0)\,ABCD}\left[\hat{C}\right] =& \frac{A_L^{AB} A_L^{CD\,*}}{(2L+1)(L(L+1))^2}\sum_{\ell_1\ell_2} g^{AB}_{\ell_1 L\ell_2} \times \\ &\times \left[\hat{C}^{AC}_{\ell_1}\hat{C}^{BD}_{\ell_2} g^{CD\,*}_{\ell_1 L\ell_2} + (-1)^{\ell_1+L+\ell_2}\hat{C}^{AD}_{\ell_1}\hat{C}^{BC}_{\ell_2} g^{CD\,*}_{\ell_2 L\ell_1}\right].\end{aligned} \tag{2.59}$$

If the weights, g, are chosen to be optimal according to Eq. 2.49 and $AB = CD$, this reduces to

$$N_L^{(0)\,ABAB} = A_L^{AB}. \tag{2.60}$$

This is the zeroth order bias term, which is present even for purely Gaussian random fields $\hat{a}_{\ell m}$, i.e. in the absence of lensing. It is the most dominant bias term in the expansion Eq. 2.57. In Fig. 2.3 one can see $N_L^{(0)}$-bias curves for some examples of different noise properties and ℓ-cut-offs, $\ell_{\rm max}$ in the quadratic estimator. The rough scaling of the bias is

$$(L(L+1))^2 N_L^{(0)} \sim \frac{1}{N_{\rm modes}}, \tag{2.61}$$

where $N_{\rm modes}$ is the number of signal-dominated modes of the corresponding CMB fields [145]. Assuming all modes below $\ell_{\rm eff}$ are signal dominated, then $N_{\rm modes} \sim \ell_{\rm eff}(\ell_{\rm eff}+1)$.

2.5.2 FIRST ORDER BIAS

From statistical isotropy follows [162] that we can write the connected four point function in terms of the reduced trispectrum T as

$$\left\langle \hat{a}^{A\,\dagger}_{\ell_1 m_1} \hat{a}^{B}_{\ell_2 m_2} \hat{a}^{C}_{\ell_3 m_3} \hat{a}^{D\,\dagger}_{\ell_4 m_4} \right\rangle_C = \sum_{LM} \begin{pmatrix} \ell_1 & \ell_2 & L \\ m_1 & m_2 & -M \end{pmatrix} \begin{pmatrix} \ell_3 & \ell_4 & L \\ m_3 & m_4 & M \end{pmatrix} (-1)^M T^{\ell_1\ell_2}_{\ell_3\ell_4}(L).$$

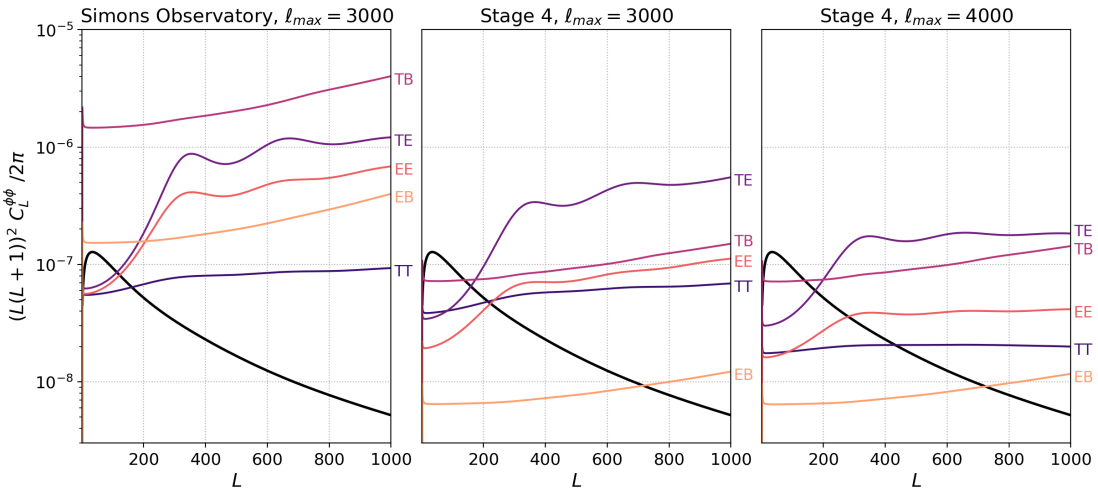

Figure 2.3: Examples of $N_L^{(0)}$-bias terms for different experimental configurations. One observes a change and relative strength of the bias level depending on the noise level and the ℓ-cut-off. Details on the experimental properties are given in Chapter 5. The fiducial signal power spectrum, $C_L^{\phi\phi}$ is shown in the black line.

This results on one hand in the term

$$\hat{C}_L^{ABCD} = \left(\frac{A_L^{AB}}{2L+1}\sum_{\ell ell'} g_{\ell L\ell'}^{AB} f_{\ell L\ell'}^{AB}\right)\left(\frac{A_L^{CD}}{2L+1}\sum_{\ell ell'} g_{\ell L\ell'}^{CD} f_{\ell L\ell'}^{CD}\right) C_L^{\phi\phi}, \tag{2.62}$$

which, by choice of the optimal weights tells us that there is no multiplicative bias in estimating the potential (i.e. the prefactor of $C_L^{\phi\phi}$ is 1). On the other hand there are two additional contractions causing an additive bias, $N_L^{(1)}$. Analytical flat-sky expressions for this bias are for example given in Ref. [186]. Since this bias starts to become important only at small scales, curved- and flat-sky computations are expected to be non-differiantiable. Fig. 2.4 shows examples of $N_L^{(1)}$-bias curves, computed in the flat-sky approximation.

2.5.3 HIGHER ORDER BIASES

Higher-order biases can be obtained by going to higher perturbative orders in the deflection operator. Properties of the bias at second order, $N_L^{(2)}$, are that it is negative and dominant at large-L, such that it suppresses the peak in $\hat{C}_L^{\phi\phi}$. However, as pointed out in Ref. [145], the replacement of unlensed with lensed power spectra made in Eq. 2.37 can largely suppress this bias. To obtain sub-percent precision it is necessary to replace the lensed power spectra, $\tilde{C}_\ell$, in the f-functions (Eq. 2.37) of the normalization A_L (Eq. 2.46) with the gradient power spectra, C_ℓ^g, following the arguments in [145, 213]. Fig. 2.5 shows the $N_L^{(2)}$-bias for the TT, EE and EB estimator auto-power spectrum for our fiducial CMB-S4 experimental configuration, obtained as a residual bias in simulations.

2.5.4 POWER SPECTRUM COVARIANCE

For the final power spectrum, as well as eventual cosmological parameter extraction from it, it is necessary to have knowledge of the covariance

$$\mathrm{cov}\left(\hat{C}_L^{\phi\phi}, \hat{C}_{L'}^{\phi\phi}\right) = \left\langle \hat{C}_L^{\phi\phi}\hat{C}_{L'}^{\phi\phi}\right\rangle - \left\langle \hat{C}_L^{\phi\phi}\right\rangle\left\langle \hat{C}_{L'}^{\phi\phi}\right\rangle. \tag{2.63}$$

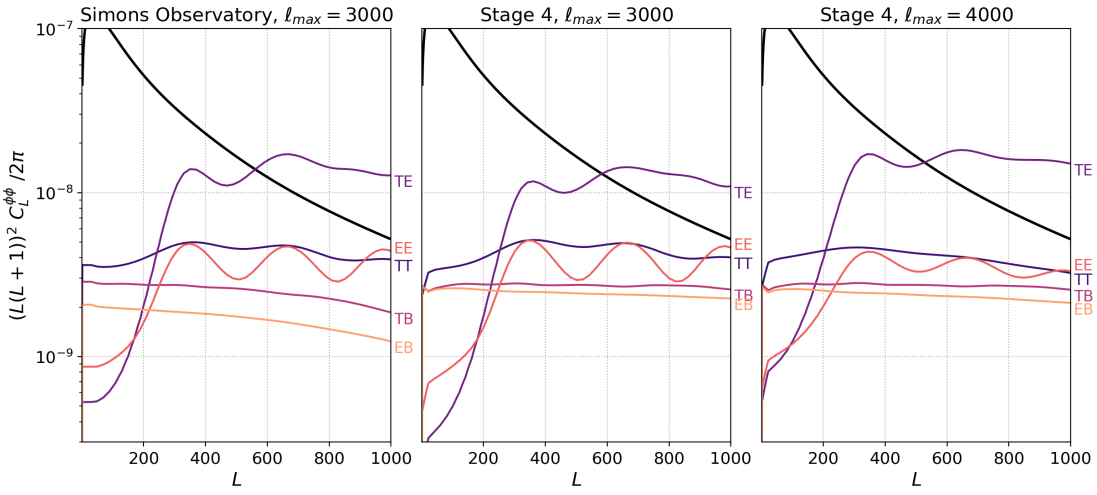

Figure 2.4: Same as Fig. 2.3, but for the $N_L^{(1)}$-bias. It is always well below the corresponding $N_L^{(0)}$-curve and only becomes relevant at small-scales. The computation of these curves uses parts of the publicly available code LENSINGBIASES (https://github.com/JulienPeloton/lensingbiases).

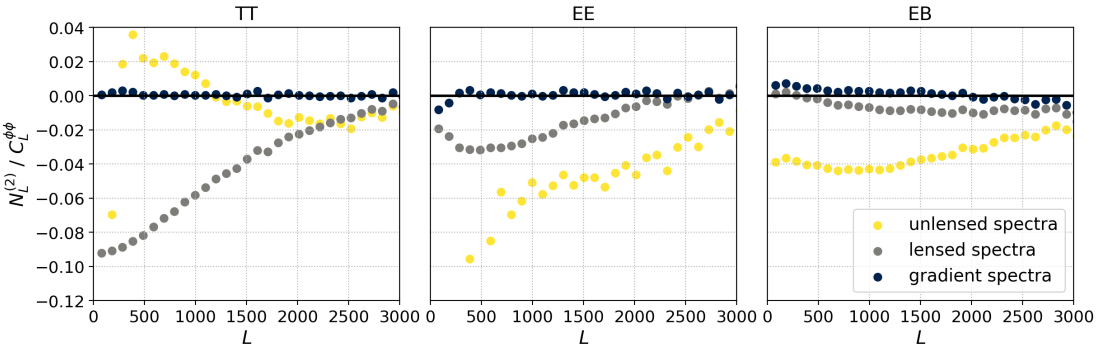

Figure 2.5: Examples of the $N_L^{(2)}$-bias for a CMB-S4-like experiment, assuming $\ell_{\rm max} = 4000$. The figure shows the second-order bias relative to the signal $C_L^{\phi\phi}$ obtained from 100 Gaussian CMB simulations and subsequent lensing reconstruction. To properly isolate the bias from the dominant zero- and first-order bias, we make use of the assumption from [145], that the dominant part of $N^{(2)}$ is given by $2\langle\phi^{\rm input}\hat{\phi}\rangle$. We use different set-ups of weight functions, either including unlensed power spectra, C_ℓ, lensed power spectra, $\tilde{C}_\ell$, or gradient power spectra, C_ℓ^g.

To compute the first term we have to evaluate the four-point function of the reconstructed potentials, which amounts to the evaluation of up to the eight-point function of the CMB,

$$\begin{aligned}\left\langle \hat{C}_L^{\phi\phi}\hat{C}_{L'}^{\phi\phi}\right\rangle =& \frac{A_L^2 A_{L'}^2}{(L(L+1))^2(L'(L'+1))^2}\sum_{\ell_1 m_1}\dots\sum_{\ell_8 m_8}(-1)^{m_2+m_4+m_6+m_8}\times \\ &\times\begin{pmatrix}\ell_1 & \ell_2 & L\\ -m_1 & m_2 & -M\end{pmatrix}\begin{pmatrix}\ell_3 & \ell_4 & L\\ -m_3 & m_4 & -M\end{pmatrix}\begin{pmatrix}\ell_5 & \ell_6 & L'\\ -m_5 & m_6 & -M'\end{pmatrix}\begin{pmatrix}\ell_7 & \ell_8 & L'\\ -m_7 & m_8 & -M'\end{pmatrix}\times \\ &\times g_{\ell_1 L\ell_2}g^*_{\ell_3 L\ell_4}g_{\ell_5 L'\ell_6}g^*_{\ell_7 L'\ell_8}\left\langle \hat{a}^\dagger_{\ell_1 m_1}\hat{a}_{\ell_2 m_2}\hat{a}_{\ell_3 m_3}\hat{a}^\dagger_{\ell_4 m_4}\hat{a}^\dagger_{\ell_5 m_5}\hat{a}_{\ell_6 m_6}\hat{a}_{\ell_7 m_7}\hat{a}^\dagger_{\ell_8 m_8}\right\rangle,\end{aligned} \tag{2.64}$$

where we omitted the superscripts for clarity. One can use Wick's theorem to decompose the eight-point function into connected four-, six- and eight-point. The latter two are of order $\mathcal{O}(\phi^4)$ [188] and we will neglect them in the following. Consequently the evaluation of the connected four-point functions remains. Arguments similar to the case of the CMB power spectrum yield [186, 145]

$$\mathrm{cov}\left(\hat{C}_L^{\phi\phi},\hat{C}_{L'}^{\phi\phi}\right)\approx\delta_{LL'}\frac{2}{2L+1}\left\langle\hat{C}_L^{\phi\phi}\right\rangle^2. \tag{2.65}$$

Hence, the reconstructed lensing potential $\hat{\phi}$ behaves approximately as a Gaussian field, in the sense that it gives the known result for the cosmic variance of the power spectrum of Gaussian variables. It differs, however, from the usual case of Gaussian random field in the fact that it arises from correlation of many fields and broad range of multipoles. There are also cross-multipole correlations arising, which can cause cross-correlations of up to 10% [145, 270]. In practice that can be alleviated by a method presented in Sec. 2.5.6.

2.5.5 MINIMUM-VARIANCE ESTIMATOR

We have seen that the bias terms

$$N_L^{\phi\phi}=N_L^{(0)}+N_L^{(1)}+\dots \tag{2.66}$$

can be treated as statistical noise of the power spectrum estimate, analogue to the case of CMB auto-power spectra. This leads directly to the idea of combining the different quadratic estimators $\hat{\phi}^{AB}$ to minimize the noise in a quadratic estimator, $\hat{\phi}^{\mathrm{mv}}$, which has minimal variance. It can be computed by inverse noise weighting the single estimators

$$\hat{\phi}^{\mathrm{mv}}_{LM}=\sum_{AB}w_L^{AB}\hat{\phi}^{AB}_{LM}, \tag{2.67}$$

with L-dependent weights given by

$$w_L^{AB}\equiv\frac{\sum_{(CD)}\left(\mathbf{N}_L^{-1}\right)_{(AB)(CD)}}{N_L^{\mathrm{mv}}} \tag{2.68}$$

$$N_L^{\mathrm{mv}}\equiv\sum_{(AB)}\sum_{(CD)}\left(\mathbf{N}_L^{-1}\right)_{(AB)(CD)}. \tag{2.69}$$

Fig. 2.6 shows the weight functions for the three experimental examples shown above. Generally, the relative importance of the TT estimator decreases with increasing instrumental sensitivity and constant resolution. In principle, however, the TT-estimator can gain the most by going to higher ℓ_{max}, due to the degraded signal-to-noise of polarization at small scales. This, on the other hand, is limited by small scale foregrounds that are more prominent in temperature (see Sec. 1.8).

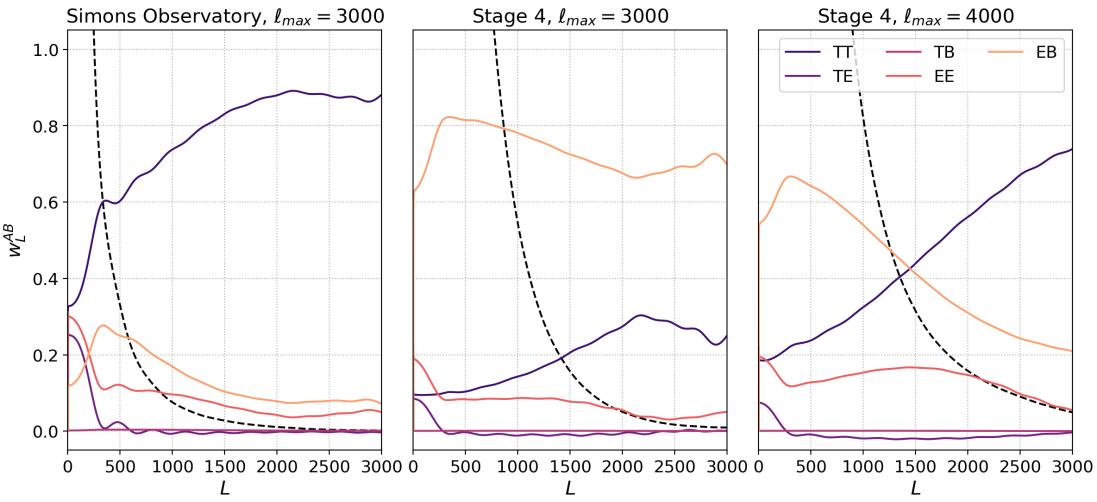

Figure 2.6: The weighting functions defined in Eq. 2.68 that act as coefficients when combining the quadratic estimators from TT, TE, TB, EE and EB. The dashed line shows the signal-to-noise ratio $C_L^{\phi\phi}/N_L^{\phi\phi}$. The relative importance of the TT-estimator decreases with decreasing map-level noise.

2.5.6 REALIZATION-DEPENDENT BIAS

To improve the modeling of the zeroth order bias, $N_L^{(0)}$, accounting for the fluctuations of the particular realization of the CMB and the noise, and to suppress the off-diagonal correlations of the covariance of $\hat{C}_L^{\phi\phi}$, we can define the so-called realization dependent bias

$$N^{(0)\,\mathrm{rd}} = 2\check{N}_L^{(0)} - N_L^{(0)}. \tag{2.70}$$

As introduced in [145, 321, 270], the new function $\check{N}_L^{(0)}$ is similar to $N_L^{(0)}$, but is estimated using power spectra of the observed realization, $\check{C}_\ell$,

$$2\check{N}_L^{(0)\,ABCD} \equiv \sum_{XY}\sum_{\ell} \frac{\partial N^{(0)\,ABCD}}{\partial \hat{C}_\ell^{XY}} \check{C}_\ell^{XY} = \tag{2.71}$$

$$= \frac{A_L^{AB} A_L^{CD\,*}}{(2L+1)(L(L+1))^2} \sum_{\ell_1\ell_2} g_{\ell_1 L \ell_2}^{AB} \Big[\left(\check{C}_{\ell_1}^{AC} \hat{C}_{\ell_2}^{BD} + \hat{C}_{\ell_1}^{AC} \check{C}_{\ell_2}^{BD} \right) g_{\ell_1 L \ell_2}^{CD\,*} +$$

$$+ (-1)^{\ell_1+L+\ell_2} \left(\check{C}_{\ell_1}^{AD} \hat{C}_{\ell_2}^{BC} + \hat{C}_{\ell_1}^{AD} \check{C}_{\ell_2}^{BC} \right) g_{\ell_2 L \ell_1}^{CD\,*} \Big]. \tag{2.72}$$

This form of bias-subtraction can also be obtained as a result of the Edgeworth expansion of the CMB likelihood (see Eq. 1.165) [304, 251].

2.5.7 IMPACT OF SKY CUTS

Until now we have discussed the quadratic estimator being unbiased and optimal (in the sense of having minimum variance) in the case of statistical isotropic CMB fields. In a realistic situation, however, there will be only a fraction of the sky observed by the instrument or selected to be suitable for the analysis. Naively applying the quadratic estimator on masked CMB fields will result in a biased result

$$\langle \hat{\phi}_{LM} \rangle_{\mathrm{CMB}} \neq \phi_{LM}. \tag{2.73}$$

We can characterize this bias with a multiplicative part, accounting for the deviation from optimality of the normalization, and an additive bias, due to the mode-mixing of CMB fields introduced by the mask,

$$\langle \hat{\phi}_{LM} \rangle_{\rm CMB} = \sum_{L'M'} \mathbf{M}_{LML'M'} \phi_{L'M'} + \phi^{\rm MF}_{LM}. \tag{2.74}$$

The matrix $\mathbf{M}$ is the coupling matrix, analogous to the case of CMB power spectra from masked fields. The mean field, $\phi^{\rm MF}$, is the signal introduced by the mask's mode-mixing even in the absence of lensing, which already appeared in the derivation of the maximum likelihood estimator in the two terms of Eq. 2.21. We assume that we can write the diagonal part of the covariance as

$$\langle \hat{\phi}_{LM} \hat{\phi}^{\dagger}_{LM} \rangle = \sum_{L'} \mathbf{M}^2_{LML'} C^{\phi\phi}_{L'} + N^{(0)}_{LM} + N^{(1)}_{LM} + C^{\rm MF}_{L}, \tag{2.75}$$

assuming that ϕ and $\phi^{\rm MF}$ are uncorrelated. All terms involve, in principle, complex sums including multiple Wigner-3j symbols. However, in most cases one can approximate the mixing matrix $\mathbf{M}^2_{LML'}$ reasonably well as a constant normalization factor [40], which is given by W_4, where

$$W_n = \int d\Omega \, m^n(\mathbf{n}), \tag{2.76}$$

is the average over the n-th power of the pixel-space mask $m(\mathbf{n})$.

The most efficient (and often only tractable) way to compute the mean-field is by using Monte-Carlo simulations, which are generated as random Gaussian fields of the lensed power spectra and masked in the same way as the signal. To obtain an unbiased estimate of the mean-field one has to average over the set of quadratic reconstructions on these simulations

$$\hat{\phi}^{\rm MF}_{LM} = \frac{1}{N_{\rm MF}} \sum_{i}^{N_{\rm MF}} \hat{\phi}^{\text{unlensed MC i}}_{LM}. \tag{2.77}$$

The mean field's variance can be computed as

$$\left\langle \hat{\phi}^{\rm MF}_{LM} \hat{\phi}^{\rm MF\,\dagger}_{L'M'} \right\rangle = \delta_{LL'} \delta_{MM'} \left(C^{\rm MF}_{L} + \frac{1}{N_{\rm MF}} N^{(0)}_{L} \right). \tag{2.78}$$

To conclude, as a crude but effective approximation, especially when using an apodized mask which renders the mask-mixing-matrix, $\mathbf{M}^2_{LML'}$, almost diagonal and reduces the mean-field power [39], one can write an estimator for the lensing power spectrum as

$$\hat{C}^{\phi\phi}_{L} = \frac{1}{W_4} \sum_{LM} \bar{\phi}_{LM} \bar{\phi}^{\dagger}_{LM} - \left(1 + \frac{1}{N_{\rm MF}} \right) N^{(0)}_{L} - N^{(1)}_{L}, \tag{2.79}$$

where $\bar{\phi}_{LM}$ are the mean field subtracted lensing potential estimates

$$\bar{\phi}_{LM} \equiv \hat{\phi}_{LM} - \hat{\phi}^{\rm MF}_{LM}. \tag{2.80}$$

The variance of this estimate is, since it is given by the CMB eight-point function, given by

$$\text{var}\left(\hat{C}^{\phi\phi}_{L} \right) = \frac{W_8}{W_4^2} \frac{2}{2L+1} \left\langle \hat{C}^{\phi\phi}_{L} \right\rangle^2 \approx \frac{1}{f_{\rm sky}} \frac{2}{2L+1} \left\langle \hat{C}^{\phi\phi}_{L} \right\rangle^2. \tag{2.81}$$

2.5.8 BIAS-HARDENING

Gravitational lensing breaks the Gaussianity of the primordial CMB fields and causes statistical anisotropy of the measured fields, which can be used to extract the lensing information via the quadratic estimator. In practice, CMB lensing is not the only source of statistical anisotropy, causing potential contamination in the CMB lensing measurement. Effects from masking, inhomogeneous noise, point sources and instrumental systematics like beam asymmetry and polarization angle misestimation can introduce such non-diagonal terms in the two-point correlation function [251, 252, 261]. Generally one can write down the expansion

$$\left\langle \tilde{\mathbf{s}}_{\ell m} \tilde{\mathbf{s}}^{\dagger}_{\ell' m'} \right\rangle_{\text{CMB}} = \delta_{\ell\ell'}\delta_{mm'}\mathbf{C}_{\ell} + \sum_{LM}(-1)^{m} \begin{pmatrix} \ell & \ell' & L \\ -m & m' & M \end{pmatrix} \sum_{i} \mathbf{f}^{i}_{\ell L \ell'} x^{i}_{LM}, \tag{2.82}$$

by extending Eq. 2.29 by arbitrary fields x^i_{LM} with response functions $\mathbf{f}^i_{\ell L\ell'}$, defined by

$$\mathbf{f}^{i}_{\ell L \ell'} \equiv \sum_{mMm'} (-1)^{m} \begin{pmatrix} \ell & \ell' & L \\ -m & m' & M \end{pmatrix} \frac{\delta}{\delta x^{i}_{LM}} \left\langle \tilde{\mathbf{s}}_{\ell m} \tilde{\mathbf{s}}^{\dagger}_{\ell' m'} \right\rangle_{\text{CMB}}. \tag{2.83}$$

MASKING

The harmonic coefficients of masked T, Q and U maps can be expressed in terms of the harmonic coefficients of the true CMB as

$$\begin{aligned} \tilde{\mathbf{s}}_{\ell m} &= \mathbf{Y}^{\dagger} \cdot \mathbf{m}(\mathbf{n}) \mathbf{Y} \cdot \mathbf{s}_{\ell m} = & (2.84) \\ &= \sum_{\ell' m'} \sum_{LM} \int d\Omega \mathbf{Y}^{\dagger} \mathbf{Y} Y_{LM} \mathbf{s}_{\ell' m'} m_{LM} & (2.85) \end{aligned}$$

where $\mathbf{m}(\mathbf{n})$ is a pixel space mask or, more generally, any pixel-dependent amplitude of the true T, Q and U maps, with corresponding harmonic coefficients m_{LM}. This results in following response functions

$$\begin{aligned} f^{m\,TT}_{\ell L\ell'} &= \left(H_{\ell' L \ell} C^{TT}_{\ell} + H_{\ell L \ell'} C^{TT}_{\ell'}\right) \epsilon_{\ell L \ell'} \\ f^{m\,TE}_{\ell L\ell'} &= \left({}_2H_{\ell' L \ell} C^{TE}_{\ell} + H_{\ell L \ell'} C^{TE}_{\ell'}\right) \epsilon_{\ell L \ell'} \\ f^{m\,TB}_{\ell L\ell'} &= i \left({}_2H_{\ell' L \ell} C^{TE}_{\ell}\right) \beta_{\ell L \ell'} \\ f^{m\,EE}_{\ell L\ell'} &= \left({}_2H_{\ell' L \ell} C^{EE}_{\ell} + {}_2H_{\ell L \ell'} C^{EE}_{\ell'}\right) \epsilon_{\ell L \ell'} \\ f^{m\,EB}_{\ell L\ell'} &= i \left({}_2H_{\ell' L \ell} C^{EE}_{\ell} + {}_2H_{\ell L \ell'} C^{BB}_{\ell'}\right) \beta_{\ell L \ell'} \\ f^{m\,BB}_{\ell L\ell'} &= \left({}_2H_{\ell' L \ell} C^{BB}_{\ell} + {}_2H_{\ell L \ell'} C^{BB}_{\ell'}\right) \epsilon_{\ell L \ell'}, \end{aligned} \tag{2.86}$$

with

$${}_{\pm s}H_{\ell L \ell'} \equiv \sqrt{\frac{(2\ell+1)(2L+1)(2\ell'+1)}{4\pi}} \begin{pmatrix} \ell & L & \ell' \\ \pm s & 0 & \mp s \end{pmatrix}. \tag{2.87}$$

INHOMOGENEOUS NOISE

The effect of inhomogeneous noise can be the easiest expressed in pixel-space, where the diagonal noise covariance is given by

$$\left\langle \mathbf{n}(\mathbf{n}) \mathbf{n}^{\dagger}(\mathbf{n}) \right\rangle = \mathbf{N}(\mathbf{n}), \tag{2.88}$$

where $\mathbf{N}$ can be in general a 3×3 matrix for each pixel, $\mathbf{n}$. This directly results in corresponding response functions given by

$$\begin{aligned}
f^{n\,TT}_{\ell L\ell'} &= (H_{\ell' L\ell} + H_{\ell L\ell'})\,\epsilon_{\ell L\ell'} \\
f^{n\,TE}_{\ell L\ell'} &= ({}_2H_{\ell' L\ell} + H_{\ell L\ell'})\,\epsilon_{\ell L\ell'} \\
f^{n\,TB}_{\ell L\ell'} &= i\,({}_2H_{\ell' L\ell})\,\beta_{\ell L\ell'} \\
f^{n\,EE}_{\ell L\ell'} &= ({}_2H_{\ell' L\ell} + {}_2H_{\ell L\ell'})\,\epsilon_{\ell L\ell'} \\
f^{n\,EB}_{\ell L\ell'} &= i\,({}_2H_{\ell' L\ell} + {}_2H_{\ell L\ell'})\,\beta_{\ell L\ell'} \\
f^{n\,BB}_{\ell L\ell'} &= ({}_2H_{\ell' L\ell} + {}_2H_{\ell L\ell'})\,\epsilon_{\ell L\ell'},
\end{aligned} \tag{2.89}$$

POINT SOURCES

We model the stokes parameters including point sources given a (usually Gaussian) profile b_ℓ following Ref. [261] as

$$\tilde{T}(\mathbf{n}) = T(\mathbf{n}) + \sum_i \sum_{\ell m} S_i \delta(\mathbf{n} - \mathbf{n}_i) b^i_\ell Y_{\ell m}(\mathbf{n}) \tag{2.90}$$

$$\tilde{Q}(\mathbf{n}) = Q(\mathbf{n}) + \sum_i \sum_{\ell m} S_i p_i \delta(\mathbf{n} - \mathbf{n}_i) b^i_\ell Y_{\ell m}(\mathbf{n}) \tag{2.91}$$

$$\tilde{U}(\mathbf{n}) = U(\mathbf{n}) + \sum_i \sum_{\ell m} S_i p_i \delta(\mathbf{n} - \mathbf{n}_i) b^i_\ell Y_{\ell m}(\mathbf{n}), \tag{2.92}$$

where S_i and p_i are the flux and the polarization fraction of source i, respectively. Assuming the same shape function $b^i_\ell = b_\ell$ for each source, i, we find the quadratic estimator responses

$$\begin{aligned}
f^{s\,TT}_{\ell L\ell'} &= (H_{\ell' L\ell} b_\ell + H_{\ell L\ell'} b_{\ell'})\,\epsilon_{\ell L\ell'} \\
f^{s\,TE}_{\ell L\ell'} &= ({}_2H_{\ell' L\ell} b_\ell + H_{\ell L\ell'} b_{\ell'})\,\epsilon_{\ell L\ell'} \\
f^{s\,TB}_{\ell L\ell'} &= i\,({}_2H_{\ell' L\ell} b_\ell)\,\beta_{\ell L\ell'} \\
f^{s\,EE}_{\ell L\ell'} &= ({}_2H_{\ell' L\ell} b_\ell + {}_2H_{\ell L\ell'} b_{\ell'})\,\epsilon_{\ell L\ell'} \\
f^{s\,EB}_{\ell L\ell'} &= i\,({}_2H_{\ell' L\ell} b_\ell + {}_2H_{\ell L\ell'} b_{\ell'})\,\beta_{\ell L\ell'} \\
f^{s\,BB}_{\ell L\ell'} &= ({}_2H_{\ell' L\ell} b_\ell + {}_2H_{\ell L\ell'} b_{\ell'})\,\epsilon_{\ell L\ell'}.
\end{aligned} \tag{2.93}$$

DEPROJECTING MEAN-FIELD BIASES

The known response of some systematic effects to the CMB lensing quadratic estimator makes it possible to build an estimator, which is more robust to these effects. It is called bias-hardened estimator, following Refs. [251, 252]. The expectation value of the quadratic estimator over an ensamble of CMB realizations is then given by

$$\left\langle \hat{\phi}_{LM} \right\rangle = \phi_{LM} + \frac{A_L}{L(L+1)(2L+1)} \sum_{i \in m,n,s,\ldots} \sum_\ell \sum_{\ell'} g_{\ell L\ell'} \mathbf{f}^i_{\ell L\ell'} x^i_{LM} \equiv \sum_j R^{0j} y^j_{LM}, \tag{2.94}$$

where

$$R^{ij}_L \equiv \frac{A^{ii}_L}{A^{ij}_L} \quad \text{and} \quad A^{ij}_L = L(L+1)(2L+1) \left[\sum_{\ell\ell'} g^i_{\ell L\ell'} f^j_{\ell L\ell'} \right]^{-1}. \tag{2.95}$$

The bias-hardened lensing potential estimator is then obtained after inverting the $\mathbf{R}$-matrix

$$\hat{\phi}^{\text{BH}}_{LM} = \sum_j \left(\mathbf{R}^{-1}_L\right)^{ij} y^j_{LM}. \tag{2.96}$$

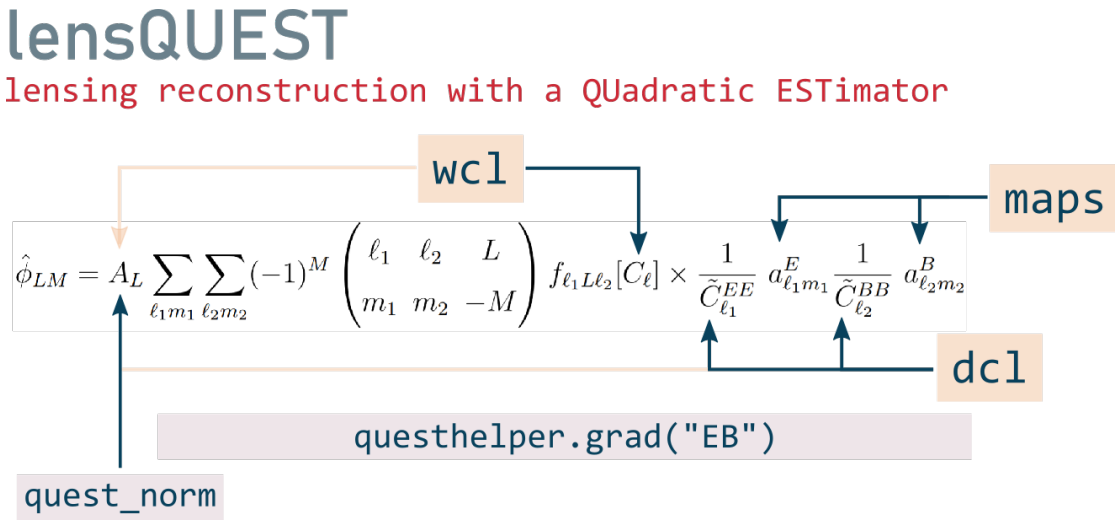

Figure 2.7: Summary of the main functions within LENSQUEST, the computation of the quadratic estimator normalization and the evaluation of the (un-normalized) quadratic estimator itself, shown in the particular example of the EB-estimator.

2.6 LENSQUEST

In Sec. 2.4 I outlined an approach to efficiently evaluate the quadratic estimator over CMB fields. I have implemented this approach in the form of a now publicly available[24] code LENSQUEST [25] makes use of this method. In this section I will give a brief documentation of the code. The code consists of a Python layer, which wraps parts in C++ to perform the computationally expensive parts. These expensive parts are A) the computation of Wigner-3js and B) (inverse) spherical harmonic transforms.

2.6.1 QUEST_NORM

There are two main functionalities of the software as summarized in Fig. 2.7. To compute the quadratic estimator introduced in Sec. 2.3 it is necessary to compute the normalization, A_L, separately. The reason is to be able to pre-compute the quantity, which does not depend on actual CMB maps, but just on the fiducial power spectra. Without much computational overhead it also can compute the noise power spectra $N_L^{(0)}$ in Eq. 2.59 for each estimator in auto- and cross-correlation.

The API of the corresponding function is documented in Appendix B.2. At the center of this function is the recursive computation of Wigner-3j function based on [325, 324], implemented in the C++ code-package WIGNERSYMBOLS[26], which is shared under a GNU Lesser General Public License. It is able to compute the vectors

$$W3J_{\ell_1}(\ell_2, \ell_3, m_1, m_2, m_3) = \begin{pmatrix} \ell_1 & \ell_2 & \ell_3 \\ m_1 & m_2 & m_3 \end{pmatrix}, \tag{2.97}$$

[24] At the time of writing the publicly available part is just a subset of the code described here. The public version only contains the well tested parts. The remaining modules are planned to be released shortly.

[25] https://github.com/doicbek/lensquest

[26] https://github.com/joeydumont/wignerSymbols

quest
+ maps : array + wcl : array + dcl : array + lmin : int = 2 + lmax : int = None + lminCMB : int = 2 + lmaxCMB : int = None + nside: int = None
+ grad(type : "TT", "TE", "TB", "EE", "EB" or "BB" , store : bool=False) + curl(type : "TT", "TE", "TB", "EE", "EB" or "BB" , store : bool=False) + mask(type : "TT", "TE", "TB", "EE", "EB" or "BB" , store : bool=False) + noise(type : "TT", "TE", "TB", "EE", "EB" or "BB" , store : bool=False) + make_minvariance(N0 : array) + make_biashardened(Rinv : array)

Figure 2.8: The class diagram for the `quest`-class within LENSQUEST. It shows its main attributes in the middle row, as well as its member functions in the bottom row.

which are only non-zero if

$$m_1 + m_2 + m_3 = 0, \tag{2.98}$$

$$-\ell_i \leq m_i \leq \ell_i \text{ and} \tag{2.99}$$

$$|\ell_1 - \ell_2| \leq \ell_3 \leq \ell_1 + \ell_2. \tag{2.100}$$

Using this function, one can compute the $f_{\ell L \ell'}$ and $g_{\ell L \ell'}$ functions used for the quadratic estimator (normalization). The sum over ℓ and ℓ' is implemented embarrassingly parallel with OPENMP.

2.6.2 QUEST

The central part of LENSQUEST is the `quest`-class, which allows for the computation of the quadratic estimator $\hat{\phi}_{LM}/A_L$. Its attributes and member functions are summarized in Fig. 2.8. At initialization it is given an array of CMB fields $(a^T_{\ell m}, a^E_{\ell m}, a^B_{\ell m})$ (or alternatively of pixel-space fields T, Q and U which are subsequently transformed into harmonic coefficients), as well as arrays of power spectra for the computation of weights $g_{\ell L \ell'}$. The first set of power spectra, `wcl`, is used to compute the $f_{\ell L \ell'}$ functions, while the second set, `dcl`, is employed as the power spectra in the denominator of the $g_{\ell L \ell'}$ functions and hence are the spectra used in the denominator of the isotropic total-power-filter applied to the input fields. The latter can be alternatively set to 1, if the input CMB fields are filtered in a previous step. The `lmin` and `lmax` attributes set the minimal and maximal multipole of the output lensing potential, while `lminCMB` and `lmaxCMB`, if set, cuts the lowest or highest multipoles of the input CMB fields. The `nside` parameter determines the resolution of the maps at the intermediate stage of the lensing reconstruction and is by default set to appropriately capture the input CMB fields up to `lmaxCMB`.

The actual reconstruction is then initiated by calling the `grad` member function with the estimator type specified as a string in the function's argument. It then returns the (un-normalized) quadratic estimator of this type as a complex NUMPY array or can be alternatively stored as an attribute of the

object. The ordering of $\hat{\phi}_{LM}/A_L$ inside the output array follows the HEALPY convention. It also includes functions to compute the analogue curl-estimator [254]. Furthermore, it can compute relevant estimators for the bias-hardening of the CMB lensing quadratic estimator [251, 252]. The two functions `make_minvariance()` and `make_biashardened()` allow to compute the minimum variance or the bias-hardened estimator upon providing the lensing noise (in dictionary format) or inverse R-matrix (as defined in Ref. [251]), respectively.

The by far most expensive operation within this class are the (inverse) spherical harmonic transformations. Hence they are performed inside the more efficient C++-layer, making use of the LIBSHARP[27] library [307] provided under the GNU General Public License. Parts of the HEALPIX C++[28] [132] and HEALPY[29] packages are used as well.

2.6.3 PYTHON AND PARALLEL COMPUTING

Due to ever increasing data sets in cosmology it becomes more and more important to be able to run the data-analysis pipeline on a supercomputer, allowing to run many processes in parallel. In this section I will summarize the topic of parallel computing, based on [47], in the context of cosmological data-analysis and Python, the predominant programming language in the field.

SERIAL VS. PARALLEL COMPUTING

Serial program of software is the more traditional way of executing several, discrete instructions sequentially. Hence, the program can be executed on a single processor. Parallel computing on the other hand is possible when a problem can be broken down in such a way that those parts can be executed simultaneously. In that sense, a parallel program can be seen as a set of sequential programs that run at the same time. This requires the usage of multiple processors, which, thanks to the rapid development of ever smaller and more powerful processors as well as their efficient production, is easily realizable in superclusters.

To execute parallel programs parallel computers are necessary. Today most computers in use are parallel in the sense that they have multiple cores, which in turn can have multiple hardware threads. Computer clusters are composed of multiple computers (so-called nodes) that are connected in a network. Usually each computing node is a multi-processing in itself with multiple CPUs/GPUs, containing multiple cores, which in turn can contain multiple hardware threads. Usually the power of such a cluster is measured in floating point operations per second, $Flop/s$. As of June 2019 the largest computing cluster in the world located at the Oak Ridge National Laboratory in the United States is able to perform 200, 794.9 $TFlop/s$ on 2,414,592 cores [178]. One of the largest graphics processing units (GPU) for use in personal computers produced by NVIDIA contains 4,352 cores [128]. Fig. 2.9 shows the the statistics of the 500 largest supercomputers in the world over time, showcasing a nearly linear evolution of processing power over time, which is called Moore's law.

Virtually all modern computers follow the so-called von-Neuman architecture, which consists of four basic components: the memory, the control unit, the arithmetic logic unit and the input/output. The memory is used to store data and instructions of the program. The control unit reads these instructions, decodes them and coordinates the execution of said program sequentially. The Arithmetic

[27] https://github.com/Libsharp/libsharp
[28] https://healpix.sourceforge.io
[29] https://healpy.readthedocs.io

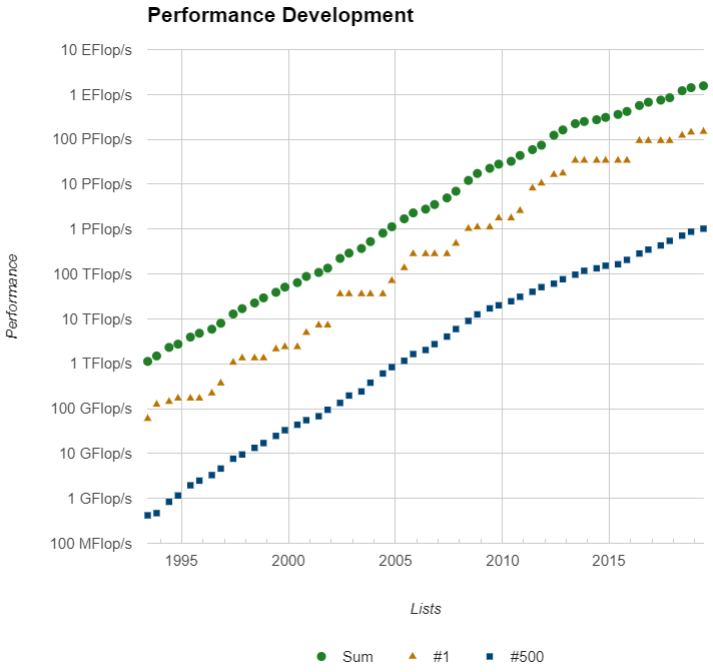

Figure 2.9: The development of computing performance over time of the 500 largest supercomputers in the world, the so-called Top500. The plot is taken from [271]. It shows in green bullets the total sum of the performance in $Flop/s$, in yellow triangles the largest and in blue squares the 500th largest supercomputer in the world in the respective year.

unit performs the basic arithmetic operations. This remains the fundamental architecture of computer clusters. There are two main memory models for parallel computers. With the so-called shared memory all cores have access to the same memory. In contrast, with distributed memory cores can only see local memory and communication protocols are necessary to access memory of other cores. Modern superclusters employ a hybrid architecture with shared memory machines (e.g. a node) or GPUs with shared memory, connected in a network of multiple such machines which require some network communication to access each other's memory. This is illustrated in Fig. 2.10.

In the following we call a program which is executed sequentially a process (or sometimes called task). To discuss the different parallel programming model we consider the relation between processes. We have seen that processes can share a common address space in memory, called shared memory. Another case of shared memory programming is the so-called thread model, where a thread is a single execution path within a process. Threads share data, code and system resources of the process, but can execute independently. Creating multiple thread is usually more economical, is however rather limiting in memory per task and prone to errors, for example memory conflicts. Major application programming interfaces (APIs) supporting threads are POSIX Threads and OpenMP. The latter is available in C, C++ and Fortran. As mentioned the distributed memory model (also called message passing model) requires a communication protocol to communicate between processes and their local memory. The industry standard API for message passing is the Message Passing Interface (MPI).

In practice hybrid models are used, combining the previously discussed programming models. A usual example is the combination of MPI and OpenMP. Here threads perform simple, but intensive computations within a process within a node in a cluster. The communication between processes on the same or different nodes is handled over the network via MPI. Another example is the usage of GPU programming with CUDA, an API similar to OpenMP. Compared to CPUs, GPUs contain a much larger amount of (usually slower) cores with limited shared memory. This allows to run massively parallel processes on large blocks of data more efficiently.

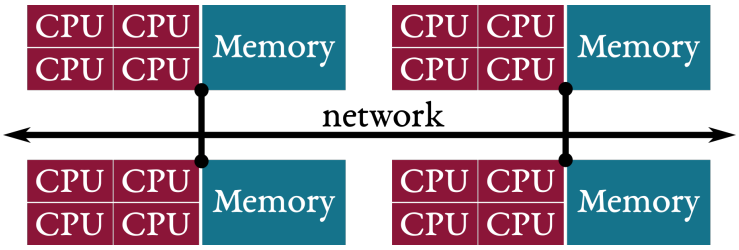

Figure 2.10: Example of the memory architexture of modern parallel computers. A single node's cores share the memory within that node (shared memory), while network communication is necessary to access the memory on other nodes (distributed memory).

MASSIVELY PARALLEL COMPUTING ON NERSC

A supercomputer facility that is extensively used for cosmological computation is the National Energy Research Scientific Computing Center (NERSC) [30]. Since May 2019 its main computational system is named Cori after the American biochemist Gerty Cori. As of June 2019 it is placed 14th on the Top500 list of largest supercomputers [178]. The system is divided in two architectures using two different processor types within the same network. It houses 2,388 computing nodes accommodating 2 sockets of Intel® Xeon® E5 processors (code name *Haswell*) a 16 cores at 2.3 GHz. Each core supports 2 threads, totalling 64 threads per node. Each node has 128 GB shared memory. Furthermore, next to the Haswell nodes, there are 9,688 nodes housing one socket of a Intel® Xeon Phi™ Processor (code name *Knights Landing* (KNL)) with 68 cores at 1.4 GHz. Each core has 4 hardware threads, which results in 272 threads per node. Each node has 96 GB of shared memory. [87]

Until May 2019, a second machine at NERSC was operating, named after the American inventor and businessman Thomas Alva Edison. It consisted of 5,586 nodes, each containing two sockets, populated with a 12-core Intel® Ivy Bridge processor at 2.4 GHz, with up to 2 threads per core. Each node had 64 GB of shared memory. [103]

This thesis made use of both systems extensively, amounting to over 4.5 million CPUh over three years. In 2020 a new machine named Perlmutter (after the Nobel Prize-winning astrophysicist) will be delivered[31]. It will lay the focus on a GPU-heavy architecture, which has a promising field of application in machine learning.

MASSIVELY PARALLEL COMPUTING WITH PYTHON

The difficulty of parallelism with the Python programming languages is the so-called global interpreter lock (GIL), which is necessary since the Python interpreter is not thread-safe. This means that only the thread which holds the GIL can access Python objects [172]. However, there are ways to evade the GIL. For example, third-party Python modules can run code in C that does not recognize the thread structure of the Python interpreter and can run in multiple threads. This is why modules like NUMPY can run in multiple threads. LENSQUEST is wrapping Python to C++ using CYTHON[32]. It allows to create data structures in C++ which point to Python objects, namely NUMPY arrays. These structures can then be used by the C++ internal routines, especially the quadratic estimator normalization computation, which is parallelized with OPENMP, as well as the spherical harmonic transformations with the multithreading-supporting LIBSHARP.

[30] https://www.nersc.gov/

[31] https://www.energy.gov/articles/doe-build-next-generation-supercomputer-lawrence-berkeley-national-laboratory

[32] https://cython.org/

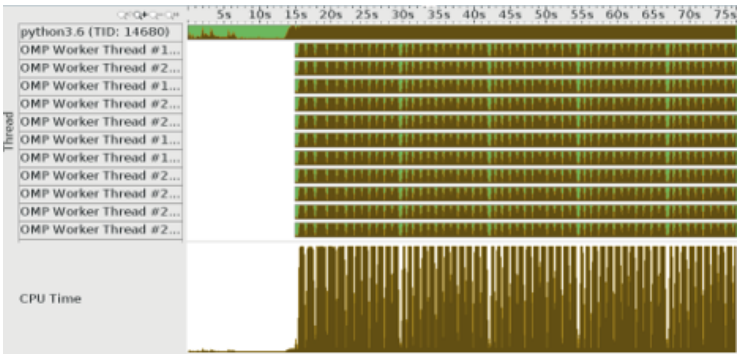

Figure 2.11: Screenshot of the profiling of the LENSQUEST code using the shareware Intel® VTune™ Amplifier. It shows the activity of a subset of all OPENMP threads, in this case 32, of a process while evaluating a quadratic estimator. It shows that, after some time for initialization and input/output, all threads are active.

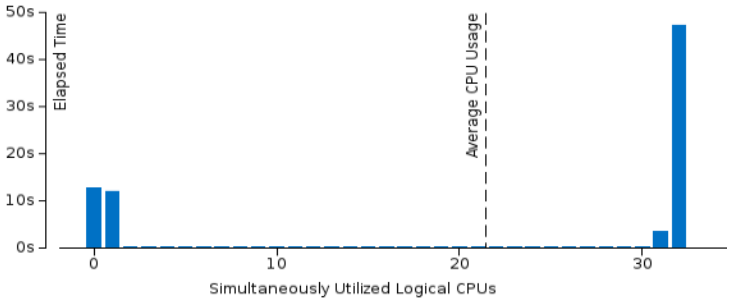

Figure 2.12: Summary of the profiling of Fig. 2.11 after evaluating a quadratic estimator with LENSQUEST, showing that for the most time all 32 threads are active.

It is common that the quadratic estimator has to be evaluated over a large set of CMB simulations for all types of estimators. Both can be parallelized in a trivial way (embarrassingly parallel) using MPI with little communication between nodes. The module MPI4PY[33] is an MPI API for Python, providing simplified and full-functional wrappers to the C++ MPI communication functions.

2.7 WIENER FILTERING

For either the maximum likelihood solving or the quadratic estimator reconstruction, one requires the total-power-filtered, measured CMB maps (e.g. Eq. 2.25). Since this filtering operation is similar to so-called Wiener-filtering[34], up to a final application of the signal covariance matrix, we can make use of the extensive work done in this field. The goal is to obtain the filtered quantities

$$\bar{\mathbf{s}} = \mathbf{B}^\dagger \hat{\mathbf{C}}^{-1} \hat{\mathbf{s}} = \mathbf{B}^\dagger (\tilde{\mathbf{C}} + \mathbf{N})^{-1} \hat{\mathbf{s}}. \tag{2.101}$$

In cases where the lensed CMB covariance as well as the noise covariance both reduce to be diagonal matrices in harmonic space, this simplifies to

$$\bar{a}^T_{\ell m} = \frac{1}{\tilde{C}^{TT}_\ell + b_\ell^{-2} N^{TT}_\ell} \hat{a}^T_{\ell m} \tag{2.102}$$

$$\bar{a}^E_{\ell m} = \frac{1}{\tilde{C}^{EE}_\ell + b_\ell^{-2} N^{EE}_\ell} \hat{a}^E_{\ell m} \tag{2.103}$$

$$\bar{a}^B_{\ell m} = \frac{1}{\tilde{C}^{BB}_\ell + b_\ell^{-2} N^{BB}_\ell} \hat{a}^B_{\ell m}, \tag{2.104}$$

neglecting any cross-correlation between T, E and B, most notably the TE correlation, which is usually done in quadratic estimator analyses to significantly simplify the computation (cf. Ref. [258]).

[33] https://mpi4py.readthedocs.io/

[34] and is often used interchangeably

In the presence of inhomogeneous noise or limited sky coverage this assumption breaks down and the estimated lensing potential becomes non-optimal if isotropic weights are employed. Already for the first detection of CMB lensing with WMAP, a more optimal weighting scheme was used [344]. The basic idea is to solve the linear equation directly in pixel domain

$$(\tilde{\mathbf{C}} + \mathbf{N})\mathbf{B}\bar{\mathbf{s}} = \hat{\mathbf{s}}, \tag{2.105}$$

where we can use the fact that $\tilde{\mathbf{C}}$ is diagonal in harmonic space, while, in the case of stationary, anisotropic noise, $\mathbf{N}$ is diagonal in pixel-space. This allows efficient application of the matrix $\tilde{\mathbf{C}} + \mathbf{N}$ on a vector, granted it can be efficiently transformed between pixel- and harmonic-space. In practice, it can be useful to bring this equation in the form

$$\mathbf{N}\mathbf{Y} f_\ell^{-1/2} \tilde{\mathbf{C}}_\ell^{1/2} (\tilde{\mathbf{C}}_\ell^{-1} + f_\ell \mathbf{Y}^\dagger \mathbf{N}^{-1} \mathbf{Y} f_\ell) f_\ell^{-1} \mathbf{Y}^\dagger \tilde{\mathbf{C}}_\ell^{1/2} f_\ell^{-1/2} \bar{\mathbf{s}} = \hat{\mathbf{s}}, \tag{2.106}$$

where we made the harmonic transformation steps and the beam- and transfer-functions, f_ℓ, explicit. The operators $\mathbf{Y}$ denote backward transformations from harmonic- to pixel-space, while $\mathbf{Y}^\dagger$ transforms forward from pixel- to harmonic-space. This formulation reduces it to a common problem in linear algebra of large systems of equations. Several solving strategies has been proposed, which include methods in the context of cosmological analysis, namely the multigrid preconditioned conjugate gradient [344] or the messenger-field (MF) technique [106, 264]. The former is extensively used in the CMB lensing context, most prominently in the latest Planck lensing analysis [287], where it helped to further shrink the errorbars of the measured lensing power spectrum. The results in Sec. 4.3 are produced with a code based on the publicly available implementation of the multigrid preconditioner, QCINV[35].

2.8 DISCUSSION

In this section I summarized the basic steps necessary to estimate the CMB lensing power spectrum from CMB data. In this context I laid out the details of the LENSQUEST software, that I developed during my thesis and implements the methods described in Sec. 2.3 and following sections. This code is the basis of the work in the remainder of the thesis, either applied on simulated or real data sets.

[35] https://github.com/dhanson/qcinv

I did not continue (with studying the CMB), because I had trouble imagining that such tiny disturbances to the CMB could be detected.

Jim Peebles in Ref. [269]

3 Zooming on B-modes

In this chapter I will describe the methods I used to produce realistic forecast of the delensed B-mode power spectrum and subsequent tensor-to-scalar ratio estimation. This includes a set of methods to analyse polarized CMB maps and power spectra, including component separation methods, lensing of CMB fields and noise simulations.

A measurement of the primordial gravitational wave signal, or alternatively the tensor-to-scalar ratio r, is limited in temperature and E-modes by cosmic variance from the Sachs-Wolfe and integrated Sachs-Wolfe power at large scales. Large scale B-modes, however, are only generated by primordial gravitational waves or non-linear effects, which is why the current constraint on r from B-modes is limited by instrumental noise and secondary anisotropies such as galactic foregrounds and gravitational lensing. In this chapter I will summarize the mentioned three effects that pose the major challenges to improved constraints on r from CMB B-modes. We will generalize the notation of the measured signal (data) vector as

$$\hat{\mathbf{d}} \equiv \mathbf{BAc} + \mathbf{n}, \tag{3.1}$$

$$\hat{\mathbf{d}}_\nu \equiv \mathbf{B}_\nu \mathbf{A}_{\nu i} \mathbf{c}_i + \mathbf{n}_\nu \tag{3.2}$$

where $\mathbf{c}$ contains the Stokes parameters of the various sky components, i.e. lensed CMB and foregrounds. One can write it as

$$\mathbf{c} = \begin{pmatrix} T_{\rm CMB} \\ Q_{\rm CMB} \\ U_{\rm CMB} \\ T_{\rm dust} \\ Q_{\rm dust} \\ U_{\rm dust} \\ \vdots \end{pmatrix}. \tag{3.3}$$

$\mathbf{A}$ is the so-called mixing matrix, which, applied to such a component vector, produces corresponding linear combinations of components as measured at a given frequency (or in a frequency channel with given bandpass). Then $\mathbf{B}$ applies the beam smoothing corresponding to the frequency channel. The last term contains the instrumental noise for each Stokes parameter in each frequency channel. Finally,

one obtains a data vector which has the form

$$\hat{\mathbf{d}} = \begin{pmatrix} T_{\nu_1} \\ Q_{\nu_1} \\ U_{\nu_1} \\ \vdots \\ T_{\nu_N} \\ Q_{\nu_N} \\ U_{\nu_N} \end{pmatrix}, \tag{3.4}$$

for frequency channels ν_1 to ν_N, $N \leq 1$.

3.1 INSTRUMENTAL NOISE

We call the noise of a pixelised map white noise if $\mathbf{n}_i$ has uniform variance and is uncorrelated for all pixels, i.e.

$$\langle \mathbf{n}_i \mathbf{n}_j \rangle = \sigma^2_{\text{pix}} \delta_{ij} \tag{3.5}$$

for all pairs of pixels i and j [192]. Another property of white noise is that the variance is inverse proportional to the pixel size above the beam scale, Ω_{pix},

$$\sigma^2_{\text{pix}} \sim \frac{1}{\Omega_{\text{pix}}}. \tag{3.6}$$

A quantity independent of the pixel size is the weight per solid angle

$$w \equiv \frac{1}{\sigma^2_{\text{pix}} \Omega_{\text{pix}}} \equiv \sigma_T^{-2}, \tag{3.7}$$

where we call σ_T the (white) noise level in temperature with units often given in μKarcmin. The noise level depends on the detector sensitivity which is given in terms of the noise-equivalent temperature for a full detector array, NET_{array}, as

$$\sigma_T = \sqrt{\frac{f_{\text{sky}}}{T_{\text{obs}} \epsilon}} NET_{\text{array}}, \tag{3.8}$$

where

- f_{sky} is the observed fraction of the sky,
- T_{obs} is the observation time and
- ϵ is the observation efficiency.

It will be useful to consider beam-deconvolved data, which we will use in the following without a change in notation

$$\hat{\mathbf{d}} \equiv \mathbf{A}\mathbf{c} + \mathbf{B}^{-1}\mathbf{n}, \tag{3.9}$$

where the operation in the latter term is usually understood to be evaluated in harmonic domain. This has the advantage that the signal has no multiplicative bias in the data. In the case of a Gaussian beam this lets us write a white noise power spectrum as [192]

$$N_\ell^{TT} = (\sigma_T \, [\mu K \text{rad}])^2 \exp\left(\ell(\ell+1) \frac{(\theta)^2}{8 \ln 2} \right), \tag{3.10}$$

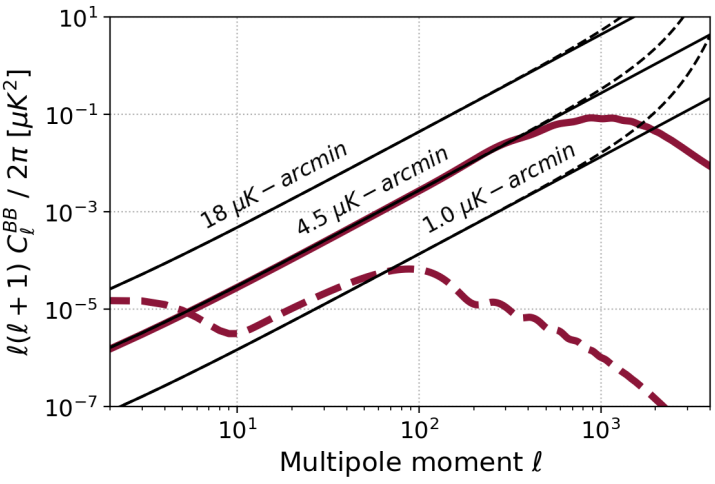

Figure 3.1: This figure shows three exemplary white noise curves, for noise levels in polarization $18\ \mu\mathrm{K}-$ arcmin, $4.5\ \mu\mathrm{K}-$arcmin, $1.0\ \mu\mathrm{K}-$ arcmin. In red the B-mode power spectra from gravitational lensing (solid line) and primordial tensor perturbations with $r = 10^{-3}$ (dashed line) are shown.

where θ is the FWHM of the Gaussian beam expressed in radians. If the polarization data is obtained from the same experiment as the temperature data (e.g. by subtracting the latter between two orthogonal axes or alternatively see Sec. 4.3.2), then the pixel-level noise is related by

$$\left(\sigma^P_{\rm pix}\right)^2 = 2\left(\sigma^T_{\rm pix}\right)^2, \tag{3.11}$$

which leads to

$$\sigma_P = \sqrt{2}\sigma_T, \tag{3.12}$$

called noise level in polarization. To model correlated noise we write

$$N_\ell = N_\ell^{\rm white}\left(1+\left(\frac{\ell}{\ell_{\rm knee}}\right)^{\alpha_{\rm knee}}\right), \tag{3.13}$$

where we add to the previously introduced white noise spectrum a red spectrum with knee multipole $\ell_{\rm knee}$ and slope $\alpha_{\rm knee}$. Fig. 3.1 shows three examples of white noise power spectra, N_ℓ^{BB}, on top of the B-mode power spectrum. Note that the white part of the power spectrum caused by lensing corresponds roughly to a white noise level of $4.5\ \mu\mathrm{K}-$ arcmin in polarization for our fiducial cosmology (Tab. 1.5).

3.2 GALACTIC FOREGROUNDS

Polarized galactic foregrounds are seen to be a major obstacle in measuring large scale primordial B-modes currently and in the future [371, 109]. As measured by the Planck satellite, the emission from dust and synchrotron in our galaxy is highly polarized, such that the measured B-mode power from galactic foregrounds alone can be of order, or even orders of magnitude larger than the cosmological signal that we want to measure [296]. Note that this is not the case for temperature and E-mode measurements of the CMB. Fig. 3.2 shows typical levels of foreground contamination for B-modes from galactic dust and synchrotron in 5% of the sky from simulations based on Planck measurements.

The basis of galactic component separation are the differing spectral and statistical properties of the CMB, which is a black-body, and the foreground components. Assuming the polarized galactic sky to be constituted by two components, dust and synchrotron emission, Planck [285] found for the variance of the polarization signal as shown in Fig. 3.3.

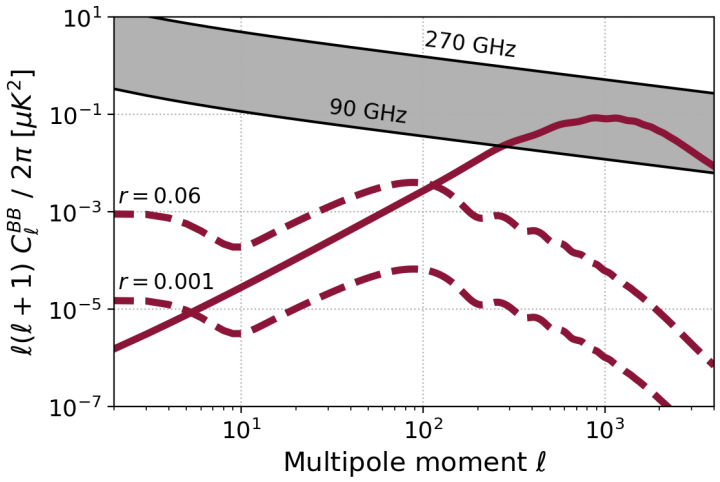

Figure 3.2: The level of galactic foreground emission in the B-mode power spectrum for 5% of the sky, avoiding foreground intensity as much as possible. The combined contribution from dust and synchrotron emission is shown for frequencies between 90 GHz and 270 GHz. The two components of the CMB B-mode power spectrum from lensing and tensor perturbations, for the cases of $r = 10^{-3}$ targeted by future experiments and the current upper limit of $r = 0.06$ [375] are shown in red.

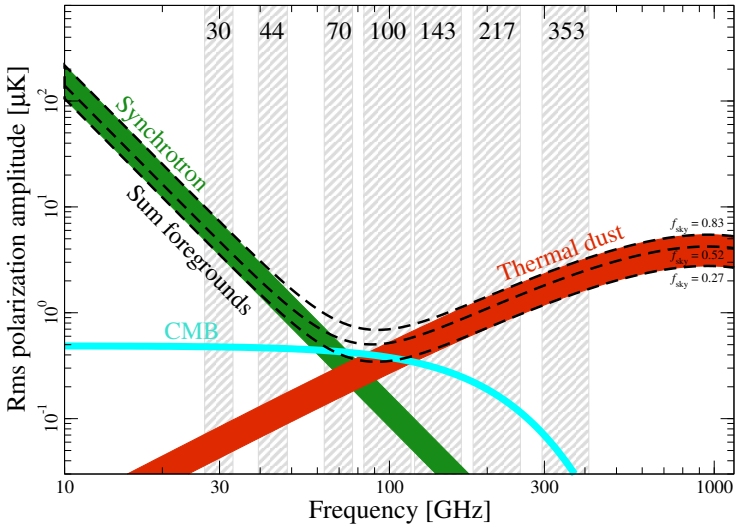

Figure 3.3: The spectral behaviour of CMB, thermal dust and synchrotron polarized emission. Figure taken from Ref. [285].

On the basis of all component separation algorithms lies the simple data model

$$\hat{\mathbf{d}} = \hat{\mathbf{A}}\mathbf{c} + \overline{\mathbf{n}}, \tag{3.14}$$

where $\overline{\mathbf{n}}$ is the beam-deconvolved noise. In this section we focus on the mixing matrix

$$\mathbf{A} = \left(\begin{array}{c|c|c} & & \\ \mathbf{A}^{\mathrm{CMB}} & \cdots & \mathbf{A}^{\mathrm{fg}} \cdots \\ & & \end{array} \right) \tag{3.15}$$

which produces data vectors of single-frequency signal maps as linear combinations of the sky components in $\mathbf{c}$. Hence, $\mathbf{d}$ is a vector of length $3 \times N_f \times N_{\mathrm{pix}}$, where N_f is the number of frequency channels, and $\mathbf{c}$ is a vector of length $3 \times N_c \times N_{\mathrm{pix}}$, where N_c is the number of assumed components in the sky signal. The true mixing matrix is indicated with a $\hat{\bullet}$, while any modelled mixing matrix as needed for foreground cleaning is denoted $\mathbf{A}$.

3.2.1 PARAMETRIC FOREGROUND CLEANING

In the case we can model the spectral emission of all components given some spectral parameters θ_i for component i,

$$A_{\nu i} = s_i(\theta, \nu) \tag{3.16}$$

we can introduce a Gaussian likelihood given by

$$-2\log\mathcal{L}(\mathbf{d}|\mathbf{c},\theta_i) = (\mathbf{d}-\mathbf{A}\mathbf{c})^T\mathbf{N}^{-1}(\mathbf{d}-\mathbf{A}\mathbf{c}) + \text{const.}\,, \tag{3.17}$$

where $\mathbf{N}$ is the noise covariance matrix in pixel space with rank $N_f \cdot N_c$. The maximum likelihood value is obtained by differentiating with respect to θ_i and $\mathbf{c}$ leading to [357]

$$-\left(\frac{\partial\mathbf{A}}{\partial\theta_i}\mathbf{c}\right)\mathbf{N}^{-1}(\mathbf{d}-\mathbf{A}\mathbf{c}) = 0 \tag{3.18}$$

$$\mathbf{c} = \left(\mathbf{A}^T\mathbf{N}^{-1}\mathbf{A}\right)^{-1}\mathbf{A}^T\mathbf{N}^{-1}\mathbf{d}. \tag{3.19}$$

From that one can obtain the spectral likelihood by evaluating the likelihood above at the maximum-likelihood position with respect to the components $\mathbf{c}$

$$-2\log\mathcal{L}_{\text{spec.}}(\mathbf{d}|\theta_i) = -\left(\mathbf{A}^T\mathbf{N}^{-1}\mathbf{d}\right)^T\left(\mathbf{A}^T\mathbf{N}^{-1}\mathbf{A}\right)^{-1}\mathbf{A}^T\mathbf{N}^{-1}\mathbf{d} + \text{const.}\,. \tag{3.20}$$

In contrast to the marginalized likelihood $\int d\mathbf{c}\mathcal{L}(\mathbf{d}|\mathbf{c},\theta_i)$ the maximum values of the spectral likelihood coincide with the maximum-likelihood estimates of the full likelihood [357]. While the best-fit value is an (asymptotically) unbiased estimator, the widths of the true and spectral likelihood do not coincide. In order to compute the covariance of the spectral parameters we compute the second derivative of the (log-)likelihood

$$\frac{\partial^2(-2\log\mathcal{L})}{\partial\theta_i\partial\theta_j} = \left(\frac{\partial^2\mathbf{A}}{\partial\theta_i\partial\theta_j}\mathbf{c} + \frac{\partial\mathbf{A}}{\partial\theta_i}\frac{\partial\mathbf{c}}{\partial\theta_j}\right)^T\mathbf{N}^{-1}(\mathbf{d}-\mathbf{A}\mathbf{c}) - \left(\frac{\partial\mathbf{A}}{\partial\theta_i}\mathbf{c}\right)^T\mathbf{N}^{-1}\left(\frac{\partial\mathbf{A}}{\partial\theta_j}\mathbf{c} + \mathbf{A}\frac{\partial\mathbf{c}}{\partial\theta_j}\right).$$

3.2.2 FORECASTING

This allows us to write the covariance matrix of spectral parameters as estimated from the spectral likelihood, which results in [110, 109]

$$\begin{aligned}\left(\mathbf{\Sigma}^{-1}\right)_{ij} &= -\left\langle\frac{\partial^2\log\mathcal{L}_{\text{spec.}}}{\partial\theta_i\partial\theta_j}\right\rangle_{\text{noise}}\Bigg|_{\theta=\theta^*} = \\ &= -\text{Tr}\left(\left(\frac{\partial\mathbf{A}^T}{\partial\theta_i}\mathbf{N}^{-1}\mathbf{A}\left(\mathbf{A}^T\mathbf{N}^{-1}\mathbf{A}\right)^{-1}\mathbf{A}^T\mathbf{N}^{-1}\frac{\partial\mathbf{A}}{\partial\theta_j} - \frac{\partial\mathbf{A}^T}{\partial\theta_i}\mathbf{N}^{-1}\frac{\partial\mathbf{A}}{\partial\theta_j}\right)\mathbf{c}\mathbf{c}^T\right)\end{aligned} \tag{3.21}$$

where θ^* is the maximum-likelihood estimate. We obtained this ensamble-averaged covariance matrix, the so-called Fisher information matrix, by averaging over possible noise realizations, allowing to forecast the performance of an experiment given a noise covariance matrix $\mathbf{N}$. Assuming Gaussianity the uncertainty on a given spectral parameter is then given by the square root of the respective inverse covariance matrix element

$$\sigma(\theta_i) = \sqrt{(|\mathbf{\Sigma}_{ii}|)}. \tag{3.22}$$

This *statistical uncertainty* on the spectral parameter fit due to instrumental noise will eventually propagate to residuals in the cleaned CMB and will cause biases in the resulting power spectra and derived cosmological parameters. Systematic uncertainties arise if the modelling of the true sky, $\mathbf{A}$ in Eq. 3.14, which is implicitly given in the multifrequency data maps, and the assumed sky, $\hat{\mathbf{A}}$ in Eq. 3.17, does not conform. The latter uncertainties may result in systematic biases in the cleaned CMB maps and final summary statistic. Inconsistencies in the scaling laws or their variability on the sky, for example, may introduce such systematic biases.

3.2.3 FOREGROUND RESIDUALS

From the maximization of the likelihood we can obtain an estimator for the components

$$\hat{\mathbf{c}} = \left(\mathbf{A}^{*\,T}\mathbf{N}^{-1}\mathbf{A}^{*}\right)^{-1}\mathbf{A}^{*\,T}\mathbf{N}^{-1}\hat{\mathbf{d}} \equiv \mathbf{W}|_{\theta=\theta_*}\hat{\mathbf{d}}, \tag{3.23}$$

given the best-fit value of the spectral likelihood, θ_*, determining $\mathbf{A}^*$. The residuals in the component maps are then defined as

$$\mathbf{r} = \hat{\mathbf{c}} - \mathbf{c}. \tag{3.24}$$

If the model for the CMB scaling is the same in the true data and the model, one finds for the residual in the cleaned CMB map

$$\mathbf{r}^{\mathrm{CMB}} = \sum_{\nu\in\text{frequencies}} \mathbf{W}^{\mathrm{CMB},\nu}|_{\theta_*}\mathbf{f}^{\nu}, \tag{3.25}$$

where $\mathbf{f}^{\nu}$ are the foreground maps in the frequency channel ν of the data. To characterize its behaviour around the best-fit value we perform a Taylor expansion up to second order around this value [356]

$$\mathbf{r}^{\mathrm{CMB}} \equiv \mathbf{r}^{(0)} + \mathbf{r}^{(1)\,i}\delta\theta_i + \mathbf{r}^{(2)\,ij}\delta\theta_i\delta\theta_j, \tag{3.26}$$

where

$$\mathbf{r}^{(0)} = \sum_{\nu} \mathbf{W}^{\mathrm{CMB},\nu}|_{\theta_*}\mathbf{f}^{\nu} \tag{3.27}$$

$$\mathbf{r}^{(1)\,i} = \sum_{\nu} \frac{\partial\mathbf{W}^{\mathrm{CMB},\nu}}{\partial\theta_i}|_{\theta_*}\mathbf{f}^{\nu} \tag{3.28}$$

$$\mathbf{r}^{(2)\,ij} = \sum_{\nu} \frac{\partial^2\mathbf{W}^{\mathrm{CMB},\nu}}{\partial\theta_i\partial\theta_j}|_{\theta_*}\mathbf{f}^{\nu}, \tag{3.29}$$

which are in total $1 + N_c + N_c(N_c+1)/2$ independent vectors of $3 \times N_{\mathrm{pix}}$ entries.

We can evaluate the effect of these residuals, while treating the errors on the spectral parameters estimation statistically, for the CMB power spectra and CMB lensing power spectrum. For the power spectrum we have up to second order in the error on the spectral parameters

$$\left\langle \mathbf{r}^{\mathrm{CMB}}\mathbf{r}^{\mathrm{CMB}\,\dagger}\right\rangle = \left\langle \mathbf{r}^{(0)}\mathbf{r}^{(0)\,\dagger}\right\rangle + \left\langle \mathbf{r}^{(1)\,i}\mathbf{r}^{(1)\,j\,\dagger}\right\rangle \Sigma_{ij} + \left\langle \mathbf{r}^{(0)}\mathbf{r}^{(2)\,ij\,\dagger}\right\rangle \Sigma_{ij} + \left\langle \mathbf{r}^{(2)\,ij}\mathbf{r}^{(0)\,\dagger}\right\rangle \Sigma_{ij}, \tag{3.30}$$

where we recognize the covariance of spectral parameters after noise averaging

$$\Sigma_{ij} = \langle \delta\theta_i\delta\theta_j \rangle . \tag{3.31}$$

Another crucial effect, besides leaving residuals in the cleaned CMB maps due to errors on the foreground model fitting and foreground mis-modeling, component separation from multifrequency maps is propagating the noise in a non-optimal way. The estimator in Eq. 3.23 leaves a noise in the cleaned CMB map given by

$$\mathbf{n}^{\mathrm{CMB}} = \sum_{\nu\in\text{frequencies}} \mathbf{W}^{\mathrm{CMB},\nu}|_{\theta_*}\mathbf{n}^{\nu}, \tag{3.32}$$

depending on the noise in each frequency map, $\mathbf{n}^{\nu}$. The pixel-space noise covariance follows directly giving

$$\sigma^{\mathrm{CMB}} = \left[\left(\mathbf{A}^{T}\mathbf{N}^{-1}\mathbf{A}\right)^{-1}\right]_{\mathrm{CMB,CMB}}. \tag{3.33}$$

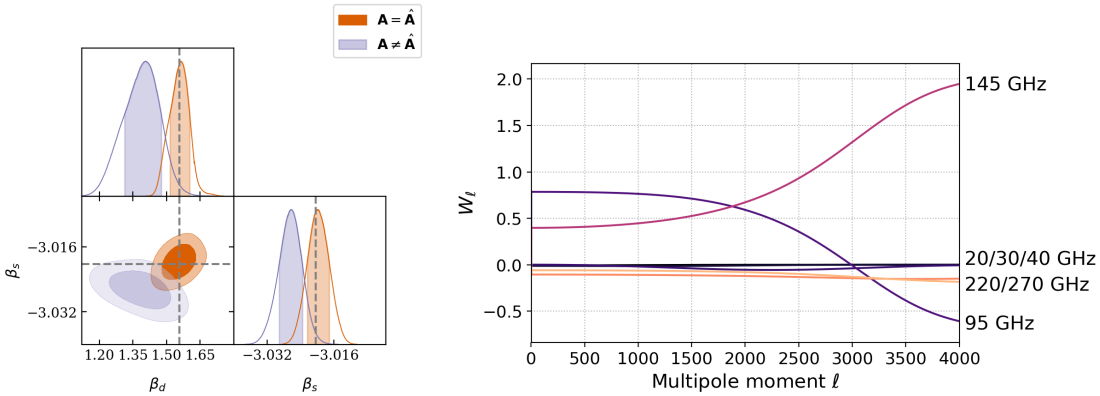

Figure 3.4: Examples for the two main steps of the presented parametric component separation. The left figure shows the two-dimensional and marginalised one-dimensional posteriors of the spectral parameter estimation using the spectral likelihood for two different models of the input foreground scaling including dust and synchrotron emission. The assumed scaling model is the same in both cases, such that the assumed and input model is the same for the case in orange and different for the case in red. The right figure shows the weights used in the cleaning of foregrounds by combining, in this case, six frequency channels. Details on the experimental configurations are given in Sec. 6.2.

Furthermore, we can write some of these expressions explicitly in multipole space assuming statistically isotropic noise and constant spectral indices across the sky. We then have

$$\mathbf{W}_\ell^* = \left(\mathbf{A}^{*\,T}\mathbf{N}_\ell^{-1}\mathbf{A}^*\right)^{-1}\mathbf{A}^{*\,T}\mathbf{N}_\ell^{-1}, \tag{3.34}$$

giving an ℓ-dependent weight function each frequency map has to multiplied with before combining it into a cleaned CMB map. Furthermore, the noise after component separation is then simply given by

$$N_\ell^{\text{cleaned}} = \left[\left(\mathbf{A}^{*\,T}\mathbf{N}_\ell^{-1}\mathbf{A}^*\right)^{-1}\right]_{\text{CMB,CMB}}. \tag{3.35}$$

Fig. 3.4 shows two steps of an exemplary component separation pipeline, the estimation of the spectral parameters and the computation of the cleaned CMB map by combining single frequency maps. It shows an example of systematic bias introduced when the assumed model for the mixing matrix does not conform with the mixing in the true sky ($\mathbf{A} \neq \hat{\mathbf{A}}$). The component-separation-weights show the relative contribution of high- medium and low-frequency channels to the cleaned CMB map. Owed to the minimum of foreground emission around 90 GHz, the medium frequency channels (in this case 90 and 145 GHz) contribute the most to the cleaned CMB map. In the example the 145 GHz channel dominates at high multipoles due to the better resolution in these maps.

In Fig. 3.5 the power spectrum of the foreground residuals in the CMB maps are shown, arising due to systematic and statistical errors. The degradation of the noise compared to a simple inverse-noise-weighting of the CMB channels is shown as well.

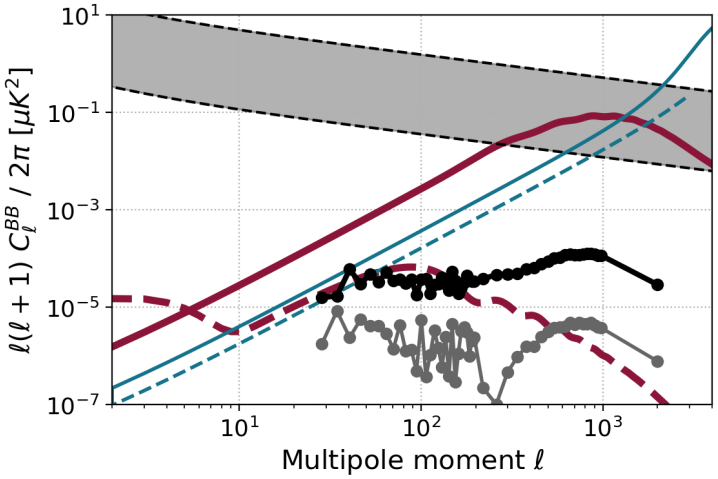

Figure 3.5: This figure is similar to Fig. 3.2, but also shows the level of foreground residuals, to be compared with the shown level of primordial B-modes for $r = 10^{-3}$. The 1σ-level of statistical residuals is shown in gray points, while the systematic error, due to imperfect foreground model assumed in the cleaning, is shown in black points. The noise power spectrum in the cleaned CMB map is shown in the orange solid line, which is larger than expected from a simple inverse noise weighting of the 95 and 145 GHz channels in the orange dashed line. The assumed instrumental configuration and foreground model corresponds to CMB-S4 with the non-Gaussian foreground simulations of Sec. 6.1.1.

3.3 GRAVITATIONAL LENSING

3.3.1 REMOVING LENSING IN THE B-MODES: DELENSING

The effect weak gravitational lensing has on the B-mode power spectrum is explained in Secs. 1.6.2 and 2.1. As we have seen, the effect of a lensing deflection field $\mathbf{d}$ on the CMB can be expressed with the deflection operator

$$\tilde{\mathbf{s}} = \mathbf{D}_{\mathbf{d}}\mathbf{s}, \tag{3.36}$$

where $\tilde{\mathbf{s}} = \mathbf{c}^{\rm CMB}$ in the context of the previous sections. As introduced in Sec. 2.1, the inverse of this deflection operator is given by $\mathbf{D}_{-\mathbf{d}'}$, where the inverse deflection field $\mathbf{d}'$ is implicitly given by

$$\mathbf{d}(\mathbf{n}) = \mathbf{d}'(\mathbf{n} + \mathbf{d}(\mathbf{n})) \tag{3.37}$$

In principle, this operation introduces a curl potential in the inverse lensing operation

$$\mathbf{d}'(\mathbf{n}) = \nabla\phi^{\rm inv}(\mathbf{n}) + \star\nabla\omega^{\rm inv}(\mathbf{n}), \tag{3.38}$$

which, however, is sub-dominant [16]. In practice the inverse lensing deflection field can be obtained iteratively in a Newton-Raphson method [67]

$$\mathbf{d}'^{(N+1)}(\mathbf{n}) = \mathbf{d}'^{(N)}(\mathbf{n}) + \mathbf{M}^{-1}(\mathbf{n} - \mathbf{d}'^{(N)}(\mathbf{n})) \cdot (\mathbf{d}'^{(N)}(\mathbf{n}) + \mathbf{d}(\mathbf{n} - \mathbf{d}'^{(N)}(\mathbf{n}))), \tag{3.39}$$

where $\mathbf{M}$ is the magnification matrix for the forward deflection $\mathbf{d}$ as defined in Eq. 1.250. The iteration can be started at $\mathbf{d}'^{(0)} = 0$. In current experimental configurations the inverse lensing can be approximated by $\mathbf{d}' = \mathbf{d}$ (in Ref. [16] called *anti-lensing*), which, however, might lead to significant errors in the low-noise regime [67].

To allow for an inversion of the lensing effect in practice, in the presence of noisy CMB data and a noisy estimate of the lensing deflection field, estimators are required. Such so-called delensing algorithms that allow for such a separation of lensing and primordial CMB statistically have been proposed in the literature [193, 187, 159, 332, 346, 338, 66, 240]. Before trying to obtain a delensing estimator

from the Likelihood formalism we have been using in this section so far, it is instructive to focus on the delensing of B-modes (in the ideal case of isotropic noise and full sky coverage) using the first order perturbative expansion first. The delensing of polarization Stokes parameters can be written in a general form as

$$(Q^{\text{del}} \pm iU^{\text{del}})(\mathbf{n}) = f \star (\hat{Q} \pm i\hat{U})(\mathbf{n}) + h \star (\hat{Q} \pm i\hat{U})(\mathbf{n} - g \star \nabla\phi(\mathbf{n})) \tag{3.40}$$

and in harmonic space

$$a^{B\,\text{del}}_{\ell m} = (f^B_\ell + h^B_\ell)\hat{a}^B_{\ell m} - \sum_{\ell' m'}\sum_{LM} g_L \hat{\phi}_{LM}(-1)^m {}_2F_{\ell L \ell'} \begin{pmatrix} \ell & L & \ell' \\ m & -M & -m' \end{pmatrix} \times \\ \times \left(\epsilon_{\ell L \ell'} h^B_{\ell'} \hat{a}^B_{\ell' m'} - \beta_{\ell L \ell'} h^E_{\ell'} i\hat{a}^E_{\ell' m'}\right), \tag{3.41}$$

where the $\star$-operator applies an arbitrary isotropic and real filter function in harmonic space. In the idealistic case, where the lensing potential and the unlensed CMB signal is perfectly known, one recovers the expressions of 1.6.2 with $h = g = 1,\ f = 0$, obtaining the primordial contribution to the B-modes by subtracting the lensing signal (lensing template) from the total signal (to first order in ϕ). In the case of noisy data, one has to use estimates of the lensing potential and the primary CMB, which is usually done by filtering the observed CMB and reconstructed lensing potential in an optimal way, motivating the equation above.

Simply remapping (anti-lensing) the (Wiener-filtered) Q and U Stokes parameter in every pixel according to the Wiener-filtered reconstructed lensing potential, $\hat{\phi}$, translates up to first order in ϕ to the following set of filters in harmonic space

$$g_L = \frac{C^{\phi\phi}_L}{C^{\phi\phi}_L + N^{\phi\phi}_L} \tag{3.42}$$

$$f^B_\ell = 0 \tag{3.43}$$

$$h^E_\ell = \frac{\tilde{C}^{EE}_\ell}{\tilde{C}^{EE}_\ell + N^{EE}_\ell} \tag{3.44}$$

$$h^B_\ell = \frac{\tilde{C}^{BB}_\ell}{\tilde{C}^{BB}_\ell + N^{BB}_\ell}, \tag{3.45}$$

The formalism in Ref. [346] is called *template delensing* and yields

$$g_L = \frac{C^{\phi\phi}_L}{C^{\phi\phi}_L + N^{\phi\phi}_L} \tag{3.46}$$

$$f^B_\ell = 1 \tag{3.47}$$

$$h^E_\ell = \frac{C^{EE}_\ell}{\tilde{C}^{EE}_\ell + N^{EE}_\ell} \tag{3.48}$$

$$h^B_\ell = 0, \tag{3.49}$$

by minimizing the variance in the delensed power spectrum.

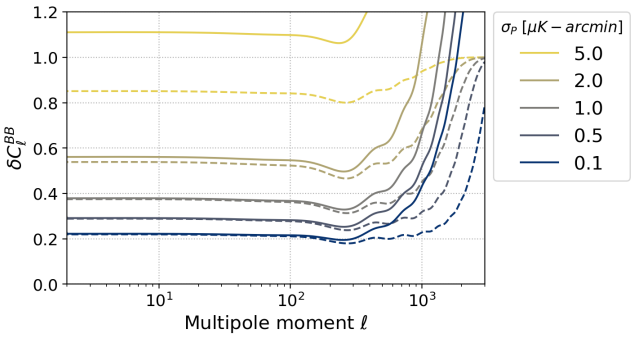

Figure 3.6: The ratio of the B-mode power spectra after delensing compared to B-mode power spectra without delensing for two different choices of filtering. For the solid lines the filter of Eqs. 3.42-3.45 is used, while delensing with the filtering of Eqs. 3.46-3.49 is shown in the dashed lines. The additional lensing of the noise in the B-mode spectrum in the former case causes the noise-level-dependent degradation of the delensing efficiency relative to the latter case.

The delensed B-mode power spectrum, assuming zero primordial B-mode power, in the former case is then given by

$$C_\ell^{BB\,\mathrm{del}} = \left(\frac{\tilde{C}_\ell^{BB}}{\tilde{C}_\ell^{BB}+N_\ell^{BB}}\right)^2 \left(\tilde{C}_\ell^{BB}+N_\ell^{BB}\right) + \frac{1}{2\ell+1}\sum_{\ell' L} |{}_2F_{\ell\ell' L}\epsilon_{\ell L\ell'}|^2 \frac{\left(\tilde{C}_{\ell'}^{BB}\right)^2}{\tilde{C}_{\ell'}^{BB}+N_{\ell'}^{BB}} \frac{\left(C_L^{\phi\phi}\right)^2}{C_L^{\phi\phi}+N_L^{\phi\phi}} + \\ + \left(1-2\frac{\tilde{C}_\ell^{BB}}{\tilde{C}_\ell^{BB}+N_\ell^{BB}}\right) \frac{1}{2\ell+1}\sum_{\ell' L} |{}_2F_{\ell\ell' L}\beta_{\ell L\ell'}|^2 \frac{\left(\tilde{C}_{\ell'}^{EE}\right)^2}{\tilde{C}_{\ell'}^{EE}+N_{\ell'}^{EE}} \frac{\left(C_L^{\phi\phi}\right)^2}{C_L^{\phi\phi}+N_L^{\phi\phi}} \tag{3.50}$$

and in the latter case by

$$C_\ell^{BB\,\mathrm{del}} = \tilde{C}_\ell^{BB} + N_\ell^{BB} - \frac{1}{2\ell+1}\sum_{\ell' L} |{}_2F_{\ell\ell' L}\beta_{\ell L\ell'}|^2 \frac{\left(C_{\ell'}^{EE}\right)^2}{\tilde{C}_{\ell'}^{EE}+N_{\ell'}^{EE}} \frac{\left(C_L^{\phi\phi}\right)^2}{C_L^{\phi\phi}+N_L^{\phi\phi}}. \tag{3.51}$$

The negligence of the primordial B-mode signal in the filters is justified by its smallness compared to the E-mode signal. It is noted that these methods assume known signal covariances. The naive remapping of the (Wiener-filtered) Q and U parameters translates in an additional term including the Wiener-filtered observed B-mode field in harmonic space. The difference in terms of the delensing efficiency obtained by employing one of the two sets of filters in Eqs. 3.42-3.45 and Eqs. 3.46-3.49 is shown in Fig. 3.6. It depicts the degradation of the delensing efficiency using the filters of Eqs. 3.42-3.45 caused by the additional lensing of the B-mode noise, which is not present in the template delensing regime (Eqs. 3.46-3.49).

Fig. 3.7 shows an example of the residual delensed B-mode power spectrum given different noise curves, computed with Eq. 3.51. The ratio between residual delensed B-mode power spectrum and lensed power spectrum is almost constant at scales $\ell < 250$ relevant for a primordial B-mode detection. Hence, it is common to quote a corresponding lensing amplitude, A_{lens}, to a delensed power spectrum

$$C_\ell^{BB\,\mathrm{del}} \approx A_{\mathrm{lens}}\tilde{C}_\ell^{BB}\,,\ (r=0). \tag{3.52}$$

Fig. 3.8 shows the dependence of this amplitude on the white noise level of the CMB, on which the lensing potential is reconstructed, and the E-modes used in the delensing convolution in Eq. 3.41. Since the E-modes are already measured at a high signal-to-noise for the noise levels considered, A_{lens} only depends weakly on the E-mode white noise. Note that, due to the cosmic variance of the lensed CMB used in the reconstruction of ϕ with the quadratic estimator, even in the limit of no noise there is residual delensed B-mode power (cosmic-variance limit).

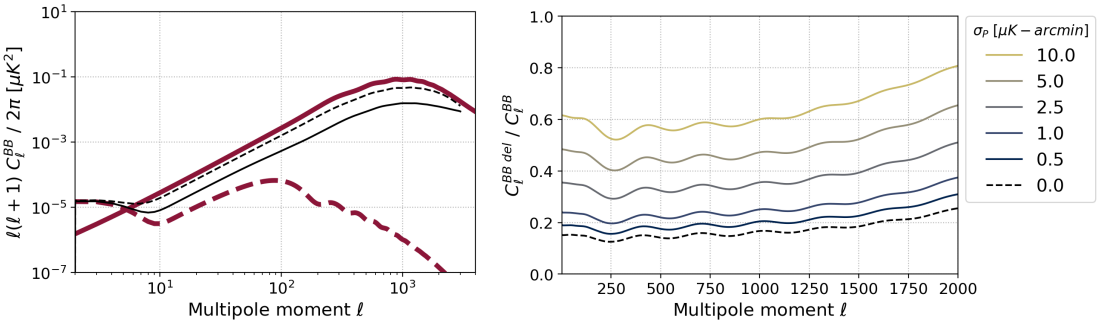

Figure 3.7: The figure on the left-hand-side shows an example of the B-mode power spectrum for our fiducial cosmology before and after delensing. Ignoring foregrounds, the signal includes large-scale power from primordial gravitational waves ($r = 10^{-3}$) and power at small scales from lensing. Delensing reduces the lensing B-mode power, as well as the corresponding cosmic variance, as given in two examples in the black line. They correspond to different instrumental configurations, where the solid line is for a low-noise experiment with $\sigma_P = 0.5\ \mu$Karcmin and the dashed line for a relatively high-noise experiment with $\sigma_P = 10.0\ \mu$Karcmin. In both an experimental beam of $\theta = 1$ arcmin is assumed. The right-hand-side figure shows the ratio between the delensed and lensed power spectra (without primary contribution). For scales $\ell < 250$ this ratio is almost constant.

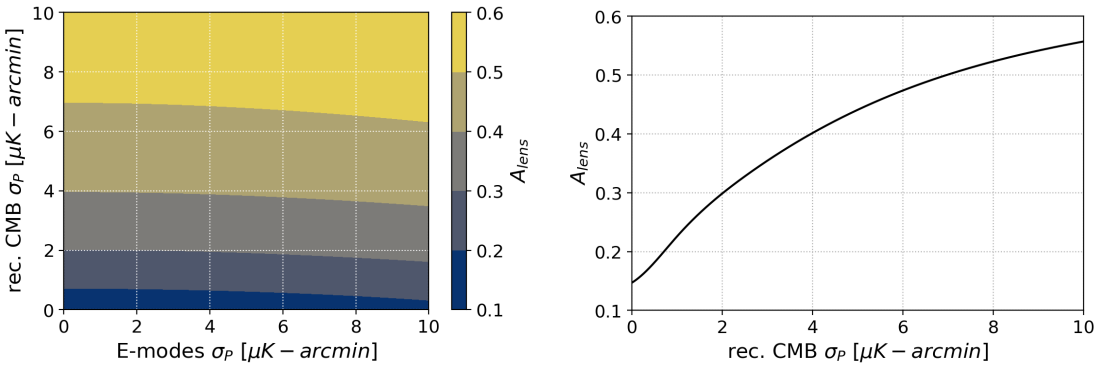

Figure 3.8: The figure on the left shows the delensing amplitude $A_{\rm lens}$ obtained for different experimental configurations, with the possibility to obtain the lensing potential reconstruction and the E-modes for the delensing convolution from two different experiments with two different white noise levels. The right hand side shows a slice at E-mode $\sigma_P = 1.0\ \mu$K $-$ arcmin.

Fig. 3.9 shows the importance of small-scale E-modes for the delensing, e.g. using E-modes solely from an experiment with a resolution $\theta \ll 10$ arcmin could heavily degrade the delensing performance. In practice, considering the split of large-scale and small-scale experiments, the E-mode information could come from a combination of two data sets.

3.3.2 ITERATIVE DELENSING

Another concept which can be qualitatively introduced in this context and more formally derived in a maximum likelihood formalism is iterative delensing. For low-noise experiment the variance from gravitation lensing is dominant over the instrumental noise in the B-mode power spectrum. Hence, the reconstruction of the lensing potential with the quadratic estimator in the EB combination is limited by the mixing of modes due to lensing in the power spectrum. This limiting factor, however, can be reduced by delensing the B-mode power spectrum, to which the quadratic estimator can be reapplied with a adopted weighting. One obtains an improved estimate of the lensing potential which can in turn used to further delens the B-mode signal. In the limit of no instrumental noise, infinite

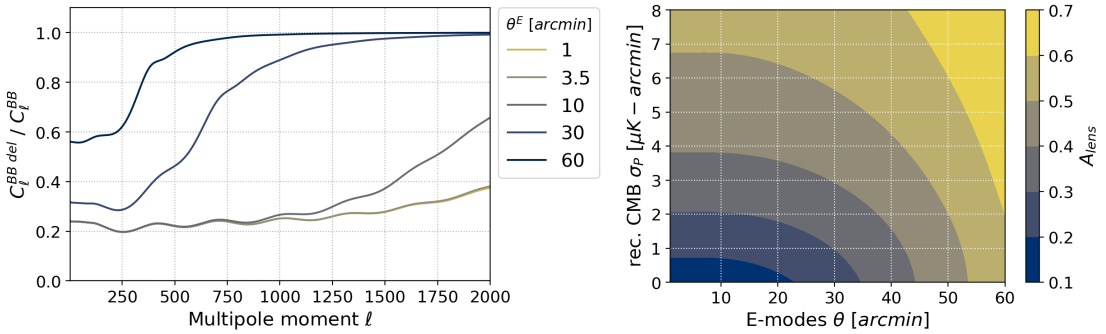

Figure 3.9: Considering varying resolutions of the E-mode measurement used in the delensing convolution Eq. 3.41, showing the importance of small-scale E-modes. The left hand side shows the ratio of the delensed residual B-mode power compared to lensing B-modes power for different beam-sizes θ of the E-mode data. The right hand side shows the delensing amplitude depending on the white noise level of the data used for the lensing reconstruction and the beam-size of the E-mode data set.

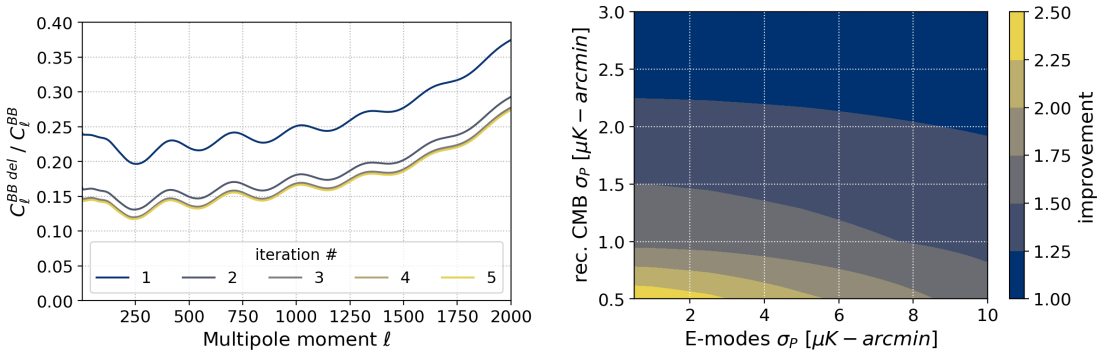

Figure 3.10: The figure on the left shows the residual lensing B-mode power spectrum after N iterations relative to the lensed B-mode power spectrum. It is assuming internal delensing with a white noise level $\sigma_P = 1.0\,\mu$K-arcmin and a 1 arcmin beam. The right figure is showing the ratio of delensing amplitudes after iterative delensing, stopping after 5 iterations relative to stopping after the first one, assuming two different white noise levels for lensing reconstruction and the E-mode measurements.

resolution and the absence of foregrounds as well as a rotational component of the lensing deflection fields, there is no fundamental limitation in reconstructing ϕ and removing the lensing B-mode power with this method [159]. Care has to be taken to not accidentally remove B-mode power of primordial origin. One way to ameliorate this is to ignore the large-scale B-mode signal in the reconstruction of ϕ, since most of the lensing signal lies in the small-scale B-mode signal [159].

Fig. 3.10 shows the improvement iterative delensing can have for low-noise data for the fiducial cosmology and simplistic instrumental configurations assumed here. For experiments with a white-noise level $< 2\,\mu$Karcmin, iterative delensing can achieve an improvement of about a factor 2.

3.3.3 DELENSING WITH THE QUADRATIC ESTIMATOR

For this section we define shorthand notations for the delensing operation using filters in Eqs. 3.46-3.49

$$a^{B\,\mathrm{del}}_{\ell m} = \hat{a}^B_{\ell m} - \hat{a}^E \hat{\otimes}_{\ell m} \hat{\phi} \equiv \hat{a}^B_{\ell m} - \sum_{\ell' m'} \sum_{LM} g_L \hat{\phi}_{LM} (-1)^m {}_2F_{\ell L \ell'} \begin{pmatrix} \ell & L & \ell' \\ m & -M & -m' \end{pmatrix} \times \\ \times \left(\epsilon_{\ell L \ell'} h^B_{\ell'} \hat{a}^B_{\ell' m'} - \beta_{\ell L \ell'} h^E_{\ell'} i \hat{a}^E_{\ell' m'} \right) \tag{3.53}$$

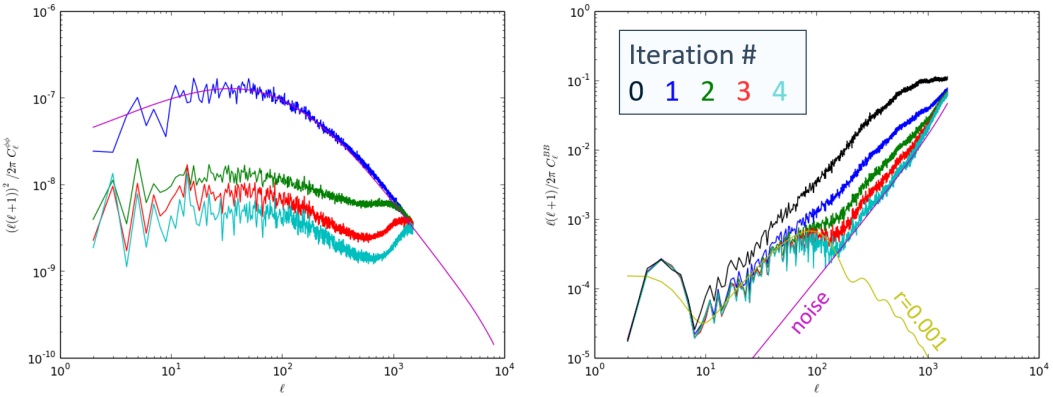

Figure 3.11: Example of iterative delensing, showing the reconstructed lensing potential on the left hand side for each iteration as well as the total B-mode power spectrum for one realization after N iterations. The simulations use $\ell_{\rm max} = 1500$, $N_{\rm side} = 2048$, $1\,\mu$K $-$ arcmin white noise and a 3.5 arcmin beam.

and the lensing reconstruction with the quadratic estimator

$$\hat{\phi}_{LM} = \hat{a}^X \odot_{LM} \hat{a}^Y \equiv \frac{A_L^{XY}}{L(L+1)} \sum_{\ell m} \sum_{\ell' m'} (-1)^{m'} \begin{pmatrix} \ell & \ell' & L \\ -m & m' & -M \end{pmatrix} g^{XY}_{\ell L \ell'} \hat{a}^{X\,\dagger}_{\ell m} \hat{a}^Y_{\ell' m'}. \quad (3.54)$$

The power spectrum of Eq.3.53, assuming ϕ to be an isotropic Gaussian field with power spectrum $C_L^{\phi\phi}$, is given by Eq. 3.51. However, as we have already seen in the computation of the two-point correlation of the reconstructed lensing potential, disconnected correlation functions of the CMB will arise, causing additional terms that bias the power spectrum. The delensed B-mode power spectrum is generally given by

$$\begin{aligned} \left\langle a^{B\,\rm del\,\dagger}_{\ell m} a^{B\,\rm del}_{\ell' m'} \right\rangle &= \left\langle \left(\hat{a}^B_{\ell m} - \hat{a}^E \hat{\otimes}_{\ell m} \hat{a}^X \odot_{LM} \hat{a}^Y\right)^\dagger \left(\hat{a}^B_{\ell' m'} - \hat{a}^E \hat{\otimes}_{\ell' m'} \hat{a}^X \odot_{L'M'} \hat{a}^Y\right) \right\rangle = \\ &= + \left\langle \hat{a}^{B\,\dagger}_{\ell m} \hat{a}^B_{\ell' m'} \right\rangle - \\ &\quad - \left\langle \hat{a}^{B\,\dagger}_{\ell m} \hat{a}^E \hat{\otimes}_{\ell' m'} \hat{a}^X \odot_{L'M'} \hat{a}^Y \right\rangle - \\ &\quad - \left\langle \hat{a}^{E\,\dagger} \hat{\otimes}^\dagger_{\ell m} \hat{a}^{X\,\dagger} \odot^\dagger_{LM} \hat{a}^{Y\,\dagger} \hat{a}^B_{\ell' m'} \right\rangle + \\ &\quad + \left\langle \hat{a}^{E\,\dagger} \hat{\otimes}^\dagger_{\ell m} \hat{a}^{X\,\dagger} \odot^\dagger_{LM} \hat{a}^{Y\,\dagger} \hat{a}^E \hat{\otimes}_{\ell' m'} \hat{a}^X \odot_{L'M'} \hat{a}^Y \right\rangle, \end{aligned} \quad (3.55)$$

where the latter two terms introduces bias depending on the four- and six-point functions of CMB fields [369, 67, 249].

3.4 CONCLUSION

In this Chapter I have summarized some of the key, high-level CMB polarization data analysis methods which I employ in the following chapters. Here I have not included methods for which readily available, general software packages exist. For instance, for B-mode power spectrum estimation based on the pure pseudo-spectrum technique I used the X^{2}PURE software [342, 134, 133] and I used primarily PySM to simulate galactic foregrounds, described in more detail in Sec 6.2.

Science is science and facts are facts.

The 45th President of the United States of America in the Scientific American (2016)

4

Extracting Cosmological information from CMB data sets on the Example of the POLARBEAR & Simons Array Experiments

I am a member of the POLARBEAR/Simons Array collaboration since 2016. My main contributions to the POLARBEAR and Simons Array consisted of contributing to the map-making of the second season small-patch data analysis, leading to a sub-degree scale B-mode power spectrum [379]. Furthermore I helped in the writing and review of follow-up papers [255, 82, 380]. More recently I have been one of the lead data analysts for the third season data set, focusing on a larger CMB patch (large patch). This analysis lead to measurements of tropospheric ice clouds [363] and the polarized CMB on degree scales, relevant for Inflation science [380], as well as sub-degree scales, the regime of CMB lensing [377]. In particular, I have been the leader of the CMB lensing analysis of this data set and build the pipeline between map-making and CMB lensing potential estimation. As part of this project, I built a curved-sky CMB lensing pipeline for Simons Array which is able to optimally account for the large expected footprint of the Simons Array CMB survey. Hence, I have been leading the effort for the CMB lensing preparation for the Simons Array analysis. Furthermore, I'm responsible for the pointing calibration analysis for POLARBEAR-2/Simons Array, a major instrumental systematic in CMB lensing reconstruction. Since 2017 I have been also a member of the Simons Observatory collaboration, participating in analysis working groups and helping in forecasting efforts [386, 385]. To set my work in context I also provide an overview of the experimental landscape and its brief history focusing on the experiments I have been working on. This is followed by Secs. 4.3 and 4.4.1, which present my major contributions to the projects. This chapter is in parts based on a presentation I gave on behalf of the POLARBEAR collaboration, which is published in the conference proceedings to be found in Ref. [34].

4.1 THE HISTORY OF OBSERVING THE CMB

The first measurement of the CMB anisotropy at scales $> 10°$ as well as the most precise measurement of the CMB spectrum until today (2019) was achieved by the team of the DMR [349] and FIRAS [121] instruments on board of the COBE satellite, respectively. In the years following the COBE results many ground-based and balloon-borne experiments measured the degree- to arcminute-scale CMB anisotropy. Starting in 1998 the MAT (Microwave Anisotropy Telescope) or TOCO [241], BOOMERanG [44], MAXIMA [143] and Archeops [41] experiments measured the theoretically pre-

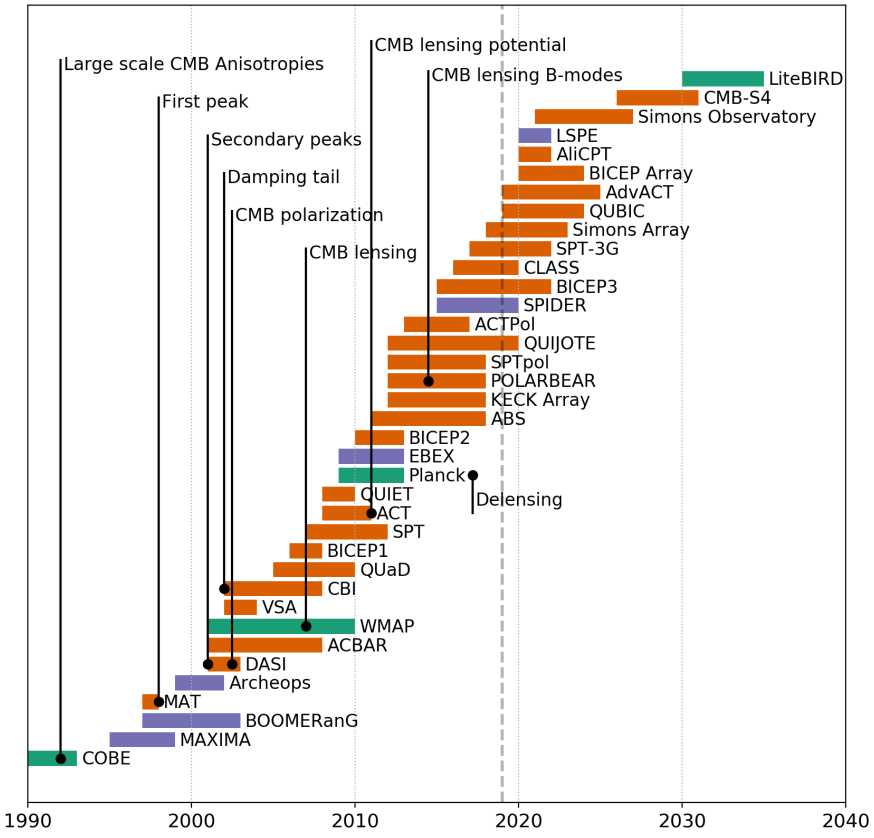

Figure 4.1: A timeline of CMB experiments, showing their approximate starting and ending dates. The list is not complete and omits many experiments, especially in the past (see for example Tab. 1 of Ref. [168]). Most dates are coming from Ref. [205]. The three major types of CMB experiments are satellites in green, balloon-borne in purple and ground-based in orange.

dicted first acoustic peak in the CMB power spectrum. The secondary peaks were discovered by DASI (Degree Angular Scale Interferometer) [140], BOOMERanG [45] and VSA (Very Small Array) [327] in 2001 and 2002. In 2002 the CBI (Cosmic Background Imager) experiment published [266] the CMB power spectrum up to $\ell = 3500$ and hence made a first measurement of the CMB damping tail, followed by measurements on similar scales from ACBAR [203]. It was also in 2002 when the DASI experiment made the first detection of CMB polarization [197] by detecting E-mode polarization at 4.9σ.

In 2001 the Wilkinson Microwave Anisotropy Probe (WMAP) satellite was launched into space and subsequently observed the sky for nine years. NASA's successor satellite of COBE utilized two 1.5 m primary mirrors to detect microwave photons with 10 high-electron-mobility transistor (HEMT) amplifier detectors. It had a full-sky coverage in five frequency bands given in Tab. 4.1. Besides measuring CMB temperature and E-mode power spectra as well as cosmological parameters to unprecedented precision, it was possible for the first time to provide evidence for weak gravitational lensing of the CMB by cross-correlating the reconstructed lensing potential with radio galaxy counts[344].

band names	K	Ka	Q	V	W
central frequency [GHz]	23	33	41	61	94
bandwidth [GHz]	5.5	7.0	8.3	14.0	20.5
resolution [arcmin]	53	40	31	21	13

Table 4.1: The instrumental configuration of the WMAP satellite, taken from Tab. 2 in Ref. [38]. The nominal specifications of the frequency channels (central value and width) as well as the FWHM beam size is given.

central frequency [GHz]	30	44	70	100	143	217	353	545	857
resolution [arcmin]	32.29	27.94	13.08	9.66	7.22	4.90	4.92	4.67	4.22
noise level σ_T [μK-arcmin]	150	162	210	77.4	33.0	46.8	154		
noise level σ_P [μK-arcmin]	210	240	300	118	70.2	105	439		

Table 4.2: The instrumental configuration of the Planck satellite, taken from Tab. 2 in Ref. [284]. The mean FWHM of the effective beam fit and estimates of the noise in temperature and polarization on 1° scale, assuming it to be white.

In 2009, Planck, a satellite of the European Space Agency (ESA), launched into space, towards the second Lagrange point (L2). It was taking data for five years in nine frequency bands spread over two instruments, the low-frequency and high-frequency instruments (LFI and HFI). The LFI covers frequency bands between 30 and 70 GHz, detecting light with pseudo-correlation radiometers, while the HFI measures light at frequencies above 100 GHz with bolometers. Both are fed by a 1.5 m telescope [368, 291]. Tab. 4.2 shows the frequency coverage as well as the sensitivity in each frequency channel. Besides measuring the temperature, polarization and lensing of the CMB to (to date) highest precision, allowing for sub-percent measurements of 5 of the 6 standard cosmological parameters, it allowed to demonstrate delensing of the temperature power spectrum for the first time [206].

Since the late 2000s the current generation of CMB experiments has been deployed, in alphabetical order the Atacama Cosmology Telescope[36] (ACT: ACT, ACTpol, AdvACT), Background Imaging of Cosmic Extragalactic Polarization[37] (BICEP: BICEP1, BICEP2, KECK Array, BICEP3, BICEP Array), Polarization of the Background Radiation[38] (POLARBEAR: POLARBEAR-1, POLARBEAR-2a, Simons Array) and the South Pole Telescope[39] (SPT: SPT, SPTpol, SPT-3G) experiments.

The ACT is a 6 m telescope located on Cerro Toco in the Atacama desert in northern Chile at an altitude of 5190 m. It allows for arcminute resolution measurements at millimeter wavelengths. The first-generation receiver, Millimeter Bolometric Array Camera (MBAC), observed between 2007 and 2010 at 148 GHz. With the second generation, ACTPol, ACT started to become polarization sensitive, with 3068 TES bolometric detectors sensitive in either 90 or 146 GHz [248]. ACT achieved a first measurement of the microwave background temperature distortions due to the kinematic Sunyaev-Zel'dovich effect [144] and the first detection of the CMB lensing potential auto power spectrum at 4σ [92]. The third-generation receiver, AdvACT, will expand both in low- and high-frequency channels, adding sensitivity in 27, 38, 150 and 230 GHz. It started observing in 2017 [195].

BICEP is a series of experiments starting in 2006 with BICEP1, followed by BICEP2, BICEP3 and the KECK Array are located at the Amundsen-Scott South Pole Station. All stages of the experiment are housed in on-axis small aperture telescopes. Starting with the KECK Array, the initially single frequency observations of BICEP1 and BICEP2 at 150 GHz could be amended with sensitivity in 90 and 220 GHz. The ongoing observations of BICEP3 in 95 GHz was producing the deepest maps of large-scale polarization to date in a sky region of more than 400 deg^2 centered at RA 0h, Dec. 57.5°. In 2020 BICEP Array will replace KECK array with additional sensitivity and frequency coverage of 30, 40 and 220 GHz [376]. In 2014 BICEP2 and KECK Array were able to achieve a first detection of degree angular scale B-modes [5], however not of primordial origin [122]. Together with data from Planck and WMAP, BICEP2/KECK Array set the tightest constraints on the tensor-to-scalar ratio, $r < 0.06$ at 95% confidence [375] (see also Tab. 4.3).

[36] https://act.princeton.edu
[37] https://bicepkeck.org/
[38] https://bolo.berkeley.edu/polarbear/
[39] https://pole.uchicago.edu/

Year	Experiment	$\sigma(r)$
2004	DASI	7.5
2009	BICEP1	0.28
2010	WMAP	1.1
2010	QUIET-Q	0.97
2012	QUIET-W	0.85
2013	BICEP1	0.25
2014	BICEP2	0.10
2015	BICEP2 + Planck	0.034
2015	BICEP2 + KECK Array	0.024
2018	ABS	0.7
2018	BICEP2 + KECK Array	0.02
2019	POLARBEAR-1	0.3

Table 4.3: Published sensitivities to the tensor-to-scalar ratio r. Table content largely from Ref. [376].

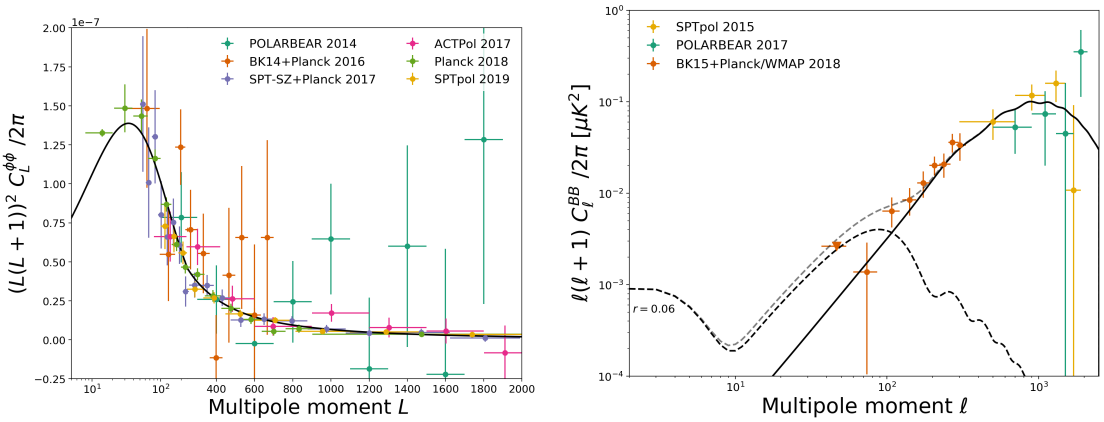

Figure 4.2: The left hand side shows the current status of CMB lensing potential power spectrum measurements, including data points from Polarbear [382], BICEP/Keck Array cross-correlated with Planck [374], SPT-SZ combined with Planck [259], ACTPol [337], Planck alone [287] and SPTpol [403]. On the right the current status of CMB B-mode power spectrum measurements is shown, including B-mode power spectra from SPTpol [184], Polarbear [378] and BICEP/Keck Array [375]. In both figures the black solid line shows the respective prediction of the best-fit ΛCDM model of Planck 2018 [286]. The black dashed line in the right-hand side corresponds to the current primordial gravitational wave upper-limit of $r = 0.06$ [375].

The SPT is a 10 m telescope surveying the CMB from close to the geographic South Pole at Amundsen-Scott South Pole Station and is able to achieve arcminute resolution. The SPT experiments have successfully conducted two major surveys, the SPT-SZ survey with SPT and the polarization sensitive survey SPT-POL with SPTpol. The former observed 2500 deg^2 in 95, 150 and 220 GHz, the latter 500 deg^2 in 150 and 220 GHz at a sensitivity of 8.3 μK-arcmin in polarization within $1000 < \ell < 3000$ [42, 403]. The third generation receiver is called SPT-3G and started observing in 2017 with 16140 tri-chroic detectors in 95, 150 and 220 GHz [36]. SPT demonstrated for the first time the delensing of B-modes using CIB data [230].

The POLARBEAR, Simons Array and Simons Observatory experiments will be presented in greater detail in the following parts of this chapter.

4.2 THE POLARBEAR-1 EXPERIMENT

The POLARBEAR experiment has been observing the polarized CMB signal since 2012 from the Atacama desert in Chile aiming at measuring the extremely faint B-mode signal, the curl-like pattern in the polarization field of the CMB. In the contrary to the temperature and E-mode signal, the gradient-like component of the polarization field, which are sourced by scalar density perturbations of the primordial plasma, the B-mode signal contains information about the tensor fluctuations, i.e. gravitational waves in the early universe and is therefore a decisive probe of inflation theories, predicting a measurable tensor-to-scalar ratio r. After measurements of the temperature and E-mode power spectra by the Planck collaboration [288] that indicate a remarkable consistency with predictions of the simplest inflationary models, a measurement of large scale B-modes, which allows for constraints on r, will be a tantalizing confirmation of these theories and will eventually permit differentiation between its different models.

As introduced in Sec. 1.6.2, B-modes are also produced by the conversion from E-modes via weak-gravitational lensing, an effect which is dominant on degree and smaller scales. This signal, tracing the line-of-sight integrated matter distribution in the Universe, enables vast possibilities of cosmological inference of the formation and distribution of large-scale structure and dark matter, but is also a primary foreground to primordial gravitational wave measurements. Furthermore, several secondary effects act as foregrounds to high sensitivity B-mode measurements. Most importantly, the ability to clean polarized thermal emission of our Galaxy, mainly coming from dust grain alignment with and synchrotron radiation produced in the galactic magnetic field, from the measured signal with the help of multi-frequency observations will be critical for a successful measurement of the primordial gravitational wave signal in the CMB. For ground-based experiments the emission of rotational and vibrational excited states of oxide and water molecules in the atmosphere gives rise to 1/f correlated noise in the relevant microwave spectrum, which, due to temperature to polarization leakage through systematic effects, can also be a main contaminant for a large scale B-mode measurement.

An understanding of and controlling these effects, together with various other sources of systematics, is crucial for a robust measurement of the extremely faint B-mode signal. In 2014, the POLARBEAR collaboration published the first evidence for non-zero B-mode signal at sub-degree scales derived from CMB polarization data only [379]. Since then complementary or similar results were derived from analysis of data of BICEP2 [5], *Keck Array* [372], SPTpol [184], combined BICEP2/*Keck Array* Planck and WMAP [371, 373, 375], and ACTPOL [222].

4.2.1 INSTRUMENT

The POLARBEAR-1 experiment [185] is located at the James Ax Observatory in the Atacama desert in Chile, 5, 190 m above sea level. It is designed to target both the small- and the large-angular-scales of the CMB polarization, in particular the B-modes. The Huan Tran Telescope (HTT) is composed of a two-mirror off-axis Gregorian telescope satisfying the Mizuguchi-Dragone condition, allowing for low cross polarization and astigmatism over a large field of view, see Fig. 4.3 [388]. The focus created by the primary and secondary mirror is reimaged by the cold optical system in the cryogenic receiver to a flat focal plane. The 2.5 m primary mirror allows a small angular resolution with a beam size of 3.5′ full-width at half-maximum (FWHM) at 150 GHz. The focal plane consists of 637 dual polarization pixels cooled at 250 mK with a 2.4° diameter field of view. The incoming light is measured at a frequency of 150 GHz through lenslet-coupled transition-edge sensors (TES).

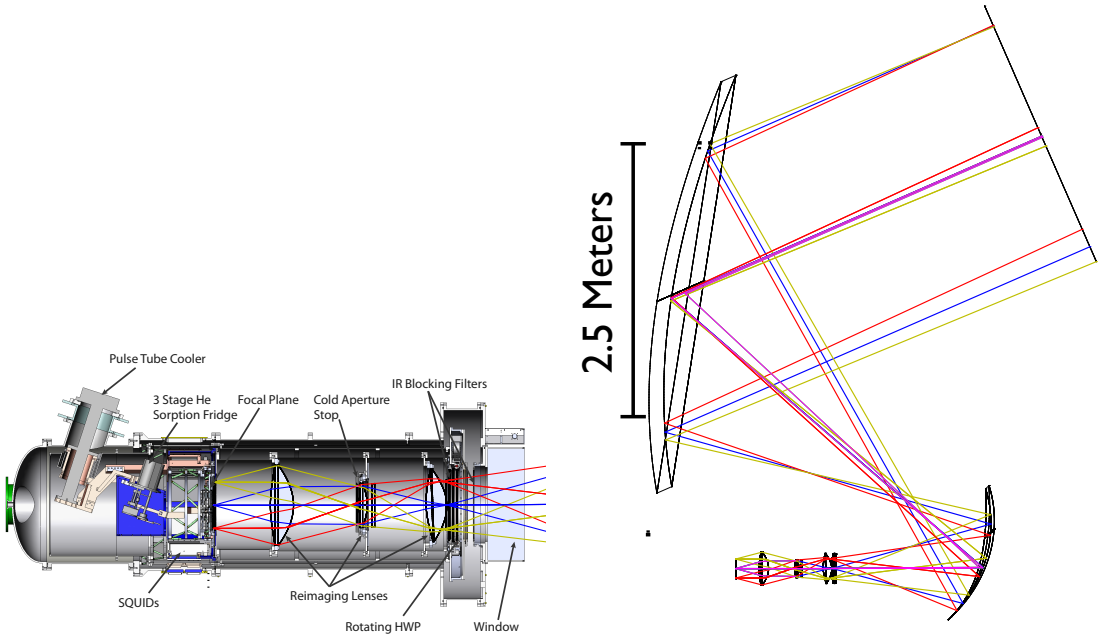

Figure 4.3: Figure showing the optical configuration (right) and the cross-section of the Polarbear receiver (left). Both showing a ray-tracing of light entering from the (top) right. Figures taken from [185]

4.2.2 SCAN STRATEGY

POLARBEAR-1 saw its first light in January 2012. During the first two seasons three small patches, each of $3° \times 3°$) with minimal foreground contamination and a combined 24 h availability from Chile have been observed. The first season lasted until October 2014, resulting in a first release of results described below. The second season of small patch observations went on until May 2014, increasing the data volume by about 61%. Since May 2014, we observe a larger sky area of roughly 700 square-degrees with a continuously rotating half-wave plate, which was installed at prime focus of the HTT. The time line of observation time and the CMB patch locations on the sky are shown in Fig. 4.4.

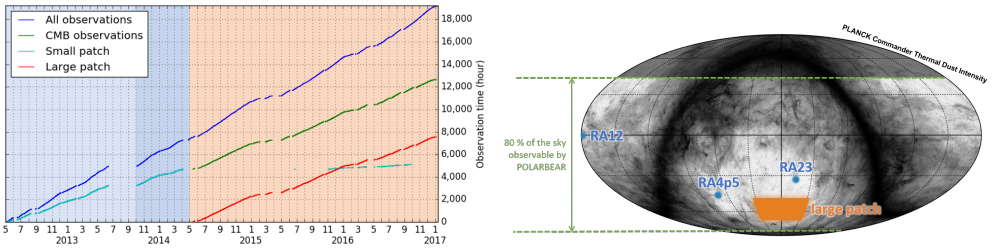

Figure 4.4: Left: Timeline of Polarbear-1 observation, showing the accumulation of CMB data on the three small and the large patch in terms of observation time, as well as the total observation time, including auxiliary dedicated calibration observations. Right: The location of the four patches on the sky on top of the dust foreground contamination at 150 GHz from Planck COMMANDER. The observed regions on the sky are the three small patches RA4.5, RA12 and RA23 (named by its right-ascension hour-angle), as well as the large patch.

4.2.3 SMALL-PATCH RESULTS

In the first publications using POLARBEAR-1 first season data we reported a first detection of the CMB lensing potential power spectrum using CMB polarization data alone at 4.2σ [382], a measurement of CMB lensing potential and HERSCHEL-ATLAS CIB cross-correlation at 4.0σ [383], a measurement of the B-mode polarization power spectrum at sub-degree scales, rejecting no lensing B-mode power with a 97.1 % confidence level [379] and set constraints on the Faraday rotation from anisotropic cosmic birefringence ($<$ 93 nG (95% C.L.) primordial magnetic field equivalent) and strength of the primordial magnetic fields ($<$ 3.9 nG (95% C.L.)) [384].

In the final release of the two-season B-mode power spectrum [378], we re-analyzed the first season data set and combined it with the second season data set. This enabled us, together with improved calibration, to report B-mode band power uncertainties reduced by a factor of two compared to the first release. We also employed a second, alternative pipeline for the data analysis. It is based on a unbiased map-making algorithm described in [297] and differs primarily in the way it accounts for the filtering of the time-ordered data to remove atmospheric noise and ground pickup. While the first pipeline (labeled "Pipeline A") is based on the MASTER method [160] and performs this filtering and map-making sequentially to eventually account for the filtered signal in the transfer function on power spectrum level, the second pipeline ("Pipeline B") attempts to account for the filtering in the map-making more optimally by performing these steps simultaneously. Therefore, the latter approach produces an unbiased representation of the microwave sky, with the drawback of being more expensive computationally. Both pipelines then generate power spectra based on the pure pseudo-C_ℓ method. The resulting polarization white-noise levels reach 7, 6, and 5 μK $-$ arcmin for RA4.5, RA12, and RA23, respectively. Compared to [379], we also updated estimates of polarized galactic foreground contamination from thermal dust and synchrotron in our three patches using Planck and WMAP data and improved the instrumental systematic effects simulations, which now follow all the data analysis pipeline steps. We performed a suite of null tests to evaluate the calibration, data-selection criteria and filtering methods, and to test for unknown systematic errors, before unblinding the data. We show in figure 4.5 the reported B-mode power spectrum at sub-degree scales from the POLARBEAR-1 season one and two data set and the estimated level of instrumental systematic uncertainties in the four bins between $\ell = 500$ and $\ell = 2100$, as reported in [378].

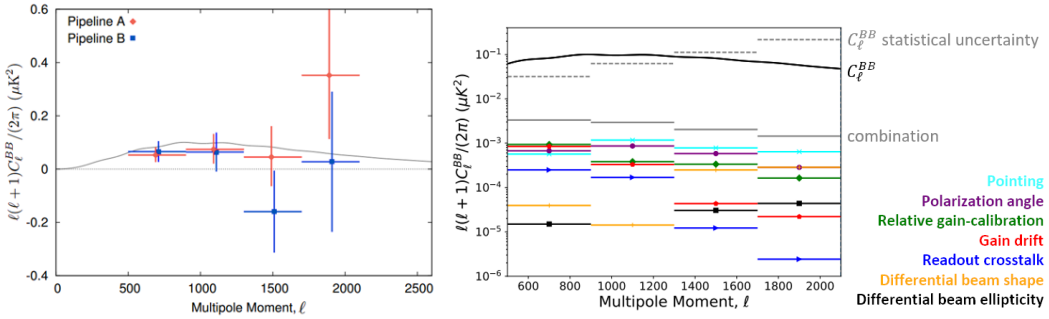

Figure 4.5: Left: Polarbear-1 B-mode angular power spectrum from the two-season data set. Red diamonds (blue squares) show the measured band powers from pipeline A (pipeline B). The plotted error bars correspond to the 68.3% confidence intervals of the statistical uncertainty only. Right: Estimated levels or upper bounds on instrumental systematic uncertainties in the four bins of the B-mode power spectrum. Both figures are from Ref. [378].

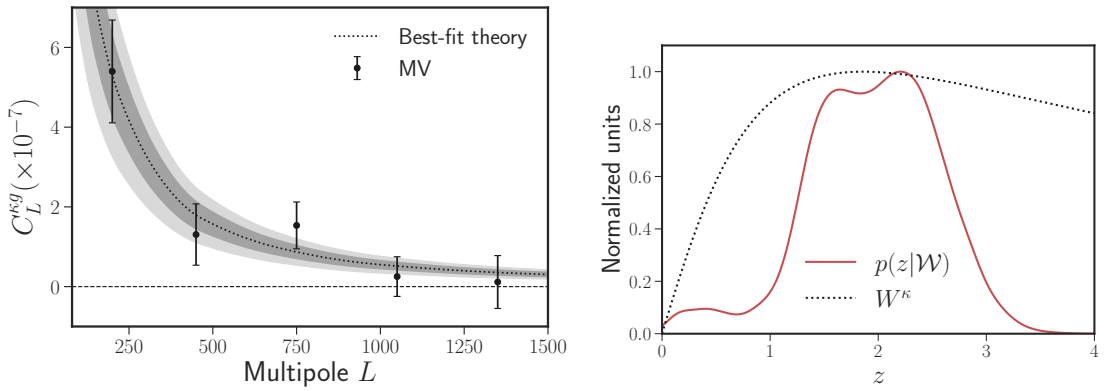

Figure 4.6: The Polarbear CMB lensing Herschel-ATLAS galaxy density cross power spectrum, coadded from measurements in the overlap regions of RA12 and RA23 on the left hand side. The right hand side shows the normalized galaxy redshift distribution, showing the main contribution is from galaxies within redshifts $z \approx 1-3$.

We are able to reject the null-hypothesis of no B-mode power with 3.1 σ and measure the amplitude of lensing B-modes after foreground subtraction as

$$A_L = 0.60^{+0.26}_{-0.24}(\text{stat.})^{+0.00}_{-0.04}(\text{inst.}) \pm 0.14(\text{foreground}) \pm 0.04(\text{multi.}),$$

where the uncertainty terms include the systematic uncertainty associated with possible biases from the instrument, the total foreground uncertainty, and the multiplicative calibration uncertainties. An updated measurement of the lensing auto-power spectrum from the two-season small-patch data set is in progress.

In a 2019 release, POLARBEAR reported a successful measurement of CMB lensing cross-correlations with cosmic shear of HSC [255] and CIB of Herschel[82]. The HSC (Hyper Suprime Cam) is an optical imager mounted on the Subaru Telescope at the summit of Mauna Kea. We made use of the first year data from a wide, deep galaxy imaging survey, compiled in a shape catalog which is detailed in Ref. [227]. The 13.3 deg^2 HSC WIDE12H field, with a number density of 23.4 arcmin^{-2}. This field has a 11.1 deg^2 overlap with RA12 with a noise level of $\sim 6\ \mu$K $-$ arcmin. We measured the lensing amplitude $A_{\rm lens}$ of the cross-correlation power spectrum, where $A_{\rm lens} = 1$ corresponds to a Planck 2018 ΛCDM cosmology. We rejected the null-hypothesis of no lensing at 3.5 σ with $A_{\rm lens} = 1.70 \pm 0.48$. The cross-correlation with the clustering of bright sub-millimeter galaxies detected by the Herschel satellite. The Astrophysical Terahertz Large Area Survey (ATLAS) covered the sky in a 600 deg^2 patch in five frequency bands between 100 and 500 μm. The survey coverage overlaps with POLARBEAR RA12 and RA23. The detected galaxies span a redshift range between $z \approx 0$ and $z \approx 6$, of which the low redshift galaxies are mainly composed of late-type and star-burst galaxies with low to moderate star formation rates [102, 136], while galaxies at $z > 1$ are much more strongly clustered and have higher star formation rates [225, 404]. The measured CMB lensing convergence cross Herschel-ATLAS galaxy counts together with the lensing kernels entering Eq. 1.297 are shown in Fig. 4.6. We achieved a 4.8σ measurement of no-lensing-hypothesis rejection. The measurement of the cross-correlation allowed us to infer the bias parameter b_1, measured to be $b_1 \approx 5.74 \pm 1.25$.

We were also able to exploit the small-patch CMB lensing measurement to delens our angular-scale B-mode measurement [381]. We achieved a B-mode power reduction employing the quadratic estimator lensing reconstruction of 14% and could increase that to 22% when using iterative lensing estimation as detailed in [66].

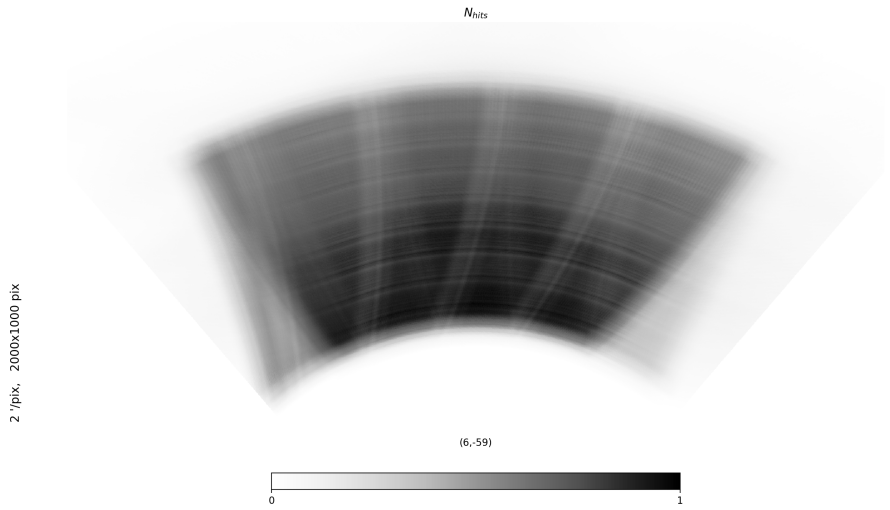

Figure 4.7: The N_{hits} map of Polarbear-1 large-patch observations, normalized to 1.

4.3 THE POLARBEAR LARGE PATCH LENSING ANALYSIS

Since May 2014 we have been observing a larger, effectively 670 deg^2 patch of the sky in the southern galactic hole centered at RA $= -59.3°$, dec $= 0^h12^m$. The observation is composed of few hours-long constant elevation scans (CES) at a speed of $0.4° \ s^{-1}$, after which detector tuning and gain calibration was performed. The CMB patch scans are grouped in three types; one scan of the patch when it is rising above the horizon, one high-elevation scan and one scanning the patch while it is setting, A complete map of the full coverage of the patch is produced in a ten-day cycle. The signal is modulated by a continuously rotating half-wave plate (CRHWP) at 2 Hz installed near the prime focus of the telescope. We used a subset of the full three-year data set to show that this setup allows targeting degree scale B-mode anisotropies and therefore inflationary physics [364]. This is because the CRHWP efficiently mitigates the correlated part of the atmospheric noise, therefore allowing for a production of single-detector polarization maps and thus avoiding numerous sources of systematic effects like intensity to polarization leakage typical of the orthogonal detector pair differencing method as used for example for the first two seasons of POLARBEAR-1. This leakage is a major obstacle in measuring large-scale B-modes from the ground with a medium aperture, high resolution telescope like POLARBEAR-1 due to atmospheric correlated, 1/f noise. We verified that a characterization and subtraction of this leakage is possible and a knee frequency of the order of $\ell = 39$ is achievable [364]. The large-patch science observations with the HWP began on 25 July 2014 and ended 30 December 2016.

In the following sections I will outline the full POLARBEAR data analysis pipeline, starting at the data selection on the raw timestream level and going over the various calibration steps to the making of maps. This includes the application of filters to the calibrated data and modeling of the noise. Once we have maps available, we can perform our power spectra and lensing reconstruction analysis. My work was focusing on the latter.

4.3.1 PRE-PROCESSING AND CALIBRATION

DATA SELECTION

The final science product uses $\sim$ 3000 hour-long CES observations, left over after applying a suite of data selection criteria. This amounts to an efficiency of around 15%. These criteria include time-

localized glitches in the timestreams and detector noise property changes during a scan, as well as time domain array noise and map-domain noise. The data is flagged and removed on the subscan level, the constant drift scans between the turnarounds of the telescope. The turnarounds, when the telescope boresight is accelerating, are discarded from the science analysis as well.

DATA SPLITS

In order to characterize the data and check it for systematics, we split the full data set in 14 uncorrelated halves, both with approximately even map-depth. Those splits are

- *first half versus second half*, the chronological split in two halves of the data with equal map-weight,
- *rising versus middle and setting*, *middle versus rising and setting* and *setting versus rising and middle*, splitting the data across the three types of CES scans,
- *left-going versus right-going subscans*, split according to the scan direction of the telescope,
- *high gain versus low gain observations*, splitting the data at the mean gain coefficient,
- *high PWV versus low PWV*, splitting the data by precipitable water vapor (PWV) measured by the nearby APEX radiometer,
- *mean temperature leakage by bolometer*, split by detectors that see large and small temperature-to-polarization leakage,
- $2f$ *amplitude by bolometer* and $4f$ *amplitude by bolometer*, split the data by HWP signal amplitude,
- *Q versus U pixels*, where the data is split in the two detector types in the focal planes, having different nominal polarization angles,
- *Sun above or below the horizon* and *moon above or below the horizon*, splitting by boresight distance to the sun or moon,
- *left half versus right half*, splitting the detectors in the focal plane by the boresight symmetry axis.

Other splits that are used in POLARBEAR-1 analyses are splits in common mode Q and U knee frequency, top half versus bottom half of detectors and top versus bottom detectors, splitting the detectors in detector-pairing on the focal plane (cf. [380]).

POINTING CALIBRATION

The pointing calibration is done similar to the small-patch analysis [378]. Prior to each CMB observation, raster scans of bright point sources are performed. The sources are chosen from PCCS [283] and ATCA [247] point source catalogues, matched with the azimuth and elevation ranges of the science scans. Jupiter and Tau A observations are also included in the pointing reconstructions. Details on the pointing reconstruction method are given in Sec. 4.4.1. The pointing model predicts a residual uncertainty of $50''$ root mean square (RMS).

BEAM CALIBRATION

Beam calibration is done on raster scans of Jupiter. The beam window function, b_ℓ, is reconstructed from the averaged Fourier transforms of the coadded Planet maps. In that, the analysis is similar to that in [378] and described in more detail in [380]. The resulting effective FWHM of the beam is 3.6 arcmin.

GAIN CALIBRATION

The time variation of detectors is measured with a chopped thermal source before and after every four observations. The detector time constants are measured by sweeping the frequency of the chopper in front of the thermal source from 4 to 44 Hz.

POLARIZATION ANGLE CALIBRATION

The polarization angle is calibrated with raster scans of Tau A, a polarized supernova remnant. The time ordered data is then fit to the beam convolved Tau A map measured by the IRAM 30 m telescope [22]. It allows to calibrate the absolute polarization angle to sub-degree precision. Furthermore, we apply a self-calibration step by requiring $C_\ell^{EB} = 0$ and rotate the final E- and B-fields accordingly [183].

4.3.2 DATA ANALYSIS

DATA MODEL

The raw time ordered data, d_m, recorded from one bolometer is modeled by

$$d_m(t) = I(t) + \epsilon \mathrm{Re}\left((Q(t) + iU(t))e^{-i(4\chi(t)+2\theta_{\mathrm{det}})}\right) + A(\chi(t), t) + N_m(t), \tag{4.1}$$

where $\chi \approx \omega t$ is the HWP angle, spinning at an angular velocity ω. The polarization efficiency is given by ϵ and θ_{det} is the detector angle with respect to the instrument. Instrumental polarization, intensity-to-polarization (I→P) leakage and non-idealities of the HWP can create a HWP-synchronous signal (HWPSS), $A(\chi, t)$, which comes on top of the HWP-modulated signal from the astrophysical signal $Q(t)$ and $U(t)$. One can apply filters and modulations to this model in such a way that we can recover the intensity and polarization signal from the sky in the following way

$$d_0(t) = \mathrm{LPF}_{\nu_0}\left(d_m(t)\right) \tag{4.2}$$

$$d_4(t) = \mathrm{LPF}_{\nu_0}\left(d_m(t) 2e^{i(4\chi(t)+2\theta_{\mathrm{det}})}\right). \tag{4.3}$$

This, and the data downsampling done in the same step, simplifies the subsequent map-making. The low-pass filter, LPF_{ν_0}, with cut-off frequency ν_0, set at the HWP rotation frequency, ensures that only the unmodulated signal is recovered. In the second equation the modulated signal at four times the HWP frequency, namely the polarization signal $(Q(t) + iU(t))e^{-2i\theta_{\mathrm{det}}}$, gets first demodulated and then recovered in the low-pass filter. These demodulated timestreams, sampled at 8 Hz, are used as the input for the following analysis. The signal contaminating the sky signal is the demodulated signal of the HWPSS, which can be decomposed in a constant part and a part proportional to the intensity signal

$$\mathrm{LPF}_{\nu_0}\left(A(\chi(t), t) 2e^{i(4\chi(t)+2\theta_{\mathrm{det}})}\right) = A_0 + \lambda_4 I(t). \tag{4.4}$$

The factor λ_4 comes from the instrumental polarization as well as I→P leakage. This coefficient can be measured from the data which allows partial subtraction of the I→P leakage from the demodulated data (cf. [364]).

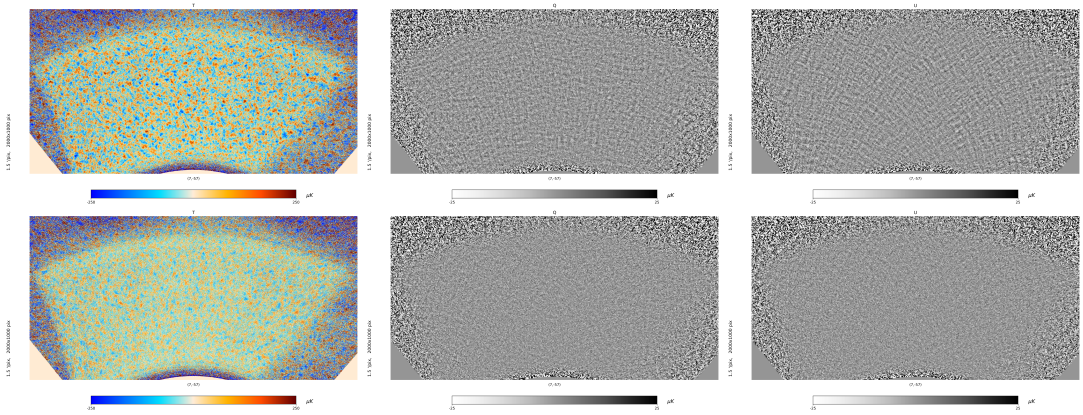

Figure 4.8: The full-season coadded real data CMB intensity (T), Q and U maps of the Polarbear-1 large-patch dataset, produced with the biased filter-and-bin map-maker in the top row. The bottom row shows noise estimates obtained by adding daily real-data maps with a random sign.

MAP-MAKING

After demodulation and leakage subtraction we are left with the two timestreams (neglecting any HWPSS)

$$d_0(t) = I(t) + N_0(t) \tag{4.5}$$

$$d_4(t) = \mathrm{Re}\left((Q(t) + iU(t))e^{-2i\theta_{\mathrm{det}}}\right) = Q(t)\cos(2\theta_{\mathrm{det}}) + U(t)\sin(2\theta_{\mathrm{det}}). \tag{4.6}$$

Using the information of the position on the sky, or pixel p, a given detector is pointing to at any given time, $A_p(t)$, we can compute a map of T, Q and U components out of the T, Q and U timestreams. It essentially comes down to the inversion of the system of linear equations

$$\mathbf{d} = \begin{pmatrix} I(t) \\ Q(t) \\ U(t) \end{pmatrix} = \mathbf{A}\mathbf{m} + \mathbf{n}, \tag{4.7}$$

where $\mathbf{m}$ is a pixelized map of the CMB Stokes parameters and the $\mathbf{n}$-vector contains the noise. There is no fundamental difference of noise properties between the two common methods of measuring CMB polarization. The matrix $\mathbf{A}$ is called pointing matrix and is of size $3 \times N_t \times N_p$, where N_t is the number of time samples and N_p is the number of pixels in the maps, and is, thanks to the pointing reconstruction/calibration, known. Hence, map-making is a linear statistical problem, which can be solved by the generalized-least-square estimator

$$\hat{\mathbf{m}} = (\mathbf{A}^T\mathbf{M}\mathbf{A})^{-1}\mathbf{A}^T\mathbf{M}\mathbf{d}, \tag{4.8}$$

which gives an unbiased estimate of the map given a positive definite weight matrix $\mathbf{M}$. If $\mathbf{M} = \mathbf{N}^{-1}$, where $\mathbf{N}$ is the covariance matrix of $\mathbf{n}$, and the noise is Gaussian, then we obtain the minimum variance or maximum likelihood estimator. In practice, however, the data model of Eq. 4.7 is not correct, since we apply a suite of filters, sumarized in the operator $\mathbf{F}$, to the raw data timestreams. This makes this estimator biased. In order to obtain an unbiased, maximum likelihood estimator in the presence of filtering, we used the method described in Ref. [297] in the past for POLARBEAR-1 analysis [378]. In the large-patch analysis, we have been using a so-called filter-and-bin map-maker, which allows for a much faster production of maps with the caveat of them being biased. The filter-and-bin estimator can be written as

$$\hat{\mathbf{m}} = (\mathbf{A}^T\mathbf{N}^{-1}\mathbf{A})^{-1}\mathbf{A}^T\mathbf{N}^{-1}\mathbf{F}\mathbf{d}, \tag{4.9}$$

i.e. the filters are applied to the timestream data, but are not accounted for in the matrix $(\mathbf{A}^T\mathbf{N}^{-1}\mathbf{A})^{-1}$. This reduces the computational cost if $\mathbf{N}$ can be approximated to be diagonal. In the following we will employ this approximation. It allows to produce daily maps, $\hat{\mathbf{m}}^i$, which are about 3000 for the POLARBEAR-1 large-patch analysis, and coadd those like

$$\hat{\mathbf{m}} = \mathbf{w}^{-1} \sum_i \mathbf{w}^i \hat{\mathbf{m}}^i, \tag{4.10}$$

where the weights, $\mathbf{w}^i$, are defined as

$$\mathbf{w}^i = \mathbf{A}^T \mathbf{N}_i^{-1} \mathbf{A} \tag{4.11}$$

and combine to a total coadded weight as

$$\mathbf{w}^{-1} = \sum_i \left(\mathbf{w}^i\right)^{-1}. \tag{4.12}$$

These weights maps can be used as an estimate of the noise per pixel, assuming only uncorrelated detector white noise. This is largely following the filter-and-bin MASTER mapmaker of Ref. [160]. We also apply an extra factor to the temperature map weights

$$\mathbf{w}^{T\,i} \rightarrow f^{T\,i} \mathbf{w}^{T\,i}, \tag{4.13}$$

computed as

$$f^{T\,i} = \mathrm{var}\left(\hat{m}^{T\,i}\right). \tag{4.14}$$

With this operation we achieved a lower noise level in the final coadded map by $\mathcal{O}(10)$. The final coadded real data maps are shown in Fig. 4.8. The map projection used for the lensing analysis is HEALPIX C++[40] [132] with a resolution of $N_{\mathrm{side}} = 2048$, corresponding roughly to pixels with 1.7 arcmin in size.

FILTERS

In this section I will summarize the operations that go into the $\mathbf{F}$-operator that was introduced int he previous section, in the order they are applied to the demodulated data. The first filter is applied in the Fourier domain and removes signal above 1.2 Hz and notch filters glitches that were flagged in the dataselection pipeline. If a high-significant glicth is seen in more than 50 detectors, a notch filter with width of 10 mHz is applied. Next, a ninth order polynomial is fit to each detector timestream and removed, to account for thermal fluctuations in the receiver. The third filter removes a template of ground-fixed signal. Telescope sidelobes are suspected to pick up signal from the surrounding landscape (ground, mountain, facilities). Each CES's timestreams are projected in coordinates fixed to the ground (azimuth and elevation), where the azimuth signal is binned into bins of 15 arcmin width. This template is then removed from each detector timestream, separately for each CES. Following Ref. [176, 364], we can estimate the temperature-to-polarization leakage due to detector non-linearity and instrumental polarization from the CES scans themselves by performing a PCA (principal component analysis). Each subscan is first-order-polynomial- and low-pass-filtered at 400 mHz before the leakage coefficients are estimated from each CES, based in principle on

$$\hat{\lambda}_4 \approx \frac{\langle d_4(t) d_0(t) \rangle}{\langle d_0(t) d_0(t) \rangle}. \tag{4.15}$$

[40] https://healpix.sourceforge.io

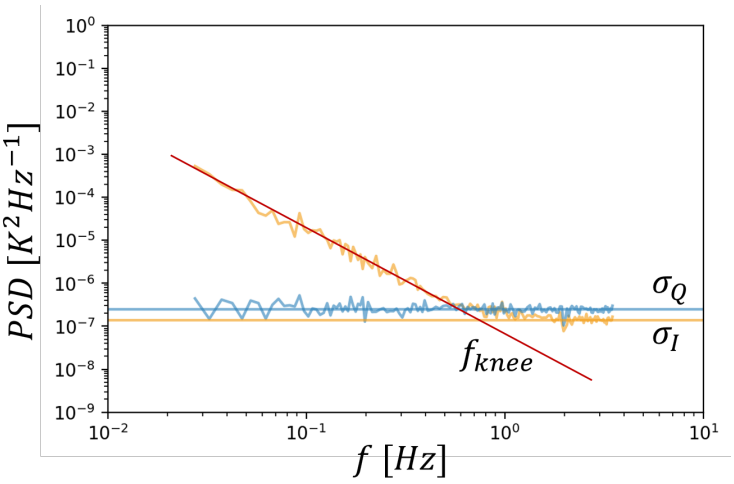

Figure 4.9: Example of a Polarbear-1 PSD of a single CES, showing the distinct features of low-frequency correlated noise in the temperature PSD (orange) and a polarization ($P = Q, U$) PSD (blue) exhibiting a two-times larger white noise than in temperature.

In practice, we compute the covariance matrix of all T, Q and U timestreams, perform a PCA and estimate λ_4 from the eigenvalues. We assume that the following leakage subtraction is heavily dominated by atmospheric fluctuations, and we do not expect it to bias the cosmological signal. Hence, this filtering operation is not included in the simulation pipeline (see Ref. [380]). Following that we apply a second-order-polynomial filter to each subscan in each timestream. The last filter removes the common frequency mode of the signal that is seen by all detectors.

NOISE MODEL

On the detector timestream level the noise is characterized by the timestream power-spectrum density (PSD). It is the Fourier transform of the filtered timestream.

$$P(f) = \left| \int \frac{dt}{2\pi} e^{ift} X(t) \right|^2 \sim A_X \left(\frac{f_{\text{knee},\,X}}{f} \right)^{\alpha} + \sigma_X^2 \quad , X = T, Q, U. \tag{4.16}$$

representing the timesteam-level equivalent of Eq. 3.13. In practice, noise weights in $\mathbf{N}$ are taken to be uncorrelated white noise levels, obtained by averaging individual detector's PSDs between 1 and 3 Hz. Fig. 4.9 shows an example of a POLARBEAR-1 PSD of the large-patch dataset with its distinctive features, f_{knee} and white noise levels.

A noise model used for correlated noise simulations can be constructed relying on Fourier-transformed timestreams in groups of subscans (scans between the telescope turnarounds). To do so, a CES is divided in N_{ss} groups of subscans. The demodulated $T(t)$, $Q(t)$ and $U(t)$ detector timestreams, that are filtered as described above, are separately Fourier transformed in each group. The resulting Fourier representations of the timestreams are denoted with $T_i^s(f)$, $Q_i^s(f)$ and $U_i^s(f)$, for detector i, subscan s and frequency f. This allows to construct the estimator [76, 379]

$$C_{ij}^b = \left\langle \left\langle (X_i^s(f))^* \, X_j^s(f) \right\rangle_{f \in b} \right\rangle_s , \tag{4.17}$$

by averaging first over frequency in a given frequency bin, b and then over all subscans in a CES. It allows to quantify the frequency dependent correlation between two detectors i and j. Per CES, we use $N_{\text{ss}} = 15$ groups of subscans in 10 logarithmically-spaced bins between 0.0008 and 4 Hz (the HWP frequency is 2 Hz). In Fig. 4.11 we show an example of a C_{ij}^b matrix, obtained from POLARBEAR-1 temperature timestreams.

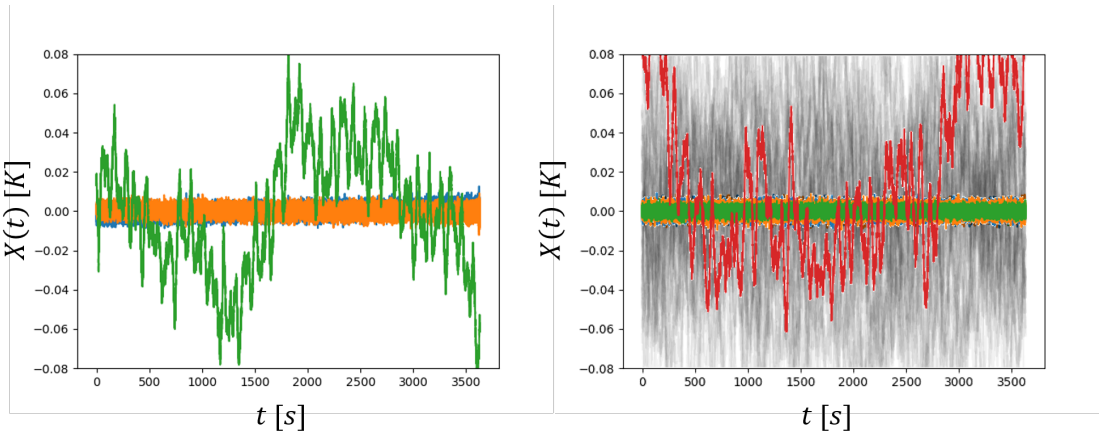

Figure 4.10: The right hand side shows real data timestream of a given CES and day. The green, blue, and orange lines are the T, Q and U timestreams described in this section. The corresponding lines on the left hand side are simulated timestreams assuming white noise, uncorrelated between detectors. An example of a simulated timestream using the C_{ij}^b-matrix formalism is shown in red. More realizations of simulated, correlated timestreams are shown in the background as faint black lines.

Using the C_{ij}^b covariance matrix for timestreams in the Fourier-domain, we can simulate timestreams including detector-detector correlations with the same Gaussian properties. To do so, we perform a Cholesky decomposition

$$\mathbf{C}^b = \mathbf{L}^b \mathbf{L}^{b\,\dagger} \tag{4.18}$$

and simulate correlated timestream out of uncorrelated, white-noise time streams with unit covariance

$$\hat{X}_i(t) = \int df e^{-ift} \sum_j L_{ij}^{b(f)} \xi_j(f), \tag{4.19}$$

where $\xi_j(f) \leftarrow \mathcal{N}(0,1)$, i.e. it is drawn for every frequency sample from a Gaussian distribution with zero mean and variance one. An example of a simulated timestream in comparison with the real data timestream is shown in Fig. 4.10. The qualitative reproduction of the low-frequency noise modes in the simulated, correlated timestreams compared to white noise simulations is apparent. Also, comparing the maps in Fig. 4.12, shows the higher fidelity qualitatively.

Modeling the single-scan detector covariance matrix as shown above is only used as a validation of our noise model. The noise estimate which is used to perform simulations including realistic signal and noise comes from the real data itself, making use of the availability of single-day maps from our data. To create random realizations of realistic noise, including low-frequency noise and accurate levels of white noise, we coadd single-day real-data maps with a random sign. We further require that for each of the noise realizations

$$\sum_{i \in \text{positive sign}} \left(\mathbf{w}^i\right)^{-1} = \sum_{i \in \text{negative sign}} \left(\mathbf{w}^i\right)^{-1}, \tag{4.20}$$

i.e. we require that the signal is weighted equally in the maps contributing with a positive sign and maps contributing with a negative sign, which results in signal-free noise-only coadded maps.

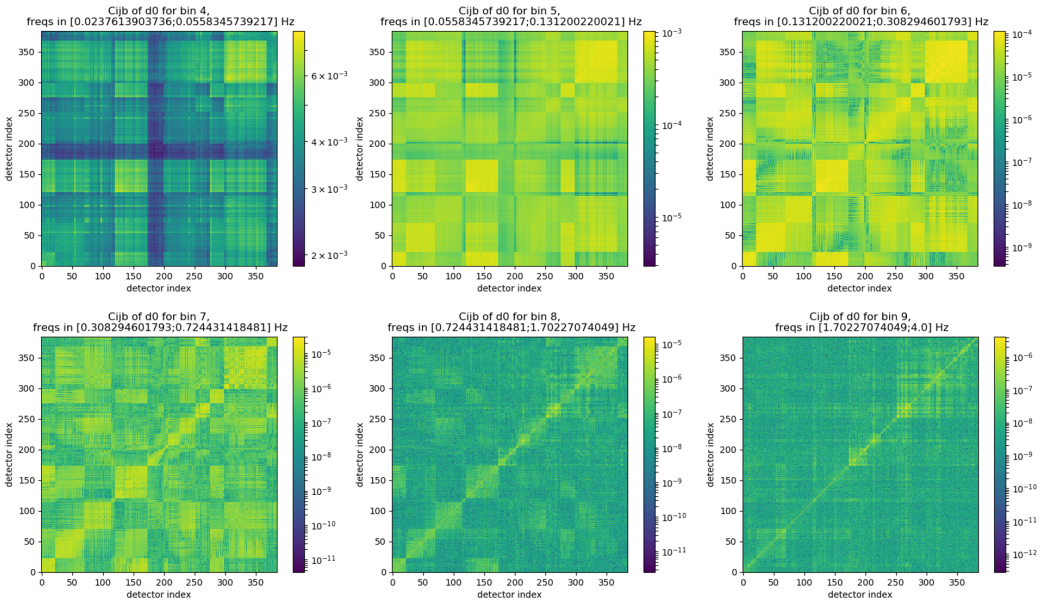

Figure 4.11: Example of a Polarbear-1 temperature C_{ij}^b matrix, for a subset of detectors remaining after data selection and bins between 0.02 and 4 Hz. It shows large correlations at low frequencies < 1 Hz and a dominant diagonal (uncorrelated detectors) part at high frequencies > 1 Hz.

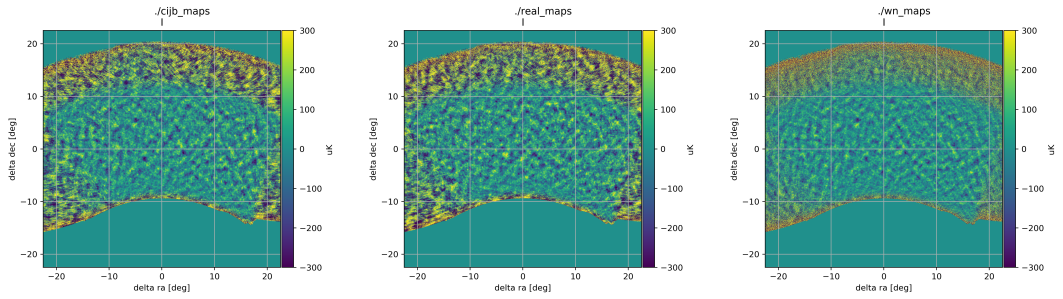

Figure 4.12: Simulating signal and noise, projected on the sky. The left hand figure shows simulations employing a C_{ij}^b noise model, the middle figure shows the real data and the right hand figure shows simulations from a white noise model, all for total intensity.

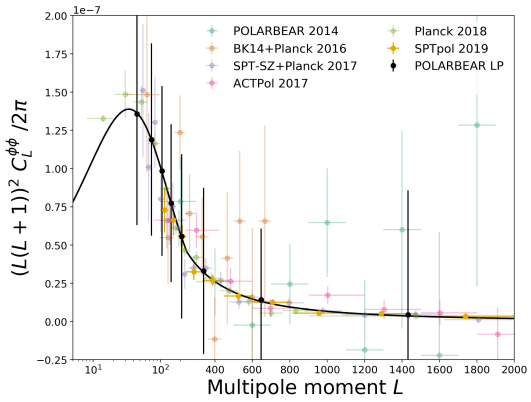

Figure 4.13: Same as Fig. 4.2, including the forecast of the Polarbear-1 large-patch lensing power spectrum sensitivity.

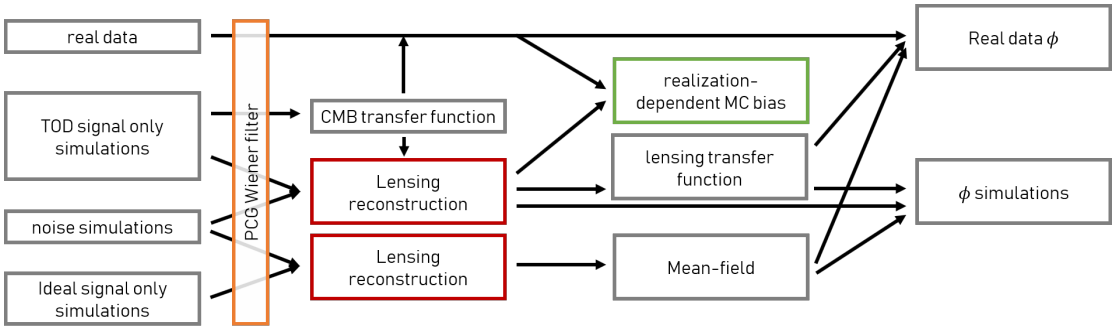

Figure 4.14: The Polarbear-1 large-patch lensing pipeline, starting from real data and simulated maps, going through optimal filtering, transfer function and lensing reconstruction, as well as estimation of biases.

4.3.3 CMB LENSING ANALYSIS

In this section I will detail the lensing reconstruction pipeline for the POLARBEAR-1 large-patch analysis. Although the science target of the large-patch survey were the large scale B-modes and constraints on r, due to the medium aperture size and beam size of 3.5 arcmin, POLARBEAR-1 has access to a broad range of scales, including the small-scales relevant for the lensing analysis. Hence, although not competitive in terms of the noise level to the small-patch surveys of POLARBEAR, the access to more modes due to the larger patch size allows for comparable constraints on the lensing power spectrum. Fig. 4.13 includes forecasted errorbars for this dataset in the context of the latest power spectrum measurements.

Fig. 4.14 shows the pipeline to produce lensing potential estimates from real data and simulated maps. We compute power spectra of CMB maps to get an estimate of the power spectrum of the noise in the map as well as to obtain the transfer functions to correct for the introduced bias in the maps due to filtering. Before lensing reconstruction, the maps go through a Wiener filtering step, accounting for noise inhomogeneity. From the reconstructed lensing potential simulations we compute transfer functions at the lensing potential level and its mean-field. We also compute a realization dependent bias correction for the lensing potential power spectrum. These steps will be detailed in the following.

POWER SPECTRUM ESTIMATION

Contrary to the power spectrum estimation analysis done in Refs. [379, 378], we simplify the pipeline to produce noise-bias power spectra for the lensing pipeline significantly. Most importantly, the lensing analysis lends the filter transfer functions from this analysis. In this analysis we do not account for the $E \rightarrow B$-leakage due to filtering.

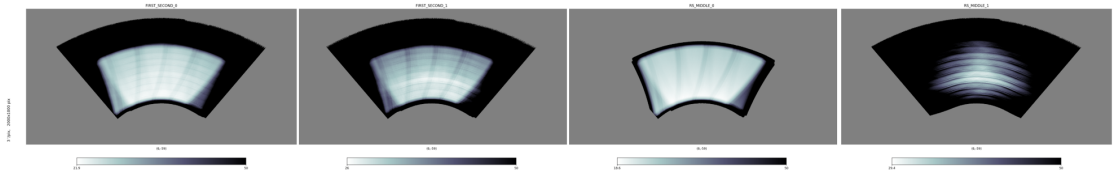

Figure 4.15: Qualitative representations of possible (normalized) inverse noise matrices, $\mathbf{N}^{-1}$, as they appear within different data splits of the Polarbear-1 large-patch data set. The figure shows an exemplary selection of two data splits, dividing the data in time (*first half versus second half*, left-hand-side) and dividing the data by scanning type (*rising and setting versus middle*, right-hand-side).

We define filter transfer functions that correct for the bias introduced in the map-making on the power spectrum level

$$C_\ell^{TT} \approx \left(f_\ell^T\right)^2 \hat{C}_\ell^{TT} \tag{4.21}$$

$$C_\ell^{EE} \approx \left(f_\ell^E\right)^2 \hat{C}_\ell^{EE} \tag{4.22}$$

$$C_\ell^{BB} \approx \left(f_\ell^B\right)^2 \hat{C}_\ell^{BB}. \tag{4.23}$$

The power spectra, $\hat{C}_\ell^{XX}$, are obtained from noiseless simulations going through the same filtering and map-making pipeline as the real data. We obtain binned power spectrum estimates by applying the X^{2}PURE code [342, 134, 133], which implements the pure-pseudospectrum technique to minimize E-to-B leakage caused by sky masking, to our maps. The transfer functions, f_ℓ^X are then computed by comparing the output power spectra with the input power spectra. For the computation of f^E the B-modes are set to zero in the simulations and to compute f^B we assume zero E-modes in the simulations.

WIENER FILTER

We apply a filter as explained in Sec. 2.7 on all maps before using them as input for the lensing reconstruction code. We want to obtain the quantities

$$\bar{\mathbf{a}} = \left(\mathbf{C}_\ell + b_\ell^{-2}\mathbf{f}_\ell^2\mathbf{Y}^T\mathbf{N}\mathbf{Y}\right)^{-1} b_\ell^{-1}\mathbf{f}_\ell\hat{\mathbf{a}}, \tag{4.24}$$

where b_ℓ is the beam function in harmonic space. In practice, the filtered quantities $\bar{\mathbf{a}}$ are obtained by solving

$$\left(\mathbf{C}_\ell^{-1} + b_\ell^2\mathbf{f}_\ell^{-2}\mathbf{Y}^T\mathbf{N}^{-1}\mathbf{Y}\right)\mathbf{C}_\ell\bar{\mathbf{a}} = \mathbf{f}_\ell^{-1}b_\ell\mathbf{Y}^T\mathbf{N}^{-1}\hat{\mathbf{a}} \tag{4.25}$$

with a conjugate gradient decent method with multigrid preconditioner [344]. The $\mathbf{N}$-matrix is taken to be the weight matrix $\mathbf{w}^{-1}$, i.e. assuming uncorrelated white noise per pixel (after filtering). Fig. 4.15 shows examples of the inverse noise matrix used in the filtering. We performed tests with different configurations of the multigrid preconditioner and found that a 2-level multigrid, the lowest having a resolution of $N_{\text{side}} = 1024$, to be best (see Fig. 4.16 for an example). We furthermore apply a mask, effectively setting the noise to infinite in the pixels where the mask is zero. The mask removes the high-noise outer regions of the patch. No polarized point sources are detected by Planck within the POLARBEAR-1 large-patch, neither does an internal source finder detect any point sources in our polarization maps. We nevertheless mask out the point sources detected in the Planck 143 GHz intensity maps, reported in the second Planck catalogue of compact sources (PCCS2) [283], with an radius of 5 arcmin. Furthermore, the mask is tapered at the edges with an analytic apodization shape with apodization length of 1 deg (see Ref. [134]). The final inverse noise map is shown in Fig. 4.17. The resulting filtered harmonic coefficients $\bar{a}^T$, $\bar{a}^E$ and $\bar{a}^B$ are then used to reconstruct the lensing potential.

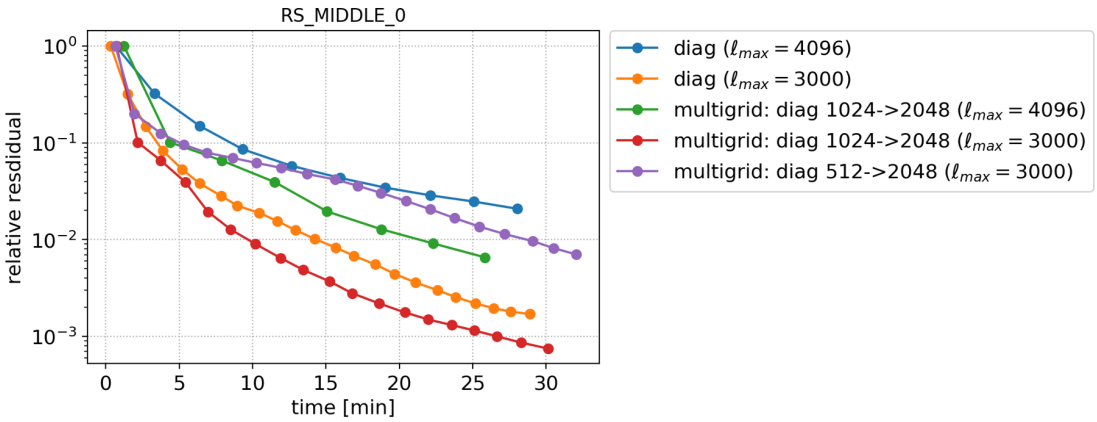

Figure 4.16: Different configurations of the (multigrid) preconditioner to perform the Wiener filter operation on Polarbear-1 large-patch data set. The multigrid preconditioner uses a diagonal preconditioner on a lower resolution grid, which is used to precondition the problem in the full resolution. The dependence of the maximum multipole ℓ_{max} is tested as well.

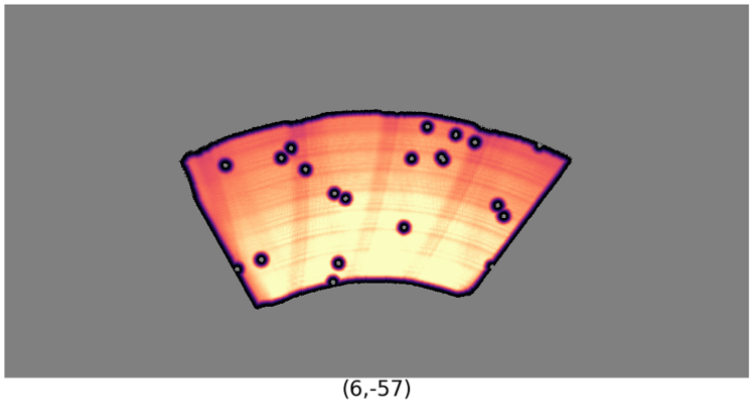

Figure 4.17: The normalized matrix $\mathbf{N}^{-1}$ of the full data set, with a mask applied to remove the high-noise outer regions and point sources detected by Planck.

LENSING RECONSTRUCTION

We employ a curved-sky quadratic estimator for the reconstruction of the lensing potential, which is detailed in Sec. 2.3. The quadratic estimator weights are taken to be the lensed power spectra of a Planck 2015 fiducial cosmology.

LENSING POTENTIAL TRANSFER FUNCTION

We introduce a further transfer function for the lensing potential

$$\hat{\phi}^{XY}_{LM} \to A^{XY\ \mathrm{MC}}_{L} \hat{\phi}^{XY}_{LM}, \quad \text{by requiring that} \quad \langle \hat{\phi}\phi \rangle \sim \langle \phi\phi \rangle, \tag{4.26}$$

where $\hat{\phi}$ is the reconstructed lensing potential on a simulation including realistic scanning and filtering in the CMB map-making and ϕ is the input lensing potential of the simulation. We can then compute the transfer function by averaging over N simulations

$$A^{XY\ \mathrm{MC}}_{L} = \frac{\sum_i^N \sum_M \phi^i_{LM} \phi^i_{LM}}{\sum_i^N \sum_M \hat{\phi}^{i\ XY}_{LM} \phi^i_{LM}}. \tag{4.27}$$

This extra filtering also accounts for the sky masking with an effective W_4 factor (see Eq. 2.76).

MEAN-FIELD

We use signal and noise simulations to compute the mean-field for each estimator. To do so we reconstruct the lensing potential, applying the same transfer functions and filtering as for the real data. The averaged reconstructed potentials

$$\hat{\phi}^{\mathrm{MF}}_{LM} = \frac{1}{N_{\mathrm{MF}}} \sum_i^{N_{\mathrm{MF}}} \hat{\phi}^i_{LM} \tag{4.28}$$

are then an estimate of the real mean field, ϕ^{MF} with power spectrum C^{MF}_L. The variance of the estimated mean-field is then given by

$$\hat{C}^{\mathrm{MF}}_L = C^{\mathrm{MF}}_L + \frac{1}{N_{\mathrm{MF}}} N^{(0)}_L, \tag{4.29}$$

where N_{MF} is the number of simulations going into the mean-field computation. Fig. 4.18 is showing the resulting mean-field, projected back into map space, for the polarization-only estimators. The power spectra are shown in Fig. 4.19, demonstrating that the mean-field at large scales is lower for polarization estimators. This is expected due to the lack of a monopole and dipole.

REALIZATION-DEPENDENT BIAS

We employ the realization-dependent bias computation method of Ref. [251] by computing appropriate four-point combinations between lensing potentials reconstructed on the real data and simulations, to account for any mismatch between the two [280]

$$\begin{aligned}\hat{N}^{(0)\ \mathrm{RD}}_L = \Bigg\langle & \hat{C}^{\phi\phi}_L \left[A^i, \hat{B}, C^i, \hat{D}\right] + \hat{C}^{\phi\phi}_L \left[\hat{A}, B^i, C^i, \hat{D}\right] + \hat{C}^{\phi\phi}_L \left[A^i, \hat{B}, \hat{C}, D^i\right] + \\ & + \hat{C}^{\phi\phi}_L \left[\hat{A}, B^i, \hat{C}, D^i\right] - \hat{C}^{\phi\phi}_L \left[A^i, B^j, C^j, D^i\right] - \hat{C}^{\phi\phi}_L \left[A^i, B^j, C^i, D^j\right] \Bigg\rangle_{i\neq j},\end{aligned}$$

where $\hat{X}$ are the real data CMB fields and X^i are the CMB fields of the ith simulation ($X = A, B, C, D$).

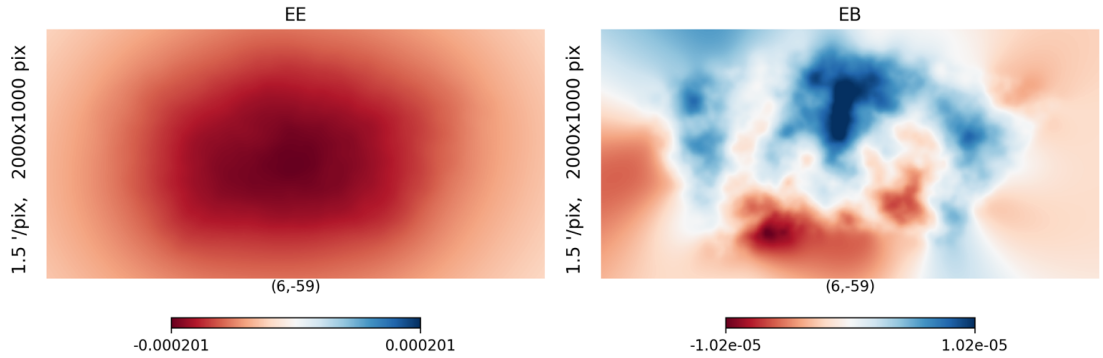

Figure 4.18: The mean-field of the full coadded Polarbear-1 large-patch data set, for the two polarization estimators, EE and EB.

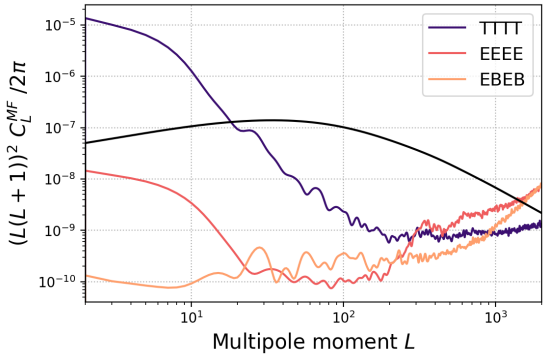

Figure 4.19: The auto-power spectra of estimated mean-fields $\hat{\phi}^{\mathrm{MF}}$, for the TT, EE and EB estimators, computed for the Polarbear-1 large-patch lensing analysis. The fiducial signal, $C_L^{\phi\phi}$, is shown in the black line.

THE LENSING AUTO-POWER SPECTRUM

At this point we can estimate the CMB lensing auto power spectrum from our measurements as

$$\hat{C}_L^{\phi\phi} = A_L^{\mathrm{MC}} \frac{1}{2L+1} \sum_M \hat{\phi}^*_{LM} \hat{\phi}_{LM} - \hat{N}_L^{(0)\ \mathrm{RD}} - \frac{1}{N_{\mathrm{MF}}} N_L^{(0)} - N_L^{(1)}, \tag{4.30}$$

where $N_L^{(1)}$ is computed analytically. This allows to compute the power spectrum of all kinds of four-point combinations of T, E and B-fields, as well as the auto-power spectrum of the minimum-variance (MV) estimator.

SCIENCE VALIDATION

In Polarbear we perform strict science validation tests before we can unblind our science product, such as a B-mode or CMB lensing power spectrum. Before these predefined tests are not passing, the science result will be blinded to avoid human bias in the data analysis. In the CMB lensing analysis we build CMB null spectra out of reconstructed lensing potentials in two halves of the data, $\hat{\phi}^1$ and $\hat{\phi}^2$, in the following way

$$C_L^{\mathrm{null}} \equiv C_L^{\phi^1\phi^1} + C_L^{\phi^2\phi^2} - 2C_L^{\phi^1\phi^2}, \tag{4.31}$$

where each of the three spectra is computed as in Eq. 4.30. Obviously, in the absence of any systematics, these spectra are supposed to consistent with zero. Additional to the check for systematic, these spectra can be an indicator of how well the lensing bias can be subtracted. We specifically defined various data splits, as outlined in Sec. 4.3.1, to test for specific potential systematics in our data. Any uncorrected temporal drift of the data should be detectable in the null spectrum between the first and second half

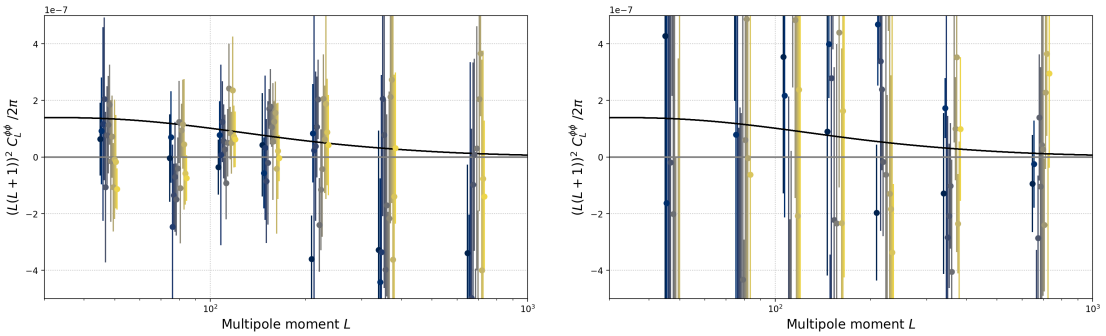

Figure 4.20: A demonstration of the null spectra of 14 splits of the Polarbear-1 large-patch data set, using the $EEEE$ (left) and $EBEB$ (right) lensing power spectrum estimators. Each color corresponds to a different split.

of the data, any uncorrected sensitivity to atmospheric emission should be seen in the null spectrum split by PWV, etc. . Fig. 4.20 shows an overview of the null spectra computed for the POLARBEAR-1 large-patch lensing analysis. Further, we check the power spectrum of the CMB lensing curl mode, ω, which is expected to be consistent with zero to first order [159, 85, 86, 254].

To systematically check for failures in the null tests we compile them into summary statistics, based in their χ value per bandpower defined by

$$\chi_b^\alpha \equiv \frac{\hat{C}_b^\alpha}{\sigma\left(\hat{C}_b^\alpha\right)}, \tag{4.32}$$

where $\hat{C}_b^\alpha$ is the null spectrum corresponding to the data split α and b denotes the bin. Furthermore, we have null spectra for every combination of quadratic estimators X. In total, we obtain

$$N = N_{\text{spectra}} \times N_{\text{splits}} \times N_{\text{bins}} \tag{4.33}$$

numbers, which we require to be Gaussian distributed. We test that by computing probabilities to exceed (PTEs) of summary statistics by summing either χ_b^α or $(\chi_b^\alpha)^2$ over bins, splits or spectra. Specifically, we focus on a subset of five statistics per spectrum, X, which are

- the average χ overall, $\sum_b \sum_\alpha \chi_b^\alpha$,
- the most extreme χ^2 by bin, $\min_b \left(\sum_\alpha (\chi_b^\alpha)^2\right)$,
- the most extreme χ^2 by test, $\min_\alpha \left(\sum_b (\chi_b^\alpha)^2\right)$,
- the most extreme χ^2 overall, $\min\left((\chi_b^\alpha)^2\right)$ and
- the total χ^2 overall, $\sum_b \sum_\alpha (\chi_b^\alpha)^2$,

and require them all to be larger than 5% to pass the null test. Furthermore, we check if the three distributions

- by bin, $\sum_\alpha (\chi_b^\alpha)^2$,
- by test, $\sum_b (\chi_b^\alpha)^2$ and
- overall, $(\chi_b^\alpha)^2$,

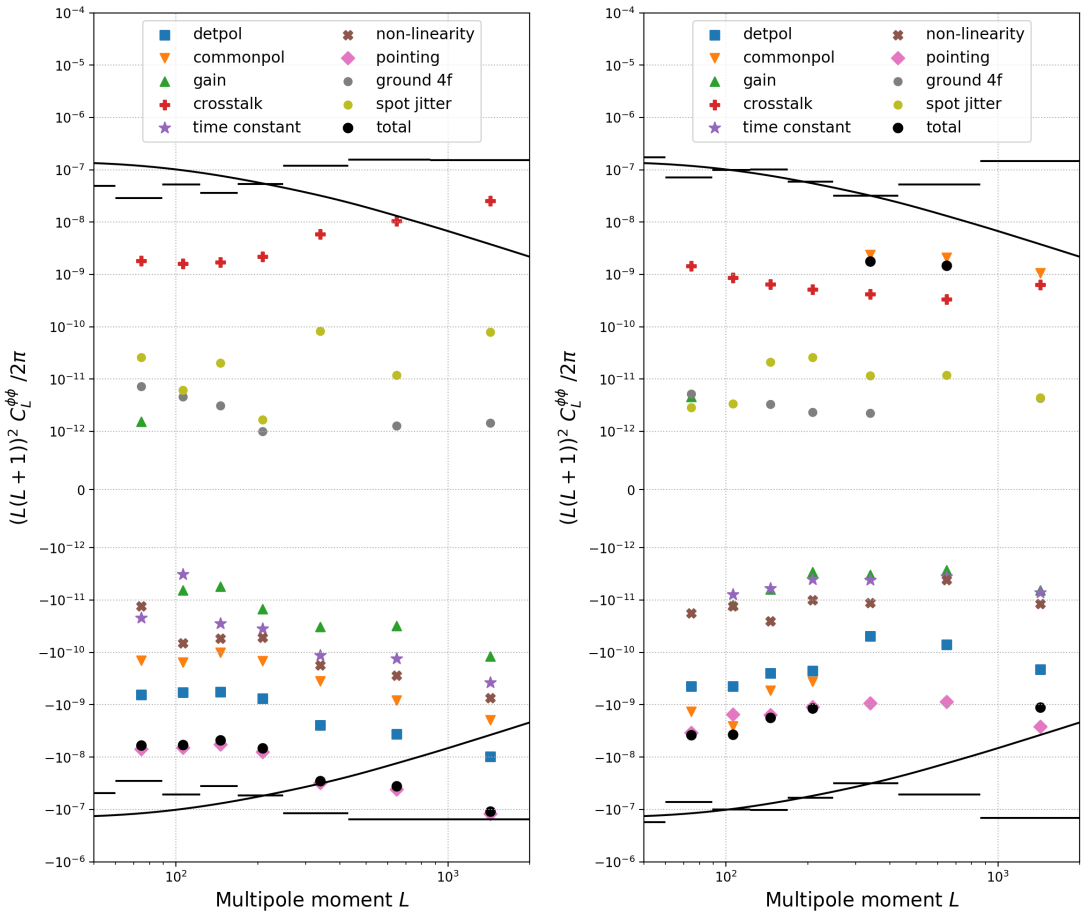

Figure 4.21: Instrumental systematic simulations for the Polarbear-1 large-patch data set, propagated to the CMB lensing power spectrum. The introduced biases from systematics are shown in the $EEEE$ (left) and $EBEB$ (right) spectra. The black lines show the lensing potential signal amplitude, with positive and negative signs, respectively. The black bars depict the statistical uncertainties in each of the seven bins. The labels are described in Sec. 4.3.3.

conform with a uniform distribution, employing a Kolmogorov–Smirnov (KS) test. The p-values of the latter are required to not exceed 5% as well to pass the null test. Cumulative false positive rate of these eight tests are 33.7 %. As of summer 2019, the POLARBEAR-1 data set is currently undergoing these checks for the CMB lensing analysis, which is why we cannot show final results here.

SYSTEMATICS SIMULATIONS

We simulate instrumental systematics on the detector timestream level as described in detail in Ref. [380]. In Fig. 4.21 we show nine categories of systematics, briefly described in the following.

- detpol: The detector polarization angle calibration angle is simulated on timestream level, assuming that the calibrated values are Gaussian distributed around the true ones with a standard deviation of $1.2°$.
- commonpol: Given the systematic error estimate of TauA's polarization angle in [22] we simulate it by rotating the polarization angle of the input sky with an RMS of $0.5°$.
- gain: The relative gain calibration uncertainty in each detector of 4.7% is propagated to CMB lensing power spectra by timestream level simulations. This error comes from the thermal source amplitude and the detector noise.

- time constant drift: We simulate the drift of the detector time constants by creating a template from the downsampled $\arg(Q(t) + iU(t))$ real data timestreams.
- non-linearity: We simulate the non-linearity of the detectors by creating a template from downsampling and normalizing the $\sqrt{Q(t)^2 + U(t)^2}$ real data timestreams.
- crosstalk: The amplitude of the electrical crosstalk between detectors read out by the same cables is estimated from Jupiter observations. To simulate systematic errors, we inject electric crosstalk at the timestream level, where the perturbed timestream, $\hat{d}$, for detector i is given in terms of the unperturbed ones, d_i, as

$$\hat{d}_i(t) = d_i(t) + \sum_j \Lambda_{ij} d_j(t), \tag{4.34}$$

  where $\mathbf{\Lambda}$ is the cross-talk matrix. We find this matrix to be sparse, with non-zero off-diagonal elements having a median of 0.01, which is measured in Jupiter observations.
- pointing: We compare the sky projection after using different pointing models, where the fiducial one only includes radio point sources in the calibration and the other additionally includes Jupiter observations. Details on the pointing reconstruction can be found in Sec. 4.4.1.
- ground 4f: We simulate variations in the ground emission, which could not be subtracted out in the ground-pickup template removal described above. One possibility for this variation can be the detector non-linearity, which modulates the $4f$ signal amplitude. The resulting modulation of the detector gain can be simulated similar to the non-linearity described above.
- spot jitter: We observed a small air-bubble in the anti-reflection coating of the half-wave plate. We estimate the added variance due to an HWP angle jitter, which leaks $0f$- into the $4f$-signal.

FOREGROUNDS

Due to the low temperature sensitivity in our POLARBEAR-1 large-patch dataset, we almost exclusively rely on polarization information in our lensing estimation. This is why we focus on the main foregrounds for polarization, including galactic polarized dust and synchrotron emission as well as polarized point source emission. Luckily, the number of polarized foregrounds is believed to be lower than foregrounds in total intensity of the CMB, including the CIB and radio point sources [107, 261], the kinematic Sunyaev-Zeldovich (kSZ) [118] as well as the thermal Sunyaev-Zeldovich (tSZ) effect [226].

GALACTIC FOREGROUNDS Galactic foregrounds contaminating CMB lensing estimation have been investigated in Refs. [116, 73] as well as Chapter 6 of this thesis. These results as well as dedicated simulations motivate the assumption that the systematic errors due to galactic foregrounds are negligible compared to the statistical uncertainty and a final estimation of the level of systematic errors will be made after finalizing the dataselection and reconstruction parameters.

POLARIZED POINT SOURCES Estimates of the biases due to unresolved (polarized) radio sources have been made in [345]. Neither Planck nor our own internal point source detection measured any polarized point sources in our patch. To estimate the bias due to unresolved, and hence unmasked, point sources in both temperature and polarization with a flux lower than 100 mJy, we use the NVSS (NRAO VLA Sky Survey) catalog survey [84] at a resolution of $43''$ at 1.4 GHz to obtain an estimate

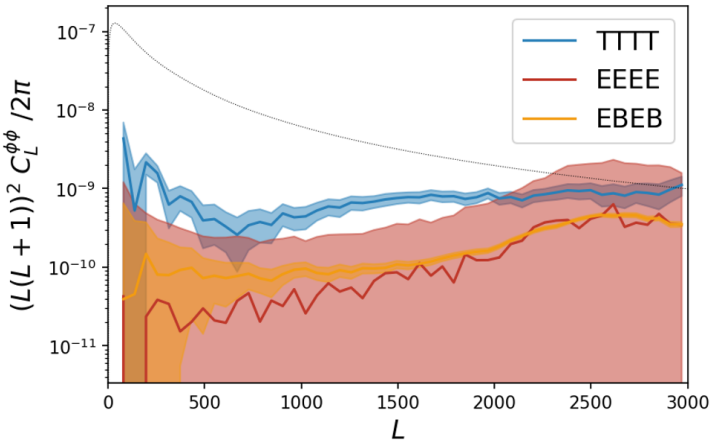

Figure 4.22: Systematic bias from unresolved polarized point sources in the large-patch for different quadratic estimators as marked in the legend. The shaded area indicate the statistical uncertainty of the simulations.

of the polarization fraction and simulate maps of Poisson distributed point sources with radii < 3.5 arcmin [302]. The resulting bias from unresolved point sources in our POLARBEAR-1 large-patch CMB lensing spectra are shown in Fig. 4.22. The bias levels are well below the statistical uncertainty.

OUTLOOK

The CMB lensing analysis of the POLARBEAR-1 large-patch data set will complete the wide range of observed multipoles of one single data set. Together with the degree-scale B-mode analysis of [380], we accomplished polarized CMB measurements from the ground within scales between $\ell \approx 100$ and $\ell \approx 3000$. This serves as an important proof of concept of the Simons Array, which targets low-multipoles as well as high-multipoles and aims to constrain both, the tensor-to-scalar ratio, r, as well as the total mass of neutrinos, M_ν. Currently, this analysis is still blinded, but we expect to be able to pass our null tests soon, such that the results of the analysis presented in this section will become public soon.

4.4 POLARBEAR-2A AND SIMONS ARRAY

4.4.1 POLARBEAR-2A

In December 2018, as the first step of a major upgrade to the existing POLARBEAR experiment, POLARBEAR-2a was deployed [354, 360]. The new instrument will observe the CMB with 7,588 sinuous-antenna-coupled superconducting TES in two frequency bands, 95 GHz and 150 GHz, with a 4.8° field of view. A broadband half-wave plate will be mounted at secondary focus [156] and we expect a nominal array sensitivity 5.8 $\mu K_{CMB}\sqrt{s}$, in terms of noise-equivalent temperature, in both frequency bands. Fig. 4.23 shows a picture of the fully assembled POLARBEAR-2a focal plane consisting of 7 wafers of 1,088 detectors, a factor six more compared to POLARBEAR-1.

FIRST LIGHT

In December 2018 we achieved first light. Fig. 4.24 shows the first POLARBEAR-2 planet scan of Venus, from a single detector. Since the first light, POLARBEAR-2a has been undergone testing and calibration work such as focusing of the focal plane and beam calibration, detector biasing and readout noise testing.

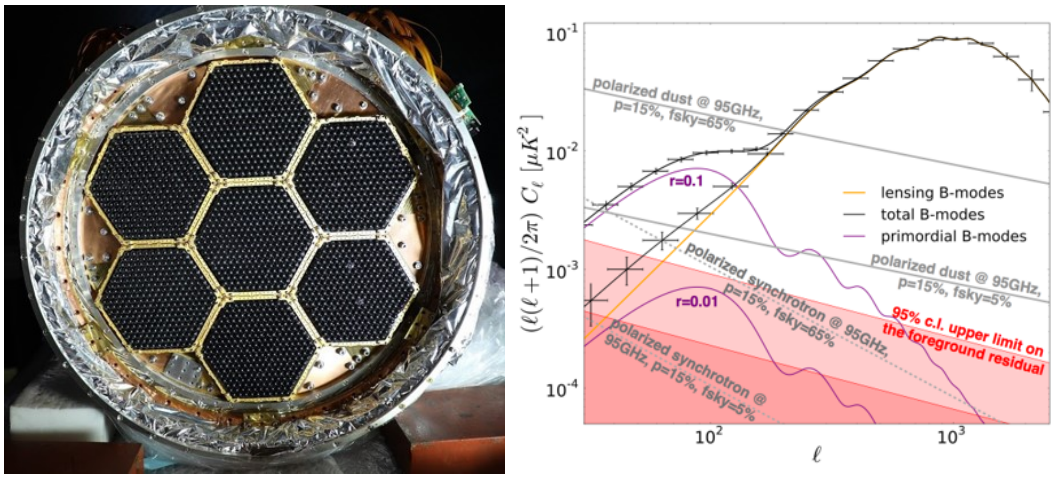

Figure 4.23: Left: The assembled Polarbear-2a focal plane at KEK in Japan for testing in 2018. It has a radius of roughly 36.5 cm, nearly twice as large as Polarbear-1. Right: Forecast for Simons Array science goals, showing the B-mode power spectrum and how, with new internal foreground cleaning capabilities, we are able to clean the level of the galactic foregrounds, which are dominating at large scales, down to the level of equivalent primordial B-modes with $r = 0.01$. From Ref. [354].

POINTING RECONSTRUCTION

To accurately produce maps out of measured timestreams, one has to know the exact pointing of the telescope at each moment in time. The pointing reconstruction denotes the translation between the pointing coordinates which are read out from the telescope's mechanical encoder and the true pointing coordinates. At the same time one can also account for structural imperfections as well as environmental effects. An accurate pointing reconstruction is achieved by calibrating with the help of celestial objects with known position on the sky, such as planets, extra-galactic objects or radio point sources. The required accuracy is usually determined by the science target, e.g. the systematic effect on the B-mode power spectrum. As shown in Ref. [112], the effect of an pointing error RMS, θ_{pointing}, on the B-mode power spectrum can be modelled as an additional beam convolution with effective beam function given by

$$b_\ell^{\text{pointing}} = \exp\left(-\ell(\ell+1)\frac{(2\theta_{\text{pointing}})^2}{8\log 2}\right). \tag{4.35}$$

In Fig. 4.25 the systematic bias due to the extra smoothing of a non zero pointing error RMS is shown, in the context of a fiducial (i.e. not yet finalized) Simons Array survey.

The telescope coordinates are parametrized by the angular distance parallel to the horizon, the azimuth (az), ranging between $0°$ and $360°$, and the distance perpendicular to the horizon with increasing values in upward direction, the elevation (el), ranging between $0°$ and $90°$. We have rough information of the telescope pointing from the telescope encoder, which measures the az and el through the physical rotation position of the azimuth and elevation bearings. The specified accuracy of this information, given by the manufacturer, is 30 arcsec. But environmental effects can physically deform the telescope in such a way to significantly distort the pointing direction compared to the nominal one given by the telescope encoder, which may vary with time, temperature and pressure, among others. Hence, a calibration of the pointing is necessary to maintain the pointing error requirement below 30 arcsec of Simons Array.

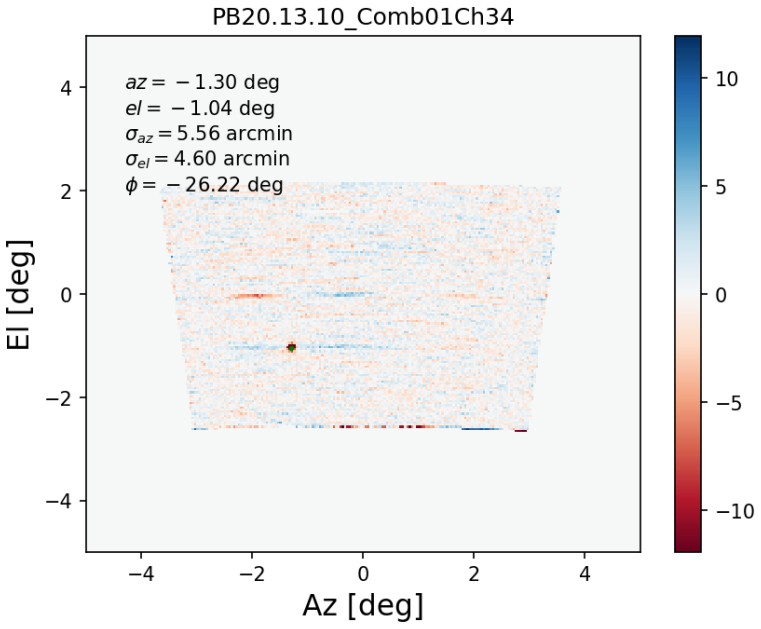

Figure 4.24: Map of a Venus observation of one Polarbear-2 detector, including Gaussian fit parameters. The central point is shown in green within the map. The unit of the colorscale are ADC counts.

To calibrate the telescope pointing, we produce coadded maps from the full focal plane array of a celestial object with known response to the detectors, usually a point source convolved with the telescope beam. From that we can fit for the position in az and el coordinates of the measured object and compare those to the expected positions. Those position can either be obtained from astronomical algorithms computing the current planet positions from tabulated data (ephermerides), using tools like SKYFIELD[41], or the tabulated position of fixed celestial objects from point source catalogues like Australia Telescope 20 GHz survey (AT20G) [247], NVSS [84] or of Planck [283]. Given the telescope location on the Earth and the exact time from a GPS clock, the true positions usually given in equatorial coordinates, right-ascension (ra) and declination (dec), can be transformed to telescope coordinates (az, el) by accounting for the rotation of the Earth.

In pointing reconstruction, we try to find a linear equation transforming between the true pointing direction (az, el) and the one given by the telescope encoder $(\tilde{az}, \tilde{el})$

$$\begin{pmatrix} az \\ el \end{pmatrix} = \begin{pmatrix} \Delta az + \tilde{az} \\ \Delta el + \tilde{el} \end{pmatrix} = \mathbf{A}\mathbf{s} + \begin{pmatrix} \tilde{az} \\ \tilde{el} \end{pmatrix}, \tag{4.36}$$

where $\mathbf{A}$ is a $2 \times N$ matrix defining the pointing model with N parameters contained in $\mathbf{s}$. We assume five parameters accounting for various structural imperfections of the telescope [174, 135]

$$\mathbf{A}_0 \equiv \begin{pmatrix} \cos(\tilde{el}) & 0 & -1 & -\sin(\tilde{az})\sin(\tilde{el}) & -\cos(\tilde{az})\sin(\tilde{el}) \\ 0 & -1 & 0 & \cos(\tilde{az}) & -\sin(\tilde{az}) \end{pmatrix} \tag{4.37}$$

$$\mathbf{s}_0^T \equiv (ia, ie, ca, an, aw), \tag{4.38}$$

where

- ia specifies the azimuth offset,
- ie accounts for the elevation offset and collimation error in elevation,
- ca parametrizes the collimation error in azimuth,

[41] https://rhodesmill.org/skyfield/

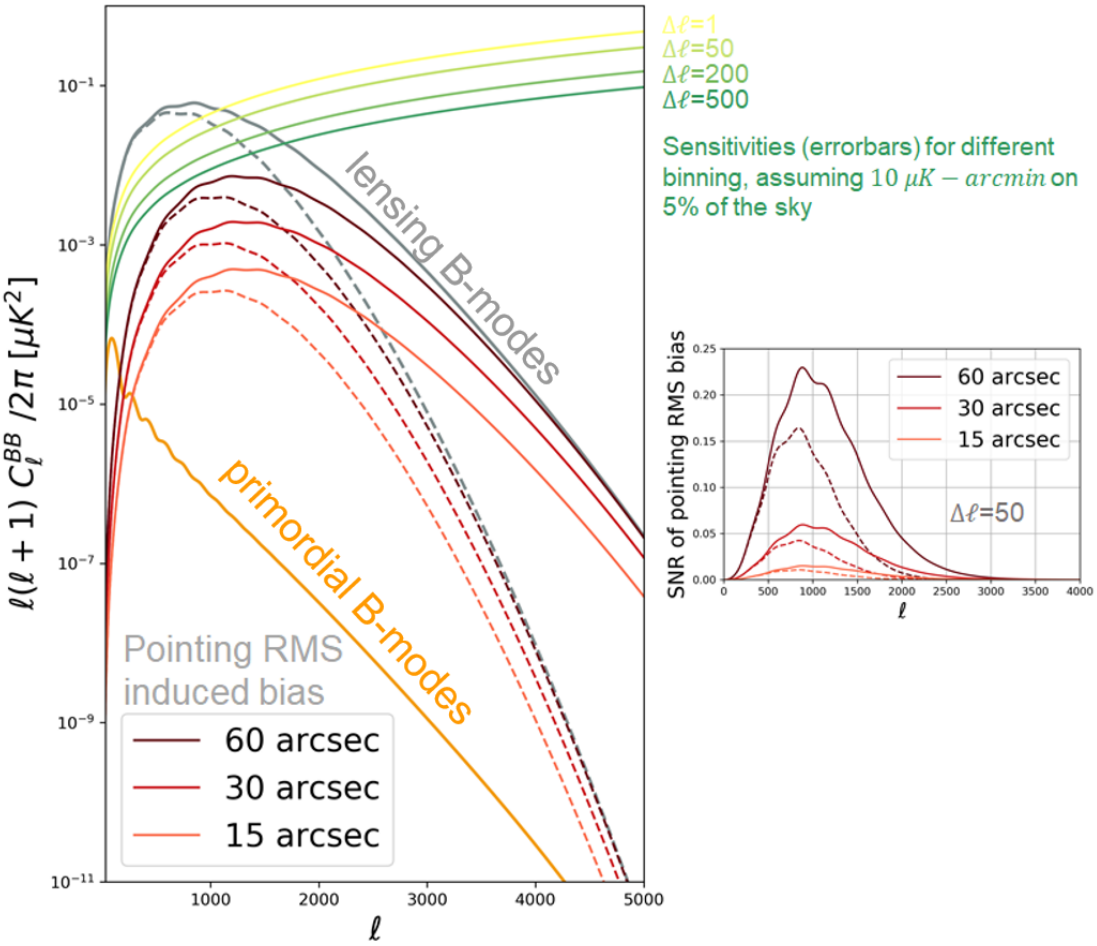

Figure 4.25: Pointing systematic study for Polarbear-2, showing systematic biases in the B-mode power spectrum due to different pointing model error RMSs on the left. On the right are the corresponding signal-to-noise curves. Solid lines correspond to beam-convolved spectra at 150 GHz with a beam-size of 3.5 arcmin, while dashed lines correspond to 95 GHz with 5.2 arcmin. The sensitivity curves in green correspond to fiducial Simons Array surveys.

- an specifies the tilt of azimuth axis from vertical in north direction and
- aw parametrizes the tilt of azimuth from vertical in west direction.

Furthermore, we can assume a timing error correction, dt, caused by synchronization errors between clocks used to compute celestial positions [235]

$$\mathbf{A}_t \equiv \begin{pmatrix} -\sin(l) + \cos(\tilde{az})\cos(l)\tan(\tilde{el}) \\ -\cos(l)\sin(\tilde{az}) \end{pmatrix} \tag{4.39}$$

$$\mathbf{s}_t^T \equiv (dt), \tag{4.40}$$

where l is the latitude of the telescope location. Additionally we introduced ancillary parameters during the POLARBEAR small-patch observing seasons [235] accounting for the effects of solar radiation and ambient temperature

$$\mathbf{A}_s \equiv \begin{pmatrix} T & 0 & \sin(\theta_s)\sin(\phi_s) & 0 \\ 0 & T & 0 & \sin(\theta_s)\cos(\phi_s) \end{pmatrix} \tag{4.41}$$

$$\mathbf{s}_s^T \equiv (ta1, te1, sa, se), \tag{4.42}$$

where

- $ta1$ is the linear order in temperature flexure in azimuth,
- $te1$ is the linear order in temperature flexure in elevation,
- sa is the differential solar heating flexure in azimuth and
- se is the differential solar heating flexure in elevation.

Here we explicitly account for changes in the ambient temperature, T, as well as the position of the Sun (θ_s, ϕ_s) with respect of the telescope boresight pointing. This was necessary due to the fact that gradients up to $5°C$ were measured across the POLARBEAR-1 telescope, causing structural contractions depending on incident solar radiation. Alternatively one can use the solar irradiance, I_S, measured at site and parametrize a pointing model as [235]

$$\mathbf{A}_i \equiv \begin{pmatrix} \left(\frac{I_S}{I_{S,0}}\right)^{1/4}\sin(\theta_s)\sin(\phi_s) & 0 \\ 0 & \left(\frac{I_S}{I_{S,0}}\right)^{1/4}\sin(\theta_s)\cos(\phi_s) \end{pmatrix} \tag{4.43}$$

$$\mathbf{s}_i^T \equiv (sai, sei), \tag{4.44}$$

where

- sai is the differential solar heating flexure in azimuth and
- sei is the differential solar heating flexure in elevation.

For even higher precision, atmospheric refraction has to be taken into account. One can introduce it as an elevation dependent error [174]

$$\Delta el = R(P, T, RH, el), \tag{4.45}$$

where R is the atmospheric refraction correction depending on the ambient pressure, P, temperature, T, relative humidity, RH, and the elevation, el. In the Ulich model [391], one can write it as two separable terms

$$R(P, T, RH, el) = R_0(P, T, RH) f(el). \tag{4.46}$$

In Refs. [174, 391, 56] one can find expressions for these terms as

$$R_0[\text{arcsec}] = 16.01 \frac{K}{mb}\frac{P}{T} - 1.15 \frac{K}{mb}\frac{P_w}{T} + 7.73493 \cdot 10^4 \frac{K^2}{mb}\frac{P_w}{T^2} \tag{4.47}$$

$$f = \frac{\cos(el)}{\sin(el) + 0.00175 \tan(87.5^\circ - el)}, \tag{4.48}$$

where P_w is the pressure of water vapor at the surface. Alternative models used at the IRAM and ALMA telescopes can be found in Refs. [341, 174, 135].

In the first season of POLARBEAR-1 small-patch observation [379] we used the pointing model

$$\mathbf{A} = (\mathbf{A}_0)\,, \tag{4.49}$$

which was improved in the second-season analysis [378] by

$$\mathbf{A} = (\mathbf{A}_0, \mathbf{A}_t, \mathbf{A}_s)\,. \tag{4.50}$$

In the POLARBEAR-1 large-patch analysis we use the 8-parameter pointing model

$$\mathbf{A} = (\mathbf{A}_0, \mathbf{A}_t, \mathbf{A}_i)\,. \tag{4.51}$$

Fitting the pointing model can be done by solving a generalized least-square problem, by acquiring a sufficiently large vector of pointing observations data points

$$\mathbf{d} = \begin{pmatrix} \Delta az_1 \\ \Delta el_1 \\ \vdots \\ \Delta az_{N_d} \\ \Delta el_{N_d} \end{pmatrix}, \tag{4.52}$$

containing N_d data points of azimuth and elevation offsets from separate point source observations. The system matrix $\mathbf{A}$ is then a $2N_d \times N$ matrix and, given an unknown noise term $\mathbf{n}$ with covariance $\mathbf{N}$, the system of linear equations can be written as

$$\mathbf{d} = \mathbf{A}\mathbf{s} + \mathbf{n}, \tag{4.53}$$

which, as shown in e.g. Sec. 3.2.3, leads to the unbiased estimator [108]

$$\hat{\mathbf{s}} = \left(\mathbf{A}^T \mathbf{N}^{-1} \mathbf{A}\right)^{-1} \mathbf{A}^T \mathbf{N}^{-1} \mathbf{d}. \tag{4.54}$$

One challenge in the pointing reconstruction for POLARBEAR-2 and Simons Array is the envisioned survey over a large fraction of sky $> 10\%$ within two patches in the southern and northern galactic

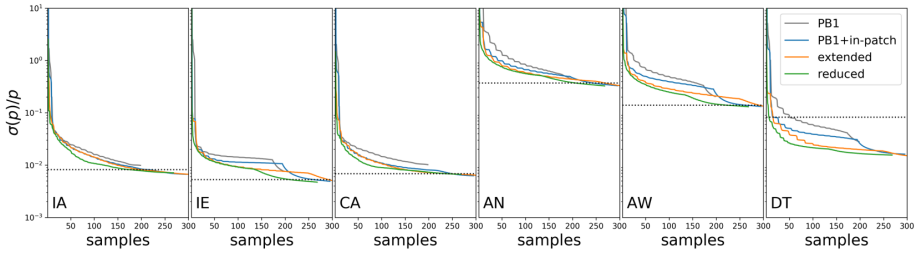

Figure 4.26: Forecasting of the sensitivity to the six-parameter pointing model $(\mathbf{A}_0, \mathbf{A}_t)$, depending on the number of measured samples, N_d. We show four different selections of point sources included in the observing rotation, which are observed depending on their availability, marked in different colors.

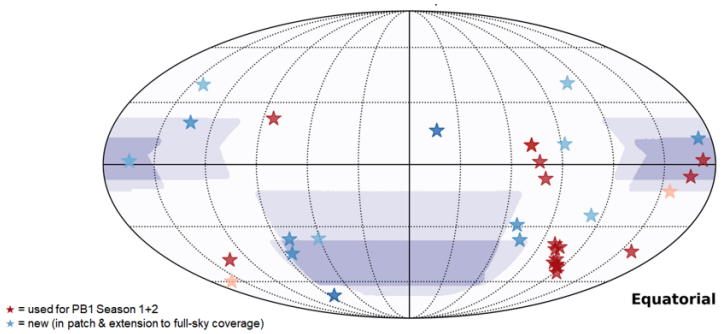

Figure 4.27: The distribution of point-sources of the *reduced* source selection, maximizing the sensitivity of the fitted pointing model parameters.

hole. This requires accurate pointing reconstruction on the full-sky. While previous POLARBEAR analyses restricted the selection of observed point sources to ranges in (az, el) which were traversed by the relatively small science patches, the source selection has to span a larger range in both (az, el)-space as well as (ra, dec)-space, maintaining roughly the same amount of allocated time for point source observations per day ($\sim$ 1 h). To optimize the source selection and more efficiently reconstruct the pointing model on the full-sky, we forecast the error on the pointing model parameters after N_d measurements of a variable set of point sources. We compute the covariance matrix as

$$\mathbf{\Sigma} = \left(\mathbf{A}^T \mathbf{N}^{-1} \mathbf{A}\right)^{-1} \sim \left(\mathbf{A}^T \mathbf{A}\right)^{-1}. \tag{4.55}$$

Fig. 4.26 shows a result of that forecast for four different sets of point sources that are included in the rotation of point sources that are each observed for 10 minutes within the daily total of one-hour-long pointing observations. The noise covariance is assumed to be diagonal with diagonal elements to be taken the POLARBEAR-1 pointing error RMS of 30 arcsec. The six parameters of the $(\mathbf{A}_0, \mathbf{A}_t)$ are shown. We compare the set which was used for the POLARBEAR-1 analyses, with sets including also the point sources which are automatically available within potential CMB patches (PB1+in-patch) and test a new (extended and reduced) set of point sources. The latter two sets are chosen such that all point-sources are observed with a signal-to-noise ratio larger than three within the 10 minutes of observation. Furthermore, they were selected by eye to be evenly distributed in (ra, dec) sky-coordinates. The source candidates are taken from the Planck Point Source Catalog [283] and are partly cross-matched with NVSS [84], IRAS [150] GAIA [54] observations, to increase accuracy. The distribution across the sky, in comparison with the potential CMB patches of Simons Array are shown in Fig. 4.27.

central frequency [GHz]	95	150	220	270
resolution [arcmin]	5.2	3.5	2.7	2.2
NET [$\mu K\sqrt{s}$]	5.8	5.8	19	41

Table 4.4: The instrumental configuration of the Simons Array.

4.4.2 SIMONS ARRAY

POLARBEAR-2a will be mounted on the first telescope of Simons Array[360], an array of three similar telescopes and receivers, observing the sky in four frequency bands. POLARBEAR-2a will be followed by POLARBEAR-2b, in 2019, both observing in bands centered around 95 GHz and 150 GHz. The POLARBEAR-2b receiver is currently undergoeing extensive cryogenic tests. In 2019/2020, POLARBEAR-1 will be retrofitted to house the third new receiver, POLARBEAR-2c, observing at higher frequencies of 220 GHz and 270 GHz, to monitor the dust foreground contamination.

Simons Array will consist of these three receivers and telescopes. The full array will observe in different frequency bands : 95 GHz and 150 GHz for POLARBEAR-2a and 2b, and 220 GHz and 270 GHz for POLARBEAR-2c. The full array will have 22,764 bolometers, where each pixel consist of four bolometers in two frequency bands and two orthogonal polarizations. The sensitivity in each frequency channels is shown in Tab. 4.4. Thanks to the multi-frequency capabilities of Simons Array we believe to be able to deliver competitive results on large- and small-scale polarized CMB science. We expect constraints on the total neutrino mass $\sigma(\sum m_\nu) = 40$ meV (with DESI-BAO, including foreground contamination) through CMB lensing measurements, new cross-correlation possibilities due to overlap with external surveys and constraints on the tensor-to-scalar ratio r of the order 10^{-2}, with possible detections on the $\sigma(r = 0.1) = 6 \times 10^{-3}$ level [354].

4.5 THE FUTURE OF CMB OBSERVATIONS

It is now well established [109, 24] that future high-sensitivity measurements of CMB observables such as the tensor-to-scalar ratio or the total mass of neutrinos require low-noise measurements of CMB polarization in a broad range of frequencies to have the ability to remove foregrounds accurately. This is reflected in the design of next-generation CMB observatories, of which I will focus on three particular projects.

4.5.1 SIMONS OBSERVATORY

The first one is the Simons Observatory, which resulted from a merger of the Advanced-ACT and Simons Array collaborations to join the effort of CMB observation from the Atacama desert. It now grew to a collaboration of 287 researchers from 53 institutions and five continents. The Simons Observatory will be a completely new CMB experiment, that is currently being built on Cerro Roco in Chile, next to the current ACT, CLASS and Simons Array telescopes. It is scheduled to start observations in the early 2020s. It aims to measure both degree-scale and sub-degree/small-scale CMB temperature and polarization, which motivates the design of two types of telescopes. The Simons Observatory will consist of three small-aperture, 42-cm telescopes (SATs) and one large-aperture, 6-m telescope (LAT), with a total of 60,000 cryogenic bolometers spread over the four receivers in the four telescopes. The nominal frequency bands and baseline noise properties are shown in Tab. 4.5. The anticipated survey of the SATs will have a footprint of about 10% of the sky, while we will target 40% of the sky with the LAT with major overlap with galaxy surveys such as DESI or LSST.

	central frequency [GHz]	27	39	93	145	225	280
SAT	resolution [arcmin]	91	63	30	17	11	9
	noise level σ_T [μK-arcmin]	35	21	2.6	3.3	6.3	16
LAT	resolution [arcmin]	7.4	5.1	2.2	1.4	1.0	0.9
	noise level σ_T [μK-arcmin]	71	36	8.0	10	22	56

Table 4.5: The instrumental configuration of Simons Observatory, taken from Tab. 1 in Ref. [386]. The anticipated white noise levels are given for temperature, where the corresponding noise levels for polarization are larger by $\sqrt{2}$.

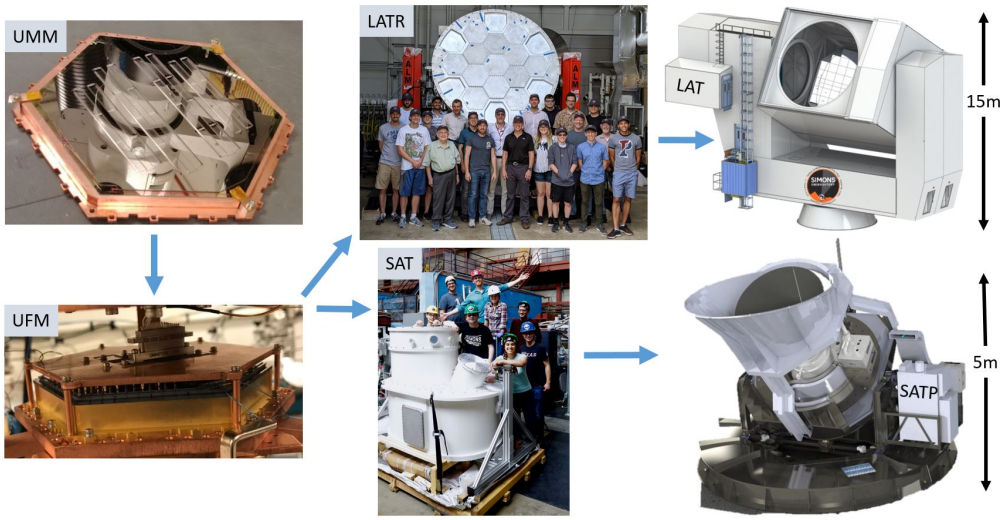

Figure 4.28: Overview of the instrumentation of Simons Observatory. The focal planes follow a modular system, consisting of a universal-microwave multiplexing module (UMM) for read out which, together with silicon wafers, form the universal focal plane module (UFM). These modules will be used for SAT and LAT telescope receivers (SATR and LATR). The SATR will be installed on the SAT platform (SATP) and the LATR on the LAT. Figure is taken from Ref. [385].

The key science goals are constraining cosmological parameters derived from the large-scale B-modes, the damping tail, CMB lensing, the primordial bispectrum, and the thermal and kinematic Sunyaev-Zel'dovich (SZ) effects. These include putting new constraints on primordial gravitational waves, measuring the number of relativistic species and the total mass of neutrinos, testing for deviations from a cosmological constant, improving our understanding of galaxy evolution, and constraining the duration of reionization. Furthermore, the LAT survey will provide a legacy catalog of 16,000 galaxy clusters and more than 20,000 extragalactic sources. The forecasted sensitivities to our science goals are shown in Tab. 4.6.

An overview of the Simons Observatory instrument design is shown in Fig. 4.28. Each SAT will house a single optics tube, containing seven detector arrays operated at 100 mK. There will be two medium-frequency (MF) tubes, one ultra-high frequency (UHF) tube and one low-frequency (LF) tube. The latter two will share the time in one SAT (in the nominal design). Together they will contain 30,000 detectors. Each optics tube will have a 35° field-of-view and a continuously rotating half-wave plate cooled at 40 K. To avoid ground pickup, each SAT will have a forebaffle attached to the cryostat, a co-moving shield attached to the elevation stage of the platform and a fixed ground screen. The LAT design is similar to the one of CCAT-prime [265], which will be built in parallel by *Vertex Antennentechnik*[42], both due to be installed in Chile in 2021. It is a 6 m cross-Dragone telescope with an 8° field-of-view. The receiver (LATR) will have a diameter of 2.5 m and will be able to house up to

[42] https://www.vertexant.com/

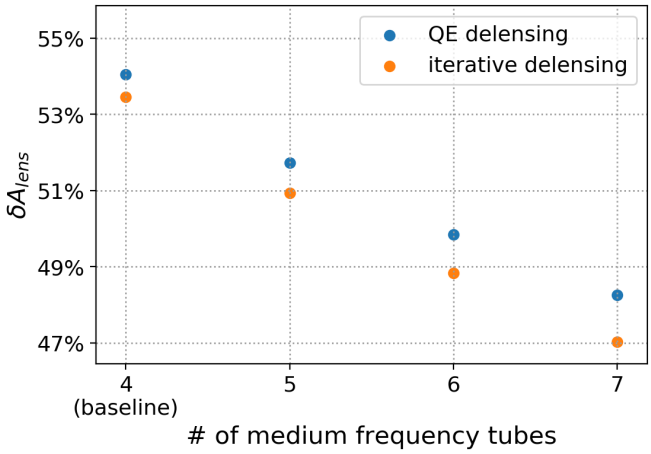

Figure 4.29: Forecast of the delensing efficiency, $\delta A_{\rm lens}$, for an increase in medium-frequency (MF) tubes after the end of the nominal survey of Simons Observatory of five years, after which the survey strategy focuses on 10% of the sky to optimally overlap with the SAT survey.

13 optics tubes. The nominal design for first deployment foresees 7 optics tubes installed in the LATR, 1 LF, 4 MF and 2 UHF. Further optics tubes in the LAT are part of extended Simons Observatory programs [385]. For example, an increase in MF tubes for the LAT could slightly increase the efficiency of internal delensing, as shown in Fig. 4.29.

The Simons Observatory detectors will be dichroic TES bolometric polarimeters, housed in so-called universal focal plane modules (UFMs). There will be two types of detector arrays, either coupled through orthomode transducers to aluminium feedhorns, produced at NIST (National Institute of Standards and Technology), or coupled through dual-polarization sinuous antennas and lenslets, produced at UC Berkeley. One major technological advancement of Simons Observatory will be the microwave multiplexing readout scheme [96]. It allows for a readout of one UFM with a single pair of coaxial cables. The achieved multiplexing factor is anticipated to be 1.800, with a recent demonstration of 528 [151]. For comparison, the multiplexing factor of Simons Array is 40 [149]. The entire Simons Observatory will require the production of 49 UFMs.

4.5.2 CMB STAGE IV

As an ultimate ground-based CMB observatory the CMB Stage IV (CMB-S4) experiment was conceived [2]. Similar to the Simons Observatory, the anticipated design of CMB-S4 consists of small- and large-aperture telescopes, targeting low-ℓ and high-ℓ CMB measurements. It will provide low-resolution ultra-deep measurements with noise levels $< 1\ \mu K$-arcmin, covering 3% of the sky as well as high-resolution measurements over 60% of the sky [3]. The total detector count of CMB-S4 is anticipated to be 511,184, distributed over multiple receivers in multiple telescopes at two sites: the Atacama desert in Chile and the South Pole. The science goals can be grouped into four subjects

- primordial gravitational waves and inflation,
- the dark Universe,
- mapping matter in the cosmos and
- the time-variable millimeter-wave sky.

	Current[b]	SO-Nominal (2022-27) Baseline	Goal	Method[d]
Primordial perturbations				
r ($A_L = 0.5$)	0.03	0.003	0.002[e]	BB + external delensing
n_s	0.004	0.002	0.002	TT/TE/EE
$e^{-2\tau}\mathcal{P}(k = 0.2\text{Mpc})$	3%	0.5%	0.4%	TT/TE/EE
$f_{\rm NL}^{\rm local}$	5	3	1	$\kappa\times$ LSST-LSS
		2	1	kSZ + LSST-LSS
Relativistic species				
$N_{\rm eff}$	0.2	0.07	0.05	TT/TE/EE + $\kappa\kappa$
Neutrino mass				
M_ν (eV, $\sigma(\tau) = 0.01$)	0.1	0.04	0.03	$\kappa\kappa$ + DESI-BAO
		0.04	0.03	tSZ-N $\times$ LSST-WL
M_ν (eV, $\sigma(\tau) = 0.002$)		0.03[f]	0.02	$\kappa\kappa$ + DESI-BAO + LB
		0.03	0.02	tSZ-N $\times$ LSST-WL + LB
Beyond standard model				
$\sigma_8(z = 1 - 2)$	7%	2%	1%	$\kappa\kappa$ + LSST-LSS
		2%	1%	tSZ-N $\times$ LSST-WL
H_0 (km/s/Mpc, ΛCDM)	0.5	0.4	0.3	TT/TE/EE + $\kappa\kappa$
Galaxy evolution				
$\eta_{\rm feedback}$	50-100%	3%	2%	kSZ + tSZ + DESI
$p_{\rm nt}$	50-100%	8%	5%	kSZ + tSZ + DESI
Reionization				
Δz	1.4	0.4	0.3	TT (kSZ)

Table 4.6: The Simons Observatory science goals. The table is taken from Ref. [385] and details on the assumptions and forecasting methods can be found in Ref. [386].

	central frequency [GHz]	20	30	40	95	145	220	270
LAT	resolution [arcmin]	10	7.4	5.1	2.2	1.4	1.0	0.9
	noise level σ_T [μK-arcmin]	48.1	16.2	9.07	1.53	1.57	5.01	12.0

Table 4.7: The instrumental configuration of the CMB-S4 LAT.

Detailed forecasts and achievable sensitivities can be found in Refs. [2, 3]. We use the publicly availabe CMB-S4 noise calculator [43] to present anticipated white noise levels and a Gaussian beam sizes for the CMB-S4 LAT shown in Tab. 4.7.

4.5.3 LITEBIRD

In May 2019 the LiteBIRD[44] satellite proposal was selected by the Japanese space agency as an L-Class mission, anticipated to launch in 2028 [45]. It is a satellite CMB experiment specifically designed to target a high-sensitivity tensor-to-scalar ratio measurement. The target is a sensitivity of $\sigma(r) < 10^{-3}$ without delensing, by measuring the B-mode power spectrum in a multipole range $2 \leq \ell \leq 200$ [361, 244]. Furthermore, it will deliver cosmic-variance limited measurement of the optical depth to reionization, $\tau_{\rm reio.}$, from the E-mode power spectrum [392] and set new constraints on cosmic birefringence [242] It will consist of three telescopes (LFT, MFT and HFT) all measuring half-wave plate modulated CMB in 15 frequency bands with 4676 detectors over the full-sky [244]. A fiducial instrumental configuration of LiteBIRD is given in Tab. 4.8.

central frequency [GHz]	40.0	50.0	60.0	68.4	78.0	88.5	100.0	118.6
resolution [arcmin]	60	56	48	43	39	35	29	25
noise level σ_P [μK-arcmin]	42.4	25.8	20.1	15.6	12.5	10.1	11.8	9.5
central frequency [GHz]	140.0	166.0	195.0	234.9	280.0	337.4	402.1	
resolution [arcmin]	23	21	20	19	24	20	17	
noise level σ_P [μK-arcmin]	7.6	6.7	5.1	6.3	10.1	10.1	19.1	

Table 4.8: The fiducial instrumental configuration of the LiteBIRD satellite, which is not finalized yet.

[43] https://cmb-s4.org/wiki/images/Lat-noise-181002.pdf

[44] http://litebird.jp/eng/

[45] http://www.isas.jaxa.jp/home/rikou/godo/2019/0602/gbi7uzhxfxmz/misison_selection_announcement_may2019.pdf

Those who study the complex interplay of cause and effect in the history of the Universe say that this sort of thing is going on all the time, but that we are powerless to prevent it.

Douglas Adams, *The Hitchhiker's Guide to the Galaxy*

5

Cosmological Large-Scale Structure and CMB Lensing

In this chapter I present my work on the effects of non-linear structure formation and post-Born CMB lensing on CMB lensing extraction methods used to measure the CMB lensing power spectrum, as well as cross-correlation power spectra. The content is largely based on published work in Ref. [33] and Ref. [114]. While these have been collaborative projects I have made major contributions to them comprising of the high-fidelity CMB lensing potential reconstruction from full-sky simulations, the computation of theoretical bispectra and statistical comparison with the lensed CMB simulations, the computation of CMB lensing power spectra and delensed B-mode power spectra, as well as the estimation of cosmological parameters using MCMC sampling as well as intrinsic alignment parameter estimation. The relevant work capitalized on the tools and techniques described in chapters 1 and 2.

CMB lensing is one of the key signals exploited by current and future experiments to obtain constraints on cosmological models. It is sourced by growing matter perturbations between the last-scattering surface ($z \approx 1100$) and $z = 0$, and contains thus valuable information on the parameters affecting the formation of the large-scale structures (LSS) of the universe such as the sum of neutrino masses (M_ν) and the properties of the dark energy (see Ref. [212] for a review). Achieving high-sensitivity measurements of the lensed CMB polarization is a crucial step to increase the precision of the CMB lensing potential reconstruction.

With decreasing noise levels, higher angular resolutions and larger areas observed by future experiments (e.g. CMB-S4 [2]), the accuracy of reconstruction techniques and theoretical modeling of the measurements has to improve alike. To date, CMB lensing potential reconstruction analyses commonly rely on the assumption of Gaussianity of the unlensed CMB temperature field and of the lensing potential itself. The lensing potential, however, becomes non-Gaussian due to nonlinear structure formation mainly at late times. Although the level of non-Gaussianity is expected to be small due to the large number of potential wells that deflect CMB photons, the impact of this effect has to be quantified in light of future high-precision measurements [238, 250, 301].

Moreover, the Born approximation (i.e. the evaluation of the deflections of the photons with respect to the original unperturbed line of sight), usually employed for modeling CMB lensing, does not account accurately for all features of the actual deflection process (e.g. the correlation between subsequent lensing events) neglecting therefore some of the sources of non-Gaussian statistics in the

lensing potential. Earlier attempts to model CMB lensing including the effects of nonlinear structure formation were presented in [62, 60, 238]. Recent works investigated the effect of the relaxation of the Born approximation on lensed CMB power spectra and CMB lensing power spectra, from both an analytical and a numerical point of view [138, 301, 215, 113]. Similar analytical studies were previously performed also in the context of the weak lensing shear power spectrum [85, 335, 201, 274]. While the most recent studies showed that the main post-Born effects are observed on the higher-order statistics of the CMB lensing potential rather than on its power spectrum, the impact of such effects on lensing reconstruction has not yet been evaluated. Recent theoretical investigations further suggested that the presence of non-Gaussianities in the CMB lensing potential could lead to percent level biases in the reconstructed CMB lensing potential power spectrum if they are left unaccounted for [48]. This could in turn lead to a biased estimation of cosmological parameters.

In this chapter we evaluate the impact of the non-Gaussian statistics of the CMB lensing potential on the commonly employed quadratic estimator techniques for the CMB lensing reconstruction. As these effects are often too complex to model analytically, we use the simulations of [113] that include both the nonlinear evolution of LSS and post-Born effects to model and investigate this problem numerically.

5.1 GRAVITATIONAL LENSING FORMALISM

In the weak lensing formalism the effect of deflections of light rays coming from a source plane is described by the lens equation. This maps the final angular position $\mathbf{s}(\mathbf{n}, 0)$ of a ray to the angular position of its source $\mathbf{n}$ using Eq. 1.263

$$\mathbf{n}' \equiv \mathbf{s}(\mathbf{n}, 0) = \mathbf{n} - 2\int_0^{\chi_*} d\chi W(\chi)\nabla\Psi_W\left(\mathbf{s}(\mathbf{n}, \chi'), \chi'\right). \tag{5.1}$$

The derivatives in the small angle limit should be computed using a coordinate system orthogonal to the current light ray's direction of travel. Numerical tests have shown that using angular derivatives causes a negligible error (see e.g. [35] and references therein). The linearized mapping between an image at the source plane and the lensed image at a given lens plane is described by the lensing magnification matrix (or lensing Jacobian) defined in Eq. 1.250. This can be computed as the simple derivative of the equation above.[46]

$$M_{ij}(\mathbf{n}, \chi) = \delta_{ij} - 2\int_0^{\chi_*} d\chi' W(\chi')\nabla_i\nabla_j\Psi_W\left(\mathbf{s}(\mathbf{n}, \chi'), \chi'\right) M_{kj}(\mathbf{n}, \chi'), \tag{5.2}$$

In the leading-order computations of the lensing effect, the photon path is approximated by the unperturbed photon geodesic $\mathbf{s}(\mathbf{n}, \chi) \approx \mathbf{n}\chi$, such that the line integral of the Weyl potential Ψ_W simplifies to

$$\mathbf{n}' = \mathbf{n} - 2\int_0^{\chi_*} d\chi' W(\chi')\nabla\Psi_W\left(\mathbf{n}, \chi'\right). \tag{5.3}$$

At linear order in Ψ_W, the overall deflection of a photon $\boldsymbol{\alpha}$ is then given by Eq. 1.266

$$\boldsymbol{\alpha}(\mathbf{n}) = -2\int_0^{\chi_*} d\chi W(\chi)\nabla\Psi_W(\chi\mathbf{n}, \tau) = \nabla\phi(\mathbf{n}).$$

[46] We note that the following formula can be extended to the full-sky case by promoting the partial derivatives to covariant derivatives.

We note that the lensing potential, ϕ, and the lensing convergence, κ, can be connected in the weak lensing regime through the relations [47]

$$\kappa = -\frac{1}{2}\nabla^2\phi, \tag{5.4}$$

$$C_L^{\kappa\kappa} = \frac{[L(L+1)]^2}{4} C_L^{\phi\phi}. \tag{5.5}$$

If we want to evaluate the lens equation at higher order, i.e. beyond the Born approximation (post-Born), we have to account for the fact that photons do not travel along the unperturbed background geodesics. Higher-order corrections are typically introduced perturbatively in Eq. (5.1) by Taylor expanding the potential Ψ_W around the unperturbed geodesic position.

The distinct additional couplings that arise reflect the change in the shape of a light ray bundle by one lensing event affecting the amount of lensing generated by a later lensing event (lens-lens coupling) as well as by changing gravitational potentials in the direction in which the ray path is bent. We refer the reader to [85, 301, 201, 232] for further details. Post-Born corrections affect the angular power spectrum of CMB lensing observables in a minor way. In particular, the amplitude of $C_L^{\kappa\kappa}$ is suppressed on scales $L \lesssim 1000$ by roughly 0.2% due to lens-lens coupling and enhanced above the cosmic variance uncertainties at $L \gtrsim 1000$, mimicking thus an additional nonlinear large-scale structure growth [301]. Higher-order correlations of the κ field, such as the bispectrum, are, however, more affected and we will discuss these effects in the following sections.

A characteristic signature of post-Born corrections is the appearance of curl-like modes in the overall lensing deflection angle [159, 301], such that (cf. Eq. 1.263)

$$\mathbf{n}' = \mathbf{n} + \nabla\phi(\mathbf{n}) + \nabla \times \Omega(\mathbf{n}). \tag{5.6}$$

Here we define $(\nabla \times \Omega)_i \equiv \epsilon_{ij}\partial_j\Omega$, where ϵ_{ij} is the Levi-Civita symbol in two dimensions and Ω is a pseudo-scalar field. In analogy to the case of κ and ψ, Ω is related to the lensing rotation ω as

$$\omega = -\frac{1}{2}\nabla^2\Omega, \tag{5.7}$$

$$C_L^{\omega\omega} = \frac{[L(L+1)]^2}{4} C_L^{\Omega\Omega}. \tag{5.8}$$

The technique to reconstruct the lensing potential from simulations is described in Sec. 2.3 and following sections. The formalism derived in that section assumes that all the non-Gaussianity in the CMB is entirely due to the lensing effect and that the lensing potential is a Gaussian field. However, this is just an approximation and if the lensing potential (or equivalently the lensing convergence) has nonzero higher-order correlations, there are additional terms involving four-point functions of lensed CMB fields that create distinct biases. This problem was first studied in [48] in the context of assessing the impact of the nonlinear evolution of the matter distribution in the lensing reconstruction. In this work the authors derived expressions for the bias induced by a nonzero bispectrum in the lensing potential caused by the nonlinear gravitational collapse that is of order

$$\mathcal{O}\left(\left(C_L^{\phi\phi}\right)^{3/2}\right) \tag{5.9}$$

[47] Despite being derived in the Born approximation, these relations hold in the post-Born regime at subpercent accuracy as discussed in [113].

and is referred to as $N_L^{(3/2)}$. Hence the bias expansion of Eq. 2.57 now reads

$$\left\langle \hat{C}_L^{\phi\phi} \right\rangle = C_L^{\phi\phi} + N_L^{(0)} + N_L^{(1)} + N_L^{(3/2)} + N_L^{(2)} + ...$$

The TT reconstruction channel was found to be the most sensitive on angular scales $\ell \lesssim 1000$ considered in their work and could reach the level of 2.5% for low noise and large sky coverage experiments. This level of bias is significant in light of the expected future experimental sensitivity. Understanding the amplitude and nature of higher-order biases and their effect on our ability of constraining the cosmology is therefore crucial.

It is particular to this kind of bias that, while the Gaussian bias arising from CMB fields within the quadratic estimator are not present when cross-correlating the CMB reconstructed lensing potential, $\hat{\phi}$, with an external tracer, $\phi_{\rm ext}$, the higher-order terms, most prominently three-point correlations in ϕ remain [49, 114]. Hence the $N_L^{(3/2)}$-bias is present in cross-correlations as well, so that we can write

$$\left\langle \hat{C}_L^{\phi\phi_{\rm ext}} \right\rangle \equiv \frac{1}{2L+1} \sum_M \hat{\phi}^\dagger_{LM} \phi_{{\rm ext},LM} = C_L^{\phi\phi{\rm ext}} + N_L^{(3/2)} \tag{5.10}$$

Modeling these effects analytically becomes cumbersome very quickly. Therefore, we decided to adopt a numerical approach and assess the impact of these biases through accurate and realistic numerical simulations. In order to tackle the problem in its full complexity we decide to use simulations that include not only the nonlinear evolution of matter studied in [48] but also post-Born effects including the resulting non-Gaussian corrections. Analytical predictions of the shape and amplitude of these non-Gaussian correlations have recently been computed in [301, 215, 231]. The detailed shape and sign of $N_L^{(3/2)}$ depends on the lensing potential bispectrum, where there can be a partial cancellation between the post-Born and non-linear matter evolution (LSS) terms as explained in Ref. [301]. For the CMB lensing auto-spectrum, the cancellation can be significant, substantially reducing the size of the overall bias [48, 33, 49, 114]. However, the LSS bispectrum can become larger for lower-redshift tracers, and the post-Born contribution smaller, so there is substantially less cancellation for cross-correlation with low-redshift tracers, giving a larger net bias.

5.2 MODELING CMB LENSING AT HIGHER ORDER

To test the bias in the lensing reconstruction induced by non-Gaussian evolution of the matter and post-Born effect we need to simulate the lensing of CMB anisotropies including both these effects. For this purpose we use the simulation method and results of Ref. [113] (hereafter FCC18). This work produced a collection of lensing observables $\kappa, \omega, \phi, \Omega$, derived from a ΛCDM N-body simulation of the DEMNUni suite [61, 68] in the Born approximation and using multiple-lens ray tracing techniques. The N-body simulation employed in FCC18 used 2048^3 dark matter particles and a box size of 2 Gpc/h from $z = 99$ to $z = 0$. This redshift range cover allows to reproduce the CMB lensing kernel, $W^{\rm CMB}(\chi)$, with sub-percent precision. The mass resolution of the simulation at $z = 0$ is $M_{\rm CDM} = 8.27 \times 10^{10} M_\odot/h$ and the gravitational softening length is set to $\epsilon_s = 20$ kpc/h corresponding to 0.04 times the mean linear inter-particle separation. Below, we briefly summarize the specificities of the light-cone construction and ray tracing algorithm adopted in these simulations as well as further tests complementary to the one presented in FCC18 and specifically performed for this work. We refer the reader to FCC18 for a more detailed discussion.

5.2.1 RAY TRACING ALGORITHM FOR CMB LENSING

Starting from a series of snapshots in time of an N-body simulation, the algorithm adopted in FCC18 reconstructs the full-sky past light cone of the observer from redshift $z = 0$ to the maximum redshift covered by the simulation $z_{\rm max}$ (in our case $z_{\rm max} = 99$). Because the universe volume simulated in the N-body is finite, we replicate the box volume in space to fill the whole observable volume between $0 \leq z \leq z_{\rm max}$. To avoid repeating the same structures along the line of sight and to recover (at least partially) structures on scales comparable to the box size, the algorithm employs a specific randomization procedure for the particle positions as in [62, 58]. The lightcone was then divided into spherical shells of comoving thickness $\Delta\chi \approx 150\,{\rm Mpc}/h$. The particles located inside each of these volumes, s, were projected onto spherical shells of surface mass density $\Sigma^{(s)}$ sampled on a HEALPIX grid at $N_{\rm side} = 4096$ [123] so that each pixel, p, the surface density is

$$\Sigma_p^{(s)} = \sum_0^n m/\Delta\Omega_{\rm pix} \tag{5.11}$$

where n is the number of particle per pixel, $\Delta\Omega_{\rm pix}$ its area in steradians, and m the mass of one dark matter particle. The s-th surface mass density plane was converted into surface mass overdensity $\Delta_\Sigma^{(s)} = \Sigma^{(s)}/\bar{\Sigma}^{(s)} - 1$ The algorithm then converts the surface mass density planes into convergence fields. With this discrete version of the light cone at hand, it is convenient to use the discretized lens equation of Eq. (1.265) [175, 141, 323]

$$\mathbf{n}' = \mathbf{n} - \sum_{s=0}^{N-1} \frac{S_k(\chi - \chi_s)}{S_k(\chi)} \boldsymbol{\alpha}^{(s)}(\mathbf{s}^s). \tag{5.12}$$

Here s is the shell index and we define the gradient of the two-dimensional (2D) projected gravitational potential as

$$\boldsymbol{\alpha}^{(s)}(\mathbf{s}^{(s)}) = 2\frac{1}{S_k(\chi_s)} \int_{\chi_s - \Delta\chi/2}^{\chi_s + \Delta\chi/2} d\chi \nabla\Psi(\mathbf{s}^{(\chi)}, \chi). \tag{5.13}$$

$\boldsymbol{\alpha}^{(s)}$ is easily computed starting from the convergence field of each shell (s), $\kappa^{(s)}$,

$$\kappa^{(k)} = \kappa_{\chi_*}^{(k)} \equiv 4\pi G \frac{S_k(\chi_* - \chi_k)}{S_k(\chi_*)} \frac{(1+z_s)}{S_k(\chi_s)} \Delta_\Sigma^{(s)}, \tag{5.14}$$

using a spin-1 spherical harmonic transform [becker2013, 90] in the E and B decomposition

$${}_1\alpha_{\ell m}^{(s),E} = \frac{2\kappa_{\ell m}^{(s)}}{\sqrt{\ell(\ell+1)}} \qquad {}_1\alpha_{\ell m}^{(s),B} = 0. \tag{5.15}$$

The $\Delta_\Sigma^{(k)}$ maps will also be used as proxy of the galaxy density distribution as described in Sec. 5.2.3. The latest operation requires the computation of the spherical harmonic coefficients $\kappa_{\ell m}^{(s)}$ using a fast spherical harmonic transform up to a given cut-off in power $\ell_{\rm max}$. The choice of $\ell_{\rm max}$ for each different shell is optimized to ensure the total deflection is computed with sub-percent precision for scales $\ell \lesssim 8000$. The magnification matrix follows straightforwardly from Eq. (5.12) as

$$M_{ij}^N(\mathbf{n}, \chi_N) = \delta_{ij} - \sum_{s=0}^{N-1} \frac{S_{s,N}}{S_N} U_{ip}^{(s)}(\mathbf{s}^{(s)}, \chi_s) A_{pj}^{(s)} \mathbf{n}, \chi_s), \tag{5.16}$$

where N is the number of planes necessary to reach the source at comoving distance χ_N and U_{ij} is the matrix of the second derivatives of the gravitational potential, $\nabla_i \nabla_j \Psi_W$. U_{ij} can be computed easily

as derivatives of the component of the spin-1 field $\boldsymbol{\alpha}^{(k)}$ (see Appendix A of FCC18). In Eq. (5.16) we use the notation $S_{s,N} \equiv S_k(\chi_N - \chi_s)$ and $S_s \equiv S_k(\chi_s)$ for simplicity. Implementing Eq. (5.16) in numerical simulations becomes quickly prohibitive for a large number of lens planes and large sky fraction. FCC18 adopted the multiple lens approach of [153], who showed that the equation can be rewritten in a more efficient form that requires one to store in a memory for a given sth iteration just the position of the light rays at the two previous positions $\mathbf{s}^{(s-2)}$ and $\mathbf{s}^{(s-1)}$,

$$\mathbf{s}^{(s)} = \left(1 - \frac{D_{s-1}}{D_s}\frac{D_{s-2,s}}{D_{s-2,s-1}}\right)\mathbf{s}^{(s-2)} + \\ + \frac{D_{s-1}}{D_s}\frac{D_{s-2,s}}{D_{s-2,s-1}}\mathbf{s}^{(s-1)} - \frac{D_{s-1,s}}{D_s}\mathbf{s}^{(s-1)}(\mathbf{s}^{(s-1)}). \tag{5.17}$$

By differentiating with respect to $\mathbf{n}$ as in Eq. (5.2), we obtain the recurrence relation for the magnification matrix

$$M_{ij}^{(s)} = \left(1 - \frac{D_{s-1}}{D_s}\frac{D_{s-2,s}}{D_{s-2,s-1}}\right)M_{ij}^{(s-2)} + \\ + \frac{D_{s-1}}{D_s}\frac{D_{s-2,s}}{D_{s-2,s-1}}M_{ij}^{(s-1)} - \frac{D_{s-1,s}}{D_s}U_{ip}^{(s-1)}M_{pj}^{(s-1)}. \tag{5.18}$$

This algorithm was originally developed in the context of galaxy lensing, but adapted to spherical geometry in [90] and developed first in [58, 113] for CMB lensing. This approach is also convenient to derive the magnification matrix and lensing observables in the Born approximation that we will use later to isolate the contribution coming from post-Born effects. Assuming the background distortion, the first-order magnification matrix is

$$M_{ij}^{(N),\mathrm{1st}}(\mathbf{n}, \chi_s) = \delta_{ij} - \sum_{s=0}^{N-1}\frac{D_{s,N}}{D_N}U_{ij}^{(s)}(\mathbf{n}, \chi_s). \tag{5.19}$$

We note that the U_{ij} matrix is symmetric because mixed covariant derivatives of scalar fields commute and thus the field rotation, ω, is identically zero.

5.2.2 GALAXY LENSING

We produce 5 simulated maps of convergence κ_z for a Dirac delta source distribution around specific redshifts $z \in \{0.2, 0.35, 0.6, 1, 2\}$ and no shot-noise. We are neglecting complications connected to conversion between observed shear estimators and convergence maps, as well as all the instrumental and theoretical systematic effects in these kind of measurements, such as redshift estimation and distribution of background galaxies, multiplicative biases in the cosmic shear estimates, intrinsic alignments and the impact of the baryons in the signal modelling.

We show in Ref. [114] that the power spectrum of the post-Born simulated convergence maps κ_z are consistent with the Born results, showing differences to the Born result of about 0.05% for $z = 2$ on all angular scales and consistent with zero to within sample variance. Such differences are negligible for all practical purposes and are in rough agreement with analytic estimates based on the results of Ref. [201, 301], which predicts them to be lower than 0.01%.

We find that the measured post-Born corrections grow slightly with decreasing redshifts as a result of numerical artefacts and power aliasing (as an additional shot-noise bias), but stay below 3% at $z = 0.2$. The power spectrum of the rotation component of the magnification matrix comes entirely from

second-order lens-lens coupling terms and provides a stringent test of the accuracy of the post-Born modelling in our observables. For the bins $z \geq 0.6$, where the signal is stronger and the RMS rotation angle has a magnitude much higher than the raytracing resolution ($\simeq 50, 20, 7$ arcsec respectively), we obtain agreement at the few-percent level between the power spectrum of the simulated rotation fields and the analytic predictions from Ref. [301] using Halofit for the non-linear matter power spectrum. At $z = 0.35$ and $z = 0.2$ the magnitude of the rotation angle is well below our spatial resolution (2 and 0.5 arcsec respectively) and thus the agreement is degraded to $\simeq 20\%$. As the post-Born effects are very small at these low redshifts, this accuracy level is more than enough for our purposes.

5.2.3 DENSITY FIELD

Another observable we consider for the cross-correlation is the projected density. This is usually reconstructed through the observation of galaxy overdensities δ_g. We ignore the complications associated with the ability to model how galaxies trace the true underlying matter field, i.e. to the knowledge of their bias parameters as a function of scale and redshift, by directly using the $\Delta_\Sigma^{(k)}$ field without resorting to the creation of mock galaxy catalogs using abundance matching or Halo Occupation Distribution (HOD) techniques. This is equivalent to setting $b_1 = 1$ and constant over redshift in Eq. (1.306). We will report results for $N_L^{(3/2)}$ in terms of relative bias with respect to the true cross-correlation power spectrum, so the impact of changes in overall normalization is minimized. We produced simulated density fields for 7 different redshift bins with an approximately constant width of 1 Gpc. The details of the bin boundaries are shown in Tab. 5.1.

We will be correlating simulated density fields with Born and post-Born CMB lensing, so for each redshift bin we produced lensed and unlensed density fields such that the density field is modeled to consistent perturbative order (so the signals observed in a given direction on the sky are probing densities at consistently perturbed locations along the line of sight). The first-order unlensed results are obtained by simply summing together the $\Sigma^{(s)}$ planes falling within the boundaries of each redshift bin and then computing the surface mass overdensity $\Delta_\Sigma^{\bar{z}}$ of this map. To model the lensed surface mass density we first created an integrated convergence map $K^{(s)}$ for each $\Sigma^{(s)}$ falling within a redshift bin in the Born approximation, i.e.

$$K^{(s)} = \sum_{j<k} \kappa_{\chi_s}^{(j)}. \tag{5.20}$$

We lensed each $\Sigma^{(s)}$ with a displacement field extracted from $K^{(s)}$[48] using a modified version of the LensPix code, and then sum together each lensed $\Sigma^{(s)}$ within a redshift bin to get the lensed surface mass density $\Delta_\Sigma^{\bar{z},\mathrm{ML}}$. This procedure is necessary to take into account the fact that at the next perturbative order, the density field is observed at the lensed position. Neglecting this would lead to a loss of correlation, since the background and perturbed light ray paths would then see lensing by different small-scale structure (e.g. the perturbative cross power spectrum would be missing a 2×2-order term that is important on small scales). In Ref. [114] we compare the power spectrum $C_\ell^{gg,\bar{z}} = C_\ell^{\Delta\Delta,\bar{z}}$ of the simulated galaxy density maps compared with analytic predictions using Eq. (1.297) and the Halofit fitting formula. The two results agree at better than 4% level. We found that the difference between the lensed and unlensed $C_\ell^{gg,\bar{z}}$ is below 0.2% for the highest and below 0.05% for the lowest redshift bin.

[48] This operation requires solving the Poisson equation in the harmonic domain and for this purpose we set a maximum multipole $L_{\max} = 6144$.

$\bar{z}$	$z_{\rm min}$	$z_{\rm max}$	$\Delta\chi$ [Gpc]
0.2	0.06	0.33	1.1
0.35	0.25	0.46	0.8
0.6	0.41	0.78	1.2
1	0.75	1.3	1.5
2	1.19	2.85	2.5
5	2.85	7.04	2.5
9.45	7.04	11.85	1.2

Table 5.1: Details of the redshift bins used to model the density field and its cross-correlation with CMB lensing, where $\Delta\chi$ gives the comoving thickness of the each top-hat bin.

5.2.4 CONSISTENCY CHECK WITH THE LSS AND POST-BORN BISPECTRA

FCC18 carried out an accurate characterization of the post-Born corrections on κ, ω and lensed CMB power spectra and compared extensively with their analytical predictions derived in [301, 215, 232, 231, 214]. However, the analysis did not investigate in detail the impact of the nonlinear evolution of large-scale structures and how simulation properties match with analytical predictions of the higher-order statistics of the κ field. Below we present additional validation tests performed to assess the reliability of these simulations in modeling higher-order statistics of post-Born corrections and nonlinear LSS evolution. We limit our analysis to the statistics of the κ field and its cross-correlation with ω. Higher-order statistics of the curl mode of the deflection field beyond the mixed $\kappa\kappa\omega$ bispectrum [301], which appear at higher order in the perturbative expansion, are lacking theoretical predictions. The measurement of the $\kappa\kappa\omega$ and $\kappa\omega\omega$ bispectrum in the simulations used in this work through its effect on lensed B-modes power spectrum was presented in FCC18, together with the measurement of the post-Born induced curl mode on lensed CMB power spectra. We refer the reader to that work for a more in-depth discussion and comparison with theoretical predictions.

HIGHER-ORDER STATISTICS OF THE CMB CONVERGENCE

To verify the accuracy of the simulations in reproducing the expected level of non-Gaussianity in κ, we compare its skewness as measured in the simulations with the values obtained by contracting the predicted theoretical bispectrum including LSS nonlinearity and post-Born corrections. The definition of skewness given a pixelized map of a scalar field, X, is

$$S_3[X] = \langle XXX \rangle = \frac{1}{N_{\rm pix}} \sum_p^{N_{\rm pix}} X_p^3, \tag{5.21}$$

where p is the pixel index and $N_{\rm pix}$ the total number of pixels in the map. Following [352, 194], we compute the skewness in terms of the reduced bispectrum $b_{L_1L_2L_3}$ as

$$S_3[b_{L_1L_2L_3}] = \sum_{L_1L_2L_3}^{L_{\rm max}} \frac{(2L_1+1)(2L_2+1)(2L_3+1)}{(4\pi)^2} \begin{pmatrix} L_1 & L_2 & L_3 \\ 0 & 0 & 0 \end{pmatrix}^2 b_{L_1L_2L_3}, \tag{5.22}$$

with corresponding variance dominated by the disconnected six-point function

$$\sigma^2_{S_3} \simeq \frac{6}{4\pi} \sum_{L_1L_2L_3}^{L_{\rm max}} \frac{(2L_1+1)(2L_2+1)(2L_3+1)}{(4\pi)^2} \begin{pmatrix} L_1 & L_2 & L_3 \\ 0 & 0 & 0 \end{pmatrix}^2 C_{L_1} C_{L_2} C_{L_3}. \tag{5.23}$$

In particular, the skewness of the Born-approximated convergence, κ^F, obtained from the first-order magnification matrix, provides a measurement of the LSS-induced bispectrum. The bispectrum

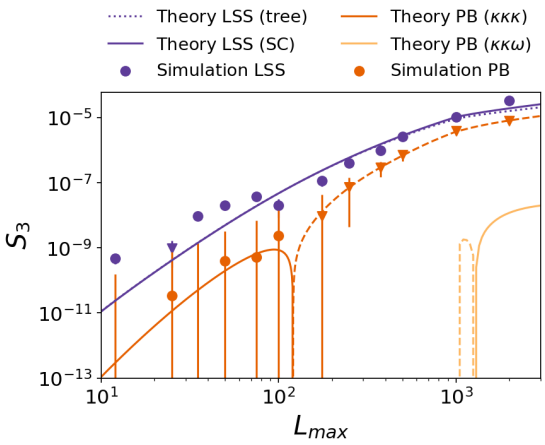

Figure 5.1: Comparison of the skewness for different cutoff values of the convergence multipoles. The theory curves are computed using the tree-level expression of the LSS convergence bispectrum including the Scoccimarro & Couchman fit of [326], as well as post-Born corrections of the $b^{\kappa\kappa\kappa}$ and $b^{\kappa\kappa\omega(+)}$ bispectra of [301]. Only the absolute values are shown; negative values are marked by a dashed line or triangular marker.

of the convergence computed using the multiple lens ray tracing algorithm, κ^R, receives a contribution from the LSS-induced bispectrum as well as from the post-Born corrections induced bispectrum. The difference of the skewness of κ^R and κ^F gives thus a direct measurement of the collapsed post-Born-induced bispectrum.

We use the formulas presented in [43] and [301] to compute the bispectrum of κ due to LSS nonlinearity (at tree level in density perturbations or adopting the nonlinear fitting formula from [326]) and post-Born effects, respectively. In Fig. 5.1 we show a comparison between the skewness measured in the low-pass-filtered simulations and their expected theoretical value as a function of the maximum multipole cutoff used in the calculations. We find a good agreement between simulation and theoretical expectations for the post-Born bispectrum part, confirming the findings of FCC18 on the level of the lensed CMB B-mode power spectrum. For this observable, the post-Born $\kappa\kappa\kappa$ bispectrum is the dominant correction while the contribution of the curl mode in terms of the $\kappa\kappa\omega$ bispectrum is negligibly small (see also [215]). The LSS skewness agrees well with theoretical expectation on scales $75 \lesssim L_{\rm max} \lesssim 2000$ and starts deviating outside this range, yet still with reasonable agreement. On the largest scales, the discrepancy might be due to the adoption of Limber approximation or by spurious numerical correlations induced by the box size replication during the light-cone construction or simply sample variance of the matter bispectrum. In fact, [314] measured the three-dimensional matter bispectrum from the same N-body simulation used for this work and found an excess of power at low values of $k \lesssim 0.1\,{\rm Mpc}^{-1}h$ for both squeezed and equilateral configurations. These scales contribute significantly to the signal on angular scales $\ell \lesssim 100$ (see e.g. [212]) and could be responsible of the excess of skewness observed when only such scales are included. Although in FCC18 the replication procedure was shown to produce accurate results on the large scales of $C_L^{\kappa\kappa}$ and no significant spurious excess of power was observed, we tested the stability of our results on lensing reconstruction with respect to the minimum multipole employed in the analysis. We found negligible differences when excluding CMB angular scales $\ell \leq 100$.

At angular scales $L_{\rm max} \gtrsim 2000$ we expect to see discrepancies due to the limitation of the fitting formulas used to compute the theoretical expectation as well as theoretical uncertainties in the modeling of the nonlinear matter power spectrum used to compute the theoretical expectation of the skewness. In particular, at $L \approx 2000$, the CMB convergence receives a non-negligible contribution from structures at scales $k \gtrsim 1\,{\rm Mpc}^{-1}h$ [113, 212] and on these angular scales uncertainties on the matter power spectrum are already of the order of 15% [362]. The use of nonlinear fitting formulas improves the agreement with simulation results with respect to the tree-level bispectrum. We note that we do not investigate possible improvement using alternative nonlinear bispectrum fitting formulas, as, for

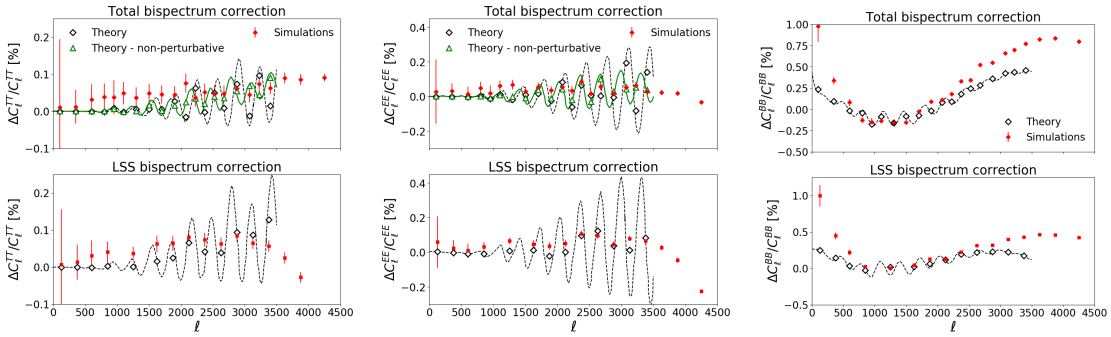

Figure 5.2: Impact of CMB convergence bispectrum on lensed temperature (left), E-mode (middle) and B-mode (right) power spectra. The top panel shows the total correction accounting for the LSS and post-Born induced bispectrum, while the bottom panel shows the correction due to only nonlinear LSS evolution. The theoretical predictions of [215] are shown in black and simulation results in red. The green curves show the values of the nonperturbative corrections computed in [215] for the temperature and E-mode power spectra. Binned theoretical predictions are shown with empty markers. The error bars include only the uncertainty on the average over the Gaussian MC realizations and do not include the sample variance of the convergence bispectrum.

example, the one introduced in Ref. [129]. The validity of these equations at high redshifts was not validated and the differences with respect to the Scoccimarro & Couchman formulas formulas [326] were shown to be marginal and relevant only for a subset of the bispectrum configurations (see discussion in Ref. [301]).

LSS BISPECTRUM EFFECT ON LENSED CMB

Non-Gaussianity in the lensing potential can affect the shape of the lensed CMB power spectra. The authors of Ref. [215] computed the effect on the CMB power spectrum induced by the bispectrum of the CMB convergence due to the nonlinear evolution of matter (hereafter LSS term) and the one due to post-Born corrections (hereafter PB term). FCC18 showed that the corrections computed by Ref. [215] for the PB term match very well the results extracted from ray tracing simulations. As a validation test for this work, we focused on measuring the corrections to lensed CMB power spectra generated by the LSS term alone, as well as those due to the combination of LSS and PB terms. We then compared the results of the simulations with the theoretical prediction of Ref. [215]. To isolate the LSS term, we lens 100 Gaussian realizations of unlensed CMB maps with a deflection field extracted from the κ^F map as performed in FCC18. From the average of the power spectra of these maps we subtract the average power spectrum of the 100 CMB realizations that were lensed with a deflection field computed from a Gaussian realization of the lensing convergence κ^G with power spectrum $C_L^{\kappa^F\kappa^F}$. Similarly, to measure the total correction, we repeat the same procedure with κ^R and $C_L^{\kappa^R\kappa^R}$ to produce the Gaussian realizations of the deflection field. In Fig. 5.2 we show the results of this analysis together with a comparison with the prediction of Ref. [215].

The theoretical predictions for both the total and LSS bispectrum (which is the dominant term) agree quite well with the simulation results on the relevant angular scales, especially the ones implementing the nonperturbative formalism for the TT and EE power spectrum as discussed in PL16 and FCC18. This approach accounts for the fact that even in the Gaussian approximation lensing is a $\mathcal{O}(1)$ effect at small scales and therefore treating the corrections due to non-Gaussianity as perturbations around an unlensed field leads to inaccurate results.

Despite the overall good agreement, some differences can be observed. This is expected because, unlike the analytical approximations, simulations include the effects of non-Gaussianity nonperturbatively and the exact shape of the correction depends on the detailed shape of the bispectrum. In particular, simulation results show an excess of power on the B-mode power spectrum compared to analytical predictions. This is consistent since B-modes are more sensitive to small-scale lenses [115] and thus non-Gaussianities due to strongly nonlinear density fields are expected to give larger corrections where the perturbative expansion becomes less accurate. The discrepancies at scales $\ell \lesssim 100$ could conversely arise due to the excess of skewness discussed in the previous section, although we stress that a larger skewness does not seem to affect significantly the temperature and E-mode power spectrum, where the corrections are dominated by structures at $\ell \lesssim 300$. We further expect discrepancies at large scales due to the use of the Limber and flat-sky approximations in the theory computations. Nevertheless, we decide to perform dedicated robustness tests in the following section to assess the impact of this discrepancy as a potential systematic effect.

5.3 RESULTS

5.3.1 NUMERICAL SETUP

To measure the $N_L^{(3/2)}$ bias, we produce several sets of lensed CMB maps using the LensPix code[49]. These are later combined in different ways to isolate different contributions to this bias and to perform consistency and robustness tests. A subset of these simulations is briefly described in Sec. 5.2.4, and here we review the procedure in more detail.

First, we simulate 100 Gaussian realizations of the primordial CMB. Each of these simulations is then lensed using seven different simulated deflection fields

$$\boldsymbol{\alpha}^{\rm eff} = \nabla\phi + \nabla \times \Omega$$

and adopting the effective remapping for the CMB photons as in Eq. (5.6). The ϕ and Ω potentials are obtained from the κ and ω field of FCC18 using the consistency relations in Eqs. (5.4) and (5.7) in the harmonic domain. For this operation as well as in the synthesis of the unlensed CMB, we adopted a bandlimit parameter $\ell_{\rm max} = 6200$. According to the findings of [115], this setup allows us to recover the lensed CMB power spectrum with a precision of $\mathcal{O}(10^{-3})$ on scales $\ell \lesssim 4000$ and $\mathcal{O}(10^{-2})$ at $\ell \approx 5000$. The full set of deflection fields used to lens the CMB are therefore as follows:

- κ^G. A Gaussian realization of convergence with power spectrum $C_L^{\kappa^F\kappa^F}$.
- $\pm\kappa^F$. These simulations measure the bias including only the effects of the nonlinear LSS evolution.
- $\pm\kappa^R$ alone. These simulations measure the bias due to LSS nonlinearity and PB effects in the convergence field.
- $\pm\kappa^R$ and $\pm\omega^R$ ($\pm\kappa^{R\omega}$ hereafter). They include the full set of nonlinearity of LSS and PB corrections, including the so-called mixed bispectrum correlations $\kappa\kappa\omega$ and $\kappa\omega\omega$ (we refer the reader to [301, 113] for further discussion).

[49] We found consistent results when analyzing maps simulated with the LenS^{2}HAT code [115] which implements a different interpolation scheme to resample the unlensed CMB realization at the displaced ray position.

We denote the resulting lensed CMB simulations with a given deflection field by a superscript G, $\pm F$, $\pm R$ or $\pm R\omega$, respectively. For the results described in this paper we use maps having an angular resolution of 52 arcsec in HEALPIX pixelization, corresponding to $N_{\rm side} = 4096$. On each of these sets we run the lensing reconstruction using a quadratic estimator and compare them to extract different sources of biases. Each simulation set is designed to contain a lensing potential with the same mean power spectrum $C_L^{\phi\phi}$[50]. Remaining relative deviations from the fiducial $C_L^{\phi\phi}$ due to post-Born corrections are below 0.2% on the relevant scales considered in this paper. Hence, in the following, we assume $N_L^{(0)}$ and $N_L^{(1)}$ to be equal for all simulations. Under this assumption we can write

$$\begin{aligned} \hat{C}_L^{\phi\phi}[\kappa] &= \frac{1}{2L+1}\sum_M \hat{\phi}^\dagger_{LM}\hat{\phi}_{LM} \\ &\approx C_L^{\phi\phi} + N_L^{(0)} + N_L^{(1)} + N_L^{(3/2)}[\kappa] + \mathcal{O}\left(\phi^4, \Omega^2\right), \end{aligned} \tag{5.24}$$

where only the $N_L^{(3/2)}$ bias depends on the specific statistic of the κ field used to lens a specific simulation. We will test the validity of this assumption in Sec. 5.3.4.

In order to evaluate the bias in a given experimental configuration we add Gaussian noise realizations with corresponding power spectrum $N_\ell = \sigma_n^2 B_\ell^2$, with white noise level, σ_n, and a circular Gaussian beam with FHWM size, θ [192],

$$B_\ell = \exp\left(\ell(\ell+1)\frac{\theta^2}{16\log 2}\right). \tag{5.25}$$

5.3.2 MEASUREMENTS OF $N_L^{(3/2)}$ BIAS IN THE CMB LENSING AUTO-POWER SPECTRUM

To measure the $N_L^{(3/2)}$ biases from the simulations and distinguish the contributions to the biases originating from all the different contributions of the κ bispectrum and correlations involving curl modes ($\kappa\kappa\omega + \kappa\omega\omega$, PB$\omega$ hereafter), we combine the reconstructed CMB lensing potential power spectrum on each set of lensed CMB realizations as follows:

$$\text{LSS} \quad N_L^{(3/2)} = \left\langle \hat{C}_L^{\phi\phi}[\kappa^F] - \hat{C}_L^{\phi\phi}[\kappa^G] \right\rangle_{\text{Lensed CMB}} \tag{5.26}$$

$$\text{PB} \quad N_L^{(3/2)} = \left\langle \hat{C}_L^{\phi\phi}[\kappa^R] - \hat{C}_L^{\phi\phi}[\kappa^F] \right\rangle_{\text{Lensed CMB}} \tag{5.27}$$

$$\text{PB}\omega \quad N_L^{(3/2)} = \left\langle \hat{C}_L^{\phi\phi}[\kappa^{R\omega}] - \hat{C}_L^{\phi\phi}[\kappa^R] \right\rangle_{\text{Lensed CMB}} \tag{5.28}$$

$$\text{Total} \quad N_L^{(3/2)} = \left\langle \hat{C}_L^{\phi\phi}[\kappa^{R\omega}] - \hat{C}_L^{\phi\phi}[\kappa^G] \right\rangle_{\text{Lensed CMB}}, \tag{5.29}$$

where we denote in squared brackets the corresponding set of CMB realizations used in the lensing reconstruction.

[50] $C_L^{\phi\phi}$ extracted from a N-body simulation has a potential bias at small angular scales due to the presence of shot noise due to the finite number of particles in the N-body simulation. According to the estimates of FCC18, the shot noise accounts for roughly 15% of the amplitude of the power spectrum on the maximum multipole relevant for this analysis. Because in the following text we compare simulated quantities, all including the shot-noise term, the impact of the shot-noise term on the results is expected to be highly reduced.

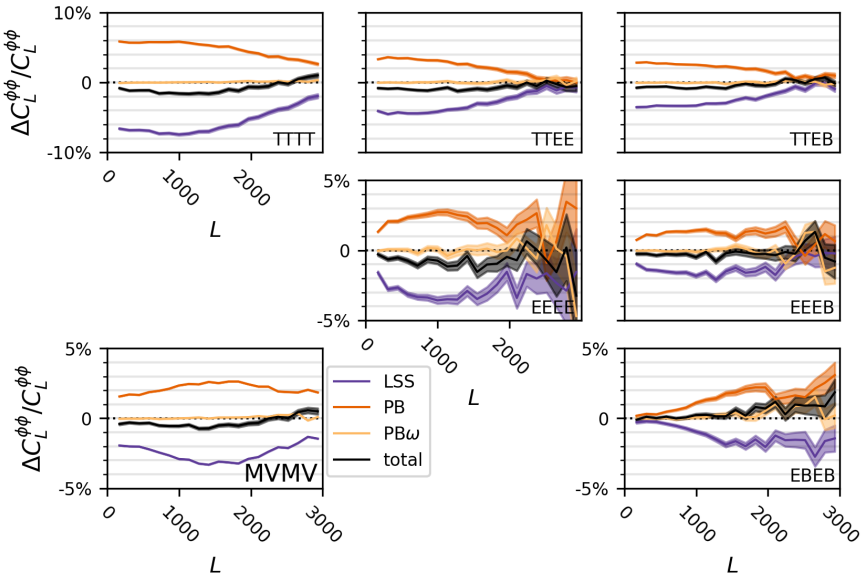

Figure 5.3: Relative biases in the estimated lensing potential power spectrum induced by non-Gaussian statistics of the underlying lensing potential (black curves) as measured in the FCC18 simulations. This case included lensed CMB modes up to $\ell_{\rm max} = 4000$ and CMB-S4-like experimental configuration. We differentiate the effects caused by nonlinearities of large-scale structures (LSS, purple curve), post-Born lensing effects (PB, orange curve) as well as post-Born mixed bispectrum terms (PBω, yellow curve) accounting for higher-order correlation between the lensing gradient and curl potential. The shaded areas show the uncertainty on the bias computed from the dispersion of 100 lensed CMB simulations with a common underlying lensing potential.

We report the measurement of the $N_L^{(3/2)}$ as the average over the 100 lensed CMB simulations at our disposal for each deflection field configuration. The error bars shown in the following figures are computed from the dispersion of the lensed CMB simulations and represent the uncertainty on the mean of the simulations. Due to the fact that the realizations of primordial CMB are the same for all sets of simulations, we avoid realization-dependent biases (up to bispectrum terms) and cosmic variance noise. In the following we discuss the impact of $N_L^{(3/2)}$ bias in terms of the ratio between the bias and the lensing potential power spectrum measured in the FCC18 simulations. The reported signal-to-noise ratio (SNR) is computed as the ratio between $N_L^{(3/2)}$ and the error bar expected for a given experimental configuration

$$\sigma\left(\hat{C}_L^{\phi\phi}\right) \approx \sqrt{\frac{2}{2L+1}\frac{1}{f_{\rm sky}\Delta L}}\left(C_L^{\phi\phi} + N_L^{(0)} + N_L^{(1)}\right), \tag{5.30}$$

where we assume the observed sky fraction to be $f_{\rm sky} = 40\%$, to match the expected sky coverage of CMB-S4, and the bin size $\Delta L \approx 140$. For all configurations the minimal CMB multipole used is $\ell_{\rm min} = 2$.

In Fig. 5.3 we show the total $N_L^{(3/2)}$ bias for the minimum-variance quadratic estimator due to non-Gaussianity in the lensing deflection field, along with the breakdown of the contribution of each source of non-Gaussianity (LSS, PB, and PBω). These results are derived performing lensing reconstruction using a sharp cutoff in harmonic space that removed all the CMB harmonic coefficients having $\ell \geq \ell_{\rm max} = 4000$ and assuming an experiment with 1.4 μK-arcmin white noise in polarization (1 μK-arcmin in temperature) and a 1 arcmin beam size to match CMB-S4 configuration. We find that post-Born effects produce a positive bias in the lensing reconstruction, while LSS effects sup-

press power in the reconstructed potential. This leads to an important cancellation of the two effects and, in fact, the total $N_L^{(3/2)}$ bias becomes a subpercent effect. The amplitude of $N_L^{(3/2)}$, however, changes quite significantly depending on which combination of the quadratic estimator is used for the lensing reconstruction. At low multipoles the individual relative contributions to the biases induced by LSS and PB can reach up to 7% in the autopower spectrum of the TT estimator. Generally, the bias amplitude grows with the number of contributing temperature fields used in the estimator. For polarization-based estimators the overall bias can reach 2% for both LSS and PB terms when considered separately. In our experimental setup, the polarization-based estimators provide the most important contribution to the minimum variance combination below $L \approx 1500$, while for larger multipoles the temperature reconstruction, which is more sensitive to small-scale lenses, starts to dominate in the minimum-variance combination.

The cancellation effect observed between LSS and PB term can be understood noting that post-Born effects tend to reduce significantly the bispectrum amplitude for a large fraction of bispectrum configurations. The post-Born bispectrum has, in fact, mainly negative contributions while the LSS bispectrum due to nonlinearities has strictly positive contributions. This effect and its analytical modeling was discussed first in [301], and FCC18 observed it as a general reduction of the amplitude of higher-order moments on numerical simulations (see also the results in Fig. 5.1). Fig. 5.4 shows the ratio between the CMB convergence bispectrum including post-Born and LSS nonlinear evolution effects and the one including only the latter. The LSS bispectrum is strictly positive, since density perturbations grow faster if they are denser and, hence, large-scale overdensities correlate with small-scale lenses. One can observe a suppression of the bispectrum in the flattened configurations, when $L_1 \approx L_2 + L_3$, while for equilateral configurations, i.e. $L_1 \approx L_2 \approx L_3$, the bispectrum gets enhanced. Simple arguments can be made to understand why there is a sign difference in the bispectrum when all the convergence modes are aligned, i.e. in the flattened limit [301]. In this case lens-lens deflection, i.e. the deflection of a light ray bundle off two consecutive lenses, dominates. In this case, the first lens induces a contraction of the light bundle area. This in turn causes the second lens to have a smaller effect than it would have without the first lens. This results in an anti-correlation between large and small scale convergence modes, leading to a negative sign of the bispectrum in the flattened limit. The positive contributions conversely represent a change in the deflection field along the direction in which the ray is deflected. A ray passing the edge of an overdensity could be deflected towards the center, where the potential gradients are larger. This generates more lensing than if the two contributions had been added independently and a positive correlation between angular scales. The fact that the post-Born and LSS contributions roughly match in amplitude is coincidental and not anymore the case when the source plane is at low redshifts [301].

We note, however, that due to the complex convolution of the bispectrum configurations in the quadratic estimator, the details of the cancellations happening on the $N_L^{(3/2)}$ bias are nontrivial and their analytical modeling for the different combinations of quadratic estimators is challenging. A more detailed discussion can be found in [48, 49]. The important cancellation effects between the LSS and PB terms observed for CMB lensing might not be as effective in the case of lensing of other diffuse background emissions that have a redshift kernel peaking at lower redshift, such as the cosmic infrared background or line intensity mapping data [319]. With a shorter line of sight integration, the relative importance of the post-Born effect is in fact decreased and the LSS term for the $N_L^{(3/2)}$ bias will become the leading one, thus increasing the impact of $N_L^{(3/2)}$ on the reconstructed power spectrum.

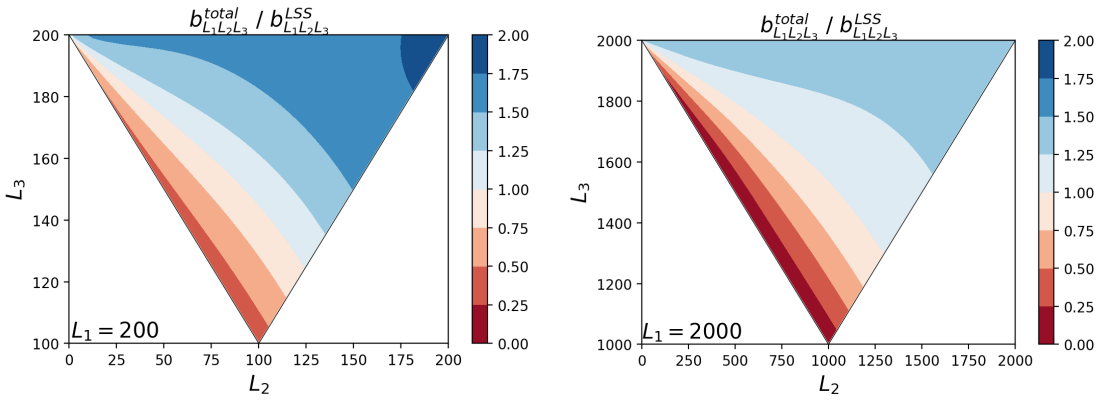

Figure 5.4: The relative change of the convergence bispectrum from large-scale structure nonlinearity (derived using the fitting formula of Ref. [326]) due to post-Born effects, for $L_1 = 200$ and $L_1 = 2000$.

The shape of the $N_L^{(3/2)}$ biases depends not only on the type of reconstruction channel used, but also on the range of multipoles included in the reconstruction. We perform the lensing reconstruction using different cutoff values $\ell_{\rm max}$ for the harmonic coefficient used in the lensing reconstruction and show the value of $N_L^{(3/2)}$ for the minimum-variance estimator for a cosmic-variance limited experiment in Fig. 5.5. Because of the differences with analytical predictions discussed in Sec. 5.2.4, we test the stability of our results with respect to the choice of $\ell_{\rm min}$ and verified that increasing the cutoff to $\ell_{\rm min} = 200$ did not affect our results. As expected, we can observe that the non-Gaussian effects become more prominent when we include progressively smaller angular scales in the lensing reconstruction. For $\ell_{\rm max} = 2000$ the bias is not detectable and its signal-to-noise ratio is smaller than one. In the case of $\ell_{\rm max} = 3000$, at small scales the LSS bias becomes positive, such that the total bias includes positive contributions from LSS and the post-Born gradient and curl fields, which causes the previously detected cancellation to fail. The total bias can therefore reach levels up to 4%, although at multipoles with poor SNR. Including progressively smaller scales causes the LSS terms to increase in amplitude faster than the PB term, and as a result, the cancellation become less effective, causing the $N_L^{(3/2)}$ bias to grow. In this scenario the bias becomes very significant and its SNR could be larger than 10. We warn the reader that such an extreme case serves an illustrative purpose and should be taken with a grain of salt. In fact, the matter distribution on scales $k \geq 2\,{\rm Mpc}^{-1}h$ affects significantly the CMB lensing signal at $\ell \simeq 5000$ and the simulations employed for this work have significant uncertainties on these scales due to the limited resolution of the N-body simulations used to model the deflection field and the absence of baryonic effects. These might become more important when analyzing non-Gaussian effects (see, e.g., [69, 256]). Furthermore, one can observe that the cross-bispectrum contribution from the curl potential dominates at scales $\ell \lesssim 2000$ and gets subsequently downweighted in the reconstruction including larger multipoles.

The changes in the weighting of the CMB harmonic coefficients used in the lensing reconstruction in the presence of experimental noise — even with CMB-S4 sensitivity — reduces the sharp features observed in the results of Fig. 5.5 and the total $N_L^{(3/2)}$ gets suppressed compared to the cosmic-variance limit case. Reducing the cutoff in power for the reconstruction to $\ell_{\rm max} = 3000$ has a net effect of making the bias practically disappearing, despite that the individual LSS and PB effects can be of order of the error bar.

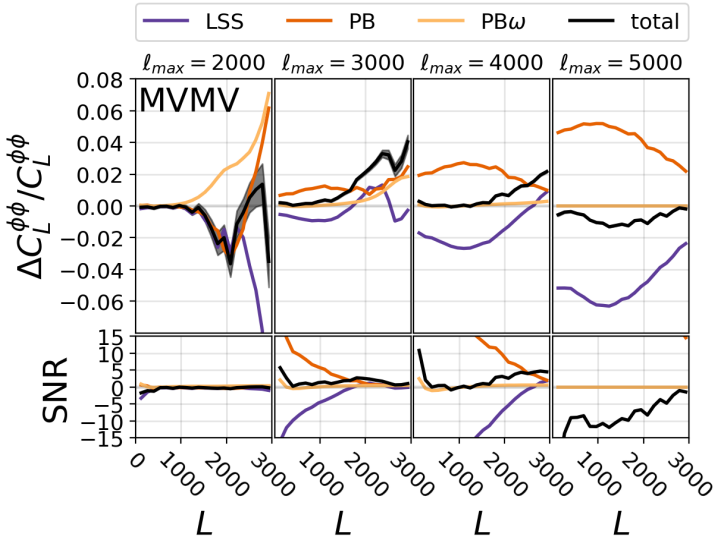

Figure 5.5: Dependence of the $N_L^{(3/2)}$ bias for the minimum-variance lensing estimator on the maximum lensed CMB multipole used in the reconstruction algorithm in the limit of no instrumental noise. The shaded areas show the uncertainty on the bias, computed from the dispersion of the 100 simulations.

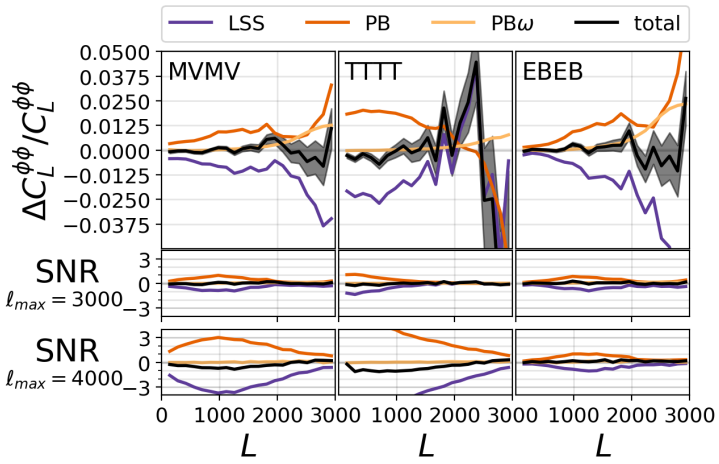

Figure 5.6: The bias in the reconstructed minimum-variance, TTTT and EBEB lensing power spectrum for an instrument with $1.4\ \mu K$-arcmin white noise in polarization, 1 arcmin beam, and including only lensed CMB multipoles up to $\ell_{\rm max} = 3000$ in the reconstruction. For comparison the signal-to-noise ratios of the biases in this case ($\ell_{\rm max} = 3000$) and the case with $\ell_{\rm max} = 4000$ (cf. Fig. 5.3) are shown in the bottom two rows.

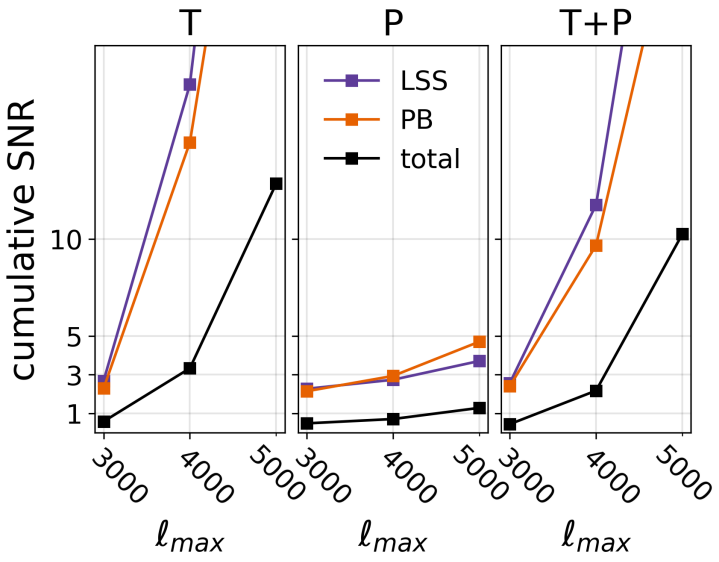

Figure 5.7: Summary of cumulative signal-to-noise ratio of the bias for an instrument with $1.4\ \mu K$-arcmin white noise in polarization, 1 arcmin beam, and different CMB multipole cutoffs $\ell_{\rm max}$, comparing temperature (T), polarization (P), and minimum-variance (T+P) estimators.

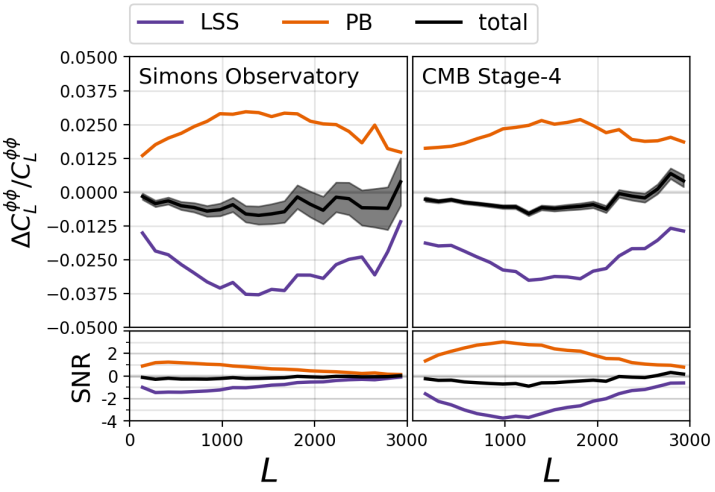

Figure 5.8: Comparison of the $N_L^{(3/2)}$-biases in a lensing potential measurement of Simons Observatory and CMB-S4. Since the former is dominated by the temperature lensing estimation, both are biased on the same level.

In Fig. 5.6 we show a comparison of the SNR obtained using these two cutoffs in CMB multipoles. As can be seen in this figure, we observe a rapid increase in the bias amplitudes between the two cases, in particular in the temperature reconstruction channels. Using polarization-only lensing reconstruction and comparing the results with temperature-only reconstruction can be appropriate tools to identify and potentially mitigate the $N_L^{(3/2)}$ biases. Since the TTTT reconstruction is the most sensitive for the CMB-S4 experimental configurations for $L \gtrsim 1500$, dropping this reconstruction channel has an important effect in terms of the sensitivity of the reconstruction and thus, using a different cutoff in power for the temperature-based and polarization-based reconstruction might be an effective strategy to minimize the effect of $N_L^{(3/2)}$ biases while mitigating the loss of sensitivity. The contamination by unresolved extragalactic foreground residual might in any case prevent the use of multipoles $\ell \gg 3000$ of temperature anisotropies. The significance to measure the bias in the lensing power spectrum, when combining all bins, is summarized in Fig. 5.7 in terms of the cumulative signal-to-noise ratio for different CMB multipole cutoffs.

Fig. 5.8 shows a forecast for Simons Observatory in comparison with CMB-S4. For SO we considered the so-called "goal" N_ℓ observed over 40% of the sky, which is tabulated numerically to include the effects of component separation on the final sensitivity based on an internal linear combination (ILC) of frequencies (called *Standard ILC* in Ref. [386]). Although the CMB sensitivities for the Simons Observatory LAT survey are lower, the level of $N_L^{(3/2)}$-bias is on the same level as for CMB-S4. This is because the SO measurement is dominated by the temperature polarization estimators.

5.3.3 MEASUREMENTS OF $N_L^{(3/2)}$ BIAS IN CROSS-POWER SPECTRA

We measure the effect of the $N_L^{(3/2)}$ in the cross-correlation power spectrum between the reconstructed lensing potential and the input lensing power spectrum. The bias of the cross-spectrum, induced by a nonzero CMB lensing potential bispectrum, is mainly caused by the correlation of the external large-scale structure tracer with the second-order response of the reconstructed lensing potential to the true lensing potential. For the sake of simplicity we limit our analysis to the case of the cross-correlation with a perfect tracer of the CMB lensing potential, i.e., the lensing potential directly extracted from the FCC18 simulations. Since in the cross-correlation case the tracer is almost uncorrelated with CMB fields, there are fewer contractions of the matter field that contribute to the $N_L^{(3/2)}$ bias, and thus we should see a reduction in the amplitude of $N_L^{(3/2)}$ by a factor of roughly 2 with respect to the bias on

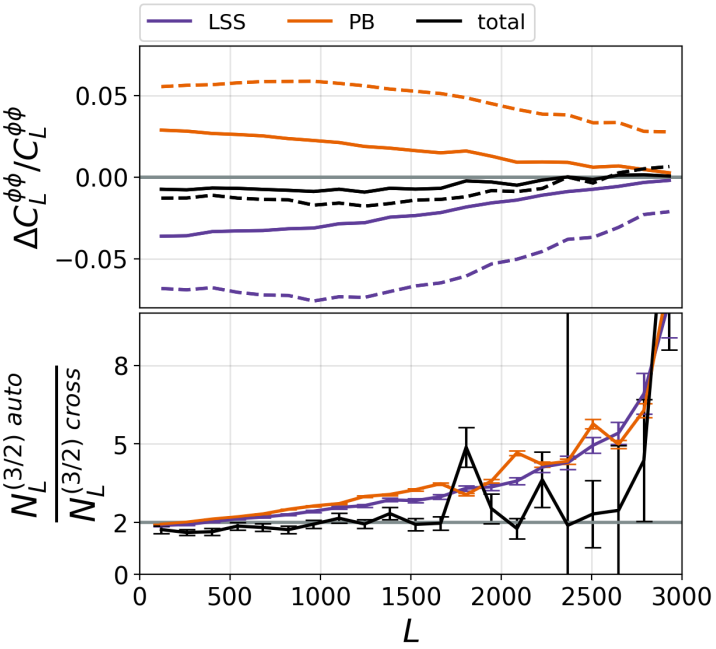

Figure 5.9: Top: $N_L^{(3/2)}$ bias for the reconstructed CMB lensing potential autospectrum (dashed lines) and cross-correlation with the input CMB lensing potential of FCC18 simulations (solid lines) for a CMB-S4 experiment and a cutoff in power $\ell_{\rm max} = 4000$ for the lensing reconstruction with the temperature estimator. Bottom: The ratio of the $N_L^{(3/2)}$ biases for the cross-correlation and autopower spectrum compared with the leading order predictions of [48] (dashed black lines).

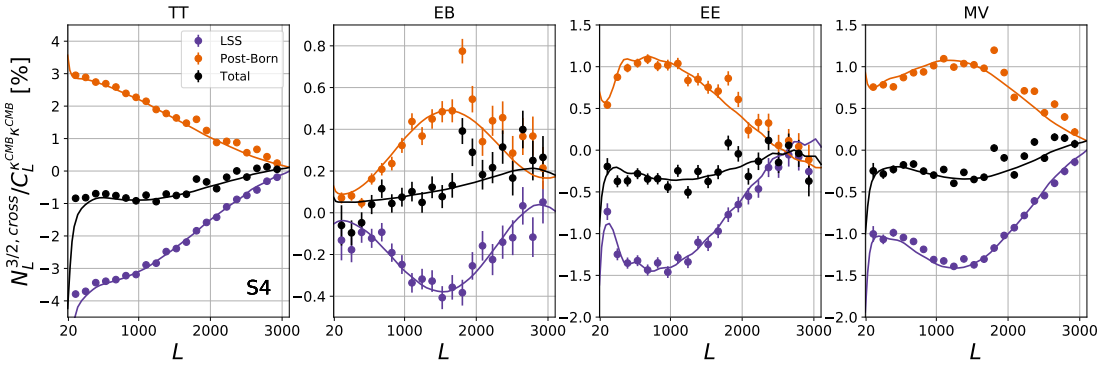

Figure 5.10: Fractional $N_L^{(3/2)}$ bias in the cross-correlation power spectrum between the reconstructed CMB lensing potential and the true one measured from simulation for CMB-S4. Theoretical predictions based on results of Ref. [114] and matter bispectrum fitting formulas of [129] are shown as solid lines while binned simulation measurements are shown as dots. Different contributions to the $N_L^{(3/2)}$ signal are shown.

the autospectrum, in particular for the TTTT estimator [48]. We verify that this prediction holds, as we show in Fig. 5.9. A similar level of suppression is observed also for other estimators and, in particular, for EBEB we saw a reduction of more than a factor of 4 for $L \gtrsim 2000$.

This analysis might suggest that cosmological constraints based on cross-correlations of CMB lensing with an external tracer sufficiently correlated with the CMB lensing potential might be less biased if we cannot account for the $N_L^{(3/2)}$ bias in the autospectrum analysis. However, we stress that due to the distinctive impact of the post-Born term with respect to the LSS one in the case of CMB lensing, the overall variation in amplitude of the bias in cross-correlation might change significantly if a tracer of structures at lower redshift is considered. Nevertheless, these techniques might be affected by other type of biases, such as those due to the galaxy intrinsic alignements in the case of galaxy weak lensing [239, 206, 389]. In addition, the tracers at lower redshift are in fact more sensitive to the non-Gaussianity due to matter nonlinearity and less sensitive to post-Born effects. Therefore we expect to observe an increase in the $N^{3/2}$ bias as the cancellation between LSS and post-Born becomes less effective in this case. In Fig. 5.10 we show the analytical predictions for $N_L^{3/2}$-biases compared to simulations. The agreement between the theoretical prediction and simulations is very good for all the reconstruction channels.

Figs. 5.11 (lensing correlation) and 5.12 (density cross-correlation) show the comparison between the theoretical predictions of $N_L^{(3/2)}$ discussed in Ref. [114] with simulation results for CMB-S4 using the various different lensing reconstruction estimators. Corresponding relative bias curves for a Simons Observatory-like experimental configuration can be found in Ref. [114]. $N_L^{(3/2)}$ becomes a progressively larger fraction of the signal when using lower redshift tracers of the Universe's matter distribution. In the case of density cross-correlation, the LSS contribution to $N_L^{(3/2)}$ increases by factor of 3 going from $z = 2$ to $z = 0.35$. A similar trend, though less pronounced, is observed for the cross-correlation with galaxy lensing. The fractional post-Born bias has weaker variations of the order of $\lesssim 50\%$, since the size of the post-Born contribution and the signal itself both scale roughly the same way with path length. The stronger scaling of the LSS density cross-correlation bias can be explained by the fact that post-Born effects are less important at low redshifts, leading to less cancellation between the two terms and a net increase of the total bias. Note that the amplitude of the large-scale $N_L^{(3/2)}$ for galaxy lensing tends to saturate for sources located at $0.35 < z < 0.6$ and gets reduced for the $z = 0.2$ case that mainly traces matter at $z \approx 0.1$, as the sharp decrease in the lensing kernel of CMB lensing overcomes the effect of the increased non-linearities of the LSS. Lensing of galaxies at $z \approx 0.35(0.6)$ mainly probes the matter distribution halfway between the source and the observer. We see the same saturation effect in the cross-correlation with the density at lower redshift with respect to the galaxy lensing case, i.e. $z < 0.35$. As shown in Ref. [114], the largest contribution to the fractional bias on large scales comes from semi-squeezed bispectrum triangles coupling large-scale tracer modes to the small-scale lensing potential modes that enter the small-scale lensed temperature that dominates the large-scale lensing reconstruction.

The level of agreement between theoretical modeling and simulations for the LSS term depends on the uncertainty in the modeling of the non-linear matter bispectrum. There is also cosmic variance because only a single realization of the non-linear matter field from the LSS simulation is available. The model uncertainty for the post-Born theory is lower. Furthermore, our measurement technique suppresses the bulk of the sample variance for this term. Hence, the agreement of the post-Born curves between simulations and theoretical predictions is better, in the worse cases within $\simeq 25\%$. Especially in the case for CMB-S4 the approach adopted for the non-linear modeling is important and can generate differences in amplitude of about 50% in the case of galaxy lensing cross-correlation using the

very small-scale temperature. In this regime, simulation results often lie between theoretical predictions computed with fitting formulas for the non-linear matter bispectrum of Ref. [326] (SC) or of Ref. [129] (GM) and lean towards one or the other approach depending on the redshift bin and on the reconstruction channel. Hence the accuracy of $N_L^{(3/2)}$-bias predictions relies on the accuracy of the bispectrum modeling. At $z \geq 5$ the LSS contribution is strongly suppressed, as structures are mainly in the linear regime[51], so the leading source of bias comes from post-Born effects alone as shown in Fig. 5.13.

As shown in Ref. [114], in the case of Simons Observatory minimum-variance lensing reconstruction cross-correlated with galaxy lensing, the detection significance of $N_L^{(3/2)}$ will always stay below 1σ for redshift bins at $z \lesssim 0.6$, but it would become significant for galaxy lensing at higher redshift, though with a strong dependence on the exact number density of the galaxy population used in the analysis. The detection significance depends on the number density of the galaxy population as well as the bias of the galaxy sample. For $b_1^2 \bar{n}_g = 4$ gal/arcmin^2, we have $\sigma \approx 1$ for all redshift bins at $z < 2$. At CMB-S4 sensitivities and for the same shot noise levels, the effect will be detected at $\approx 4\sigma$ in each redshift bin for cross-correlation with galaxy density at $z \leq 1$. These numbers reduce to $\approx 2\sigma$ in the case of cross-correlation with galaxy lensing, but could quickly rise if a lower shot noise level can be achieved in each redshift bin, in particular at $z \gtrsim 0.6$. For Lyman break galaxies (LBG) at $z \gg 2$ [400] or radio-continuum surveys at $z \geq 5$, $N_L^{(3/2)}$ will be unobservable for EB reconstruction, while the detection significance is enhanced for TT lensing reconstruction, where $N_L^{(3/2)}$ is higher, even in the case of Simons Observatory, where the detection significance is low in each separate redshift bin, the significance of $N_L^{(3/2)}$ in a full combined analysis including multiple redshift bins would quickly increase above 2σ. Moreover, for a full combined analysis including all the tracers in multiple redshift bins, as well as their cross-correlation with CMB lensing, the significance of $N_L^{(3/2)}$ could be substantially larger due to the effective large-scale cosmic-variance cancellation [331, 322].

5.3.4 CONSISTENCY CHECKS

To ensure that the reported biases were not caused by a mismatch in the CMB and lensing potential power spectra and therefore are not residual $N_L^{(0)}$ and $N_L^{(1)}$ biases, we check the consistency of our measurements in the auto-spectrum-case with an alternative method to extract the $N_L^{(3/2)}$ bias. In particular, we compare the spectra

$$\Delta C_L^{\phi\phi,1}[\kappa^X] = \left\langle \hat{C}_L^{\phi\phi}[\kappa^X] - \hat{C}_L^{\phi\phi}[\kappa^G] \right\rangle_{100\ \text{sims}} \tag{5.31}$$

$$\Delta C_L^{\phi\phi,2}[\kappa^X] = \frac{1}{2} \left\langle \hat{C}_L^{\phi\phi}[\kappa^X] - \hat{C}_L^{\phi\phi}[-\kappa^X] \right\rangle_{100\ \text{sims}}, \tag{5.32}$$

where $X \in \{F, R\}$. The averaging in Eq. (5.31) is performed over the 100 realizations of lensed CMB derived with the set of simulations including a Gaussian convergence, and the averaging in Eq. (5.32) is computed over the 100 realizations of lensed CMB lensed with the non-Gaussian convergence κ^X.

[51] We note that in the computation of $N_L^{(3/2)}$ we used the results of the tree-level LSS bispectrum for contributions at $z > 5$.

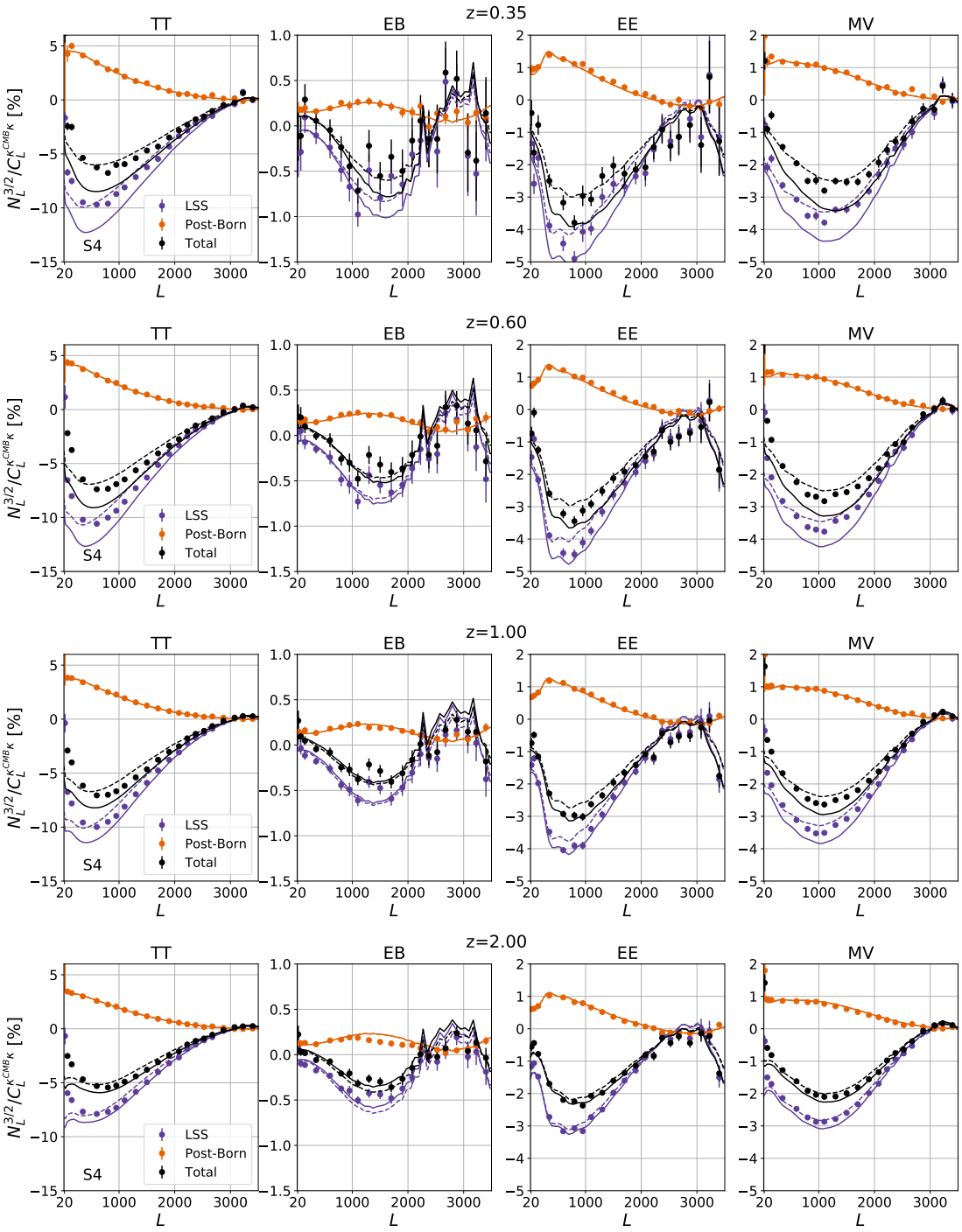

Figure 5.11: This figure shows the fractional $N_L^{(3/2)}$ bias for the cross-correlation power spectrum between the reconstructed CMB lensing potential reconstruction on CMB-S4-like data and galaxy lensing at different redshift bins. The redshift increases moving from top to bottom. Theoretical predictions using GM fitting formulas for the matter bispectrum are shown as solid lines while those based on SC fitting formulas are shown as dashed lines. Different contributions to the $N_L^{(3/2)}$ signal are shown in different colors.

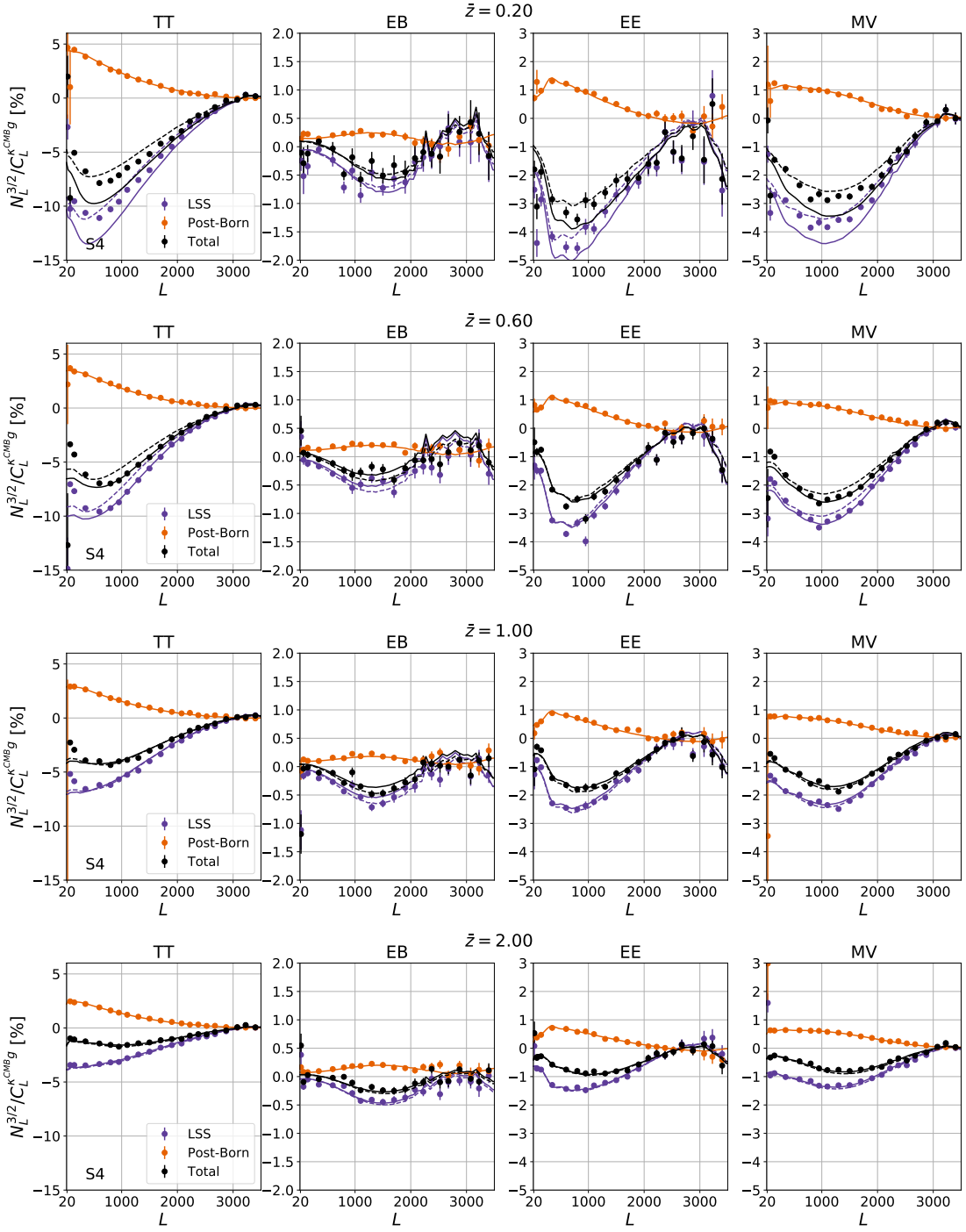

Figure 5.12: Same as Fig. 5.11 but showing cross-correlation power spectra the reconstructed CMB lensing potential and galaxy counts in different redshift bins.

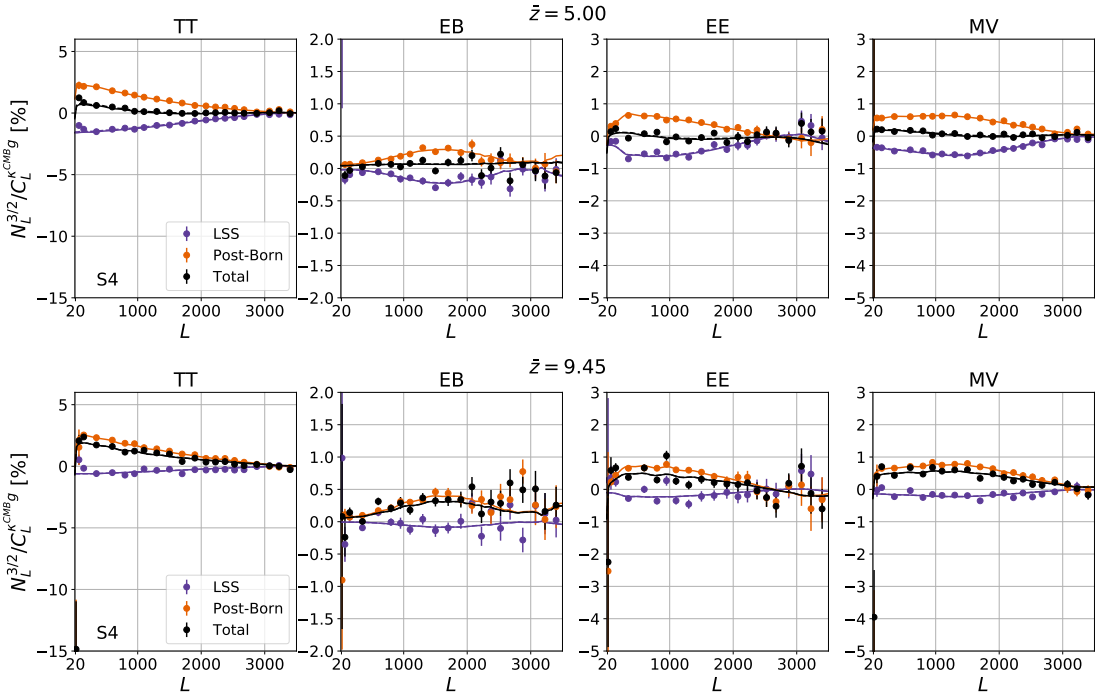

Figure 5.13: Results for CMB-S4 lensing potential correlated with a density tracer, same as Fig. 5.12 but for high-redshift bins. The theoretical predictions model the non-linear matter bispectrum using tree-level prediction for $z > 5$. At these redshifts the structure formation is mainly in the linear regime on relevant scales, so the main source of $N_L^{(3/2)}$ is post-Born effects.

We have that

$$\begin{aligned}\left\langle \hat{C}_L^{\phi\phi}[\kappa^X] \right\rangle \approx & N_L^{(0)}\left[C_\ell^{\mathrm{CMB}}\right] + C_L^{\phi\phi} + \\ & + N_L^{(1)}\left[C_\ell^{\mathrm{CMB}}, C_L^{\phi\phi}\right] + \\ & + \mathrm{sgn}(\kappa^X) N_L^{(3/2)}\left[C_\ell^{\mathrm{CMB}}, C_L^{\phi\phi}, b_{L_1L_2L_3}^{\phi\phi\phi}\right], \end{aligned} \tag{5.33}$$

where we denote in squared brackets the functional dependencies of the biases for clarity. Hence both techniques in Eqs. (5.31) and (5.32) isolate in principle the $N_L^{(3/2)}$ bias. However, a mismatch of $N_L^{(0)}$ and $N_L^{(1)}$ between simulations lensed with κ^F, κ^R and κ^G or correlations at order higher than the bispectrum should manifest themselves in a discrepancy between the two spectra. We constructed null spectra and computed Welch's t-test statistics for both the κ^F and the κ^R sets of simulations to test separately LSS effects alone and LSS and PB together. In both cases we use the spectra from the three most relevant reconstruction channels (TTTT, EBEB, and the autopower spectrum of the minimum-variance estimator (MVMV)) binned in 21 bins within $L \in [30, 3000]$. With this approach we test the hypothesis that the two curves are realizations of a common underlying distribution and quantify the validity of the assumptions used to isolate the biases above. The variances used in the tests are obtained from simulations. We show a subset of the null spectra $\Delta C_L^{\phi\phi,2} - \Delta C_L^{\phi\phi,1}$ in Fig. 5.14. The deviations from zero in the high signal-to-noise regions are subdominant, while small deviations at mostly large multipoles are well within the 1σ error bar. We furthermore obtained global p values by averaging over the bins for each estimator and find no PTE lower than 5%, as summarized in Table 5.2. These results made us conclude that the simulation and reconstruction pipeline up to the lensing power spectrum step are internally consistent, increasing our confidence in the results shown in Sec. 5.3.2.

p-value [%]	LSS	Total
MVMV	13.8	47.2
TTTT	38.9	52.7
TTTE	16.0	17.8
TTEE	87.8	96.0
TTTB	76.3	87.5
TTEB	67.6	99.6
TETE	43.6	47.6
TEEE	5.3	9.2

p-value [%]	LSS	Total
TETB	97.8	86.0
TEEB	83.6	98.9
EEEE	30.5	27.9
EETB	21.7	20.7
EEEB	46.1	49.0
TBTB	45.2	20.4
TBEB	60.1	73.4
EBEB	17.3	51.5

Table 5.2: Global p-values of null spectra of noiseless configuration and $\ell_{\rm max} = 3000$.

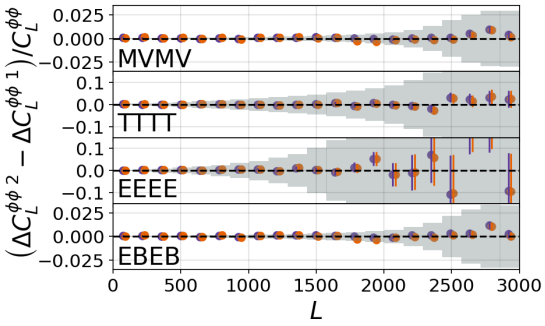

Figure 5.14: The null spectra obtained taking the difference between $\Delta C_L^{\phi\phi,1}$ and $\Delta C_L^{\phi\phi,2}$ as defined in Eqs. (5.31) and (5.32) for the minimum-variance, TTTT, EEEE, and EBEB lensing reconstruction in the limit of no instrumental noise. The reconstructions on κ^F-lensed CMB fields are shown in purple (LSS only contribution), the same with κ^R are shown in orange [LSS and PB (total) contributions]. The error bars show the uncertainties as measured from the scatter in the simulations while the shaded area show the expected statistical uncertainty in the respective bin.

5.4 $N_L^{3/2}$ IMPACT ON COSMOLOGICAL PARAMETER ESTIMATION

Future sensitive measurements of the CMB lensing potential will provide important constraints on cosmological parameters. Therefore a biased reconstruction of the lensing potential power spectrum could affect their estimation. For example, we find that at the high sensitivities envisioned for CMB-S4 measurements the total $N_L^{(3/2)}$ bias could produce deviations of more than 3σ from the fiducial value of 1 when fitting the lensing amplitude parameter $A_{\rm lens}$. In Table 5.3 we show the fitted $A_{\rm lens}$ parameter for different CMB multipole cutoffs obtained by maximizing the simple one-parameter likelihood defined by

$$-2\ln\mathcal{L} = \sum_L (2L+1) f_{\rm sky} \left(\ln\left(\frac{C_L}{D_L}\right) + \frac{D_L}{C_L} - 1 \right), \tag{5.34}$$

where $C_L = A_{\rm lens} \times C_L^{\rm fid.} + N_\ell^{\phi\phi,\rm tot.}$, $D_L = C_L^{\rm fid.} + N_\ell^{\phi\phi,\rm tot.} + N_L^{(3/2)}$, and $N_L^{\phi\phi,\rm tot.} = N_L^{(0)} + N_L^{(1)}$.

Total bias	$\ell_{\rm max} = 3000$	$\ell_{\rm max} = 4000$	$\ell_{\rm max} = 5000$
T	0.997 ± 0.006	$\mathbf{0.988 \pm 0.003}$	$\mathbf{0.973 \pm 0.002}$
P	$\mathbf{1.005 \pm 0.002}$	$\mathbf{1.009 \pm 0.001}$	$\mathbf{1.005 \pm 0.001}$
T+P	$\mathbf{1.004 \pm 0.002}$	$\mathbf{1.004 \pm 0.001}$	$\mathbf{0.992 \pm 0.001}$

Table 5.3: Fitted $A_{\rm lens}$ parameter of the biased reconstructed lensing power spectrum with a fiducial value of $A_{\rm lens} = 1$ for temperature-only (T), polarization-only (P), and minimum variance (T+P) lensing estimators and no noise in the CMB. Cases with significant bias are marked in bold.

Because of the nontrivial scale dependence of the $N_L^{3/2}$ bias, we expand our cosmological parameter estimation study to the exploration of a broader parameter space using Markov chain Monte Carlo (MCMC) techniques. The goal is to quantify the significance of possible biases in parameters like the total neutrino mass, M_ν, or the amplitude of primordial inflationary perturbations, A_s, if $N_L^{3/2}$ is unaccounted for in the power-spectra modeling and cosmological parameters sampling. For this purpose we use the publicly available package MontePython [52] [53, 21] based on the Metropolis-Hastings sampling algorithm. In this analysis we consider the CMB and lensing likelihood for a set of parameters θ given the measured power spectra of CMB temperature, E-modes and lensing potential as Gaussian in the respective fields. Under these assumptions the likelihood function is given by (e.g., [392])

$$-2\log\mathcal{L}(\theta|\hat{\mathbf{C}}) = \sum_\ell (2\ell+1) f_{\rm sky}\left(\ln\frac{|\mathbf{C}_\ell|}{|\hat{\mathbf{C}}_\ell|} + \mathbf{C}_\ell^{-1}\hat{\mathbf{C}}_\ell - 3\right), \tag{5.35}$$

where the covariance matrix for the fiducial model $\hat{\mathbf{C}}_\ell$ and the theoretical signal $\mathbf{C}_\ell$ are constructed as

$$\mathbf{C}_\ell = \begin{pmatrix} C_\ell^{TT}+N_\ell^{TT} & C_\ell^{TE} & C_\ell^{T\phi} \\ C_\ell^{TE} & C_\ell^{EE}+N_\ell^{EE} & 0 \\ C_\ell^{T\phi} & 0 & C_\ell^{\phi\phi}+N_\ell^{\phi\phi,\rm tot.} \end{pmatrix},$$

where $N_\ell^{\rm TT}$ and $N_\ell^{\rm EE}$ are the white noise power spectra for the temperature and the E-modes and $N_\ell^{\phi\phi,\rm tot.} = N_\ell^{(0)} + N_\ell^{(1)}$. All these quantities are computed assuming the fiducial cosmology with CMB-S4 sensitivities and considered to be independent of the cosmological parameters in order to simplify and speed up the sampling. In the evaluation of the fiducial $\hat{\mathbf{C}}_\ell$ we use the biased lensing potential power spectrum, $\tilde{C}_L^{\phi\phi}$, which includes the $N_L^{(3/2)}$ bias measured in the simulations and depends on the cosmological parameters of the fiducial model as

$$\tilde{C}_L^{\phi\phi} \equiv C_L^{\phi\phi}[\theta^{\rm fid.}] + N_L^{(0)} + N_L^{(1)} + \frac{C_L^{\phi\phi}[\theta^{\rm fid.}]}{C_L^{\phi\phi\ \rm sims}} N_L^{(3/2)}. \tag{5.36}$$

This definition allows one to mitigate the impact of the shot-noise term and the difference in the modeling of the nonlinear evolution between the simulation results and the Boltzmann solvers which typically employ the Halofit fitting formulas [362]. This enables us to have a consistent modeling of nonlinearity between the fiducial and the fitted model, reducing the chance to obtain spurious results in the fitting that are driven by the differences in the CMB lensing potential power spectrum modeling. We note, however, that the uncertainties in the modeling of nonlinearity on the CMB lensing power spectrum reach the 10 – 15% level on the scales considered in this work [301, 362] and might become non-negligible. In the construction of the covariance we neglect the ϕE correlation because it is confined at very large angular scales and carries little information on the parameters of interest in our analysis. For the sake of simplicity we do not include the B-mode power spectrum in $\hat{\mathbf{C}}_\ell$ and $\mathbf{C}_\ell$ to avoid the need to model the non-Gaussian covariance between C_ℓ^{BB} and $C_L^{\phi\phi}$ [343]. We note that more optimal formalisms to deal with the non-Gaussian correlations between CMB and lensing power spectra have been discussed in the literature [321, 270, 40]. As the present analysis is intended to quantify biases on cosmological parameters estimation due to mismodeling of the lensing potential bias rather than to provide an accurate forecast of future CMB experiment constraints, the approximations adopted here are not expected to affect our conclusions at the level of accuracy considered in this work.

[52] http://baudren.github.io/montepython.html

$\Omega_b h^2$	0.02225 ± 0.00016
$\Omega_c h^2$	0.1198 ± 0.0015
$\tau_{\text{reio.}}$	0.058 ± 0.012
$\ln 10^{10} A_s$	3.094 ± 0.034
n_s	0.9645 ± 0.0049
$100\theta_s$	1.04077 ± 0.00032
M_ν [meV]	$[0, 300]$

Table 5.4: The cosmological parameters from Planck 2015 [279, 294] together with their 1σ proposal scale or parameter bounds used in the cosmological parameter inference.

In the likelihood construction we assume a fiducial ΛCDM cosmology taken from Planck 2015 results [279, 294] devoid of massive neutrinos, while we allow for a single neutrino to be massive in the parameter fit. We include angular scales $30 \leq \ell \leq 3000$ and assume an observed sky fraction $f_{\text{sky}} = 40\%$ to mimic a CMB-S4-like survey with $1.4\ \mu K$-arcmin white noise in polarization and a 1 arcmin beam size in the likelihood. We summarize the values of our fiducial cosmology as well as the details of the priors adopted for the cosmological parameters sampled in our analysis in Table 5.4.

We neglect the effects of the LSS non-Gaussianity and post-Born corrections on the lensed CMB TT and EE power spectra since the cumulative signal-to-noise ratio for these corrections is below the detection thresholds even for CMB-S4 sensitivity. In Fig. 5.15 we show the 2D posteriors obtained for the parameter combinations of $\Omega_c h^2$, $\ln\left(10^{10} A_s\right)$, and M_ν for the minimum-variance lensing estimator and CMB-S4 sensitivity. The figure shows an example of the main biases in the parameter estimation induced by different sources (LSS, PB, total) of unaccounted $N_L^{(3/2)}$ bias. Similar to what was observed in Sec.5.3.2, the compensating effect between the LSS and PB biases observed at the level of the lensing power spectrum is also visible in the cosmological parameter estimation, where we find a cancellation of the parameter biases when both these terms are included. Each source of $N_L^{(3/2)}$ bias might considerably affect the estimation of the cosmological parameters when considered alone at the level of CMB-S4 sensitivity. Assuming we can model these biases analytically we need to include both the terms in the modeling as the inclusion of only one of the LSS or PB term would lead to an overcorrection of the effect. This is clearly visible in the case the LSS-induced $N_L^{(3/2)}$ for A_s and M_ν, where the large negative bias over a large range of scales in the power spectrum causes a significant false detection of a 169^{+50}_{-30} meV neutrino mass. The cancellation due to post-Born corrections mitigates this bias, reducing it to 83^{+40}_{-50}, what is still compatible with zero neutrino mass, but only at the 2σ-level.

The same analysis carried out adding only the $N_L^{(3/2)}$ biases of polarization-based estimators indicates that using these reconstruction channels leads to more robust constraints on cosmological parameters, even when including the smaller angular scales in the lensing reconstruction. In Tab. 5.5 and Fig. 5.16 we show the best-fit values and marginalized posteriors obtained including the total $N_L^{(3/2)}$ computed varying the CMB multipole cutoff used in the reconstruction for the two different cases including and excluding temperature data when forming the minimum-variance estimator. Including multipoles up to $\ell = 5000$ in the reconstruction leads to a neutrino mass bias larger than 1σ, even after excluding temperature data. Nevertheless, on the level of the parameter estimation we can observe that the polarization lensing estimator is more robust to these kinds of biases, which can be attributed in part to the slightly worse reconstruction lensing noise when excluding small-scale temperature data and in part to the smaller amplitude of the $N_L^{(3/2)}$ bias for polarization estimators.

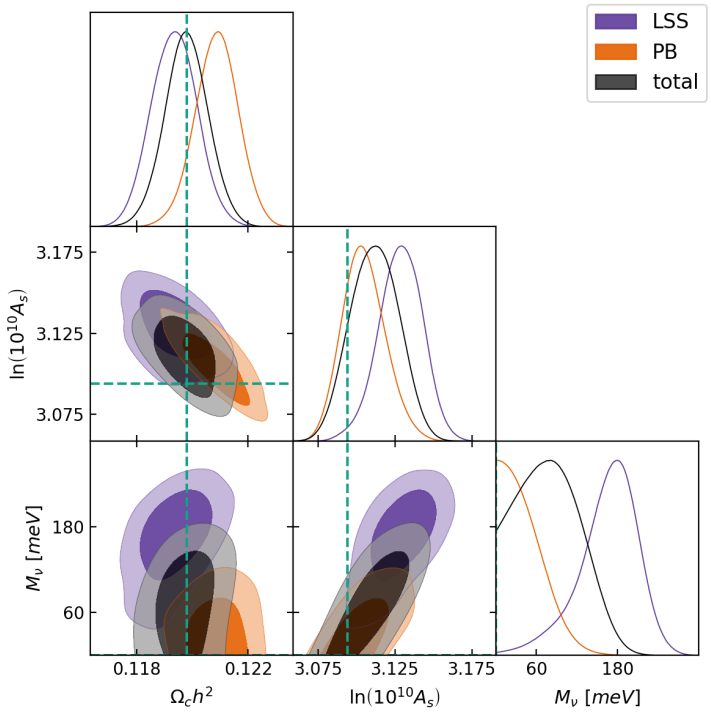

Figure 5.15: The 2D posteriors for the cold dark matter density, $\Omega_c h^2$, the amplitude of primordial inflationary perturbations, A_s and the neutrino mass, M_ν, including biases from LSS nonlinearities and post-Born effect in $\hat{C}_L^{\phi\phi}$, reconstructed using the minimum variance estimator, CMB modes up to $\ell_{\rm max} = 4000$ and CMB-S4 experimental specifications. The posteriors showing biases, comparing with the fiducial values in the green dashed lines. No massive neutrinos were assumed in the simulations, $M_\nu = 0$.

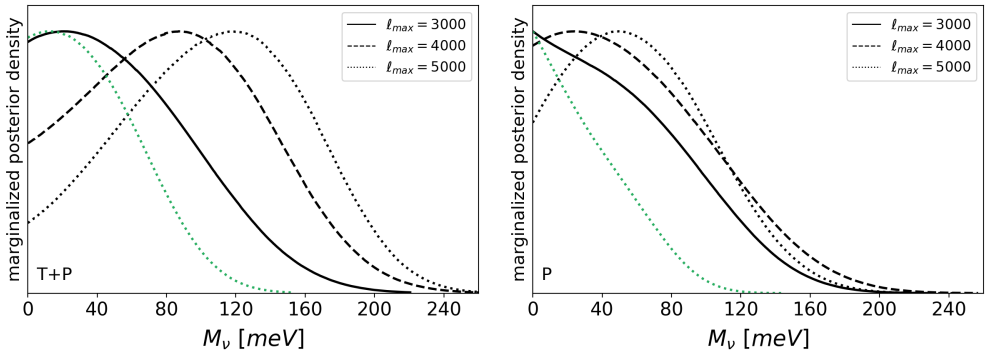

Figure 5.16: The one-dimensional posteriors for the total neutrino mass M_ν for different CMB multipole cutoffs used in the lensing reconstruction. $\ell_{\rm max} = 3000$ case is shown as a solid line, while $\ell_{\rm max} = 4000$ and $\ell_{\rm max} = 5000$ are shown as dashed and dotted lines, respectively. The left figure shows the results obtained including all reconstruction estimators including temperature (T+P), while the right figure uses only polarization-based estimators (P). Each figure also includes the posterior after including a prior using DESI BAO data [18] in the sampling in green, for the most extreme case of $\ell_{\rm max} = 5000$.

		$\ell_{\rm max} = 3000$		$\ell_{\rm max} = 4000$		$\ell_{\rm max} = 5000$		$\ell_{\rm max} = 5000$+DESI	
		Bias	1σ (stat.)	Bias	1σ (stat.)	Bias	1σ (stat.)	Bias	1σ (stat.)
T+P	$\Omega_c h^2 \times 10^5$	25	85	14	88	-45	85	-66	55
	$\tau_{\rm reio.} \times 10^3$	5	9	9	8	14	9	9	10
	$\ln\left(10^{10} A_s\right) 10^3$	11	15	18	18	27	16	16	14
	M_ν [meV]	0	79	90	60	110	50	0	55
P	$\Omega_c h^2 \times 10^5$	16	84	26	82	25	80	-37	56
	$\tau_{\rm reio.} \times 10^3$	6	9	7	10	7	9	8	9
	$\ln\left(10^{10} A_s\right) 10^3$	12	16	13	16	14	15	15	16
	M_ν [meV]	0	75	0	84	65	60	0	44

Table 5.5: This table shows the deviation of the best-fit from the fiducial values (bias) and 68% confidence level (1σ) uncertainties for the cold dark matter density, $\Omega_c h^2$, the optical depth to reionization, $\tau_{\rm reio.}$, the amplitude of primordial inflationary perturbations, A_s and the neutrino mass M_ν. A configuration with $1.4\,\mu K$-arcmin white noise and 1 arcmin beam with different CMB multipole cutoff and estimator combinations was used. We show biases using minimum-variance lensing reconstruction including CMB temperature (T+P) and using polarization only (P). Upper limits are given in terms of 95% confidence level.

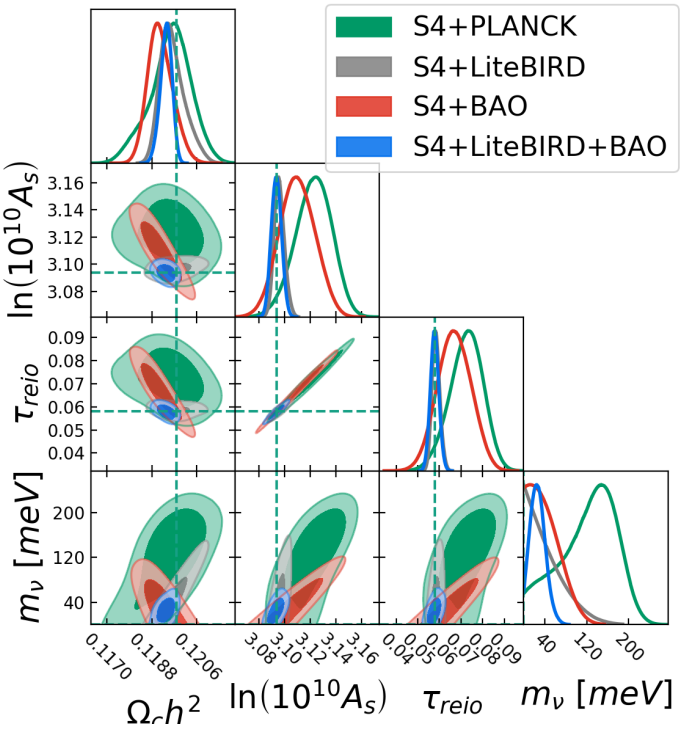

Figure 5.17: The parameter estimation for the most extreme case of $\ell_{\rm max} = 5000$, including measurements from Planck, LiteBIRD, BAOs and PIXIE. The inclusion of LiteBIRD and PIXIE provide a cosmic-variance limited measurement of $\tau_{\rm reio.}$, which largely ameliorates the bias on M_ν.

		$\ell_{\rm max} = 3000$		$\ell_{\rm max} = 4000$		$\ell_{\rm max} = 5000$		$\ell_{\rm max} = 5000$+DESI	
		Bias	1σ (stat.)	Bias	1σ (stat.)	Bias	1σ (stat.)	Bias	1σ (stat.)
T+P	$\Omega_c h^2 \times 10^5$	7	76	-7	81	-36	81	-55	50
	$\tau_{\rm reio.} \times 10^3$	1	9	3	9	9	8	1	6
	$\ln\left(10^{10} A_s\right) 10^3$	3	15	6	16	16	14	0	11
	M_ν [meV]	< 94		25	40	67	40	-19	20
P	$\Omega_c h^2 \times 10^5$	17	76	8	77	17	75	-41	53
	$\tau_{\rm reio.} \times 10^3$	1	8	1	8	1	8	1	7
	$\ln\left(10^{10} A_s\right) 10^3$	3	14	2	15	2	14	0	12
	M_ν [meV]	< 97		< 89		< 86		-23	20

Table 5.6: The same as Tab. 5.5, but for a fiducial value of the total mass of neutrinos of $M_\nu = 60$ meV.

		$\ell_{\rm max} = 3000$		$\ell_{\rm max} = 4000$		$\ell_{\rm max} = 5000$	
		Bias	1σ (stat.)	Bias	1σ (stat.)	Bias	1σ (stat.)
T+P	$\Omega_c h^2 \times 10^5$	13	53	8	54	-1	82
	$\ln\left(10^{10} A_s\right) 10^3$	0.3	3.9	0.2	3.8	1.5	4.7
	M_ν [meV]	6	30	4	40	39	50
P	$\Omega_c h^2 \times 10^5$	11	52	11	53	15	49
	$\ln\left(10^{10} A_s\right) 10^3$	0.1	4.5	0.3	4.2	0.2	3.9
	M_ν [meV]	4	30	3	20	1	20

Table 5.7: The same as Tab. 5.5, but for a fiducial total mass of neutrinos of $M_\nu = 60$ meV and a cosmic-variance limited prior on $\tau_{\rm reio.}$ ($\sigma\left(\tau_{\rm reio.}\right) = 0.002$).

We note, however, that the error on the total neutrino mass does not decrease significantly with decreasing noise in the CMB lensing potential power spectrum. This is due to the degeneracy of the total neutrino mass with the A_s parameter and the sensitivity of the constraint on the latter (or, more precisely, on the combination $A_s e^{-2\tau_{\rm reio.}}$). Since we are assuming future data from ground-based CMB-S4 instruments, which are limited to multipoles $\ell \geq 30$, we are not able to push the uncertainty on $\tau_{\rm reio.}$ to the cosmic-variance limit. However, accessing the reionization bump at $\ell \leq 20$ down to cosmic-variance precision could be achieved by proposed (nearly) all-sky polarized CMB surveys like CLASS [397], CORE [392], LiteBIRD [361] or PIXIE [57]. This would provide a tighter constraint on $\tau_{\rm reio.}$ [11], and would lead to the expected decrease in statistical uncertainty with increasing multipole cut-off in the lensing reconstruction. Furthermore, a $N^{(3/2)}$-bias in the lensing potential estimation would bias A_s and $\tau_{\rm reio.}$ high. We observe that being able to include the constraining power of the reionization bump at large-scales would reduce the bias on $\tau_{\rm reio.}$, and consequently significantly reduce the bias on estimate of A_s. The bias in the total neutrino mass, which is correlated with the latter, is consequently ameliorated as well, at the expense of a small total bias on cold-dark matter density, Ω_m, within the 1σ uncertainty, and a negligibly larger χ^2 goodness of fit. This effect can be seen in Fig. 5.17, showing the vanishing of any bias after including a cosmic-variance limited measurement of $\tau_{\rm reio.}$ from the large-scale E-mode power spectrum.

Finally, assuming a weak cosmological dependence of the $N^{3/2/}$-bias, we test for the case of a non-zero fiducial neutrino mass. Consequently, Tab. 5.6 shows the parameter biases derived from the best-fit values obtained from the MCMC posteriors. It shows that the slight increase in parameter error bars while reducing the lensing reconstructing noise as well as the vanishing bias in some cases observed in Tab. 5.5 are artifacts of restricting the total neutrino mass parameter to positive values, while in part fitting a positively biased lensing power spectrum. We show that in this case, even after the inclusion of an extrenal BAO dataset like DESI, biases of the order of the 1σ-error can arise. Tab. 5.7 is listing the biases for the considered values of $\ell_{\rm max}$ in the case of a cosmic-variance-limited measurement of $\tau_{\rm reio.}$, as well as an assumed fiducial total mass of neutrinos of $M_\nu = 60$ meV. Fig. 5.18 shows the

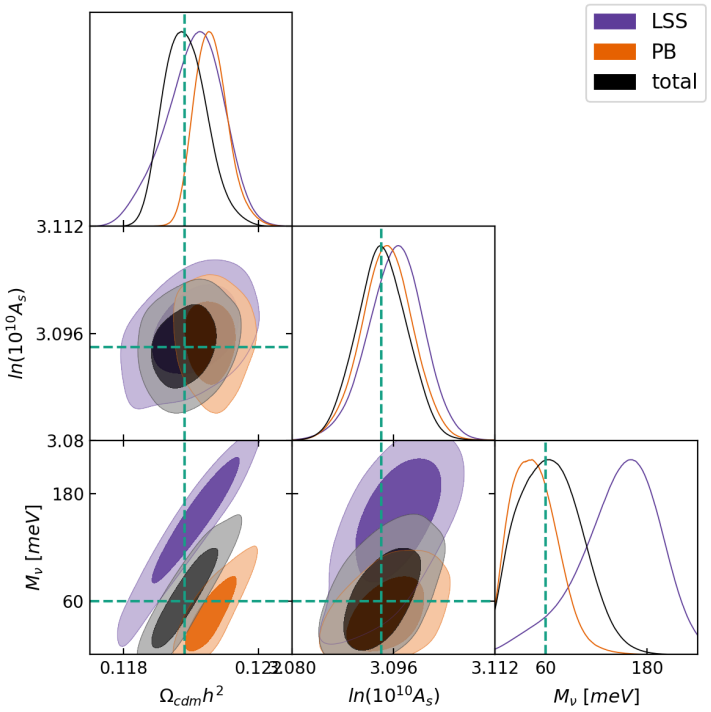

Figure 5.18: The analogue to Fig. 5.15 for a fiducial total mass of neutrinos of $M_\nu = 60$ meV and a cosmic-variance limited prior on $\tau_{\text{reio.}}$ ($\sigma(\tau_{\text{reio.}}) = 0.002$).

two-dimensional posterior densities for the case of $\ell_{\text{max}} = 4000$. Again, a tighter constraint on $\tau_{\text{reio.}}$ can largely mitigate the biases in the neutrino mass estimation.

Also in the case of CMB lensing galaxy counts/lensing cross-correlation, the $N_L^{(3/2)}$ can potentially bias cosmological parameters and galaxy bias measurements. Furthermore it could impact efforts to use cross-correlations to tighten constraints on nuisance parameters describing instrumental systematics and contaminating signals. In the specific case of galaxy lensing measurements, the use of cross-correlations is emerging as standard practice to improve determination of nuisance parameters and minimize the impact of systematics [77, 260, 147]. As a concrete example, we consider the case of intrinsic alignments (IA): in addition to the correlation with observed galaxy shapes due to gravitational lensing, the galaxy shapes can also be intrinsically aligned with the same local tidal field that contributes to the CMB lensing signal [158]. This manifests itself in an additive bias in the CMB lensing convergence cross-correlation spectra estimated from CMB lensing and galaxy shapes [389, 139, 206],

$$\Delta\langle\hat{C}_L^{\kappa_{\text{CMB}}\kappa}\rangle = C_L^{\kappa_{\text{CMB}}I}. \tag{5.37}$$

IA forms a non-zero bispectrum with CMB lensing that gives rise to an additional term to $N_L^{(3/2)}$, but we neglect this effect in this work as it is a small correction to the main signal (see Appendix C.2 of Ref. [114]). $C_L^{\kappa_{\text{CMB}}I}$ can be modelled with the non-linear intrinsic alignment model (NLA) of [52, 206] using the non-linear matter power spectrum in Eq. (1.304) with the free and dimension-less parameter A^{IA}, an amplitude parameter usually constrained from the data through a joint fit with $C_L^{\kappa\kappa}$. As a working example, we derived the bias in the A^{IA} parameter due to misidentification of the $N_L^{3/2}$-bias as intrinsic alignment using the likelihood

$$-2\ln\mathcal{L} = \sum_L \frac{(2L+1)f_{\text{sky}}\left(\hat{C}_L - C_L\right)^2}{\left(C_L^{\kappa_{\text{CMB}}\kappa_{\text{CMB}}} + N_L^{\kappa_{\text{CMB}}\kappa_{\text{CMB}}}\right)\cdot\left(C_L^{\kappa\kappa} + N_L^{\kappa\kappa}\right) + \left(C_L^{\kappa_{\text{CMB}}\kappa}\right)^2} + \text{const.} \tag{5.38}$$

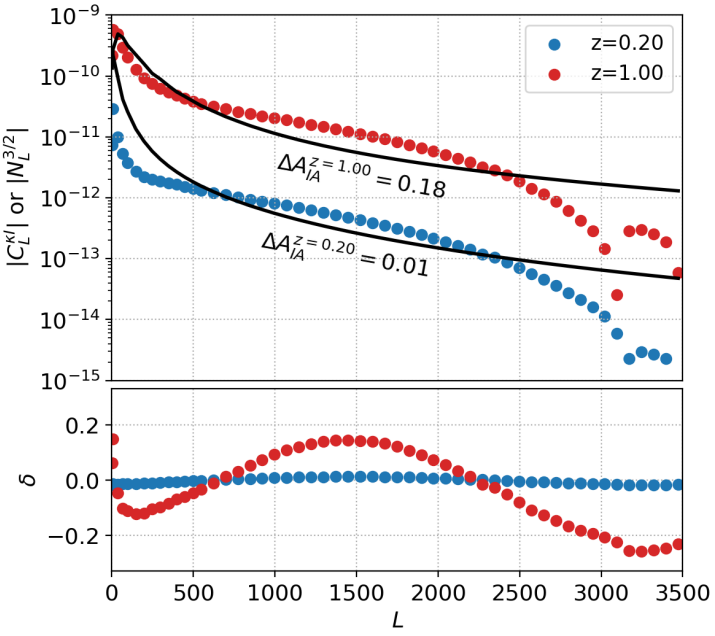

Figure 5.19: Comparison of an intrinsic alignment power spectrum (thick markers) with the $N_L^{3/2}$-bias (thin lines) in cross-correlation for two redshift bins. The intrinsic alignment amplitudes $\Delta A^{\rm IA}$ are the deviations of the best-fit values from the fiducial value $A^{\rm IA} = 1$.

To quantify the importance of modeling of $N_L^{3/2}$, we include it in the measured signal but neglect it in the assumed model, so that[53]

$$\text{Signal:} \qquad \hat{C}_L = C_L^{\kappa_{\rm CMB}\kappa} + C_L^{\kappa_{\rm CMB} I}\big|_{A^{\rm IA}=1} + N_L^{3/2} \tag{5.39}$$

$$\text{Model:} \qquad C_L = C_L^{\kappa_{\rm CMB}\kappa} + C_L^{\kappa_{\rm CMB} I}. \tag{5.40}$$

Fig. 5.19 shows an example of a fitted intrinsic alignment power spectrum to $N_L^{3/2}$ in cross-correlation of CMB lensing with galaxy lensing data in two redshift bins. In Table 5.8 we show the shift $\Delta A^{\rm IA}$ in the best fit values of the intrinsic alignment amplitude $A^{\rm IA}$ induced by $N_L^{(3/2)}$ for CMB-S4 sensitivity and a LSST/Euclid-like survey shot noise. For LSST, assuming the redshift distribution of the so-called golden sample given in Refs. [223, 243], there is a total density of 50 (26) gal/arcmin^2 for galaxy density (lensing). Assuming a uniform distribution of objects over the 10 redshift bins as a baseline analysis (see e.g. [78]), we obtain $\bar{n} \approx 3$ (5) gal/arcmin^2 in each redshift bin. This roughly matches the shot noise expected for Euclid [15]. We therefore take 4 gal/arcmin^2 as an indicative number for the shot-noise in those surveys at each redshift. For this setup we found that $\Delta A^{\rm IA}$ is detected at 2 to 4σ significance when using minimum-variance lensing reconstruction for galaxy convergence at $z \gtrsim 0.6$. Going to higher redshifts, the intrinsic alignment power spectrum decreases more rapidly than the $N_L^{3/2}$-bias, such that the apparent relative bias on the intrinsic alignment parameter increases. For polarization estimators, e.g. EB, $N_L^{(3/2)}$ is too low to be confused with an intrinsic alignment amplitude and thus the overall bias in the minimum-variance is hence driven by the temperature estimator. For SO sensitivity we never detect $\Delta A^{\rm IA}$ even assuming no galaxy survey noise. Recent measurements of intrinsic alignment from DES constrained $A^{\rm IA}$ for different galaxy populations and in different redshift bins between $0.2 < z < 1.3$ [316]. For a mixed sample of early and late type galaxies $A^{\rm IA} \approx 0.5$ and constant in redshift, while using their best-fit model for the redshift evolution of $A^{\rm IA}$ for early-type galaxies $A^{\rm IA} \approx 3$–0.5 for the redshift bins we considered in our analysis. In light of these numbers the $\Delta A^{\rm IA}$ we found could introduce significant errors in the fitting.

[53] As our theoretical predictions do not include any dn/dz we assumed a Gaussian window function centered on a given redshift bin with a width in redshift $\sigma_z = 0.01$. The results are broadly insensitive to this parameter.

$\Delta A^{\rm IA}$	$z = 0.20$	$z = 0.35$	$z = 0.60$	$z = 1.00$	$z = 2.00$
TT	0.02 ± 0.07	0.09 ± 0.07	0.27 ± 0.07	0.57 ± 0.08	1.08 ± 0.11
EB	0.00 ± 0.7	0.00 ± 0.07	0.01 ± 0.07	0.02 ± 0.08	0.05 ± 0.10
MV	0.01 ± 0.06	0.03 ± 0.06	0.10 ± 0.06	0.21 ± 0.07	0.42 ± 0.08

Table 5.8: Values of the bias in terms of galaxy intrinsic alignment amplitude $A^{\rm IA}$ induced by an unmodeled $N_L^{(3/2)}$ assuming S4-like noise in the CMB and 3 gal/arcmin^2 in each redshift bin. The theory expectation including $N_L^{(3/2)}$ is calculated using the SC fit to the non-linear matter bispectrum, neglecting IA contributions to the bispectrum.

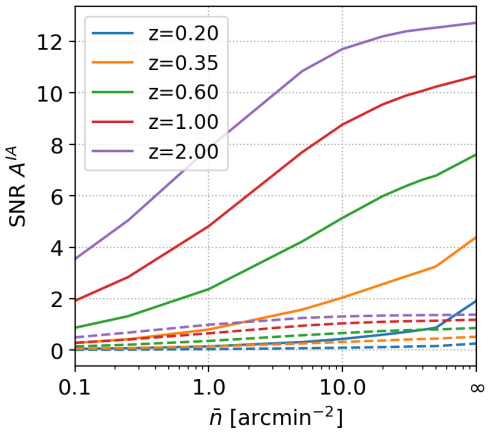

Figure 5.20: Dependence of the significance of the bias in $A^{\rm IA}$ on the galaxy lensing shot noise given in Eq. 1.305. Two configurations used in the CMB reconstruction are shown: CMB-S4-like noise in the solid lines, while SO-like noise is used in the dashed lines.

Fig. 5.20 shows the significance of the bias in $A^{\rm IA}$ depending on the noise of the galaxy survey, determined by the mean galaxy density $\bar{n}$. Although the quantitative details of the detection significance and $A^{\rm IA}$ estimates presented here depend on the choice of redshift bins of the LSS surveys and the approximations assumed, they clearly show that $N_L^{(3/2)}$ cannot be neglected in the data analysis of future experiments and will have to be taken into account. In addition, it will also be mandatory to correctly include post-Born corrections in simulations and analytical models, as neglecting the post-Born contribution would lead to an important misestimation of the size of $N_L^{(3/2)}$. At CMB-S4 sensitivity neglecting post-Born contributions would increase the $N_L^{(3/2)}$ detection significance by 2σ to 4σ for cross-correlation with galaxy lensing, and by 3σ for correlation with galaxy density if small-scale temperature is used. However, at SO sensitivity, neglecting the post-Born contribution to $N_L^{(3/2)}$ seems to be a good-enough approximation for tracers at $z \lesssim 0.6$ since the increase of detection significance would be marginal (less than 0.5σ). Nevertheless, the analytic predictions we developed allow $N_L^{(3/2)}$ to be modeled with sufficient precision. The detection significance of the residual between our theoretical predictions and the simulation measurements is in fact always below 1σ for both S4 and SO, for all the tracers and at all redshifts even assuming a galaxy survey with no shot-noise. As such no statistically significant effect of $N_L^{(3/2)}$ should be observed in a consistent analysis of future experiments. However, in the case where multiple redshift bins are combined using the full covariance for all the tracers, partial cosmic variance cancellation could make the residual more important and would deserve more detailed investigation.

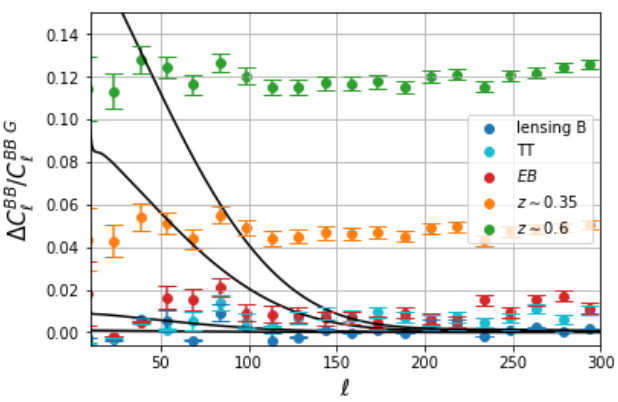

Figure 5.21: The bias on the B-mode power spectrum after delensing, due to post-Born and LSS effects. In dark blue (*lensing B*) the difference between Non-Gaussian and Gaussian lensing simulations B-mode power spectra is shown. Denoted with TT and EB shows the internally delensed B-mode power spectra, using the respective estimators in the reconstruction. B-mode spectra, delensed with external tracers in two redshift bins, are shown in orange and green. The black lines correspond to a primordial gravitational wave signal with r equal to $2 \cdot 10^{-3}, 10^{-3}, 10^{-4}$ and 10^{-5}.

5.5 IMPACT ON THE DELENSED B-MODE POWER SPECTRUM

Similar to the work performed in Ref. [253], we propagate the non-Gaussian lensing simulations to the level of delensed B-mode power spectra in a preliminary analysis. Similar to the analysis above, we look at differences between two sets of simulations, one using a non-Gaussian lensing potential including nonlinear LSS and post-Born effects and the other doesn't. For both cases we compute delensed B-mode power spectra, either by creating a B-mode template using the internally reconstructed lensing potantial or using the convergence map corresponding to galaxy density in a given redshift bin. Delensing with external galaxy density tracers is set to become an important tool to improve tensor-to-scalar ratio constraints in the future [386]. In Fig. 5.21 we show that delensing with a galaxy density measurement at low redshift can bias an tensor-to-scalar ratio estimation on the order of 10^{-3} at $\ell = 80$. The shape of this bias is relatively constant over multipoles relative to C_ℓ^{BB}. Internal delensing on the other hand doesn't show any significant additional bias. Nevertheless, this bias will have to be accounted for in a multi-tracer delensing analysis [338, 405].

5.6 CONCLUSIONS

We investigated the properties of higher-order correlations of the CMB lensing deflection field arising from nonlinear evolution of the matter as well as post-Born corrections, modeled through numerical simulations, and their impact on the CMB lensing potential reconstruction using quadratic estimators ($N_L^{(3/2)}$ bias). We validate the numerical simulations used to model these effects comparing the expected corrections on the lensed CMB power spectrum due to both LSS nonlinearity and post-Born corrections modeled analytically, finding a good agreement. We find that both the matter nonlinearity and post-Born non-Gaussianity cause significant biases of the reconstructed CMB lensing potential power spectrum. However, when these effects are jointly included in the modeling, the amplitude of the total $N_L^{(3/2)}$ bias is greatly reduced both on the CMB lensing autospectrum and in the cross-correlation. This is directly related to the different shape and sign properties of the post-Born bispectrum and the matter bispectrum. The cancellation is more effective in the presence of experimental noise. Despite this fact, we find that the estimation of the $A_{\rm lens}$ parameter from the CMB lensing potential could be biased by more than 3σ for future high-sensitivity experiments like CMB-S4.

The cancellation of $N_L^{(3/2)}$-biases from post-Born lensing and large-scale structure growth becomes redshift-dependent for cross-correlations between CMB lensing and external matter tracers. At lower redshift the post-Born signal decreases due to the decreased path length and the large-scale structure bispectrum grows, so there is relatively less cancellation. However, the fractional bias decreases at very low redshift due to suppression by the CMB lensing window function, so the bias remains relatively

small ($\lesssim 10\%$) for all redshifts, and therefore does not need to be modeled to high precision. However, including both bias-terms, from post-Born and large-scale structure effects, will become important to obtain correct results in future high-precision cosmology measurements. If the effect is modeled via simulations, the simulations should self-consistently include the post-Born lensing effect, otherwise the bias may be overestimated.

We further perform a MCMC analysis to evaluate the impact of the residual $N_L^{(3/2)}$ bias on the estimation of other cosmological parameters at the CMB-S4 sensitivity. We find that the best-fit value of cosmological parameters such as M_ν and A_s could be biased due to the $N_L^{(3/2)}$ bias by up to 2σ, but the significance of these biases greatly depends on the type of quadratic estimator and the maximum multipole used for the lensing reconstruction. Using multipoles $\ell \leq 3000$ for the lensing reconstruction and parameter fitting would not produce any significant bias on cosmological parameters. However the inclusion of smaller angular scales in the lensing reconstruction in order to improve the sensitivity, will also bring the lensing reconstruction in a regime where the details of the cancellation of the post-Born and LSS term becomes trickier and less effective. As a consequence, the total bias due to LSS nonlinearity and post-Born effects, if unaccounted for, becomes more important. In general we find that the CMB temperature-based reconstruction channels are more prone to these biases due to their higher sensitivity to small scale lenses and a lower signal-to-noise ratio. In the small-scale temperature regime, however, foreground contaminations might be the major limiting effects [107, 261, 118]. Various foreground-mitigation techniques [318, 226, 287] can be used in addition to a simple $\ell_{\rm max}$ cut, which means the bias will need to be computed for a particular adopted analysis scheme (see the Appendix of Ref. [114]). Specifically in our cross-correlation analysis we have made a few unrealistic assumptions. This includes not including nonlinear bias effects, intrinsic alignments, and other contributions causing a non-zero bispectrum and need to be accounted for in a realistic scenario.

Using only polarization-based estimators for the lensing reconstruction usually leads to cosmological constraints which are more robust to both the foreground and $N_L^{(3/2)}$ effects. The latter, in particular, is caused by a consistently more effective cancellation of LSS and post-Born effects. As an illustrative case, we perform the cosmological parameter analysis including multipoles up to $\ell = 5000$. In this case we find a shift of the likelihood peak causing a detection of a nonzero neutrino mass at the 2σ level when including all the lensing reconstruction channels. The inclusion of external data sets such as DESI BAO seems to help remove the biases, though 1σ tensions might still remain. Nevertheless, based on the results above, we could expect inconsistencies between the inferred neutrino mass estimates from different data sets, if the $N_L^{(3/2)}$ bias is not accounted for in the parameter estimation for future, high-sensitivity/high-resolution CMB experiments. Finally, we find that the $N_L^{(3/2)}$ bias in the cross-correlation with a perfect tracer of the CMB lensing potential is reduced by a factor of roughly 2 with respect to the bias on the autospectrum, in agreement with the prediction of [48].

We specifically investigated the $N_L^{(3/2)}$ bias in the context of simple quadratic estimators. More optimal estimators, for example iterative maximum-likelihood [159, 66] or Bayesian sampling-based methods [240], are expected to behave differently and future work should determine if bispectrum biases remain as significant. We compared our results on the auto-spectrum $N_L^{(3/2)}$-bias with those of Ref. [49], who performed a similar analysis using a CMB lensing field extracted from different N-body simulations. Despite their N-body simulations differing in resolution and box size, and the simulated sky area used for the lensing reconstruction being smaller than the full-sky results of our work, we find similar conclusions. This suggests that, while some conclusion of this work might still be simulation dependent and more complex physical effects may need to be included in our modeling, the higher-order effects in CMB lensing should be treated carefully in future analyses if the full scientific capacity of a CMB-S4-like observation is to be thoroughly exploited.

A still more glorious dawn awaits
Not a sunrise, but a galaxy rise
A morning filled with 400 billion suns
The rising of the milky way

Carl Sagan, *Cosmos*

6

Assessing Galactic Foreground Impact on CMB Lensing Science

This chapter is based on a publication in preparation [32]. I am the lead author of this work with the objective of assessing the possible systematic biases due to galactic foregrounds on CMB lensing reconstruction as well as CMB B-mode delensing. I have developed a simulation pipeline, which includes the generation of high-resolution, multi-frequency maps of galactic dust and synchrotron and a computation of realistic foreground residuals following a map-level component separation technique, based on xForecast [109, 356, 111]. I have also developed a semi-analytical approach to compute foreground residuals in the context of CMB lensing and estimate biases in the CMB lensing power spectrum and delensed B-mode power spectrum.

In the context of CMB lensing we are interested in understanding the small-scale anisotropies in the CMB. With increasing sensitivity in CMB lensing potential measurements, usual approaches by simulating small-scale galactic foregrounds as Gaussian realizations of an extrapolated power-law from low-resolution Planck maps have become too simplistic. Only with the current onset of multi-frequency, high-sensitivity observations from the ground, we will be able to understand galactic foregrounds from our data beyond the multipole of $\ell \approx 300$, where the polarized dust power spectrum from Planck is signal dominated at high galactic latitudes. Multi-frequency observations and inherent component separation, however, are no fail-safe systems. We know that, given the possible complexity of polarized galactic foregrounds, neither avoiding galactic foregrounds in the survey strategy [289, 199, 200] nor component separation techniques [109, 111] can assure with certainty an unbiased estimate of a primordial gravitational wave signal in the B-mode power spectrum. Since future CMB lensing potential power spectrum measurements will be dominated by measuring the non-Gaussian correlations in the CMB polarization, those measurements, and subsequent parameter estimations, might be biased, even after attempting multi-frequency galactic foreground cleaning. Furthermore, any higher-order correlations in the galactic foregrounds between small- and large-scales might introduce unexpected biases in the delensed B-mode power spectrum and hence bias a tensor-to-scalar ratio measurement. Those higher-order correlations of foregrounds have already been detected in data [179, 88]. In this chapter we start by reviewing the Galactic foreground simulations we use, continue by assessing the component separation performance for the future ground-based CMB experiment CMB-S4 and characterize foreground biases after component separation. Next, we will characterize following biases in the CMB lensing potential and delensed B-mode power spectra, before propagating it to the two major cosmological parameters of interest, r and M_ν.

6.1 HIGH-RESOLUTION GALACTIC FOREGROUNDS

6.1.1 SIMULATING THE GALACTIC MAGNETIC FIELD

To simulate the diffuse polarized emission from galactic dust, the spin orientation of the dust grains has to be taken into account. We have seen in Sec. 1.8.2, that this orientation roughly aligns perpendicularly with the field lines of the galactic magnetic field (GMF). There are several ways proposed in the literature to account for that. All of them rely on some sort of simulation of the three-dimensional GMF, whose structure is then projected on the two-dimensional sphere to be related to the measured I, Q and U Stokes parameters. We use the common decomposition expressing the GMF as the sum of its mean, $\mathbf{B}_0$, and turbulent component, $\mathbf{B}_t$,

$$\mathbf{B} = \mathbf{B}_0 + \mathbf{B}_t. \tag{6.1}$$

Since we are interested in in the contamination to the CMB observed in a small fraction of the sky at high galactic latitudes, we ignore the variation of structures on galaxy-wide scales and hence we assume that $\mathbf{B}_0$ has a fixed orientation, representing the mean orientation of the GMF in the solar neighbourhood.

To simulate the $\mathbf{B}_t$-field one can use simulations of magnetohydrodynamic (MHD) turbulence of the interstellar medium [202]. Ref. [190] were able to produce low-resolution polarized dust maps from MHD simulations for large-scale power spectrum studies. Furthermore, a similar approach lead to simulations of polarized synchrotron emission [395]. An alternative approach is presented in Refs. [293, 393], who propose to statistically model the turbulent component as a Gaussian realization in each component of $\mathbf{B}_t$. It allows for a simple parametrization of effects due to line-of-sight projections of the galactic magnetic field. However, it does not encapsulate the non-Gaussian structure of the turbulent galactic magnetic field component, as seen in MHD simulations [202]. By modeling each component of the turbulent part as a Gaussian field, correlated between line-of-sights, one can accurately reproduce observations from Planck, in particular the correlations in p and ψ maps of thermal dust [393].

Following Refs. [293, 393], one can define a Cartesian coordinate system centered on the observer, where $\hat{\mathbf{e}}_x^T = (1, 0, 0)$ is the unit vector towards the galactic center, $\hat{\mathbf{e}}_y^T = (0, 1, 0)$ pointing towards positive Galactic longitude and $\hat{\mathbf{e}}_z^T = (0, 0, 1)$ pointing towards the Galactic north pole. The direction of the mean component is parametrized by the two parameters, the longitude, l_0, and the latitude, b_0,

$$\hat{\mathbf{B}}_0 = \begin{pmatrix} \cos l_0 \cos b_0 \\ \sin l_0 \cos b_0 \\ \sin b_0 \end{pmatrix}. \tag{6.2}$$

Given the unit vector along the line-of-sight, $\mathbf{n}$, one can project any normalized vector field $\hat{\mathbf{B}}$ on the tangential plane of the sphere, by

$$\hat{\mathbf{B}}_\perp = \hat{\mathbf{B}} - \left(\hat{\mathbf{B}} \cdot \mathbf{n}\right) \mathbf{n}. \tag{6.3}$$

Defining a coordinate system on the tangent space of the unit sphere, one gets the following vectors

in Cartesian coordinates, pointing in north and east directions, respectively,

$$\hat{\mathbf{e}}_n = \frac{(\mathbf{n} \times \hat{\mathbf{e}}_z) \times \mathbf{n}}{|(\mathbf{n} \times \hat{\mathbf{e}}_z) \times \mathbf{n}|}, \tag{6.4}$$

$$\hat{\mathbf{e}}_e = -\frac{\mathbf{n} \times \hat{\mathbf{e}}_n}{|\mathbf{n} \times \hat{\mathbf{e}}_n|}. \tag{6.5}$$

The total vector field of the GMF is then given by

$$\mathbf{B}(\mathbf{n}) = |\mathbf{B}_0(\mathbf{n})| \left(\hat{\mathbf{B}}_0(\mathbf{n}) + f_M \hat{\mathbf{B}}_t(\mathbf{n}) \right), \tag{6.6}$$

where each component of $\mathbf{B}_t$ is a Gaussian realization of a power law

$$C_\ell \sim \ell^{\alpha_M}. \tag{6.7}$$

The relative strength of the turbulent component is defined as $f_M \equiv |\mathbf{B}_t(\mathbf{n})| \,/\, |\mathbf{B}_0(\mathbf{n})|$, which is assumed to be isotropic. The model of the GMF hence comprises of six parameters, l_0, b_0, p_0, N, α_M and f_M.

The Stokes parameters of an optically thin emission at frequency ν are given by Eq. 1.323. Ref. [393] approximates the integrals along the line-of-sight with finite sums over source functions $S_i(\nu) = \overline{n}_d B_\nu(T_d) \overline{C}_{\text{avg}}$ in N layers of dust, resulting in

$$I_\nu(\mathbf{n}) = \sum_{i=1}^{N} S_i(\nu) \left[1 - p_0 \left(\cos^2 \gamma_i - \frac{2}{3} \right) \right] \tag{6.8}$$

$$Q_\nu(\mathbf{n}) = \sum_{i=1}^{N} S_i(\nu) p_0 \cos(2\phi_i) \cos^2 \gamma_i \tag{6.9}$$

$$U_\nu(\mathbf{n}) = \sum_{i=1}^{N} S_i(\nu) p_0 \sin(2\phi_i) \cos^2 \gamma_i. \tag{6.10}$$

To compute the angles ϕ and γ which describe the orientation of the GMF projected on the sphere, we use

$$\phi = \pi - \arccos \left(\frac{\hat{\mathbf{B}}_\perp \cdot \hat{\mathbf{e}}_n}{\left| \hat{\mathbf{B}}_\perp \right|} \right), \tag{6.11}$$

$$\gamma = \arccos \left(\sqrt{1 - \left| \hat{\mathbf{B}} \cdot \mathbf{n} \right|} \right). \tag{6.12}$$

Then, assuming $S_i(\nu)$ is independent of the layer, i, we use the intensity map of dust at a given frequency as a template for $S(\nu)$

$$S(\nu_0) = I_{\nu_0} / \sum_{i=1}^{N} \left[1 - p_0 \left(\cos^2 \gamma_i - \frac{2}{3} \right) \right]. \tag{6.13}$$

Then, a measurement of the galactic dust intensity at high signal-to-noise can be used to compute the Q and U maps with an effective polarization fraction and polarization angle given by the projected three-dimensional GMF simulation. In practice we use the thermal dust intensity template of

l_0	b_0	p_0	α_M	f_M	N
$70°$	$24°$	0.25	-2.5	0.9	4

Table 6.1: The fiducial parameters of the polarized dust emission simulations obtained by fitting simulations to Planck data in Ref. [393].

the PySM[54] [387] package, which uses a realization of the extrapolated power spectrum below scales of $\approx$ 7 arcmin. Possible extensions of this formalism could take into account the galactic magnetic field structure in radial direction along the line-of-sight [233]. In the simulations we neglect the TE as well as EB correlations of galactic dust. A formalism to simulate those is given in Ref. [393]. Furthermore, we naively simulate galactic synchrotron emission in the same way, using the synchrotron emission template in intensity from PySM.

Fig. 6.1 shows the polarized dust Q and U Stokes parameters for six different realizations of the GMF. Also the effective polarization fraction, p (Eq. 1.329), and polarization angle, ϕ_+ (Eq. 1.330), are shown, such that

$$Q = I \times p \times \cos\phi_+ \tag{6.14}$$
$$U = I \times p \times \sin\phi_+, \tag{6.15}$$

given a PySM diffuse dust intensity template, I. Figs. 6.2 and 6.3 show the polarization fraction and polarization angle in comparison with data from Planck. The qualitative agreement, at least statistically, is apparent. Fig.6.4 shows the histogram of polarization fractions obtained from one simulation. For the simulations, the fiducial parameters of Ref. [393] are used. They are summarized in Tab. 6.1.

In Fig. 6.5 the B-mode power spectra of the galactic dust simulations are shown, including their dependence on the four parameters p_0, α_M, f_M and N.

6.2 SKY SIMULATIONS AND METHODS FOR SCIENCE EXTRACTION

The lensing power spectrum can be estimated from maps of the three Stokes parameters of the simulated T, Q and U. We have seen in Sec. 2.5 that for smaller instrumental noise levels, the estimation from CMB temperature data becomes less relevant. This can be a blessing in the sense that foregrounds and other systematic effects are numerous in temperature and consequential temperature-based lensing estimation, a feature that might also stem from the relative ignorance of the polarized CMB signal. For temperature, several contaminants have been identified and treated, like dust and synchrotron emission [116], radio point sources [107, 261], the kinematic Sunyaev-Zeldovich (kSZ) effect [118] and the thermal Sunyaev-Zeldovich (tSZ) effect [226], as well as issues in the common analysis such as the mis-modelling of the underlying lensing deflection as a Gaussian field [33, 49, 114]. For polarization on the other hand, all these effects were found to be less severe or, as in the case of the some galactic components and SZ effects, non existent.

[54] https://github.com/bthorne93/PySM_public

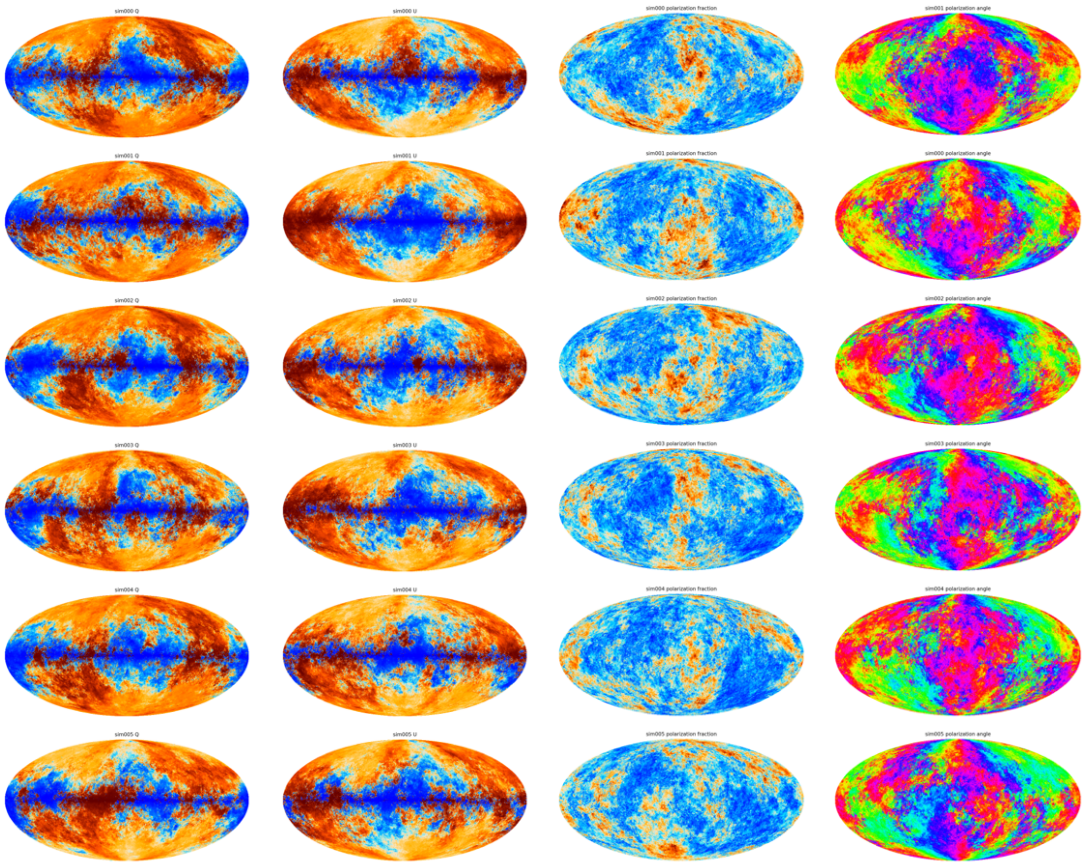

Figure 6.1: Simulated realizations of the thermal dust polarization given the PySM dust intensity map and six different Gaussian realization of the GMF, showing the qualitative statistical properties , terms of, from left to right column, Q, U, p and ϕ_+.

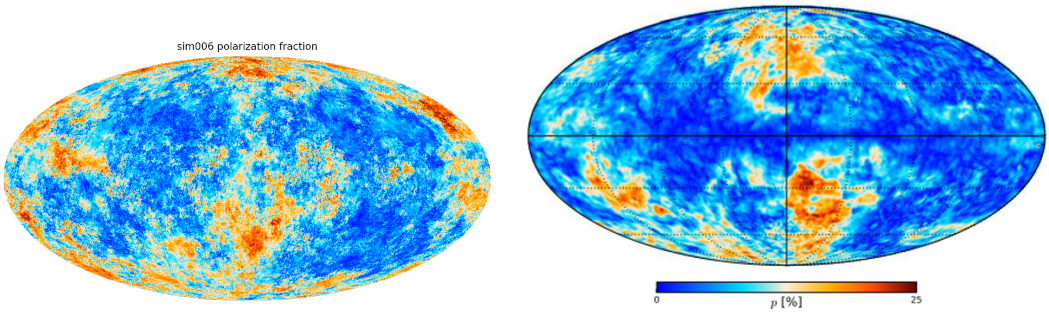

Figure 6.2: Comparing the polarization fraction, p, from one simulation with a random realization of the GMF (left) with the one measured by Planck, produced with the GNILC component separation algorithm (right). The latter is shown at a 80 arcmin resolution. The uncertainty for the GNILC map is everywhere below 3%. The right figure is taken from Ref. [290]. Both maps have the same colorscale.

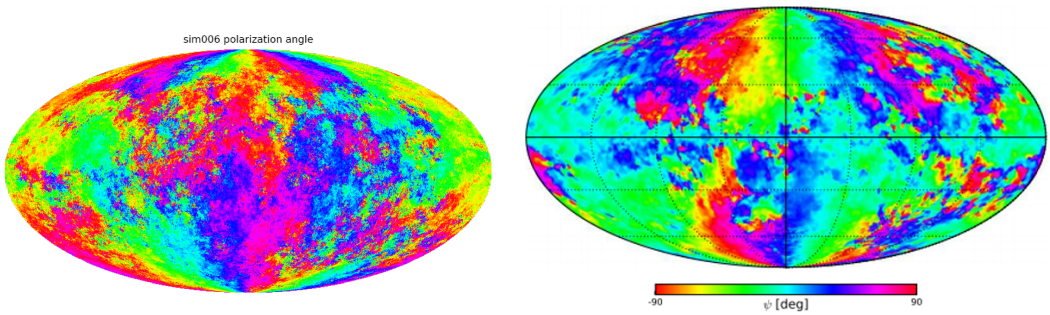

Figure 6.3: Comparing the polarization fraction, ϕ_+, from one simulation with a random realization of the GMF (left) with the the one measured by Planck, produced with the GNILC component separation algorithm (right). The latter is shown at a 80 arcmin resolution. The uncertainty for the GNILC map is everywhere at the sub-degree level. The right figure is taken from Ref. [290]. Both maps have the same colorscale.

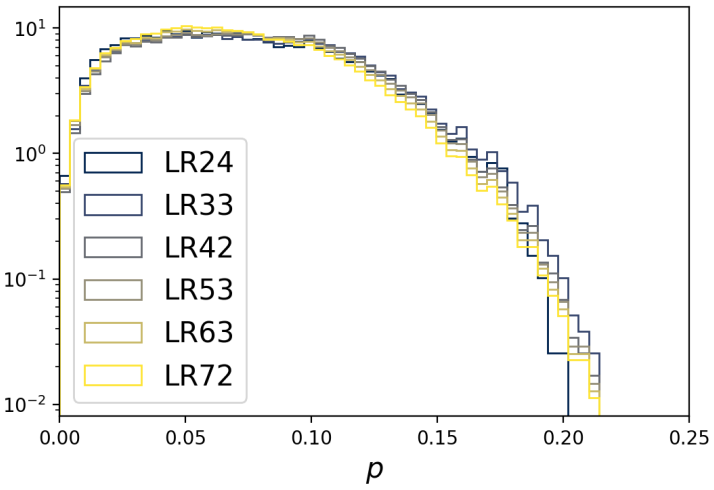

Figure 6.4: The histogram of polarization fraction per pixel for one simulation of polarized dust for different sky fractions. The Planck masks are used here, where the number in the label gives the rough sky fraction in percent.

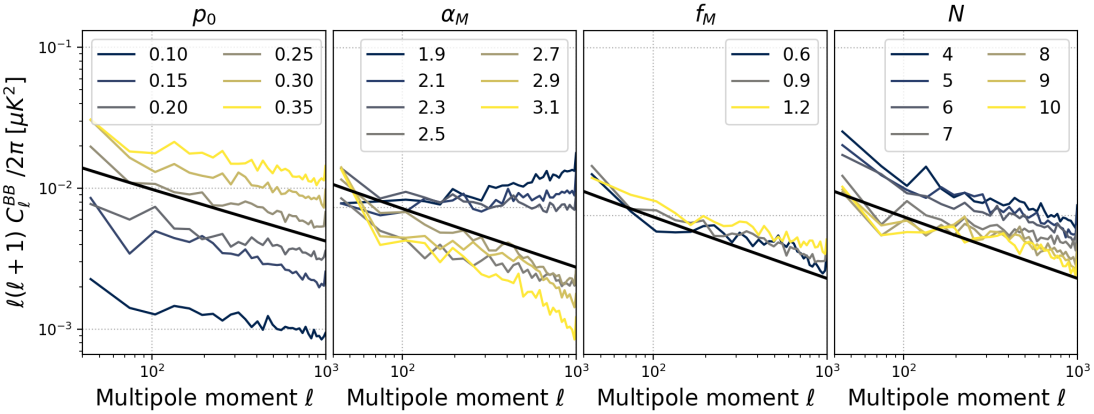

Figure 6.5: The B-mode power spectra from diffuse galactic dust, simulated with the fiducial parameters of Tab. 6.1, varying one of the four parameters at a time. Each of the power spectra is computed from a single GMF realization with X^{2}PURE, on a 5% mask around the southern galactic pole (see following sections).

6.2.1 PYSM FOREGROUND SIMULATIONS

Additional to the foreground simulations of Sec. 6.1.1 we use a second set of simulations based on the polarized dust and synchrotron templates of PySM[55] [387]. For synchrotron these are a combination of the 408 MHz Haslam maps [148, 308] and WMAP 9-year 23 GHz maps [37] smoothed to five degrees. For thermal dust the template is based on the COMMANDER astrophysical component maps of CIB-suppressed polarized galactic dust emission of the Planck 2015 data release (PR2) [278], smoothed to two degrees.

Small scales are added, similar to the processing in [387], by fitting the power spectrum at large-scales with a power-law in ℓ,

$$C_\ell^{EE/BB} = A \left(\frac{\ell}{80} \right)^\alpha , \tag{6.16}$$

and by generating a Gaussian random realization of Q and U Stokes parameters at small-scales, such that the sum of large- and small-scale maps have a power spectrum given by the earlier fitted power-law. The pure, cut-sky power spectra are computed with X^{2}Pure [134] on the patch given by the observing strategy we consider (see below), using an apodization length of 8°.

6.2.2 MULTI-FREQUENCY GALACTIC FOREGROUND SIMULATIONS

The procedure described in the last section results in two sets of templates, including polarized thermal dust emission at $\nu_{\rm dust} = 353$ GHz, $Q^{\rm dust}(\mathbf{n})$ & $U^{\rm dust}(\mathbf{n})$, and polarized synchrotron emission at $\nu_{\rm sync} = 23$ GHz, $Q^{\rm sync}(\mathbf{n})$ & $U^{\rm sync}(\mathbf{n})$. These can be used to simulate frequency maps using PySM and following scaling factors (cf. Sec. 1.8.2)

$$A^{\nu\ \rm dust} = \left(\frac{\nu}{\nu_{\rm dust}} \right)^{\beta_d - 2} \frac{B_\nu(T_d)}{B_{\nu_{\rm dust}}(T_d)} \tag{6.17}$$

$$A^{\nu\ \rm sync} = \left(\frac{\nu}{\nu_{\rm sync}} \right)^{\beta_s} , \tag{6.18}$$

where β_d and β_s are the dust and synchrotron spectral index, T_d the dust temperature and $B_\nu(T_d)$ Planck's law given by

$$B_\nu(T_d) = \frac{2h\nu^3/c^2}{\exp\left(\frac{h\nu}{kT_d}\right) - 1}. \tag{6.19}$$

The (noise-free) data model of an observed Stokes parameter in the direction $\mathbf{n}$ at frequency ν, assuming delta-shaped band-passes, is then given by

$$\tilde{Q}(\mathbf{n}, \nu) = Q^{\rm CMB}(\mathbf{n}) + A^{\nu\ \rm dust}(\mathbf{n}) \times Q^{\rm dust}(\mathbf{n}) + A^{\nu\ \rm sync}(\mathbf{n}) \times Q^{\rm sync}(\mathbf{n}), \tag{6.20}$$

and corresponding expression for U. Here we explicitly allow for the frequency scaling factors to vary over the sky, corresponding to spatially varying spectral indices β_d and β_s [56], a fact established but weakly constrained by observations [289, 200]. In the simulations we either use constant spectral indices or spectral indices maps from Planck's COMMANDER or GNILC pipeline [278, 308] for dust and a combination of Haslam and WMAP maps, provided within PySM [387].

[55] https://github.com/bthorne93/PySM_public

[56] We assume a spatially constant dust temperature throughout this chapter.

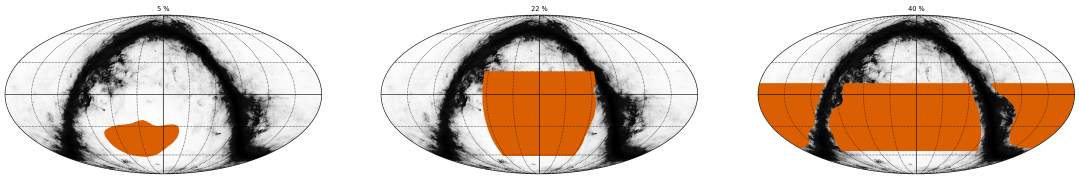

Figure 6.6: The survey footprints used throughout this chapter, spanning 5%, 22% and 40% of the sky, shown in orange shade on a map in celestial coordinates. The galactic dust intensity template of PySM is shown in black.

6.2.3 THE OTHER SKY COMPONENTS

To recap, we model (single-frequency or foreground-cleaned) T, Q and U maps, which contain lensed CMB, $\mathbf{s}$, instrumental noise, $\mathbf{n}$, and an additional galactic foreground component, $\mathbf{f}$

$$\mathbf{d} = \tilde{\mathbf{s}} + \mathbf{n} + \mathbf{f}. \tag{6.21}$$

CMB

For the CMB we generate random realizations of unlensed T, Q and U maps, as well as the lensing potential ϕ from power spectra computed with CAMB according to the Planck 2015 best-fit cosmology of Tab. 1.5 and produce lensed maps with LenS^{2}HAT [115].

NOISE AND OBSERVATION STRATEGY

We assume a CMB-S4-like experimental configuration, populating all available atmospheric windows in the microwave spectrum between 20 and 270 GHz with detectors observing the sky in seven frequency channels. As an observational strategy we investigate a deep, a wide and an ultra-wide survey. The survey footprints are shown in Fig. 6.6. The deep survey spans 5% of the sky at an area, where galactic dust emission is expected to be at its lowest level in the southern galactic hole. It is designed to be used in the delensing study. The wide survey, spanning about 22% of the sky, arises from a realistic scanning strategy for a ground based CMB experiment at Chile (Atacama desert) and corresponds to the *shallow scan* of the S4CMB code[57]. The ultra-wide survey, spanning about 40% of the sky, spans the whole observable sky from the Atacama desert, applying first the 80% galactic mask of Planck[58] and given a minimal observation elevation of 57°[59].

To simulate realistic noise levels we take noise power-spectra computed with the publicly availabe CMB-S4 noise calculator [60]. The white noise levels and Gaussian beam sizes are given in Tab. 4.7. Additional to the large-aperture telescope (LAT) configuration targeting the small-scale CMB we assume a small-aperture telescope (SAT) setup, which is capable of observing atmosphere-free polarized CMB down to multipoles of $\ell = 30$ in the same frequency channels with similar white noise levels to allow for the galactic foregrounds cleaning. This could be achieved from the ground with a continuously-rotating half-wave plate [364]. The upper multipole cut-off used in this study is $\ell = 3000$. In Fig 6.7 we show the corresponding beam-deconvolved noise curves for our SAT and LAT configuration. In the following we denote the noise power spectra with N_ℓ and the harmonic multipoles of its Gaussian realizations with $n_{\ell m}$.

[57] https://github.com/JulienPeloton/s4cmb
[58] https://wiki.cosmos.esa.int/planck-legacy-archive/index.php/Frequency_maps
[59] This is chosen such that the resulting footprint is $f_{\rm sky} = 40\%$.
[60] https://cmb-s4.org/wiki/images/Lat-noise-181002.pdf

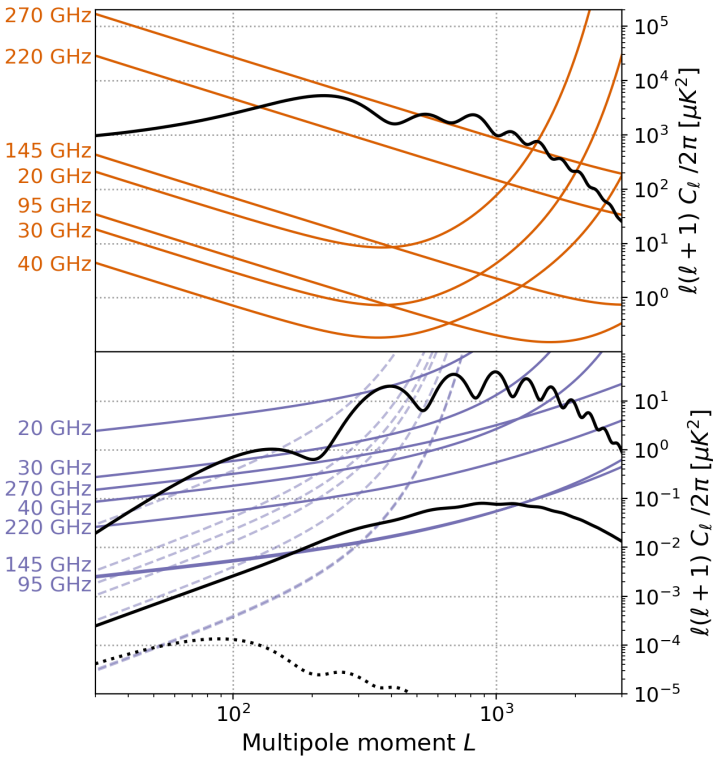

Figure 6.7: The temperature (top) and polarisation (bottom) beam-deconvolved noise power-spectra for each of the seven frequency channels. The dashed lines in the bottom plot are the corresponding noise curves without the atmospheric component at lower resolution, to mimic a small-aperture telescope configuration for delensing. The thick black lines are the fiducial TT, EE and BB power-spectra, in that order from top to bottom. The target, the primordial B-mode power-spectrum corresponding to $r = 10^{-3}$, is shown in the dotted black line.

Since we are interested in systematic biases due to different levels of foreground contamination, we make the simplification to keep the noise the same for each survey footprint. This allows us to isolate the effect from different foreground structures, without the effects changing noise levels will have on the resulting biases. The noise power spectrum curves are calculated assuming $f_{\rm sky} = 22\%$. Hence the noise levels used are rather pessimistic for the deep survey and optimistic for the ultra-wide survey.

6.2.4 FOREGROUND CLEANING

The basis of the foreground cleaning algorithm we use is a maximum-likelihood estimator with parametric foreground modeling, as described in e.g. Refs. [357, 356] and Sec. 3.2. The first step is the maximization of the spectral likelihood resulting in a set of spectral parameters θ, which can be used to build an estimate of the mixing matrix $\hat{\mathbf{A}} = \hat{\mathbf{A}}(\mathbf{x}, \beta)$. If this estimate does not to coincide with the true mixing matrix, $\mathbf{A}(\mathbf{x})$, systematic foreground residuals in the estimated, cleaned CMB map will arise. We have two ways at hand to estimate the resulting bias due to foreground residuals in the B-mode power spectrum. We can either use MC simulations and average over CMB and noise realizations, or we use the semi-analytical approach of Eq. 3.30 given the covariance of the spectral parameters following the maximum-likelihood estimation. The implementation of the maximum-likelihood estimation and residual calculation makes extensive use of the FGBUSTER library[61].

[61] https://github.com/fgbuster/fgbuster

6.2.5 LENSING POTENTIAL RECONSTRUCTION

We follow the formalism laid-out in Chap. 2 to estimate the lensing potential, $\hat{\phi}$, and the associated power spectrum, $\hat{C}_L^{\phi\phi}$, as

$$\hat{C}_L^{\phi\phi} = W_4^{-1} \frac{1}{2L+1} \sum_M \left(\hat{\phi}_{LM} - \hat{\phi}^{\rm MF}_{LM}\right) \left(\hat{\phi}_{LM} - \hat{\phi}^{\rm MF}_{LM}\right)^\dagger - N_L, \tag{6.22}$$

where $W_4 = \int d\mathbf{x}\, m(\mathbf{x})^4$ with the apodized sky mask $m(\mathbf{x})$. The used apodization length is chosen to be 1°. N_L includes the bias terms, in the present case the analytic computations of $N_L^{(0)}$ [258] and $N_L^{(1)}$ [186]. We use MC simulations on the basis of Gaussian realizations of the full power spectrum including CMB, noise and foreground (residuals) to compute the mean-field, $\hat{\phi}^{\rm MF}$.

6.2.6 B-MODE TEMPLATE

We follow the procedure in Sec. 3.3.3 of creating a template of lensing-induced B-modes, that can be used to subtract from the measured, total data to minimally reduce the lensing variance in the final B-mode power spectrum, leaving a residual in the B-mode power spectrum given by

$$C_\ell^{BB\,\text{res.}} = \frac{1}{2\ell+1} \sum_{\ell' L} |f^{EB}_{\ell\ell' L}|^2 \left[C^{EE}_{\ell'} C^{\phi\phi}_L - \frac{\left(C^{EE}_{\ell'}\right)^2}{C^{EE}_{\ell'} + N^{EE}_{\ell'}} \frac{\left(C^{\phi\phi}_L\right)^2}{C^{\phi\phi}_L + N^{\phi\phi}_L} \right]. \tag{6.23}$$

In the case of internal delensing, when $\hat{\phi}$ is a quadratic combination of two CMB fields, extra terms due two four- and six-point correlations.

6.2.7 CMB POWER SPECTRUM ESTIMATION

We use the pure pseudo-cross-spectrum approach to compute polarized CMB (cross-)power spectra of cut-sky CMB maps [342, 134], implemented in the X^{2}Pure code. In the following we will report differences between B-mode power spectra including the same noise realizations.

6.3 FORMAL CHARACTERIZATION OF BIASES IN THE CMB LENSING POWER SPECTRUM ESTIMATION

6.3.1 BIAS IN THE QUADRATIC ESTIMATOR

From Eqs. 6.21, 2.52 and 6.22 we obtain following bias-terms including contribution of the foreground components after averaging over the statistically isotropic components signal and noise, $\tilde{s}_{\ell m} + n_{\ell m}$, (see Appendix C)

$$\left\langle \hat{C}_L^{\phi\phi} \right\rangle = C_L^{\phi\phi} + N_L^{(0)} \left[\hat{C}_\ell + F_\ell\right] + F_L^{\rm syst.}, \tag{6.24}$$

up to zeroth order in $C_L^{\phi\phi}$, where the contributions of the foregrounds to the power spectrum is included in the total measured power spectrum in the computation of $N_L^{(0)}$ (cf. Eq. 2.59) and

$$F_L^{\rm syst.} = W_4^{-1} \frac{1}{2L+1} \sum_M \left[f \odot_{LM} f\right]^\dagger \left[f \odot_{LM} f\right] - N_L^{(0)}\left[F_\ell\right], \tag{6.25}$$

We used here the notation introduced in Eq. 3.54 to denote a quadratic combination of CMB fields to a lensing potential estimate with $\odot$. Due to the nature of the quadratic estimator, Eq. 6.24 is true even though the foreground fields, $f_{\ell m}$, are non-isotropic (cf. Appendix C). Following its definition in Eq. 2.59, this equation includes two $N_L^{(0)}$ terms. One computed with the full, measured power spectra, $\hat{C}_\ell + F_\ell$, and one only including the total foreground power spectrum, F_ℓ. This spectrum is defined as

$$F_\ell \equiv \frac{1}{2\ell+1} \sum f_{\ell m} f^\dagger_{\ell m}, \tag{6.26}$$

or its respective equivalent estimator which corrects for the sky masking. The $N_L^{(0)}$-terms including the two-point function of the foregrounds are naturally accounted for in a realization-dependent bias subtraction [251]. The unknown trispectrum of the foregrounds in the last term of Eq. 6.25 is the potentially problematic one, as it will bias the lensing potential power spectrum estimate. In the presence of sky-masking and more complex noise than white noise, Eq. 6.24 becomes inaccurate.

After component separation, similar to the case of the two point function, we can account for the uncertainty in the spectral parameters and obtain an expression for the resulting statistical bias in the lensing power spectrum. Using the definitions in Eqs. 3.27, 3.28 and 3.29 in Eq. 6.22, we obtain (see Appendix C)

$$F_L^{\text{stat.}} = W_4^{-1} \frac{1}{2L+1} \sum_M \left[\mathbf{z} \odot_{LM} \mathbf{r}^{(0)}\right]^\dagger \left[\mathbf{r}^{(0)} \odot_{LM} \mathbf{r}^{(0)}\right] + \text{cycl.} + \tag{6.27}$$

$$+ W_4^{-1} \frac{1}{2L+1} \sum_M \sum_{ij} \Sigma_{ij} \left[\mathbf{r}^{(1)\,i} \odot_{LM} \mathbf{r}^{(1)\,j}\right]^\dagger \left[\mathbf{r}^{(0)} \odot_{LM} \mathbf{r}^{(0)}\right] + \text{perm.}\ , \tag{6.28}$$

where $\mathbf{z} \equiv \sum_{ij} \Sigma_{ij} \mathbf{r}^{(2)\,ij}$. This amounts to $2 + 4 \times n + 2 \times n^2$ quadratic estimator evaluations, where n is the number of spectral parameters. Hence we can write the bias expansion of Eq. 2.57 to zeroth order

$$\left\langle \hat{C}_L^{\phi\phi} \right\rangle = C_L^{\phi\phi} + N_L^{(0)} \left[\hat{C}_\ell + F_\ell\right] + F_L^{\text{syst.}} + F_L^{\text{stat.}} + \ldots,$$

where the last term is zero before component separation and and $F^{\text{syst.}}$ would also be using foregrounds residuals instead of full-power-input foregrounds, substituting in Eq. 6.25

$$f = \mathbf{r}^{(0)}. \tag{6.29}$$

6.3.2 POST DELENSING

As mentioned in Sec. 3.3.3, there are biases arising in the internally delensed B-mode power spectrum due to disconnected, Gaussian correlations in higher order n-point functions. We account for this bias, the so-called delensing bias, $N_\ell^{\text{del. bias}}$, with Monte Carlo simulations including our purely Gaussian foreground model. This bias has two contributions, one from a four-point functions and one from a six-point functions of CMB fields [67, 249]

$$N_\ell^{\text{del.}} \equiv \left\langle \left| \hat{a}^B - \left[\hat{a}^E \hat{\otimes} \left[\hat{a}^X \odot \hat{a}^Y\right]\right] \right|^2 \right\rangle - C_\ell^{\text{res.}} = \tag{6.30}$$

$$= -2 \left\langle \hat{a}^{B\,\dagger} \left[\hat{a}^E \hat{\otimes} \left[\hat{a}^X \odot \hat{a}^Y\right]\right] \right\rangle + \tag{6.31}$$

$$+ \left\langle \left[\hat{a}^E \hat{\otimes} \left[\hat{a}^X \odot \hat{a}^Y\right]\right]^\dagger \left[\hat{a}^E \hat{\otimes} \left[\hat{a}^X \odot \hat{a}^Y\right]\right] \right\rangle + \tag{6.32}$$

$$- C_\ell^{\text{res.}}. \tag{6.33}$$

$\frac{\Delta\sigma(M_\nu)}{\sigma(M_\nu)}$ [%]	$f_{\rm sky} = 5\%$	$f_{\rm sky} = 22\%$
temperature	0.3	1.1
polarization	2.3	5.7
minimum-variance	1.8	4.2

Table 6.2: The relative degradation of the total neutrino mass error, $\Delta\sigma\,(M_\nu) > 0$, after including the total foreground power in the lensing weights for our two different observation strategies, 5% and 22% of the sky. We show both for temperature-only and polarization-only lensing reconstruction separately as well as the minimum-variance combination.

The final, total B-mode power spectrum, $\hat{C}_\ell^{BB}$, that can be used to estimate r, can then be written in following separate components

$$\hat{C}_\ell = rC_\ell^{\rm prim.} + C_\ell^{\rm lens} + N_\ell + F_\ell^{\rm res.} \qquad \text{(before delensing)}, \tag{6.34}$$

$$\hat{C}_\ell = rC_\ell^{\rm prim.} + C_\ell^{\rm res.} + N_\ell + F_\ell^{\rm res.} + N_\ell^{\rm del.}(r) + F_\ell^{\rm del.} \qquad \text{(after delensing)}, \tag{6.35}$$

where $F_\ell^{\rm res.}$ is the power spectrum of foreground residuals

$$F_\ell^{\rm res.} = \frac{1}{2\ell+1}\sum_m r_{\ell m}^{B\ \rm CMB\ \dagger} r_{\ell m}^{B\ \rm CMB}, \tag{6.36}$$

and $F_\ell^{\rm del.}$ arises from the non-Gaussian statistics of the foregrounds to the delensing bias, which will be looked at isolated in the following. In the upcoming results we will neglect the r-dependence of the delensing bias, $N_\ell^{\rm del.}$, to compute the uncertainty in the parameter estimation.

6.4 FOREGROUND BIASES IN CMB LENSING

6.4.1 GAUSSIAN AND ISOTROPIC FOREGROUNDS

To first order approximation, the galactic foreground emission can be described solely by its second moment, such that it is natural to absorb it within the weights and analytic normalization calculation of the quadratic estimator [73]

$$\hat{C}_\ell = \tilde{C}_\ell + N_\ell + F_\ell. \tag{6.37}$$

This maintains optimality in the sense that it minimizes the resulting variance following the derivation in Ref. [258]. It can be seen as downweighting the modes with respect to their foreground power and is in that sense similar to the strategy proposed in Ref. [116] of introducing a high-pass filter to mitigate galactic foreground biases. In Fig. 6.8 we observe no bias-reducing effect for the temperature reconstruction, in which case the two-point spectrum is signal dominated. For the polarization (EBEB) reconstruction, this filtering, effectively applying a low-pass filter on the polarization signal, is reducing the bias on scales up to $L = 1000$. This filtering comes, however, with the caveat of increased noise in the final lensing power spectrum. Furthermore, the mean field for the EB estimator gets reduced at the largest scales, reducing one simulation-dependent factor in the analysis well below the signal. The relative increase in the error on the total neutrino mass, M_ν, is shown in Tab. 6.2, for different sizes of the observed sky patch. The latter is estimated with a Fisher-matrix formalism as described in [109], estimating the neutrino mass from the CMB lensing power spectrum alone.

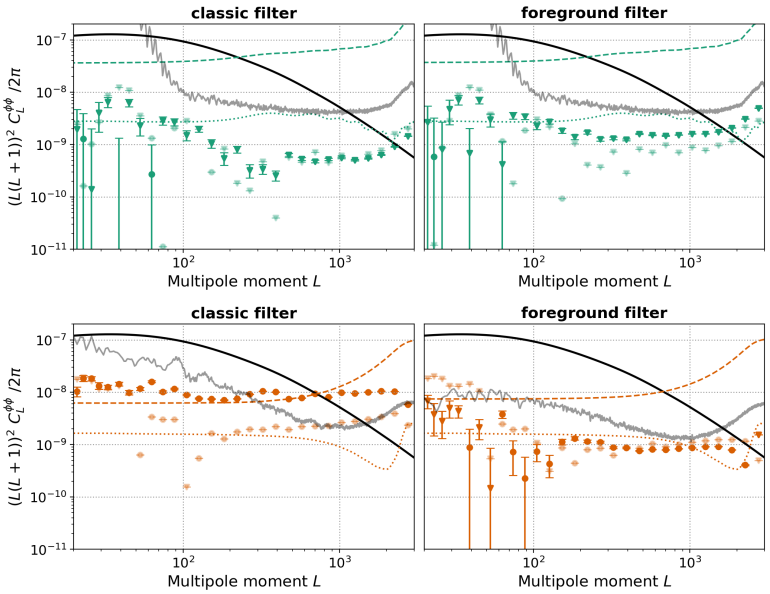

Figure 6.8: The residual biases, $F_L^{\text{syst.}}$ of Eq. 6.25, of the lensing power spectrum after subtracting analytic $N^{(0)}$ and $N^{(1)}$ biases. We compare different weighting schemes of the quadratic estimator auto-power spectra of the temperature (top row) and polarization (bottom row) lensing estimations on the foreground simulations of Ref. [393], assuming a combination of the 95 and 145 GHz channel in our CMB-S4-like configurations for 5% (light colors) and 22% (bright colors) of the sky. The dashed and dotted lines show the analytic $N^{(0)}$ and $N^{(1)}$ biases, respectively, which are subtracted from the estimated spectra. On the left hand side the two-point contamination from foregrounds is not taken in account in the estimator's weights, on the right hand side we applied the substitution in equation 6.37. In grey, we also show the mean-field power spectrum of the respective estimator on the bigger patch.

6.4.2 ISOLATING FOREGROUND BIASES

To test the effect of sky masking on the assumption made in Eq. 6.24, i.e. isotropy of the CMB and the noise, we compare the foreground bias obtained by explicitly computing Eq. 6.25 with the one obtained from Monte-Carlo simulations. These Monte Carlo simulations include 100 realizations of lensed CMB, 100 realizations of white noise and the template of the foreground contribution. Before we apply any foreground cleaning algorithm, we investigate the bias obtained by simply coadding the maps of CMB-dominated frequency channels, 95 and 145 GHz, with weights given by the inverse noise to obtain minimal noise in the final maps. For this analysis we use two types of foreground templates. The first one is described in Sec. 6.1.1, which accounts for complex correlations of the polarization angle of the galactic emission of dust and synchrotron using parameters in Tab. 6.1, in the following denoted by a (V). The second one is obtained by creating a Gaussian realization of the dust and synchrotron power spectra obtained from the respective PySM T, Q and U templates on each observation patch, and in the following denoted by (G). We ensure that both templates have the same T, E and B auto-power spectra by appropriately weighting the harmonic coefficients of the (V)-template by ratios of simple pseudo-power spectra of (G) and (V). After lensing reconstruction on each realization we are left with two sets of 100 lensing potentials for each quadratic estimator type. We estimate a power spectrum from those using Eq. 2.79 and form the average of the difference between the power spectra of the two sets. We moreover define a Monte-Carlo-computed bias, N^{MC}, as the difference of the averaged lensing power spectra from (G)-simulations and the input lensing power spectrum. In Fig. 6.9 we show the comparison between the residual bias of the simulations and the analytical prediction of the foreground trispectrum bias of Eq. 6.25. It shows a reasonable agreement, given the full-sky assumption made in Eq. 6.25. This result motivates us to report the model and parameter-dependent biases in the following sections.

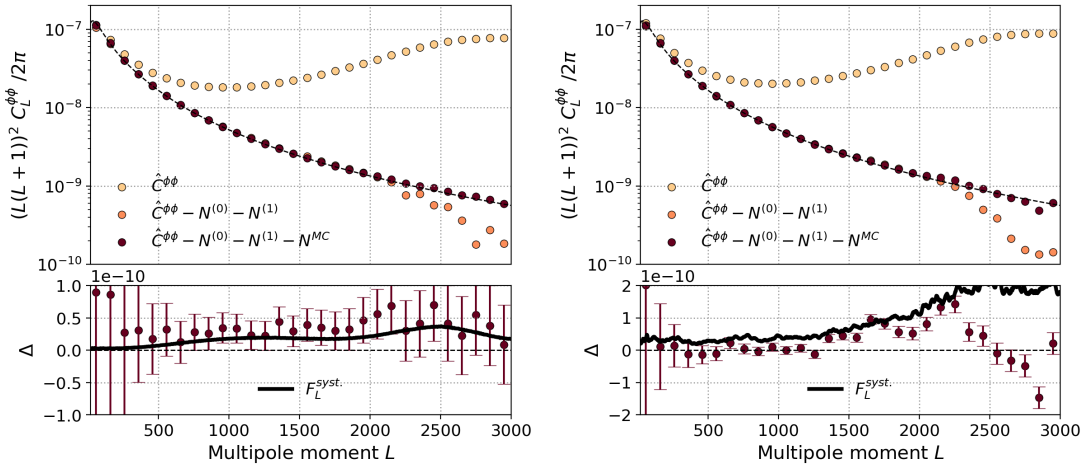

Figure 6.9: The left (right) figure shows the lensing power spectrum, measured on the 5% (22%) patch with the EB-estimator, in different stages of the bias subtraction. The respective bottom row shows the residual after Monte-Carlo-bias subtraction, which is caused by the foreground trispectrum, as well as potentially mode-mixing due to masking. The black line in the bottom figures shows the analytical prediction of Eq. 6.25, which follow the simulation points up to small L-scales in the larger patch.

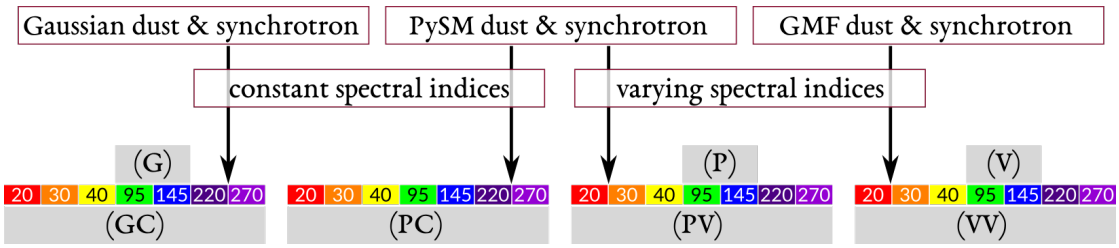

Figure 6.10: Diagram summarizing the procedure to obtain the different foreground simulations used in this section. We start with three kind of dust and synchrotron emission template at a given frequency and combine them into multi-frequency maps, using either constant spectral indices, $\bar{\beta}$, or line-of-sight varying spectral indices, β (see Sec. 6.2.2 for details). To asses the foreground contamination without foreground cleaning, we combine the 95 and 145 GHz channels to obtain simulations (G), (P) and (V).

6.4.3 MODEL-DEPENDENT BIASES

We have introduced three different models to create a foreground template, being

(G) purely Gaussian realizations of the power spectra computed from the masked regions of the PySM foreground templates,

(P) the PySM templates themselves, based on data from Planck, Haslam and WMAP at limited resolution for polarization and

(V) (as in Vansyngel et al. (2016)[62]) the simulation procedure introduced in Refs. [293, 393] to simulate non-Gaussian small scale diffuse foreground emission.

The process to create them is summarized in Fig. 6.10. We show the resulting $F_L^{\text{syst.}}$ relative to the signal power spectrum in Fig. 6.11 for our two patches and three foreground models. As expected,

[62] We thank Flavien Vansyngel for providing a set of dust and synchrotron emission simulations, which were used for some results of this section as well as to cross-check with our own simulation pipeline presented in Sec. 6.1.1.

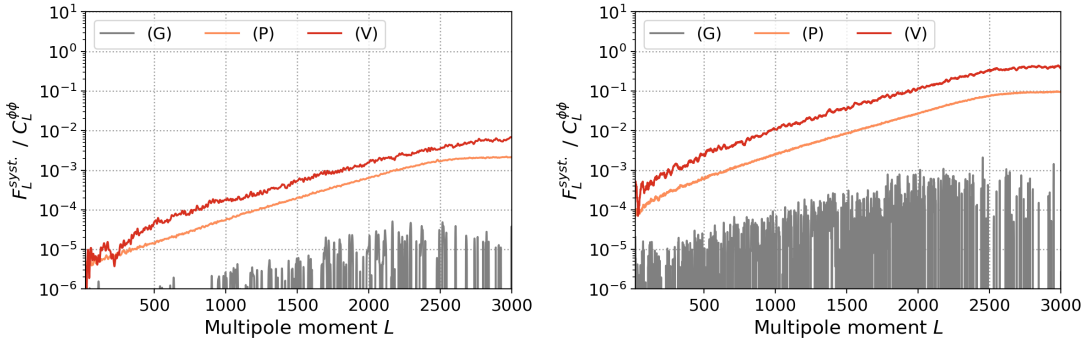

Figure 6.11: The left (right) figure shows the relative foreground bias, $F_L^{\text{syst.}}$, measured on the 5% (22%) patch with the EB-estimator. We show the bias for the three foreground simulations considered in this section. Note that the (V)-simulation harmonic coefficients are rescaled in such a way that their power spectra match those of the (G) and (P), which effectively corresponds to setting $p_0 = 0.26$ for the small patch and $p_0 = 0.16$ for the big patch.

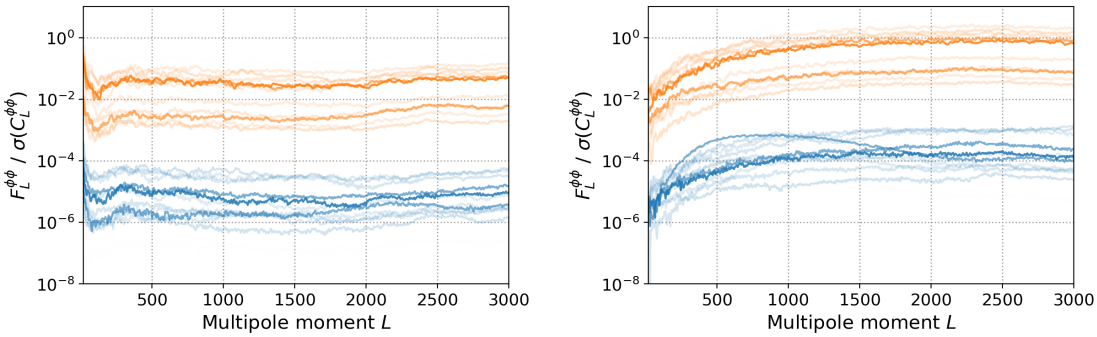

Figure 6.12: The signal-to-noise ratio of the foreground bias for our CMB-S4 configurations, measured in the $EEEE$ (left) and $EBEB$ (right) estimators. We produce 10×3 foreground simulations, spanning the (p_0, f_M) parameter-space, using the given 1σ intervals of Ref. [393] for p_0 (0.03) and f_M (0.1). We base the color intensity on their likelihood, assuming both parameters to be uncorrelated and the likelihood to be Gaussian, i.e. a bright color means a more likely value of the GMF parameter and a barely visible one corresponds to a 2σ deviation. The bias in the 5% patch is shown in blue, the bias in the 22% patch is shown in orange.

it is consistent with zero for the (G)-simulations, in line with the expectation. The bias from (P)-simulations is below 1% for the small patch, but can reach levels as high as 10% for the larger patch, at scales, however, where signal-to-noise is relatively low. The (V) simulations cause a bias which is always larger than (P) and can reach few percent even in the small patch.

6.4.4 SIMULATION PARAMETER DEPENDENT BIASES

We make use of the simulation pipeline of Sec. 6.1.1 and produce foreground-bias-curves depending on statistical parameters of the GMF and dust grains. We change parameters of the [393] foreground model (see Tab. 6.1) and propagate the foreground trispectrum to a lensing power spectrum estimate in Fig. 6.13 for varying p_0, f_M, N and α_M parameters. For each parameter we produce a number of realizations with a different value of this parameter each, while the other parameters are kept fixed. All results are obtained on the 5%-sky-patch, without any foreground cleaning algorithm applied yet. We use the 1σ-errors of Ref. [393], which were obtained in their fit to current Planck data within the Planck 24% mask, to get an estimate of possible ranges in CMB lensing power these biases could lead to. The results are shown in Fig. 6.12, showing a mostly constant signal-to-noise ratio, which is negligible for the small patch, but can reach single-digit percent levels for the larger patch.

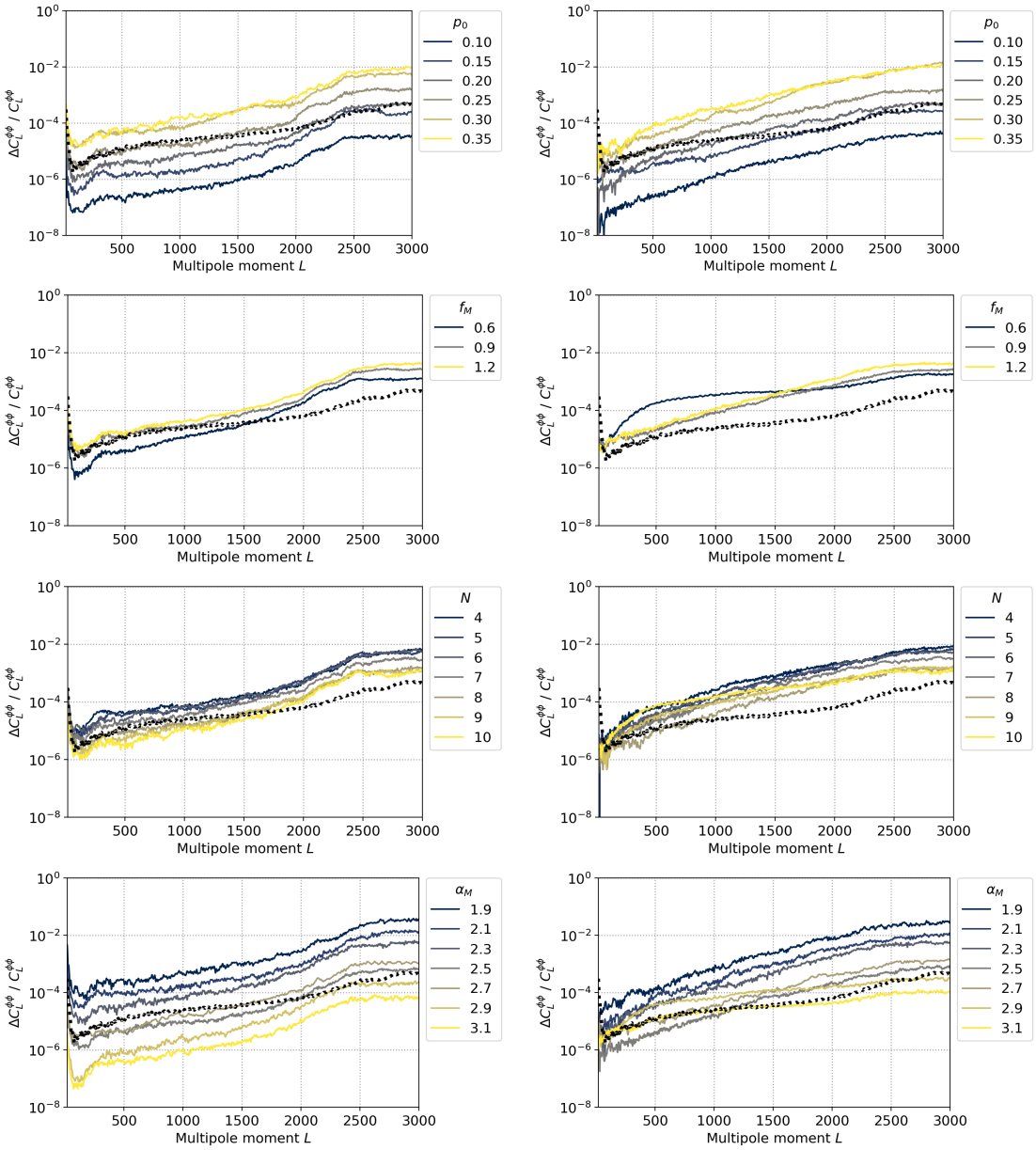

Figure 6.13: The top row shows the change of the p_0 parameter in the (V) foreground model. It results in a steady increase of the residual foreground bias in the $EEEE$ estimator (left column) and $EBEB$ estimator (right column). The fiducial, best-fit value of Ref. [393] is $p_0 = 0.25$. In black, the foreground bias of the $TTTT$ estimator is shown. The following rows show the same for f_M, N and α_M. The fiducial values are $0.9, 4$ and -2.5, respectively.

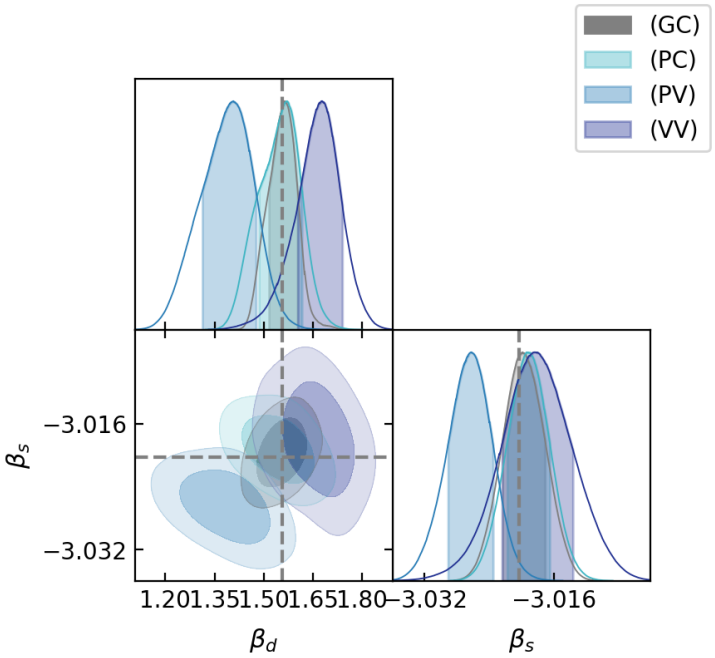

Figure 6.14: This figure is showing the distribution of the peaks of the spectral likelihoods, computed for 100 CMB and noise simulations and the four different foreground simulations. We compare the spectral parameters, β_d and β_s, estimated on 5% of the sky using the different foreground models described in Sec. 6.5.

6.5 BIASES AFTER COMPONENT SEPARATION

In the context of component separation we add a second layer of complexity[63], the frequency scaling of the foregrounds. The procedure is described in Sec. 6.2.2. We produce four sets of multi-frequency maps from the three foreground templates at hand (cf. Fig. 6.10), leading to

(GC) the Gaussian foreground templates, scaled with a constant spectral index, given as the averaged spectral index over the considered sky region in the PySM spectral index maps,

(PC) the PySM foreground templates, scaled with a constant spectral index,

(PV) the PySM foreground templates, scaled with a line-of-sight varying spectral index, given in the PySM spectral index template map and

(VV) the simulations obtained by the method of Sec. 6.1.1, scaled with a line-of-sight varying spectral index.

6.5.1 FOREGROUND CLEANING PERFORMANCE

In Fig. 6.14 we show the result of the maximum-likelihood fit of our four cases of galactic foreground modeling on 100 simulations each, using routines of the FGBUSTER software package. In the fit we assume two foreground components, a modified black-body for dust and power-law SED for synchrotron, with a single, spatially constant spectral index for both, β_d and β_s, and a spatially constant dust temperature, T_dust. The grey, dashed horizontal lines mark the input value for the simulations with constant spectral indices. We are able to recover the correct values if the input and the assumed model are the same (for (GC) and (PC)), with slight systematic biases if this is not the case.

[63] To be precise, these have been already used in the previous sections to get the total foreground contamination at $90 + 145$ GHz.

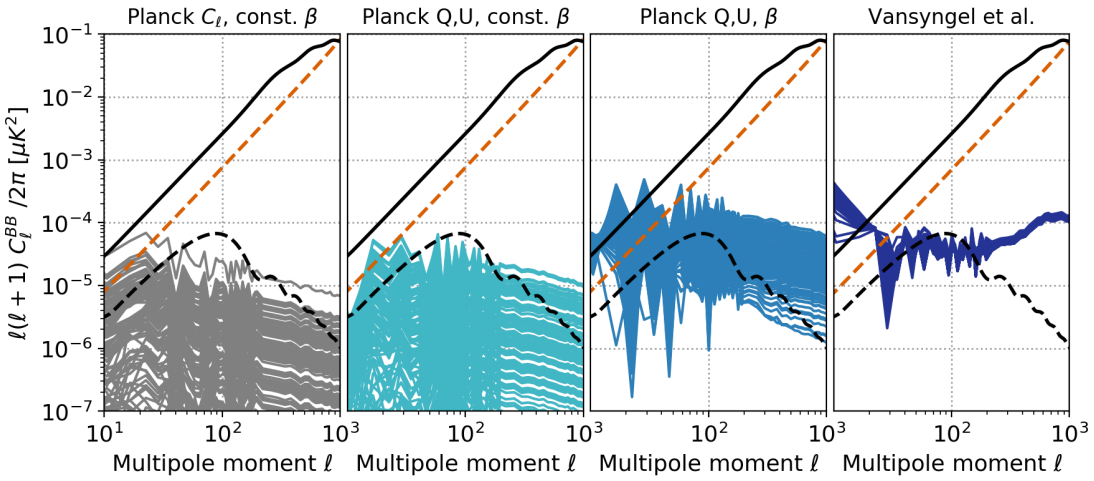

Figure 6.15: The different components of the B-mode power spectrum after foreground cleaning for our four foreground models: the lensing B-mode power spectrum in the solid black line, the noise power after component separation in the dashed orange line, the primordial B-mode power spectrum corresponding to our fiducial value of the tensor-to-scalar ratio, $r = 10^{-3}$, and the foreground residuals from our 100 simulations in the solid colored lines.

$\frac{\Delta\sigma(M_\nu)}{\sigma(M_\nu)}$ [%]	$f_{\rm sky} = 5\%$	$f_{\rm sky} = 22\%$
temperature	1.1	1.3
polarization	32	35
minimum-variance	30	32

Table 6.3: The relative degradation of the total neutrino mass error, $\Delta\sigma\,(M_\nu)$, after component separation and reconstructing the lensing potential on foreground cleaned, but noise-degraded, maps, on 5% and 22% of the sky. We show both for temperature-only and polarization-only lensing reconstruction separately as well as the minimum-variance combination.

In Fig. 6.15 we show the residual B-mode auto-power spectrum obtained as described in Sec. 3.2.3 using the aforementioned best-fit values. The scatter of the spectra in our 100 simulations illustrates the additional uncertainty introduced in the B-mode power spectrum due to the uncertainty in the foreground SED estimations [356, 111]. The simple propagation of the degraded noise properties after component separation to the Fisher forecast of the neutrino mass sensitivity from a CMB lensing potential measurement alone (cf. Sec. 6.4.1) results in a 1% degradation for the temperature and a 30% degradation for the polarization estimator (see Tab. 6.3).

6.5.2 BIASES IN CMB LENSING

Similar to the method of Sec. 6.4.2, we isolate the bias due to higher-order correlations of the foregrounds by comparing and subtracting the lensing power spectra, obtained from two distinct basis sets of foreground templates. The process is summarized in Fig. 6.16. We add to the 100 realizations of CMB and noise the template of foreground residuals computed according to Eq. 3.25, computed from the (GC) for one set and (VV) for the other. For both, the same best-fit values of spectral parameters are used, obtained on the respective realization of CMB and noise, added to the (VV) simulation. In a realistic situation, one would have access to the single-frequency-map power spectra, from which one could obtain a power-law fit for the foreground contamination, compute a Gaussian realization from that, which could then go through the same component separation pipeline as the real data. The Gaussian simulations can then be used to debias the estimated lensing power spectrum, or

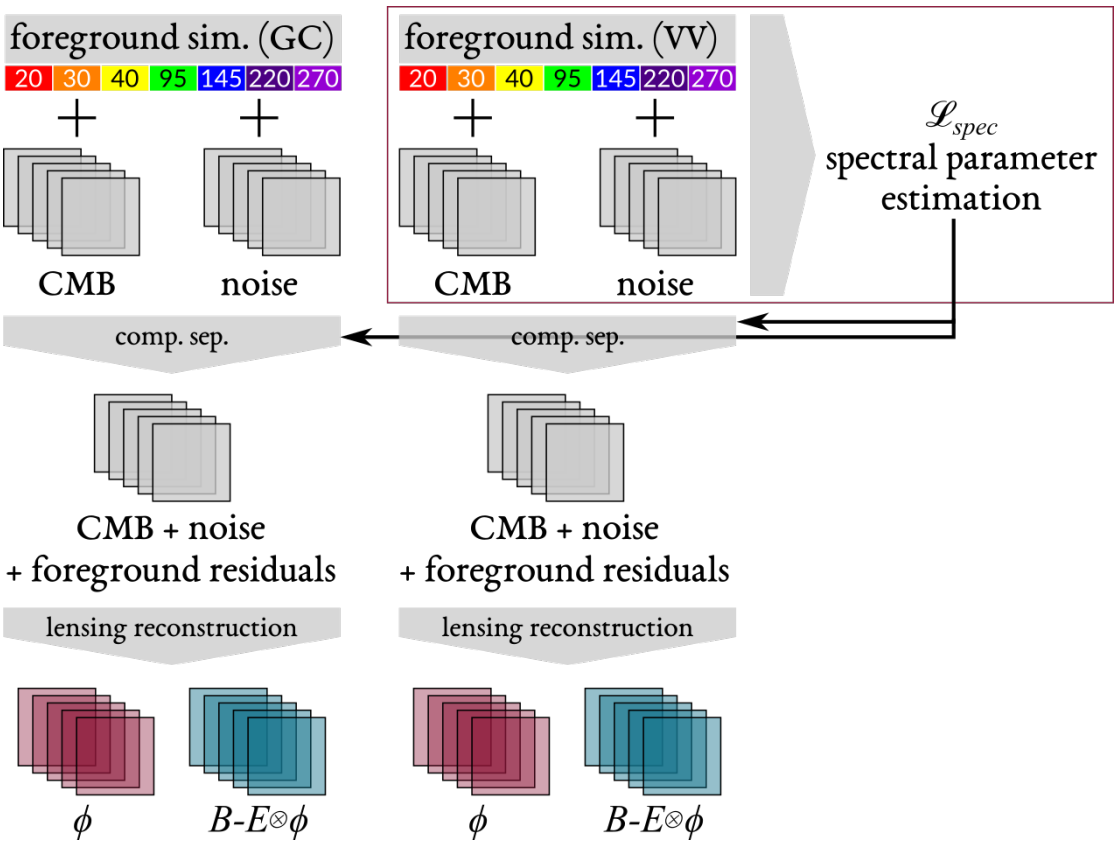

Figure 6.16: This diagram summarizes the simulation pipeline to obtain two sets of foreground cleaned CMB simulations, one containing Gaussian foregrounds and one containing non-Gaussian foreground simulations of Sec. 6.1.1. Both sets run through the same component separation (comp. sep.) pipeline, with spectral parameters estimated on the (VV) foreground simulations with the help of the spectral likelihood, Eq. 3.20.

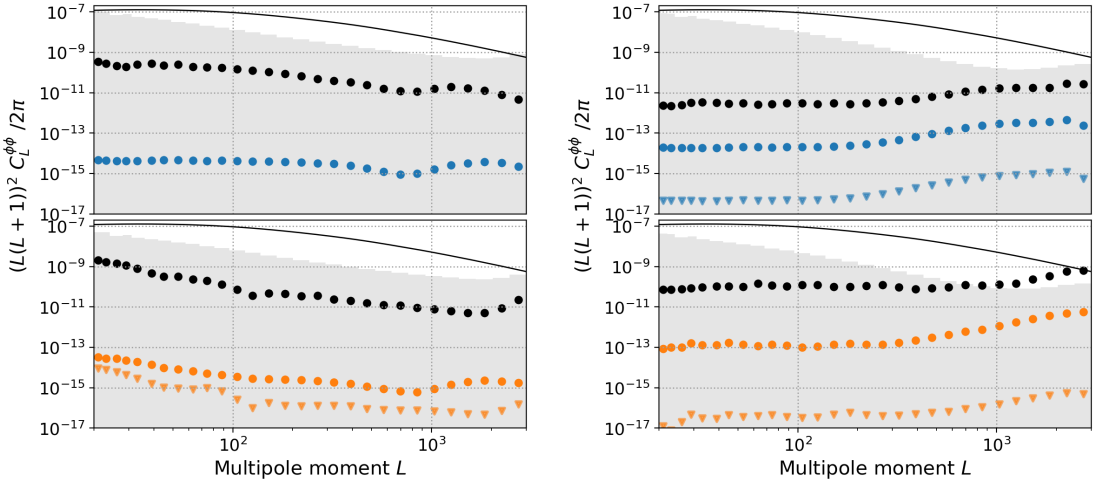

Figure 6.17: The bias in the CMB lensing power spectrum estimator before (black markers) and after (colored markers) component separation. Both cases account for foregrounds (residual) power spectra in the filtering (see Secs. 6.4.1 and 6.5.2). The two major types of estimators, from temperature (left) and polarization (right) CMB data are shown, for both cases of observed sky patches, 5% (top) and 22% (bottom). The signal is shown as a black line, the statistical uncertainty in each bandpower as grey bars. The corresponding statistical foreground residuals, $F_L^{\text{stat.}}$, are shown as triangles in the respective plots.

get an estimate of the foreground residual bias in it, and reflect the prior knowledge we have about the foregrounds, i.e. their power spectrum and constant frequency scaling. Hence, the residual biases are caused by two effects, the variation of spectral indices across the sky and the non-Gaussian structure of the foreground components. The resulting biases from foreground residuals in the lensing power spectrum are shown in Fig. 6.17. The bias in both estimators is significantly reduced, by at least two orders of magnitude and are therefore well below the statistical uncertainty in our chosen bandpowers.

In Fig. 6.18 we show residual biases in the temperature on polarization lensing estimator using two kinds of filters, analogous to Sec. 6.4.1. We model power spectra of systematic foreground residuals from single- and cross-frequency power spectra as [356]

$$\hat{C}_\ell^{\text{res.}} = \mathbf{W}_\ell^T \mathbf{F}_\ell \mathbf{W}_\ell, \tag{6.38}$$

where $\mathbf{F}_\ell$ is a $N_{\text{freq.}} \times N_{\text{freq.}}$ matrix for each ℓ, containing the multi-frequency foreground (cross)-spectra, obtained by fitting a power-law foreground spectrum to each (cross-)frequency power spectrum. The expression for the weight function, $\mathbf{W}_\ell$, is given in Eq. 3.34. This is similar to what is described in as described in Sec. 3.2.3 and shown in Fig. 6.15. We show that the difference between the two cases are small if the foreground residual is sufficiently low, as in our small-patch case. For larger (systematic) foreground residuals, as we see them in the larger patch. This can further reduce biases.

In Fig. 6.19 we show the resulting statistical uncertainty due to the uncertainty in the foreground residual modeling. Similar to the case of the statistical bias of the two-point correlation [356] (see Sec. 3.2.3), we propagate this uncertainty to the lensing power spectrum by computing the residual power spectrum, $\hat{C}_\ell^{\text{res.}}$, for each of the 100 simulations and obtain the corresponding $N_L^{(0)}\left[\hat{C}_\ell^{\text{res.}}\right]$ for each CMB and noise realization. Naturally, this uncertainty could be mitigated in a realization-dependent bias subtraction in the lensing potential power spectrum estimate.

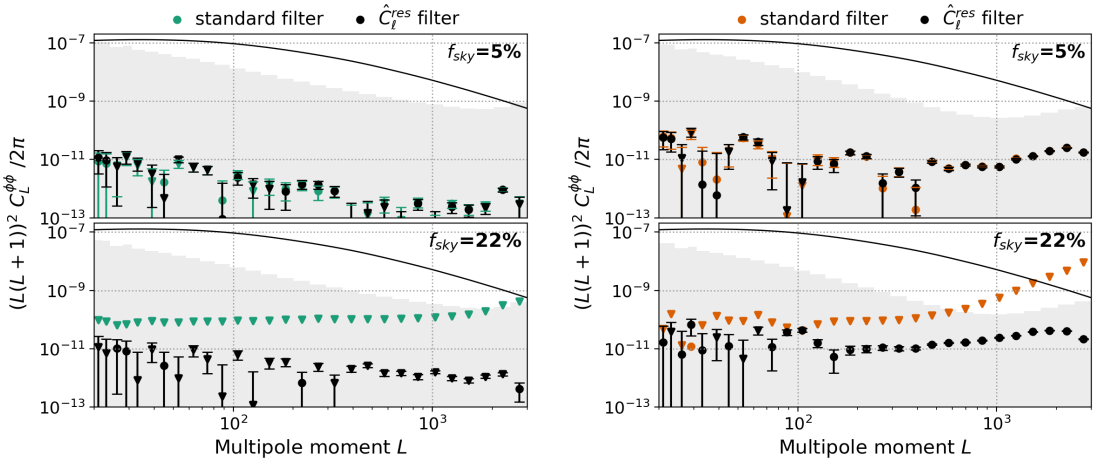

Figure 6.18: Similar to Fig. 6.8 we show the arising biases if the foreground power is neglected in the filtering of the input CMB fields to the quadratic estimator. The temperature estimator is shown on the left, polarization on the right. In the following we will use the foreground residual modeling of Eq. 6.38 in the filtering, which can significantly reduce residual biases. The errorbar from cosmic-variance and noise in each band is shown as grey bars. Triangles correspond to negative values.

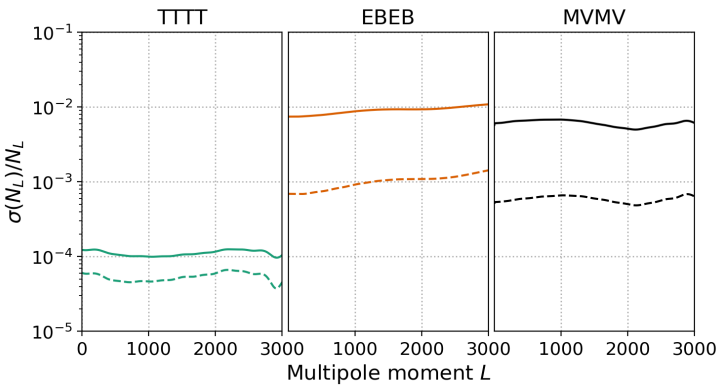

Figure 6.19: The 1σ statistical uncertainty of the noise bias $N_L^{(0)}$ due to the statistical uncertainty of the foreground model, i.e. the uncertainty in the residual foregrounds. This is computed by inserting the spectra of the 100 simulations obtained from the maximum likelihood fitting in the computation of $N_L^{(0)}$. This figure shows the cases of 5% (solid) and 22% (dashed) sky coverage, for $TTTT$ (left), $EBEB$ (middle) and minimum-variance (right) lensing estimators.

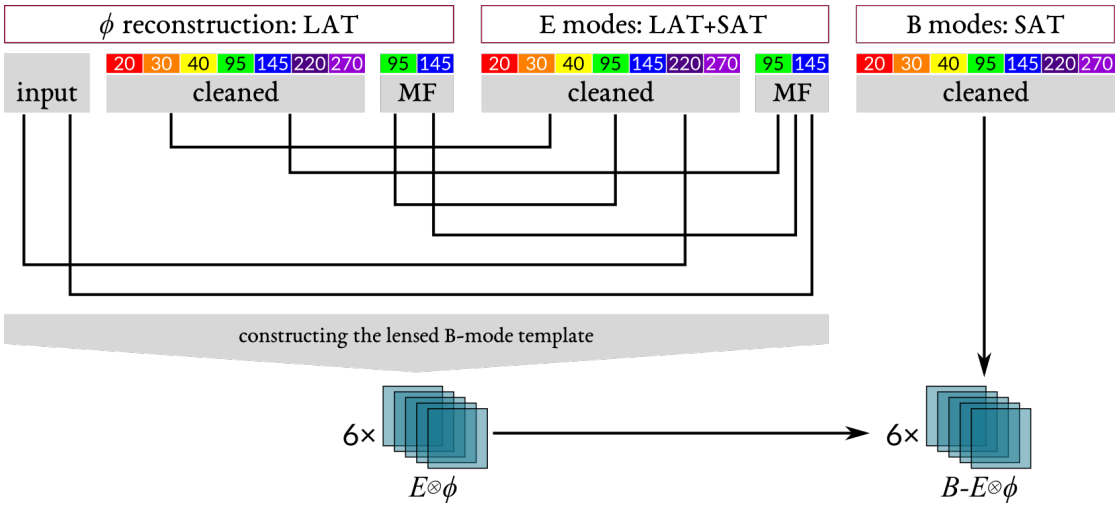

Figure 6.20: Diagram summarizing the procedure to obtain delensed B-mode maps from various combinations of lensing reconstruction, including the ideal case of the input ϕ, and E-mode configurations.

6.6 DELENSING

In the previous section, we ended up with two sets of simulations, one starting from Gaussian realizations of foreground power spectra (GC) and one starting from templates of PySM and simulated small scales with the method of Sec. 6.1.1 (VV). Both sets of multi-frequency simulations had been cleaned from foregrounds, leaving us with 100 realizations of uncleaned and cleaned CMB T, E and B fields, as well as uncleaned and cleaned ϕ estimates. This can be used (cf. Sec. 3.3.3), to estimate $F_\ell^{\rm del.}$ of Eq. 6.35 by differentiating estimated B-mode power spectra between the (GC) and (VV) simulations. We estimate the B-mode power spectra with X^{2}Pure. Fig. 6.20 depicts schematically the procedure to obtain delensed B-mode maps. It also shows the various combinations of different experimental configurations we consider. We assume for both, lensing potential reconstruction and E-mode measurement, either a cleaned map or a simple coadded map from medium-frequency (MF) channels, where the foreground contamination is not accounted for. We also compare with the case where the lensing potential is not correlated with CMB fields, by taking the input lensing potential and adding to it a Gaussian realization of the lensing reconstruction noise. Fig. 6.23 shows the resulting binned $F_\ell^{\rm del.}$-bias, for three different cases of the B-mode template ingredients used for the delensing. The E-modes used for the delensing convolution can either be cleaned, i.e. have lower foreground bias but higher noise, or uncleaned, i.e. including the total foreground bias after coadding the 95 and 145 GHz channels. Similar, we can either use the lensing potential estimated from foreground-contaminated or foreground-cleaned maps. We see that external delensing, i.e. using the input ϕ potential as the delensing tracer, as well as TT delensing, is mainly free of this bias. When the lensing potential is estimated from E and B fields, it introduces complex correlations with the E and B fields that are used in the delensing procedure, causing a bias which is of the order the primordial signal with $r = 10^{-3}$ at its $\ell = 80$ peak. It also effectively doubles the foreground residual in the delensed map. However, this bias goes away if the LAT fields are cleaned from the foreground emission, i.e. both the E-mode field used for the B-mode template creation as well as the E and B fields used for the lensing tracer estimation.

As an example we show in Fig. 6.21 the full B-mode power spectra, comparing theory power spectra with the results from simulations. We can see by eye an agreement of the simulated delensed spectra with a delensing amplitude of about $A_{\rm lens} = 0.4$, up to the lowest multipole bins at $\ell \approx 30$, where the foreground residual, $F_\ell^{\rm syst.}$, is starting to be visible.

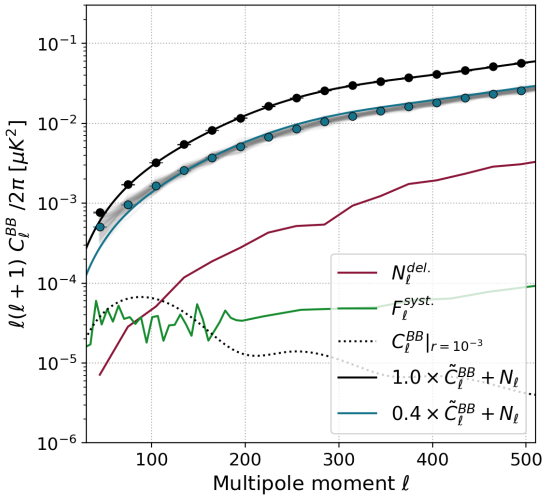

Figure 6.21: An example of lensed, delensed and unlensed B-mode power spectra, The lines show the theory curves, where in solid black is the pure lensing power spectrum and in dotted black is the primordial B-mode power spectrum with $r = 10^{-3}$. The blue line shows the lensed power spectrum, with a lensing amplitude of $A_{\rm lens} = 0.4$, which is expected to be achieved by CMB-S4 with the quadratic estimator ($A_{\rm lens} = 0.1$ for iterative delensing [2]). The lensing power spectra have the instrumental noise bias term added to them. The red line shows the amplitude of the delensing bias, $-N_\ell^{\rm del.}$, computed with Gaussian simulations, following Ref. [249]. The dots show the mean of the 100 simulations on the cleaned (VV) simulation set, black for the lensed case, blue for the delensed case with the delensing and noise bias not removed. For the latter case the spectra from the 100 realizations are shown in light grey. We can achieve close agreement with 40% delensing.

We propagate this bias to a likelihood on the tensor-to-scalar-ratio, r [109, 356, 65]. Following Refs. [366, 142, 111], we employ a CMB-and-noise-averaged Gaussian likelihood on the CMB fields, which leads to

$$-2\log\mathcal{L}\left(r|\hat{C}_\ell^{BB}\right) = f_{\rm sky}\left(\sum_\ell \frac{2\ell+1}{2}\frac{\hat{C}_\ell^{BB}}{C_\ell^{BB}} + \log\left(\det\left(C_\ell^{BB}\right)\right)\right). \tag{6.39}$$

The assumed covariance matrix is modeled including primordial and lensing contributions, as well as the noise and an estimate of the foreground residuals and Gaussian delensing biases (estimated from simulations including Gaussian foreground simulations)

$$C_\ell(r) = rC_\ell^{\rm prim.} + C_\ell^{\rm res.} + N_\ell + F_\ell^{\rm res.} + N_\ell^{\rm del.}. \tag{6.40}$$

The biases and 1σ-errors on r for different configurations and reconstruction or delensing parameters are shown in Fig. 6.22. The fiducial value is $r = 10^{-3}$. We include the B-mode auto-power spectrum between $\ell = 30$ and $\ell = 300$ in the r-likelihood. The measured B-mode map comes from foreground-cleaned SAT multi-frequency maps, with white noise specifications given in Tab. 4.7 without additional atmospheric noise. We investigate three bias mitigation strategies:

I: Only using the internal lensing potential reconstruction from CMB temperature. We have seen that delensing with only the temperature quadratic estimator mitigates additional foreground biases, however, with the downside of having lower delensing efficiency.

II: We remove multipoles of the CMB fields which are used for the lensing reconstructions below a certain $\ell_{\rm min}$-value. This has the advantage that it reduces biases due to higher-order mode-mixing correlations [332, 369, 329].

III: We perform the galactic foreground cleaning technique introduced in the previous sections prior to lensing reconstruction and delensing.

Compared to the naive, fiducial case of performing no galactic foreground cleaning nor any other bias mitigation strategy prior to lensing reconstruction and delensing, which inhibits a 1σ-bias to positive values, all mitigation strategies can remove the bias. Hence, the optimal choice comes down to

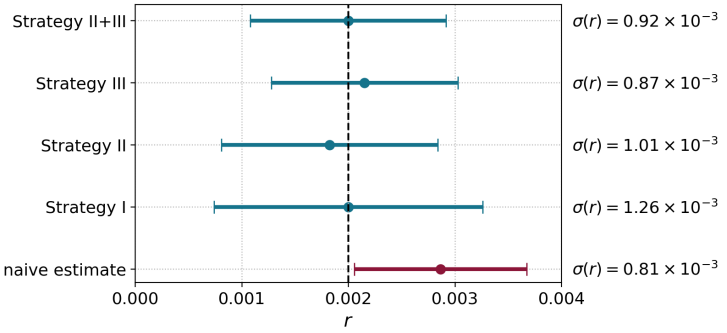

Figure 6.22: From the maximum-likelihood fit on the B-mode power spectrum, we obtain a best-fit value and 1σ error estimate on r, which is plotted in this figure. We show a fiducial, naive case and three proposed bias mitigation strategies as proposed in the text.

the strategy which recovers the best signal-to-noise, which is a simple foreground cleaning technique. However, we show that even in the cases where this is not possible (i.e. there are no sufficient multi-frequency observations), the delensing estimator can be made more robust against biases from higher-order correlations of foregrounds.

6.7 DISCUSSION

We have investigated state-of-the-art small-scale diffuse foreground simulations, which can accurately reproduce one- and two-point statistics of dust and synchrotron emission data. We use those to investigate biases on the estimates of the CMB lensing potential, arising from complex small-scale diffuse foregrounds can have on CMB lensing potential estimates. We find possible significant biases in large footprint surveys, as planned for Simons Observatory or CMB-S4. We showed ranges of signal-to-noise levels of foreground biases, covering best- and worst-case scenarios in terms of the real realization of the magnetic field of our Galaxy, constrained by current Planck data. We claim that these biases can essentially be mitigated by using multi-frequency observations and apply simple foreground cleaning methods. Furthermore, we tested for biases in the B-mode power spectrum, showing the necessity to clean the CMB of galactic foreground emission not only for the large-scale SAT survey, but also the LAT survey to achieve the most sensitive and unbiased measurement of r. Not cleaning the latter can lead to significant biases in the r-estimation after internal delensing with the EB quadratic estimator.

The GMF simulation method used allows to produce extreme cases of statistical properties of the GMF by tuning the parameters of the simulation. But still, simulating the GMF's turbulent component as a Gaussian random field, which, given the observation of non-Gaussian GMF correlations in MHD simulations, could be overly optimistic. We leave the inclusion of small-scale GMF simulations from MHD for future studies. Polarized small-scale galactic dust and synchrotron emission in the high signal-to-noise regime will be measured by next-generation CMB observatories such as Simons Observatory or CMB-S4. Also dedicated experiments like BLAST[64] will be critical in further characterizing possible biases in CMB lensing and delensing.

Additional mitigation strategies proposed in the literature, especially in the context of extragalactic contamination, are only cleaning one field of the two within the quadratic estimator to reduce biases while loosing less in terms of signal-to-noise [226] or using a sub-set of the information of the lensing potential estimator, the so-called shear estimator, which is less sensitive to foreground biases [318]. Moreover, there are bias-hardening proposals against a varying dust amplitude with given power spectrum [287], similar to the formalism outlined in Appendix C.4. A less viable idea is the usage of cross-frequency quadratic estimators to clean from foreground contamination (see Appendix C.3), which would degrade the noise level in the final lensing potential estimate by a factor $\mathcal{O}(10)$.

[64] https://sites.northwestern.edu/blast/

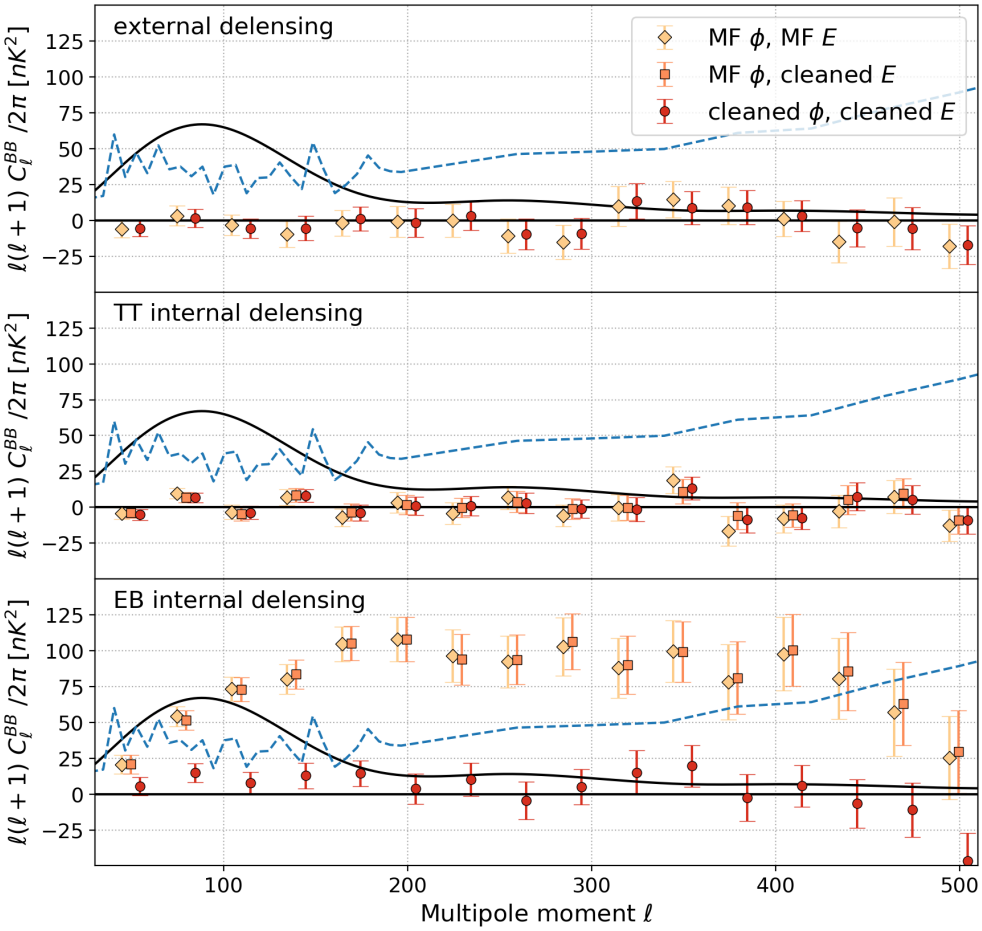

Figure 6.23: Figure showing the $F_\ell^{\rm del.}$-bias term of Eq. 6.35, originating from higher-order correlations of the diffuse foregrounds and computed from simulations, is shown as points. Contributions to the B-mode auto-power spectrum (in nK^2 units!) are shown. The dashed blue line is the average foreground residual in the 5% patch (same as the right hand figure of Fig. 6.15). The solid black line is the primordial gravitational wave power spectrum, corresponding to $r = 10^{-3}$. The two components of the B-mode template used for delensing, the E-mode field and the ϕ estimate can either be cleaned or uncleaned (MF: medium frequency, 95 and 145 GHz, only).

7 Conclusions

In this thesis I described my work in the context of an ever growing field in observational cosmology. CMB lensing, now detected by more than 40σ [287], is one of the major observables of the future in CMB science, one major avenue for future CMB observatories to reach their science goals. I introduced these major open questions to be answered with experimental cosmology which set the scientific context of this thesis: the total mass of the elusive particles called neutrinos on one side and probing the very beginning of our Universe, searching for a primordial superluminal expansion explaining missing links in the current Standard Model of the Universe.

I outlined my development of a framework for extracting the CMB lensing information from CMB data sets, which is successfully applied to one of the most complex current data set produced by the POLARBEAR telescope. In this context I described the full data analysis pipeline of POLARBEAR in which I was involved, starting at the raw data timestreams and going all the way to the CMB lensing potential estimation. I also showed the status of the CMB lensing reconstruction effort for the POLARBEAR-I third season dataset, which I am leading, demonstrating the scientific capability of probing a wide range of multipoles with POLARBEAR and eventually Simons Array. My work of developing a quadratic estimator, which is ready to be applied to massive CMB datasets, is also part of the analysis pipeline preparation effort of one of the next-generation CMB experiments, the Simons Array.

Beyond current data analysis effort, I described my work on characterizing the sensitivity to astrophysical systematic effects of future CMB lensing and large-scale B-mode measurements. This included the effect of realistic photon propagation within an evolving, non-linear large-scale structure distribution. I showed that for future experiments, simple assumption made on these effects which worked until now can lead to dangerous biases, possibly biasing a total neutrino mass detection measurement, which is a major science target for future experiments. Similar biases arise when cross-correlating the CMB lensing signal with external LSS tracers, with a possible weaker bias cancellation effect seen in the CMB lensing auto-spectrum when considering low redshift tracers. This bias could be significant in future CMB experiments, however, as we show, can be modeled quite accurately with the help of LSS bispectrum fitting formulas and the post-Born bispectrum from higher order perturbative expansions. This bias is also correlated with other systematics in lensing cross-correlations like intrinsic alignment. Finally, we observe a significant bias in the B-mode power spectrum after delensing with a low-redshift LSS tracer.

Furthermore, I worked on the characterization of foreground biases in the context of CMB lensing, potentially biasing both, a CMB lensing potential power spectrum and subsequent neutrino mass estimation, as well as a tensor-to-scalar ratio measurement, when using a CMB lensing quadratic estimate as a mass tracer of the Universe for delensing. Especially given the tarnished record on primordial gravitational wave announcements and the ever growing reliance of future CMB experiments on delensing to reach their science goals,a careful characterization of biases due to higher-order foreground correlations is expedient. This kind of analysis, delensing in the presence of complex galactic foregrounds, is an important subject in near-future CMB data analysis, since many experimental efforts are hoping to increase their sensitivity of r through delensing. Examples are the efforts of the BICEP/Keck collaborations to delens their B-mode spectrum with high-resolution CMB data from SPT, the planned delensing effort of Simons Observatory to delens with a multi-tracer approach [338, 405, 386] and eventually the natural synergy between the LiteBIRD satellite's large-scale B-mode measurement and the small-scale CMB measurement of CMB-S4 [2].

In my future work I would like to combine all these building blocks and be a part of the next-generation CMB measurement efforts to detect the total mass scale of neutrinos with cosmological data as well as primordial gravitational waves as a smoking gun for Inflation. I plan to continue to work on the interface between theoretical or phenomenological cosmology and data analysis, to prepare ongoing and future CMB efforts for the ever growing complexity of datasets, both in terms of sheer data volume as well as the complexity of the signal, foregrounds and noise.

A

Generalities

A.1 DEFINITIONS

A.1.1 RICCI TENSOR AND SCALAR

The Ricci curvature tensor, $R_{\mu\nu}$, and Ricci scalar, R, are given in terms of Christoffel symbols, Γ, and corresponding metric tensor, g, as

$$R_{\mu\nu} = 2\Gamma^{\rho}{}_{\mu[\nu,\rho]} + 2\Gamma^{\rho}{}_{\lambda[\rho}\Gamma^{\lambda}{}_{\nu]\mu} \tag{A.1}$$

$$R = g^{\mu\nu}R_{\mu\nu}, \tag{A.2}$$

where

$$\Gamma^{\mu}_{\alpha\beta} \equiv \frac{g^{\mu\nu}}{2}\left[g_{\alpha\nu,\beta} + g_{\nu\beta,\alpha} - g_{\alpha\beta,\nu}\right]. \tag{A.3}$$

The comma denotes partial derivatives with respect to the following coordinate. The square brackets around indices indicate to take the asymmetric part with respect to these indices.

A.1.2 COORDINATE DEFINITIONS

We define the direction of the line-of-sight, with us, the observer, at the origin of the coordinate system, as

$$\mathbf{n} = \begin{pmatrix} \sin\theta\cos\phi \\ \sin\theta\sin\phi \\ \cos\theta \end{pmatrix}. \tag{A.4}$$

The infinitesimal area element of the unit sphere around the observer is given by

$$d\Omega = d\theta \sin\theta d\phi. \tag{A.5}$$

A.2 WIGNER-3J RELATIONS

Following useful relations between Wigner-3j symbols and spherical harmonic functions Refs. [258, 394].

$$\int d\Omega_{s_1} Y_{\ell_1 m_1 s_2} Y_{\ell_2 m_2 s_3} Y_{\ell_3 m_3} = = \sqrt{\frac{(2\ell_1+1)(2\ell_2+1)(2\ell_3+1)}{4\pi}} \begin{pmatrix} \ell_1 & \ell_2 & \ell_3 \\ -s_1 & -s_2 & -s_3 \end{pmatrix} \begin{pmatrix} \ell_1 & \ell_2 & \ell_3 \\ m_1 & m_2 & m_3 \end{pmatrix}.$$

Wigner-3j symbols also satisfy the following summation relations [258, 394]

$$\sum_{m_1 m_2} \begin{pmatrix} \ell_1 & \ell_2 & L \\ m_1 & m_2 & M \end{pmatrix} \begin{pmatrix} \ell_1 & \ell_2 & L' \\ m_1 & m_2 & M' \end{pmatrix} = \frac{1}{2L+1} \delta_{LL'} \delta M M' \tag{A.6}$$

$$\sum_{m} (-1)^{\ell+m} \begin{pmatrix} \ell & \ell & L \\ m & -m & 0 \end{pmatrix} = \sqrt{\frac{2\ell+1}{2L+1}} \delta_{L0}. \tag{A.7}$$

B

Lensing Reconstruction with the Quadratic Estimator

B.1 EXACT FLAT-SKY NON-PERTURBATIVE MODE RESPONSE FUNCTIONS

The exact flat-sky non-perturbative mode response functions are given in Tab B.1. To a $\sim 0.5\%$ accuracy the $\tilde{C}_l^{TP_\perp}$ and $\tilde{C}_l^{PP_\perp}$ terms can be neglected. Approximating the gradient spectra with equivalent lensed CMB spectra (and taking $\tilde{C}_l^{TP_\perp} = \tilde{C}_l^{PP_\perp} = 0$) is a good approximation for $\ell_{\rm max} > 2000$ [145]. Their derivation, starting from Eq. 2.83, follows.

XY	$f^{XY}(\mathbf{l}_1, \mathbf{l}_2)$
TT	$\mathbf{l}_1 \cdot \mathbf{L} C_{l_1}^{T\nabla T} + \mathbf{l}_2 \cdot \mathbf{L} C_{l_2}^{T\nabla T}$
EE	$\cos(2(\varphi_{l_1} - \varphi_{l_2}))\left[\mathbf{l}_1 \cdot \mathbf{L}\tilde{C}_{l_1}^{E\nabla E} + \mathbf{l}_2 \cdot \mathbf{L}\tilde{C}_{l_2}^{E\nabla E}\right] + \frac{1}{2}\sin(2(\varphi_{l_1} - \varphi_{l_2}))\left[\mathbf{l}_1 \times \mathbf{L}\tilde{C}_{l_1}^{PP_\perp} - \mathbf{l}_2 \times \mathbf{L}\tilde{C}_{l_2}^{PP_\perp}\right]$
EB	$\sin(2(\varphi_{l_1} - \varphi_{l_2}))\left[\mathbf{l}_1 \cdot \mathbf{L}\tilde{C}_{l_1}^{E\nabla E} + \mathbf{l}_2 \cdot \mathbf{L}\tilde{C}_{l_2}^{B\nabla B}\right] - \frac{1}{2}\cos(2(\varphi_{l_1} - \varphi_{l_2}))\left[\mathbf{l}_1 \times \mathbf{L}\tilde{C}_{l_1}^{PP_\perp} + \mathbf{l}_2 \times \mathbf{L}\tilde{C}_{l_2}^{PP_\perp}\right]$
BB	$\cos(2(\varphi_{l_1} - \varphi_{l_2}))\left[\mathbf{l}_1 \cdot \mathbf{L}\tilde{C}_{l_1}^{B\nabla B} + \mathbf{l}_2 \cdot \mathbf{L}\tilde{C}_{l_2}^{B\nabla B}\right] - \frac{1}{2}\sin(2(\varphi_{l_1} - \varphi_{l_2}))\left[\mathbf{l}_1 \times \mathbf{L}\tilde{C}_{l_1}^{PP_\perp} - \mathbf{l}_2 \times \mathbf{L}\tilde{C}_{l_2}^{PP_\perp}\right]$
TE	$\cos(2(\varphi_{l_1} - \varphi_{l_2}))\mathbf{l}_1 \cdot \mathbf{L}\tilde{C}_{l_1}^{T\nabla E} + \sin(2(\varphi_{l_1} - \varphi_{l_2}))\mathbf{l}_1 \times \mathbf{L}\tilde{C}_{l_1}^{TP_\perp} + \mathbf{l}_2 \cdot \mathbf{L}\tilde{C}_{l_2}^{T\nabla E}$
TB	$\sin(2(\varphi_{l_1} - \varphi_{l_2}))\mathbf{l}_1 \cdot \mathbf{L}\tilde{C}_{l_1}^{T\nabla E} - \cos(2(\varphi_{l_1} - \varphi_{l_2}))\mathbf{l}_1 \times \mathbf{L}\tilde{C}_{l_1}^{TP_\perp} - \mathbf{l}_2 \times \mathbf{L}\tilde{C}_{l_2}^{TP_\perp}$

Table B.1: The exact non-perturbative mode response functions for the flat-sky case, to be used in the CMB lensing quadratic estimator. We define $\mathbf{a} \times \mathbf{b} \equiv \epsilon_{ij} a^i b^j$. The definitions of the lensed gradient spectra can be found in the Appendix of Ref. [213].

We start by introducing the flat-sky definitions for the Fourier transforms

$$T(\mathbf{n}) = \int \frac{d^2\mathbf{l}}{(2\pi)^2} T(\mathbf{l}) e^{i\mathbf{l}\cdot\mathbf{n}} \tag{B.1}$$

$$_{\pm}X(\mathbf{n}) = \int \frac{d^2\mathbf{l}}{(2\pi)^2} {}_{\pm}X(\mathbf{l}) e^{\pm 2i\varphi_{\mathbf{l}}} e^{i\mathbf{l}\cdot\mathbf{n}}, \tag{B.2}$$

where $\varphi_{\mathbf{l}}$ is the azimuthal angle of $\mathbf{l}$, and

$$T(\mathbf{l}) = \int d^2\mathbf{n} T(\mathbf{n}) e^{-i\mathbf{l}\cdot\mathbf{n}} \tag{B.3}$$

$$_{\pm}X(\mathbf{l}) = \int d^2\mathbf{n} {}_{\pm}X(\mathbf{n}) e^{\mp 2i\varphi_{\mathbf{l}}} e^{-i\mathbf{l}\cdot\mathbf{n}}. \tag{B.4}$$

The power spectra are defined as

$$\langle X(\mathbf{l}) Y^*(\mathbf{l}') \rangle = (2\pi)^2 \delta(\mathbf{l} - \mathbf{l}') C^{XY}_{|\mathbf{l}|}. \tag{B.5}$$

The lensing response function definition of Eq. 2.83 is given by

$$\left\langle \frac{\delta}{\delta\phi(\mathbf{L})} X(\mathbf{l}) Y(\mathbf{l}') \right\rangle_G = \delta(\mathbf{l} + \mathbf{l}' - \mathbf{L}) f^{XY}_{lLl'}, \tag{B.6}$$

where

$$\begin{aligned}
\frac{\delta}{\delta\phi(\mathbf{L})} X(\mathbf{l}) &= \int d^2\mathbf{n} \frac{\delta}{\delta\phi(\mathbf{L})} X(\mathbf{n} + \nabla\phi(\mathbf{n})) e^{\mp si\varphi_{\mathbf{l}}} e^{-i\mathbf{l}\cdot\mathbf{n}} = \\
&= \int d^2\mathbf{n} \widetilde{\nabla X}(\mathbf{n}) \frac{\delta \nabla\phi(\mathbf{n})}{\delta\phi(\mathbf{L})} e^{\mp si\varphi_{\mathbf{l}}} e^{-i\mathbf{l}\cdot\mathbf{n}} = \\
&= i\mathbf{L} \int d^2\mathbf{n} \widetilde{\nabla X}(\mathbf{n}) e^{\mp si\varphi_{\mathbf{l}}} e^{-i(\mathbf{l}-\mathbf{L})\cdot\mathbf{n}} = \\
&= i\mathbf{L} e^{\pm si(\varphi_{\mathbf{l}-\mathbf{L}} - \varphi_{\mathbf{l}})} \widetilde{\nabla X}(\mathbf{l} - \mathbf{L}).
\end{aligned} \tag{B.7}$$

The functional derivative of the lensing potential gradient with respect to the lensing potential can then be written as

$$\frac{\delta\nabla\phi(\mathbf{n})}{\delta\phi(\mathbf{L}')} = \frac{\delta}{\delta\phi(\mathbf{L}')} \nabla \int \frac{d^2\mathbf{L}}{(2\pi)^2} \phi(\mathbf{L}) e^{i\mathbf{L}\cdot\mathbf{n}} = \int \frac{d^2\mathbf{L}}{(2\pi)^2} i\mathbf{L}\delta(\mathbf{L} - \mathbf{L}') e^{i\mathbf{L}\cdot\mathbf{n}} = \frac{i\mathbf{L}'}{(2\pi)^2} e^{i\mathbf{L}'\cdot\mathbf{n}}, \tag{B.8}$$

such that for two lensed fields, $\tilde{X}$ and $\tilde{Y}$, one has

$$\left\langle \frac{\delta}{\delta\phi(\mathbf{L})}\tilde{X}(\mathbf{l})\tilde{Y}(\mathbf{l}')\right\rangle_G = \left\langle i\mathbf{L}e^{\pm si(\varphi_{\mathbf{l}-\mathbf{L}}-\varphi_{\mathbf{l}})}\widetilde{\nabla X}(\mathbf{l}-\mathbf{L})\tilde{Y}(\mathbf{l}') + \tilde{X}(\mathbf{l})i\mathbf{L}e^{\pm s'i(\varphi_{\mathbf{l}'-\mathbf{L}}-\varphi_{\mathbf{l}'})}\widetilde{\nabla Y}(\mathbf{l}'-\mathbf{L})\right\rangle_G .$$

We use the definitions of the gradient spectra from Ref. [213]

$$\begin{aligned}
\left\langle \widetilde{\nabla T}(\mathbf{l})\tilde{T}(\mathbf{l}')\right\rangle &\equiv i\mathbf{l}\tilde{C}_l^{T\nabla T}\delta(\mathbf{l}+\mathbf{l}')(2\pi)^2 \\
\left\langle \widetilde{\nabla_\pm X}(\mathbf{l})_\mp\tilde{X}(\mathbf{l}')\right\rangle &\equiv i\mathbf{l}\left(\tilde{C}_l^{E\nabla E}+\tilde{C}_l^{B\nabla B}\right)\delta(\mathbf{l}+\mathbf{l}')(2\pi)^2 \\
\left\langle \widetilde{\nabla_{i\pm} X}(\mathbf{l})_\pm\tilde{X}(\mathbf{l}')\right\rangle &\equiv i\left[\mathbf{l}_i\left(\tilde{C}_l^{E\nabla E}-\tilde{C}_l^{B\nabla B}\right)\mp i\epsilon_{ji}\mathbf{l}^j\tilde{C}_l^{PP\perp}\right]\delta(\mathbf{l}+\mathbf{l}')(2\pi)^2 \\
\left\langle \widetilde{\nabla_{i\pm} X}(\mathbf{l})\tilde{T}(\mathbf{l}')\right\rangle &\equiv i\left[\mathbf{l}_i\tilde{C}_l^{T\nabla E}\mp i\epsilon_{ji}\mathbf{l}^j\tilde{C}_l^{TP\perp}\right]\delta(\mathbf{l}+\mathbf{l}')(2\pi)^2.
\end{aligned}$$

We are now set to compute the 5 response functions given in Tab. B.1 The TT correlation gives

$$\begin{aligned}
\left\langle \frac{\delta}{\delta\phi(\mathbf{L})}T(\mathbf{l})T(\mathbf{l}')\right\rangle_G &= i\mathbf{L}\left(\left\langle\nabla X(\mathbf{l}-\mathbf{L})T(\mathbf{l}')\right\rangle_G\left\langle\nabla X(\mathbf{l}'-\mathbf{L})T(\mathbf{l})\right\rangle_G\right) = \\
&= i\mathbf{L}\left(i(\mathbf{l}-\mathbf{L})\tilde{C}_{l-L}^{T\nabla T}\delta(\mathbf{l}-\mathbf{L}+\mathbf{l}')+i(\mathbf{l}'-\mathbf{L})\tilde{C}_{l'-L}^{T\nabla T}\delta(\mathbf{l}'-\mathbf{L}+\mathbf{l})\right) = \\
&= \delta(\mathbf{l}+\mathbf{l}'-\mathbf{L})\left(\mathbf{L}\cdot\mathbf{l}'\tilde{C}_{l'}^{T\nabla T}+\mathbf{L}\cdot\mathbf{l}\tilde{C}_l^{T\nabla T}\right).
\end{aligned}$$

For the polarization fields auto-spectra we use

$$\begin{aligned}
E(\mathbf{l}) &= -\frac{{}_+X(\mathbf{l})+{}_-X(\mathbf{l})}{2} \\
B(\mathbf{l}) &= -\frac{{}_+X(\mathbf{l})-{}_-X(\mathbf{l})}{2i},
\end{aligned}$$

resulting for EE in

$$\begin{aligned}
\left\langle \frac{\delta}{\delta\phi(\mathbf{L})}E(\mathbf{l})E(\mathbf{l}')\right\rangle_G &= \frac{1}{4}\left\langle \frac{\delta}{\delta\phi(\mathbf{L})}\left({}_+X(\mathbf{l})_+X(\mathbf{l}')+{}_-X(\mathbf{l})_+X(\mathbf{l}')+{}_+X(\mathbf{l})_-X(\mathbf{l}')+{}_-X(\mathbf{l})_-X(\mathbf{l}')\right)\right\rangle_G = \\
&= \frac{1}{4}i\mathbf{L}\Big\langle \Big(e^{2i(\varphi_{\mathbf{l}-\mathbf{L}}-\varphi_{\mathbf{l}})}\nabla_+X(\mathbf{l}-\mathbf{L})_+X(\mathbf{l}')+e^{2i(\varphi_{\mathbf{l}'-\mathbf{L}}-\varphi'_{\mathbf{l}})}{}_+X(\mathbf{l})\nabla_+X(\mathbf{l}'-\mathbf{L}) \\
&\quad +e^{-2i(\varphi_{\mathbf{l}-\mathbf{L}}-\varphi_{\mathbf{l}})}\nabla_-X(\mathbf{l}-\mathbf{L})_+X(\mathbf{l}')+e^{2i(\varphi_{\mathbf{l}'-\mathbf{L}}-\varphi'_{\mathbf{l}})}{}_-X(\mathbf{l})\nabla_+X(\mathbf{l}'-\mathbf{L}) \\
&\quad +e^{2i(\varphi_{\mathbf{l}-\mathbf{L}}-\varphi_{\mathbf{l}})}\nabla_+X(\mathbf{l}-\mathbf{L})_-X(\mathbf{l}')+e^{-2i(\varphi_{\mathbf{l}'-\mathbf{L}}-\varphi'_{\mathbf{l}})}{}_+X(\mathbf{l})\nabla_-X(\mathbf{l}'-\mathbf{L}) \\
&\quad +e^{-2i(\varphi_{\mathbf{l}-\mathbf{L}}-\varphi_{\mathbf{l}})}\nabla_-X(\mathbf{l}-\mathbf{L})_-X(\mathbf{l}')+e^{-2i(\varphi_{\mathbf{l}'-\mathbf{L}}-\varphi'_{\mathbf{l}})}{}_-X(\mathbf{l})\nabla_-X(\mathbf{l}'-\mathbf{L})\Big)\Big\rangle_G
\end{aligned}$$

Using the definitions of this section leads directly to the expression in Tab. B.1. Analogous computations lead to the terms for EB and BB.

The temperature-polarization cross-correlation, TE, results in following terms

$$\begin{aligned}
\Big\langle \frac{\delta}{\delta\phi(\mathbf{L})} T(\mathbf{l})E(\mathbf{l}')\Big\rangle_G &= -\frac{1}{2}\Big\langle \frac{\delta}{\delta\phi(\mathbf{L})}\Big(T(\mathbf{l})_+ X(\mathbf{l}') + T(\mathbf{l})_- X(\mathbf{l}')\Big)\Big\rangle_G = \\
&= -\frac{1}{2} i\mathbf{L}\Big\langle \Big(\nabla T(\mathbf{l}-\mathbf{L})_+ X(\mathbf{l}') + e^{2i(\varphi_{\mathbf{l}'-\mathbf{L}}-\varphi'_{\mathbf{l}})} T(\mathbf{l})\nabla_+ X(\mathbf{l}'-\mathbf{L}) \\
&\qquad + \nabla T(\mathbf{l}-\mathbf{L})_+ X(\mathbf{l}') + e^{-2i(\varphi_{\mathbf{l}'-\mathbf{L}}-\varphi'_{\mathbf{l}})} T(\mathbf{l})\nabla_- X(\mathbf{l}'-\mathbf{L})\Big)\Big\rangle_G = \\
&= -\frac{1}{2} i\mathbf{L}\Big\langle \Big(i\left[(\mathbf{l}-\mathbf{L})_i \tilde{C}^{T\nabla E}_{l-L} - i\epsilon_{ji}(\mathbf{l}-\mathbf{L})^j \tilde{C}^{TP\perp}_{l-L}\right] + e^{2i(\varphi_{\mathbf{l}'-\mathbf{L}}-\varphi'_{\mathbf{l}})} i\left[(\mathbf{l}'-\mathbf{L})_i \tilde{C}^{T\nabla E}_{l'-L} - i\epsilon_{ji}(\mathbf{l}'-\mathbf{L})^j \tilde{C}^{TP\perp}_{l'-L}\right] \\
&\qquad + i\left[(\mathbf{l}-\mathbf{L})_i \tilde{C}^{T\nabla E}_{l-L} + i\epsilon_{ji}(\mathbf{l}-\mathbf{L})^j \tilde{C}^{TP\perp}_{l-L}\right] + e^{-2i(\varphi_{\mathbf{l}'-\mathbf{L}}-\varphi'_{\mathbf{l}})}\left[(\mathbf{l}'-\mathbf{L})_i \tilde{C}^{T\nabla E}_{l'-L} + i\epsilon_{ji}(\mathbf{l}'-\mathbf{L})^j \tilde{C}^{TP\perp}_{l'-L}\right]\Big)\Big\rangle_G \delta(\mathbf{l}+\mathbf{l}'-\mathbf{L}),
\end{aligned}$$

which can be simplified to the expression of Tab. B.1, and similar computations lead to the expression for TB.

B.2 LENSQUEST QUEST_NORM

Listing B.1: First lines of the `quest_norm` function to compute the quadratic estimator normalization.

```
def quest_norm(wcl, dcl, lmin=2, lmax=None, lminCMB=2, lmaxCMB=None, lminCMB2=None,
        lmaxCMB2=None, curl=False, rdcl=None, bias=False, wclgrad=None):

    """Computes the normalization of the quadratic estimator.

    Parameters
    ----------
    wcl : array-like, shape (1,lmaxCMB) or (4, lmaxCMB)
        The input power spectra (lensed or unlensed) used in the weights of the
        normalization a la Okamoto & Hu, either TT only or TT, EE, BB and TE (
        polarization).
    dcl : array-like, shape (1,lmaxCMB) or (4, lmaxCMB)
        The (noisy) input power spectra used in the denominators of the normalization
        (i.e. Wiener filtering), either TT only or TT, EE, BB and TE (polarization).
    lmin : int, scalar, optional
        Minimum l of the normalization. Default: 2
    lmax : int, scalar, optional
        Maximum l of the normalization. Default: lmaxCMB
    lminCMB : int, scalar, optional
        Minimum l of the CMB power spectra. Default: 2
    lmaxCMB : int, scalar, optional
        Maximum l of the CMB power spectra. Default: given by input cl arrays
    curl : bool, optional
        Computing normalization for the curl estimator. Default: False
    bias: bool, scalar, optional
        Additionally computing the N0 bias. Default: False
    wclgrad: array-like, shape (1,lmaxCMB) or (4, lmaxCMB)
        Optional array of gradient power spectra, only used in the f, not the g
        functions

    Returns
    -------
    AL: dictionary
        Normalization for (TT,TE,EE,TB,EB) quadratic estimators.
    NL: dictionary (only if bias=True)
        Zeroth order lensing noise for (TT,TE,EE,TB,EB) quadratic estimators and all (
        non-zero) cross-correlations.
    """
```

C

Foregrounds and CMB lensing

C.1 FOREGROUND BIAS IN LENSING POWER SPECTRUM

We assume that the harmonic coefficients are biased by a constant field $f^X_{\ell m}$ such that

$$\tilde{a}^X_{\ell m} = a^X_{\ell m} + n^X_{\ell m} + f^X_{\ell m} \tag{C.1}$$

and

$$\langle \tilde{a}^X_{\ell m} \rangle = f^X_{\ell m}. \tag{C.2}$$

The inferred lensing power spectrum from these multipoles is then given by

$$\begin{aligned}
\left\langle \frac{1}{2L+1} \sum_M \phi^{AB\,\dagger}_{LM} \phi^{CD}_{LM} \right\rangle =& \frac{1}{2L+1} \sum_M \sum_{\ell_1 m_1} \sum_{\ell_2 m_2} \sum_{\ell_3 m_3} \sum_{\ell_4 m_4} A^{AB}_L A^{CD}_L \begin{pmatrix} \ell_1 & \ell_2 & L \\ m_1 & m_2 & -M \end{pmatrix} \begin{pmatrix} \ell_3 & \ell_4 & L \\ m_3 & m_4 & -M \end{pmatrix} \\
& g^{AB\,*}_{\ell_1 L \ell_2} g^{CD}_{\ell_3 L \ell_4} \left\langle \tilde{a}^{\dagger\,A}_{\ell_1 m_1} \tilde{a}^{\dagger\,B}_{\ell_2 m_2} \tilde{a}^{C}_{\ell_3 m_3} \tilde{a}^{D}_{\ell_4 m_4} \right\rangle \\
=& \frac{1}{2L+1} \sum_M \sum_{\ell_1 m_1} \sum_{\ell_2 m_2} \sum_{\ell_3 m_3} \sum_{\ell_4 m_4} A^{AB}_L A^{CD}_L \begin{pmatrix} \ell_1 & \ell_2 & L \\ m_1 & m_2 & -M \end{pmatrix} \begin{pmatrix} \ell_3 & \ell_4 & L \\ m_3 & m_4 & -M \end{pmatrix} \\
& g^{AB\,*}_{\ell_1 L \ell_2} g^{CD}_{\ell_3 L \ell_4} \\
& \big(\tilde{C}^{AC}_{\ell_1 m_1} \delta_{\ell_1 \ell_3} \delta_{m_1 m_3} \tilde{C}^{BD}_{\ell_2 m_2} \delta_{\ell_2 \ell_4} \delta_{m_2 m_4} + \tilde{C}^{AD}_{\ell_1 m_1} \delta_{\ell_1 \ell_4} \delta_{m_1 m_4} \tilde{C}^{BC}_{\ell_2 m_2} \delta_{\ell_2 \ell_3} \delta_{m_2 m_3} \\
& - \tilde{F}^{AC}_{\ell_1 m_1} \delta_{\ell_1 \ell_3} \delta_{m_1 m_3} \tilde{F}^{BD}_{\ell_2 m_2} \delta_{\ell_2 \ell_4} \delta_{m_2 m_4} - \tilde{F}^{AD}_{\ell_1 m_1} \delta_{\ell_1 \ell_4} \delta_{m_1 m_4} \tilde{F}^{BC}_{\ell_2 m_2} \delta_{\ell_2 \ell_3} \delta_{m_2 m_3} \\
& + \tilde{f}^{\dagger\,A}_{\ell_1 m_1} \tilde{f}^{\dagger\,B}_{\ell_2 m_2} \tilde{f}^{C}_{\ell_3 m_3} \tilde{f}^{D}_{\ell_4 m_4} \big) + C^{\phi\phi}_L + N^{(1)}_L + \dots \\
=& N^{(0)}_L \left[\tilde{C}_\ell + F_\ell \right] + C^{\phi\phi}_L \left[f_{\ell m} \right] - N^{(0)}_L \left[F_\ell \right] + C^{\phi\phi}_L + N^{(1)}_L + \dots
\end{aligned} \tag{C.3}$$

C.2 FOREGROUND RESIDUAL BIAS IN THE LENSING POWER SPECTRUM

After cleaning, which is essentially a linear combination of frequency maps, the corresponding equation to the full-foreground-equivalent Eq. C.1 can be written as

$$\tilde{a}^X_{\ell m} = a^X_{\ell m} + n^X_{\ell m} + \sum_\nu A^\nu_{\ell m \ell' m'} f^X_{\ell' m'}, \tag{C.4}$$

where $a^X_{\ell m}$ is, as before, the harmonic transform of the lensed CMB and $n^X_{\ell m}$ is the noise field after component separation. The residual CMB is then a linear combination of the single frequency foreground maps $f^X_{\ell' m'}$ with weights, $A^\nu_{\ell m \ell' m'}$, obtained from the foreground cleaning algorithm. For slight improvement in readability we redefine the quantities of Eqs. 3.27-3.29

$$y \equiv \mathbf{r}^{(0)} \tag{C.5}$$

$$Y_i \equiv \mathbf{r}^{(1)\,i} \tag{C.6}$$

$$X_{ij} \equiv \mathbf{r}^{(2)\,ij} \tag{C.7}$$

$$z \equiv \sum_{ij} \Sigma_{ij} X_{ij} \tag{C.8}$$

and omit writing most of the indices and summations explicitly. Similar, the calculation in the previous Appendix, the foreground residual bias can be written as

$$\frac{1}{2L+1}\sum_M \phi^{AB\,\dagger}_{LM}\phi^{CD}_{LM} =$$

$$\frac{1}{2L+1}\sum_M \sum_{\ell_1 m_1}\sum_{\ell_2 m_2}\sum_{\ell_3 m_3}\sum_{\ell_4 m_4} A^{AB}_L A^{CD}_L \begin{pmatrix} \ell_1 & \ell_2 & L \\ m_1 & m_2 & -M \end{pmatrix}\begin{pmatrix} \ell_3 & \ell_4 & L \\ m_3 & m_4 & -M \end{pmatrix} g^{AB\,*}_{\ell_1 L \ell_2} g^{CD}_{\ell_3 L \ell_4}$$

$$\Big((a^{A\dagger}_{\ell_1 m_1} + y^{A\dagger}_{\ell_1 m_1} + \delta^\dagger Y^{A\dagger}_{\ell_1 m_1} + \delta^\dagger X^{A\dagger}_{\ell_1 m_1}\delta)(a^{B\dagger}_{\ell_2 m_2} + y^{B\dagger}_{\ell_2 m_2} + \delta^\dagger Y^{B\dagger}_{\ell_2 m_2} + \delta^\dagger X^{B\dagger}_{\ell_2 m_2}\delta)$$

$$(a^C_{\ell_3 m_3} + y^C_{\ell_3 m_3} + Y^C_{\ell_3 m_3}\delta + \delta^\dagger X^C_{\ell_3 m_3}\delta)(a^D_{\ell_4 m_4} + y^D_{\ell_4 m_4} + Y^D_{\ell_4 m_4}\delta + \delta^\dagger X^D_{\ell_4 m_4}\delta)\Big).$$

Averaging over CMB and noise, while neglecting uneven powers of δ leads to

$$
\begin{aligned}
&\frac{1}{2L+1}\sum_M \phi^{AB\,\dagger}_{LM}\phi^{CD}_{LM} = \\
&\frac{1}{2L+1}\sum_M \sum_{\ell_1 m_1}\sum_{\ell_2 m_2}\sum_{\ell_3 m_3}\sum_{\ell_4 m_4} A^{AB}_L A^{CD}_L \begin{pmatrix} \ell_1 & \ell_2 & L \\ m_1 & m_2 & -M \end{pmatrix}\begin{pmatrix} \ell_3 & \ell_4 & L \\ m_3 & m_4 & -M \end{pmatrix} g^{AB\,*}_{\ell_1 L \ell_2} g^{CD}_{\ell_3 L \ell_4} \\
&\Big((C^{AC}_{\ell_1}+F^{AC}_{\ell_1})(C^{BD}_{\ell_2}+F^{BD}_{\ell_2})\delta_{\ell_1\ell_3}\delta_{m_1m_3}\delta_{\ell_2\ell_4}\delta_{m_2m_4} + (C^{AD}_{\ell_1}+F^{AD}_{\ell_1})(C^{BC}_{\ell_2}+F^{BC}_{\ell_2})\delta_{\ell_1\ell_4}\delta_{m_1m_4}\delta_{\ell_2\ell_3}\delta_{m_2m_3} - \\
&- F^{AC}_{\ell_1}F^{BD}_{\ell_2}\delta_{\ell_1\ell_3}\delta_{m_1m_3}\delta_{\ell_2\ell_4}\delta_{m_2m_4} - F^{AD}_{\ell_1}F^{BC}_{\ell_2}\delta_{\ell_1\ell_4}\delta_{m_1m_4}\delta_{\ell_2\ell_3}\delta_{m_2m_3} \\
&+ \Big(y^{A\dagger}_{\ell_1m_1}y^{B\dagger}_{\ell_2m_2} + \delta^\dagger Y^{A\dagger}_{\ell_1m_1}y^{B\dagger}_{\ell_2m_2} + \delta^\dagger X^{A\dagger}_{\ell_1m_1}\delta y^{B\dagger}_{\ell_2m_2} + y^{A\dagger}_{\ell_1m_1}\delta^\dagger Y^{B\dagger}_{\ell_2m_2} + \delta^\dagger Y^{A\dagger}_{\ell_1m_1}\delta^\dagger Y^{B\dagger}_{\ell_2m_2} + \\
&\quad + \delta^\dagger X^{A\dagger}_{\ell_1m_1}\delta\delta^\dagger Y^{B\dagger}_{\ell_2m_2} + y^{A\dagger}_{\ell_1m_1}\delta^\dagger X^{B\dagger}_{\ell_2m_2}\delta + \delta^\dagger Y^{A\dagger}_{\ell_1m_1}\delta^\dagger X^{B\dagger}_{\ell_2m_2}\delta + \delta^\dagger X^{A\dagger}_{\ell_1m_1}\delta\delta^\dagger X^{B\dagger}_{\ell_2m_2}\delta\Big)\times \\
&\times\Big(y^{C}_{\ell_3m_3}y^{D}_{\ell_4m_4} + Y^{C}_{\ell_3m_3}\delta y^{D}_{\ell_4m_4} + \delta^\dagger X^{C}_{\ell_3m_3}\delta y^{D}_{\ell_4m_4} + y^{C}_{\ell_3m_3}Y^{D}_{\ell_4m_4}\delta + Y^{C}_{\ell_3m_3}\delta Y^{D}_{\ell_4m_4}\delta + \\
&\quad + \delta^\dagger X^{C}_{\ell_3m_3}\delta Y^{D}_{\ell_4m_4}\delta + y^{C}_{\ell_3m_3}\delta^\dagger X^{D}_{\ell_4m_4}\delta + Y^{C}_{\ell_3m_3}\delta\delta^\dagger X^{D}_{\ell_4m_4}\delta + \delta^\dagger X^{C}_{\ell_3m_3}\delta\delta^\dagger X^{D}_{\ell_4m_4}\delta)\Big),
\end{aligned}
$$

where

$$
F^{AB}_\ell = \frac{1}{2\ell+1}\sum_m \left(y^{A\dagger}_{\ell m}y^{B}_{\ell m} + y^{A\dagger}_{\ell m}z^{B}_{\ell m} + z^{A\dagger}_{\ell m}y^{B}_{\ell m} + Y^{A\dagger}_{\ell m}\Sigma Y^{B}_{\ell m}\right)
$$

Average over spectral indices uncertainty, assuming Gaussian errors, $\langle\delta\delta\rangle = \Sigma$ and throwing away powers of δ of order three or higher then gives us

$$
\begin{aligned}
&\frac{1}{2L+1}\sum_M \phi^{AB\,\dagger}_{LM}\phi^{CD}_{LM} = \\
&N^{(0)}_L\left[C_\ell + F_\ell\right] + N^{(1)}_L\left[C_\ell + F_\ell\right] + C^{\phi\phi}_L + \\
&\otimes_L\left(\phi^\dagger\left[y^A_{\ell m}y^B_{\ell m}\right],\phi\left[y^C_{\ell m}y^D_{\ell m}\right]\right) + \otimes_L\left(\phi^\dagger\left[y^A_{\ell m}y^B_{\ell m}\right],\phi\left[y^C_{\ell m}z^D_{\ell m}\right]\right) + \\
&\otimes_L\left(\phi^\dagger\left[y^A_{\ell m}y^B_{\ell m}\right],\phi\left[z^C_{\ell m}y^D_{\ell m}\right]\right) + \otimes_L\left(\phi^\dagger\left[y^A_{\ell m}z^B_{\ell m}\right],\phi\left[y^C_{\ell m}y^D_{\ell m}\right]\right) + \\
&\otimes_L\left(\phi^\dagger\left[z^A_{\ell m}y^B_{\ell m}\right],\phi\left[y^C_{\ell m}y^D_{\ell m}\right]\right) + \Sigma_{ij}\otimes_L\left(\phi^\dagger\left[Y^A_{i\ell m}Y^B_{j\ell m}\right],\phi\left[y^C_{\ell m}y^D_{\ell m}\right]\right) + \\
&\Sigma_{ij}\otimes_L\left(\phi^\dagger\left[y^A_{\ell m}Y^B_{i\ell m}\right],\phi\left[y^C_{\ell m}Y^D_{j\ell m}\right]\right) + \Sigma_{ij}\otimes_L\left(\phi^\dagger\left[y^A_{\ell m}Y^B_{i\ell m}\right],\phi\left[Y^C_{j\ell m}y^D_{\ell m}\right]\right) + \\
&\Sigma_{ij}\otimes_L\left(\phi^\dagger\left[y^A_{\ell m}y^B_{\ell m}\right],\phi\left[Y^C_{i\ell m}Y^D_{j\ell m}\right]\right) + \Sigma_{ij}\otimes_L\left(\phi^\dagger\left[Y^A_{i\ell m}y^B_{\ell m}\right],\phi\left[y^C_{\ell m}Y^D_{j\ell m}\right]\right) + \\
&\Sigma_{ij}\otimes_L\left(\phi^\dagger\left[Y^A_{i\ell m}y^B_{\ell m}\right],\phi\left[Y^C_{j\ell m}y^D_{\ell m}\right]\right) - N^{(0)}_L\left[F_\ell\right],
\end{aligned}
$$

which leads to Eq. 6.28.

C.3 CROSS-FREQUENCY QUADRATIC ESTIMATOR CLEANING

The goal is to use the information in all the quadratic combination of available frequency maps. Similar to the map-level case, we write down our data model as

$$\hat{\phi}^{\nu_1\nu_2}_{LM} = A^{\nu_1\nu_2}_L \sum_{\ell_1 m_1}\sum_{\ell_2 m_2}(-1)^M \begin{pmatrix} \ell_1 & \ell_2 & L \\ m_1 & m_2 & -M \end{pmatrix} g^{\nu_1\nu_2}_{\ell_1\ell_2}(L) A^{\nu_1 k_1} a^{k_1}_{\ell_1 m_1} A^{\nu_2 k_2} a^{k_2}_{\ell_2 m_2} + n^{\nu_1\nu_2}_{LM},$$

with known noise covariance $\langle n^{\dagger\,\nu_1\nu_2}_{LM} n^{\nu'_1\nu'_2}_{LM}\rangle = N^{(0)\,\nu_1\nu_2\nu'_1\nu'_2}_L$, omitting the superscript (0) in the following text. Following directly from the calculations in [258], the expression, which is diagonal in harmonic space, is given by

$$N^{(0)\,\nu_1\nu_2\nu'_1\nu'_2}_L = \frac{A^{*\nu_1\nu_2}_L A^{\nu'_1\nu'_2}_L}{2L+1}\sum_{\ell_1\ell_2}\left(g^{*\nu_1\nu_2}_{\ell_1\ell_2}(L)\left(C^{\nu_1\nu'_1}_{\ell_1} C^{\nu_2\nu'_2}_{\ell_2} g^{\nu'_1\nu'_2}_{\ell_1\ell_2}(L) + (-1)^{L+\ell_1+\ell_2} C^{\nu_1\nu'_2}_{\ell_1} C^{\nu_2\nu'_1}_{\ell_2} g^{\nu'_1\nu'_2}_{\ell_2\ell_1}(L)\right)\right)$$

We write down a Gaussian likelihood as

$$-2\ln\mathcal{L} = -\frac{1}{2}\sum_{\nu_1\nu_2\nu'_1\nu'_2}\left(\hat{\phi}^{\nu_1\nu_2}_{LM} - \sum_{k_1k_2} A^{\nu_1 k_1} A^{\nu_2 k_2}\hat{\phi}^{k_1k_2}_{LM}\right)^\dagger \left(N^{-1}_L\right)^{\nu_1\nu_2,\nu'_1\nu'_2}\left(\hat{\phi}^{\nu'_1\nu'_2}_{LM} - \sum_{k_1k_2} A^{\nu'_1 k_1} A^{\nu'_2 k_2}\hat{\phi}^{k_1k_2}_{LM}\right),$$

following in the maximum likelihood estimator, given an estimate for $A^{\nu k}$,

$$\bar{\phi}^{k_1k_2}_{LM} = \sum_{k'_1k'_2}\left[\sum_{\nu_1\nu_2\nu'_1\nu'_2} A^{\nu_1 k_1} A^{\nu_2 k_2}\left(N^{-1}_L\right)^{\nu_1\nu_2,\nu'_1\nu'_2} A^{\nu'_1 k'_1} A^{\nu'_2 k'_2}\right]^{-1}\sum_{\nu_1\nu_2\nu'_1\nu'_2} A^{\nu_1 k'_1} A^{\nu_2 k'_2}\left(N^{-1}_L\right)^{\nu_1\nu_2,\nu'_1\nu'_2}\hat{\phi}^{\nu'_1\nu'_2}_{LM}.$$

The corresponding lensing noise is then given by

$$N^{(0)\,\text{comb.}}_L = \left[\left[\sum_{\nu_1\nu_2\nu'_1\nu'_2} A^{\nu_1 k_1} A^{\nu_2 k_2}\left(N^{-1}_L\right)^{\nu_1\nu_2,\nu'_1\nu'_2} A^{\nu'_1 k'_1} A^{\nu'_2 k'_2}\right]^{-1}\right]_{00}$$

Fig. C.1 depicts the noise curves of the quadratic estimator before components separation, of all multi-frequency quadratic combinations and cross-combinations and the final combinaed multi-frequency quadratic estimator cleaning noise. Fig. C.2 shows the relative degradation of noise using multi-frequency quadratic estimator cleaning.

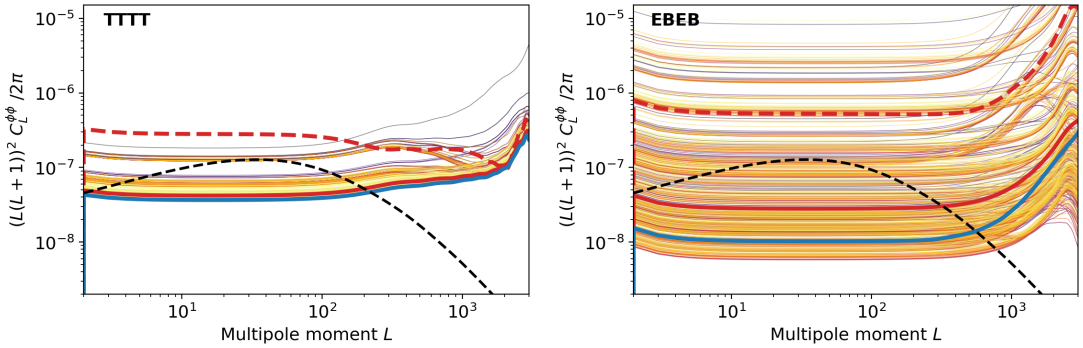

Figure C.1: Zero order noise comparison of different cleaning schemes. The blue curve is produced after linearly combining the I, Q & U single-frequency maps to subtract out galactic foreground emission, the red curve is obtained by combining the $N_{\rm freq} \times N_{\rm freq}$ cross-frequency quadratic estimators. The dashed red line is the result of using one frequency channel only once in the lensing power spectrum estimation. The other curves in the background are the single noise spectra of the $N_{\rm freq}^4$ frequency-channel combinations.

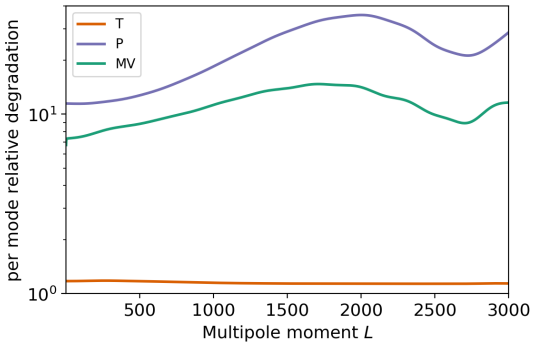

Figure C.2: Relative degradation of noise, comparing cross-frequency quadratic estimator cleaning with single-frequency map cleaning.

C.4 BIAS HARDENING AGAINST SPATIALLY VARYING SPECTRAL PARAMETERS

We allow the spectra parameters in our foreground frequency scaling laws to vary, as it is suggested to be the case in nature by recent Planck data. We split the spectral parameters of dust and synchrotron emission in constant and small spatially varying parts

$$\beta_d \to \beta_d + \delta\beta_d(\mathbf{x})$$

$$\beta_s \to \beta_s + \delta\beta_s(\mathbf{x}),$$

which allows us to write the mixing matrix as

$$A^{\nu i} \to A^{\nu i} + A^{\nu i}\delta A^i(\mathbf{x}),$$

with $\delta A^i(\mathbf{x}) = \log\left(\frac{\nu}{\nu_{\rm ref}}\right)\delta\beta^i(\mathbf{x})$, for $i = $ dust, sync.

For every frequency and component, the measured harmonic coefficients can be written as

$$a^{X\nu}_{\ell m} = a^{X\ \rm CMB}_{\ell m} + n^{X\nu}_{\ell m} + A^{\nu i}a^{Xi}_{\ell m} + A^{\nu i}\log\left(\frac{\nu}{\nu_{\rm ref}}\right)\int {}_XY^*_{\ell m}(\mathbf{x})\delta\beta^i(\mathbf{x}){}_YY_{\ell' m'}(\mathbf{x})d\Omega\, a^{Yi}_{\ell' m'}.$$

With the SHT of $\delta\beta^i(\mathbf{x}) = \sum_{LM}\delta\beta^i_{LM}Y_{LM}(\mathbf{x})$ the last term can be re-written as

$$\delta a^{X\nu}_{\ell m} = A^{\nu i}\log\left(\frac{\nu}{\nu_{\rm ref}}\right)(-1)^m \begin{pmatrix} \ell & \ell' & L \\ m & -m' & -M \end{pmatrix} {}_{s_X}H_{\ell L\ell'}\delta\beta^i_{LM}\left(\epsilon_{\ell L\ell'}a^{Xi}_{\ell' m'} + \beta_{\ell L\ell'}a^{\bar{X}i}_{\ell' m'}\right),$$

where

$${}_sH_{\ell L\ell'} = \sqrt{\frac{(2\ell+1)(2\ell'+1)(2L+1)}{4\pi}}\begin{pmatrix} \ell & L & \ell' \\ s & 0 & -s \end{pmatrix}. \tag{C.9}$$

The foreground-only two-point function can then be written as

$$\left\langle a^{X\nu_1\ \rm fg}_{\ell_1 m_1}a^{Y\nu_2\ \rm fg}_{\ell_2 m_2}\right\rangle = \delta_{\ell_1\ell_2}\delta_{m_1-m_2}(-1)^{m_1}A^{\nu_1 i}A^{\nu_2 j}C^{Xi Yj\ \rm fg}_{\ell_1} + (-1)^M\begin{pmatrix} \ell & \ell' & L \\ m & m' & -M \end{pmatrix}h^{X\nu_1 Y\nu_2\ i}_{\ell_1 L\ell_2}\delta\beta^i_{LM},$$

with

$$h^{X\nu_1 Y\nu_2\, i}_{\ell_1 L\ell_2} = \sum_j {}_{s_X}H_{\ell_1 L\ell_2}\log\left(\frac{\nu_1}{\nu_{\rm ref}}\right) A^{\nu_1 i}A^{\nu_2 j}\left(\epsilon_{\ell_1\ell_2 L}\tilde{C}^{XiYj}_{\ell_2} + \beta_{\ell_1\ell_2 L}\tilde{C}^{\bar{X}iYj}_{\ell_2}\right)$$
$$+ \ {}_{s_Y}H_{\ell_2 L\ell_1}\log\left(\frac{\nu_2}{\nu_{\rm ref}}\right) A^{\nu_1 j}A^{\nu_2 i}\left(\epsilon_{\ell_1\ell_2 L}\tilde{C}^{XjYi}_{\ell_1} - \beta_{\ell_1\ell_2 L}\tilde{C}^{Xj\bar{Y}i}_{\ell_1}\right),$$

which allows us to in principle write down the estimators for the spectral parameters

$$\hat{\delta\beta^i}^{XY}_{LM} = \frac{A^{XY}_L(h)}{L(L+1)}\sum_{\ell_1 m_1}\sum_{\ell_2 m_2}(-1)^M \begin{pmatrix} \ell_1 & \ell_2 & L \\ m_1 & m_2 & -M \end{pmatrix} g^{XY}_{\ell_1 L\ell_2}(h)\bar{a}^X_{\ell_1 m_1}\bar{a}^Y_{\ell_2 m_2},$$

with the same definitions as in the previous section, but replacing f with h. These quantities will appear in a lensing potential estimator as a mean-field, as well as the lensing potential will appear as a mean field in a spectral parameter estimation. Following the formalism introduced in Refs. [251, 252], we can formulate a bias-hardened estimator to alleviate this by defining the "transfer-functions"

$$A_L(x,y) = L(L+1)(2L+1)\left(\sum_{\ell_1\ell_2} g^*_{L\ell_1\ell_2}(x)y_{Ll_1l_2}\right)^{-1}$$

and

$$R_L(x,y) = \frac{A_L(x,x)}{A_L(x,y)},$$

such that one can write

$$\begin{pmatrix} \langle\hat{\phi}_{LM}\rangle \\ \langle\hat{\delta\beta}^i_{LM}\rangle \end{pmatrix} = \begin{pmatrix} R_L(f,f) & R_L(f,h^i) \\ R_L(h^i,f) & R_L(h^i,h^i) \end{pmatrix}\begin{pmatrix} \hat{\phi}_{LM} \\ \hat{\delta\beta}^i_{LM} \end{pmatrix} = \mathbf{R}_L(f,h^i)\begin{pmatrix} \hat{\phi}_{LM} \\ \hat{\delta\beta}^i_{LM} \end{pmatrix}.$$

The bias-hardened estimator can then be obtained by inverting a matrix for every multipole of size, in the case of two foreground components, 3×3

$$\begin{pmatrix} \hat{\phi}^{\rm BHE}_{LM} \\ \hat{\delta\beta}^{\rm BHE\ dust}_{LM} \\ \hat{\delta\beta}^{\rm BHE\ sync}_{LM} \end{pmatrix} = \mathbf{R}^{-1}_L \begin{pmatrix} \hat{\phi}_{LM} \\ \hat{\delta\beta}^{\rm dust}_{LM} \\ \hat{\delta\beta}^{\rm sync}_{LM} \end{pmatrix}.$$

Bibliography

[1] K. N. Abazajian, G. M. Fuller, and M. Patel "Sterile neutrino hot, warm, and cold dark matter" in: *Phys. Rev. D* 64:2 (May 2001), 023501 DOI: 10.1103/PhysRevD.64.023501 arXiv: astro-ph/0101524 (see p. 16).

[2] K. N. Abazajian et al. "CMB-S4 Science Book, First Edition" Oct. 2016 arXiv: 1610.02743 (see pp. 134, 136, 137, 193, 198).

[3] K. N. Abazajian et al. "CMB-S4 Science Case, Reference Design, and Project Plan" July 2019 arXiv: 1907.04473 (see pp. 134, 136).

[4] L. Ackerman, M. R. Buckley, S. M. Carroll, and M. Kamionkowski "Dark matter and dark radiation" in: *Phys. Rev. D* 79:2 (Jan. 2009), 023519 DOI: 10.1103/PhysRevD.79.023519 arXiv: 0810.5126 (see p. 16).

[5] P. A. R. Ade et al. "BICEP2 I: Detection Of B-mode Polarization at Degree Angular Scales" in: *Phys. Rev. Lett.* 112:24 (Mar. 2014), 241101 DOI: 10.1103/PhysRevLett.112.241101 arXiv: 1403.3985 (see pp. 103, 105).

[6] N. Aghanim, S. Majumdar, and J. Silk "Secondary anisotropies of the CMB" in: *Reports Prog. Phys.* 71:6 (June 2008), 066902 DOI: 10.1088/0034-4885/71/6/066902 arXiv: 0711.0518 (see p. 39).

[7] A. Aguilar-Arevalo et al. "The DAMIC dark matter experiment" Oct. 2015 arXiv: 1510.02126 (see p. 17).

[8] E. Akhmedov, G. Branco, and M. Rebelo "Seesaw mechanism and structure of neutrino mass matrix" in: *Phys. Lett. B* 478:1-3 (Apr. 2000), 215–223 DOI: 10.1016/S0370-2693(00)00282-3 arXiv: hep-ph/9911364 (see p. 12).

[9] A. Albrecht and P. J. Steinhardt "Cosmology for Grand Unified Theories with Radiatively Induced Symmetry Breaking" in: *Phys. Rev. Lett.* 48:17 (Apr. 1982), 1220–1223 DOI: 10.1103/PhysRevLett.48.1220 (see p. 31).

[10] Y. Ali-Haïmoud, C. M. Hirata, and C. Dickinson "A refined model for spinning dust radiation" in: *Mon. Not. R. Astron. Soc.* 395:2 (May 2009), 1055–1078 DOI: 10.1111/j.1365-2966.2009.14599.x arXiv: 0812.2904 (see p. 57).

[11] R. Allison, P. Caucal, E. Calabrese, J. Dunkley, and T. Louis "Towards a cosmological neutrino mass detection" in: *Phys. Rev. D* 92:12 (2015), 123535 DOI: 10.1103/PhysRevD.92.123535 arXiv: 1509.07471 (see pp. 39, 54, 165).

[12] R. A. Alpher, H. Bethe, and G. Gamow "The Origin of Chemical Elements" in: *Phys. Rev.* 73:7 (Apr. 1948), 803–804 DOI: 10.1103/PhysRev.73.803 (see p. 7).

[13] R. A. Alpher and R. C. Herman "On the Relative Abundance of the Elements" in: *Phys. Rev.* 74:12 (Dec. 1948), 1737–1742 DOI: 10.1103/PhysRev.74.1737 (see p. 7).

[14] R. A. Alpher and R. C. Herman "Remarks on the Evolution of the Expanding Universe" in: *Phys. Rev.* 75:7 (Apr. 1949), 1089–1095 DOI: 10.1103/PhysRev.75.1089 (see p. 7).

[15] L. Amendola et al. "Cosmology and Fundamental Physics with the Euclid Satellite" in: *Living Rev. Relativ.* 16:1 (Dec. 2013), 6 DOI: 10.12942/lrr-2013-6 arXiv: 1206.1225 (see p. 167).

[16] E. Anderes, B. Wandelt, and G. Lavaux "Bayesian inference of CMB gravitational lensing" in: *Astrophys. J.* 808:2 (Dec. 2014), 152 DOI: 10.1088/0004-637X/808/2/152 arXiv: 1412.4079 (see p. 94).

[17] E. Aprile et al. "XENONnT dark matter data analysis: Signal and background models and statistical inference" in: *Phys. Rev. D* 99:11, 112009 (June 2019), 112009 DOI: 10.1103/PhysRevD.99.112009 arXiv: 1902.11297 (see p. 17).

[18] M. Archidiacono, T. Brinckmann, J. Lesgourgues, and V. Poulin "Physical effects involved in the measurements of neutrino masses with future cosmological data" in: *J. Cosmol. Astropart. Phys.* 2017:02 (Feb. 2017), 052–052 DOI: 10.1088/1475-7516/2017/02/052 arXiv: 1610.09852 (see p. 163).

[19] E. Armengaud et al. "Performance of the EDELWEISS-III experiment for direct dark matter searches" in: *J. Instrum.* 12:8 (Aug. 2017), P08010 DOI: 10.1088/1748-0221/12/08/P08010 arXiv: 1706.01070 (see p. 17).

[20] V. N. Aseev et al. "Upper limit on the electron antineutrino mass from the Troitsk experiment" in: *Phys. Rev. D* 84:11 (Dec. 2011), 112003 DOI: 10.1103/PhysRevD.84.112003 arXiv: 1108.5034 (see p. 15).

[21] B. Audren, J. Lesgourgues, K. Benabed, and S. Prunet "Conservative Constraints on Early Cosmology: an illustration of the Monte Python cosmological parameter inference code" in: *J. Cosmol. Astropart. Phys.* 2013:02 (), 001–001 DOI: 10.1088/1475-7516/2013/02/001 arXiv: 1210.7183 (see p. 161).

[22] J. Aumont et al. "Measurement of the Crab nebula polarization at 90 GHz as a calibrator for CMB experiments" in: *Astron. Astrophys. Vol. 514, id.A70, 8 pp.* 514: (Dec. 2009) DOI: 10.1051/0004-6361/200913834 arXiv: 0912.1751 (see pp. iii, 123).

[23] J. M. Bardeen "Gauge-invariant cosmological perturbations" in: *Phys. Rev. D* 22:8 (Oct. 1980), 1882–1905 DOI: 10.1103/PhysRevD.22.1882 (see pp. 33, 35).

[24] D. Barron et al. "Optimization study for the experimental configuration of CMB-S4" in: *J. Cosmol. Astropart. Phys.* 2018:02 (Feb. 2018), 009–009 DOI: 10.1088/1475-7516/2018/02/009 arXiv: 1702.07467 (see p. 132).

[25] M. Bartelmann and P. Schneider "Weak gravitational lensing" in: *Phys. Rep.* 340:4-5 (Jan. 2001), 291–472 DOI: 10.1016/S0370-1573(00)00082-X arXiv: astro-ph/9912508 (see p. 45).

[26] N. Bartolo, V. De Luca, G. Franciolini, A. Lewis, M. Peloso, and A. Riotto "The Primordial Black Hole Dark Matter - LISA Serendipity" in: *Phys. Rev. Lett.* 122:21 (Oct. 2018), 211301 DOI: 10.1103/PhysRevLett.122.211301 arXiv: 1810.12218 (see p. 18).

[27] B. A. Bassett, S. Tsujikawa, and D. Wands "Inflation dynamics and reheating" in: *Rev. Mod. Phys.* 78:2 (May 2006), 537–589 DOI: 10.1103/RevModPhys.78.537 arXiv: astro-ph/0507632 (see p. 32).

[28] L. Baudis "The Search for Dark Matter" in: *Eur. Rev.* 26:1 (Feb. 2018), 70–81 DOI: 10.1017/S1062798717000783 arXiv: 1801.08128 (see p. 17).

[29] D. Baumann "Cosmology Lecture Notes" July 2018 URL: http://cosmology.amsterdam/education/cosmology/ (visited on 05/31/2019) (see pp. 2, 18, 19, 23, 24).

[30] D. Baumann "TASI Lectures on Inflation" July 2009 arXiv: 0907.5424 (see pp. 2, 8, 32, 35).

[31] D. Baumann, D. Green, and B. Wallisch "New Target for Cosmic Axion Searches" in: *Phys. Rev. Lett.* 117:17 (Oct. 2016), 171301 DOI: 10.1103/PhysRevLett.117.171301 arXiv: 1604.08614 (see p. 16).

[32] D. Beck, J. Errard, and R. Stompor "Diffuse polarized foregrounds contamination to gravitational lensing reconstruction" in: *Prep.* (2019) (see pp. v, 171).

[33] D. Beck, G. Fabbian, and J. Errard "Lensing reconstruction in post-Born cosmic microwave background weak lensing" in: *Phys. Rev. D* 98:4 (Aug. 2018), 043512 DOI: 10.1103/PhysRevD.98.043512 arXiv: 1806.01216 (see pp. v, 137, 140, 174).

[34] D. Beck et al. "Latest results, current data-analysis and upcoming upgrades of the Polarbear/Simons Array experiments" in: *53rd Rencontres Moriond* Aug. 2018, 7 (see pp. v, 101).

[35] M. R. Becker "calclens: weak lensing simulations for large-area sky surveys and second-order effects in cosmic shear power spectra" in: *Mon. Not. R. Astron. Soc.* 435:1 (Oct. 2013), 115–132 DOI: 10.1093/mnras/stt1352 arXiv: 1210.3069 (see p. 138).

[36] A. N. Bender et al. "Year two instrument status of the SPT-3G cosmic microwave background receiver" in: *Millimeter, Submillimeter, Far-Infrared Detect. Instrum. Astron. IX* (Aug. 2018) ed. by J. Zmuidzinas and J.-R. Gao, 2 DOI: 10.1117/12.2312426 arXiv: 1809.00036 (see p. 104).

[37] C. L. Bennett et al. "Nine-Year Wilkinson Microwave Anisotropy Probe (WMAP) Observations: Final Maps and Results" in: *Astrophys. J. Suppl. Ser.* 208:2 (Dec. 2012), 20 DOI: 10.1088/0067-0049/208/2/20 arXiv: 1212.5225 (see p. 177).

[38] C. L. Bennett et al. "The Microwave Anisotropy Probe (MAP) Mission" in: *Astrophys. Journal, Vol. 583, Issue 1, pp. 1-23.* 583: (Jan. 2003), 1–23 DOI: 10.1086/345346 arXiv: astro-ph/0301158 (see p. 102).

[39] A. Benoit-Lévy, T. Déchelette, K. Benabed, J.-F. Cardoso, D. Hanson, and S. Prunet "Full-sky CMB lensing reconstruction in presence of sky-cuts" in: *Astron. Astrophys.* 555: (Jan. 2013), 37 DOI: 10.1051/0004-6361/201321048 arXiv: 1301.4145 (see p. 76).

[40] A. Benoit-Lévy, K. M. Smith, and W. Hu "Non-Gaussian structure of the lensed CMB power spectra covariance matrix" in: *Phys. Rev. D* 86:12 (Dec. 2012), 123008 DOI: 10.1103/PhysRevD.86.123008 arXiv: 1205.0474 (see pp. 76, 161).

[41] A. Benoît et al. "The cosmic microwave background anisotropy power spectrum measured by Archeops" in: *Astron. Astrophys.* 399:3 (Mar. 2003), L19–L23 DOI: 10.1051/0004-6361:20021850 arXiv: astro-ph/0210305 (see p. 101).

[42] B. A. Benson et al. "SPT-3G: a next-generation cosmic microwave background polarization experiment on the South Pole telescope" in: *Proc. SPIE* ed. by W. S. Holland and J. Zmuidzinas July 2014, 91531P DOI: 10.1117/12.2057305 arXiv: 1407.2973 (see p. 104).

[43] F. Bernardeau, S. Colombi, E. Gaztañaga, and R. Scoccimarro "Large-scale structure of the Universe and cosmological perturbation theory" in: *Phys. Rep.* 367:1-3 (Sept. 2002), 1–248 DOI: 10.1016/S0370-1573(02)00135-7 arXiv: astro-ph/0112551 (see pp. 40, 41, 145).

[44] P. de Bernardis et al. "A flat Universe from high-resolution maps of the cosmic microwave background radiation" in: *Nature* 404:6781 (Apr. 2000), 955–959 DOI: 10.1038/35010035 (see p. 101).

[45] P. de Bernardis et al. "Multiple Peaks in the Angular Power Spectrum of the Cosmic Microwave Background: Significance and Consequences for Cosmology" in: *Astrophys. J.* 564:2 (Jan. 2002), 559–566 DOI: 10.1086/324298 arXiv: astro-ph/0105296 (see p. 102).

[46] F. Bezrukov and M. Shaposhnikov "The Standard Model Higgs boson as the inflaton" in: *Phys. Lett. B* 659:3 (Jan. 2008), 703–706 DOI: 10.1016/j.physletb.2007.11.072 arXiv: 0710.3755 (see p. 33).

[47] Blaise Barney "Introduction to Parallel Computing" URL: https://computing.llnl.gov/tutorials/parallel%7B%5C_%7Dcomp/ (visited on 06/18/2019) (see p. 81).

[48] V. Böhm, M. Schmittfull, and B. D. Sherwin "Bias to CMB lensing measurements from the bispectrum of large-scale structure" in: *Phys. Rev. D* 94:4 (Aug. 2016), 043519 DOI: 10.1103/PhysRevD.94.043519 arXiv: 1605.01392 (see pp. 138–140, 150, 154, 155, 170).

[49] V. Böhm, B. D. Sherwin, J. Liu, J. C. Hill, M. Schmittfull, and T. Namikawa "Effect of non-Gaussian lensing deflections on CMB lensing measurements" in: *Phys. Rev. D* 98:12 (Dec. 2018), 123510 DOI: 10.1103/PhysRevD.98.123510 arXiv: 1806.01157 (see pp. 140, 150, 170, 174).

[50] S. Borsanyi et al. "Calculation of the axion mass based on high-temperature lattice quantum chromodynamics" in: *Nature* 539:7627 (Nov. 2016), 69–71 DOI: 10.1038/nature20115 arXiv: 1606.07494 (see p. 11).

[51] A. Bosma "21-cm line studies of spiral galaxies. II. The distribution and kinematics of neutral hydrogen in spiral galaxies of various morphological types." in: *Astron. J.* 86: (Dec. 1981), 1825–1846 DOI: 10.1086/113063 (see p. 1).

[52] S. Bridle and L. King "Dark energy constraints from cosmic shear power spectra: impact of intrinsic alignments on photometric redshift requirements" in: *New J. Phys.* 9:12 (Dec. 2007), 444–444 DOI: 10.1088/1367-2630/9/12/444 arXiv: 0705.0166 (see pp. 50, 166).

[53] T. Brinckmann and J. Lesgourgues "MontePython 3: boosted MCMC sampler and other features" Apr. 2018 arXiv: 1804.07261 (see p. 161).

[54] A. G. A. Brown et al. "Gaia Data Release 2" in: *Astron. Astrophys.* 616: (Aug. 2018), A1 DOI: 10.1051/0004-6361/201833051 (see p. 131).

[55] L. M. Brown "The idea of the neutrino" in: *Phys. Today* 31:9 (Sept. 1978), 23–28 DOI: 10.1063/1.2995181 (see p. 12).

[56] G. Brussaard and P. A. Watson "Atmospheric modelling and millimetre wave propagation" 1st ed. Springer Netherlands, 1995, 329 (see p. 130).

[57] E. Calabrese, D. Alonso, and J. Dunkley "Complementing the ground-based CMB-S4 experiment on large scales with the PIXIE satellite" in: *Phys. Rev. D* 95:6 (Mar. 2017), 063504 DOI: 10.1103/PhysRevD.95.063504 arXiv: 1611.10269 (see p. 165).

[58] M. Calabrese, C. Carbone, G. Fabbian, M. Baldi, and C. Baccigalupi "Multiple lensing of the cosmic microwave background anisotropies" in: *J. Cosmol. Astropart. Phys.* 2015:03 (Mar. 2015), 049–049 DOI: 10.1088/1475-7516/2015/03/049 arXiv: 1409.7680 (see pp. 141, 142).

[59] F. Capozzi, E. Di Valentino, E. Lisi, A. Marrone, A. Melchiorri, and A. Palazzo "Global constraints on absolute neutrino masses and their ordering" in: *Phys. Rev. D* 95:9 (May 2017), 096014 DOI: 10.1103/PhysRevD.95.096014 arXiv: 1703.04471 (see p. 14).

[60] C. Carbone, C. Baccigalupi, M. Bartelmann, S. Matarrese, and V. Springel "Lensed CMB temperature and polarization maps from the Millennium Simulation" in: *Mon. Not. R. Astron. Soc.* 396:2 (June 2009), 668–679 DOI: 10.1111/j.1365-2966.2009.14746.x arXiv: 0810.4145 (see p. 138).

[61] C. Carbone, M. Petkova, and K. Dolag "DEMNUni: ISW, Rees-Sciama, and weak-lensing in the presence of massive neutrinos" in: *J. Cosmol. Astropart. Phys.* 2016:07 (July 2016), 034–034 DOI: 10.1088/1475-7516/2016/07/034 arXiv: 1605.02024 (see p. 140).

[62] C. Carbone, V. Springel, C. Baccigalupi, M. Bartelmann, and S. Matarrese "Full-sky maps for gravitational lensing of the cosmic microwave background" in: *Mon. Not. R. Astron. Soc.* 388:4 (Aug. 2008), 1618–1626 DOI: 10.1111/j.1365-2966.2008.13544.x arXiv: 0711.2655 (see pp. 138, 141).

[63] B. Carr "Primordial black holes as dark matter and generators of cosmic structure" Jan. 2019 arXiv: 1901.07803 (see p. 18).

[64] E. Carretti et al. "S-band Polarization All Sky Survey (S-PASS): survey description and maps" Mar. 2019 arXiv: 1903.09420 (see p. 57).

[65] J. Carron "Optimal constraints on primordial gravitational waves from the lensed CMB" in: *Phys. Rev. D* 99:4 (Feb. 2019), 043518 DOI: 10.1103/PhysRevD.99.043518 arXiv: 1808.10349 (see p. 193).

[66] J. Carron and A. Lewis "Maximum a posteriori CMB lensing reconstruction" in: *Phys. Rev. D* 96:6 (2017), 063510 DOI: 10.1103/PhysRevD.96.063510 arXiv: 1704.08230 (see pp. 63, 66, 94, 108, 170).

[67] J. Carron, A. Lewis, and A. Challinor "Internal delensing of Planck CMB temperature and polarization" in: *J. Cosmol. Astropart. Phys.* 2017:05 (May 2017), 035–035 DOI: 10.1088/1475-7516/2017/05/035 arXiv: 1701.01712 (see pp. 94, 99, 181).

[68] E. Castorina, C. Carbone, J. Bel, E. Sefusatti, and K. Dolag "DEMNUni: the clustering of large-scale structures in the presence of massive neutrinos" in: *J. Cosmol. Astropart. Phys.* 2015:07 (July 2015), 043–043 DOI: 10.1088/1475-7516/2015/07/043 arXiv: 1505.07148 (see p. 140).

[69] T. Castro, M. Quartin, C. Giocoli, S. Borgani, and K. Dolag "The effect of baryons in the cosmological lensing PDFs" in: *Mon. Not. R. Astron. Soc.* 478:1 (July 2018), 1305–1325 DOI: 10.1093/mnras/sty1117 arXiv: 1711.10017 (see p. 151).

[70] P. Catelan, M. Kamionkowski, and R. D. Blandford "Intrinsic and extrinsic galaxy alignment" in: *Mon. Not. R. Astron. Soc.* 320:1 (Jan. 2001), L7–L13 DOI: 10.1046/j.1365-8711.2001.04105.x arXiv: astro-ph/0005470 (see p. 50).

[71] S. Chabanier, M. Millea, and N. Palanque-Delabrouille "Updated matter power spectrum constraints from the Lyα forest and other probes" May 2019 arXiv: 1905.08103 (see pp. 48, 49).

[72] A. Challinor and A. Lewis "Lensed CMB power spectra from all-sky correlation functions" in: *Phys. Rev. D* 71:10 (May 2005), 103010 DOI: 10.1103/PhysRevD.71.103010 arXiv: astro-ph/0502425 (see p. 48).

[73] A. Challinor et al. "Exploring cosmic origins with CORE: Gravitational lensing of the CMB" in: *J. Cosmol. Astropart. Phys.* 2018:04 (Apr. 2018), 018–018 DOI: 10.1088/1475-7516/2018/04/018 arXiv: 1707.02259 (see pp. 124, 182).

[74] C. Cheung, A. L. Fitzpatrick, J. Kaplan, L. Senatore, and P. Creminelli "The effective field theory of inflation" in: *J. High Energy Phys.* 2008:03 (Mar. 2008), 014–014 DOI: 10.1088/1126-6708/2008/03/014 arXiv: 0709.0293v2 (see pp. 34, 35).

[75] M. Chevallier and D. Polarski "Accelerating Universes with Scaling Dark Matter" in: *Int. J. Mod. Phys. D* 10:02 (Sept. 2000), 213–223 DOI: 10.1142/S0218271801000822 arXiv: gr-qc/0009008 (see p. 22).

[76] H. C. Chiang et al. "Measurement of Cosmic Microwave Background Polarization Power Spectra from Two Years of BICEP Data" in: *Astrophys. J.* 711: (June 2009), 1123–1140 DOI: 10.1088/0004-637X/711/2/1123 arXiv: 0906.1181 (see p. 114).

[77] N. E. Chisari, J. Dunkley, L. Miller, and R. Allison "Contamination of early-type galaxy alignments to galaxy lensing–CMB lensing cross-correlation" in: *Mon. Not. R. Astron. Soc.* 453:1 (Oct. 2015), 682–689 DOI: 10.1093/mnras/stv1655 arXiv: 1507.03906 (see p. 166).

[78] N. E. Chisari et al. "Core Cosmology Library: Precision Cosmological Predictions for LSST" in: *Astrophys. J. Suppl. Ser.* 242:1 (Dec. 2018), 2 DOI: 10.3847/1538-4365/ab1658 arXiv: 1812.05995 (see p. 167).

[79] J. Chluba "Science with CMB spectral distortions" May 2014 arXiv: 1405.6938 (see p. 20).

[80] D. Chowdhury, J. Martin, C. Ringeval, and V. Vennin "Inflation after Planck: Judgment Day" Feb. 2019 arXiv: 1902.03951 (see p. 33).

[81] J. M. Cline "Baryogenesis" Sept. 2006 arXiv: hep-ph/0609145 (see p. 12).

[82] T. P. Collaboration et al. "Cross-correlation of POLARBEAR CMB Polarization Lensing with High-z Sub-mm Herschel-ATLAS galaxies" Mar. 2019 arXiv: 1903.07046 (see pp. v, 101, 108).

[83] M. Compiègne, L. Verstraete, A. Jones, J.-P. Bernard, F. Boulanger, N. Flagey, J. Le Bourlot, D. Paradis, and N. Ysard "The global dust SED: tracing the nature and evolution of dust with DustEM" in: *Astron. Astrophys.* 525: (Jan. 2011), A103 DOI: 10.1051/0004-6361/201015292 arXiv: 1010.2769 (see p. 58).

[84] J. J. Condon, W. D. Cotton, E. W. Greisen, Q. F. Yin, R. A. Perley, G. B. Taylor, and J. J. Broderick "The NRAO VLA Sky Survey" in: *Astron. J.* 115:5 (May 1998), 1693–1716 DOI: 10.1086/300337 (see pp. 124, 127, 131).

[85] A. Cooray and W. Hu "Second-Order Corrections to Weak Lensing by Large-Scale Structure" in: *Astrophys. J.* 574:1 (July 2002), 19–23 DOI: 10.1086/340892 arXiv: astro-ph/0202411 (see pp. 122, 138, 139).

[86] A. Cooray, M. Kamionkowski, and R. R. Caldwell "Cosmic shear of the microwave background: The curl diagnostic" in: *Phys. Rev. D* 71:12 (June 2005), 123527 DOI: 10.1103/PhysRevD.71.123527 arXiv: astro-ph/0503002 (see p. 122).

[87] "Cori Configuration" URL: https://www.nersc.gov/users/computational-systems/cori/configuration/ (visited on 06/18/2019) (see p. 83).

[88] W. R. Coulton and D. N. Spergel "The bispectrum of polarized galactic foregrounds" Jan. 2019 arXiv: 1901.04515 (see p. 171).

[89] L. Danese and G. de Zotti "Double Compton process and the spectrum of the microwave background" in: *Astron. Astrophys.* 107: (1982), 39–42 (see p. 20).

[90] S. Das and P. Bode "A Large Sky Simulation of the Gravitational Lensing of the Cosmic Microwave Background" in: *Astrophys. J.* 682:1 (July 2008), 1–13 DOI: 10.1086/589638 arXiv: 0711.3793 (see pp. 44, 141, 142).

[91] S. Das, J. Errard, and D. Spergel "Can CMB Lensing Help Cosmic Shear Surveys?" Nov. 2013 arXiv: 1311.2338 (see p. 50).

[92] S. Das et al. "Detection of the Power Spectrum of Cosmic Microwave Background Lensing by the Atacama Cosmology Telescope" in: *Phys. Rev. Lett.* 107:2 (2011), 021301 DOI: 10.1103/PhysRevLett.107.021301 arXiv: 1103.2124 (see p. 103).

[93] J. Davis Leverett and J. L. Greenstein "The Polarization of Starlight by Aligned Dust Grains." in: *Astrophys. J.* 114: (Sept. 1951), 206 DOI: 10.1086/145464 (see p. 58).

[94] V. Desjacques, D. Jeong, and F. Schmidt "Large-scale galaxy bias" in: *Phys. Rep.* 733: (Feb. 2018), 1–193 DOI: 10.1016/j.physrep.2017.12.002 arXiv: 1611.09787 (see p. 51).

[95] C. Dickinson "CMB foregrounds - A brief review" in: *52nd Rencontres Moriond* June 2016 arXiv: 1606.03606 (see p. 60).

[96] B. Dober et al. "Microwave SQUID multiplexer demonstration for cosmic microwave background imagers" in: *Appl. Phys. Lett.* 111:24 (Dec. 2017), 243510 DOI: 10.1063/1.5008527 (see p. 134).

[97] S. Dodelson "Modern Cosmology" Amsterdam: Academic Press, 2003 (see pp. 8, 9, 19, 21, 25, 36).

[98] A. Dolgov "Neutrinos in cosmology" in: *Phys. Rep.* 370:4-5 (Nov. 2002), 333–535 DOI: 10.1016/S0370-1573(02)00139-4 arXiv: hep-ph/0202122 (see p. 16).

[99] B. T. Draine "Physics of the Interstellar and Intergalactic Medium" Princeton: Princeton University Press, 2011 (see p. 57).

[100] B. T. Draine and A. Lazarian "Electric Dipole Radiation from Spinning Dust Grains" in: *Astrophys. J.* 508:1 (Nov. 1998), 157–179 DOI: 10.1086/306387 arXiv: astro-ph/9802239 (see p. 57).

[101] B. Draine "Interstellar Dust Models: Extinction, Absorption and Emission" in: *EAS Publ. Ser.* 35: (Feb. 2009), 245–268 DOI: 10.1051/eas/0935013 (see pp. 57, 58).

[102] L. Dunne et al. "Herschel-ATLAS: Rapid evolution of dust in galaxies in the last 5 billion years" in: *Mon. Not. R. Astron. Soc.* 417:2 (Dec. 2010), 1510–1533 DOI: 10.1111/j.1365-2966.2011.19363.x arXiv: 1012.5186 (see p. 108).

[103] "Edison Configuration" URL: https://www.nersc.gov/users/computational-systems/retired-systems/edison-retired-on-5132019/configuration/ (visited on 06/18/2019) (see p. 83).

[104] A. Einstein "Cosmological Considerations in the General Theory of Relativity" in: *Sitzungsber. Preuss. Akad. Wiss. Berlin (Math. Phys.)* 1917: (1917), 142–152 (see p. 22).

[105] S. R. Elliott and P. Vogel "Double Beta Decay" in: *Annu. Rev. Nucl. Part. Sci.* 52:1 (Feb. 2002), 115–151 DOI: 10.1146/annurev.nucl.52.050102.090641 arXiv: hep-ph/0202264 (see p. 15).

[106] F. Elsner and B. D. Wandelt "Efficient Wiener filtering without preconditioning" in: *Astron. Astrophys.* 549: (Jan. 2013), A111 DOI: 10.1051/0004-6361/201220586 arXiv: 1210.4931 (see p. 85).

[107] A. van Engelen, S. Bhattacharya, N. Sehgal, G. P. Holder, O. Zahn, and D. Nagai "CMB Lensing Power Spectrum Biases from Galaxies and Clusters using High-angular Resolution Temperature Maps" in: *Astrophys. J.* 786:1 (Oct. 2013), 13 DOI: 10.1088/0004-637X/786/1/13 arXiv: 1310.7023 (see pp. 124, 170, 174).

[108] J. Errard "A hunt for cosmic microwave background B-modes in the sytematic contaminants jungle" PhD thesis Jan. 2012 (see p. 130).

[109] J. Errard, S. M. Feeney, H. V. Peiris, and A. H. Jaffe "Robust forecasts on fundamental physics from the foreground-obscured, gravitationally-lensed CMB polarization" in: *J. Cosmol. Astropart. Phys.* 2016:03 (Sept. 2015), 052–052 DOI: 10.1088/1475-7516/2016/03/052 arXiv: 1509.06770 (see pp. 89, 91, 132, 171, 182, 193).

[110] J. Errard and R. Stompor "Astrophysical foregrounds and primordial tensor-to-scalar ratio constraints from CMB B-mode polarization observations" in: *Phys. Rev. D* 85:8 (Mar. 2012), 083006 DOI: 10.1103/PhysRevD.85.083006 arXiv: 1203.5285 (see p. 91).

[111] J. Errard and R. Stompor "Characterizing bias on large scale CMB B-modes after galactic foregrounds cleaning" in: *Phys. Rev. D* 99:4 (Nov. 2018), 043529 DOI: 10.1103/PhysRevD.99.043529 arXiv: 1811.00479 (see pp. 171, 188, 193).

[112] G. Fabbian "Modeling and measuring the weak lensing of CMB polarization in current and future ground-based experiments" PhD thesis Jan. 2013 (see p. 126).

[113] G. Fabbian, M. Calabrese, and C. Carbone "CMB weak-lensing beyond the Born approximation: a numerical approach" in: *J. Cosmol. Astropart. Phys.* 2018:02 (Feb. 2018), 050–050 DOI: 10.1088/1475-7516/2018/02/050 arXiv: 1702.03317 (see pp. 138–140, 142, 145, 147).

[114] G. Fabbian, A. Lewis, and D. Beck "CMB lensing reconstruction biases in cross-correlation with large-scale structure probes" June 2019 arXiv: 1906.08760 (see pp. v, 67, 137, 140, 142, 143, 154–156, 166, 170, 174).

[115] G. Fabbian and R. Stompor "High-precision simulations of the weak lensing effect on cosmic microwave background polarization" in: *Astron. Astrophys.* 556: (Aug. 2013), A109 DOI: 10.1051/0004-6361/201321575 arXiv: 1303.6550 (see pp. 147, 178).

[116] Y. Fantaye, C. Baccigalupi, S. Leach, and A. Yadav "CMB lensing reconstruction in the presence of diffuse polarized foregrounds" in: *J. Cosmol. Astropart. Phys.* 2012:12 (Dec. 2012), 017–017 DOI: 10.1088/1475-7516/2012/12/017 arXiv: 1207.0508 (see pp. 124, 174, 182).

[117] C. Feng and G. Holder "Polarization of the Cosmic Infrared Background Fluctuations" July 2019 arXiv: 1907.12085 (see p. 60).

[118] S. Ferraro and J. C. Hill "Bias to CMB lensing reconstruction from temperature anisotropies due to large-scale galaxy motions" in: *Phys. Rev. D* 97:2 (Jan. 2018), 023512 DOI: 10.1103/PhysRevD.97.023512 arXiv: 1705.06751 (see pp. 124, 170, 174).

[119] D. J. Fixsen "The Temperature of the Cosmic Microwave Background" in: *Astrophys. J.* 707:2 (Nov. 2008), 916–920 DOI: 10.1088/0004-637X/707/2/916 arXiv: 0911.1955 (see p. 22).

[120] D. J. Fixsen, E. S. Cheng, J. M. Gales, J. C. Mather, R. A. Shafer, and E. L. Wright "The Cosmic Microwave Background Spectrum from the Full COBE FIRAS Data Set" in: *Astrophys. J.* 473:2 (Dec. 1996), 576–587 DOI: 10.1086/178173 (see p. 22).

[121] D. J. Fixsen et al. "Cosmic microwave background dipole spectrum measured by the COBE FIRAS instrument" in: *Astrophys. J.* 420: (Jan. 1994), 445 DOI: 10.1086/173575 (see p. 101).

[122] R. Flauger, J. C. Hill, and D. N. Spergel "Toward an understanding of foreground emission in the BICEP2 region" in: *J. Cosmol. Astropart. Phys.* 2014:08 (Aug. 2014), 039–039 DOI: 10.1088/1475-7516/2014/08/039 arXiv: 1405.7351 (see p. 103).

[123] P. Fosalba, E. Gaztañaga, F. J. Castander, and M. Manera "The onion universe: all sky light-cone simulations in spherical shells" in: *Mon. Not. R. Astron. Soc.* 391:1 (Nov. 2008), 435–446 DOI: 10.1111/j.1365-2966.2008.13910.x arXiv: 0711.1540 (see p. 141).

[124] C. Frenk and S. White "Dark matter and cosmic structure" in: *Ann. Phys.* 524:9-10 (Oct. 2012), 507–534 DOI: 10.1002/andp.201200212 arXiv: 1210.0544 (see pp. 17, 18).

[125] A. Gabrielli, F. Sylos Labini, M. Joyce, and L. Pietronero "Statistical physics for cosmic structures" 1st ed. Berlin, Heidelberg: Springer, 2005, 424 (see p. 5).

[126] G. Gamow "Expanding Universe and the Origin of Elements" in: *Phys. Rev.* 70:7-8 (Oct. 1946), 572–573 DOI: 10.1103/PhysRev.70.572.2 (see p. 7).

[127] A. Gando et al. "Search for Majorana Neutrinos Near the Inverted Mass Hierarchy Region with KamLAND-Zen" in: *Phys. Rev. Lett.* 117:8 (Aug. 2016), 082503 DOI: 10.1103/PhysRevLett.117.082503 arXiv: 1605.02889 (see p. 15).

[128] "GeForce RTX 2080 Ti Graphics Card | NVIDIA" URL: https://www.nvidia.com/en-us/geforce/graphics-cards/rtx-2080-ti/ (visited on 06/18/2019) (see p. 81).

[129] H. Gil-Marín, C. Wagner, F. Fragkoudi, R. Jimenez, and L. Verde "An improved fitting formula for the dark matter bispectrum" in: *J. Cosmol. Astropart. Phys.* 2012:02 (Feb. 2012), 047–047 DOI: 10.1088/1475-7516/2012/02/047 arXiv: 1111.4477 (see pp. 42, 146, 154, 156).

[130] J. N. Goldberg, A. J. Macfarlane, E. T. Newman, F. Rohrlich, and E. C. G. Sudarshan "Spin-s Spherical Harmonics and ð" in: *J. Math. Phys.* 8:11 (Nov. 1967), 2155–2161 DOI: 10.1063/1.1705135 (see p. 27).

[131] M. H. Goroff, B. Grinstein, S.-J. Rey, and M. B. Wise "Coupling of modes of cosmological mass density fluctuations" in: *Astrophys. J.* 311: (Dec. 1986), 6 DOI: 10.1086/164749 (see p. 41).

[132] K. M. Gorski, E. Hivon, A. J. Banday, B. D. Wandelt, F. K. Hansen, M. Reinecke, and M. Bartelmann "HEALPix: A Framework for High-Resolution Discretization and Fast Analysis of Data Distributed on the Sphere" in: *Astrophys. J.* 622:2 (Apr. 2005), 759–771 DOI: 10.1086/427976 arXiv: astro-ph/0409513 (see pp. 81, 113).

[133] J. Grain, M. Tristram, and R. Stompor "CMB EB and TB cross-spectrum estimation via pseudospectrum techniques" in: *Phys. Rev. D* 86:7 (Oct. 2012), 076005 DOI: 10.1103/PhysRevD.86.076005 arXiv: 1207.5344 (see pp. 99, 118).

[134] J. Grain, M. Tristram, and R. Stompor "Polarized CMB power spectrum estimation using the pure pseudo-cross-spectrum approach" in: *Phys. Rev. D* 79:12 (June 2009), 123515 DOI: 10.1103/PhysRevD.79.123515 arXiv: 0903.2350 (see pp. 99, 118, 177, 180).

[135] A. Greve, J. .-.-F. Panis, and C. Thum "The pointing of the IRAM 30-m telescope." in: *Astron. Astrophys. Suppl.* 115: (Feb. 1996), 379 DOI: 1996A&AS..115..379G (see pp. 127, 130).

[136] Q. Guo et al. "Which halos host Herschel-ATLAS galaxies in the local Universe?" in: *Mon. Not. R. Astron. Soc.* 412:4 (Nov. 2010), 2277–2285 DOI: 10.1111/j.1365-2966.2010.18051.x arXiv: 1011.3048 (see p. 108).

[137] A. H. Guth "Inflationary universe: A possible solution to the horizon and flatness problems" in: *Phys. Rev. D* 23:2 (Jan. 1981), 347–356 DOI: 10.1103/PhysRevD.23.347 (see p. 31).

[138] S. Hagstotz, B. M. Schäfer, and P. M. Merkel "Born-corrections to weak lensing of the cosmic microwave background temperature and polarisation anisotropies" in: *Mon. Not. R. Astron. Soc.* 454:1 (Oct. 2014), 831–838 DOI: 10.1093/mnras/stv1977 arXiv: 1410.8452 (see p. 138).

[139] A. Hall and A. Taylor "Intrinsic alignments in the cross-correlation of cosmic shear and CMB weak lensing" in: *Mon. Not. R. Astron. Soc. Lett.* 443:1 (Jan. 2014), L119–L123 DOI: 10.1093/mnrasl/slu094 arXiv: 1401.6018 (see pp. 39, 166).

[140] N. W. Halverson et al. "DASI First Results: A Measurement of the Cosmic Microwave Background Angular Power Spectrum" in: *Astrophys. J.* 568:1 (Apr. 2001), 38–45 DOI: 10.1086/338879 arXiv: astro-ph/0104489 (see p. 102).

[141] T. Hamana and Y. Mellier "Numerical study of the statistical properties of the lensing excursion angles" in: *Mon. Not. R. Astron. Soc.* 327:1 (Oct. 2001), 169–176 DOI: 10.1046/j.1365-8711.2001.04685.x arXiv: astro-ph/0101333 (see p. 141).

[142] S. Hamimeche and A. Lewis "Likelihood analysis of CMB temperature and polarization power spectra" in: *Phys. Rev. D* 77:10 (May 2008), 103013 DOI: 10.1103/PhysRevD.77.103013 arXiv: 0801.0554 (see p. 193).

[143] S. Hanany et al. "MAXIMA-1: A Measurement of the Cosmic Microwave Background Anisotropy on Angular Scales of 10[arcmin]–5°" in: *Astrophys. J.* 545:1 (Dec. 2000), L5–L9 DOI: 10.1086/317322 arXiv: astro-ph/0005123 (see p. 101).

[144] N. Hand et al. "Evidence of Galaxy Cluster Motions with the Kinematic Sunyaev-Zel'dovich Effect" in: *Phys. Rev. Lett.* 109:4 (July 2012), 041101 DOI: 10.1103/PhysRevLett.109.041101 arXiv: 1203.4219 (see pp. 51, 103).

[145] D. Hanson, A. Challinor, G. Efstathiou, and P. Bielewicz "CMB temperature lensing power reconstruction" in: *Phys. Rev. D* 83:4 (Feb. 2011), 043005 DOI: 10.1103/PhysRevD.83.043005 arXiv: 1008.4403 (see pp. 67, 71–75, 201).

[146] J. Harnois-Déraps et al. "CFHTLenS and RCSLenS Cross-Correlation with Planck Lensing Detected in Fourier and Configuration Space" in: *Mon. Not. R. Astron. Soc. Vol. 460, Issue 1, p.434-457* 460: (Mar. 2016), 434–457 DOI: 10.1093/mnras/stw947 arXiv: 1603.07723 (see p. 51).

[147] J. Harnois-Déraps et al. "KiDS-450: Tomographic Cross-Correlation of Galaxy Shear with {\it Planck} Lensing" in: *Mon. Not. R. Astron. Soc. Vol. 471, Issue 2, p.1619-1633* 471: (Mar. 2017), 1619–1633 DOI: 10.1093/mnras/stx1675 arXiv: 1703.03383 (see pp. 51, 166).

[148] C. G. T. Haslam, C. J. Salter, H. Stoffel, and W. E. Wilson "A 408 MHz all-sky continuum survey. II. The atlas of contour maps" in: *Astron. Astrophys. Suppl. Ser.* 47: (1982), 1–142 DOI: 1982A&AS...47....1H (see p. 177).

[149] K. Hattori et al. "Development of Readout Electronics for POLARBEAR-2 Cosmic Microwave Background Experiment" in: *J. Low Temp. Phys.* 184:1-2 (July 2016), 512–518 DOI: 10.1007/s10909-015-1448-x arXiv: 1512.07663 (see p. 134).

[150] G. Helou and D. W. Walker "Infrared astronomical satellite (IRAS) catalogs and atlases. Volume 7: The small scale structure catalog" in: *Infrared Astron. Satell. Cat. atlases. Vol. 7, p.1-265* 7: (1988), 1–265 (see p. 131).

[151] S. W. Henderson et al. "Highly-multiplexed microwave SQUID readout using the SLAC Microresonator Radio Frequency (SMuRF) electronics for future CMB and sub-millimeter surveys" in: *Millimeter, Submillimeter, Far-Infrared Detect. Instrum. Astron. IX* ed. by J. Zmuidzinas and J.-R. Gao vol. 10708 SPIE, July 2018, 43 DOI: 10.1117/12.2314435 (see p. 134).

[152] C. Heymans et al. "The Shear TEsting Programme 1: Weak lensing analysis of simulated ground-based observations" in: *Mon. Not. R. Astron. Soc. Vol. 368, Issue 3, pp. 1323-1339.* 368: (June 2005), 1323–1339 DOI: 10.1111/j.1365-2966.2006.10198.x arXiv: astro-ph/0506112 (see p. 50).

[153] S. Hilbert, J. Hartlap, S. D. M. White, and P. Schneider "Ray-tracing through the Millennium Simulation: Born corrections and lens-lens coupling in cosmic shear and galaxy-galaxy lensing" in: *Astron. Astrophys.* 499:1 (May 2009), 31–43 DOI: 10.1051/0004-6361/200811054 arXiv: 0809.5035 (see p. 142).

[154] R. H. Hildebrand "Magnetic fields and stardust" in: *R. Astron. Soc. Q. J.* 29: (Sept. 1988), 327–351 (see p. 60).

[155] R. H. Hildebrand, L. Kirby, J. L. Dotson, M. Houde, and J. E. Vaillancourt "Dispersion of Magnetic Fields in Molecular Clouds. I" in: *Astrophys. J.* 696: (Nov. 2008), 567–573 DOI: 10.1088/0004-637X/696/1/567 arXiv: 0811.0813 (see p. 59).

[156] C. A. Hill et al. "Design and development of an ambient-temperature continuously-rotating achromatic half-wave plate for CMB polarization modulation on the POLARBEAR-2 experiment" in: *Proc. SPIE* ed. by W. S. Holland and J. Zmuidzinas July 2016, 99142U DOI: 10.1117/12.2232280 arXiv: 1607.07399 (see p. 125).

[157] C. M. Hirata and U. Seljak "Analyzing weak lensing of the cosmic microwave background using the likelihood function" in: *Phys. Rev. D* 67:4 (), 043001 DOI: 10.1103/PhysRevD.67.043001 arXiv: astro-ph/0209489 (see p. 65).

[158] C. M. Hirata and U. Seljak "Intrinsic alignment-lensing interference as a contaminant of cosmic shear" in: *Phys. Rev. D* 70:6 (Sept. 2004), 063526 DOI: 10.1103/PhysRevD.70.063526 arXiv: astro-ph/0406275 (see p. 166).

[159] C. M. Hirata and U. U. Seljak "Reconstruction of lensing from the cosmic microwave background polarization" in: *Phys. Rev. D* 68:8 (June 2003), 083002 DOI: 10.1103/PhysRevD.68.083002 arXiv: astro-ph/0306354 (see pp. 94, 98, 122, 139, 170).

[160] E. Hivon, K. M. Gorski, C. B. Netterfield, B. P. Crill, S. Prunet, and F. Hansen "MASTER of the CMB Anisotropy Power Spectrum: A Fast Method for Statistical Analysis of Large and Complex CMB Data Sets" in: *Astrophys. Journal, Vol. 567, Issue 1, pp. 2-17.* 567: (May 2001), 2–17 DOI: 10.1086/338126 arXiv: astro-ph/0105302 (see pp. 107, 113).

[161] D. W. Hogg "Distance measures in cosmology" May 1999 arXiv: astro-ph/9905116 (see p. 5).

[162] W. Hu "Angular trispectrum of the cosmic microwave background" in: *Phys. Rev. D* 64:8 (Sept. 2001), 083005 DOI: 10.1103/PhysRevD.64.083005 arXiv: astro-ph/0105117 (see p. 71).

[163] W. Hu "CMB temperature and polarization anisotropy fundamentals" in: *Ann. Phys. (N. Y).* 303:1 (Jan. 2003), 203–225 DOI: 10.1016/S0003-4916(02)00022-2 arXiv: astro-ph/0210696 (see p. 38).

[164] W. Hu "Dark Energy Probes in Light of the CMB" in: *ASP Conf. Ser.* 339: (July 2004), 215 arXiv: astro-ph/0407158 (see p. 38).

[165] W. Hu "Lecture Notes on CMB Theory: From Nucleosynthesis to Recombination" Feb. 2008 arXiv: 0802.3688 (see p. 37).

[166] W. Hu "Weak lensing of the CMB: A harmonic approach" in: *Phys. Rev. D* 62:4 (July 2000), 043007 DOI: 10.1103/PhysRevD.62.043007 arXiv: astro-ph/0001303 (see pp. 46, 47, 50).

[167] W. Hu and A. Cooray "Gravitational time delay effects on cosmic microwave background anisotropies" in: *Phys. Rev. D* 63:2 (Dec. 2000), 023504 DOI: 10.1103/PhysRevD.63.023504 arXiv: astro-ph/0008001 (see p. 43).

[168] W. Hu and T. Okamoto "Mass Reconstruction with CMB Polarization" in: *Astrophys. J.* 574:2 (Nov. 2001), 566–574 DOI: 10.1086/341110 arXiv: astro-ph/0111606 (see pp. 38, 102).

[169] W. Hu and M. White "A CMB polarization primer" in: *New Astron.* 2:4 (Oct. 1997), 323–344 DOI: 10.1016/S1384-1076(97)00022-5 arXiv: astro-ph/9706147 (see p. 37).

[170] E. P. Hubble "Cepheids in Spiral Nebulae" in: *Popular Astronomy* 33: (1925) (see p. 1).

[171] E. P. Hubble "NGC 6822, a remote stellar system." in: *Astrophys. J.* 62: (Dec. 1925) DOI: 10.1086/142943 (see p. 1).

[172] "Initialization, Finalization, and Threads — Python 3.7.3 documentation" URL: https://docs.python.org/3/c-api/init.html%7B%5C#%7Dthread-state-and-the-global-interpreter-lock (visited on 06/18/2019) (see p. 83).

[173] F. Iocco, G. Mangano, G. Miele, O. Pisanti, and P. D. Serpico "Primordial nucleosynthesis: From precision cosmology to fundamental physics" in: *Phys. Rep.* 472:1-6 (Mar. 2009), 1–76 DOI: 10.1016/j.physrep.2009.02.002 arXiv: 0809.0631 (see p. 18).

[174] J. G. Mangum "A Telescope Pointing Algorithm for ALMA" 2001 URL: http://legacy.nrao.edu/alma/memos/html-memos/abstracts/abs366.html (see pp. 127, 130).

[175] B. Jain, U. Seljak, and S. White "Ray-tracing Simulations of Weak Lensing by Large-Scale Structure" in: *Astrophys. J.* 530:2 (Feb. 2000), 547–577 DOI: 10.1086/308384 arXiv: astro-ph/9901191 (see p. 141).

[176] B. R. Johnson et al. "MAXIPOL: Cosmic Microwave Background Polarimetry Using a Rotating Half-Wave Plate" in: *Astrophys. J.* 665:1 (Aug. 2007), 42–54 DOI: 10.1086/518105 arXiv: astro-ph/0611394 (see p. 113).

[177] A. P. Jones "Depletion patterns and dust evolution in the interstellar medium" in: *J. Geophys. Res. Sp. Phys.* 105:A5 (May 2000), 10257–10268 DOI: 10.1029/1999JA900264 (see p. 57).

[178] "June 2019 | TOP500 Supercomputer Sites" URL: https://www.top500.org/lists/2019/06/ (visited on 06/18/2019) (see pp. 81, 83).

[179] G. Jung, B. Racine, and B. van Tent "The bispectra of galactic CMB foregrounds and their impact on primordial non-Gaussianity estimation" in: *J. Cosmol. Astropart. Phys.* 2018:11 (Nov. 2018), 047–047 DOI: 10.1088/1475-7516/2018/11/047 arXiv: 1810.01727 (see p. 171).

[180] N. Kaiser and N. "On the spatial correlations of Abell clusters" in: *Astrophys. J.* 284: (Sept. 1984), L9 DOI: 10.1086/184341 (see p. 51).

[181] M. Kamionkowski, A. Kosowsky, and A. Stebbins "Statistics of cosmic microwave background polarization" in: *Phys. Rev. D* 55:12 (June 1997), 7368–7388 DOI: 10.1103/PhysRevD.55.7368 arXiv: astro-ph/9611125 (see p. 37).

[182] A. Kashlinsky "Cosmic Infrared Background and Early Galaxy Evolution" in: *Phys. Rep.* 409:6 (Dec. 2004), 361–438 DOI: 10.1016/j.physrep.2004.12.005 arXiv: astro-ph/0412235 (see p. 60).

[183] B. Keating, M. Shimon, and A. Yadav "Self-Calibration of CMB Polarization Experiments" in: *Astrophys. J.* 762:2 (Nov. 2012), L23 DOI: 10.1088/2041-8205/762/2/L23 arXiv: 1211.5734 (see p. 111).

[184] R. Keisler et al. "Measurements of Sub-degree B-mode Polarization in the Cosmic Microwave Background from 100 Square Degrees of SPTpol Data" in: *Astrophys. J.* 807:2 (Mar. 2015), 151 DOI: 10.1088/0004-637X/807/2/151 arXiv: 1503.02315 (see pp. 104, 105).

[185] Z. D. Kermish et al. "The POLARBEAR experiment" in: *Proc. SPIE* ed. by W. S. Holland Sept. 2012, 84521C DOI: 10.1117/12.926354 arXiv: 1210.7768 (see pp. 105, 106).

[186] M. Kesden, A. Cooray, and M. Kamionkowski "Lensing reconstruction with CMB temperature and polarization" in: *Phys. Rev. D* 67:12 (June 2003), 123507 DOI: 10.1103/PhysRevD.67.123507 arXiv: astro-ph/0302536 (see pp. 72, 74, 180).

[187] M. Kesden, A. Cooray, and M. Kamionkowski "Separation of Gravitational-Wave and Cosmic-Shear Contributions to Cosmic Microwave Background Polarization" in: *Phys. Rev. Lett.* 89:1 (June 2002), 011304 DOI: 10.1103/PhysRevLett.89.011304 arXiv: astro-ph/0202434 (see p. 94).

[188] M. Kesden, A. Cooray, and M. Kamionkowski "Weak lensing of the CMB: Cumulants of the probability distribution function" in: *Phys. Rev. D* 66:8 (Oct. 2002), 083007 DOI: 10.1103/PhysRevD.66.083007 arXiv: astro-ph/0208325 (see p. 74).

[189] M. Kilbinger "Cosmology with cosmic shear observations: a review" in: *Reports Prog. Phys.* 78:8 (July 2015), 086901 DOI: 10.1088/0034-4885/78/8/086901 (see p. 50).

[190] C.-G. Kim, S. K. Choi, and R. Flauger "Dust Polarization Maps from TIGRESS: E/B power asymmetry and TE correlation" Jan. 2019 arXiv: 1901.07079 (see p. 172).

[191] D. Kirk et al. "Cross-correlation of gravitational lensing from DES Science Verification data with SPT and Planck lensing" in: *Mon. Not. R. Astron. Soc. Vol. 459, Issue 1, p.21-34* 459: (Dec. 2015), 21–34 DOI: 10.1093/mnras/stw570 arXiv: 1512.04535 (see p. 51).

[192] L. Knox "Determination of inflationary observables by cosmic microwave background anisotropy experiments" in: *Phys. Rev. D* 52:8 (Oct. 1995), 4307–4318 DOI: 10.1103/PhysRevD.52.4307 arXiv: astro-ph/9504054 (see pp. 88, 148).

[193] L. Knox and Y.-S. Song "Limit on the Detectability of the Energy Scale of Inflation" in: *Phys. Rev. Lett.* 89:1 (June 2002), 011303 DOI: 10.1103/PhysRevLett.89.011303 arXiv: astro-ph/0202286 (see pp. 35, 94).

[194] E. Komatsu and D. N. Spergel "Acoustic signatures in the primary microwave background bispectrum" in: *Phys. Rev. D* 63:6 (Feb. 2001), 063002 DOI: 10.1103/PhysRevD.63.063002 arXiv: astro-ph/0005036 (see p. 144).

[195] B. J. Koopman et al. "Advanced ACTPol Low-Frequency Array: Readout and Characterization of Prototype 27 and 39 GHz Transition Edge Sensors" in: *J. Low Temp. Phys.* 193:5-6 (Dec. 2018), 1103–1111 DOI: 10.1007/s10909-018-1957-5 arXiv: 1711.02594 (see p. 103).

[196] A. Kosowsky "Cosmic Microwave Background Polarization" in: *Ann. Phys. (N. Y.)* 246:1 (Feb. 1996), 49–85 DOI: 10.1006/aphy.1996.0020 arXiv: astro-ph/9501045 (see p. 37).

[197] J. M. Kovac, E. M. Leitch, C. Pryke, J. E. Carlstrom, N. W. Halverson, and W. L. Holzapfel "Detection of polarization in the cosmic microwave background using DASI" in: *Nature* 420:6917 (Dec. 2002), 772–787 DOI: 10.1038/nature01269 arXiv: astro-ph/0209478 (see p. 102).

[198] K. Koyama "Cosmological tests of modified gravity" in: *Reports Prog. Phys.* 79:4 (Apr. 2016), 046902 DOI: 10.1088/0034-4885/79/4/046902 arXiv: 1504.04623 (see p. 22).

[199] N. Krachmalnicoff, C. Baccigalupi, J. Aumont, M. Bersanelli, and A. Mennella "Characterization of foreground emission on degree angular scales for CMB B -mode observations" in: *Astron. Astrophys.* 588: (Apr. 2016), A65 DOI: 10.1051/0004-6361/201527678 arXiv: 1511.00532 (see p. 171).

[200] N. Krachmalnicoff et al. "The S-PASS view of polarized Galactic Synchrotron at 2.3 GHz as a contaminant to CMB observations" in: *Astron. Astrophys.* 618: (Feb. 2018), A166 DOI: 10.1051/0004-6361/201832768 arXiv: 1802.01145 (see pp. 57, 171, 177).

[201] E. Krause and C. M. Hirata "Weak lensing power spectra for precision cosmology: Multiple-deflection, reduced shear and lensing bias corrections" in: *Astron. Astrophys.* 523: (Oct. 2009), A28 DOI: 10.1051/0004-6361/200913524 arXiv: 0910.3786 (see pp. 138, 139, 142).

[202] A. G. Kritsuk, R. Flauger, and S. D. Ustyugov "Dust-Polarization Maps for Local Interstellar Turbulence" in: *Phys. Rev. Lett.* 121:2 (July 2018), 021104 DOI: 10.1103/PhysRevLett.121.021104 arXiv: 1711.11108 (see p. 172).

[203] C. L. Kuo et al. "High-Resolution Observations of the Cosmic Microwave Background Power Spectrum with ACBAR" in: *Astrophys. J.* 600:1 (Jan. 2004), 32–51 DOI: 10.1086/379783 arXiv: astro-ph/0212289 (see p. 102).

[204] O. Lahav, P. B. Lilje, J. R. Primack, and M. J. Rees "Dynamical effects of the cosmological constant" in: *Mon. Not. R. Astron. Soc.* 251:1 (July 1991), 128–136 DOI: 10.1093/mnras/251.1.128 (see p. 40).

[205] "LAMBDA - CMB Experiments" URL: https://lambda.gsfc.nasa.gov/product/expt/index.cfm (visited on 06/23/2019) (see p. 102).

[206] P. Larsen and A. Challinor "Intrinsic alignment contamination to CMB lensing–galaxy weak lensing correlations from tidal torquing" in: *Mon. Not. R. Astron. Soc.* 461:4 (Oct. 2016), 4343–4352 DOI: 10.1093/mnras/stw1645 arXiv: 1510.02617 (see pp. 103, 155, 166).

[207] P. Larsen, A. Challinor, B. D. Sherwin, and D. Mak "Demonstration of Cosmic Microwave Background Delensing Using the Cosmic Infrared Background" in: *Phys. Rev. Lett.* 117:15 (Oct. 2016), 151102 DOI: 10.1103/PhysRevLett.117.151102 arXiv: 1607.05733 (see p. 60).

[208] H. M. Lee and B. T. Draine "Infrared extinction and polarization due to partially aligned spheroidal grains - Models for the dust toward the BN object" in: *Astrophys. J.* 290: (Mar. 1985), 211 DOI: 10.1086/162974 (see p. 58).

[209] D. Lenz, O. Doré, and G. Lagache "Large-scale CIB maps from Planck" May 2019 arXiv: 1905.00426 (see p. 60).

[210] J. Lesgourgues and S. Pastor "Massive neutrinos and cosmology" in: *Phys. Rep.* 429:6 (Mar. 2006), 307–379 DOI: 10.1016/j.physrep.2006.04.001 arXiv: astro-ph/0603494 (see pp. 15, 54).

[211] A. Lewis "CAMB Notes" 2014 URL: https://cosmologist.info/notes/CAMB.pdf (visited on 06/06/2019) (see pp. 33, 34).

[212] A. Lewis and A. Challinor "Weak Gravitational Lensing of the CMB" in: *Phys. Rep.* 429:1 (Jan. 2006), 1–65 DOI: 10.1016/j.physrep.2006.03.002 arXiv: astro-ph/0601594 (see pp. 43, 45, 48, 137, 145).

[213] A. Lewis, A. Challinor, and D. Hanson "The shape of the CMB lensing bispectrum" in: *J. Cosmol. Astropart. Phys.* 2011:03 (Jan. 2011), 018–018 DOI: 10.1088/1475-7516/2011/03/018 arXiv: 1101.2234 (see pp. 67, 72, 201, 203).

[214] A. Lewis, A. Hall, and A. Challinor "Emission-angle and polarization-rotation effects in the lensed CMB" in: *J. Cosmol. Astropart. Phys.* 2017:08 (June 2017), 023–023 DOI: 10.1088/1475-7516/2017/08/023 arXiv: 1706.02673 (see p. 144).

[215] A. Lewis and G. Pratten "Effect of lensing non-Gaussianity on the CMB power spectra" in: *J. Cosmol. Astropart. Phys.* 2016:12 (Aug. 2016), 003–003 DOI: 10.1088/1475-7516/2016/12/003 arXiv: 1608.01263 (see pp. 138, 140, 144–146).

[216] D. N. Limber and D. Nelson "The Analysis of Counts of the Extragalactic Nebulae in Terms of a Fluctuating Density Field." in: *Astrophys. J.* 117: (Jan. 1953), 134 DOI: 10.1086/145672 (see p. 45).

[217] A. D. Linde "The inflationary Universe" in: *Reports Prog. Phys.* 47:8 (Aug. 1984), 925–986 DOI: 10.1088/0034-4885/47/8/002 (see p. 30).

[218] A. Linde "A new inflationary universe scenario: A possible solution of the horizon, flatness, homogeneity, isotropy and primordial monopole problems" in: *Phys. Lett. B* 108:6 (Feb. 1982), 389–393 DOI: 10.1016/0370-2693(82)91219-9 (see p. 31).

[219] A. Linde "Chaotic inflation" in: *Phys. Lett. B* 129:3-4 (Sept. 1983), 177–181 DOI: 10.1016/0370-2693(83)90837-7 (see p. 31).

[220] J. Liu and J. C. Hill "Cross-correlation of Planck CMB lensing and CFHTLenS galaxy weak lensing maps" in: *Phys. Rev. D* 92:6 (Sept. 2015), 063517 DOI: 10.1103/PhysRevD.92.063517 (see p. 51).

[221] M. López-Caniego et al. "The QUIJOTE CMB Experiment: status and first results with the multi-frequency instrument" Jan. 2014 arXiv: 1401.4690 (see p. 57).

[222] T. Louis et al. "The Atacama Cosmology Telescope: two-season ACTPol spectra and parameters" in: *J. Cosmol. Astropart. Phys.* 2017:06 (June 2017), 031–031 DOI: 10.1088/1475-7516/2017/06/031 arXiv: 1610.02360 (see p. 105).

[223] LSST Science Collaboration et al. "LSST Science Book, Version 2.0" Dec. 2009 arXiv: 0912.0201 (see p. 167).

[224] C.-P. Ma and E. Bertschinger "Cosmological Perturbation Theory in the Synchronous and Conformal Newtonian Gauges" in: *Astrophys. J.* 455: (June 1995), 7 DOI: 10.1086/176550 arXiv: astro-ph/9506072 (see pp. 23–25).

[225] S. J. Maddox et al. "Herschel ATLAS: The angular correlation function of submillimetre galaxies at high and low redshift" in: *Astron. Astrophys.* 518: (May 2010), L11 DOI: 10.1051/0004-6361/201014663 arXiv: 1005.2406 (see p. 108).

[226] M. S. Madhavacheril and J. C. Hill "Mitigating foreground biases in CMB lensing reconstruction using cleaned gradients" in: *Phys. Rev. D* 98:2 (July 2018), 023534 DOI: 10.1103/PhysRevD.98.023534 arXiv: 1802.08230 (see pp. 124, 170, 174, 194).

[227] R. Mandelbaum et al. "The first-year shear catalog of the Subaru Hyper Suprime-Cam SSP Survey" in: *Publ. Astron. Soc. Japan, Vol. 70, Issue SP1, id.S25* 70: (May 2017) DOI: 10.1093/pasj/psx130 arXiv: 1705.06745 (see p. 108).

[228] G. Mangano, G. Miele, S. Pastor, T. Pinto, O. Pisanti, and P. D. Serpico "Relic neutrino decoupling including flavour oscillations" in: *Nucl. Phys. B* 729:1-2 (June 2005), 221–234 DOI: 10.1016/j.nuclphysb.2005.09.041 arXiv: hep-ph/0506164 (see pp. 16, 17).

[229] A. Maniyar, G. Lagache, M. Béthermin, and S. Ilić "Constraining cosmology with the cosmic microwave and infrared backgrounds correlation" in: *Astron. Astrophys.* 621: (Jan. 2019), A32 DOI: 10.1051/0004-6361/201833765 arXiv: 1809.04551 (see p. 60).

[230] A. Manzotti et al. "CMB Polarization B -mode Delensing with SPTpol and Herschel" in: *Astrophys. J.* 846:1 (Aug. 2017), 45 DOI: 10.3847/1538-4357/aa82bb arXiv: 1701.04396 (see pp. 60, 104).

[231] G. Marozzi, G. Fanizza, E. Di Dio, and R. Durrer "CMB lensing beyond the leading order: Temperature and polarization anisotropies" in: *Phys. Rev. D* 98:2 (July 2018), 023535 DOI: 10.1103/PhysRevD.98.023535 arXiv: arXiv:1612.07263 (see pp. 140, 144).

[232] G. Marozzi, G. Fanizza, E. D. Dio, and R. Durrer "CMB-lensing beyond the Born approximation" in: *J. Cosmol. Astropart. Phys.* 2016:09 (Sept. 2016), 028–028 DOI: 10.1088/1475-7516/2016/09/028 arXiv: 1605.08761 (see pp. 139, 144).

[233] G. Martínez-Solaeche, A. Karakci, and J. Delabrouille "A 3D model of polarized dust emission in the Milky Way" in: *Mon. Not. R. Astron. Soc.* 476:1 (May 2018), 1310–1330 DOI: 10.1093/mnras/sty204 arXiv: 1706.04162 (see p. 174).

[234] J. S. Mathis, W. Rumpl, and K. H. Nordsieck "The size distribution of interstellar grains" in: *Astrophys. J.* 217: (Oct. 1977), 425 DOI: 10.1086/155591 (see p. 57).

[235] F. Matsuda "Cosmic Microwave Background Polarization Science and Optical Design of the Polarbear and Simons Array Experiments" PhD thesis University of California, San Diego, 2017, 198 (see p. 129).

[236] A. J. Mead, J. A. Peacock, C. Heymans, S. Joudaki, and A. F. Heavens "An accurate halo model for fitting non-linear cosmological power spectra and baryonic feedback models" in: *Mon. Not. R. Astron. Soc.* 454:2 (Dec. 2015), 1958–1975 DOI: 10.1093/mnras/stv2036 arXiv: 1505.07833 (see p. 41).

[237] A. Meisner and D. Finkbeiner "Modeling Thermal Dust Emission with Two Components: Application to the Planck HFI Maps" in: *Astrophys. J.* 798:2 (Oct. 2014), 88 DOI: 10.1088/0004-637X/798/2/88 arXiv: 1410.7523 (see p. 59).

[238] P. M. Merkel and B. M. Schäfer "Gravitational lensing of the cosmic microwave background by non-linear structures" in: *Mon. Not. R. Astron. Soc.* 411:2 (Feb. 2011), 1067–1076 DOI: 10.1111/j.1365-2966.2010.17739.x arXiv: 1007.1408 (see pp. 137, 138).

[239] P. M. Merkel and B. M. Schäfer "Imitating intrinsic alignments: a bias to the CMB lensing-galaxy shape cross-correlation power spectrum induced by the large-scale structure bispectrum" in: *Mon. Not. R. Astron. Soc.* 471:2 (Oct. 2017), 2431–2437 DOI: 10.1093/mnras/stx1664 arXiv: 1709.04444 (see p. 155).

[240] M. Millea, E. Anderes, and B. D. Wandelt "Bayesian delensing of CMB temperature and polarization" in: *Phys. Rev. D* 100:2 (July 2019), 023509 DOI: 10.1103/PhysRevD.100.023509 arXiv: 1708.06753 (see pp. 66, 94, 170).

[241] A. D. Miller, R. Caldwell, M. J. Devlin, W. B. Dorwart, T. Herbig, M. R. Nolta, L. A. Page, J. Puchalla, E. Torbet, and H. T. Tran "A Measurement of the Angular Power Spectrum of the Cosmic Microwave Background from l = 100 to 400" in: *Astrophys. J.* 524:1 (Oct. 1999), L1–L4 DOI: 10.1086/312293 (see p. 101).

[242] Y. Minami, H. Ochi, K. Ichiki, N. Katayama, E. Komatsu, and T. Matsumura "Simultaneous determination of the cosmic birefringence and miscalibrated polarisation angles from CMB experiments" Apr. 2019 arXiv: 1904.12440 (see p. 136).

[243] C. Modi, M. White, and Z. Vlah "Modeling CMB lensing cross correlations with CLEFT" in: *J. Cosmol. Astropart. Phys.* 2017:08 (Aug. 2017), 009–009 DOI: 10.1088/1475-7516/2017/08/009 arXiv: 1706.03173 (see p. 167).

[244] L. Montier "LiteBIRD Overview LiteBIRD-FRANCE" URL: https://indico.in2p3.fr/event/19378/sessions/12141/attachments/54391/71180/20190710%7B%5C_%7DLBDay%7B%5C_%7DOverview.pdf (visited on 07/22/2019) (see p. 136).

[245] V. F. Mukhanov and G. V. Chibisov "Quantum fluctuations and a nonsingular universe" in: *Sov. J. Exp. Theor. Phys. Lett.* 33: (1981), 532–535 (see p. 31).

[246] V. Mukhanov "Theory of cosmological perturbations" in: *Phys. Rep.* 215:5-6 (June 1992), 203–333 DOI: 10.1016/0370-1573(92)90044-Z (see p. 23).

[247] T. Murphy et al. "The Australia Telescope 20 GHz Survey: The Source Catalogue" in: *Mon. Not. R. Astron. Soc. Vol. 402, Issue 4, pp. 2403-2423.* 402: (Oct. 2009), 2403–2423 DOI: 10.1111/j.1365-2966.2009.15961.x arXiv: 0911.0002 (see pp. 110, 127).

[248] S. Naess et al. "The Atacama Cosmology Telescope: CMB Polarization at 200<ℓ<9000" in: *J. Cosmol. Astropart. Phys.* 2014:10 (May 2014), 007–007 DOI: 10.1088/1475-7516/2014/10/007 arXiv: 1405.5524 (see p. 103).

[249] T. Namikawa "CMB internal delensing with general optimal estimator for higher-order correlations" in: *Phys. Rev. D* 95:10 (May 2017), 103514 DOI: 10.1103/PhysRevD.95.103514 arXiv: 1703.00169 (see pp. 99, 181, 193).

[250] T. Namikawa "CMB lensing bispectrum from nonlinear growth of the large scale structure" in: *Phys. Rev. D* 93:12 (June 2016), 121301 DOI: 10.1103/PhysRevD.93.121301 arXiv: 1604.08578 (see p. 137).

[251] T. Namikawa, D. Hanson, and R. Takahashi "Bias-hardened CMB lensing" in: *Mon. Not. R. Astron. Soc.* 431:1 (May 2013), 609–620 DOI: 10.1093/mnras/stt195 arXiv: 1209.0091 (see pp. 75, 77, 78, 81, 120, 181, 213).

[252] T. Namikawa and R. Takahashi "Bias-hardened CMB lensing with polarization" in: *Mon. Not. R. Astron. Soc.* 438:2 (Feb. 2014), 1507–1517 DOI: 10.1093/mnras/stt2290 arXiv: 1310.2372 (see pp. 77, 78, 81, 213).

[253] T. Namikawa and R. Takahashi "Impact of nonlinear growth of the large-scale structure on CMB B-mode delensing" in: *Phys. Rev. D* 99:2 (Oct. 2018), 023530 DOI: 10.1103/PhysRevD.99.023530 arXiv: 1810.03346 (see p. 169).

[254] T. Namikawa, D. Yamauchi, and A. Taruya "Full-sky lensing reconstruction of gradient and curl modes from CMB maps" in: *J. Cosmol. Astropart. Phys.* 2012:01 (Jan. 2012), 007–007 DOI: 10.1088/1475-7516/2012/01/007 arXiv: 1110.1718 (see pp. 81, 122).

[255] T. Namikawa et al. "Evidence for the Cross-correlation between Cosmic Microwave Background Polarization Lensing from POLARBEAR and Cosmic Shear from Subaru Hyper Suprime-Cam" Apr. 2019 arXiv: 1904.02116 (see pp. v, 51, 101, 108).

[256] A. Natarajan, A. R. Zentner, N. Battaglia, and H. Trac "Systematic errors in the measurement of neutrino masses due to baryonic feedback processes: Prospects for stage IV lensing surveys" in: *Phys. Rev. D* 90:6 (Sept. 2014), 063516 DOI: 10.1103/PhysRevD.90.063516 arXiv: 1405.6205 (see p. 151).

[257] E. T. Newman and R. Penrose "Note on the Bondi-Metzner-Sachs Group" in: *J. Math. Phys.* 7:5 (May 1966), 863–870 DOI: 10.1063/1.1931221 (see p. 27).

[258] T. Okamoto and W. Hu "Cosmic microwave background lensing reconstruction on the full sky" in: *Phys. Rev. D* 67:8 (Apr. 2003), 083002 DOI: 10.1103/PhysRevD.67.083002 arXiv: astro-ph/0301031 (see pp. 67–69, 84, 180, 182, 200, 210).

[259] Y. Omori et al. "A 2500 square-degree CMB lensing map from combined South Pole Telescope and Planck data" in: *Astrophys. J.* 849:2 (May 2017), 124 DOI: 10.3847/1538-4357/aa8d1d arXiv: 1705.00743 (see p. 104).

[260] Y. Omori et al. "Dark Energy Survey Year 1 Results: Cross-correlation between DES Y1 galaxy weak lensing and SPT+Planck CMB weak lensing" Oct. 2018 arXiv: 1810.02441 (see pp. 51, 166).

[261] S. J. Osborne, D. Hanson, and O. Doré "Extragalactic foreground contamination in temperature-based CMB lens reconstruction" in: *J. Cosmol. Astropart. Phys.* 2014:03 (Mar. 2014), 024–024 DOI: 10.1088/1475-7516/2014/03/024 arXiv: 1310.7547 (see pp. 77, 78, 124, 170, 174).

[262] A. Osipowicz et al. "Letter of Intent KATRIN: A next generation tritium beta decay experiment with sub-eV sensitivity for the electron neutrino mass" 2001 arXiv: hep-ex/0109033 (see p. 15).

[263] S. Paine "The am atmospheric model" 2018 URL: https://doi.org/10.5281/zenodo.1193646 (see p. 61).

[264] J. Papez, L. Grigori, and R. Stompor "Solving linear equations with messenger-field and conjugate gradient techniques: An application to CMB data analysis" in: *Astron. Astrophys.* 620: (2018), A59 DOI: 10.1051/0004-6361/201832987 arXiv: 1803.03462 (see p. 85).

[265] S. C. Parshley et al. "CCAT-prime: a novel telescope for sub-millimeter astronomy" in: *Ground-based Airborne Telesc. VII* ed. by R. Gilmozzi, H. K. Marshall, and J. Spyromilio SPIE, July 2018, 220 DOI: 10.1117/12.2314046 arXiv: 1807.06675 (see p. 133).

[266] T. J. Pearson et al. "The Anisotropy of the Microwave Background to l = 3500: Mosaic Observations with the Cosmic Background Imager" in: *Astrophys. J.* 591:2 (July 2003), 556–574 DOI: 10.1086/375508 arXiv: astro-ph/0205388 (see p. 102).

[267] P. J. E. Peebles "Recombination of the Primeval Plasma" in: *Astrophys. J.* 153: (July 1968), 1 DOI: 10.1086/149628 (see p. 21).

[268] P. J. E. Peebles and B. Ratra "Cosmology with a time-variable cosmological 'constant'" in: *Astrophys. J.* 325: (Feb. 1988), L17 DOI: 10.1086/185100 (see p. 22).

[269] P. Peebles "Seeing Cosmology Grow" in: *Annu. Rev. Astron. Astrophys.* 50:1 (Sept. 2012), 1–28 DOI: 10.1146/annurev-astro-081811-125526 (see p. 87).

[270] J. Peloton, M. Schmittfull, A. Lewis, J. Carron, and O. Zahn "Full covariance of CMB and lensing reconstruction power spectra" in: *Phys. Rev. D* 95:4 (Feb. 2017), 043508 DOI: 10.1103/PhysRevD.95.043508 (see pp. 67, 74, 75, 161).

[271] "Performance Development | TOP500 Supercomputer Sites" URL: https://www.top500.org/statistics/perfdevel/ (visited on 06/18/2019) (see p. 82).

[272] S. Perlmutter et al. "Discovery of a supernova explosion at half the age of the Universe" in: *Nature* 391:6662 (Jan. 1998), 51–54 DOI: 10.1038/34124 arXiv: astro-ph/9712212 (see p. 1).

[273] M. E. Peskin and D. V. Schroeder "An Introduction To Quantum Field Theory" 1st ed. Reading: Perseus Books, 1995, 864 (see p. 12).

[274] A. Petri, Z. Haiman, and M. May "Validity of the Born approximation for beyond Gaussian weak lensing observables" in: *Phys. Rev. D* 95:12 (June 2017), 123503 DOI: 10.1103/PhysRevD.95.123503 arXiv: 1612.00852 (see p. 138).

[275] C. Pitrou, A. Coc, J.-P. Uzan, and E. Vangioni "Precision big bang nucleosynthesis with improved Helium-4 predictions" in: *Phys. Rep.* 754: (Sept. 2018), 1–66 DOI: 10.1016/j.physrep.2018.04.005 arXiv: 1801.08023 (see p. 19).

[276] Planck Collaboration et al. "Planck 2013 results. IX. HFI spectral response" in: *Astron. Astrophys.* 571: (Mar. 2013), A9 DOI: 10.1051/0004-6361/201321531 arXiv: 1303.5070 (see p. 56).

[277] Planck Collaboration et al. "Planck 2013 results. XI. All-sky model of thermal dust emission" in: *Astron. Astrophys.* 571: (Dec. 2013), A11 DOI: 10.1051/0004-6361/201323195 arXiv: 1312.1300 (see p. 59).

[278] Planck Collaboration et al. "Planck 2015 results. X. Diffuse component separation: Foreground maps" in: *Astron. Astrophys.* 594: (Feb. 2015), A10 DOI: 10.1051/0004-6361/201525967 arXiv: 1502.01588 (see p. 177).

[279] Planck Collaboration et al. "Planck 2015 results. XIII. Cosmological parameters" in: *Astron. Astrophys.* 594: (Feb. 2015), A13 DOI: 10.1051/0004-6361/201525830 arXiv: 1502.01589 (see pp. 52, 53, 162).

[280] Planck Collaboration et al. "Planck 2015 results. XV. Gravitational lensing" in: *Astron. Astrophys.* 594: (Feb. 2015), A15 DOI: 10.1051/0004-6361/201525941 arXiv: 1502.01591 (see p. 120).

[281] Planck Collaboration et al. "Planck 2015 results. XX. Constraints on inflation" in: *Astron. Astrophys.* 594: (Feb. 2015), A20 DOI: 10.1051/0004-6361/201525898 arXiv: 1502.02114 (see p. 55).

[282] Planck Collaboration et al. "Planck 2015 results. XXV. Diffuse low-frequency Galactic foregrounds" in: *Astron. Astrophys.* 594: (June 2015), A25 DOI: 10.1051/0004-6361/201526803 arXiv: 1506.06660 (see p. 57).

[283] Planck Collaboration et al. "Planck 2015 results. XXVI. The Second Planck Catalogue of Compact Sources" in: *Astron. Astrophys.* 594: (July 2015), A26 DOI: 10.1051/0004-6361/201526914 arXiv: 1507.02058 (see pp. 110, 118, 127, 131).

[284] Planck Collaboration et al. "Planck 2018 results. I. Overview and the cosmological legacy of Planck" July 2018 arXiv: 1807.06205 (see p. 103).

[285] Planck Collaboration et al. "Planck 2018 results. IV. Diffuse component separation" July 2018 arXiv: 1807.06208 (see pp. 56, 89, 90).

[286] Planck Collaboration et al. "Planck 2018 results. VI. Cosmological parameters" in: (July 2018) arXiv: 1807.06209 (see pp. 1, 15, 22, 39, 104).

[287] Planck Collaboration et al. "Planck 2018 results. VIII. Gravitational lensing" July 2018 arXiv: 1807.06210 (see pp. 85, 104, 170, 194, 197).

[288] Planck Collaboration et al. "Planck 2018 results. X. Constraints on inflation" in: (July 2018) arXiv: 1807.06211 (see pp. 33, 105).

[289] Planck Collaboration et al. "Planck 2018 results. XI. Polarized dust foregrounds" Jan. 2018 arXiv: 1801.04945 (see pp. 59, 60, 171, 177).

[290] Planck Collaboration et al. "Planck 2018 results. XII. Galactic astrophysics using polarized dust emission" July 2018 arXiv: 1807.06212 (see pp. 175, 176).

[291] Planck Collaboration et al. "Planck Early Results: The Planck mission" in: *Astron. Astrophys.* 536: (Jan. 2011), A1 DOI: 10.1051/0004-6361/201116464 arXiv: 1101.2022 (see p. 103).

[292] Planck Collaboration et al. "Planck intermediate results. XIX. An overview of the polarized thermal emission from Galactic dust" in: *Astron. Astrophys.* 576: (May 2014), A104 DOI: 10.1051/0004-6361/201424082 arXiv: 1405.0871 (see p. 60).

[293] Planck Collaboration et al. "Planck intermediate results. XLIV. The structure of the Galactic magnetic field from dust polarization maps of the southern Galactic cap" in: *Astron. Astrophys.* 596:1 (Apr. 2016), A105 DOI: 10.1051/0004-6361/201628636 arXiv: 1604.01029 (see pp. 172, 184).

[294] Planck Collaboration et al. "Planck intermediate results. XLVI. Reduction of large-scale systematic effects in HFI polarization maps and estimation of the reionization optical depth" in: *Astron. Astrophys.* 596: (May 2016), A107 DOI: 10.1051/0004-6361/201628890 arXiv: 1605.02985 (see pp. 52, 53, 162).

[295] Planck Collaboration et al. "Planck intermediate results. XXII. Frequency dependence of thermal emission from Galactic dust in intensity and polarization" in: *Astron. Astrophys.* 576: (May 2014), A107 DOI: 10.1051/0004-6361/201424088 arXiv: 1405.0874 (see pp. 58, 59).

[296] Planck Collaboration et al. "Planck intermediate results. XXX. The angular power spectrum of polarized dust emission at intermediate and high Galactic latitudes" in: *Astron. Astrophys.* 586: (Sept. 2014), A133 DOI: 10.1051/0004-6361/201425034 arXiv: 1409.5738 (see p. 89).

[297] D. Poletti et al. "Making maps of cosmic microwave background polarization for B -mode studies: the POLARBEAR example" in: *Astron. Astrophys.* 600: (Apr. 2017), A60 DOI: 10.1051/0004-6361/201629467 arXiv: 1608.01624v2 (see pp. 107, 112).

[298] A. G. Polnarev "Polarization and Anisotropy Induced in the Microwave Background by Cosmological Gravitational Waves" in: *Sov. Astron.* 29: (Dec. 1985), 607–613 (see p. 37).

[299] B. Pontecorvo "Inverse beta processes and nonconservation of lepton charge" in: *Zh.Eksp.Teor.Fiz.* 7: (1957), 247 (see p. 13).

[300] V. Poulin, T. L. Smith, T. Karwal, and M. Kamionkowski "Early Dark Energy can Resolve the Hubble Tension" in: *Phys. Rev. Lett.* 122:22 (June 2019), 221301 DOI: 10.1103/PhysRevLett.122.221301 arXiv: 1811.04083 (see p. 22).

[301] G. Pratten and A. Lewis "Impact of post-Born lensing on the CMB" in: *J. Cosmol. Astropart. Phys.* 2016:08 (May 2016), 047–047 DOI: 10.1088/1475-7516/2016/08/047 arXiv: 1605.05662 (see pp. 137–140, 142–147, 150, 161).

[302] G. Puglisi, V. Galluzzi, L. Bonavera, J. Gonzalez-Nuevo, A. Lapi, M. Massardi, F. Perrotta, C. Baccigalupi, A. Celotti, and L. Danese "Forecasting the Contribution of Polarized Extragalactic Radio Sources in CMB Observations" in: *Astrophys. J.* 858:2 (May 2018), 85 DOI: 10.3847/1538-4357/aab3c7 arXiv: 1712.09639 (see p. 125).

[303] M. J. Rees and D. W. Sciama "Large-scale Density Inhomogeneities in the Universe" in: *Nature* 217:5128 (Feb. 1968), 511–516 DOI: 10.1038/217511a0 (see p. 39).

[304] D. M. Regan, E. P. S. Shellard, and J. R. Fergusson "General CMB and primordial trispectrum estimation" in: *Phys. Rev. D* 82:2 (July 2010), 023520 DOI: 10.1103/PhysRevD.82.023520 arXiv: 1004.2915 (see pp. 29, 75).

[305] C. L. Reichardt "Observing the Epoch of Reionization with the Cosmic Microwave Background" in: *Underst. Epoch Cosm. Reionization* ed. by A. Mesinger 1st ed. Cham: Springer, Nov. 2016, 227–245 DOI: 10.1007/978-3-319-21957-8_8 arXiv: 1511.01117 (see p. 39).

[306] B. A. Reid et al. "Cosmological constraints from the clustering of the Sloan Digital Sky Survey DR7 luminous red galaxies" in: *Mon. Not. R. Astron. Soc.* 404:1 (Mar. 2010), 60–85 DOI: 10.1111/j.1365-2966.2010.16276.x (see p. 48).

[307] M. Reinecke and D. S. Seljebotn "Libsharp – spherical harmonic transforms revisited" in: *Astron. Astrophys.* 554: (June 2013), A112 DOI: 10.1051/0004-6361/201321494 arXiv: 1303.4945 (see p. 81).

[308] M. Remazeilles, C. Dickinson, A. J. Banday, M.-A. Bigot-Sazy, and T. Ghosh "An improved source-subtracted and destriped 408-MHz all-sky map" in: *Mon. Not. R. Astron. Soc.* 451:4 (Aug. 2015), 4311–4327 DOI: 10.1093/mnras/stv1274 arXiv: 1411.3628 (see p. 177).

[309] A. G. Riess, S. Casertano, W. Yuan, L. M. Macri, and D. Scolnic "Large Magellanic Cloud Cepheid Standards Provide a 1% Foundation for the Determination of the Hubble Constant and Stronger Evidence for Physics beyond ΛCDM" in: *Astrophys. J.* 876:1 (May 2019), 85 DOI: 10.3847/1538-4357/ab1422 arXiv: 1903.07603 (see pp. 1, 22).

[310] A. G. Riess et al. "Observational Evidence from Supernovae for an Accelerating Universe and a Cosmological Constant" in: *Astron. J.* 116:3 (Sept. 1998), 1009–1038 DOI: 10.1086/300499 arXiv: astro-ph/9805201 (see pp. 1, 22).

[311] M. Rigault et al. "Strong Dependence of Type Ia Supernova Standardization on the Local Specific Star Formation Rate" June 2018 arXiv: 1806.03849 (see p. 22).

[312] V. C. Rubin, D. Burstein, W. K. Ford Jr., and N. Thonnard "Rotation velocities of 16 SA galaxies and a comparison of Sa, Sb, and SC rotation properties" in: *Astrophys. J.* 289: (Feb. 1985), 81–98 DOI: 10.1086/162866 (see p. 1).

[313] J. A. Rubiño-Martín, C. H. López-Caraballo, R. Génova-Santos, and R. Rebolo "Observations of the Polarisation of the Anomalous Microwave Emission: A Review" in: *Adv. Astron.* 2012: (Dec. 2012), 1–15 DOI: 10.1155/2012/351836 (see p. 57).

[314] R. Ruggeri, E. Castorina, C. Carbone, and E. Sefusatti "DEMNUni: massive neutrinos and the bispectrum of large scale structures" in: *J. Cosmol. Astropart. Phys.* 2018:03 (Mar. 2018), 003–003 DOI: 10.1088/1475-7516/2018/03/003 arXiv: 1712.02334 (see p. 145).

[315] R. K. Sachs and A. M. Wolfe "Perturbations of a Cosmological Model and Angular Variations of the Microwave Background" in: *Astrophys. J.* 147: (Jan. 1967), 73 DOI: 10.1086/148982 (see pp. 26, 39).

[316] S. Samuroff et al. "Dark Energy Survey Year 1 Results: Constraints on Intrinsic Alignments and their Colour Dependence from Galaxy Clustering and Weak Lensing" Nov. 2018 arXiv: 1811.06989 (see p. 167).

[317] S. Y. Sazonov and R. A. Sunyaev "Microwave polarization in the direction of galaxy clusters induced by the CMB quadrupole anisotropy" in: *Mon. Not. R. Astron. Soc.* 310:3 (Dec. 1999), 765–772 DOI: 10.1046/j.1365-8711.1999.02981.x (see p. 39).

[318] E. Schaan and S. Ferraro "Foreground-Immune Cosmic Microwave Background Lensing with Shear-Only Reconstruction" in: *Phys. Rev. Lett.* 122:18 (May 2019), 181301 DOI: 10.1103/PhysRevLett.122.181301 arXiv: 1804.06403 (see pp. 170, 194).

[319] E. Schaan, S. Ferraro, and D. N. Spergel "Weak lensing of intensity mapping: The cosmic infrared background" in: *Phys. Rev. D* 97:12 (June 2018), 123539 DOI: 10.1103/PhysRevD.97.123539 arXiv: 1802.05706 (see p. 150).

[320] E. Schaan, E. Krause, T. Eifler, O. Doré, H. Miyatake, J. Rhodes, and D. N. Spergel "Looking through the same lens: Shear calibration for LSST, Euclid, and WFIRST with stage 4 CMB lensing" in: *Phys. Rev. D* 95:12 (June 2017), 123512 DOI: 10.1103/PhysRevD.95.123512 arXiv: 1607.01761 (see p. 50).

[321] M. M. Schmittfull, A. Challinor, D. Hanson, and A. Lewis "Joint analysis of CMB temperature and lensing-reconstruction power spectra" in: *Phys. Rev. D* 88:6 (2013), 063012 DOI: 10.1103/PhysRevD.88.063012 arXiv: 1308.0286 (see pp. 75, 161).

[322] M. Schmittfull and U. Seljak "Parameter constraints from cross-correlation of CMB lensing with galaxy clustering" in: *Phys. Rev. D* 97:12 (June 2018), 123540 DOI: 10.1103/PhysRevD.97.123540 arXiv: 1710.09465 (see p. 156).

[323] P. Schneider, J. Ehlers, and E. E. Falco "Gravitational Lenses" Astronomy and Astrophysics Library Berlin, Heidelberg: Springer Berlin Heidelberg, 1992, 112 DOI: 10.1007/978-3-662-03758-4 (see p. 141).

[324] K. Schulten and R. Gordon "Recursive evaluation of 3j and 6j coefficients" in: *Comput. Phys. Commun.* 11:2 (Mar. 1976), 269–278 DOI: 10.1016/0010-4655(76)90058-8 (see p. 79).

[325] K. Schulten and R. G. Gordon "Exact recursive evaluation of 3 j - and 6 j -coefficients for quantum-mechanical coupling of angular momenta" in: *J. Math. Phys.* 16:10 (Oct. 1975), 1961–1970 DOI: 10.1063/1.522426 (see p. 79).

[326] R. Scoccimarro and H. M. P. Couchman "A fitting formula for the non-linear evolution of the bispectrum" in: *Mon. Not. R. Astron. Soc.* 325:4 (Aug. 2001), 1312–1316 DOI: 10.1046/j.1365-8711.2001.04281.x arXiv: astro-ph/0009427 (see pp. 42, 145, 146, 151, 156).

[327] P. F. Scott et al. "First results from the Very Small Array – III. The cosmic microwave background power spectrum" in: *Mon. Not. R. Astron. Soc.* 341:4 (June 2003), 1076–1083 DOI: 10.1046/j.1365-8711.2003.06354.x arXiv: astro-ph/0205380 (see p. 102).

[328] S. Seager, D. D. Sasselov, and D. Scott "How Exactly Did the Universe Become Neutral?" in: *Astrophys. J. Suppl. Ser.* 128:2 (June 2000), 407–430 DOI: 10.1086/313388 arXiv: astro-ph/9912182 (see p. 21).

[329] N. Sehgal, M. S. Madhavacheril, B. Sherwin, and A. van Engelen "Internal delensing of cosmic microwave background acoustic peaks" in: *Phys. Rev. D* 95:10 (May 2017), 103512 DOI: 10.1103/PhysRevD.95.103512 arXiv: 1612.03898 (see p. 193).

[330] C. Seitz and P. Schneider "Steps towards nonlinear cluster inversion through gravitational distortions: III. Including a redshift distribution of the sources" in: *Astron. Astrophys. v.318, p.687-699* 318: (Jan. 1996), 687–699 arXiv: astro-ph/9601079 (see p. 49).

[331] U. Seljak "Extracting Primordial Non-Gaussianity without Cosmic Variance" in: *Phys. Rev. Lett.* 102:2 (Jan. 2009), 021302 DOI: 10.1103/PhysRevLett.102.021302 arXiv: 0807.1770 (see p. 156).

[332] U. Seljak and C. M. Hirata "Gravitational lensing as a contaminant of the gravity wave signal in CMB" in: *Phys. Rev. D* 69:4 (Oct. 2003), 043005 DOI: 10.1103/PhysRevD.69.043005 arXiv: astro-ph/0310163 (see pp. 94, 193).

[333] U. Seljak and M. Zaldarriaga "A Line-of-Sight Integration Approach to Cosmic Microwave Background Anisotropies" in: *Astrophys. J.* 469: (Oct. 1996), 437 DOI: 10.1086/177793 arXiv: astro-ph/9603033 (see p. 37).

[334] L. Senatore "Lectures on Inflation" in: *New Front. Fields Strings* WORLD SCIENTIFIC, Jan. 2017, 447–543 DOI: 10.1142/9789813149441_0008 arXiv: 1609.00716 (see pp. 31, 35).

[335] C. Shapiro and A. Cooray "The Born and lens–lens corrections to weak gravitational lensing angular power spectra" in: *J. Cosmol. Astropart. Phys.* 2006:03 (Mar. 2006), 007–007 DOI: 10.1088/1475-7516/2006/03/007 arXiv: astro-ph/0601226 (see p. 138).

[336] C. Sheehy and A. Slosar "No evidence for dust B-mode decorrelation in Planck data" in: *Phys. Rev. D* 97:4 (Sept. 2017), 043522 DOI: 10.1103/PhysRevD.97.043522 arXiv: 1709.09729 (see p. 60).

[337] B. D. Sherwin et al. "Two-season Atacama Cosmology Telescope polarimeter lensing power spectrum" in: *Phys. Rev. D* 95:12 (June 2017), 123529 DOI: 10.1103/PhysRevD.95.123529 arXiv: 1611.09753 (see p. 104).

[338] B. D. Sherwin and M. Schmittfull "Delensing the CMB with the cosmic infrared background" in: *Phys. Rev. D* 92:4 (Aug. 2015), 043005 DOI: 10.1103/PhysRevD.92.043005 arXiv: 1502.05356 (see pp. 94, 169, 198).

[339] S. Singh, R. Mandelbaum, and J. R. Brownstein "Cross-correlating Planck CMB lensing with SDSS: lensing–lensing and galaxy–lensing cross-correlations" in: *Mon. Not. R. Astron. Soc.* 464:2 (Jan. 2017), 2120–2138 DOI: 10.1093/mnras/stw2482 (see p. 51).

[340] A. Slosar, T. Davis, D. Eisenstein, R. Hložek, M. Ishak-Boushaki, R. Mandelbaum, P. Marshall, J. Sakstein, and M. White "Dark Energy and Modified Gravity" Mar. 2019 arXiv: 1903.12016 (see p. 22).

[341] W. M. Smart and R. M. Green "Textbook on spherical astronomy" 1st ed. Cambridge: Cambridge University Press, 1977, 431 (see p. 130).

[342] K. M. Smith "Pseudo- C ℓ estimators which do not mix E and B modes" in: *Phys. Rev. D* 74:8 (Oct. 2006), 083002 DOI: 10.1103/PhysRevD.74.083002 (see pp. 99, 118, 180).

[343] K. M. Smith, W. Hu, and M. Kaplinghat "Weak lensing of the CMB: Sampling errors on B modes" in: *Phys. Rev. D* 70:4 (Aug. 2004), 043002 DOI: 10.1103/PhysRevD.70.043002 (see p. 161).

[344] K. M. Smith, O. Zahn, and O. Dore "Detection of Gravitational Lensing in the Cosmic Microwave Background" in: *Phys. Rev. D* 76:4 (May 2007), 043510 DOI: 10.1103/PhysRevD.76.043510 arXiv: 0705.3980 (see pp. 85, 102, 118).

[345] K. M. Smith et al. "CMBPol Mission Concept Study: Gravitational Lensing" in: *AIP Conf. Proc.* 1141: (Nov. 2008), 121–178 DOI: 10.1063/1.3160886 arXiv: 0811.3916 (see p. 124).

[346] K. M. Smith, D. Hanson, M. Loverde, C. M. Hirata, and O. Zahn "Delensing CMB polarization with external datasets" in: *J. Cosmol. Astropart. Phys.* 2012:06 (June 2012), 014–014 DOI: 10.1088/1475-7516/2012/06/014 arXiv: 1010.0048 (see pp. 94, 95).

[347] M. S. Smith, L. H. Kawano, and R. A. Malaney "Experimental, computational, and observational analysis of primordial nucleosynthesis" in: *Astrophys. J. Suppl. Ser.* 85: (Apr. 1993), 219 DOI: 10.1086/191763 (see p. 18).

[348] R. E. Smith, J. A. Peacock, A. Jenkins, S. D. M. White, C. S. Frenk, F. R. Pearce, P. A. Thomas, G. Efstathiou, H. M. P. Couchmann, and T. V. Consortium "Stable clustering, the halo model and nonlinear cosmological power spectra" in: *Mon. Not. R. Astron. Soc. Vol. 341, Issue 4, pp. 1311-1332.* 341: (July 2002), 1311–1332 DOI: 10.1046/j.1365-8711.2003.06503.x arXiv: astro-ph/0207664 (see p. 42).

[349] G. F. Smoot et al. "Structure in the COBE differential microwave radiometer first-year maps" in: *Astrophys. J.* 396: (Sept. 1992), L1 DOI: 10.1086/186504 (see p. 101).

[350] V. Springel, C. S. Frenk, and S. D. M. White "The large-scale structure of the Universe" in: *Nature* 440:7088 (Apr. 2006), 1137–1144 DOI: 10.1038/nature04805 arXiv: astro-ph/0604561 (see p. 51).

[351] V. Springel et al. "Simulations of the formation, evolution and clustering of galaxies and quasars" in: *Nature* 435:7042 (June 2005), 629–636 DOI: 10.1038/nature03597 (see p. 51).

[352] M. Srednicki "Cosmic Variance of the Three-Point Correlation Function of the Cosmic Microwave Background" in: *Astrophys. J.* 416: (Oct. 1993), L1 DOI: 10.1086/187056 arXiv: astro-ph/9306012 (see p. 144).

[353] A. Starobinsky "A new type of isotropic cosmological models without singularity" in: *Phys. Lett. B* 91:1 (Mar. 1980), 99–102 DOI: 10.1016/0370-2693(80)90670-X (see pp. 31, 33).

[354] N. Stebor et al. "The Simons Array CMB polarization experiment" in: *Proc. SPIE* ed. by W. S. Holland and J. Zmuidzinas July 2016, 99141H DOI: 10.1117/12.2233103 (see pp. 125, 126, 132).

[355] W. Stein "Infrared Radiation from Interstellar Grains" in: *Astrophys. J.* 144: (Apr. 1966), 318 DOI: 10.1086/148606 (see p. 60).

[356] R. Stompor, J. Errard, and D. Poletti "Forecasting performance of CMB experiments in the presence of complex foreground contaminations" in: *Phys. Rev. D* 94:8 (Sept. 2016), 083526 DOI: 10.1103/PhysRevD.94.083526 arXiv: 1609.03807 (see pp. 92, 171, 179, 188, 190, 193).

[357] R. Stompor, S. Leach, F. Stivoli, and C. Baccigalupi "Maximum likelihood algorithm for parametric component separation in cosmic microwave background experiments" in: *Mon. Not. R. Astron. Soc.* 392:1 (Jan. 2009), 216–232 DOI: 10.1111/j.1365-2966.2008.14023.x arXiv: 0804.2645 (see pp. 91, 179).

[358] R. A. Sunyaev and Y. B. Zeldovich "Small-Scale Fluctuations of Relic Radiation" in: *Astrophys. Sp. Sci. Vol. 7, Issue 1, pp.3-19* 7: (1970), 3–19 DOI: 10.1007/BF00653471 (see p. 20).

[359] R. Sunyaev and Y. Zel'dovich "The Observations of Relic Radiation as a Test of the Nature of X-Ray Radiation from the Clusters of Galaxies" in: *Comments Astrophys. Sp. Phys.* 4: (Nov. 1972), 173 DOI: 1972CoASP...4..173S (see p. 39).

[360] A. Suzuki et al. "The Polarbear-2 and the Simons Array Experiments" in: *J. Low Temp. Phys.* 184:3-4 (Aug. 2016), 805–810 DOI: 10.1007/s10909-015-1425-4 arXiv: 1512.07299 (see pp. 125, 132).

[361] A. Suzuki et al. "The LiteBIRD Satellite Mission: Sub-Kelvin Instrument" in: *J. Low Temp. Phys.* 193:5-6 (Dec. 2018), 1048–1056 DOI: 10.1007/s10909-018-1947-7 arXiv: 1801.06987 (see pp. 136, 165).

[362] R. Takahashi, M. Sato, T. Nishimichi, A. Taruya, and M. Oguri "Revising the Halofit Model for the Nonlinear Matter Power Spectrum" in: *Astrophys. J.* 761:2 (Aug. 2012), 152 DOI: 10.1088/0004-637X/761/2/152 (see pp. 42, 145, 161).

[363] S. Takakura et al. "Measurements of tropospheric ice clouds with a ground-based CMB polarization experiment, POLARBEAR" in: *Astrophys. J.* 870:2 (Sept. 2018), 102 DOI: 10.3847/1538-4357/aaf381 arXiv: 1809.06556 (see pp. v, 101).

[364] S. Takakura et al. "Performance of a continuously rotating half-wave plate on the POLARBEAR telescope" in: *J. Cosmol. Astropart. Phys.* 2017:05 (Feb. 2017), 008–008 DOI: 10.1088/1475-7516/2017/05/008 arXiv: 1702.07111 (see pp. 109, 111, 113, 178).

[365] M. Tanabashi et al. "Review of Particle Physics" in: *Phys. Rev. D* 98:3 (Aug. 2018), 030001 DOI: 10.1103/PhysRevD.98.030001 (see pp. 4, 8, 11–16, 18, 52).

[366] M. Tegmark, A. N. Taylor, and A. F. Heavens "Karhunen-Loeve Eigenvalue Problems in Cosmology: How Should We Tackle Large Data Sets?" in: *Astrophys. J.* 480:1 (May 1997), 22–35 DOI: 10.1086/303939 arXiv: astro-ph/9603021 (see p. 193).

[367] M. Tegmark and M. Zaldarriaga "Separating the early universe from the late universe: Cosmological parameter estimation beyond the black box" in: *Phys. Rev. D* 66:10 (Nov. 2002), 103508 DOI: 10.1103/PhysRevD.66.103508 arXiv: astro-ph/0207047 (see p. 48).

[368] "Telescope / Planck / Space Science / Our Activities / ESA" URL: http://www.esa.int/Our%7B%5C_%7DActivities/Space%7B%5C_%7DScience/Planck/Telescope (visited on 07/03/2019) (see p. 103).

[369] W.-H. Teng, C.-L. Kuo, and J.-H. P. Wu "Cosmic Microwave Background Delensing Revisited: Residual Biases and a Simple Fix" Feb. 2011 arXiv: 1102.5729 (see pp. 99, 193).

[370] The ALEPH Collaboration, the DELPHI Collaboration, the L3 Collaboration, the OPAL Collaboration, the SLD Collaboration, the LEP Electroweak Working Group, t. S. electroweak heavy flavour Groups, and heavy flavour Groups "Precision Electroweak Measurements on the Z Resonance" in: *Phys. Rep.* 427:5-6 (Sept. 2005), 257–454 DOI: 10.1016/j.physrep.2005.12.006 arXiv: hep-ex/0509008 (see p. 12).

[371] The BICEP2 and Keck Array Collaborations et al. "A Joint Analysis of BICEP2/Keck Array and Planck Data" in: *Phys. Rev. Lett.* 114:10 (Feb. 2015), 101301 DOI: 10.1103/PhysRevLett.114.101301 arXiv: 1502.00612 (see pp. 89, 105).

[372] The BICEP2 and Keck Array Collaborations et al. "BICEP2 / Keck Array V: Measurements of B-mode Polarization at Degree Angular Scales and 150 GHz by the Keck Array" in: *Astrophys. J.* 811:2 (Feb. 2015), 126 DOI: 10.1088/0004-637X/811/2/126 arXiv: 1502.00643 (see p. 105).

[373] The BICEP2 and Keck Array Collaborations et al. "BICEP2 / Keck Array VI: Improved Constraints On Cosmology and Foregrounds When Adding 95 GHz Data From Keck Array" in: *Phys. Rev. Lett.* 116:3 (Oct. 2015), 031302 DOI: 10.1103/PhysRevLett.116.031302 arXiv: 1510.09217 (see p. 105).

[374] The BICEP2 and Keck Array Collaborations et al. "BICEP2 / Keck Array VIII: Measurement of gravitational lensing from large-scale B-mode polarization" in: *Astrophys. J.* 833:2 (June 2016), 228 DOI: 10.3847/1538-4357/833/2/228 arXiv: 1606.01968 (see p. 104).

[375] The BICEP2 and Keck Array Collaborations et al. "BICEP2 / Keck Array x: Constraints on Primordial Gravitational Waves using Planck, WMAP, and New BICEP2/Keck Observations through the 2015 Season" in: *Phys. Rev. Lett.* 121:22 (Oct. 2018), 221301 DOI: 10.1103/PhysRevLett.121.221301 arXiv: 1810.05216 (see pp. 90, 103–105).

[376] The BICEP2 and Keck Array Collaborations et al. "Measurements of Degree-Scale B-mode Polarization with the BICEP/Keck Experiments at South Pole" in: *53rd Rencontres Moriond* July 2018 arXiv: 1807.02199 (see pp. 103, 104).

[377] The POLARBEAR Collaboration "Measurement of the lensing power spectrum by POLARBEAR using three seasons of data taken with a continuously rotating half-wave plate" in: *Prep.* (2019) (see p. 101).

[378] The POLARBEAR Collaboration et al. "A Measurement of the Cosmic Microwave Background B-Mode Polarization Power Spectrum at Sub-Degree Scales from 2 years of POLARBEAR Data" in: *Astrophys. J.* 848:2 (May 2017), 121 DOI: 10.3847/1538-4357/aa8e9f arXiv: 1705.02907 (see pp. v, 104, 107, 110–112, 117, 130).

[379] The POLARBEAR Collaboration et al. "A Measurement of the Cosmic Microwave Background B-Mode Polarization Power Spectrum at Sub-Degree Scales with POLARBEAR" in: *Astrophys. J.* 794:2 (Mar. 2014), 171 DOI: 10.1088/0004-637X/794/2/171 arXiv: 1403.2369 (see pp. 101, 105, 107, 114, 117, 130).

[380] The POLARBEAR Collaboration et al. "A Measurement of the Degree Scale CMB B-mode Angular Power Spectrum with POLARBEAR" in: arXiv:1910.02608 (Oct. 2019), arXiv:1910.02608 arXiv: 1910.02608 (see pp. v, 101, 110, 111, 114, 123, 125).

[381] The POLARBEAR Collaboration et al. "Internal delensing of cosmic microwave background polarization B-modes with the POLARBEAR experiment" 2019 arXiv: 1909.13832 (see pp. v, 108).

[382] The POLARBEAR Collaboration et al. "Measurement of the Cosmic Microwave Background Polarization Lensing Power Spectrum with the POLARBEAR experiment" in: *Phys. Rev. Lett.* 113:2 (Dec. 2013), 021301 DOI: 10.1103/PhysRevLett.113.021301 arXiv: 1312.6646 (see pp. 104, 107).

[383] The POLARBEAR Collaboration et al. "Measurement of the Cosmic Microwave Background Polarization Lensing Power Spectrum with the POLARBEAR experiment" in: *Phys. Rev. Lett.* 113:2 (Dec. 2013), 021301 DOI: 10.1103/PhysRevLett.113.021301 arXiv: 1312.6646 (see p. 107).

[384] The POLARBEAR Collaboration et al. "POLARBEAR Constraints on Cosmic Birefringence and Primordial Magnetic Fields" in: *Phys. Rev. D* 92:12 (Sept. 2015), 123509 DOI: 10.1103/PhysRevD.92.123509 arXiv: 1509.02461 (see p. 107).

[385] The Simons Observatory Collaboration et al. "The Simons Observatory: Astro2020 Decadal Project Whitepaper" July 2019 arXiv: 1907.08284 (see pp. v, 101, 133–135).

[386] The Simons Observatory Collaboration et al. "The Simons Observatory: Science goals and forecasts" in: *J. Cosmol. Astropart. Phys.* 2019:02 (Aug. 2018), 056–056 DOI: 10.1088/1475-7516/2019/02/056 arXiv: 1808.07445 (see pp. v, 101, 133, 135, 153, 169, 198).

[387] B. Thorne, J. Dunkley, D. Alonso, and S. Naess "The Python Sky Model: software for simulating the Galactic microwave sky" in: *Mon. Not. R. Astron. Soc.* 469:3 (Aug. 2016), 2821–2833 DOI: 10.1093/mnras/stx949 arXiv: 1608.02841 (see pp. 174, 177).

[388] H. Tran, A. Lee, S. Hanany, M. Milligan, and T. Renbarger "Comparison of the crossed and the Gregorian Mizuguchi-Dragone for wide-field millimeter-wave astronomy" in: *Appl. Opt.* 47:2 (Jan. 2008), 103 DOI: 10.1364/AO.47.000103 (see p. 105).

[389] M. Troxel and M. Ishak "Cross-correlation between cosmic microwave background lensing and galaxy intrinsic alignment as a contaminant to gravitational lensing cross-correlated probes of the Universe" in: *Phys. Rev. D* 89:6 (Mar. 2014), 063528 DOI: 10.1103/PhysRevD.89.063528 arXiv: 1401.7051 (see pp. 155, 166).

[390] M. S. Turner and M. White "Dependence of inflationary reconstruction upon cosmological parameters" in: *Phys. Rev. D* 53:12 (June 1996), 6822–6828 DOI: 10.1103/PhysRevD.53.6822 (see p. 35).

[391] B. L. Ulich "Millimeter wave radio telescopes: Gain and pointing characteristics" in: *Int. J. Infrared Millimeter Waves* 2:2 (Mar. 1981), 293–310 DOI: 10.1007/BF01007036 (see p. 130).

[392] E. D. Valentino et al. "Exploring cosmic origins with CORE: Cosmological parameters" in: *J. Cosmol. Astropart. Phys.* 2018:04 (Apr. 2018), 017–017 DOI: 10.1088/1475-7516/2018/04/017 arXiv: 1612.00021 (see pp. 136, 161, 165).

[393] F. Vansyngel, F. Boulanger, T. Ghosh, B. D. Wandelt, J. Aumont, A. Bracco, F. Levrier, P. G. Martin, and L. Montier "Statistical simulations of the dust foreground to cosmic microwave background polarization" in: *Astron. Astrophys.* 603: (July 2017), A62 DOI: 10.1051/0004-6361/201629992 arXiv: 1611.02577 (see pp. 172–174, 183–186).

[394] D. A. Varshalovich, A. N. Moskalev, and V. K. Khersonskii "Quantum Theory of Angular Momentum" 1st ed. Singapore: World Scientific, Oct. 1988 DOI: 10.1142/0270 (see pp. 29, 200).

[395] J. Wang, T. R. Jaffe, T. A. Ensslin, and P. Ullio "hammurabi X: Simulating Galactic Synchrotron Emission with Random Magnetic Fields" June 2019 arXiv: 1907.00207 (see p. 172).

[396] M. Wardle and A. Konigl "A model for the magnetic field in the molecular disk at the Galactic center" in: *Astrophys. J.* 362: (Oct. 1990), 120 DOI: 10.1086/169249 (see p. 58).

[397] D. J. Watts et al. "A Projected Estimate of the Reionization Optical Depth Using the CLASS Experiment's Sample Variance Limited E-mode Measurement" in: *Astrophys. J.* 863:2 (Aug. 2018), 121 DOI: 10.3847/1538-4357/aad283 arXiv: 1801.01481 (see p. 165).

[398] S. Weinberg and R. H. Dicke "Gravitation and Cosmology: Principles and Applications of the General Theory of Relativity" in: *Am. J. Phys.* 41:4 (Apr. 1973), 598–599 DOI: 10.1119/1.1987308 (see p. 5).

[399] B. Westbrook et al. "The POLARBEAR-2 and Simons Array Focal Plane Fabrication Status" in: *J. Low Temp. Phys.* 193:5-6 (Dec. 2018), 758–770 DOI: 10.1007/s10909-018-2059-0 (see p. v).

[400] M. J. Wilson and M. White "Cosmology with dropout selection: Straw-man surveys and CMB lensing" Apr. 2019 arXiv: 1904.13378 (see p. 156).

[401] J. H. Wise "Cosmic reionisation" in: *Contemp. Phys.* (July 2019), 1–19 DOI: 10.1080/00107514.2019.1631548 arXiv: 1907.06653 (see p. 39).

[402] C. S. Wu, E. Ambler, R. W. Hayward, D. D. Hoppes, and R. P. Hudson "Experimental Test of Parity Conservation in Beta Decay" in: *Phys. Rev.* 105:4 (Feb. 1957), 1413–1415 DOI: 10.1103/PhysRev.105.1413 (see p. 12).

[403] W. L. K. Wu et al. "A Measurement of the Cosmic Microwave Background Lensing Potential and Power Spectrum from 500 deg^2 of SPTpol Temperature and Polarization Data" May 2019 arXiv: 1905.05777 (see p. 104).

[404] J.-Q. Xia, M. Negrello, A. Lapi, G. De Zotti, L. Danese, and M. Viel "Clustering of submillimeter galaxies in a self-regulated baryon collapse model" in: *Mon. Not. R. Astron. Soc.* 422:2 (Nov. 2011), 1324–1331 DOI: 10.1111/j.1365-2966.2012.20705.x arXiv: 1111.4212 (see p. 108).

[405] B. Yu, J. C. Hill, and B. D. Sherwin "Multitracer CMB delensing maps from Planck and WISE data" in: *Phys. Rev. D* 96:12 (Dec. 2017), 123511 DOI: 10.1103/PhysRevD.96.123511 arXiv: 1705.02332 (see pp. 169, 198).

[406] M. Zaldarriaga and U. Seljak "All-sky analysis of polarization in the microwave background" in: *Phys. Rev. D* 55:4 (Feb. 1997), 1830–1840 DOI: 10.1103/PhysRevD.55.1830 arXiv: astro-ph/9609170 (see pp. 27, 28, 37).

[407] Y. B. Zeldovich and R. A. Sunyaev "The interaction of matter and radiation in a hot-model universe" in: *Astrophys. Space Sci.* 4:3 (July 1969), 301–316 DOI: 10.1007/BF00661821 (see p. 20).

[408] F. Zwicky "Die Rotverschiebung von extragalaktischen Nebeln" in: *Helv. Phys. Acta* 6: (1933), 110–127 (see pp. 1, 17).